ISSN 0288-4534
CODEN: KONAE7

粉

KONA

POWDER AND PARTICLE

No. 15 (1997)

Published by Hosokawa Powder Technology Foundation

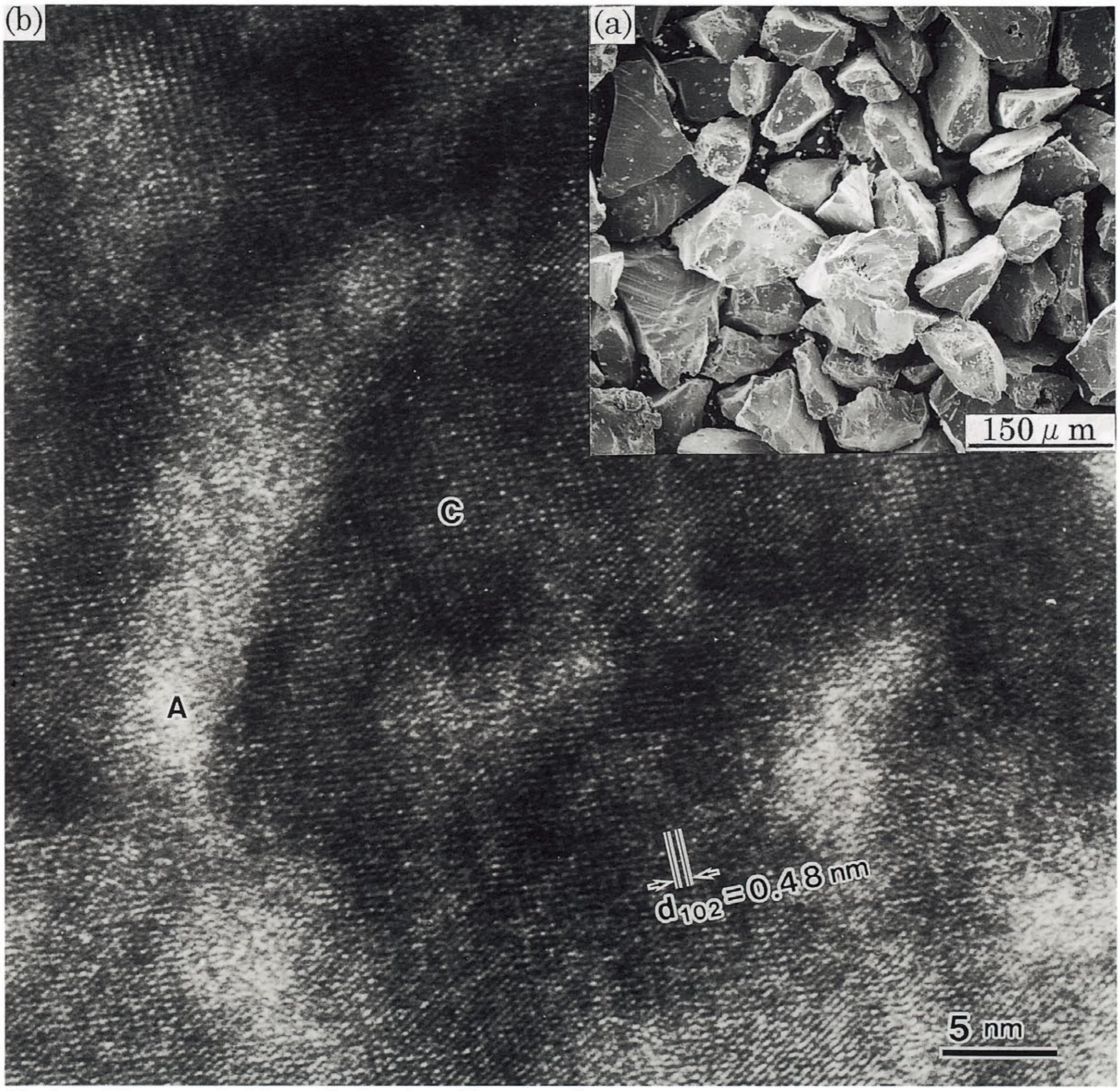

Electron Micrographs Magnetic Powders (See page 4)

KONA

POWDER AND PARTICLE

KONA is a refereed scientific journal that publishes articles on powder and particle sciences and technology. KONA has been published annually since 1983 by the Hosokawa Powder Technology Foundation in Japan. KONA is distributed to researchers, members of the scientific community, universities and research libraries throughout the world.

About the Cover of Journal "KONA"

The Chinese character "粉" is pronounced "KONA" in Japanese, and means "Powder". The hand written "粉" is after the late Mr. Eiichi Hosokawa, founder of the Hosokawa Micron Corporation.

Hosokawa Micron Corporation and its R&D Center

Editorial Board

K. Miyanami	Editor in Chief (Univ. of Osaka Prefecture, JAPAN)
Asia / Oceania Editorial Board	
Y. Kousaka	Vice Chairman (Univ. of Osaka Prefecture, JAPAN)
N. Yoshioka	(Professor Emeritus of Kyoto Univ., JAPAN)
G. Jimbo	(Chubu Powtech Plaza Lab., JAPAN)
M. Arakawa	(Former Professor of Kyoto Institute of Tech., JAPAN)
T. Oshima	(Professor Emeritus of Himeji Institute of Tech., JAPAN)
Y. Morikawa	(Professor Emeritus of Osaka Univ., JAPAN)
H. Masuda	(Kyoto Univ., JAPAN)
Y. Tsuji	(Osaka Univ., JAPAN)
H. Emi	(Kanazawa Univ., JAPAN)
Y. Kuwahara	(National Industrial Research Institute of Nagoya, JAPAN)
K. Higashitani	(Kyoto Univ., JAPAN)
P. Arnold	(Univ. of Wollongong, AUSTRALIA)
S.H. Kang	(Yeugnam Univ., KOREA)
W. Tanthapanichakoon	(Chulalongkorn Univ., THAILAND)
T. Yokoyama	(Hosokawa Micron Corp., JAPAN)
Secretariat	
F. Nakagawa	(Hosokawa Micron Corp., JAPAN)
Europe / Africa Editorial Board	
J. Schwedes	Chairman (Univ. Braunschweig, GERMANY)
B. Scarlett	Vice Chairman (Delft Univ. of Technology, THE NETHERLANDS)
K. Schönert	(Technische Univ. Clausthal, GERMANY)
H. Schubert	(Bergakademie Freiberg, GERMANY)
E. Forssberg	(Univ. Lulea, SWEDEN)
S.R. de Silva	(Postec-Research A/S, NORWAY)
J.F. Davidson	(Univ. of Cambridge, UNITED KINGDOM)
G.F. Ferrara	(Univ. di Trieste, ITALY)
J.F. Large	(Univ. de Tech. de Compiégne, FRANCE)
Secretariat	
W. Peukert	(Hosokawa MikroPul GmbH, GERMANY)
Americas Editorial Board	
D.W. Fuerstenau	Chairman (Univ. of California, U.S.A.)
T. P. Meloy	Vice Chairman (West Virginia Univ., U.S.A.)
R.K. Rajamani	(Univ. of Utah, U.S.A.)
B.H. Kaye	(Laurentian University, CANADA)
P.S. Santos	(Univ. of São Paulo, BRAZIL)
B.M. Moudgil	(Univ. of Florida., U.S.A.)
R. Hogg	(Pennsylvania State Univ., U.S.A.)
D.J.W. Grant	(Univ. of Minnesota., U.S.A.)
Secretariat	
I. Pikus	(Hosokawa Bepex Corp., U.S.A.)
D.A. Scott	(Hosokawa Micron Inter., U.S.A.)

■Publication Office

Hosokawa Powder Technology Foundation (Japan) in Hosokawa Micron Corporation
No. 9, 1-chome, Shoudai Tajika, Hirakata-shi, Osaka 573 Japan

■Notes

○ Hosokawa Powder Technology Foundation has entrusted the editorial duty to the editorial board organized by the Council of Powder Technology, Japan.

(Complimentary Copy)

Printed in Japan

The Letter from Editor

Seven papers from Americas, eight from Europe/Africa, eight from Asia/Oceania Editorial Committee, and totally 23 papers have been published in this issue. The number of pages amounts to over 200.

It is our pleasure, of course, to have this kind of balanced issue for the purpose of internationalizing KONA journal. It is slightly unfortunate, however, to have to cut down the number of excellent translated papers written originally in Japanese because of a budget limitation.

To get free of this dilemma, the editorial policies of this journal should be revised in part, which will include a restriction on the number of pages for each contribution, by mutual agreement among three editorial boards.

Hopefully, the third World Congress on Particle Technology, which is going to be held on July, 7-9, 1998 at Brighton, UK, will be the chance for discussing this matter.

Kei Miyanami

KONA

GENERAL INFORMATION

HISTORY OF THE JOURNAL

KONA journal has been published by the Council of Powder Technology, Japan. (CPT), from No.1 to No.12 issues, under the sponsorships of Hosokawa Micron Corporation (No.1 to No.9) and Hosokawa Powder Technology Foundation (No.10 to No.12).

The CPT has been established in 1969 as a non-profit organization to enhance the activities of research and development on powder science and technology in Japan under the sponsorship of Hosokawa Micron Corporation. In 1983, the CPT has decided to issue an international journal named "KONA", which publishes the excellent articles appeared in Japanese journals concerning powder science and technology, after translated into English, throughout the world. After the seventh volume issued in 1989, the CPT has changed its policy to internationalize the "KONA" from the 8th issue (1990) and on by incorporating the monographs originally written in English from the authors throughout the world. Immediately, the present editorial board including Asian, Americas' and European Blocks has been organized.

From the 13th issue and on, the Hosokawa Powder Technology Foundation has taken over the role of KONA publisher from the CPT and the Foundation has entrusted the editorial duty to the present KONA editorial board organized by the CPT without requesting any shift in our present editorial policies. This switching of publisher has been simply and only to make the aim and scope of the Foundation definite. Essentially no change has been observed in continuously editing and publishing this journal except in the designation on a part of the journal cover.

AIMS AND SCOPE OF THE JOURNAL

KONA Journal is to publish the papers in a broad field of powder science and technology, ranging from fundamental principles to practical applications. The papers discussing technological experiences and critical reviews of existing knowledge in specialized areas will be welcome.

These papers will be published only when they are judged, by the Editor, to be suitable for the progress of powder science and technology, and are approved by any of the three Editorial Committees. The paper submitted to the Editorial Secretariat should not have been previously published except the translated papers which would be selected by the Editorial Committees.

CATEGORY OF PAPERS

- Invited papers
  Original research and review papers invited by the KONA Editorial Committees.
- Contributed papers
  Original research and review papers submitted to the KONA Editorial Committees, and refereed by the Editors.
- Translated papers
  Papers translated into English, which were previously published in other languages, selected by the KONA Editorial Committees with the permission of the authors and / or the copyright holder.

SUBMISSON OF PAPERS

Papers should be sent to each KONA Editorial Secretariat.

- Asia / Oceania Editorial Secretariat
  F. Nakagawa
  Hosokawa Micron Corporation Micromeritics Laboratory
  1-9, Shoudai Tajika, Hirakata 573 JAPAN
- Europe / Africa Editorial Secretariat
  Dr.W. Peukert
  Hosokawa MikroPul GmbH
  Welserstr. 9-11, 51149 Köln
  Postfach 900749, 51117 Köln
  GERMANY
- Americas Editorial Secretariat
  Dr.I. Pikus or D.A. Scort
  Hosokawa Micron International Inc.
  10 Chatham Road, Summit, NJ 07901 USA

PUBLICATION SCHEDULE

KONA is published once a year.

SUBSCRIPTION

KONA is distributed free of charge to senior researchers at universities and laboratories as well as to institutions and libraries in the field throughout the world. The publisher is always glad to consider the addition of names of those who wish to obtain this journal regularly to the mailing list. Distribution of KONA is made by each Secretariat.

INSTRUCTIONS TO AUTHORS

(1) Manuscript format

- Two copies should be submitted to the Editorial Secretariat, in double-spaces typing on pages of uniform size.
- Authorship is to give author's names, and the mailing address where the work has been carried out on the title page.
- Abstract of 100-180 words should be given at the beginning of the paper.
- Nomenclature should appear at the end of each paper. Symbols and units are listed in alphabetical order with their definitions and dimensions in SI units.
- Literature references should be numbered and listed together at the end of paper, not in footnotes. Alphabetical order is accepted. Please give information as in the following examples:
  1) Carslaw, H.C. and J.C. Jaeger:"Conduction of Heat in Solids", 2nd ed., Clarendon Press, Oxford, England (1960).
  2) Howell, P.A.: US Patent, 3,334,603 (1963).
  3) Rushton, J.H., S.Nagata and D.L. Engle: AIChEJ., 10. 294 (1964).
  4) Seborg, D.E.: Ph.D. Dissertation, Princeton Univ., N.J., U.S.A. (1969).
- Original figures with each single copy should be submitted, on separate sheets. Authors' names and figure numbers are marked in the corner.
- Figure numbers and captions are listed on a separate sheet.
- Place of figure insertion is to be indicated in the margin of the manuscript.
- Tables should be typed on separated sheets.
- Submit an IBM-readable floppy disk ($3_{1/2}$) with your unformatted text file in ASCII code. If you use either WORD or WORD PERFECT—as word processing system, please add the formatted text file.

(2) Reprints

- The authors shall receive 50 free reprints. Additional reprints will be furnished when ordered with return of galley proofs.

(3) Publication policy

- All papers submitted for publication become immediately the property of the CPT and remain so unless withdrawn by the author prior to acceptance for publication or unless released by the Editor. Papers are not to be reproduced or published in any form without the written permission of the CPT.

KONA Powder and Particle No. 15 (1997)

Contents

<Review>

<Original Research Paper>

<Translated Research Paper>

Explanation of the Cover Photograph

High Resolution Electron Micrograph of $Sm_2(Fe, Mn)_{17}N_x$ Powder Nitrided in a Mixed Gas of NH_3+H_2

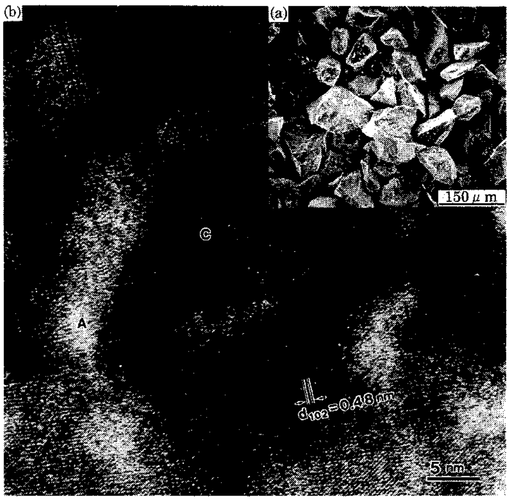

The particle size of $Sm_2Fe_{17}N_x$ powder should be finer than a few μm in order to produce high coercivity. However, a fine powder has not been considered to be preferable for manufacturing of particle magnets because of some disadvantages such as an easy oxidation and a necessity of high compaction pressure for preparing high-performance magnets. Recently, the present authors reported that the $Sm_2(Fe_{0.95}Mn_{0.05})_{17}N_x$ coarse powder such as presented in SEM image of Photo. (a) showed a high coercivity without fine grinding. And it was confirmed that the high coercivity was due to the nano-structure composed of the amorphous phase presented as A and the crystalline phase presented as C in HREM image of Photo. (b).

By courtesy of Associate Prof. K. Majima, Dr. M. Ito, Dr. S. Katsuyama and Prof. H. Nagai, Department of Materials Science and Processing, Graduate School of Engineering, Osaka University.

Review

Advances in Selective Flocculation Technology for Solid-Solid Separations†

Brij M. Moudgil, S. Mathur, T.S. Prakash
Department of Materials Science & Engineering
and Engineering Research Center for
Particle Science & Technology, University
*of Florida**

Abstract

Selective flocculation is a potential process for solid-solid separations in the fine particle size range. The critical barriers to further commercial applications of this technique are the loss in predicted single mineral selectivity in mixed mineral systems, extrapolation of mixed mineral selectivity to natural systems and scale up from bench to plant scale. A comprehensive review of the recent advances in selective flocculation technology which facilitate to overcome these barriers is presented. These include identification/design of selective reagents based on the surface chemistry of particles, use of site blocking agents to reduce heteroflocculation, and tailoring the polymer characteristics to achieve the desired separation efficiency.

1. Introduction

Removal of coarse particles suspended in a liquid can be achieved by conventional separation techniques such as, settling, forced settling, and filtration. However, in most cases where such separation is desired for fine particles, conventional separation techniques are not efficient. Flocculation of the suspension followed by separation by a conventional method has been proposed as an alternative strategy. Flocculation of fine particles using polymeric materials (flocculants) and separation of such aggregates from particles of other component(s) in the dispersed phase is known as selective flocculation. The competition between different surfaces for the flocculant has to be controlled to achieve adsorption on the targeted component(s). The aggregates of the polymer coated particles or the "flocs" thus formed are separated from the suspension either by sedimentation/elutriation or floc-flotation. The flocs can be further cleaned, provided they are robust enough, to improve the concentrate grade.

The surface-colloid chemistry of a selective flocculation separation system is similar to flotation separation in many respects except that the reagents used for selective dispersion-flocculation are mostly long chain polymers instead of short chain surfactants in flotation. The main purpose of reagents in selective flocculation is to achieve selective aggregation/dispersion as opposed to imparting hydrophobicity to particles in flotation. The principles of selective flocculation as well as the underlying surface chemistry has been reviewed earlier by Yarar and Kitchener [1], Friend and Kitchener [2], Attia and Kitchener [3], Attia and Fuerstenau [4], Sresty et al. [5], Somasundaran [6], and more recently by Attia [7-9], and Moudgil et al. [10].

2. Commercial Applications

The selective flocculation technology is used on an industrial scale for beneficiation of taconites at Tilden Mine of the Cleveland Cliffs Co. in USA [11] where the selective adsorption of starch on iron particles is exploited to achieve separation from silica. Recently, Engelhard Corporation has been reported to evaluate a selective flocculation process for removal of titania from clays [12]. The selective flocculation process for separation of titania from clays has also been developed at Thiele Kaolin, Georgia where a major difficulty from a commercial standpoint has been the low solids loadings (about 20 wt.%) during the conditioning stage with the flocculant [13]. Although primary application of selective flocculation has been in the mineral processing industry, many potential uses exist also

---

*Gainesville, Florida 32611, USA
†Received September, 1996

in biological and other colloidal systems. These include purification of ceramic powders, separation of hazardous solids from chemical wastes, and removal of deleterious components from paper pulp [7].

3. Selective Flocculation Process

The selective flocculation process involves three steps: (1) dispersion of the fine particles (typically dispersants are added at this stage), (2) selective adsorption of the polymer on the flocculating component and formation of the flocs, (3) floc growth which is generally achieved by conditioning at low shear, and (4) floc separation either through sedimentation/elutriation/sieving or flotation followed by cleaning of flocs by repeated redispersion and flocculation, if necessary.

It is obvious that correct choice of dispersants and flocculants is a prerequisite for developing a successful selective flocculation separation scheme. In the following sections the advances made in the understanding of the dispersion and selective flocculation phenomena in multi component and natural ore systems are discussed.

4. Dispersion

A stable dispersion of particles in aqueous systems can be obtained by either electrostatic and/or steric stabilization. Commonly used dispersants such as sodium silicate and sodium hexametaphosphate (SHMP) adsorb strongly on the particle surface and as a consequence of the high negative surface charge developed on the constituent components the system is electrostatically stabilized. Certain low molecular weight polymeric dispersants such as polyethylene oxide (PEO) and polyvinyl pyrrolidone (PVP) adsorb at the interface and prevent coagulation due to "entropic" and "mixing" interactions [14]. These dispersants are called steric stabilizers. In those cases where the polymeric additives are also charged, (e.g. polyacrylates), the stabilization is termed electrosteric since both the electrostatic and steric repulsion mechanisms are operating simultaneously. The choice of a dispersant is an important parameter in developing successful separation schemes.

5. Polymeric Dispersants

Much of the earlier work on selective flocculation was carried out in the presence of inorganic dispersants, like sodium silicate and SHMP [15, 16]. In separation systems involving clays, SHMP was found to be a better dispersant than sodium silicate due to its higher adsorption leading to a higher surface charge. Later, Attia and coworkers [15, 17] proposed the use of polymeric dispersants such as PEO in enhancing separation selectivity in systems where clays were one of the constituents. For example, Attia and Deason [17] used polyethylene glycol (PEG) of molecular weights of a few thousand during the separation of malachite from montmorillonite (15% by weight in the synthetic mixture) employing a modified polyacrylamide flocculant PAMG (containing chelating type glyoxal- bis-2-hydroxanil groups).

In another study, Ravishankar and Pradip [18, 19], found polyvinyl pyrrolidone (PVP) to be a good selective dispersant in the separation of hematite from kaolinite using polyacrylic acid (PAA) as the flocculant. From a practical standpoint, PVP was found to be a stable dispersant with respect to variations both in the pH and dosage.

6. Design of Selective Dispersants

A major reason for the loss in selectivity in mixed minerals and natural ore systems has been attributed to slime coating and/or unwanted activation due to soluble metal ions present in the pulp [10, 20]. These phenomena result in formation of chemically similar surfaces leading to loss in selectivity. The role of a selective dispersant is to prevent slime coating and block the possible adsorption sites on those surfaces which are not to be flocculated.

In flotation systems, the role of activators and depressants is to aid the selective adsorption of flotation collector on the component to be floated. The selective dispersant may similarly act as a poisoning agent blocking flocculant adsorption sites on the surface of the non-flocculating minerals. It has been proposed to design dispersants having functional groups selective to a particular constituent of the particulate mixture [3, 4, 21]. Low molecular weight polymers which are not capable of flocculation but adsorb strongly and selectively have thus been demonstrated to introduce/enhance selectivity in certain particulate systems [15, 22-27]. It should, however, be recognized that this approach may not always be feasible since selective dispersants may have to be designed specifically for a given component.

7. Selective Flocculants

In selective flocculation, the ideal polymer for separation should (a) consist of functional groups specific to the component(s) to be flocculated, (b) possess a backbone capable of producing strong, sturdy flocs with high shear resistance. Adsorption of the polymer on a particular surface is the result of the interactions between the functional groups of the polymer and the binding sites on the surface such as hydroxyl groups, oppositely charged ions to polymer functionality, hydrophobic groups or chemical bonding sites.

8. Design of Selective Reagents Based on Surface Chemistry

The surface property with the greatest difference between the flocculating and non-aggregating particles should be the basis of selection for a flocculant. Flocculants are high molecular weight polymers and are known to adsorb through hydrogen bonding, hydrophobic interactions, electrostatic interactions, chemical bonding, and van der Waals forces.

Flocculant Selection Based on Surface Charge

Some of the earlier successes reported in the literature were ascribed to the selective adsorption of flocculants due to differences in surface charge, either natural or induced, by a judicious control of pH and solution conditions [2, 28]. In apatite-clay system because of their surface charge characteristics (clay being negatively charged in the pH range 4-10 and apatite having a pzc at pH 6.5), the flocculation is a strong function of pH and charge on the polymer. Using a hydrolyzed polyacrylamide, e. g., an anionic flocculant like Magnafloc A155 or Superfloc A150, one can thus achieve separation of apatite from clay at an appropriate dosage and pH condition [29].

However, the possibilities of achieving adequate selectivity based on electrostatic interactions alone are limited since the particulates involved may have similar isoelectric points (e.g. apatite-dolomite system) or there may be specific interactions between the polymer and mineral surface.

Selectivity based on specificity of H-bonding

Recently it was shown that specificity of hydrogen bonding can be utilized to develop a selective flocculation scheme. The DRIFT spectra of apatite and dolomite from Florida are presented in **Figure 1** [30]. It can be observed that isolated hydroxyl groups (3619 cm^{-1}) are exclusive to the dolomite A surface, whereas hydrogen-bonded hydroxyl groups are present on both apatite and dolomite surface. Any polymer capable of hydrogen bonding such as polyacrylic acid (PAA), polyacrylamide (PAM) and polyethyleneoxide (PEO) therefore should be capable of flocculating the two materials. Among these, PEO being a weak flocculant [31], only the material with stronger interactions with the polymer molecules may be expected to flocculate. Rubio and Kitchener [32] and Cheng [33] showed that PEO is a good flocculant for a material with isolated hydroxyl groups. Experiments performed with PEO of five million molecular weight indicated that irrespective of the amount of polymer added, flocculation of apatite was not observed. On the other hand, instantaneous flocculation of dolomite occurred [30].

The specificity of hydrogen bonding of surface hydroxyls with PEO has been illustrated in the recent work by Mathur and Moudgil [34]. It was determined from a systematic study of the adsorption of PEO on a range of oxides and silicates that strong Bronsted acid sites on the surface interact with the ether oxygen, a Lewis base, of PEO to induce adsorption and consequent flocculation of the substrate particles. Thus, the presence of isolated hydroxyls does not guarantee adsorption of PEO on the oxide and silicate surfaces. It is the nature of the surface hydroxyls on the oxide surface that governs the interaction with the ether oxygen of PEO. In general, highly acidic oxides of the type MO_3, M_2O_5 and MO_2 adsorb and flocculate with PEO. Accordingly, SiO_2, MoO_2, MoO_3 and V_2O_5 were found to strongly adsorb PEO and exhibit

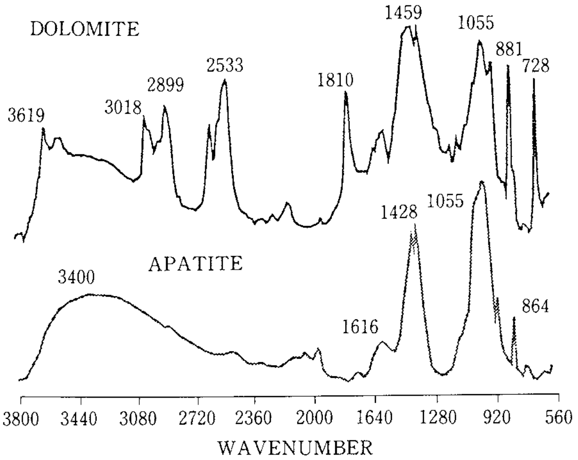

Fig. 1 DRIFT Spectra for Apatite and Dolomite from Florida (after Ref [30]).

flocculation. On the other hand, oxides with a point of zero charge (pzc) greater than that of silica such as TiO_2, Fe_2O_3, Al_2O_3 and MgO did not exhibit significant adsorption of PEO (see **Figure 2**). Amongst the silicates, layered and chain silicates (clays, pyroxenes and amphiboles) were found to strongly adsorb PEO and exhibit flocculation.

Flocculant selection based on specific interactions

A number of flocculants have been designed, synthesized and evaluated for a variety of separation systems based on the hypothesis of specific interaction as a basis of selectivity. The choice of the polymer functional group is based on the coordination-analytical chemistry and/or flotation literature. However, such an approach fails when the cations participating in the complexation reactions on the surfaces are same or chemically similar. Thus PAA, which is expected to have specific interaction with calcium ions, was found to flocculate both apatite and dolomite [35]. However, selectivity can be introduced in such systems by superposition of physical parameters such as particle size.

Tailoring Flocculant Molecular Weight To achieve Better Selectivity

Effect of Particle Size: Moudgil et al. [36-37] have recently demonstrated the significance of particle size in selective flocculation. A strong correlation between the particle size, the molecular weight, and the flocculation efficiency was observed. It was clearly demonstrated by these investigators that there exists a threshold value of the polymer molecular weight at which particles of certain size can be flocculated [36]. As illustrated in **Figure 3**, with increasing particle size, one needs higher molecular weight polymers to achieve high flocculation efficiency. This observation suggests that if the relative particle size distribution of two components in a mixture is different, one can choose an optimum molecular weight flocculant to achieve better selectivity. For instance, in a 50:50 synthetic mixture of apatite and silica, the remarkable effect of particle size on the selectivity of separation (grade) using polyacrylic acid (PAA) of 1 million MW is presented in **Figure 4** [37]. It is observed that selectivity of separation is poorer in the finer particle size range. In another case, PAA was evaluated as a selective flocculant for apatite-dolomite system [37]. PAA of 4 million MW was found to flocculate both dolomite and apatite. However, their flocculation behavior was significantly different with 450,000 MW PAA which was the lowest molecular weight fraction capable of flocculation. In single mineral tests, at a

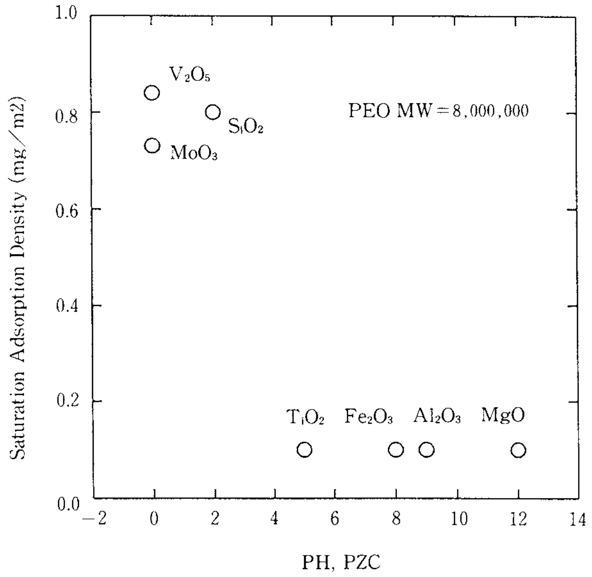

Fig. 2 Saturation adsorption density of PEO on different oxides as a function of their pzc (PEO MW=8 million; pH=9.5) (after Ref [34]).

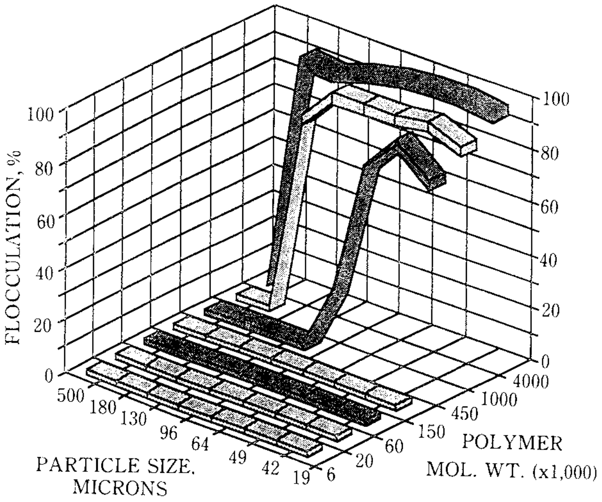

Fig. 3 Effect of Particle Size on Flocculation of Apatite (after Ref [36]).

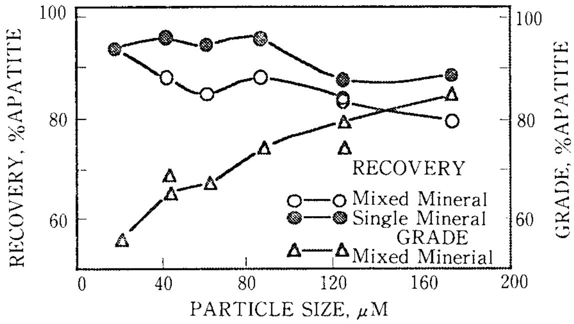

Fig. 4 Effect of Particle Size on the Separation of Apatite from Silica (after Ref [37]).

dosage of 2kg/t, 90% of dolomite and 35% of apatite flocculated. Selectivity was achieved in mixed mineral tests where apatite of 90% grade at 70% recovery level was obtained in the concentrate from a feed consisting of 80:20 mixture of apatite and dolomite.

Since in natural ore systems, one doesn't have control over the particle size distributions of various constituents, this work suggests the need to customize the flocculant for a particular separation system, and to take into account the effect of particle size distribution for developing a robust separation scheme.

Manipulation of Polymer Conformation to enhance selectivity: The conformation of polyelectrolytes commonly used in selective flocculation processes is strongly dependent on pH and ionic strength of the solution. The effect of polymer conformation on their adsorption, whether stretched or coiled, is also well documented [38]. The flocculation efficiency (or selectivity of separation) would thus be strongly influenced by the pH and ionic strength of the solution, as a consequence of the changes in polymer conformation. This effect would be in addition to the direct effect of pH and ionic strength on the dissociation, complexation, stability and surface charge characteristics.

Somasundaran and coworkers [39, 40] have studied the effect of polymer conformation on the flocculation of alumina with the help of pyrene labeled PAA. Changes in polymer conformation on alumina surface as a function of pH were monitored through fluorescence spectroscopy (see **Figure 5**). It was observed that adsorbing PAA at pH 10 in stretched conformation followed by lowering the pH to 4 did not cause the adsorbed chain to coil, as anticipated. On the other hand, raising the pH from 4 to 10 did lead to stretching of the adsorbed polymer chains and the attendant effect on its flocculation efficiency. This mechanism thus provides a method to manipulate the conformation of the adsorbed polymer in situ to optimize the flocculation efficiency. For example, if the polymer was adsorbed first at low pH and then the pH was raised, excellent flocculation of alumina was achieved as compared to the flocculation directly under the alkaline pH conditions.

Selection of flocculant for desired floc characteristics: The advantages and disadvantages of generating flocs of desired characteristics (size, shear strength, density etc.) with respect to a given floc separation scheme have not been given adequate attention in the past, even though it is well known that the nature of polymer (natural or synthetic, branched or linear, nonionic or ionic) has a remarkable effect on the floc properties.

Scheiner and coworkers [31] have compared two types of polymers, namely acrylamide based polymers (PAM) and PEO for the flocculation of a wide variety of particulate slurries including Florida phosphatic clays, potash-clay waste, uranium mill tailings, talc tailings, and coal waste slurries. PEO was observed to be particularly effective in the flocculation of waste slurries containing significant proportions of clays or clay-like materials. On the other hand, in the absence of such material, PAM based flocculants were found to be superior to PEO. Thus, for separation of a mineral-clay system PEO is expected to be a more effective flocculant. Further, the specificity of H-bonding as shown earlier with PEO could be an added advantage in enhancing the selectivity.

In general, to achieve the same level of flocculation efficiency, PEO requires a lower polymer dosage and yields a more stable dewatered product [31]. It is also observed that optimum results are obtained with polyacrylamides when dilute slurries are flocculated. However, with higher solids loading in the slurry the PEO dosage requirement for opti-

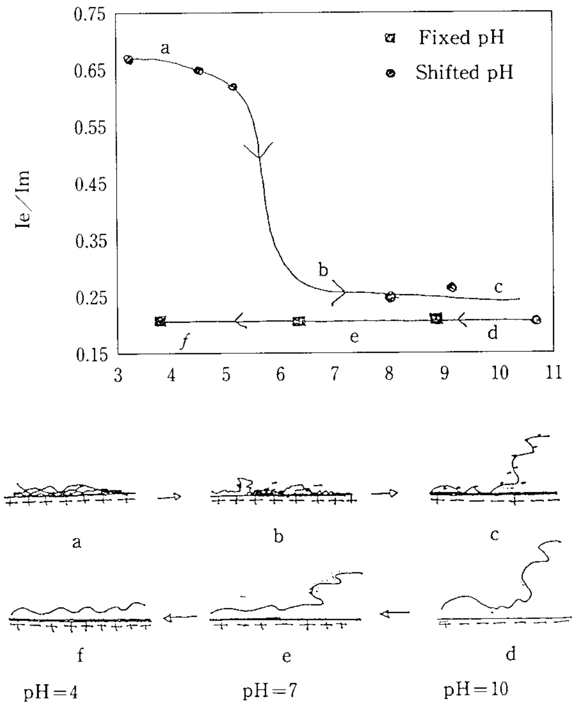

Fig. 5 Effect of PAA conformation at alumina-water interface on flocculation (after Ref [39]).

mum flocculation is lesser than with PAM. Even though initial flocs produced with PEO are strong and stable, rapid degradation takes place if the water is not removed quickly. For example, in thickeners where water is removed relatively slowly, PEO is not as effective as PAM. The choice of a flocculant thus depends on the constituent minerals, the nature of the flocs desired and their removal scheme. The nature of the flocs, such as the size, strength, density can be characterized according to the procedures developed by Vasudevan and Moudgil [41].

Ravishankar et al. [42] have made a detailed comparison between PAA and starch, the two most commonly used flocculants, on the selective flocculation efficiency of iron oxide-clay separation. The selectivity of separation with starch was observed to be better than with PAA (see **Figure 6**). The pH range of optimum separation, however, was much broader (pH 6.5-9) with PAA as compared to starch (around pH 10.5). The flocs formed with starch were smaller but more compact and resistant to shear than PAA flocs. The flocs obtained with starch, therefore, were more amenable to repeated cleanings to remove entrained and entrapped gangue. The differences observed between the two types of flocs were attributed to the mechanisms of interaction as well as the nature of the two polymers. Starch being a nonionic polymer interacts specifically with iron oxide surface. On the other hand, PAA being a highly charged polyelectrolyte complexes with Fe sites on the surface, and forms "loose" flocs due to stretched conformation.

These differences in the flocculation behavior become relevant in natural ore systems depending on the selectivity desired, the constraints on pH, the grade, the floc separation process (elutriation, thickening, or flotation) and the number of cleaning steps required.

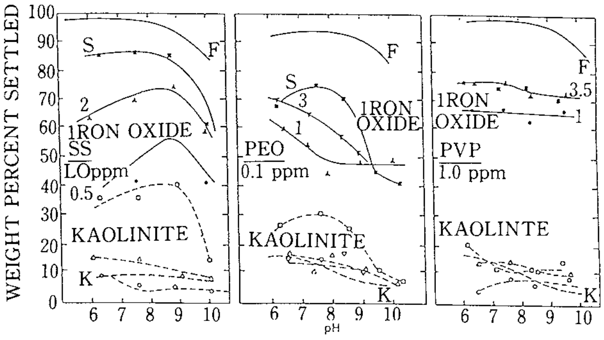

Fig. 6 Selectivity of separation in IronOxide-Kaolinite Synthetic Mixtures with two different flocculants: PAA (open symbols) and Starch (filled symbols). Note that pH scales are different for the two flocculants (after Ref [42]).

9. Technical Barriers in Process Scale-up

The major barriers to the commercial applications of the selective flocculation technology are extension of single component successes to mixed component systems, synthetic mixed component results to ground and natural systems, and scaling up of bench scale process to plant scale. In general, the selectivity observed in single component tests is invariably lost in the mixed component or natural ore systems because of one or more of the following reasons: heterocoagulation; charge patch neutralization; dissolved ion interference; slime coating; physical entrapment; entrainment and heteroflocculation and cross-contamination during the size reduction process [20]. It is important to distinguish heteroflocculation from the entrainment/entrapment effects discussed in the literature [8, 10]. Entrainment/entrapment occurs due to mechanical factors and a possible remedy is to clean the flocs (provided those are robust enough to withstand shear) repeatedly so as to wash off the entrained/entrapped gangue. Heteroflocculation, on the other hand, is a consequence of the loss of selective adsorption of the flocculant and cannot be overcome in this manner. Additionally it is important to recognize that both ion activation and slime coatings would result in heteroflocculation.

10. Loss in Selectivity

10.1 Cross Contamination during Grinding

The size reduction process involved in the generation of fine particles (slimes) has an important bearing on the type of surfaces present in mixed mineral suspensions. In general, the activity of solid surfaces is not only enhanced due to increase in surface area with size reduction, but also due to changes in the character of surface sites available. For example, the changes in surface energy per site at extremely fine sizes, (the phenomena of "mechanico-chemical activation") is well known in surface chemistry literature [6, 28, 43-44].

It is, therefore, expected that two mineral mixtures ground under different conditions (wet or dry; in presence or absence of dispersants) will exhibit differences in surface characteristics and hence in selective flocculation behavior. What is, however, most intriguing is the remarkable loss in selectivity reported by various investigators upon grinding.

Rubio and Marabini [45] for example, observed that selectivity in ground mixtures could be improved with the help of dispersants added during wet grinding of the material (see **Table 1**).

Table 1. Effects of grinding pretreatment on separation parameters; 4-stages of dispersion-flocculation on hydroxyapatite-calcite mixtures. pH 10.2; 4% solids, 16 g/t Superfloc 16, 625 g/t Cyquest and 1000 g/t sodium silicate (After Ref 45)

Type of Grinding	Grade (% P_2O_5)		Recovery (% P_2O_5)
	Feed	Concentrate	
Dry, 30 minutes	All material flocculated		(No selectivity)
Wet (with water at 60% solids; 30 minutes)	13.3	20.5	89.4
Wet (with Cyquest and sodium silicate)	12.3	25.5	86.4

Similar results with (1) dry grinding and (2) wet grinding in the presence of 5 kg/t of sodium silicate dispersant, were observed in a 1:1 apatite-silica mixture by Moudgil et al [46]. Grinding resulted in a complete loss of selectivity as seen from the results in **Table 2**. Further, the grade of apatite is significantly low (less than that of the feed) when the synthetic mixture is dry ground. This is anticipated in view of the smearing of the harder silica particles by apatite during dry grinding [46].

Table 2. Effect of Grinding on Selective Flocculation of Apatite in 1:1 Apatite-Silica System (After Ref 46)
Flocculant = (PAA Molecular Weight = 4×10^6)
Flocculant Dosage = 1.0 kg/t
pH = 9.5

Type of Feed	Grade, % Apatite	Recovery, % Apatite
Synthetic	90.7	59.2
Dry Ground	41.6	60.0
Wet Ground (Na-silicate = 5 kg/t)	78.0	40.0

Another effect of the mode of grinding is manifested in the lower recovery during wet grinding as seen in **Table 2**. This implies a decrease in the extent of flocculation when the mineral is wet ground. During a study on flocculation of wet ground apatite, it was observed that only about 66% material flocculated with a dosage of 3 kg/t PAA (molecular weight = 4 million) and only marginal improvement in flocculation was obtained with higher flocculant dosages [47]. The grinding time did not have any significant impact on the particle size distribution of −400 mesh fraction. Similar flocculation behavior was observed for wet ground apatite from other sources, whereas more than 90% material flocculated with 1 kg/t polymer if the material was dry ground instead of wet grinding. This was attributed to more efficient reduction in particle size by wet grinding. Materials of similar particle size distribution (38-44 μm fraction) exhibited identical flocculation behavior, whether dry ground or wet ground.

In dolomite-silica systems even wet grinding in the presence of dispersant could not restore the selectivity obtained in synthetic mixtures [20]. The remarkable effect of grinding of ores on the selectivity of separation is the least understood aspect of selective flocculation process. It also holds the key to the success of any selective flocculation separation scheme, particularly in natural ore systems.

Various investigators in the past have attributed the loss of selectivity in comminuted mixtures to slime coating (smearing effect) that is, coating of the smaller particles of one constituent mineral generated during grinding on larger particles of the other constituents, and rendering the surfaces indistinguishable from each other after grinding. This coating may also build up in semi-soluble systems through dissolution-precipitation type subprocesses. The presence of water and dispersants in some cases, does help to minimize this coating and hence better results are achieved. Furthermore, one may not have any control on the way the natural ore slimes are generated. Further work is warranted to restore the selectivity in such cases.

At this point, not much data is available regarding the nature of transformation of surfaces during grinding of mixtures. Furthermore, with conventional characterization techniques such as ESCA, FT-IR, Auger, SEM-EDAX, etc., it may not be possible to completely characterize these effects. There is an urgent need to understand this phenomena in multi-component and natural ore systems. Suitable remedies can only be developed after the mechanisms of the loss of selectivity due to grinding and ageing are identified and understood properly.

10.2 Heteroflocculation

Moudgil and co-workers [48-50] suggested that adsorption of the flocculant on the inert (non-flocculating) component would make it possible for it to co-flocculate with the active (flocculating) component, causing a loss in selectivity. It was argued, assuming bridging to be the flocculation mechanism, that the polymer adsorbed on the inert component bridges with the active particles to form a floc, leading to heteroflocculation. This phenomenon is illustrated in **Figure 7**. The reasons for adsorption on the inert component could be surface heterogeneity as a result of which minor adsorption occurs on the inert surface which is insufficient to lead to flocculation in single mineral tests. Also, as mentioned in an earlier section, adsorption on the inert component may occur as a consequence of grinding effects such as ion activation and slime coating. Although these effects can be minimized using suitable dispersants the possibility of heteroflocculation which requires only a minimal adsorption may still exist in such systems.

10.3 Mathematical Model of Heteroflocculation

A mathematical model to describe heteroflocculation, developed by Moudgil and coworkers [48-50], predicted the following two conditions for minimizing heteroflocculation in a system:

1. highly selective polymer adsorption
2. proper adjustment of polymer dosage to attain low surface coverage on the inert component

The former may not be easily attained since flocculants are typically high molecular weight polymers and adsorb on the solid substrate due to a number of mechanisms such as hydrogen bonding, hydrophobic bonding, specific interaction etc. Low flocculant dosages, on the other hand, could affect the floc properties, thereby making floc separation inefficient. Thus, either of the two strategies as suggested by the model is not always practical.

Aggregation of polymer coated particles is governed by the frequency and efficiency of collisions of the particles. Considering the polymer adsorption mechanism on different constituents of the mixture to be similar, the probability of adhesion would be governed by collision efficiency between the flocculant coated and the bare sites on various particles. A number of expressions suggested for floc formation have either overestimated or underestimated the collision efficiency factor except under certain specific conditions [48-52].

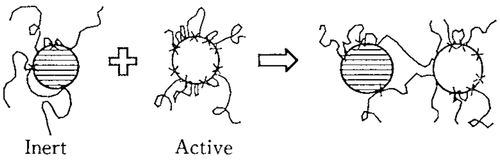

(i)Some "active"sites on the inert constituent: No selectivity

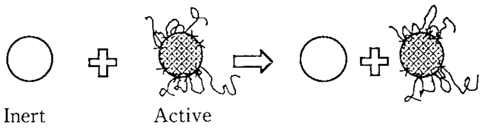

(ii)No "active" sites on the inert sudstrate: Selectivity achieved

x=active sites, ╲=polymer molecule

Fig. 7 Schematic diagram illustrating the concept of heteroflocculation (after Ref [50]).

The expressions by Hogg [51] and Moudgil et al. [48-50] can account for heteroflocculation while the others are for bulk flocculation. However, the collision efficiency is overestimated by Hogg for any fraction of the surface coverage (θ) except 0 and 1. This was attributed to the large number of sites on the surface to which the polymer molecule is attached. In other words, almost all the surface sites are implicitly considered to be capable of adsorbing polymer molecules. The expression proposed by Moudgil et al [48-50], which is based on the equivalent active sites concept, seems to correlate well with the selective flocculation data [50]. In the limiting cases Moudgil's expression for collision efficiency given below reduces to the corrected version of the one suggested by Smellie and La Mer [52].

$$E_{ij} = \Phi_i \Phi_j [\theta_i (1-\theta_j) + \theta_j (1-\theta_i)] \qquad (1)$$

where

Φ_i, Φ_j = fraction of sites on i and j that are active for polymer adsorption

θ_i, θ_j = fractional surface coverage (of active sites) at a given polymer dosage.

It should be noted that flocculation may not be observed in a system, for small θ or Φ values which would lead to near zero E_{ij}. Further the collision efficiency is shown to be a strong function of Φ and is only weakly related to θ [50]. Also Moudgil and Behl [50] proposed a critical efficiency factor (E_{ij}) and suggested that below the critical value of E_{ij}, no significant flocculation may be detected.

11. Engineered Surface Sites for Flocculant Adsorption

11.1 Concept of Site Blocking Agents (SBA)

The collision efficiency of a single flocculating mineral E_{ij}, is known to reduce with a decrease in the molecular weight of the flocculant [53]. Hence, Moudgil and coworkers proposed that a lower molecular weight fraction of the same or similar flocculant, which on its own is incapable of inducing flocculation in the active or the flocculating material, can be used as a site blocking agent (SBA) to minimize heteroflocculation [53]. A schematic of the role of SBA in enhancing adsorption of the flocculant on the active component is shown in **Figure** 8 [53]. The SBA approach is a more generic strategy to minimize loss of selectivity in mixed component systems than through design of selective dispersants as mentioned earlier.

11.2 Expression for Collision Efficiency in the Presence of SBA

To develop an expression for estimation of the collision efficiency for the particles in the presence of the site blocking agent (SBA), it is assumed that the lower molecular weight polymer (SBA) is introduced in the system prior to the injection of the flocculant. This would lead to adsorption of the SBA first and the flocculant would encounter a partially covered surface. The site on the surface can be defined, as was done earlier by Hogg [51] and Moudgil [50], to be the area occupied by the adsorbed polymer molecule. Floc formation would be observed if a coated site collides with the "active" bare site or vice versa. Any collision of a flocculant coated site with SBA coated site or vice versa will not yield flocculation.

Consider the total number of sites for the SBA on the particle I to be n_i, of these a_i are active sites. Let the dosage be such that x_i sites are covered by the site blocking agent. Similarly for the flocculant, the total number of sites is N_i of which A_i are active and at a particular dosage X_i of these active sites are covered. Schematic representation of the area of polymer adsorption site on the surface is given in **Figure 9** [53]. It can be seen from Figure 9 that more area for active sites is available for the flocculant than for the SBA. The total number of sites on the surface for the SBA and the flocculant can, however, be related, since the available area is the same, by a factor which would depend on the respective parking area of the molecules.

The probability of a given surface site on particle *i* being covered by polymer (flocculant) is given by the following expression

$$P_i=\frac{X_i}{N_i}=\frac{A_i}{N_i}\times\frac{X_i}{A_i}=\Phi_i\theta_i \qquad (2)$$

where Φ_i is the fraction of the active sites and θ_i is the fractional surface coverage of the flocculant in the absence of the SBA.

Additionally the bare "active" sites on the particle, the number of sites available for the flocculant was estimated after the SBA adsorbs. The expression for the joint probability of collision of a covered active site on particle i with a bare active site on particle j is then given by

$$P_iP_j=\Phi_i\theta_i[\Phi_j-\Phi_j\theta_j-\overline{\Phi_j}\ \overline{\theta_j}] \qquad (3)$$

$\overline{\Phi_i}$ = fraction of sites on j that are active for SBA adsorption

$\overline{\theta_j}$ = fractional surface coverage (of active sites for SBA adsorption) on j by the SBA at a given dosage.

The collision efficiency factor is given by the overall probability of adhesion by considering the joint probability of particle i having a free active site and particle j a polymer coated patch. This can be expressed as

$$\overline{E_{ij}}=\Phi_i\Phi_j[\theta_i(1-\theta_j)+\theta_j(1-\theta_i)]-\Phi_i\overline{\Phi_j}\theta_i\overline{\theta_j}-\overline{\Phi_i}\Phi_j\overline{\theta_i}\theta_j \qquad (4)$$

where $\overline{E_{ij}}$ is the collision efficiency in the presence of the SBA. It is clear from the above expression that in the absence of SBA the above equation reduces to the expression proposed by Moudgil et al. [48-50]. The use of these equations is possible only after the values of the adsorption parameters (Φ, θ, $\overline{\Phi}$, $\overline{\theta}$) are known and involves the assump-

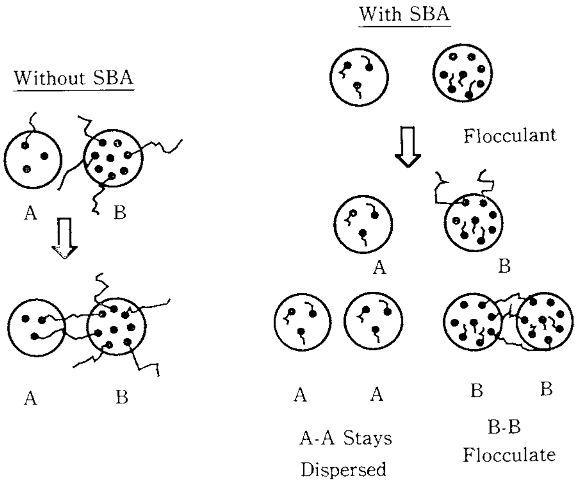

Fig. 8 Schematic showing SBA for enhanced adsorption of the flocculant (after Ref [53]).

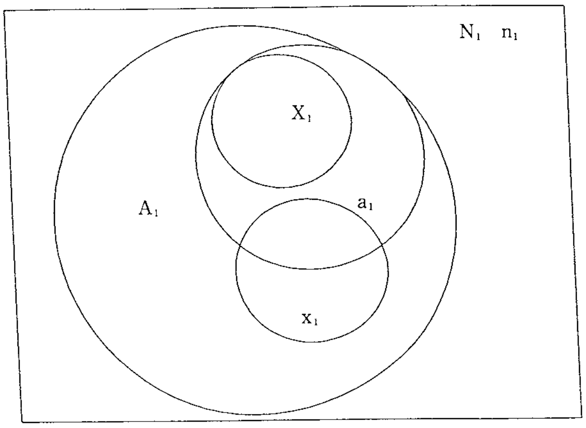

Fig. 9 Schematic representation of the solid surface for Polymer adsorption (after Ref [53]).

tion that Φ is 1 for the flocculating component.

11.3 Determination of Adsorption Parameters

Estimation of fraction of active sites on a surface can pose some problems since direct measurements are not possible. However, if a certain surface, where high adsorption density and flocculation is observed, can be considered to be totally active, the value for Φ in such a case can be arbitrarily set at one, as was done for dolomite -PEO (5 million molecular weight) system by Moudgil et al. [48-50]. Assuming the same size of an active site on another surface, Φ for a given material may be determined with reference to the active surface, by the following expression.

$$\Phi = \frac{\Gamma_{\max}}{\Gamma_{\max}^{\mathrm{ref}}} \tag{5}$$

where $\Gamma_{\max}$ is the saturation adsorption density for the two minerals.

The surface coverage (θ) may be estimated for a particular mineral by the expression

$$\theta = \frac{\Gamma}{\Gamma_{\max}} \tag{6}$$

The surface coverage $(\overline{\Phi})$ by the SBA would be given by an expression similar to equation 6. However, $\overline{\Phi}$ has to be estimated by taking into account the difference in the size of the active sites for the SBA and the flocculant molecule. A general expression based on the definition for $\overline{\Phi}$ can be given as

$$\frac{\overline{\Phi}}{\Phi} = \frac{a'}{n'} \times \frac{N'}{A'} \tag{7}$$

where a' and A' are the number of active sites for the SBA and the flocculant molecules respectively, n' and N' are the corresponding number of total sites on the surface and Φ is the fraction of active sites for a reference material. Clearly, for a molecule with the same monomeric unit the size of the active site for a SBA would be smaller than the flocculant, therefore, the total number of sites for the flocculant are smaller in number.

In general the number of active sites on a particle surface for a given polymer is directly proportional to the equilibrium adsorption density expressed in terms of moles per unit area. Further, the number of sites (both active or inert) are inversely related to the size of the polymer molecule (R_g-radius of gyration). It is well known that the radius of gyration is related to the molecular weight of the polymer by the following expression [54]

$$[R_g]^2 \propto M_w^{\frac{2}{3}(1+\nu)} \tag{8}$$

where M_w is the molecular weight of the polymer and ν is intrinsic viscosity parameter. An expression for the fraction of active sites for a SBA using the above argument can be given as

$$\frac{\overline{\Phi}}{\Phi} = \left(\frac{\overline{\Gamma}_{\max}}{\Gamma_{\max}}\right) \times \left(\frac{m}{M}\right)^{\frac{2\nu-1}{3}} \tag{9}$$

where $\Gamma_{\max}$ and $\overline{\Gamma}_{\max}$ are the saturation adsorption densities (g/unit area) for the reference (high molecular weight polymer with $\Phi = 1$) and the SBA molecule. It should be noted that the saturation adsorption for the lower molecular weight fraction is smaller than the higher molecular weight macromolecules [55,56], therefore, $\overline{\Phi}$ is less than one.

11.4 Selection of SBA

In a single mineral suspension, equation (4) reduces to

$$\overline{E} = 2\Phi^2\theta(1-\theta) - 2\Phi\overline{\Phi}\theta\overline{\theta} \tag{10}$$

which can be written as

$$\overline{E} = E - 2\Phi\overline{\Phi}\theta\overline{\theta} \tag{11}$$

where E is the collision efficiency for single mineral particles. This indicates a decrease in the collision efficiency in the presence of an SBA. As illustrated in **Figure 10** for dolomite-PEO system, flocculation is depressed with lower molecular weight polymers and the extent of depression increases with molecular weight till flocculation initiates at molecular weight beyond 6×10^6. This corresponds to the highest molecular weight polymer incapable of inducing flocculation on its own but causing a maximum decrease in the flocculation in the presence of a higher molecular weight flocculant [57]. Since reduction in collision efficiency in the single mineral system is a good indicator for reduction in the collision efficiency of a mixed mineral system, PEO of 6×10^6 molecular weight polymer was used by

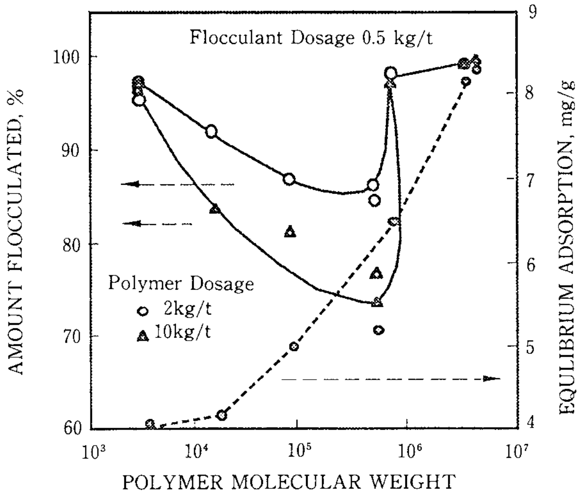

Fig. 10 Flocculation behavior of dolomite in the presence of PEO (after [57]).

Moudgil et al [57] to separate apatite from dolomite, which otherwise coflocculate. Additionally, as shown in **Figure 11** it is observed that at a given flocculant dosage, increasing the SBA concentration results in higher recovery of apatite, thereby, indicating less heteroflocculation [57]. Hence, by proper selection of SBA molecular weight and dosage heteroflocculation can be controlled. This concept was confirmed by reduction in flocculant adsorption on the apatite (inert) particles in the presence of an SBA. In a recently reported study the SBA concept was successfully used for a 80:20 mixture of apatite-palygorskite clay which was upgraded as 95% apatite at more than 80% recovery level in the product fraction [58].

12. Design of More Selective Reagents (Smart Reagents)

12.1 Creation of adsorption sites compatible with Reagent Functionality

A knowledge of polymer adsorption mechanism (s) can be applied to systems where the adsorption sites are not known a priori. In such cases the binding sites for the polymer functionality may be selectively created by altering the surface chemistry. Some of the methods by which appropriate surface bonding sites can be created are discussed below. These include modifying the surface by changing pH, heat-treatment of the substrate and selective coating onto the particles.

Effect of heat treatment: The effect of the heat treatment of the mineral on the adsorption and flocculation behavior has been demonstrated on silica [32, 33]. The pretreatment consisted of heating the material at various temperatures. It was found that the concentration of the isolated hydroxyl groups (the silanol groups) on the silica surface increased with increasing temperatures till 700°C and then decreased so as to give an essentially siloxane surface. The adsorption and flocculation behavior of pretreated silica with PEO correlated well with the concentration of silanol groups on the surface, being highest at maximum silanol concentration (see **Figure 12**).

It is known that the fully hydrated surface of silica (if precipitated at room temperature) is covered with a layer of silanol groups. The surface dehydration up to 400°C is fully reversible but above 400°C there is conversion of hydrogen-bonded silanol groups (SiOH) to siloxane (Si-O-Si) groups. PEO adsorption appears to occur through silanol groups and hence with increasing proportion of

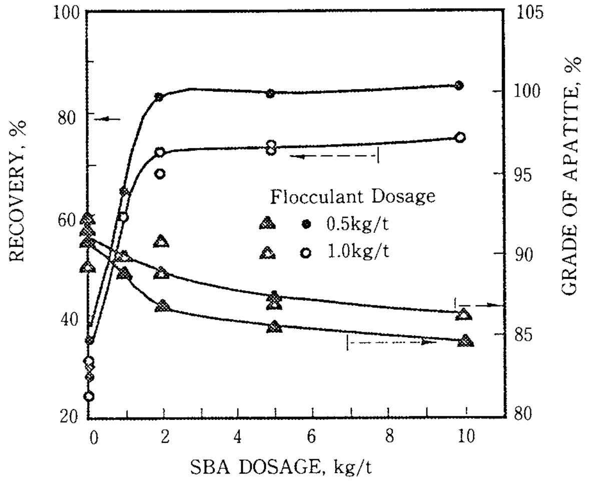

Fig. 11 Recovery of Apatite from Dolomite in the presence of SBA (after Ref [57]).

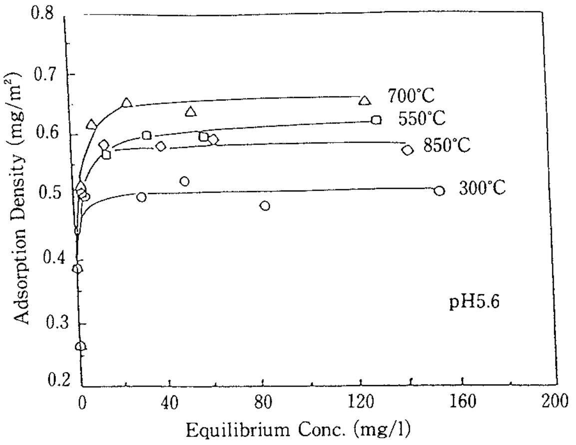

Fig. 12a Adsorption isotherms for different treated silica. Adsorption density of PEO increases with temperature till 700 °C and then decreases (after Ref [33]).

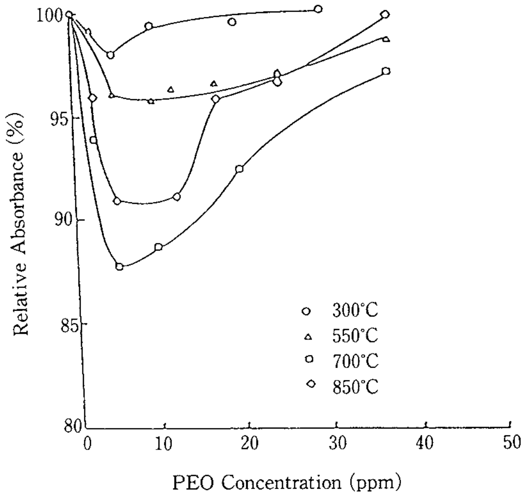

Fig. 12b Change in flocculation behavior for calcined silica particles as a function of polymer dosage. The trends in flocculation behavior correlate with the adsorption isotherms in Figure 12a (After Ref [33]).

siloxane groups both adsorption and flocculation deteriorate. Isolated silanol groups are completely removed by heating at 1000°C resulting in negligible adsorption and flocculation with PEO.

Effect of surface coating: Recently it was shown that the source of the mineral strongly influences its interaction with a given reagent. Dolomite samples from Florida exhibited flocculation with PEO whereas those from Perry Mines, Georgia and New Jersey did not flocculate at all [58-60]. Detailed characterization of dolomite samples revealed that the flocculating dolomite contains a minor amount of palygorskite which modifies its surface chemical behavior such that the surface exhibits isolated -OH groups [60]. The isolated hydroxyl groups hydrogen-bond with the ether oxygen of PEO [24, 25, 60] and result in unusually high adsorption and flocculation of Florida dolomite. The presence of the clay particles on dolomite surface was indicated by their morphology and Si-Al peaks in SEM-EDAX analysis, the existence of structural hydroxyl peak at 3619 cm^{-1} and Si-O stretching peak at 1055 cm^{-1} in IR spectra (see **Figure 13**), and XRD studies of acid insolubles. The absence of isolated hydroxyl peak at 3619 cm^{-1} in the IR spectra of dolomite samples correlated well with their lack of flocculation with PEO.

In natural systems the presence of even trace level of surface-active impurities can remarkably alter the surface characteristics and hence the flocculation behavior of the constituent minerals. In order to achieve better control of selectivity, surface characterization techniques to analyze impurities and surface contaminants are essential.

The selectivity achieved in the apatite-dolomite system with PEO [58] was possible due to the beneficial effect of the clay coating on flocculation of dolomite. Thus, in a system where the pure components are inert to the given polymer, there exists a possibility of introducing selectivity by coating of desired component(s).

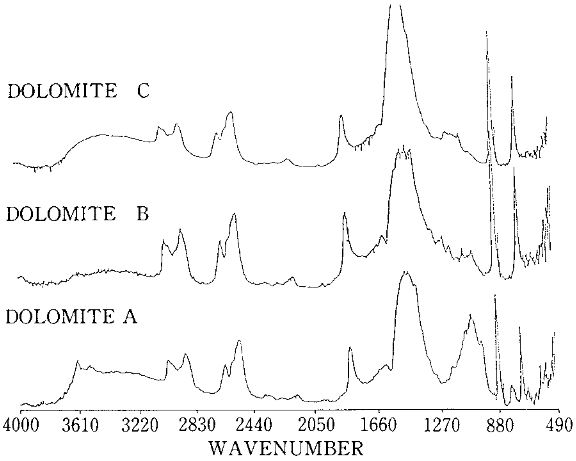

Fig. 13 DRIFT spectra of dolomite samples (after Ref [60]).

12.2 Design of Novel Selective Reagents Based on Molecular Recognition

An alternative approach to selective creation of adsorption sites on the surface appropriate to the polymer adsorption mechanism(s) would be to design the flocculant molecule such that its configuration is compatible with the molecular architecture of the surface.

Pradip [62-64] and Ravishankar et al [47], based on the molecular/ionic recognition mechanisms have suggested the need to take into account the surface structure rather than simple interactions with single sites on the surface in designing novel reagents for selective separation. A critical review of earlier investigations indicates that polymeric reagents having two or more functional groups with appropriate spacing between them to achieve structural/stereochemical compatibility with the surface are likely to exhibit enhanced structure specificity, and hence act as more selective dispersants and flocculants [64]. For instance, the unusual selectivity of starch based reagents for hematite and alumina has been attributed to the structure compatibility between the interacting oxygens in the starch end groups and the Fe-Fe distance on the surface of hematite (or Al-Al in case of Alumina). **Figure 14** schematically illustrates this concept of structural compatibility [62-64].

Starch consists of amylopectin and amylose components. Amylose having a low molecular weight (10^5) contains 200-300 amylglucose units with one end group per molecule. On the other hand, amylopectin (10^6-10^7 MW) consists of more than 5000 cross-linked anhydroglucose units with, on an average, about one end group for every 20-30 glu-

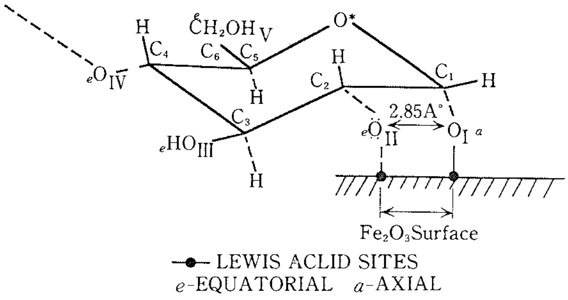

Fig. 14 Schematic diagram illustrating the mechanism of starch adsorption through binuclear complexation with Fe sites on hematite surface (after Ref [63]).

cose units. A typical end group of such a unit is shown in Figure 14. Amongst the four OH groups, O_IH is the most polarizable due to close proximity of the heterocyclic oxygen (O*). The distance between O_I and adjacent O_{II}, calculated on the basis of bond lengths and structure turns out to be 2.85 Å. As shown in Figure 14, the O-O distance in the adsorbing starch end group is remarkably close to the average Fe-Fe (or Al-Al) in corundum distance of 2.852 Å at the cleavage plane of hematite. The proposed binuclear complexation mechanism through starch end groups explains the unusually high affinity of starch molecules for alumina and iron oxide surfaces. Aluminum sites are not available on kaolinite cleavage surface and hence no flocculation is observed.

It thus appears that reagents designed on the basis of molecular recognition (structural compatibility) mechanisms could help in enhancing selectivity in natural ore systems, particularly overcoming the adverse effects of soluble ion activation, heteroflocculation, and slime coating.

13. Concluding Remarks

A critical review of the state-of-the-art of selective flocculation technology indicates that appropriate reagent schemes are critical to the successful application of the process to natural ore/particulate systems.

Recent efforts have led to a better understanding of the reasons for the loss of selectivity in mixed mineral systems. For example, heteroflocculation during the polymer addition stage has been identified also to be another major reason for the loss of selectivity in mixed mineral systems. The concept of site blocking agents (SBA) to minimize heteroflocculation is an important development for achieving the desired selectivity. However, the applicability of the SBA concept to multicomponent systems needs to be further investigated.

Cross contamination of the particles during comminution can also lead to loss of selectivity in mixed mineral and natural systems. In principle, if the ore is in a truly liberated form, i.e., no cross contamination of the component surfaces occurs during size reduction of the interlocked grains, the SBA concept should remain valid and enhanced selectivity in the system can be expected. However, if cross-contamination during comminution is encountered, the use of suitable dispersants may be necessary to restore the selectivity.

Engineering the surface sites and polymer structure for enhanced selective adsorption can be achieved through creation and control of surface sites, and designing of polymers compatible with molecular architecture of the surface through molecular modeling. In this regard, the approach of Pradip et al [62-64] to engineer highly selective reagent schemes based upon molecular structure of the surface and configuration of the adsorbing flocculant is of fundamental significance and warrants further research.

It must also be mentioned that most of the research in selective flocculation has been confined to mineral separation systems. The fundamental knowledge base generated regarding the selectivity mechanisms can be extended to other areas of solid-solid separations such as environmental restoration, preconcentration of hazardous materials, bioseparations and controlled drug delivery systems. An interdisciplinary approach is necessary to develop the science and technology of selective flocculation process in a timely manner.

14. Acknowledgments

The authors would like to acknowledge the partial financial support of this work by the Engineering Research Center (ERC) for Particle Science & Technology at the University of Florida, the National Science Foundation (NSF Grant # EEC-94-02989) and the Industrial Partners of the ERC, and the Mineral Resources Research Center, University of Florida, Gainesville, Florida.

References

1) Yarar, B. and Kitchener, J.A., “Selective Flocculation of Minerals 1 : Basic Principle ; 2. Experimental Investigations of Quartz, Calcite and Galena”, Transactions of the Institution of Mining and Metallurgy, 79, 1970, pp. C23-C33.
2) Friend, J.P. and Kitchener, J.A., “Some Physico-Chemical Aspects of the Separations of Finely-Divided Minerals by Selective Flocculation”, Chemical Engineering Science, 28, 1973, pp. 1071-1080.
3) Attia, Y.A. and Kitchener, J.A., “Development of Complexing Polymers for the Selective Flocculation of Copper Minerals”, 11th International Mineral Processing Congress, Cagliari, Italy, 1975.
4) Attia, Y.A. and Fuerstenau, D.W., “Principles of Separation of Ore Minerals by Selective Flocculation”, in Recent Development in Separation Science, Li, N.N. (Ed.), CRC Press, 4, 1978, pp. 93-105.

5) Sresty, G.C., Raja, A., and Somasundaran, P., "Selective Flocculation of Mineral Slimes Using Polymers", in Recent Development in Separation Science, Li, N.N. (Ed.), CRC Press, 4, 1978, pp. 93-105.

6) Somasundaran, P., "Selective Flocculation-Flotation of Slimes from Sylvinite Ores", in Fine Particles Processing, Somasundaran, P. (Ed.), SME-AIME, 1980, Vol. 2, pp. 947-976.

7) Attia, Y.A., "Design of Selective Polymers for Biological and Colloid Separation by Selective Flocculation", in Flocculation in Biotechnology and Separation Systems, Attia, Y.A. (Ed.), Elsevier Science Publishers, Amsterdam, 1987, pp. 227-246.

8) Attia, Y.A. and Yu, S., "Entrapment and Entrainment in Selective Flocculation Process, Part 2 : Possible Methods for Minimization of Entrapment and Entrainment", in Interfacial Phenomena in Biotechnology and Materials Processing, Attia, Y.A., Moudgil, B.M., and Chander, S. (Eds.), Elsevier Science Publishers, Amsterdam, 1988, pp. 503-514.

9) Yu, S. and Attia, Y.A., "Review of Selective Flocculation in Mineral Fines", in *Flocculation in Biotechnology and Separation Systems*, Attia, Y.A. (Ed.), Elsevier Science Publishers, Amsterdam, 1987, pp. 601-637.

10) Moudgil, B.M., Behl, S., and Pradip, "Scientific Design of a Selective Flocculation Process", Minerals and Metallurgical Processing, 10 (2), 1993, pp. 43-46.

11) Colombo, A.F., "Selective Flocculation and Flotation of Iron Bearing Minerals", in Fine Particles Processing, Somasundaran, P. (ed.), SME-AIME, 1980, Vol. 2, pp. 946-947.

12) Behl, S., Willis, M.J., and Young, R.H., "Method for Separating Mixture of Finely Divided Minerals", U.S. Patent # 535890, 1996.

13) Shi, J., "Method of Beneficiating Kaolin Clay Utilizing Ammonium Salts", U.S. Patent # 4604369, 1986.

14) Tadros, Th. F. (Ed.), *The Effect of Polymers on Dispersion Properties*, Academic Press, 1982, 423 pp.

15) Attia, Y.A., "Synthesis of PAMG Chelating Polymers for Selective Flocculation of Copper Minerals", *International Journal of Mineral Processing*, 4, 1977, pp. 209-225.

16) Krishnan, S.V. and Iwasaki, I., "Sodium Silicate as a Dispersant in Selective Flocculation of Iron Ores", *Trans. SME-AIME*, 272 : 1984-1988 (1983).

17) Attia, Y.A. and Deason, D.M., "Control of Slimes Coating in Mineral Suspensions", *Colloids and Surfaces*, 39, 1989, pp. 227-238.

18) Ravishankar, S.A. and Pradip, "Role of Organic Dispersants in the Selective Flocculation of Iron Oxide/Kaolinite Mixtures", presented at 62nd Colloid & Surface Science Symposium, ACS, Pennsylvania, USA, 1988.

19) Pradip, Ravishankar, S.A., Sankar, T.A.P., and Khosla, N.K., "Beneficiation Studies on Alumina-Rich Indian Iron Ore Slimes using Selective Dispersants, Flocculants and Flotation Collectors" *Proceedings : XVIII International Mineral Processing Congress*, Sydney, Australia, IMM, Vol. V, 1993, pp. 1289-94.

20) Moudgil, B.M. and Mehta, N., unpublished results.

21) Attia, Y.A., Kogan, R. and Driscoll, K., "Separation of Flocs from Suspension by Dissolved Air Flotation", in *Flocculation in Biotechnology and Separation Systems*, Elsevier Science Publisher, Eds., Attia, Y.A., Amsterdam, 1987, pp. 297-308.

22) Attia, Y.A., Bavarian, F. and Driscoll, K.H., "Use of Polyxanthate Dispersant for Ultrafine Pyrite Removal from High Sulfur Coal by Selective Flocculation", *Coal Preparation*, 6, 1988, pp. 35-51.

23) Attia, Y.A. and Fuerstenau, D.W., "Feasibility of Cleaning High Sulfur Coal Fines by Selective Flocculation", *Proceedings : XIV International Mineral Processing Congress*, Toronto, Canada, 1982, VII, 4.1-4.15.

24) Pradip, Kulkarni, R.A., Gandiah, S., and Moudgil, B.M., "Selective Dispersants for Apatite-Dolomite Separation", unpublished work.

25) Barbucci, R. et al. in *Reagents in the Minerals Industry*, Jones, M.J. and Oblatt, R. (Eds.), IMM, London, 1986, pp. 245-250.

26) Rinelli, G. and Marabini, A.M., "Dispersing Properties of Tanning Agents and Possibilities of Their Use in Flotation of Some Minerals", in *Fine Particles Processing*, Somasundaran, P. (Ed.), SME-AIME, 1980, pp. 1012-1033.

27) Parsonage, P. and Marsden A., "The Influence of the Structure of Reagents on Their Effectiveness as Dispersants for Cassiterite Suspensions", *International Journal of Mineral Processing*, 20, 1987, pp. 161-192.

28) Read, A.D. and Hollick, C.T., "Selective Flocculation Technologies for Recovery of Fine Particles", Mineral Science and Engineering, 8 (3), 1976, pp. 202-213.

29) Pradip, "Recovery of Phosphate Values from Slimes by Selective Flocculation" Metallurgical Research-Fundamentals & Applied Aspects, Mehrotra, S.P. and Ramrahandran, T.R., (Eds.), 1986, pp. 45-50.

30) Behl, S. and Moudgil, B.M., "Mechanisms of Polyethylene Oxide Interaction with Apatite and Dolomite", Journal of Colloid and Interface Science, 161, 1993, pp. 443-449.

31) Scheiner, B. and Wilemon, G.M., "Applied Flocculation Efficiency : A Comparison of Polyethylene Oxide and Polyacrylamides", in *Flocculation in Biotechnology & Separations Systems*, Attia, Y.A. (Ed.), Elsevier, 1987 pp. 175-185.

32) Rubio, J. and Kitchener, J.A., "The Mechanism of Adsorption of Poly (Ethylene Oxide) Flocculant on Silica", Journal of Colloid and Interface Science, 57 (1), 1976, pp. 132-141.

33) Cheng, Y.C., "The Effect of Surface Hydration on the Adsorption and Flocculation of a Model Silica Suspension Using Polyethylene Oxide", M.S. Thesis, University of Florida, Gainesville, Florida, 1985.

34) Mathur, S., and Moudgil, B.M., "Adsorption Mechanism of PEO on Oxide Surfaces", Journal of Colloid and Interface Science, in print.

35) Mathur, S., Moudgil, B.M., and Pradip, "Apatite-Dolomite Separation By Selective Flocculation Using Polyacrylic Acid", Minerals and Metallurgical Process-

ing, 13 (1), February 1996, pp. 1-3.

36) Behl, S., Moudgil, B.M., and Prakash, T.S., "Effect of Particle Size on Flocculation", Journal of Colloid and Interface Science, 158, 1993, pp. 511-512.

37) Behl, S., Moudgil, B.M., and Prakash, T.S., "Selective Flocculation in Coarse Particles", Colloids and Surfaces, 74, 1993, pp. 311-312.

38) Williams, P.A., et al, "The Relationship between Polyelectrolyte Configuration and Colloid Stability", in The Effect of Polymers on Dispersion Properties, Th. F. Tadros, ed., Academic Press, New York, 1982, pp. 361-377.

39) Somasundaran, P. and Ramachandaran, R., "Innovative Approach to Elucidate Floc Structure and Polymer Conformation at Interfaces", in *Flocculation and Dewatering*, Moudgil, B.M. and Somasundaran, P. (Eds.), Engineering Foundation, New York, 1988, pp. 217-228.

40) Tjipangandjara, K. and Somasundaran, P., "Effects of Changes in Adsorbed Polyacrylic Acid Conformation on Alumina Flocculation", *Colloids and Surfaces*, 55, 1991, pp. 245-255.

41) Moudgil, B.M., and Vasudevan, T.V., "Characterization of Flocs," in *Flocculation and Dewatering*, B. M. Moudgil and B. J. Scheiner, Eds., Engineering Foundation, New York, United Engineering Trustees, Inc., New York, NY, 1989, pp. 167-178.

42) Ravishankar, S.A., Pradip, Khosla, N.K., "Selective Flocculation of Iron Oxide from Clays : A Comparison of Polyacrylic Acids and Starches", presented at the International Symposium on Advances in Fine Particles Processing, Boston, MA, USA, 1989.

43) Liao, J., and Senna, M., "Crystallization of titania amd magnesium titanate from mechanically activated Mg $(OH)_2$ and TiO_2 gel mixture", Materials Research Bulletin, 30 (4), pp. 385-392, 1995.

44) Hamada, K., Isobe, T., and Senna, M., "Comparative studies of the mechanochemical synthesis of $MgTiO_3$ precursors by milling various mixtures containing oxides and hydroxides", Journal of Materials Science Letters, 15 (7), pp. 603-605, 1996.

45) Rubio, J. and Marabini, A.M., "Factors Affecting the Selective Flocculation of Hydroxyapatite from Quartz and/or Calcite Mixtures", *International Journal of Mineral Processing*, 20, 1987, pp. 59-71.

46) Moudgil, B.M., Mathur, S., and Behl, S., "Removal of Dolomite and Silica From Apatite By Selective Flocculation", *Minerals and Metallurgical Processing*, 11 (4), 1994, pp. 217-222.

47) Mehta, N, "Flocculation behavior of Apatite With Polyacrylic Acid", M.S. Thesis, University of Florida, Gainesville, Florida, 1993.

48) Moudgil, B.M., Shah, B.D. and Soto, H.S., "Loss of Selectivity in Apatite-Dolomite Flocculation," Minerals and Metallurgical Processing, 4 (2), (1987) pp. 27-31.

49) Moudgil, B.M. and Vasudevan, T.V., "Factors Affecting Selectivity in Purification of Fine Powders by Selective Flocculation", in *Production and Processing of Fine Particles*, A. Plumpton (Ed.), Montreal, 1988, pp. 249-256.

50) Moudgil, B.M. and Behl, S., "A Model of the Selective Flocculation Process," Journal of Colloid Interface and Science, 146 (1), pp. 1-8 (1991).

51) Hogg, R., Journal of Colloid and Interface Science, 102 (1), (1984) pp. 232-236.

52) Smellie, R.H. and La Mer,V.K., Journal of Colloid and Interface Science, 13 (6), (1957) 589-599,.

53) Behl, S., Moudgil, B.M., and Prakash, T.S., "Control of Active Sites in Selective Flocculation-Part I : A Mathematical Model", *Journal of Colloid and Interface Science*, 161, 1993, pp. 414-421.

54) Allcock, H.R. and Lampe, F.W., Contemporary Polymer Chemistry, Prentice Hall, New Jersey, (1981).

55) Cohen Stuart, M.A., Fleer, G.J., and Bijsterbosch, B.H., Journal of Colloid and Interface Science, 90 (2), pp. 310-334 (1982).

56) Blaakmeer, J., "The Adsorption of Weak Polyelectrolytes and Polyampholytes," Ph.D. Thesis, Agricultural University, Wageningen, The Netherlands (1990).

57) Behl, S. and Moudgil, B.M., "Control of Active Sites in Selective Flocculation-Part II : Role of Site Blocking Agents", *Journal of Colloid and Interface Science*, 161, 1993, pp. 422-429.

58) Mathur, S., and Moudgil, B.M., "Separation of Apatite from High MgO Phosphates by Selective Flocculation", Chapter 8, *Proceedings of the XIX International Mineral Processing Congress*, San Francisco, CA, Oct. 22-27, pp. 43-46, 1995,

59) Moudgil, B.M. and Behl, S., "Flocculation Behavior of Dolomite", XVII International Mineral Processing Congress, 23-28 May 1993, Sydney, Australia, The Australasian Institute of Mining and Metallurgy, Vol.5, pp. 1309-1314.

60) Moudgil, B.M., Mathur, S., and Behl, S., "Flocculation Behavior Of Dolomite With Poly (ethylene-oxide)", *Minerals and Metallurgical Processing*, 12 (4), November, 1995, pp. 219-224.

61) Moudgil, B.M., Mathur, S., and Behl, S., "Dolomite-Dolomite Separation by Selective Flocculation Technique", *Minerals and Metallurgical Processing*, 12 (1), February 1995, pp. 24-27.

62) Pradip, "On the Design of Selective Reagents for Mineral Processing Applications, Metals, Materials & Processes, 3 (1), 1991, pp. 15-36.

63) Pradip, "Design of Crytal-Structure Specific Surfactants Based on Molecular Recognition at Mineral Surfaces", Current Science, 63 (4), 1992, pp. 180-186.

64) Pradip, "Reagents Design and Molecular Recognition at Mineral Surfaces", Proceedings : Reagents for Better Metallurgy, Prasad, M. and Hancock, B.A. (Eds.), 1994, pp. 245-252.

Author's short biography

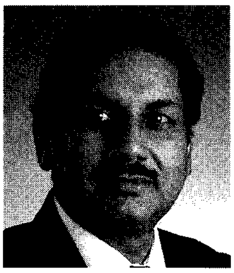

Dr. Brij M. Moudgil

Dr. Brij M. Moudgil is a Professor in the Department of Materials Science and Engineering, and Director of the Engineering Research Center for Particle Science and Technology at the University of Florida, Gainesville, FL. Dr. Moudgil also serves as the Director of the UF Mineral Resources Research Center. He received his undergraduate training in Metallurgical Engineering at the Indian Institute of Science, Bangalore. He continued his graduate studies at Columbia University, New York, and received M. S. and Eng. Sc. D. degrees in Mineral Engineering-Particulate Processing.

Prior to joining the Universtity of Florida faculty in 1981, Dr. Moudgil was associated with the Occidental Research Corporation in California as a Research Engineer. He was a visiting research fellow at the E. I. DuPont de Nemours & Co. in Wilmington, DE in 1988-89.

Sharad Mathur

Dr. Sharad Mathur is a Process Development Engineer at Engelhard Corporation, Gordon, GA. He received his Bachelor of Technology in Ceramic Engineering at Banaras Hindu University, India and a Master of Engineering in Materials Science and Engineering at McMaster University, Canada. He continued his graduate studies at the University of Florida and received a PhD in Materials Science and Engineering in 1996. Dr. Mathur has published more than fifteen papers and has presented about twenty papers at scientific meetings and seminars at academic institutions.

T.S. Prakash

Surya Prakash Thatavarthy completed his Bachelors degree in Chemical Engineering from the College of Technology, Osmania University, India in 1991 and received his M. S. degree in Materials Science and Engineering in 1996 from the University of Florida. He has started his own chemicals company in Hyderabad, India.

Review

Particle Attrition in Small Clearances[†]

C.C. Crutchley
Department of Chemical Engineering,
*University of Birminghame**
J. Bridgwater
Department of Chemical Engineering,
*University of Cambridge***

Abstract

Attrition is commonly found in the clearances of equipment where a mechanical device moves relative to a wall. Particles are trapped and broken in these regions, hence promoting attrition. This work concerns a cell where a blade rotates parallel to a wall. A cone cell design allowed for various gap sizes, particle velocities and blade tip speeds. The breakage rate of particles changed dramatically with gap size. Breakage commenced at a gap size close to a half particle diameter but had a definite minimum between one and one-and-half particle diameters. Little breakage was experienced if the gap much exceeded two particle diameters. When the other conditions of cell are changed, firstly the blade speed and secondly the flow rate of particles through the cell, the effect of gap size on breakage pattern is not changed. The product size distribution can be quite complex and is not simply related to the gap size. Segregation and a changed packing structure may each influence the breakage of a mixture.

1. Introduction

Attrition of solid particles has been and remains a major problem in processing equipment. It can change physical properties such as particle size, particle size distribution and shape. It results in the generation of fine material which may escape to the environment. Here the term "attrition" encompasses any unwanted particle breakage created during processing or handling of a material. Although the work was initially motivated by the need to reduce attrition, there are of course those processes where particle breakage or comminution is desired. Comminution has already been subject to research in great detail, resulting in a number of classical theories, but the detailed processes are still not understood and we remain far short of a scientifically-based design process.

It can be argued that attrition in the bulk of a particulate solid is caused by the occurrence of failure zones which are formed between coherent blocks of material moving against each other and creating intervening regions of high strain. These regions have been reported to be up to ten to twenty particle diameters in depth, Roscoe (1) and Bridgwater (2). Paramanathan and Bridgwater (3, 4) and Neil and Bridgwater (5, 6) showed that whilst failure zones of up to ten particle diameters exist in bulk, in an annular attrition cell a half failure zone of five particle diameters was created. They also demonstrated that attrition could be studied rationally and systematically related to stress and strain; in some cases satisfactory scaling laws could be obtained (6). Modelling of particle motion, stress transmission and particle breakage in failure zones is becoming accessible from computer-based modelling studies and are starting to show encouraging confirmation of the experimental findings, Ghadiri (7).

There is a lack of understanding of attrition even though there are many testing procedures, principally those developed for coals or grains, which can be exploited. There are no generalisations, since the various test methods are not comparable. The array of tests suitable for assessing attrition have been collected together and evaluated by Bemrose and Bridgwater (8).

The damage inflicted by mechanical equipment on solids can be quite substantial. One of the main areas of attrition occurs when a particle has to pass

---

**Pembroke Street, Cambridge CB2 3RA, England.
* Edgbaston, Birmingham, B15 2TT, England.
[†] Received April 15, 1997.

through a clearance in equipment, examples being in a screw auger used for conveying solids or in a pusher centrifuge with breakage caused by abrasion or fracture. This study is concerned with attrition in clearances. One might infer from previous work that moving mechanical equipment which breaks material at the vessel wall should do so with gaps of up to ten particle diameters, but we shall see below that this is far from the case.

When a mechanical moving part comes close to a vessel wall, creating a gap where particles can be trapped and broken, attrition products are generated. The work here concerns the construction of a new piece of testing equipment which simulates the flow of material through a gap between a moving blade and a stationary wall. It has the facility to increase or decrease the gap size whilst allowing continuous flow of material at various flowrates and different blade rotation speeds. The aim of the work is to obtain an understanding of the mechanisms existing when attrition takes place in such a clearance.

2. Equipment and Procedure

Figure 1 shows a schematic view of the design. The material under study flows downwards in a conical hopper of 60° inclined angle with an inlet diameter of 197 mm. The solids move downwards past the blade which has a height of 30 mm and a thickness of 4 mm, controlled by the rate at which solids are withdrawn from the hopper base by a vibrating feeder. The blade inserted into this flow is suspended from a motor above the conical hopper and may be rotated. Some of the solids pass through the gap between the blade edges and the sloping wall. The blade edges are arranged to be parallel to the vessel wall to achieve a constant gap thickness along the length of the blade edge. By adjustment of the vertical position of the conical hopper, the gap between the blade and the sloping hopper wall can be increased or decreased. The main design problem was to ensure the motor drive shaft was located exactly above the centre of the cone whatever the vertical position. The design allowed particles to be supplied steadily to the clearance between the wall and the rotating blade and the product to be extracted below. The volume between the blade tip and the wall was typically 100-1000 $(\mathrm{mm})^3$.

A test was conducted as follows. The separation between the blade tip and the hopper wall was set and then the hopper was filled with the material under test to the top of the cone. The material was then levelled with a brush. Beneath the hopper was placed a vibrating feeder, the setting of which determined the solids flow rate out of the cone. From the end of this feeder, the material fell onto a 40 cm diameter Russel Finex 22 shaker which captured unbroken material. The undersize material passed through a chute to a set of vibrated BS 410 sieves. The experiment was initiated when the blade, the feeder, the shaker and sieve vibrator were started simultaneously and ended when the cone emptied. Any dust left in the feeder was brushed into the nest of sieves and agitation continued until a total of 20 minutes had elapsed. The unbroken material was then weighed, the dust on the underpan wiped into the nest of sieves and the operation of the BS 410 sieves continued for five more minutes. Then sieve weighings yielded the size distribution. Semi-batch operation was employed to limit the problems of handling material and to create an experiment useable in the laboratory.

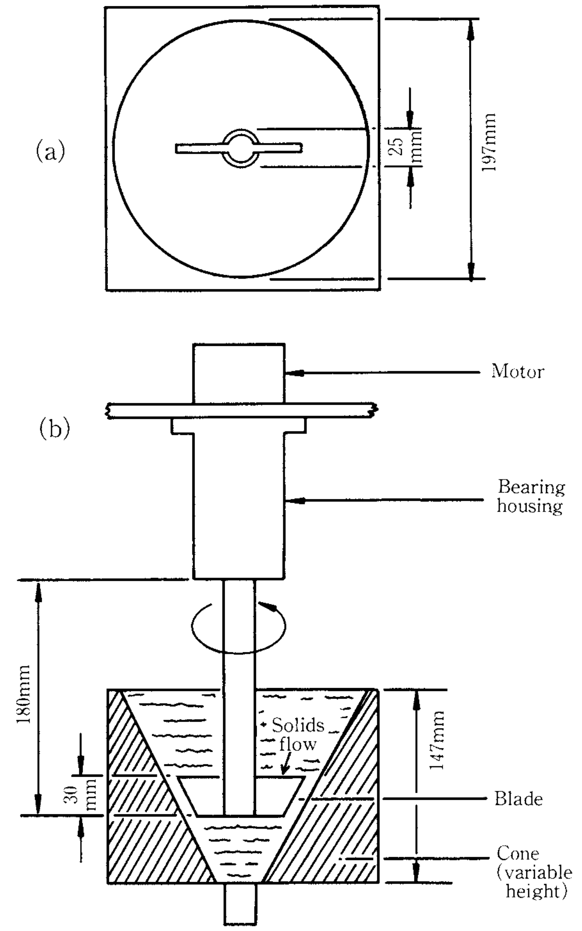

Fig. 1 Diagram of the cone cell. (a) Top view. (b) Front view, partially sectioned.

The first step in the procedure was to assess the breakage that appeared to occur in the absence of blade rotation in a so-called standard test. First of all there will be an effect due to the imperfect initial sizing there to be material outside the size range. Breakage arises since particle damage will occur during sieving, and since some breakage occurs due to the hopper wall friction and due to the action of the feeder. In this standard test switching on the feeder, sieve shaker and timing clock but not the rotating blade, the batch of material was emptied from the cone and the size distribution found. The results from this standard test were then subtracted from the experimental results obtained when the blade was rotating. The standard test was repeated after every six experiments to ensure reliability of the experimental data.

The materials used were:

	Sieve size range	Average crushing force (N)	Number tested
Urea	1.4-1.7mm	1.4	202
	1.7-2.0mm		
	3.15-3.55mm		
Molecular	1.4-1.7mm		
sieve beads	1.7-2.0mm	74	80
	3.15-3.55mm		
Catalyst	1.4-1.7mm		
base	1.7-2.0mm	46	123

Each size range had been cut from a bulk sample to give sufficient for testing. It was necessary to have 1-1.5 kg samples for use in each test in the cone cell.

Urea, the least spherical of the three, had been manufactured using a prilling tower process. The material was white with a crystalline internal structure, the crystals being 1-2 μm at the greatest dimension in particles of 1-2 mm diameter. Results varied depending if the day were dry or wet, but this was not found to be significant as the error was in the range 5-15%.

The molecular sieve beads are normally used as adsorbents in chemical processes. The manufacturing route used for these particles is agglomeration. Sub-micron crystalline metal aluminosilicates in powder form are formed into agglomerates by adding a clay binder to a wet mix. The mix is then granulated into beads which are calcined to form a strong composite. Its behaviour was not dependent on humidity.

The catalyst base particles were constituted of alumina, made by the sol-gel process, and was only available in the size range 1.4-2.0 mm. Its behaviour was not dependent on humidity.

3. Results and Discussion

Mechanisms

The tests on urea were carried out using gap increments of 0.1 mm, and sample results are given in **Figure 2** showing the percentage of material broken, or breakage, B (%), against the gap size G. If the particle size is changed, then it is found that similar behaviour is observed with the gap sizes for the maximum and minimum in breakage rates being raised by an increase in the initial particle size. If the data of Figure 2 are recast by introducing a dimensionless gap size, D, expressed as a number of particle diameters, the ratio of the gap size G to the initial particle diameter d, then we get the representation shown in **Figure 3**. Within experimental error, the maximum and minimum for the three particle sizes occur at the same dimensionless gap size.

Transferring attention to the molecular sieve beads and the catalyst particles, we find behaviour of the same character, as is shown in **Figures 4** and **5**. A dimensionless presentation is again satisfactory. In every case, the behaviour is characterised by an absence of breakage at the lowest gap widths, followed on increasing the gap width in turn by a first maximum breakage rate, a distinct minimum breakage rate and a second maximum breakage rate. Finally, breakage becomes undetectable with a further increase in gap, when D>2.2.

The findings are summarised in **Table 1**. Column A lists the gap size and the dimensionless gap at the start of breakage. This was hard to specify precise-

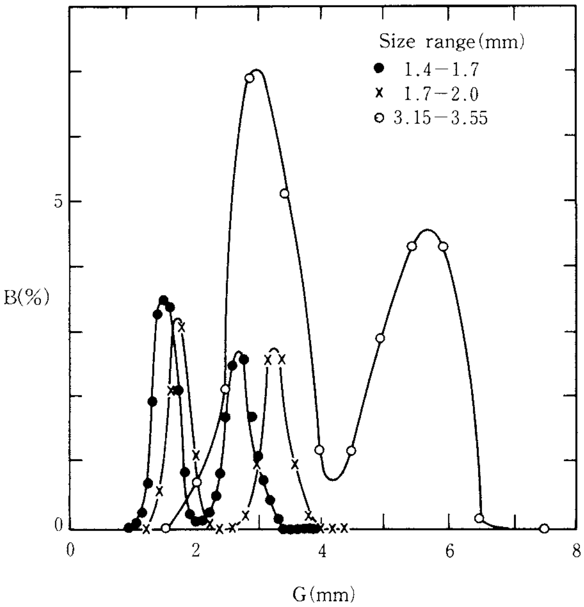

Fig. 2 A summary of the results for urea.

ly due to the small quantities of breakage product and hence there is scatter in the data. One can argue that the breakage be initiated at a gap of around 0.5D. If the gap is less than this value, the particle will need to be deformed before it passes under the blade whereas if the gap exceeds 0.5D, then the particle can be deformed by being caught between the wall and the blade. The start of breakage is rather less consistent from one material to another than the other events described below.

Examining column B, the first high breakage rate for the range 1.4-1.7 mm occurs at D=0.97 for urea and 0.71 for catalyst. This disparity may be caused by the difference in the shapes of the particles or in the friction experienced at the wall. If the initial material is of size 1.7-2.0 mm, the maximum varies from 0.76 for the catalyst, 0.81 for the molecular sieve beads and 0.97 for the urea. For the largest size, we find 0.90 for urea and 0.84 for molecular sieve beads. The high breakage rates occur at similar values for a given material i.e. urea 0.9-0.97, molecular sieve beads 0.81-0.84 and catalyst 0.71-0.76. Under such circumstances it is logical to conceive of the particle being caught and jammed against the wall and there by breaking.

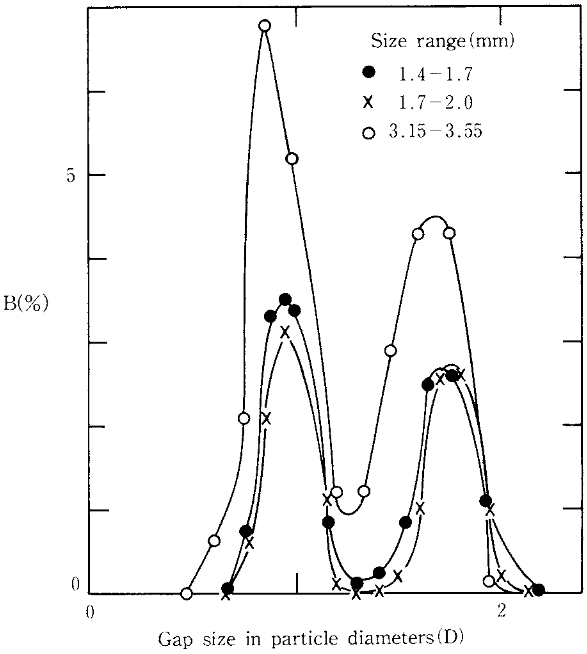

Fig. 3 The attrition of urea at various gap sizes, the latter now expressed as the ratio of gap size to mean initial particle diameter, D.

The minimum breakages listed in column C lie between D=1.10 and 1.32. One might anticipate a minimum with material simply being swept by the blade over a monolayer of particles at the wall.

The second maximum in breakage rate occurs when the dimensionless gap D is 1.6-1.8, slightly less than one particle diameter above that for the first high breakage rate. This second maximum rate is, however, sometimes markedly lower than the first maximum rate which is consistent with the particles forming a structure less prone to promote gripping and hence breakage.

The last column E gives an end point to detectable particle breakage and indicates that the dimensionless gap size giving an end of breakage is approximately independent of material. The absence of breakage in clearances larger than 2-2.2 particle diameters may be ascribed to the ability of the structure, both between the wall and the blade, and in the bulk to reorganise itself. There is thus for this system no significance of the failure zone of, say, ten particle diameters. The inference is that the particles structure can be reorganised to create free space and thereby prevent particle breakage.

A further cone was built having a small glass section within it where the particle motion could be recorded by the use of a video system. This work

Table 1 Gap sizes (mm) and dimensionless gap size (D) for various events in a series of tests on various materials

		A		B		C		D		E	
Gap size for:		Start of Breakage		First High Breakage Rate		Minimum Breakage Rate		Second High Breakage Rate		No Further Breakage	
Material	Size Range (mm)	G (mm)	D (-)	G (mm)	D (-)	G (mm)	D (-)	G (mm)	D (-)	G (mm)	D (-)
Urea	1.4-1.7	0.90	0.58	1.50	0.97	2.05	1.32	2.70	1.74	3.4	2.19
	1.7-2.0	1.20	0.65	1.80	0.97	2.40	1.30	3.30	1.78	4.0	2.16
	3.15-3.55	1.50	0.45	3.0	0.90	4.25	1.27	5.80	1.73	6.60	1.97
Molecular Sieve	1.7-2.0	0.50	0.27	1.50	0.81	2.20	1.19	3.25	1.76	3.90	2.10
	3.15-3.55	1.60	0.48	2.80	0.84	4.15	1.24	6.0	1.79	7.20	2.15
Catalyst	1.4-1.7	0.50	0.32	1.10	0.71	1.70	1.10	2.45	1.58	3.3	2.13
	1.7-2.0	0.50	0.27	1.40	0.76	2.05	1.11	2.90	1.57	3.8	2.05

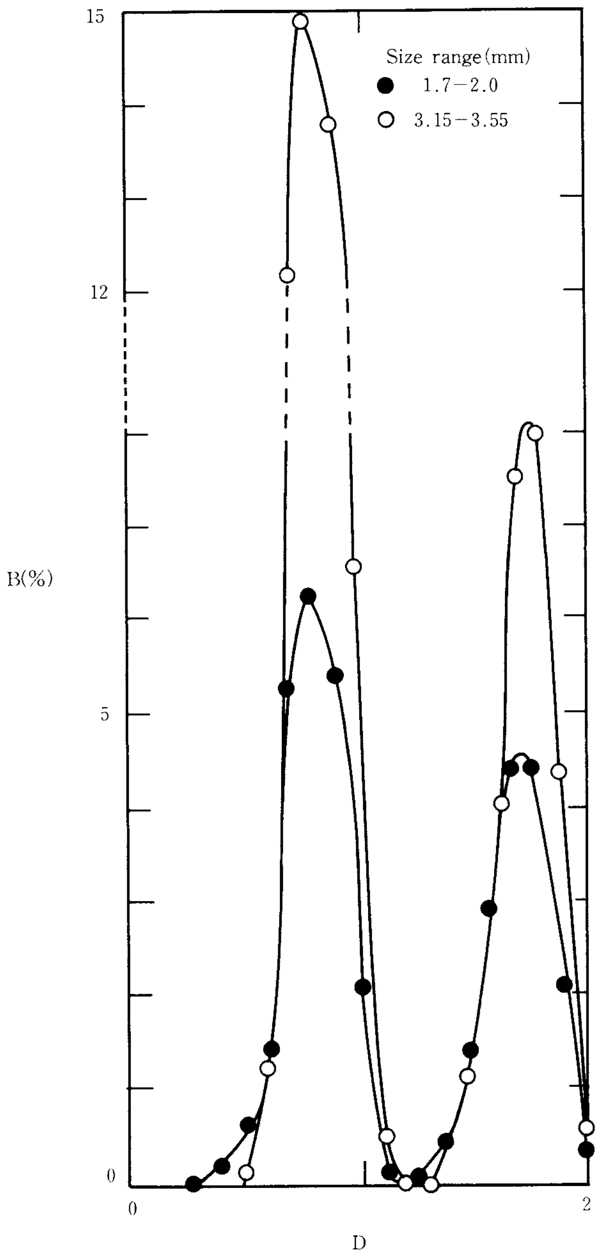

Fig. 4 The attrition of the molecular sieve beads as a function of D.

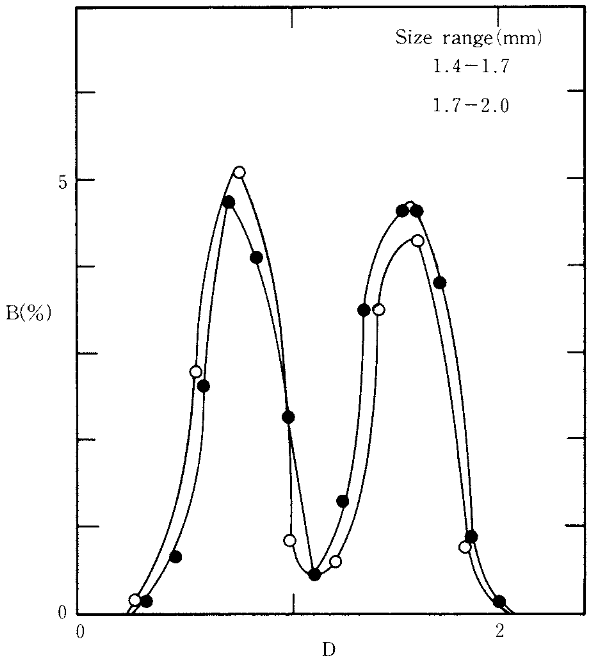

Fig. 5 The attrition of catalyst base as a function of D.

confirmed many of the above points but several other factors became evident. In a number of experiments conducted with 1.7-2.0 mm molecular sieve beads, with a blade tip speed of 0.5 cm/s and a particle velocity of 0.04 cm/s, the observations made as the gap size increased were as follows:

0.1-1.0 mm-A block of particles pushes against the blade as it rotates. These are moved along the wall by the blade with no breakage being apparent. Particles in contact with the lower blade edge move below the blade and are replaced at the top of the blade edge by others. The overall appearance is a block of particles in front of the blade being pushed along the wall with a gradual flux of material from the top to the bottom.

1.1-1.6 mm-Particles are still being pushed by the blade, but now the blade begins to nip a few particles. The space between the blade and wall is largely free of particles. Those few particles being nipped and broken are seen to break and fall immediately to the bottom of the blade via the gap existing between the blade and wall. As more particles are broken, the space begins to fill with broken particles and, at the maximum rate occurring at about 1.6 mm, becomes completely full of material. These broken particles flow from the bottom of the gap into the bulk below. It is possible to see each particle being nipped then breaking under the stress applied by the blade, all this occurring at the blade edge. The broken material then flows out of the breakage zone before it can be nipped again. However if the blade were rotating more quickly or the flow rate slower, broken particles would remain in the breakage zone. Consequently unbroken particles enter the breakage zone less quickly and less breakage takes place.

1.7-2.7 mm-Here the amount of breakage decreased with increased gap size, and particles begin to move under the blade until a state exists at around 2.1 mm where all the particles move under the blade and no breakage is evident. Up to 2.7 mm, no further change is detectable.

2.8-3.3 mm-Again an increase in breakage can be seen corresponding to the second breakage maximum. The particles at the wall, i.e. the first layer do not break, but the particles in the second layer, those directly in contact with the blade, are pushed against the first layer and broken. The fragments then pass into the area of the first layer.

3.3-4.0 mm-When the gap exceeds 3.3 mm, a decrease in particle breakage is observed until no breakage is evident and the particles flow past the blade with no disturbance being observed.

Particle Velocity and Blade Tip Speed

Two further variables of importance are the flow rate of the particles and the blade tip speed.

Figure 6(a) shows an increase in particle breakage for each gap size as the tip speed is increased. Increasing the blade tip speed allows a higher number of particles to come into contact with the blade edge. The two high breakages both show greater attrition, with the first high breakage conditions showing a more rapid increase than the second. **Figure 7(a)** shows the extent of overall attrition as a function of blade tip speed. However, the rate of increase in breakage falls with increased blade tip speed. These data show that the general relationship between breakage and gap size is unaffected by the tip speed.

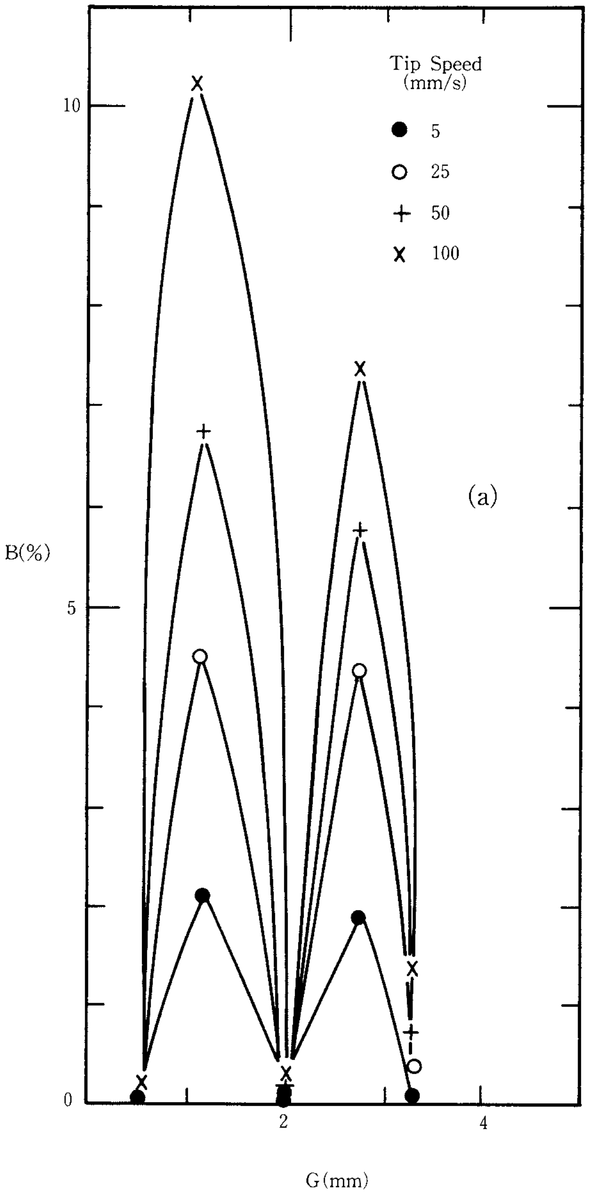

Figure 6(b) relates the breakage to the particle velocity through the cell, demonstrating how higher velocities result in lower percentages in broken material. Particle velocity is here defined as the ratio of the distance from the top of the cone to the top of the blade divided by the time taken for the

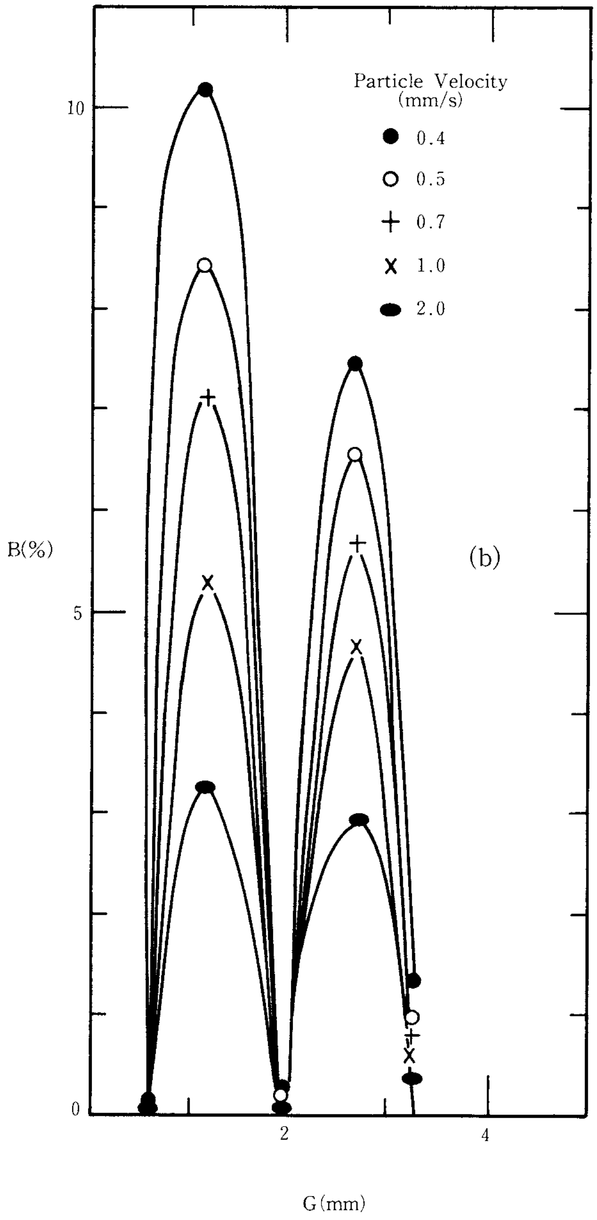

Fig. 6 Attrition of 1.4-1.7 mm molecular sieve beads.
(a) Influence of blade tip speed, t, (b) Influence of particle velocity, V.

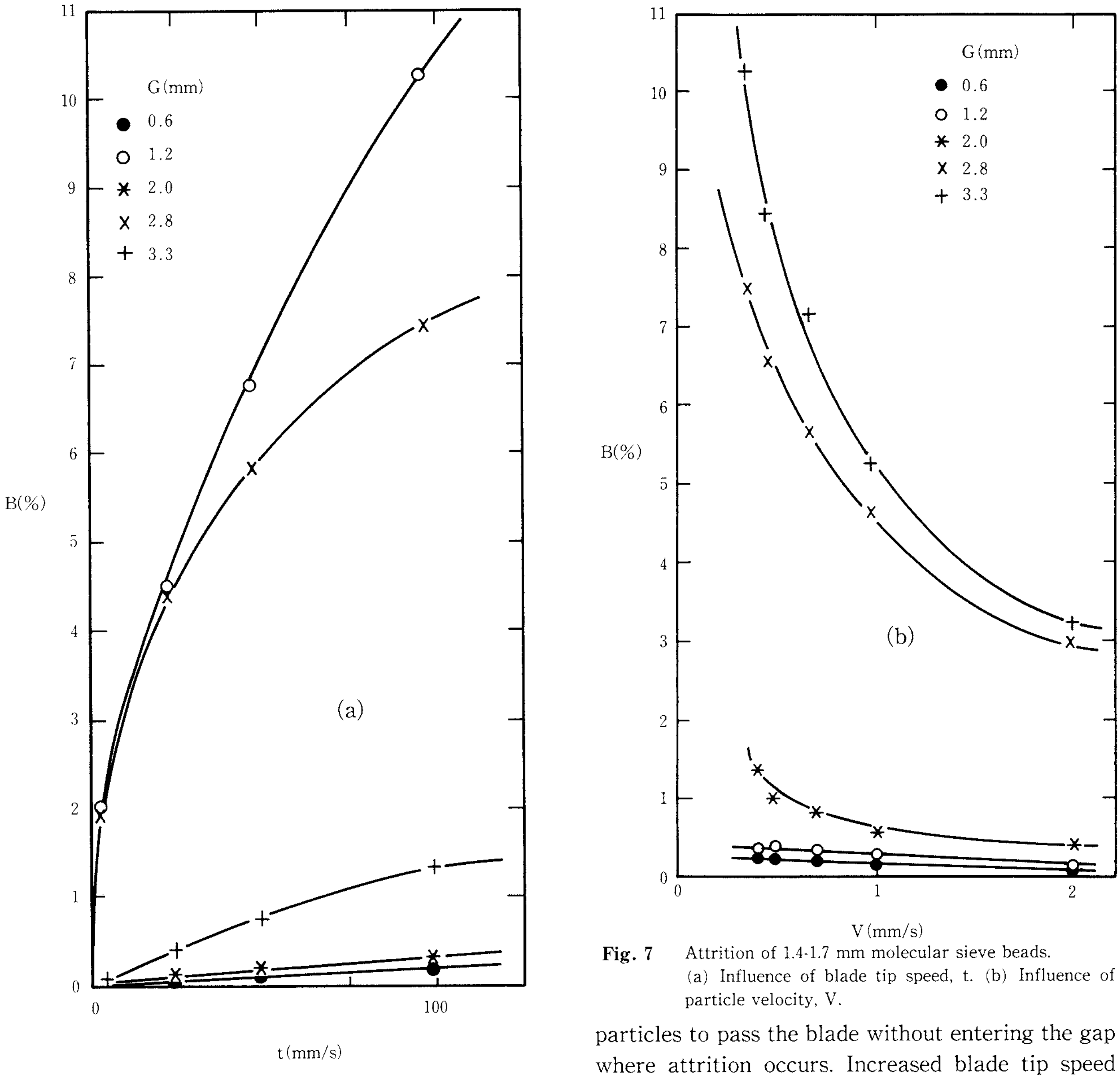

Fig. 7 Attrition of 1.4-1.7 mm molecular sieve beads.
(a) Influence of blade tip speed, t. (b) Influence of particle velocity, V.

free surface to move between these two levels. Reducing the particle velocity through the cell increases the proportion of particles coming into contact with the blade edge. The reduction in breakage rate with increased particle velocity is shown in **Figure 7(b)**. The two high breakages decrease steadily with increased particle velocity. This can be linked to the decrease in the time of the particle in the attrition zone. Lowering the particle velocity slows down the material at the wall, thus bolstering the probability that the blade will nip a particle. These data again show that the general relationships between breakage and gap size are unaffected by the particle velocity.

Despite a rapid increase in breakage as the velocity of the particles is reduced, complete breakage is never achieved as the geometry of the cell allows particles to pass the blade without entering the gap where attrition occurs. Increased blade tip speed increases the probability of breakage. Another phenomenon to consider is the percolation of broken particles through the particles at high breakage. These broken particles may begin to pack in the region of the rotating blade until they fully occupy the breakage region. If this occurs then no further unbroken particles can enter the gap.

Product size distributions

Product size distributions are now reported under the conditions pertaining to **Figures 2-5**. These are summarised in **Figures 8**, **9** and **10** for urea, molecular sieve beads and catalyst respectively. In each plot mass per cent per micron ϕ versus gap size (G) is shown, which is a bar chart distribution. For clarity of presentation, the points have been joined to allow results to be superimposed. ϕ is found by

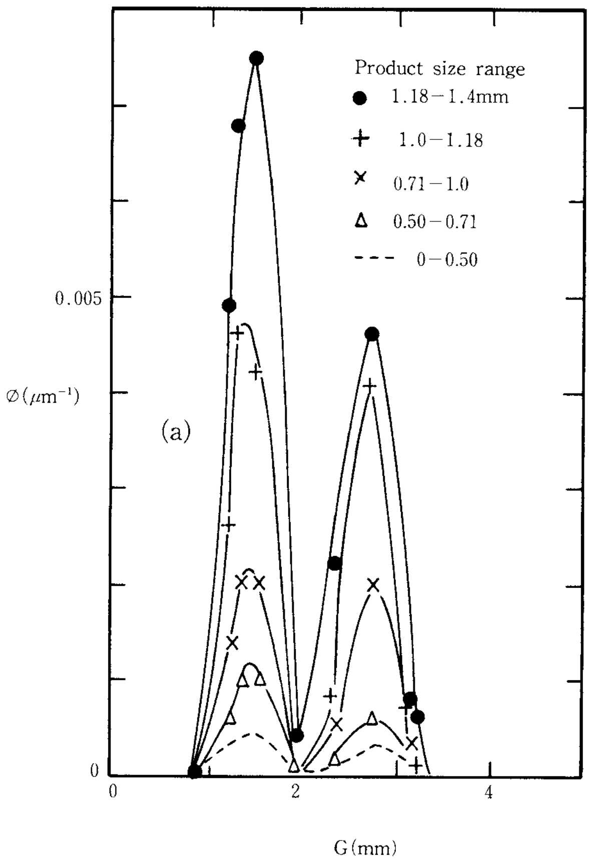

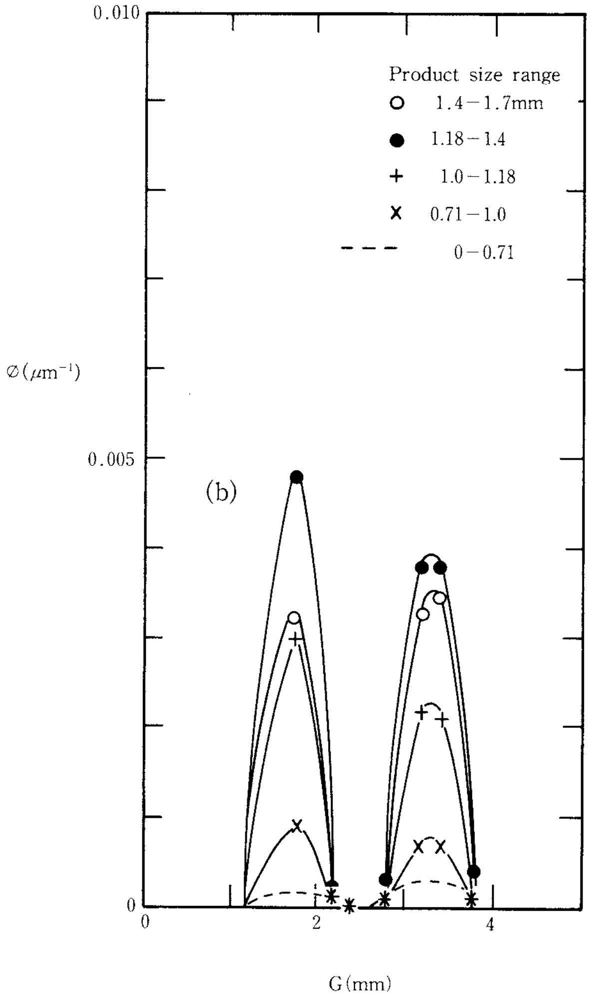

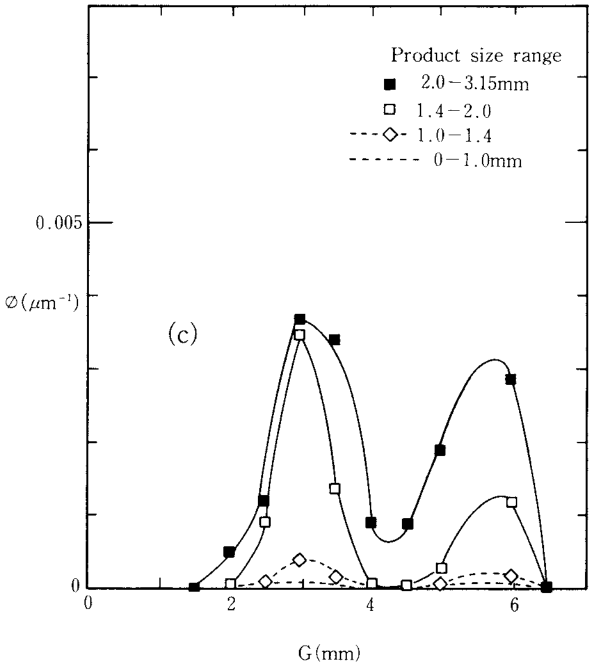

Fig. 8 Attrition product from urea at different gap sizes. Initial size: (a) 1.4-1.7 mm (b) 1.7-2.0 mm (c) 3.15-3.55 mm

considering the mass of product and dividing it by the weight of material of one product size by the size range encompassed by the limits of the sieves.

For urea, the most prominent size fraction is always that directly smaller than the feed material and the proportion of the size fraction decreases as the size of the fraction decreases. There is, however, a significant difference in behaviour linked to initial particle size in that the proportion of fine material from the larger initial particle is much less, whether argued on absolute particle size or relative particle size, than that found with the smaller initial material. The urea particles were constituted of 2 μm crystallites; this length scales does not appear in any of the attrition fragments.

For molecular sieve beads, the larger material (**Figure 9b**) shows the same general relationship as that found for the urea particles, namely a decrease in product amount with a decrease in product size. However the 1.7-2.0 mm material forms more material of intermediate size, the sieve size below the feed material then not being the most prominent. This is an indication that the breakage pattern is sensitive to initial particle size.

For the catalyst, the product size distribution displays more complex behaviour. Thus for 1.4-1.7 mm catalyst, (**Figure 10a**) the size below the top

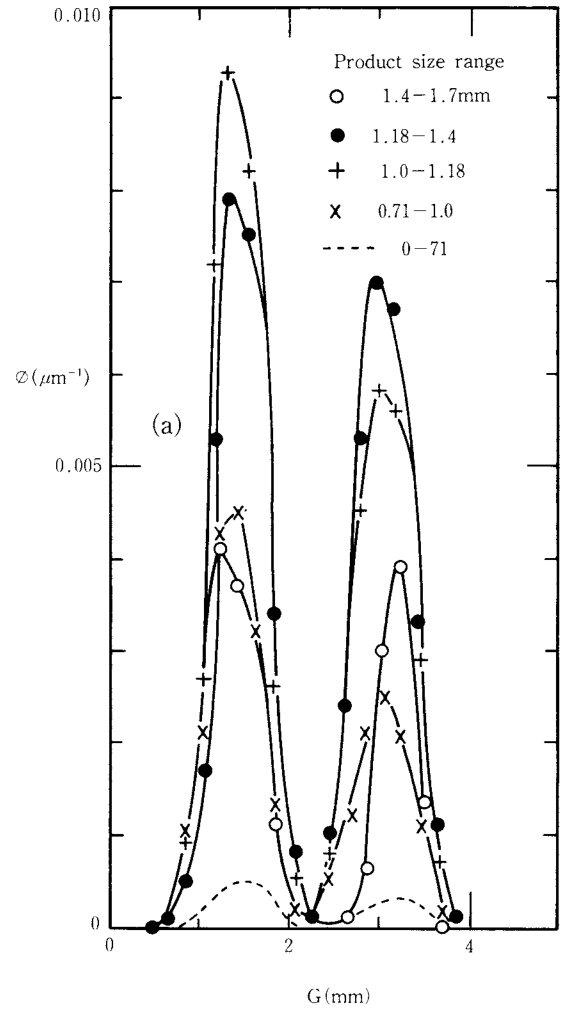

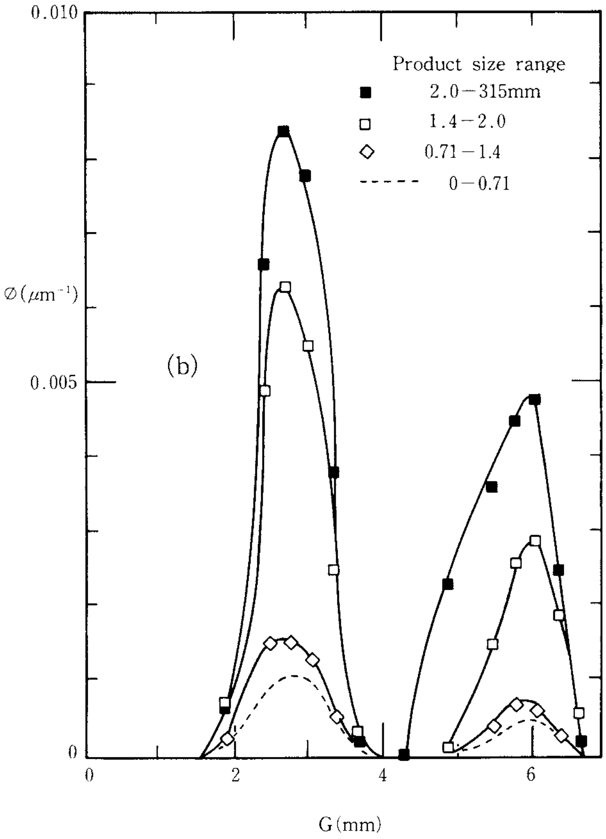

Fig. 9 Attrition product from molecular sieve beads at different gap sizes. Initial size: (a) 1.7-2.0 mm (b) 3.15-3.55 mm

sieve is not dominant in the first breakage peak. Material yet slightly smaller (1.18-1.4 mm) is virtually absent in that peak. Product of size 0.710-1.0 mm is present in abundance and there is a smaller, although appreciable, amount of material of 0-0.5 mm. In the second peak we now find a monotonic decrease in size. Thus the size directly below the initial material is the most prominent; there is still an appreciable proportion of product of size 0-0.5 mm. Related effects occur with the 1.7-2.0 mm initial material but, more strikingly, product of less than 0.5 mm is virtually absent.

Conclusions

A piece of equipment has been designed and built with the purpose of studying attrition in the clearance of a moving blade and wall. The information obtained from these tests is pertinent to a different regime of behaviour from that found in failure zones. Three spherical materials having differing internal structures, urea, catalyst and molecular sieve beads, have been used.

As the gap between the rotating blade and wall was increased, there was initially no breakage but then a maximum breakage rate was produced. The breakage rate then diminished until, at a certain gap size, a second maximum breakage rate was found. A third high breakage rate maximum might be expected, but this was not the case; attrition was not detectable once the gap exceeded 2.2 particle diameters. Similar phenomena were found with all the materials tested. Data from particles of the same type but different size could be presented in dimensionless form. There is an extreme sensitivity on breakage rate of gap size.

The pattern of breakage is somewhat affected by the gap size, the pattern is also affected by the rate of breakage. Consider now the concept of breakage function. This function commonly used to analyse breakage circuits, is that which, operating on an initial feed size distribution, gives the product size distribution. We see that the product size distribution is changed by machine design (the gap size) or an operating variable (the speed). This calls into question the concept of breakage function as found in the literature.

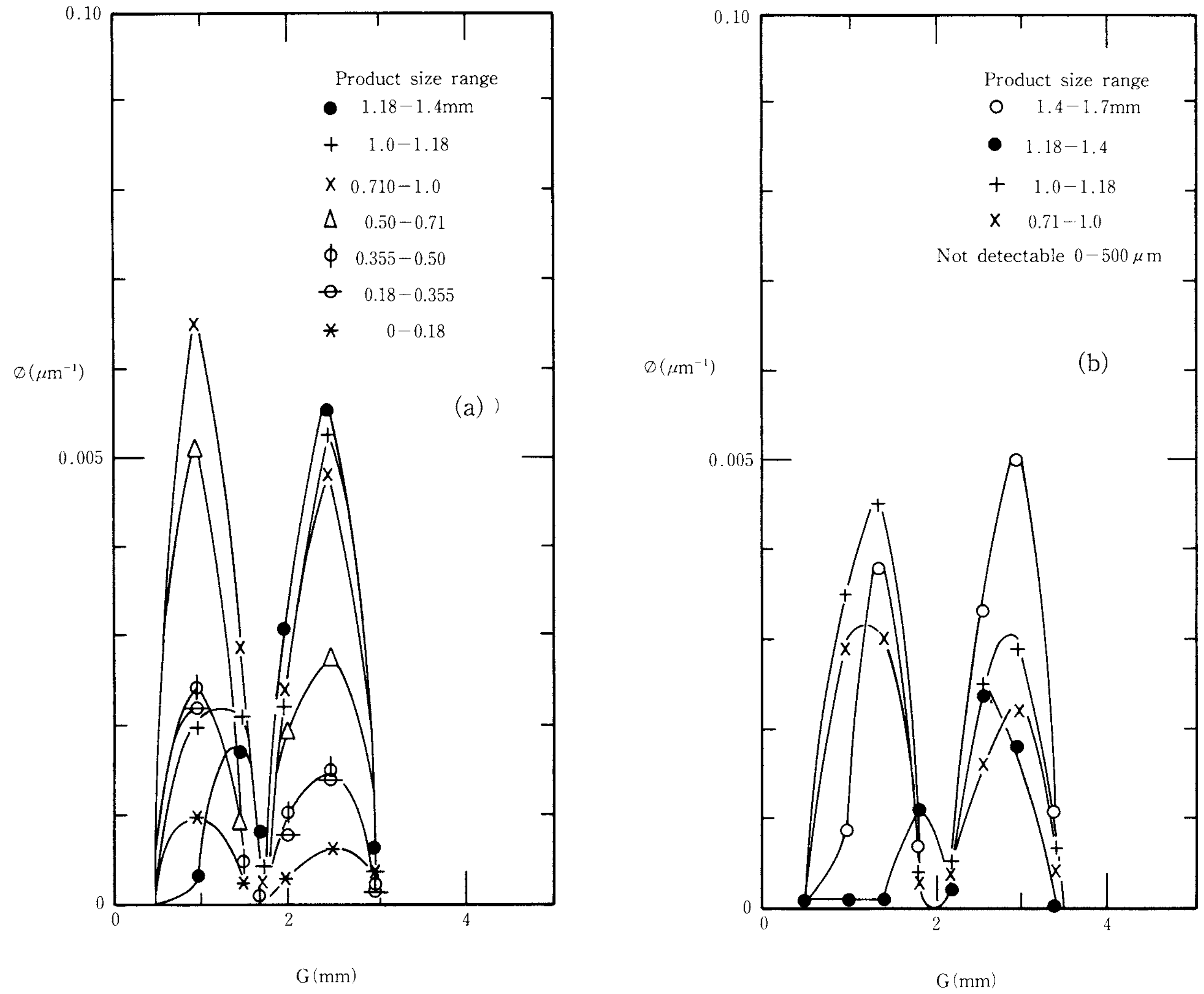

Fig. 10 Attrition product from catalyst base at different gap sizes. Initial size:
(a) 1.4-1.7 mm (b) 1.7-2.0 mm

The cone system was operated at low normal stresses, and it could be said that a system of high stress could alter the breakage. However, it can be argued that the space occupied by the particle in the gap remains constant and it is this which controls attrition. The packing would be little unchanged. If stress is important it is likely to be concerned with how particles flow into the gap as in low normal stress system. Work is required in this area.

We are now seeing the growth of the use of methods to describe inter-particle forces, packing and breakage (7). The use of these to provide information on flow of particles into a gap and the consequent breakage should give a useful comparison with the findings here.

Acknowledgements

The authors thank the International Fine Particle Research Institute and the Engineering and Physical Sciences Research Council for support.

Nomenclature

B : Breakage (percentage of feed mass that is broken) (-)%
D : Dimensionless gap size (gap size/mean initial particle size) (-)
G : Gap size (mm)
t : Blade tip speed (mm/s)
V : Particle velocity (mm/s)
∅ : Mass percent of product per micron $(\mu m)^{-1}$

References

1) Roscoe, K.H.: "The influence of strains in soil mechanics", *Géotechnique*, 1970, 20, 129-170.

2) Bridgwater, J.: "On the width of failure zones", *Géotechnique*, 1980, 30, 533-536.

3) Paramanathan, B.K. and J. Bridgwater, "Attrition of solids-I. Cell development", *Chemical Engineering Sci-*

ence, 1983, 38, 197-206.
4) Paramanathan, B.K. and J. Bridgwater, "Attrition of solids-II. Material behaviour and kinetics of attrition", *Chemical Engineering Science*, 1983, 38, 207-224.
5) Neil, A.U. and J. Bridgwater, "A test for bulk attrition", *Institution of Chemical Engineers Symposium Series*, 1985, 91, 213-226.
6) Neil, A.U. and J. Bridgwater, "Attrition of particulate solids under shear", *Powder Technology*, 1994, 80, 207-219.
7) Ning, Z. and M. Ghadiri, "Computer simulation of attrition of granular solids under shear straining by distinct element analysis", *Proceedings of the 5th World Congress of Chemical Engineering*, 1996, 5, 331-336, AIChE.
8) Bemrose, C.R. and J. Bridgwater, "Powder attrition, a review", *Powder Technology*, 1987, 47, 97-126.

Author's short biography

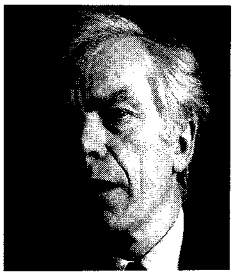

John Bridgwater

Professor Bridgwater is Shell Professor of Chemical Engineering at the University of Cambridge. Previously he was professor at the University of Birmingham where these studies were performed. He is Chairman of the Board of Editors of the journal Chemical Engineering Science and is Chairman of the Organising Committee of the 3rd World Congress in Particle Technology to be held in Brighton, England in July 1998. In 1997-98 he is President of the Institution of Chemical Engineers. His current research interests include powder mixing and the rheology and extrusion of pastes.

C.C. Crutchley

Dr. Crutchley studied Minerals Engineering in the University of Birmingham and then transferred to do a PhD in Chemical Engineering at the same University. Amongst other achievements he is an athlete of some repute-notably in throwing the javelin.

Review

Aerogels - Production, Properties and Applications

T. Burger, A. Emmerling and J. Fricke
Universität Würzburg, Experimentelle Physik II *
M. Weth
Bayerisches Zentrum für Angewandte
Energieforschung e.V (ZAE Bayern) **

Abstract

Aerogels are highly porous sol-gel derived solids. Their properties, which are extremely fascinating as well as very promising for a large number of applications, are due to their nanostructure. Aerogels can be produced from a variety of materials, whereby silica aerogels are the most thoroughly studied ones. Silica aerogels with densities ranging from a few kg/m^3 *to a few hundred* kg/m^3 *have been made as monoliths, in granular form or as powders.*

This paper describes the fundamentals of the sol-gel process, drying techniques and the basic aerogel properties. Special attention is given to their nanostructure and the resultant very low thermal conductivity. Most of the applications so far are based on the thermal, mechanical and optical properties of silica aerogels which are described.

1. History

Aerogels are highly porous sol-gel derived materials. The key to their production was found in 1931, when S.S. Kistler discovered a procedure to remove the liquid from a wet gel without causing shrinkage of the gel[1]. Up to then, the drying of a gel, still embedded in the solvent consisting mainly of alcohol with some water and catalyst, was performed by evaporation of the liquid in air. The occurring liquid-vapor interfaces (**Figure 1**) within the gel network result in capillary tensions that cause considerable shrinkage of the gel due to a partial collapse of the network. The shrinkage continues until the gel structure is strong enough to withstand these forces. The resultant "xerogels" have a remaining porosity of about 50%.

To avoid shrinkage of the gel, the build-up of capillary forces has to be prevented. Kistler's idea was to "replace the liquid with air by some means in which the surface of the liquid is never permitted to recede within the gel"[2]. He was the first to apply "supercritical drying": The aerogel is put in a pressure vessel, an autoclave. Then, the temperature and the pressure are raised above the critical point of the solvent. Since in a supercritical fluid, the liquid and vapor phases become indistinguishable, no capillary forces occur. After releasing the fluid through the outlet valve and subsequent cooling, an aerogel is obtained. Kistler produced SiO_2-Aerogels with densities between 20 and 100 kg/m^3, as well as aerogels of aluminium, ferric, stannic oxides and other materials. Kistler's original method was substainly improved by S.J. Teichner and his coworkers, who investigated the storage of oxygen and rocket propellants in porous materials[3]. A stimulating event was the application of aerogels in Cerenkov detectors in high-energy physics[4]. Today, ultralow-density aerogels with densities as low as 3 kg/m^3 can be prepared[5].

This extremely high porosity in combination with structures in the nanometer region endows aerogels with fascinating properties.

2. Preparation

2.1 Sol-Gel Process

The sol-gel process is the transition of a system of colloidal particles dispersed in a solution into a branched, continuous network which is still embedded in the liquid. Kistler's way to produce silica aerogels was the polycondensation of sodium silicates. Today, the most frequently used method to prepare monolithic aerogels is the hydrolysis and polycondensation of organometallic precursors such as tetramethoxysilane (TMOS)[6,7]. This method allows the convenient variation of reaction parameters. Up to now, aerogels of main group oxides, transition and semimetal oxides, as well as organic

---

* Am Hubland, D-97074 Würzburg, Germany
**Am Hubland, D-97074 Würzburg, Germany
† Received May 12, 1997

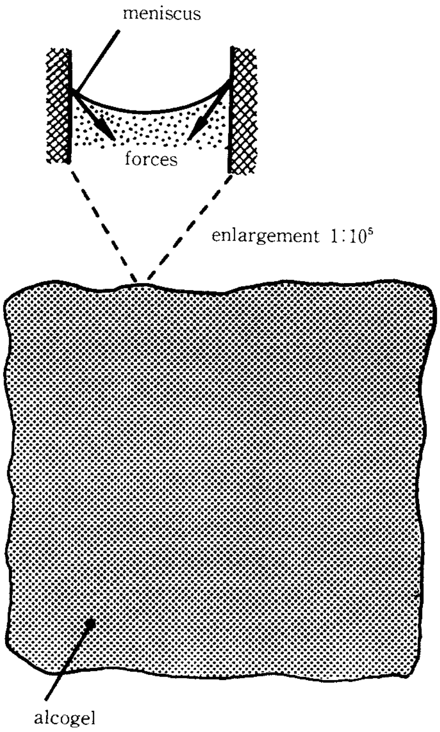

Fig. 1 Upon normal drying, the wet gel experiences strong capillary forces that cause a collapse of the tenuous network.

and carbon aerogels have been produced via the sol-gel route. Since silica aerogels are the most thoroughly studied ones, we mainly consider them in the following.

First, a liquid silicone alcoxide is hydrolysed by addition of water and a catalyst:

$$Si(OR)_4 + 4H_2O \rightarrow Si(OH)_4 + 4ROH$$

where R denotes an alkyl group. Then, the silicic acid condenses by expelling water:

$$2Si(OH)_4 \rightarrow (OH)_3Si\text{-}O\text{-}Si(OH)_3 + H_2O$$

In reality, both reactions proceed more or less simultaneously. Additional ($\equiv$Si-O-Si$\equiv$) linkages are produced by further polycondensation reactions until a tenuous network of SiO_2-tetrahedra exists. The structural growth process can be controlled by the reaction rates of hydrolysis and condensation.

Both reactions are catalysed by acids or bases and therefore exhibit a strong dependence on the pH-values. Hydrolysis, which is additionally influenced by the water-to-alcoxide ratio, shows a minimum of reaction rate at pH = 7, which strongly increases for low and high pH-values. The condensation rate has a minimum at the isoelectric point of silica (pH ≈ 2) but is large under neutral or basic conditions[7,8]. Controlling the amount of catalyst and the temperature, either polymer-like silica chains (under acidic conditions) or comparatively dense, colloidal particles[7] (basic conditions) are obtained. These substructures then aggregate to clusters, which finally build up the gel network (**Figure 2**). The aggregation rate is additionally influenced by the degree of dilution (i.e. the amount of excess alcohol) and is responsible for the final density of the gel. The gel point is reached when a cluster has formed which spans the sample vessel.

Hereafter, during the "aging" phase, the condensation reactions continue and remaining small clusters or sol particles attach to the existing network. Depending on the aging conditions, additional strengthening of the network by dissolution and precipitation, or shrinkage (syneresis) and the expulsion of water may occur.

The sol-gel process allows tailoring nanostructured materials by providing the appropriate reaction parameters. Furthermore, it permits the production of homogeneous multicomponent materials in a controlled fashion.

2.2 Drying

As already mentioned above, the crucial point is to avoid the irreversible collapse of the gel structure. The usual way of doing this is the application of supercritical drying[9]. Therefore, the gel, together with a sufficient amount of solution (e.g. methanol), is placed in a pressure vessel and heated until temperature and pressure have reached the critical point of the solvent. The gel is then immersed in a

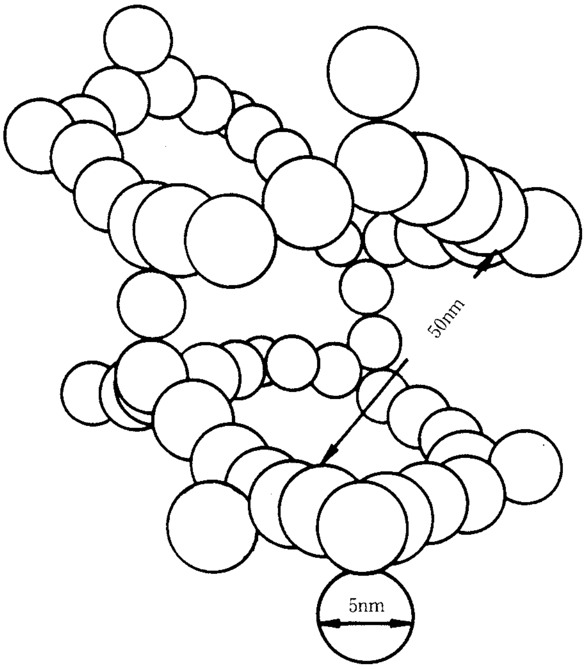

Fig. 2 Sketch of a typical structure of base-catalyzed aerogels with colloidal particles forming a branched network with open porosity.

supercritical fluid which can then be gently blown off. After cooling to ambient conditions, the vessel can be opened.

Two different modifications of the supercritical drying process are usually applied. In the so-called hot-drying process, it is performed with respect to an organic liquid (e.g. methanol or aceton). This requires temperatures of about 250℃ and pressures of about 80 bar. Since the handling of pressurized, flammable liquids is not without risks, a "cold"-drying procedure can be employed as an alternative. Here, the pore liquid is exchanged for a non-flammable liquid with low critical temperature (e.g. carbon dioxide). This is achieved by pressurizing the autoclave with liquid carbon dioxide (typically at 10℃). The gel is then rinsed until all original pore liquid is exchanged. A disadvantage of this method is that a complete solvent exchange may take a considerable time, depending on sample size and pore size distribution.

A different approach to extracting the solvent is subcritical drying. During subcritical drying, menisci develop and thus capillary forces occur (**Figure 1**). The forces increase with decreasing pore width and increasing surface tensions of the solvent. To minimize the gel shrinkage, washing steps are performed to eliminate the smallest pores and to strengthen the network[10] and/or to achieve a chemical modification of the inner surface, e.g. by silylation[11]. These silyl-modified gels contract in the expected way as capillary forces develop. However, when the liquid phase starts to form isolated droplets and surface tension ceases, a "springback" effect is observed: Since neighbouring surface silyl groups are chemically inert and can detach with little activation energy, the gel body is able to re-expand.

An advantage of subcritical drying is that the aerogel production can be performed without an autoclave.

2.3 Modifications

CO_2-dried silica aerogels have a large number of OH groups on their inner surface, which typically measures some hundred m^2/g. For that reason, they are hydrophilic and fracture into submicron-sized SiO_2 clusters if they come in contact with liquids. The same holds for alcohol-dried samples, which are first hydrophobic due to the substitution of OH-by OR-groups during the autoclave process. However, during storage, re-substitution takes place induced by ambient moisture. In terms of disposal this might be advantageous, but for handling and storage reasons, hydrophobic aerogels are preferred. Such aerogels can be made by adding about 20% of methyltrimethoxysilane to the starting precursor[12]. These aerogels float on water for months without uptake of liquid. Subcritically dried silylated aerogels are also hydrophobic.

Another important modification of silica aerogels is the enhancement of their IR-extinction and thus the reduction of radiative heat transfer by adding IR-opacifiers, e.g. carbon black. The opacification can be achieved either by adding finely dispersed carbon black particles to the sol-gel solution[13] or by pyrolysis of organic groups which are integrated in the inorganic SiO_2 network[14].

Very exciting is the modification of resorcinol formaldehyde (RF) aerogels. If pyrolysed at about 1000℃, they are transformed into highly porous electrically conductive carbon aerogels[15].

3. Characterization and Physical Properties

3.1 Structural Investigations

Many methods have been used to investigate the structure of aerogels. By using the NMR technique, the extent and kinetics of hydrolysis and condensation during gelation can be studied[16]. Thermoporometry can be used to determine the pore size distribution of the wet gel. Nitrogen sorption measurements have been used to determine the specific surface area. However, since only pores up to about 50 nm are detected, the determined pore volumes are much lower than the expected values[17], especially for densities below 200 kg/m^3. Furthermore, the condensation and surface tension of LN_2 has been shown to destructively change the structure and the mesopore size distribution[18].

Helium pycnometry is used to determine the skeletal volume and thus the skeletal density of silica aerogels. The skeletal densities were found in the range of 1700 to 2100 kg/m^3[3,19]. This would correspond to a porosity of the aerogel backbone in the order of 5% to 20%, but it could also be explained by different bond lengths compared to vitreous silica.

Mercury porometry to determine the pore volume cannot be applied to aerogels. Due to the surface tension of Hg and the low compressive modulus of aerogels, only compression of the tenuous body as a whole occurs instead of penetration[18].

Additionally, TEM studies have been performed[20]. This method might cause destruction (sintering) of the sample and only a two-dimensional projection can be obtained.

3.2 Small Angle X-Ray Scattering (SAXS)

The most powerful and reliable methods to probe aerogel structures are scattering techniques[21]. The sample is irradiated by particles (neutrons) or photons (light, X-rays) and the characteristics of the detected scattering pattern can be related to structural features. The typical arrangement of a scattering experiment is shown in **Figure 3**. In the case of x-ray scattering, the amount of scattered intensity is due to inhomogeneities in the electron (or nucleon) density of the porous body. For a statistically isotropic structure, the scattered intensity depends solely on the absolute value of the scattering vector $q=(4\pi/\lambda)\sin(\theta/2)$, where θ denotes the scattering angle and λ the wavelength. Since the structures in real space and the scattered intensity observed in q-space are connected by a Fourier transformation, a reciprocal behaviour is observed: large structural features appear at small q values and vice versa. With expected structural sizes of 1 to 100 nm and typical x-ray wavelengths of 1 to 2 Å, the scattering intensities have to be detected at small scattering angles (0.01° to 10°), i. e. close to the primary beam. This is why the technique is called small-angle x-ray scattering.

A typical scattering curve of an aerogel consisting of a particle network is shown in **Figure 4**. The characteristics of the scattering pattern can be related to the different structural features on the respective length scales[22]. At smallest scattering vectors, which correspond to a length scale much larger than the inhomogeneities, a constant scattering intensity is observed. With increasing q, a length scale is reached where the largest inhomogeneities (pores or clusters of size R) are resolved. Subsequently, a more or less extended linear decay is observed in the double-logarithmic plot. This is due to the branched appearance of the gel and may be explained by a fractal network. The intensity drops as $I \propto q^{-D}$, where the exponent D is called the mass fractal dimension[23]. A second crossover is observed at $q \approx 1/r$, when the scale approaches the particle size r. Upon further increase of the scattering vector, the scattering becomes sensitive to the nature of the particle surface. Again, a power-law behaviour is observed: $I \propto q^{D_s-6}$, where D_s is called surface fractal dimension. Smooth surfaces with $D_s=2$ lead to a decay proportional to q^{-4}; this is called Porod's law[24]. In this case, the specific surface area and the skeletal density can be calculated. Fractally rough surfaces cause a less steep decay with $D_s=2\text{-}3$[25]. A further increase of q resolves the structures on the molecular scale, where broadened Bragg peaks due to the partially ordered substructure are observed.

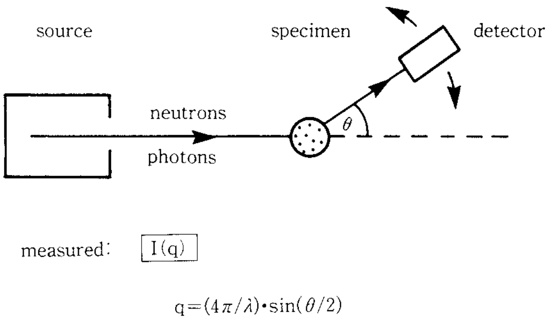

Fig. 3 Schematic representation of a scattering experiment.

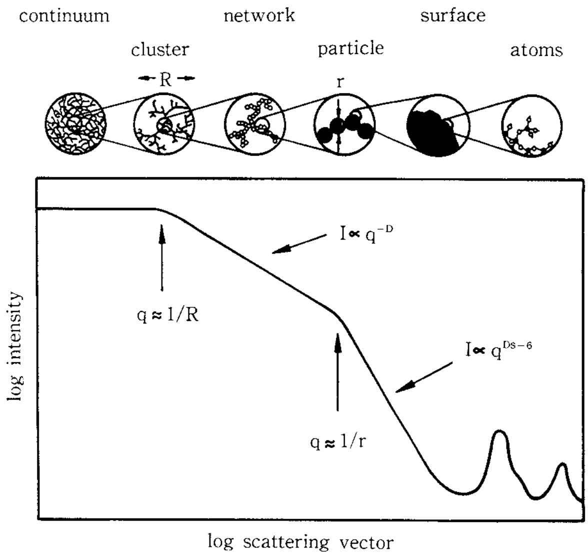

Fig. 4 Typical small angle scattering intensity for a particle network such as aerogel.

X-ray scattering curves of three different TMOS silica aerogels, catalysed at pH=9, 11 and 13 are shown in **Figure 5**[26]. All specimens had similar macroscopic densities ($\rho \approx 230$ kg/m^3). The scattering vector q, at which the scattering intensities become independent of q, is shifted to lower values for decreasing pH-values. This corresponds to an increasing cluster size R (from about 8 to 15 nm) with decreasing pH-values. Similarly, the particle radii r obtained from these scattering curves increase from approximately 1 to 3 nm[26]. For a comparison, we have included the x-ray scattering intensity of a fumed silica powder in **Figure 5**. The fumed silica powder has been pressed to a tablet with a density of 300 kg/m^3, which is comparable to the density of the presented aerogel samples. The fumed silica also shows a fractal network structure

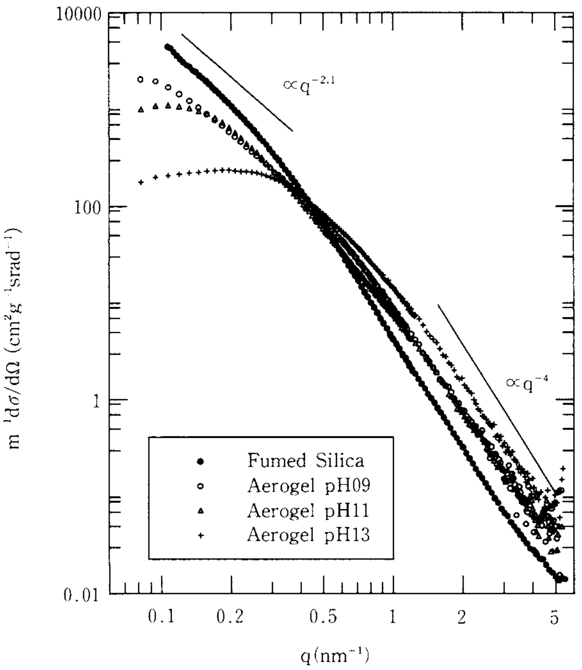

Fig. 5 SAXS patterns of three differently catalyzed aerogels of the same apparent density compared to the SAXS pattern of fumed silica.

consisting of smooth primary particles of about 10 nm (crossover at $q=0.3\ nm^{-1}$), which is about a factor of 10 larger than in the presented aerogels. The cluster size of the fumed silica could not be determined as the scattering curve still increases even at the smallest scattering vectors available. An extension of the measurement range is possible by using ultra small-angle x-ray scattering (USAXS)[26].

3.3 Optical and Infrared-Optical Properties

Silica aerogels are, if properly made, highly transparent in the visible spectral region[27]. At 630 nm, the specific extinction coefficient e_{VIS} is in the order of 0.1 m^2/kg[28]. For an aerogel with a density of $\rho=100$ kg/m^3, this corresponds to a photon mean free path of $l_{ph}=1/(e_{VIS}\cdot\rho)\approx0.1$ m at 630 nm. Due to the pore structures in the order of 1 to 100 nm, strong Rayleigh scattering is observed within the blue and ultraviolet spectral region. This leads to a bluish appearance of aerogels if viewed against a dark background. The extraction of particle diameters from optical transmission measurements is non-trivial since multiple scattering has to be taken into account.

In the infrared region, silica aerogels show besides the absorptions bands of SiO_2, additional strong absorption of water, which is chemi-or physisorbed on the huge inner surface. Specific extinction spectra for aerogels with varying water content are shown in **Figure 6**. Typically, the specific extinction is smaller than 10 m^2/kg for wavelengths below 7 μm and above 30 μm. Between 7 μm and 25 μm, a specific extinction above 100 m^2/kg is observed. Compared with the specific extinction in the visible region, a ratio of $e_{IR}/e_{VIS}>100$ is obtained. Thus, silica aerogels can be considered as transparent insulating materials that efficiently transmit solar light, but strongly block 300 K thermal infrared radiation. Integration of carbon black into the aerogel increases its IR-extinction dramatically, however, it also renders the material opaque in the visible.

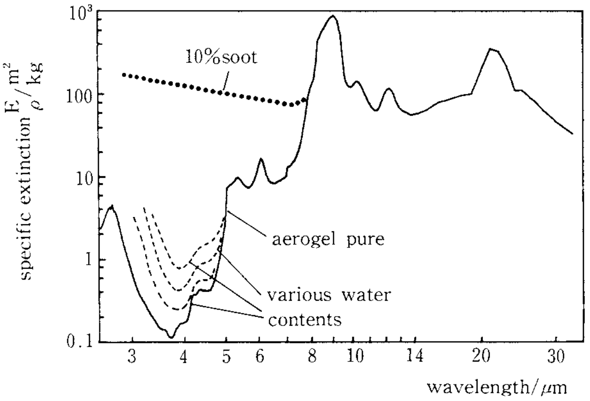

Fig. 6 Spectral specific extinction for aerogel with different water contents and for an opacified sample with 10% carbon black.

Typical SiO_2-aerogels show practically no refraction and no reflection, which is due to the fact that about 99% of their volume is air. For low-density aerogels, the correlation between the index of refraction n and the density ρ is $n-1\approx2.1\cdot10^{-4}\ \rho/(kg\cdot m^{-3})$[29], thus for $\rho\approx100\ kg\cdot m^{-3}$, one expects $n\approx1.02$.

3.4 Thermal Properties

The thermal transport in pure and opacified aerogels has been studied extensively. In principle, all three heat transfer mechanisms, i.e. gaseous and solid conduction as well as radiative transport, occur[30]. Additionally, various coupling phenomena between these heat transfer modes have been investigated[31,32].

3.4.1 Monolithic Aerogels

Due to aerogel pore sizes in the order of 50 to 100 nm and a mean free path of air at 1 bar of 70 nm, the gaseous heat conduction is partially suppressed. Evacuation to about 20 mbar is sufficient to fully eliminate gaseous conduction.

Solid conductivity λ_s is drastically reduced with respect to vitreous silica and has been found to scale with the density ρ according to[33,34]:

$$\lambda_s \propto \rho^{\gamma}, \text{ with } \gamma \approx 1.2 \dots 1.8$$

λ_s also depends on the connectivity of the network[35] and can thus be influenced by the preparation conditions.

The radiative heat transfer in aerogels is governed by their infrared absorption (see **Figure 6**). At ambient and elevated temperatures, a significant part of the thermal radiation is transmitted through the aerogel due to its relatively low specific extinction below 7 μm. As mentioned above, the radiative heat transfer can be reduced drastically if an opacifier (e.g. carbon black) is added to the silica sol and thus integrated into the gel. As can be seen in **Figure 6**, the specific extinction is strongly increased, especially below 7 μm. The radiative heat transfer in opacified aerogels can be regarded as a diffusion phenomenon. The radiative conductivity λ_r in this case is given by:

$$\lambda_r = (16\,\sigma \cdot n^2 \cdot T^3)/(3 \cdot E)_1$$

where T is the absolute temperature, n the index of refraction, σ the Stefan-Boltzmann constant and E the infrared extinction, which is related to the specific extinction $e_{IR} = E/\rho$. For $\rho = 100$ kg/m^3 and $e_{IR} = 100$ m^2/kg, one obtains $E = 10^4$ m^{-1} which corresponds to a photon mean free path $1/E$ of 10^{-4} m. Opacified aerogels with a thickness of about 0.01 m can then be considered as being optically thick. The resultant radiative conductivity at 300 K is only 0.001 W/(m·K).

The total thermal conductivity of an opacified monolitic SiO_2-aerogel of density 120 kg/m^3 is about 0.013 W/(m·K) at 300 K[36]. The contribution of the solid conduction is about 0.005 W/(m·K) and of the gaseous conduction 0.007 W/(m·K).

3.4.2 Powdery and Granular Aerogels

In powdered aerogel, the network structure which is responsible for the solid heat conduction exists only within the grain boundaries. The thermal contact resistances between the grains then cause a reduction in solid conductivity of the aerogel powder to about $\lambda_s = 0.001$ to 0.002 W/(m·K), assuming an external load of 1 bar on the powder bed. On the other hand, due to the intergranular voids, the gaseous conductivity λ_g is considerably increased to about $\lambda_s = 0.015$ W/(m·K). To suppress gaseous thermal transport, powdery aerogel fills have to be evacuated below 1 mbar.

The radiative transfer depends on the grain/void sizes ϕ_g and their ratio to the mean free path of the photons l_{ph}, which is in the order of 10^{-4} m for opacified aerogels. If $\phi_g \ll l_{ph}$, the photons "see" a homogeneous medium and are absorbed over small distances. In the case $\phi_g \gg l_{ph}$, the photons preferentially travel in the intergranular voids and the attenuation of the radiative flux is thus small.

The total thermal conductivity (**Figure 7**) of aerogel powders in air is below 0.020 W/(m·K) and can be as low as 0.003 W/(m·K) if they are evacuated. For granular aerogels, the measured conductivities are considerably higher[32].

3.5 Elastomechanical Properties

Due to the high porosity of the gels, the longitudinal sound velocity v_ℓ can be as low as 20 m/s[37] for a density of 5 kg/m^3 (**Figure 8**). Young's modulus Y for such low density aerogels is in the order of 10^4 N/m^2, i.e. about 6 orders of magnitude smaller than for vitreous silica. Generally, a scaling behaviour of v_ℓ and Y with the aerogel density is obser-

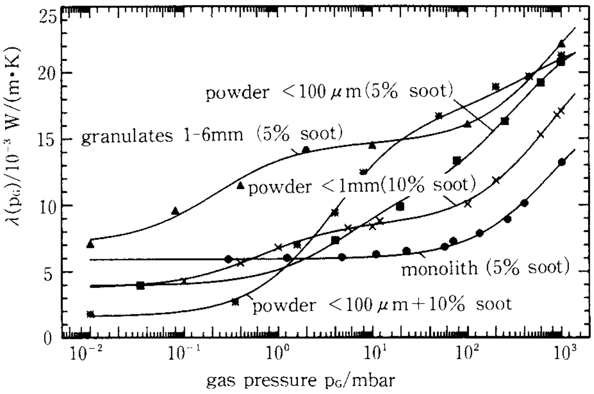

Fig. 7 Thermal conductivities of granular and powdered silica aerogels laced with carbon black as a function of air pressure.

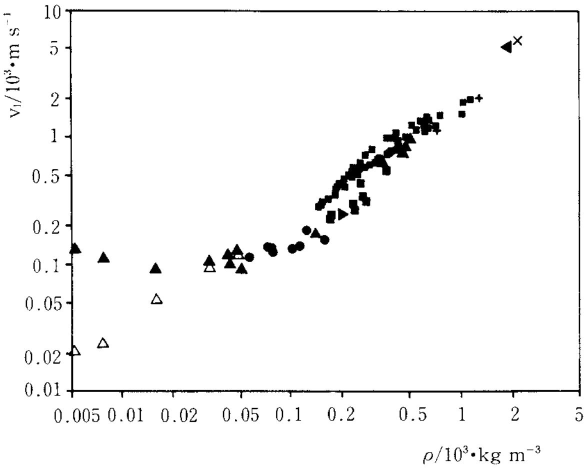

Fig. 8 Longitudinal sound velocity (v_ℓ) of porous systems versus density. Vitreous silica (x); opal (◀); xerogels for drying purposes (+) and silica aerogels of different density (ρ) produced at LLNL (Livermore) (▲); Airglass (Staffanstorp) (■); BASF (Ludwigshaven) (▶) and DESY (Hamburg) (●); open triangles are for evacuated aerogels; sintered aerogels (▪) generally display the largest sound velocities for a given density.

ved[37]:

$$v_\ell \propto \rho^\alpha, \text{ with } \alpha \approx 1.3$$
$$Y \propto \rho^\beta, \text{ with } \beta \approx 3.6$$

These scaling laws can either be explained in terms of percolation theory[38,39], or as a result of the fractal network structure[35]. The considerable deviations of the elastic properties for a given density are due to the degree of connectivity on the nanometer scale, resulting from different preparation conditions or sintering.

Additionally, the shear and rupture moduli display scaling with the density, whereas the Poisson ratio ($\mu \approx 0.22$) is independent of density.

4. Applications

All aerogel applications make use of their high porosity and nanostructure, which are responsible for the small index of refraction, the small Young's modulus, the huge inner surface and the small thermal conductivity. In some applications, a high optical transparency is also required. For carbon aerogels, the pronounced electrical conductivity is of importance.

4.1 Monolithic SiO_2-Aerogels

Most of the monolithic aerogels produced to date have been used in Cerenkov detectors[4]. For the detection of fast pions, kaons or photons, a medium with refractive index $n \approx 1$ is required. Aerogels can be made with $n \approx 1.005$ to $n \approx 1.1$, which corresponds to densities from about 20 to 500 kg/m^3 and thus happen to fit into the range of n-values that cannot be covered by compressed gases or liquids.

Also, the use of highly transparent aerogels sheets in windows was once considered feasible[40]. However, since the production of large flat crack-free and transparent aerogel sheets is extremely difficult and expensive, this application does not seem very realistic today.

4.2 Granular and Powdery SiO_2-Aerogels

4.2.1 Transparent Thermal Insulation

Studies have shown[30] that the thermal resistance and solar transmittance of granular silica aerogel fills or hot-pressed aerogel plates are sufficiently high to allow their application in transparent insulations (**Figure 9**). Aerogels for mass applications have to be cheap and thus only waterglass as a precursor can be used. The aerogel is introduced between two glass panes, and the solar radiation which passes through the aerogel/glass layer is absorbed by a black surface. The efficient thermal insulation of the aerogel fill cuts heat losses, and most of the produced thermal energy is available for heating purposes. To prevent overheating, especially during the summer months, a shading device is necessary. Another problem, the settling of the granular fill under atmospheric pressure changes, can be overcome by a partial evacuation.

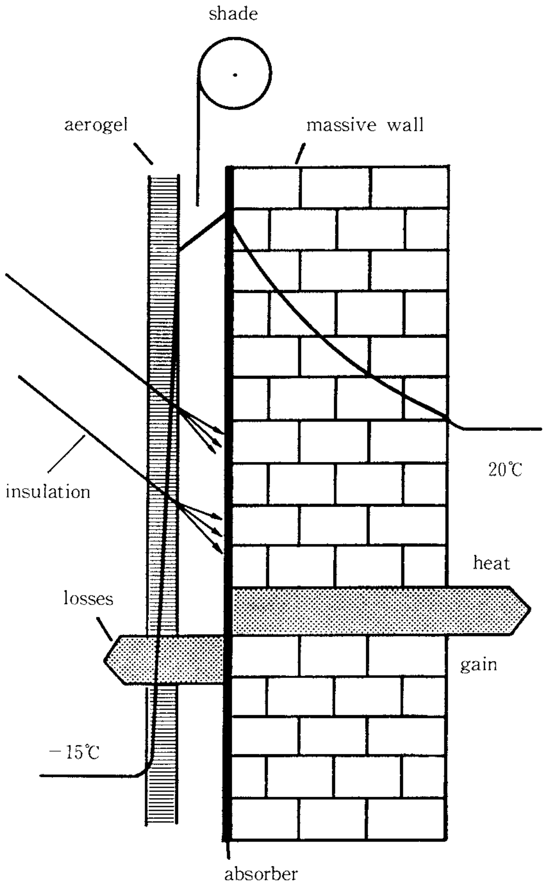

Fig. 9 Transparent insulation (TI) is installed in front of a massive, blackpainted wall. TI consists of granular silica aerogel between two protective glass panes. The solar radiation transmitted through the TI is absorbed by the black surface and most of the produced heat is transferred into the building, only little heat is lost. To prevent overheating, a shading device is necessary.

4.2.2 Opacified SiO_2-Aerogel as Thermal Insulating Materials

A very promising idea is the application of opacified granular or powdered aerogels as a substitute for glass fibres or foams in thermal insulations, e.g. for refrigerators or heat storage systems.

Recently, a thermal phase-change storage system, which uses aerogel as a superinsulating layer, was developed by BMW and Längerer & Reich in Germany[41]. The heat (700 Wh) stored in the system can be used to heat the cold motor, to warm up the passenger cell or to defrost the windscreen (**Figure**

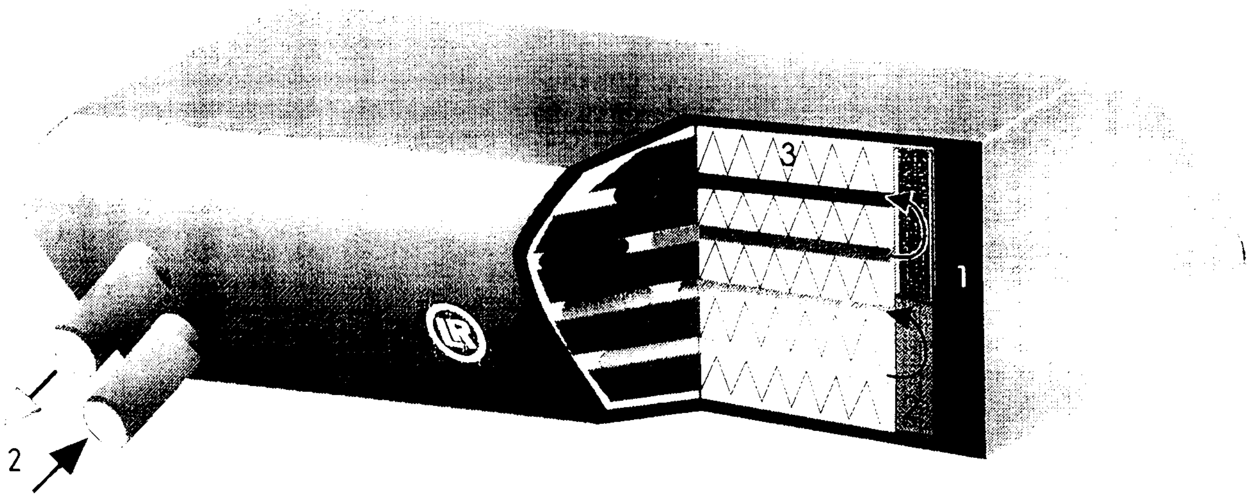

Fig. 10 Aerogel-superinsulated phase change heat storage tank developed by Längerer & Reich/Germany.

10). The evacuated aerogel insulation has a thickness of only 10 mm with an effective conductivity of 0.003 W/(m·K), which results in total heat losses of about 6 Wh/h. The phase-change medium is an eutectic salt mixture of 90 weight % magnesium nitrate-hexahydrate and 10 weight % lithium-nitrate.

One considerable advantage of powdery aerogels compared with micron-sized fumed or precipitated silicas are the better free-flow properties of aerogel powders especially when handled in vacuum. In **Figure 11**, the free-flow properties of an aerogel powder are compared with the free-flow properties of two different precipitated silicas ($d_{50} \approx 50$ μm and $d_{50} \approx 5$ μm) at approximately 1 mbar. The curves were obtained by measuring the mass flow through a hopper which was placed in a vacuum chamber.

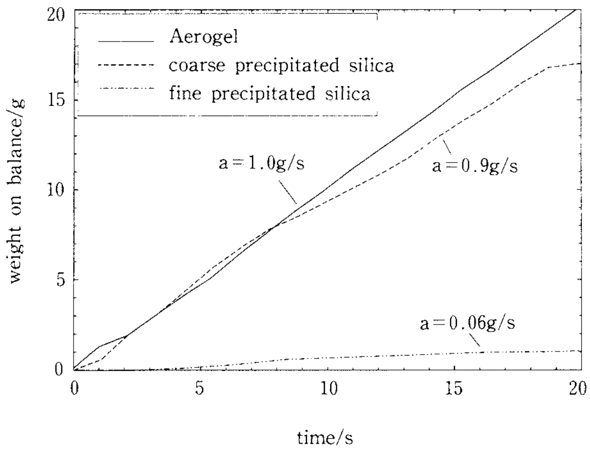

Fig. 11 Mass free flow of aerogel powder and two different precipitated silicas ($d_{50} \approx 50$ μm and $d_{50} \approx 5$ μm).

To ensure a mass flow even for powders with bad free-flow properties, the hopper is additionally equipped with a stirring device. As **Figure 11** shows, the mass flow of the aerogel and the coarse precipitated silica are comparable, however, the wiggles in the precipitated silica data indicate less favorable free-flow properties compared with the aerogel. In addition, the thermal conductivity of the coarse precipitated silica is larger than that of aerogel. This is due to the higher density of the precipitated silica particles. The thermal conductivity of the fine precipitated silica is comparable to the aerogel powder, but it has less favorable free-flow properties.

4.2.3 Miscellaneous

There are many other interesting applications of aerogels which have not been discussed so far, some of which are listed below:

1. Due to their nanostructure and large internal surface, they can be used as gas filters[42] or as substrates for catalytic materials[43].
2. Small, high-velocity particles in space can be "softly" captured by low density aerogels[44].
3. Due to their thermal stability, silica aerogels are used as transparent moulds for melt casting[45].
4. Aerogels can be used for acoustic impedance matching layers in ultrasonic transducers[46].
5. Last but not least, carbon aerogels are promising as electrodes in electrical supercapacitors[47] (**Figure 12**), which have especially large power densities.

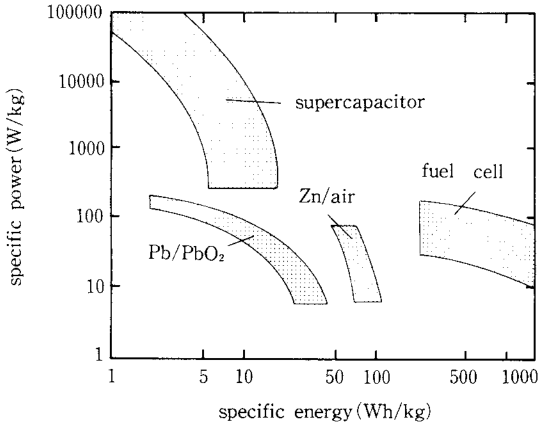

Fig. 12 Mass specific power versus mass specific energy for different energy storage and conversion systems.

5. Nomenclature

a	: mass flow	(kg/s)
D	: mass fractal dimension	(-)
D_s	: surface fractal dimension	(-)
d_{50}	: median particle diameter	(m)
E	: infrared extinction	(1/m)
e_{VIS}	: specific extinction coefficient at 630 nm	(m^2/kg)
e_{IR}	: specific extinction coefficient in the IR-region	(m^2/kg)
k	: heat transfer coefficient	(W/(m^{2}K^2))
l_{ph}	: photon mean free path	(m)
n	: refractive index	(-)
q	: scattering vector	(1/m)
R	: cluster size	(m)
r	: particle size	(m)
T	: temperature	(K)
v_ℓ	: sound velocity	(m/s)
Y	: Young's modulus	(N/m^2)
α,β,γ	: scaling constants	(-)
ϕ_g	: grain/void size	(m)
λ	: wavelength	(m)
λ_g	: gaseous thermal conductivity	(W/(mK))
λ_r	: radiative conductivity	(W/(mK))
λ_s	: solid thermal conductivity	(W/(mK))
μ	: Poisson ratio	(-)
θ	: scattering angle	(°)
ρ	: density	(kg/m^3)
σ	: Stefan Boltzmann constant	(W/(m^{2}K^4))
$d\sigma/d\Omega$	: mass specific cross section	(m^2/(kg srad))

6. References

1) Kistler, S.S.: Coherent Expanded Aerogels and Jellies, Nature (London), 127 (1931) 741.
2) Kistler, S.S.: Coherent Expanded Aerogels, J. Phys. Chem., 34 (1932) 52.
3) Nicolaon, G.A. and Teichner, S.J.: Preparation of Silica Aerogels from Methylorthsilicate in an Alcoholic Medium, and Their Properties, Bull. Soc. Chim. Fr., (1968) 1906.
4) Cantin, M.; Casse, M.; Koch, L.; Jouan, R.; Mestran, P.; Roussel, D.; Bonnin, F.; Moutel, J. and Teichner, S.J.: Silica Aerogels Used as Cerenkov Radiators, Nucl. Instrum. Meth., 118 (1974) 177.
5) Tillotson, T.M. and Hrubesh, L.W.: Transparent Ultralow-Density Silica Aerogels Prepared by a Two-Step Sol-Gel Process, J. Non-Cryst. Solids, 145 (1992) 44.
6) Aegerter, M.A.; Jalelicci, Jr.M.; Souza, D.F. and Zanotto, E.D.: Sol-Gel, Science and Technology, World Scientific, Singapore (1989).
7) Brinker, C.J. and Scherer, G.W.: Sol-Gel Science, Academic Press, Boston (1990).
8) Schmidt, H. and Scholze, H.: The Sol-Gel Process for Non-Metallic Inorganic Materials, in: Fricke, J.: Aerogels, Springer Proc. Phys. 6, Springer Verlag, Heidelberg (1986), 49.
9) Moses, J.M.; Willey, R.J. and Rouan, S. J.: Development and Processing of Aerogels in a Windowed Autoclave, Non-Cryst. Solids, 145 (1992), 41.
10) Einarsrud, M.A. and Haereid, S. Patent WO 92/20623
11) Smith, D.M.; Deshpande, R. and Brinker, C.J.: Preparation of Low-Density Aerogels at Ambient Pressures, Mat. Res. Soc. Symp. Proc. 271 (1992), 567.
12) Schwertfeger, F.; Glaubitt, W. and Schuster, U.: Hydrophobic Aerogels from Si(OMe)$_4$/MeSi(OMe)$_3$ Mixtures, J. Non-Cryst. Solids 145 (1992), 85.
13) Fricke, J.; Arduini-Schuster, M.C.; Büttner, D.; Ebert, H. P.; Heinemann, U.; Hetfleisch, J.; Hümmer, E.; Kuhn, J. and Lu, X.: Opaque Silica Aerogel Insulations as Substitutes for Polyurethane (PU) Foam, Thermal Conductivity 21, Eds. J. Cremer and H. A. Fine, Plenum New York (1990), 235.
14) Schwertfeger, F.; Kuhn, J.; Bock, V.; Arduini-Schuster, M.C.; Seyfried, E.; Schubert, U. and Fricke, J.: Infrared Opacification of Organically Modified SiO$_2$-Aerogels via Pyrolysis, Thermal Conductivity 22, Ed. T. W. Tong, Technomic Lancaster (1994), 589.
15) Pekala, R.W.: Aerogels and Xerogels from Organic Precursors, J. Mater. Sci. 24 (1989), 3221.
16) Devreux, F.; Poilot, J.P.; Chaput, F. and Sapoval, B.: NMR Determination of the Fractal Dimension in Silica Arogels, Phys. Rev. Lett., 65 (1990), 614.
17) Schuck, G.; Dietrich, W. and Fricke, J.: Pore Size Distribution of Silica Systems, in: Fricke, J.: Aerogels, Springer Proc. Phys. 6, Springer Verlag, Heidelberg (1986), 148.
18) Scherer, G.W.; Smith, D.M. and Stein, D.: Deformation of Aerogels during Characterization, J. Non-Cryst. Solids 186 (1995), 309.
19) Woignier, T. and Phalippou, J.: Skeletal Density of Silica Aerogels, J. Non-Cryst. Solids 93 (1987), 17.
20) Bourret, A.: Low-Density Aerogels Observed by High-Resolution Electron Microscopy, Europhys. Lett., 6

(1988), 731.

21) Lindner, P. and Zemb, T.: Neutron, X-ray and Light Scattering: Introduction to an Investigative Tool for Colloidal and Polymeric Systems, North-Holland, Amsterdam (1991).

22) Schaefer, D.W.: Small Angle Scattering from Disordered Systems, Mat. Res. Soc. Symp. Proc. 79 (1987), 47.

23) Teixeira, J.: J. Appl. Cryst. 21 (1988), 788.

24) Porod, G.: Die Röntgenkleinwinkelstreuung von dichtgepackten kolloidalen Systemen, Kolloidz. 124 (1951), 83.

25) Bale, H.D. and Schmitt, P.W.: Small Angle X-Ray-Scattering Investigation of Submicroscopic Porosity with Fractal Properties, Phys. Rev. Lett. 53 (1984), 596.

26) Emmerling, A.; Petricevic, R.; Beck, A.; Wang, P.; Scheller, H. and Fricke, J.: Relationship between Optical Transparency and Nanostructural Features of Silica Aerogels, J. Non-Cryst. Solids 185 (1995), 240.

27) Tewari, P.H.; Hunt, A.J. and Lofftus, K.D.: Advances in Production of Transparent Silica Aerogels for Window Glazings, in: Fricke,J.: Aerogels, Springer Proc. Phys. 6, Springer Verlag, Heidelberg (1986), 31.

28) Beck, A.; Caps, R. and Fricke, J.: Scattering of Visible Light from Silica Aerogels, J. Phys D 22 (1989), 730.

29) Poelz, G.: Aerogel in High Energy Physics, in: Fricke, J.: Aerogels, Springer Proc. Phys. 6, Springer Verlag, Heidelberg (1986), 176.

30) Fricke, J.: Thermal Transport in Porous Superinsulations, in: Fricke, J.: Aerogels, Springer Proc. Phys. 6, Springer Verlag, Heidelberg (1986), 94.

31) Caps, R. and Fricke, J.: Radiative Heat Transfer in Silica Aerogels, in: Fricke, J.: Aerogels, Springer Proc. Phys. 6, Springer Verlag, Heidelberg (1986), 110.

32) Hümmer, E.; Rettelbach, Th.; Lu, X. and Fricke, J.: Opacified Silica Aerogel Powder Insulation, Thermochimica Acta 218 (1993), 269.

33) Scheuerflug, P.: Tieftemperatureigenschaften von SiO_2-Aerogelen, PhD-Thesis, Phys. Inst. Univ. Würzburg/Germany (1993).

34) Heinemann, U.: Wärmetransport in semitransparenten nichtgrauen Medien am Beispiel von SiO_2-Aerogelen, PhD-Thesis, Phys. Inst. Univ. Würzburg/Germany (1993).

35) Emmerling, A. and Fricke, J.: Scaling Properties and Structure of Aerogels, J. Sol-Gel Sci. 8 (1997), 781.

36) Lu, X.; Arduini-Schuster, M.C.; Kuhn, J.; Nilsson, O.; Fricke, J. and Pekala, R.W.: Thermal Conductivity of Monolithic Organic Aerogels, Science 255 (1992), 971.

37) Gross, J. and Fricke, J.: Ultrasonic Velocity Measurements in Silica, Carbon and Organic Aerogels, J. Non-Cryst. Solids 145 (1992), 217.

38) Gronauer, M.; Kadur, A. and Fricke, J.: Mechanical and Acoustic Properties of Silica Aerogels, in: Fricke, J.: Aerogels, Springer Proc. Phys. 6, Springer Verlag, Heidelberg (1986), 167.

39) Woignier, T.; Phalippou, J.; Sempere, R. and Pelous, J.: Mechanical Properties of Silica Alcogels and Aerogels, J. Phys. Fr., 49 (1989), 289.

40) Dardel, G.v.; Henning, S. and Svensson, L.: A Method for the Preparation of Silica Aerogels and its Use, Eur. Pat. No. 0018 955 B1, Dec. 1, 1982.

41) Zobel, W. and Strähle, R.: Heat Storage Battery for Car Applications, C496/017 I/MechE, (1995), 379.

42) Cooper, D.W.: Part. Sci. Technol., 7 (1989), 371.

43) Pajonk, G.M.: Appl. Catal., 72 (1991), 217.

44) Hrubesh, L.W.: Rept. No. UCRL-2134, Lawrence Livermore National Laboratory, Berkeley, CA (1989).

45) Alkemper, J.; Buchholz, T.; Murakami, Y and Ratke, L.: Solidification of Aluminium Alloys in Aerogel Moulds, J. Non-Cryst. Solids 186 (1995), 395.

46) Gronauer, M. and Fricke, J.: Acoustic Properties of Microporous SiO_2-Aerogels, Acustica 59 (1986), 177.

47) Pekela, R.W.; Mayer, S.T.; Poco, J.F. and Kaschmitter, J.L.: Structure and Performance of Carbon Aerogel Electrodes, Mat. Res. Soc. Symp. Proc. Vol. 349 (1994), 79.

Author's short biography

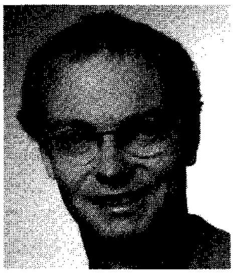

Thorsten Burger

Thorsten Burger received a diploma in physics from the Julius-Maximilians-University Würzburg, Germany, in 1995. He spent a year at the Northeastern University in Boston, where he studied the rf-properties of superconductors. He is currently continuing his graduate studies in Würzburg. His research activities are focussed on the radiative transfer in disperse media such as pharmaceutical powders, colour pigments or thermal insulating materials. He combines infrared spectroscopy and radiative transfer theory to analyse chemical and physical properties of scattering and absorbing samples. Additionally, his recent work includes the optimisation of radiative extinction and free flow-properties of thermally insulating powder mixtures.

Andreas Emmerling

Andreas Emmerling received his diploma in physics from the Julius-Maximilians-University in Würzburg. He is currently continuing his graduate studies in physics at that institution, concentrating on structural characterisation modeling and modification of highly porous, nanostructured materials. This involves experimental techniques such as small-angle scattering, development of appropriate models for data evaluation, and the application of these methods to differently prepared, modified or sintered aerogels. He has written several review articles about aerogels.

Marcus Weth

Marcus Weth studied physics at the Julius-Maximilans-University in Würzburg, Germany, and the St. Andrews University, Scotland. Right after his diploma he joined the Bavarian Center for Applied Energy Research (ZAEBayern) to pursue his doctorate.

His current research fields are the free flow properties of fine powders and their interparticulate forces.

Jochen Fricke

Jochen Fricke completed his undergraduate and graduate studies at the Technical University of Munich, receiving his Ph. D. with distinction from the Physics Department in 1967. He was a postdoctoral research fellow at that institution and the University of Pittsburg. Dr. Fricke joined the University of Würzburg as Professor of Experimental Physics in 1974, where his present research activities include investigations and optimization of porous media (powders, fibres and aerogels) with respect to structure and properties, and the development of opaque and transparent thermal superinsulation materials. In 1990 he received a medal from the German Physical Society for writing and publishing articles in the field of natural sciences. In 1991, Dr. Fricke was appointed Head of the Bavarian Center for Applied Energy Research and organized, for the second time, the International Symposium on Aerogels.

Review

Electrorheology of Non-aqueous Suspensions†

Yasufumi Otsubo
Department of Image Science,
*Faculty of Engineering, Chiba University**

Abstract

An excellent electrorheological (ER) suspension is invented with composite particles consisting of polymer core and inorganic shell. When the composite particles are subjected to jetstream agitation, the ER effects are strikingly enhanced. Since the ER effects can be attributed to the shell layers on the polymer particles, the surface of inorganic particles must be barely exposed to the surrounding oil. The importance of surface conditions is demonstrated by a scaling analysis. The creep curves at low stresses for suspensions in electric fields are composed of instantaneous elastic and retarded elastic regions. But the suspensions show no elastic recovery after the removal of stresses. The creep and recovery behavior is purely plastic. The dipole-dipole interactions cause chainlike structures of particles. The development of Bingham yield stress can be derived from the ideal chain model in which the particles all align into chains of single-particle width and equal spacing. However, the model cannot predict the solidlike deformation without recovery. The thick column formed by several chains may be responsible for purely plastic responses. The particle concentrations in column are increased in nonuniform electric fields. Since the increase in particle concentration of column lead to high yield stresses, the ER performance of suspension as an overall response can be improved by the electrode design.

1. Introduction

A rapid reversible change in viscosity of fluids on the application or removal of electric fields is referred to as the electrorheological effect and such fluids have come to be known as electrorheological or ER fluids. Typical ER fluids are suspensions of polarizable particles dispersed in insulating oils. When an electric field is increased above some critical value, the ER suspensions undergo a rapid transition from Newtonian liquids to rigid solids. Because the local fluidity can be actively controlled by the field strength, the ER fluids are attractive as vehicles in new mechanical devices such as stop valves, clutches, and dampers. Since the initial discovery by Wislow [1], the most common observation is that particles in liquids produce fibrous chains in the direction parallel to the field vector. Phenomenally the high resistance of ER fluids can be explained by the formation of fibrous structures. Klass and Martinek [2, 3] seem to have been the first to investigate the viscosity of ER fluids as a function of shear rate. Their results give the most important aspect about ER behavior of suspensions that in electric fields the flow profile is expressed by a Bingham equation. The application of electric fields induces a yield stress and an increase in viscosity after the onset of flow. The appearance of yield stress is closely associated with the rupture of chain structures.

In the chains spanning the electrode gap, the particles are connected by electric polarization forces. When the dielectric constants of the particles and the liquid are substantially different, each particle acquires an induced dipole in electric fields. The particles attract one another if they are aligned along the field direction, whereas the particles in the plane perpendicular to the field direction repel one another. The dipole-dipole interactions cause chainlike structures of particles [4-6]. Therefore, the primary method of formulating excellent ER fluids is a dielectric mismatch. According to this concept, a wide variety of ER fluids have been invented with organic and inorganic materials as the dispersed phase [7,8]. However, previous data indicate [9] that the ER effect is strongly affected by adsorbed substances at the particle surface, rather than the particle material itself. For exam-

---

*Yayoi-cho 1-33, Inage-ku, Chiba-shi 263, Japan
†Received 15 May, 1997

ple, the ER effect of silica suspensions is generated by physically adsorbed water [10]. When heated above 400°C, hydration reaction takes place. Hence the heated silica particles are almost inert in developing the ER effect. Many traditional ER fluids require a substantial amount of adsorbed water. Although it may be difficult to quantitatively predict the polarization forces due to adsorbed substances at the present stage, the surface modification of particles would be useful for improvement of ER performance.

When the ER fluid electrified in a quiescent state is subjected to shear strain, the chains spanning the electrode gap rupture above some critical strain. After the rupture the chains immediately swing back until grabbed by another chain, because the equilibrium conformation of chains is always aligned with the electric field. The total effect of steady shear at low shear rates on ER fluids is to constantly rupture and reform the chain structure. The analysis of this process is successful in deriving a Bingham constitutive equation [11]. On the other hand, the force in the direction perpendicular to the fields vector contributes to energy storage in chains, unless the strain exceeds the critical value. The ER fluids can be characterized as Voigt bodies at very small strains. However, the creep and recovery curves at different constant stresses markedly deviated from the model calculation. In creep experiments at low stresses, the strain changes almost instantaneously and reaches an equilibrium, but it is not recovered after the removal of stresses. The behavior is plastic with an infinite relaxation time. The deformation analysis of an ideal single chain predict the elastic recovery. The plastic responses can be connected with deformation of thick column consisting of aggregates of many primary chains. The yield processes of ER fluids must be understood on the basis of column structures.

In the present review, firstly, the effects of surface conditions on the ER behavior is examined for suspensions of inorganic shell/polymer core composite particles which have been developed by the authors. The importance of surface effects is demonstrated by the use of a scaling analysis. Secondly, the column structures of electrified suspensions in a quiescent state is inferred through microscopic observation. The yield stress is discussed in relation to the deformation process of thick columns. Thirdly, the effects of nonuniform electric fields is investigated from an application-oriented point. The analysis of column structures provides the feasibility of enhancing the ER performance by electrode design, which leads to new technology in application of ER fluids.

2. Formulation of ER fluids

Application and devices have different fluid requirements and limitations. To fill various needs, such as a good balance between the yield stress in electric fields and the zero-field viscosity, low current density, and long term stability against sedimentation, we have developed composite particles in which the polymer particles are coated with thin layers of fine ER-active inorganic particles. The core was 1,3-butylene glycol dimethacrylate/butyl acrylate copolymer with a monomer ratio of 25/75. The uncoated polymer particles do not show the ER effect. The diameters of ER-active inorganic particles were in the range of 20-100 nm. The composite particles were prepared by suspension polymerization in which the polymer core and inorganic shell are simultaneously formed in aqueous solutions. The following is the polymerization procedure [12].

The inorganic particles were dispersed in a mixture of 1,3-butylene glycol dimethacrylate, butyl acrylate, and polymerization initiator. The particle concentration was 9.2% by weight. The suspensions of inorganic particles in the monomer mixture were added to a 1.5wt% aqueous solution of calcium tertiary phosphate while the solution was stirred at a constant mixing speed. The initial system was an oil-in-water emulsion. Stirring was continued at 60°C for 1 hr to convert liquid droplets into solid particles. Since the monomer mixture and aqueous solution have different affinity for the particle surfaces, the migration of inorganic particles to the interface between the oil and water took place during polymerization. As a result, the organic polymer form the core, the surface of which is coated with layers of inorganic particles. After filtration and cleaning in an acid solution, the composite particles were washed with water and dried at 50°C for 48 hr. The shell layers of inorganic particles on the polymer surface are considered to be covered with a small amount of additives for the polymerization, such as initiator and dispersant. To eliminate such substances, the composite particles were subjected to jetstream agitation in air for 5 min at 6000rpm with a hybridizer. After the particles collided violently with one another, the nonvolatile contaminants were separated by filtration. The suspensions of particles without jetstream agitation show a very little ER effect. When the inactive films of dispersant and polymeric substances are removed, the striking ER effect is induced. Although the polymer particles must be coated with ER-active particles, the ER effect is much more striking under conditions where the surface of inorganic particles is barely exposed to the surrounding medium in suspensions. The jet-stream agitation is necessary for the ER effect of suspensions of composite particles. Since the jet-stream agitation did not have significant effects on the particle diameter and water content, the inorganic particles are strongly attached to polymer core and the shell layer can not be stripped away during collisions. The density of composite particles was about 1.2×10^3 kgm^{-3}. The diameter was 17μm and water content was 1.0wt% by Karl Fisher titration. **Figure 1** shows the microphotograph of composite particles coated with titanium hydroxide (C-II from Ishihara Sangyo Co.). The titanium hydroxide particles are arranged in closely packed layers on the polymer surface.

The ER fluids were suspensions of composite particles dispersed in a silicone oil. The silicone oil with a Newtonian viscosity of 0.12 Pas and density of 1.0×10^3 kgm^{-3} was obtained from Toshiba Silicone Co. and used as received. Although various inorganic particles could enhance the ER effect of composite particles, titanium hydroxide was very effective. Therefore, the discussion on ER mechanisms will be expanded by using only the experimental results for suspensions of composite particles covered with titanium hydroxide.

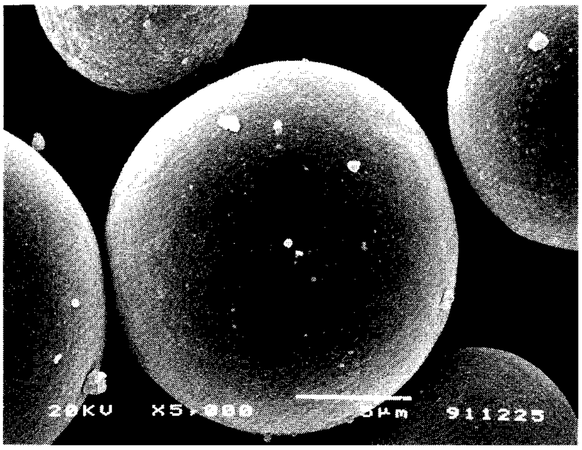

Fig. 1 Microphotograph of composite particles coated with titanium hydroxide particles.

3. Steady-shear behavior and Bingham yield stresses

3.1 Steady-shear behavior

The steady-shear viscosity was measured with a coaxial cylinder rheometer (Haake Rotovisco RV 20). The diameters of the bob and cup were 10.1 and 11.55 mm, respectively. The immersion length of the bob was 61.4 mm. A DC voltage was applied to the bob which was insulated from the upper shaft and the cup was connected to the ground (=0 V). On the application of an electric field, the shear stress (viscosity) rapidly increased and reached the equilibrium response. The response time was about 1 s (this includes the inertial effect of the bob). The equilibrium shear stress was measured at different constant shear rates in electric fields up to E=4.0 kVmm^{-1}. The time scale of viscosity decay was about 10 s after the removal of electric fields. For all runs, the current density was less than 50 mAm^{-2}.

Figure 2 shows the flow curves for a 30wt% suspension in different electric fields [13]. In the absence of electric fields, the flow is almost Newtonian. The electric fields cause an increase in shear stress over the entire range of shear rates. The stress enhancement is much larger at low shear rates and the flow curve clearly shows a plateau. Since the constant stress is generated in the limit of zero shear rate, the height of plateau which increases with field strength is considered to correspond to the Bingham (dynamic) yield stress σ_B.

Figure 3 shows the flow curves in electric fields of E=0 and E=2.0 kVmm^{-1} for suspensions at different particle concentrations [13]. On the application of electric fields, the suspensions are converted from Newtonian liquids to Bingham bodies, irre-

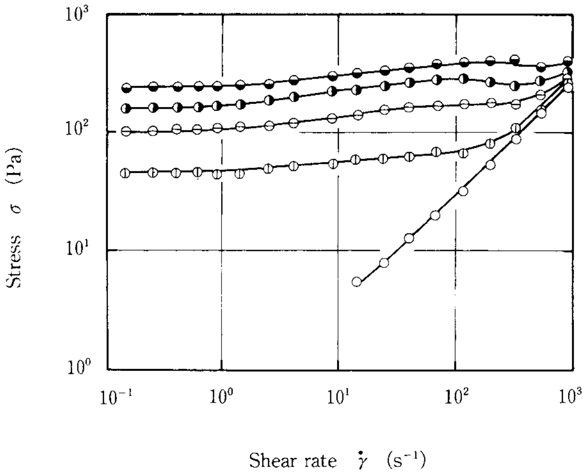

Fig. 2 Flow curves for 30wt% suspension in different electric fields: (○)0, (⦶)0.5, (⊖)1.0, (◑)1.5, and (◒) 2.0 kVmm^{-1}.

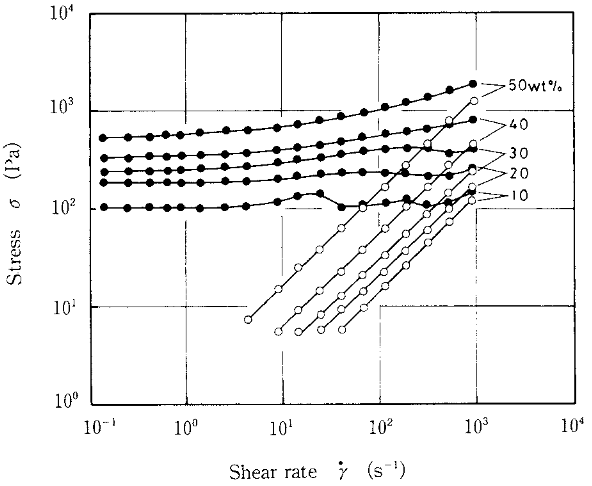

Fig. 3 Flow curves in electric fields of E=0 (open symbols) and E=2.0 kVmm^{-1} (filled symbols) for suspensions at different particle concentrations.

spective of particle concentration. The Bingham yield stress linearly increases with particle concentration. One of the important requirements of ER fluids in practical application is a good balance between the yield stress in electric fields and the zero-field viscosity. Since the zero-field viscosity slowly increases and begins to increase rapidly with particle concentration, the optimum particle concentration to achieve effective enhancement in viscosity is in the range of 30-40 wt%.

3.2 Scaling analysis

The relation among the Bingham yield stress, particle concentration and electric field has been theoretically established from the chain structuring model [11,14]. On the assumption that the particles align into chains of single-particle width and equal spacing, a Bingham constitutive equation of ER fluids has been derived through a model in which all the chains spanning the electrode gap rupture in the center and immediately swing back to reform with the nearest chain on the opposite electrode. The total effect of steady shear on the suspensions in electric fields is to constantly rupture and reform the chain structure. The stress generated at low shear rates is expressed by the following equation.

$$\sigma_B \approx \Phi \varepsilon_0 \varepsilon_c \beta^2 E^2 \qquad (1)$$

$$\beta = (\varepsilon_p - \varepsilon_c)/(\varepsilon_p + 2\varepsilon_c) \qquad (2)$$

Here, Φ is the volume concentration of particles with a dielectric constant ε_p dispersed in an oil with a dielectric constant ε_c, ε_0 is the permittivity of free space, and β is the relative polarizability. The theory predicts that the Bingham yield stress is proportional to the volume concentration of particles and the square of the electric field. However, the quadratic effect of electric field was not observed for the ER fluids studied. In the theoretical analysis, the polarization forces arise from the difference in dielectric constants between the particles and continuous liquid. The effects of colloidal forces and surface polarization are regarded as negligible.

The electric forces dominate at low shear rates, and the hydrodynamic forces dominate at high shear rates. In the intermediate region, the suspension rheology is governed by a balance between them. To characterize the relative importance of hydrodynamic to electric polarization forces, Marshall et al. [11] introduced the Mason number M_n :

$$M_n = \eta_c \dot{\gamma} / (2\varepsilon_0 \varepsilon_c \beta^2 E^2) \qquad (3)$$

where, the η_c is the viscosity of continuous phase and $\dot{\gamma}$ is the shear rate. They have shown that the relative viscosity of the electrified suspension to that of the continuous phase, η/η_c, is a function of only the Mason number, M_n. The scaling analysis [4] suggests that the chain structure ruptures and the flow becomes Newtonian when Mn is increased to unity.

In **Figure 2**, the stress curve shows a plateau at low shear rates and begins to increase above 100 s^{-1} in an electric field of 0.5 kVmm^{-1}. At about $\dot{\gamma}=100$s^{-1}, the electric polarization forces would be comparable to the hydrodynamic ones, i,e., $M_n \sim 1$. The dielectric constant of silicone oil being taken as 2.5, the dielectric constant of composite particles is estimated to be about 150. If the formulation of ER fluids was attempted only by bulk polarization effect, the particles with a high dielectric constant are required to raise the ER performance to the level of sample suspensions. However, in fact, the dielectric constant of composite particles is about 3 at frequencies from 0.1 kHz to 10 kHz (although the measurements were carried out in electric fields less than 0.1 kVmm^{-1}, because of the limitations of the apparatus). Hence, it seems difficult to apply the bulk polarization theory to the ER behavior of the suspensions of composite particles. The titanium hydroxide particles forming the shell on the surfaces of polymer particles are responsible for the ER responses. The ER behavior of sample suspensions is strongly affected by the surface properties, rather than the bulk properties. The interparticle forces due to surface polarization and conduction [15] of thin layers on the particles may play an essential role in promoting the ER effect. Although the definitive experiments are required to quantitatively understand the relation between the ER behavior and surface properties, the results demonstrate that the surface modification of particles may have great potential to improve the ER performance of suspensions.

4. Static yield stress and column structures

4.1 Creep behavior

The creep and recovery behavior was measured with a parallel plate geometry on a stress-controlled rheometer (Haake Rheo-Stress RS100) which was modified for the ER experiments. The diameter of upper plate was 35 mm and the gap between two plates was 1.000 mm. For initial conditioning, the suspensions were subjected to steady shearing at 1.0×10^2 s^{-1} for 600 s and electrified in a quiescent state for 60 s. Subsequently the stress was instantaneously applied, maintained constant for 200 s, and suddenly removed. The time dependence of strain, γ, at the plate edge was calculated from the rotation angle of upper plate. In this section, the composite particles which were covered with mixtures of titanium hydroxide and phthalocyanine blue with a mixing ratio of 80/20 were used. The highly absorbing particles like a phthalocynanine blue pigment are useful for structural analysis through microscopic observation [16,17].

Figure 4 shows the creep and recovery curves at shear stresses of 10, 20, and 50 Pa for 10 vol% suspension in an electric field of E=2.0 kVmm^{-1} [18]. By the steady-shear measurements, the Bingham yield stress was determined as 50 Pa (since the phthalocyanine blue does not contribute to the ER effect, the Bingham yield stress is lower compared with the 10wt% suspension shown in **Figure 3**). At 20 Pa and below, the strain curve comprises instantaneous and retardation regions. Since the constant-rate strain due to viscous flow is negligibly small, the creep curve can be expressed by a Voigt model. However, the most interesting feature is that the strain is not recovered after the removal of stress. The instantaneous strain does not give a physical quantity as a measure of the elastic properties. The lack of recovery implies that the suspension is plastic at low stresses. When the stress is increased beyond some critical value, the strain linearly increases with time and no elastic recovery appears. The drastic changes of creep behavior show the existence of structural transition. The electrified suspensions can be classified into two groups; plastic solids at low stresses and liquids at high stresses.

The flow curve under steady shear shows a plateau at low shear rates, the height of which generally gives the Bingham yield stress of ER fluids. At stresses less than the Bingham yield stress, the ER fluid is expected to behave as an elastic solid. However, the strain rapidly and linearly increases with time at 50 Pa. The yield stress is defined as a critical stress, below which no flow can be observed under the conditions of experimentation and above which the substance is a liquid with a plastic viscosity. From the comparison between the steady flow and creep behavior, the constant stress at low shear rates under steady flow does not necessarily give the yield stress as a transition point from a solid to liquid [13,19]. Creep experiments are useful to directly determine the static yield stress and to understand the deformation mechanisms of solid structure. For 10vol% suspension, the static yield stress, σ_0, is estimated to be 20 Pa in an electric field of 2.0 kVmm^{-1}. In many ER fluids consisting of spherical particles, the static yield stress is about 70% of the Bingham yield stress.

Figure 5 shows the creep and recovery curves at 0.2 Pa for 1vol% suspension and 0.5 Pa for 2vol% suspension. Although the strain gradually increases and reaches the equilibrium, the suspensions show

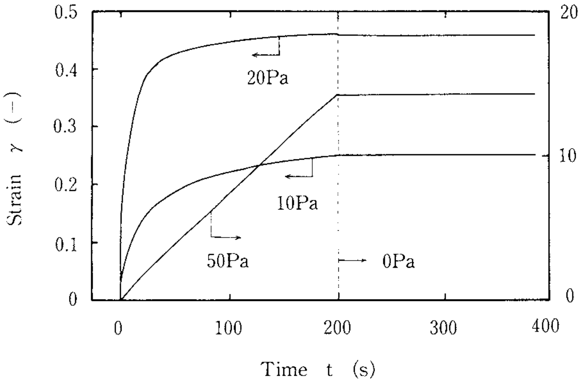

Fig. 4 Creep and recovery curves at shear stresses of 10, 20, and 50 Pa for 10vol% suspension in an electric field of E=2.0 kVmm^{-1}.

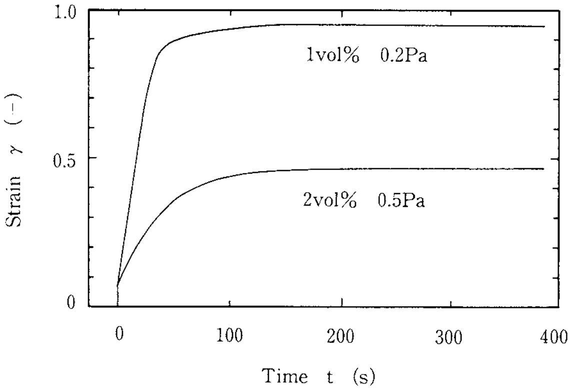

Fig. 5 Creep and recovery curves at 0.2 Pa for 1 vol% suspension and 0.5 Pa for 2 vol% suspension.

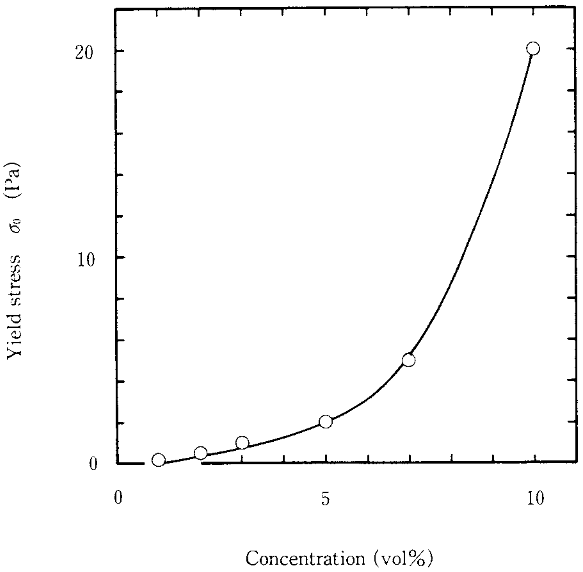

Fig. 6 Concentration dependence of static yield stress in an electric field of 2.0 kVmm^{-1}.

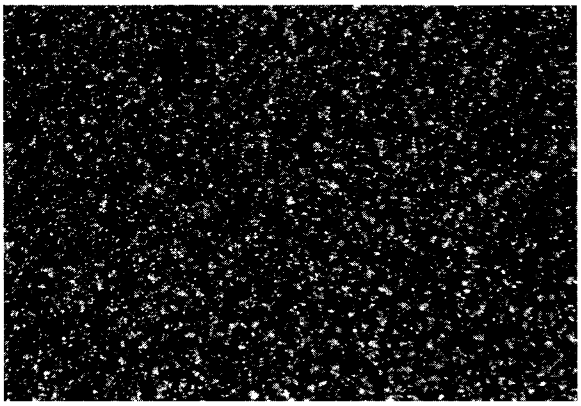

Fig. 7 Microphotograph of 7 vol% suspension without electric fields. The electric field is perpendicular to the plane of the picture.

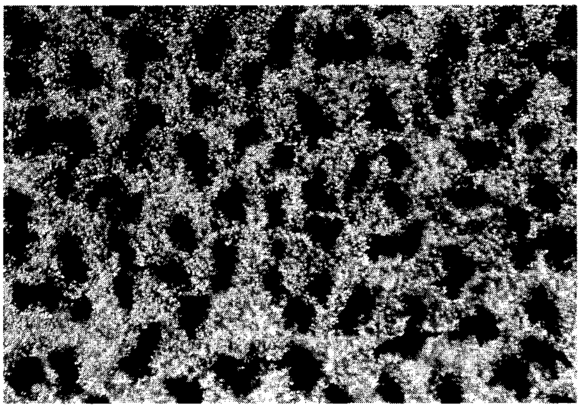

Fig. 8 Microphotograph of 7 vol% suspension in an electric field of 2.0 kVmm^{-1}. The electric field is perpendicular to the plane of the picture.

no elastic recovery. It is of interest to note that both suspensions behave as solids in an electric field. Even at a particle concentration of 1vol%, the solid structures must be fully developed between the electrode gap.

Figure 6 shows the concentration dependence of static yield stress σ_0 in an electric field of 2.0 kVmm^{-1}. The theory on the single-chain model predicts that the yield stress linearly increases with particle concentration, because each chain has the same strength and the number of chains per area is proportional to the concentration. However, the linear dependence is not established for the sample suspensions. In single chains, the force in the direction perpendicular to the field vector contributes to energy storage in strained chains, unless the strain exceed the critical value. Since the elastic modulus comes from the chains and the viscosity from the suspending fluid, the suspensions in electric fields can be characterized as Voigt bodies at very small strains. However, the suspensions show no elastic recovery after the removal of stresses. The difficulty arises in analysis of ER mechanism based on the single-chain model.

4.2 Column Structures

Figure 7 shows the microphotograph of 7vol% suspension without electric fields. Although very small aggregates can be seen, they may be uniformly distributed over the system. It is reasonably accepted that the particles are noninteracting in the absence of electric fields. **Figure** 8 shows the microphotograph of the same suspension in an electric field of 2.0 kVmm^{-1}. The system consists of large discrete aggregates. The application of electric fields causes the particles to align into chains along the field vector and at the same time to form the aggregates in the plane perpendicular to the field direction. Since the vacant area without particles cannot transmit the forces, the aggregates are responsible for the development of yield stress of electrified suspension.

By imaging analysis, the fraction of area occupied by the aggregates deposited on the electrode is found to be proportional to the volume concentration of particles. The linear relation suggests that the field-induced structures consist of columns constructed by the aggregates of many primary chains spanning the gap. If the chain-chain interactions do not exist in the columns, the yield stress would be proportional to the surface coverage as predicted by the ideal single-chain model. However, referring back to the rheological results, the yield stress cannot be directly connected with the total number of primary chains. The microscopic observation brings about an interesting finding that the average area of individual aggregates at a fixed field strength increases with particle concentration. The column diameter plays an important role in enhancing the ER effect of suspensions.

Figure 9 shows the relation between the strength and cross-sectional area per column. The calculation assumes that the sum of column strength (force at a breaking point of column) corresponds to the static yield stress. The results obviously indicate that the reinforcement of column is accelerated at high concentrations. The primary chains have a tendency to form columns and the thickening of columns effectively leads to development of high yield stress as an overall response of ER suspension.

When the chain structure of particles spanning the electrode gap is formed by the dipole-dipole interactions, an ER fluid becomes a solid in electric fields. The solid structure must be the configuration which minimized the dipolar interaction energy. Tao and Sun [20,21] have theoretically shown that the ideal structure of ER solids is not a collection of separated chains of single-particle width, but a body-centered tetragonal lattice. When placed near a chain, a particle will be repelled by the nearest particles in the chain. But the particle will be attracted by the chained particles well above and below it. Because of long-range interactions, the particles first form chains in the field direction and then the chains aggregate to develop thick columns. The lattice structure of thick column has been confirmed by an optical technique [22].

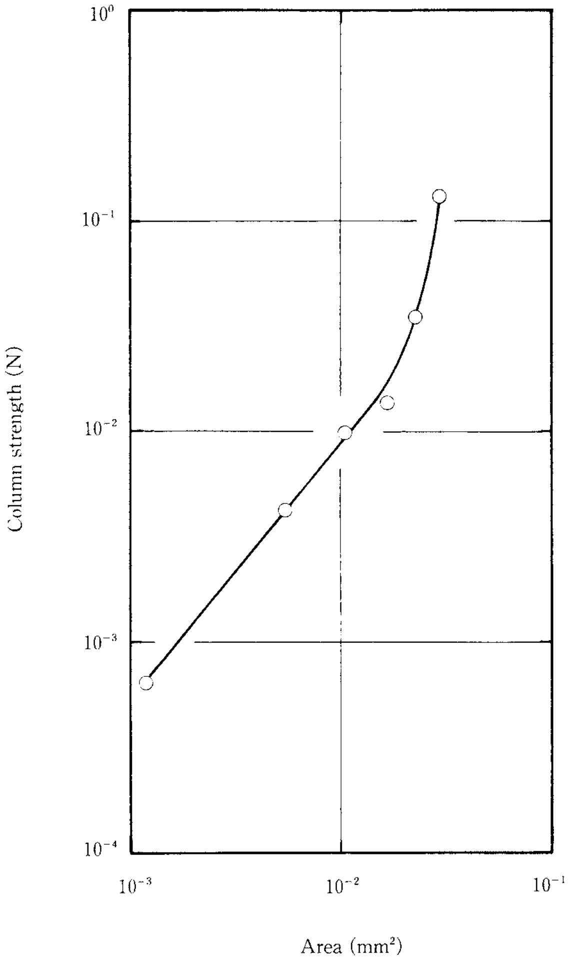

Fig. 9 Relation between the column strength and the average cross-sectional area.

However, the dipolar interaction energy per particle strongly depends on the lattice structure. For example, the particles hardly construct a simple cubic lattice. Since the forces between neighbor particles in different chains are strongly repulsive, the simple cubic lattice has higher energy than the separated chains. When the column with the body-centered tetragonal lattice is strained, the particle displacement in the chains possesses components in both the perpendicular and parallel directions to the field vector. The energy must be consumed during the motion of particles in the columns. To maintain the column structure, some critical attractive force is required, which is directly related to the strain level. When the strain is increased to the critical point, the stored energy is completely consumed and the column structure changes from the body-centered tetragonal lattice to another metastable configuration. Therefore, the suspensions in electric fields show no elastic recovery after the removal of stress. The appearance of static yield stress or purely plastic response is attributed to the deformation of thick columns. The intrinsic structure determining the yielding nature of electrified suspensions is the columns constructed by the aggregates of primary chains and the value of yield stress is controlled by the column diameter.

5. Enhancement of ER effect by device design

5.1 Double-step application of electric fields

The suspensions of composite particles containing phthalocyanine blue pigment were sandwiched between glass plates coated with transparent ITO (indium tin oxide) electrodes. The light emitted from a halogen lamp was introduced through glass fiber in the direction of electric fields. The transmittance of light through the suspensions was measured by an optical spectrum analyzer.

Figure 10 shows the effect of field strength on the spectral intensity of transmitted light for 15vol% suspension. Without electric fields, the spectrum of transmitted light shows a maximum at a wavelength of 490 nm, because the suspension is composed of the blue particles. As the field strength is raised, the light intensity increases over the entire range and the wavelength at the maximum transmittance shifts toward the red (longer wavelength) side. The wavelength at the peak is 600 nm in high electric fields and this value corresponds to that of incident light which is regarded as colorless (slightly yellowish). As shown in **Figure** 8, the system in electric fields consists of many aggregates and vacant area without particles. The generation of vacant area contributes to the discoloration of suspension in electric fields, which depends on the cross-sectional area of aggregates. The striking changes in spectral intensity arises from a purely geometrical effect. The discoloration of suspension occurs at low field strength and the effect reaches the saturation in fields above E=2.5 kVmm^{-1}.

According to the column formation theory, the field strength does not significantly influence the lattice structure. However, the intensity of transmitted light and images of aggregates vary with the field strength for suspensions sandwiched between parallel-plate electrodes. With increasing field strength, the surface coverage rapidly decreases at first and then approaches a constant (67%) beyond E=2.5 kVmm^{-1}. The particle alignment and column formation are induced in relatively low fields. When the column structure reaches the equilibrium, it is expected that the body-centered tetragonal lattice is achieved. However, the particle concentration is about 22 vol% in the columns if the cross-sectional area is constant in the direction of electric fields. In actual ER suspensions, the particles hardly construct the ideal lattice.

The dielectric polarization forces are generated instantaneously on the application of electric fields. In the column formation process, the particles must migrate. Although the response time varies with field strength, the time scale of migration is found to be of the order of 0.1 s through optical measurements. The ER fluids are always sheared in mechanical devices under operational conditions. Once the attractive forces disappear after the removal of electric fields, the columns are rapidly broken down by hydrodynamic forces and the suspension recovers the initial low viscosity level. However, it may be difficult to redisperse the particles with diameters of about 20 μm only by thermal energy. The electrooptical effects are essentially irreversible in a quiescent state. Therefore, the static structure of column is determined by the highest electric field which was previously applied to the suspension.

Figure 11 shows the static yield stress plotted against the field strength for 15 vol% suspension in different modes of electrification. In the single-step procedure, the electric field is almost instantaneously (within 0.1 s) increased from zero to the measuring strength. In the double-step procedure, the ER fluid was first exposed to an electric field of 4 kVmm^{-1} for 30 s and the field strength was decreased to the measuring strength prior to creep experiments. Obviously the double-step application leads to higher yield stresses. Since the column structuring process in electric fields is irreversible

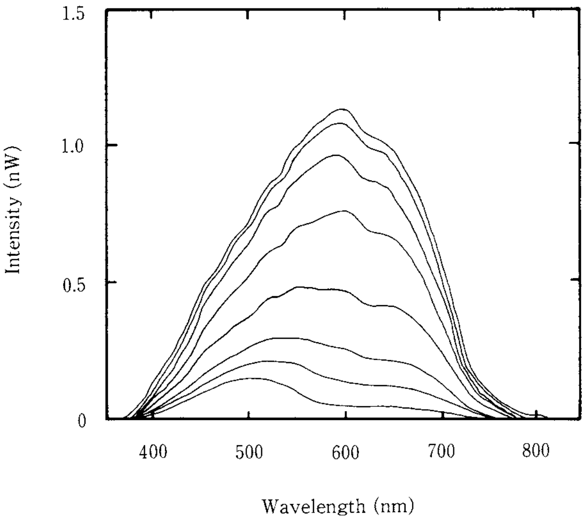

Fig. 10 Effect of field strength on the spectral intensity of transmitted light for 15vol% suspension in electric fields of different strength: 0, 0.17, 0.33, 0.50, 1.17, 1.67, 2.50, and 3.33 kVmm^{-1} from bottom to top.

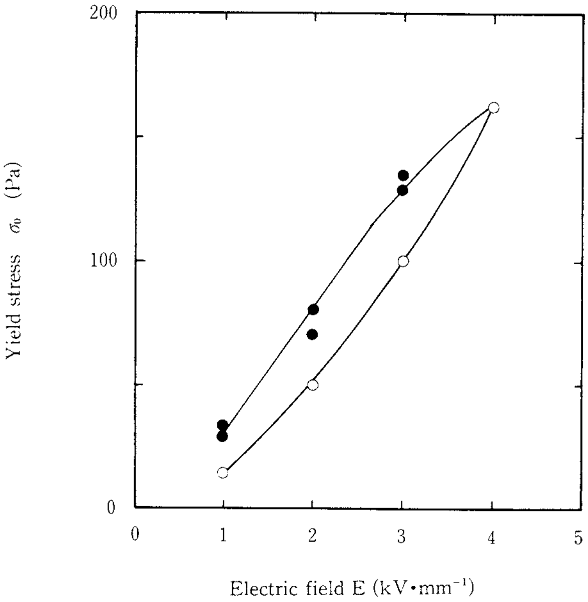

Fig. 11 Effect of electrification mode on the static yield stress for 15 vol% suspension in uniform fields: (○); single-step, (●) ; double-step.

without shear, a large part of the structure developed at 4 kVmm^{-1} remains the same even after the reduction of field strength. From **Figure 11**, the high yield stress in double-step application may be a manifestation of high density of particles in column.

5.2 ER behavior in nonuniform electric fields

The yield stress of ER fluid increases with field strength primarily due to the increase in dipole-dipole interactions between two particles. However, the column structure, i.e., the geometrical arrangement of particles may also give an important factor, because the yield process is controlled by the cooperative arrangement of particles in column.

Figure 12 shows the microphotograph of 15 vol% suspension sandwiched between the glass plates, the surfaces of which are coated with transparent ITO in a striped pattern of line and space. The thickness of conductive lines and pitch are 0.1 mm and 0.5 mm, respectively. The particles construct striped aggregates along the electrode lines and no particles remain in the insulating region. The surface coverage of particles is about 43%. Assuming that the columns are fully developed between the electrodes, the particle concentration in the columns is about 35 vol%. Although the formation of a body-centered tetragonal lattice may be impossible, the particle concentration is markedly increased in the striped electrodes. The electric field is uniform in the parallel-plate electrodes, whereas in the striped electrodes, the potential gradient is generated in the direction parallel to the glass surfaces. Therefore, the force component in direction perpendicular to individual chains is enhanced to build up the closely packed columns. The nonuniformity of electric field is responsible for the high particle concentration of columns.

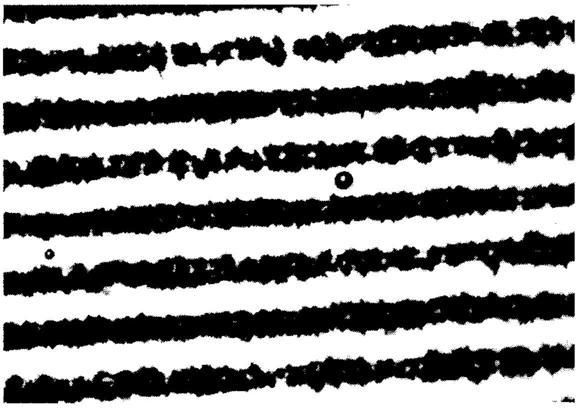

Fig. 12 Microphotograph of 15vol% suspension sandwiched between striped electrodes in an electric field of 3.3 kVmm^{-1}. The electric field is perpendicular to the plane of the picture.

To generate nonuniform electric fields, an electrode with a honeycomb pattern of conductive layer on a plastic disk was used. The area and pitch of insulating holes are 0.4 mm^2 and 0.8 mm, respectively. The area ratio of conductive part is 33%. **Figure 13** shows the comparison of static yield stresses measured by parallel-plate and honeycomb pattern electrodes for 15 vol% suspension. It is clearly shown that the honeycomb pattern electrode serves to increase the yield stress of ER suspensions, especially at high electric fields. Since the total interaction energy increases with the progress of chain aggregation, the concentrated column can bring about the high yield stress of electrified suspension. The rheological behavior in electric fields strongly depends on the column structure. Therefore, it can be stressed that the ER performance as an overall response is improved by the design of electrodes. This may provide a new aspect in application technology of ER fluids.

6. Conclusions

(1) The suspensions of inorganic shell/organic core composite particles show a striking increase in the steady-viscosity on the application of electric fields. Since the ER effect arises only from the shell layers, the surface modification of particles may have great potential to improve the ER performance of suspensions.

(2) At low stresses, the creep curve of electrified suspensions is composed of instantaneous elastic

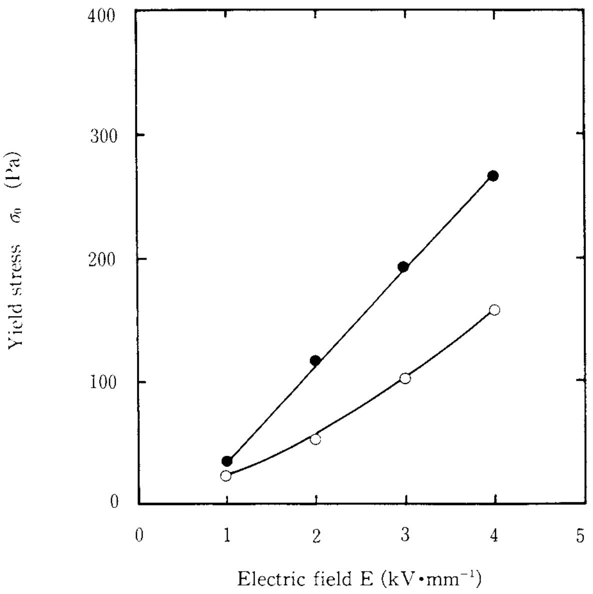

Fig. 13 Effect of electrode pattern on the static yield stress of 15vol% suspension: (○); plain electrode, (●); honeycomb pattern electrode.

and retarded elastic responses. Since the strain is not recovered after the removal of stress, the suspension is purely plastic. When the stress is increased above some critical level, the suspensions show viscous flow. The critical stress corresponds to the static yield value. The static yield stress is about 70% of the dynamic yield stress.

(3) In electric fields, the particles form chains in the field direction and then the chains aggregate to develop thick column between two electrodes. Since the dipolar interaction energy in columns strongly depends on the geometrical arrangement of particles, the appearance of static yield stress or plastic responses is attributed to the deformation of thick columns.

(4) The strong particle interactions in column lead to high yield stresses of ER fluids. When the electric fields are not uniform, the columns with high particle concentrations are achieved, which afford the high yield stresses. Since the nonuniformity of electric field is responsible for the enhanced ER effect, the electrode design may be an attractive technique in the application fields of ER fluids.

Nomenclature

E : electric field [$kVmm^{-1}$]
M_n : Mason number [-]
t : time [s]
β : relative polarizability [-]
ε_0 : permittivity of free space [Fm^{-1}]
ε_c : dielectric constant of oil [-]
ε_p : dielectric constant of particle [-]
Φ : volume concentration of particles [-]
γ : strain [-]
$\dot{\gamma}$: shear rate [s^{-1}]
η : viscosity of electrified suspension [Pas]
η_c : viscosity of oil [Pas]
σ : shear stress [Pa]
θ_B : Bingham (dynamic) yield stress [Pa]
σ_0 : static yield stress [Pa]

References

1) Winslow, W.M., J. Appl. Phys., 20, 1137 (1949)
2) Klass, D.L., and Martinek, T.W., J. Appl. Phys., 38, 67 (1967)
3) Klass, D.L., and Martinek, T.W., J. Appl. Phys., 38, 75 (1967)
4) Gast, A., and Zukoski, C.F., Adv. Colloid Interface Sci., 30, 153 (1989)
5) Chen, Y., Sprecher, A.F., and Conrad, H., J. Appl. Phys., 70, 6796 (1991)
6) Halsey, T.C., Science, 258, 761 (1992).
7) Brooks, D., Goodwin, J., Hjelm, C., Marshall, L., and Zukoski, C., Colloids Surfaces, 18, 293 (1986)
8) Block, H., and Kelly, J.P., J. Phys. D, 21, 1661 (1088)
9) Otsubo, Y., Sekine, M., and Katayama, S., J. Colloid Interface Sci., 146, 395 (1991)
10) Otsubo, Y., Sekine, M., and Katayama, S., J. Colloid Interface Sci., 150, 324 (1992)
11) Marshall, L., Zukoski, C.F., and Goodwin, J.W., J. Chem. Soc. Faraday Trans. 1, 85, 2785 (1989)
12) Otsubo, Y., and Edamura, K., J. Colloid Interface Sci., 168, 230 (1994)
13) Otsubo, Y., and Edamura, K., J. Rheol., 38, 1721 (1994)
14) Klinbenberg, D.J., and Zukoski, C.F., Langmuir, 6, 15 (1990)
15) Khusid, B., and Acrivos, A., Phys. Rev. E, 52, 1669 (1995)
16) Edamura, K., Akashi, K., and Otsubo, Y., J. Imaging Sci. Technol., 39, 564 (1995)
17) Otsubo, Y., Edamura, K., and Akashi, K., J. Colloid Interface Sci., 177, 250 (1996)
18) Otsubo, Y., and Edamura, K., Colloids Surfaces, A, 109, 63 (1996)
19) Otsubo, Y., and Edamura, K., J. Colloid Interface Sci., 172, 530 (1995)
20) Tao, R., and Sun, J.M., Phys. Rev. Lett., 67, 398 (1991)
21) Tao, R., and Sun, J.M., Phys. Rev. A, 44, 6181 (1991)
22) Chen, T., Zitter, R.N., and Tao, R., Phys. Rev. Lett., 68, 2555 (1992)

Author's short biography

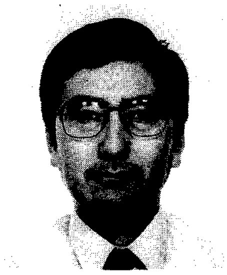

Yasufumi Otsubo

Associate Professor, Chiba University
Short vitae
1978 Ph. D.: Tohoku University (Dept. Chemical Engineering)
1987 Research Associate Princeton University (Dept. Chemical Engineering)
1988 Associate Prof. Chiba University (Dept. Imaging Science)
1994 Associate Prof. Chiba University (Center of Cooperative Research)

Research fields: Colloid Chemistry, Electrorheology, Texture of Foods, Flat Panel Display, Curing of Photosensitive Polymer

Review

Understanding Dust Explosions. The Role of Powder Science and Technology[†]

R.K. Eckhoff
Department of Physics
*University of Bergen, Norway**

Abstract

Dust explosions in the process industries most often start inside process equipment such as mills, dryers, mixers, classifiers, conveyors, and storage silos and hoppers. For any given type of dust, the ease with which the dust cloud ignites, and the rate with which it burns, vary considerably as a function of parameters well known in powder science and technology. The most important are the primary particle size distribution of the dust, the degree of de-agglomeration of the dust particles in the cloud, the dust concentration distribution in the cloud, and the cloud turbulence. The last three properties are entirely dependent on the actual process situation in which the dust cloud is generated. The paper discusses the influences of the four parameters on ignition sensitivity and explosibility, and on the design of mitigatory measures such as venting, isolation and automatic suppression. The role of powder science in understanding the development and propagation of secondary dust explosions is also outlined.

1. Introduction

1.1 General historical background

Dust explosions have been a recognized threat to humans and property for a long time. One of the earliest comprehensive written reports known is Count Morozzo's detailed analysis [1] of an explosion in the flour warehouse of Mr. Giacomelli in Turin in 1785 (see full report in Eckhoff [2]). In their report on the explosion in the Haswell coal mine (UK) in 1844, Faraday and Lyell [3] emphasized the central role of the coal dust in developing the devastating main explosion that followed the initial relatively minor explosion of firedamp. During the 150-200 years that have passed since the days of Morozzo and Faraday, the expanding chemical and metallurgical industries have given birth to a steadily increasing number of new, finely divided combustible solid materials, and dust explosions continue to be a serious hazard in many industries, as discussed by Eckhoff [2].

1.2 Objective of present paper

The scientific/technical backgrounds of people working in the area of dust explosion prevention and mitigation vary considerably. Some are electrical engineers, being mainly concerned with area classification and elimination of possible electrical ignition sources. Others have their background in statistics, and focus on the risk assessment aspects. Some are mechanical engineers, putting the main emphasis on the mechanical construction of safe process equipment. Others again have chemistry or physics as their basic education, and take a more academic approach.

In a recent issue of KONA Powder and Particle, Wolanski [4] gave an excellent overview of ignition and flame propagation processes in dust clouds generated for research purposes. The main objective of the present paper is to emphasize that a proper understanding of dust explosion phenomena in practice in the process industries requires that the relevant aspects of powder science and technology are given careful consideration.

1.3 Generation and states of explosible dust clouds

The explosible dust concentration range is rather limited. For organic dusts and coal it spans from the order of 100 g/m^3 to a few kg/m^3. The bulk density of such powders and dusts when settled in a layer or a heap is of the order of a few hundred kg/m^3. Therefore, there is a gap of a factor of at least 100 between the maximum explosible dust concentration and the bulk density in the settled state.

In some special situations such as in air jet mills, explosible dust clouds may be generated *in situ*, i.e. the dust particles become suspended in the air as

---

*Allegaten 55, N-5007 Bergen, Norway

[†] Received May 20, 1997

they are produced. However, in most cases, explosible dust clouds are generated by re-entrainment and re-dispersion of powders and dusts that have been produced at an earlier stage and allowed to accumulate as layers or heaps. Such accumulation may either be intentional, as in the collection of powders and dusts in silos, hoppers and bag filters, or unintentional, as in the deposition of dust on external surfaces of process equipment, or on beams, walls and floors in the factory building.

Re-suspension and re-dispersion of dust may either occur intentionally, e.g. during pneumatic transport in pipes, by filling of silos, in fluidized beds, in spray dryers and other types of dryers, in mixers and blenders and in screening machinery. Unintentional re-dispersion may be due to the bursting of sacks and bags containing powder, leaks of dust from process equipment, or by sudden blasts of air generated by primary explosions elsewhere in the plant.

In the present paper, the influence on dust cloud ignitability and explosibility of four central physical dust cloud properties will be discussed. These properties are:

- primary particle size of dust/powder
- degree of de-agglomeration of dust particles, i.e. real 'particle' size in dust cloud
- dust concentration in cloud
- degree of turbulence of dust cloud.

2. Particle Size

In general, the ease with which a cloud of dust of a given material ignites, and the violence with which it explodes/burns, increase with decreasing particle size in the cloud. For organic dusts and coal, particle size primarily influences the devolatilization rate. Therefore, if the combustion of the volatiles is already the rate-controlling process, a further reduction of the particle size will not increase the overall combustion rate any more. For metals such as Mg, Al and Si, the limiting particle size below which there is no further increase of ignition sensitivity and explosion violence is considerably smaller than for most organic materials. This is because particles of these metals do not devolatilize or pyrolyze, but melt and evaporate at high temperatures and burn as discrete entities. **Figure 1** shows how the combustion rate of clouds of aluminium dust in air increases systematically with the specific surface area of the dust. For aluminium, a specific surface area of 6.5 m^2/g corresponds to monosized spheres of diameter 0.34 μm.

Figure 2 summarizes some other data for the maximum rate of pressure rise for various dusts as functions of median or average particle size. The influence of the particle size of Al and Si dusts is particularly pronounced in the range below 10 μm. Eckhoff [6], discussing dusts of ferro alloys, emphasized that most published experimental data lack adequate information about the particle size in this region, and therefore are of limited value. Careful particle size measurements, at least down to 1 μm, should be regarded as an indispensable part of future experimental investigations of ignitability/explosibility/combustibility of metal dusts.

Figure 3 illustrates how the minimum explosible dust concentration is influenced by the particle size. The particles used in these experiments were close to monodisperse, i.e. of narrow size distributions. In

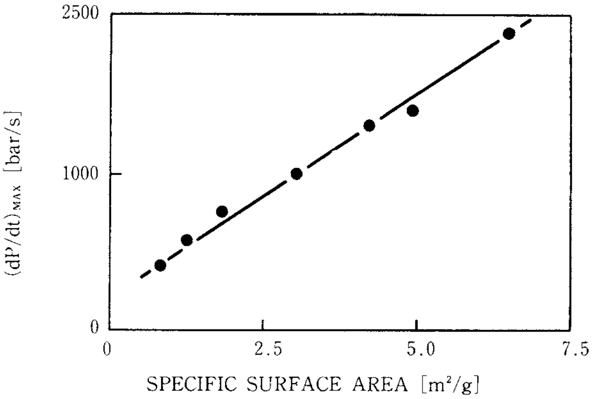

Fig. 1 Influence of specific surface area of aluminium dust on maximum rate of pressure rise in standard 1 m^3 ISO vessel. (From Bartknecht, 1978 [5])

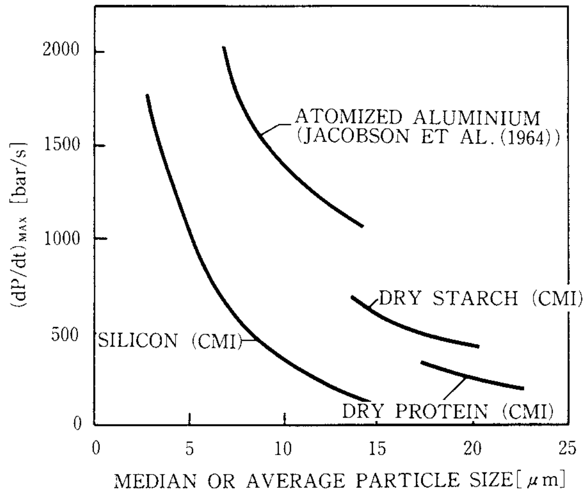

Fig. 2 $(dP/dt)_{max}$ in 1.2-litre closed vessel of clouds in air of silicon dust, aluminium dust, and dusts from natural organic materials, as functions of particle size. (From Eckhoff et al. [7])

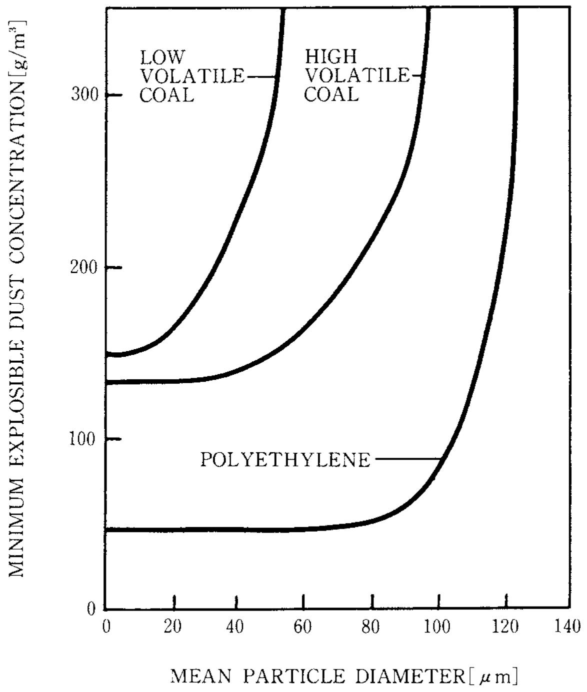

Fig. 3 Influence of mean particle diameter on minimum explosible dust concentration in 20-litre USBM vessel for three different dusts. (From Hertzberg and Cashdollar [8])

practice, the distributions may be quite wide, and simple relationships for monosized dusts may not be valid.

Figure 4 shows the strong influence of the particle size on the minimum electric spark ignition energy for three different dusts.

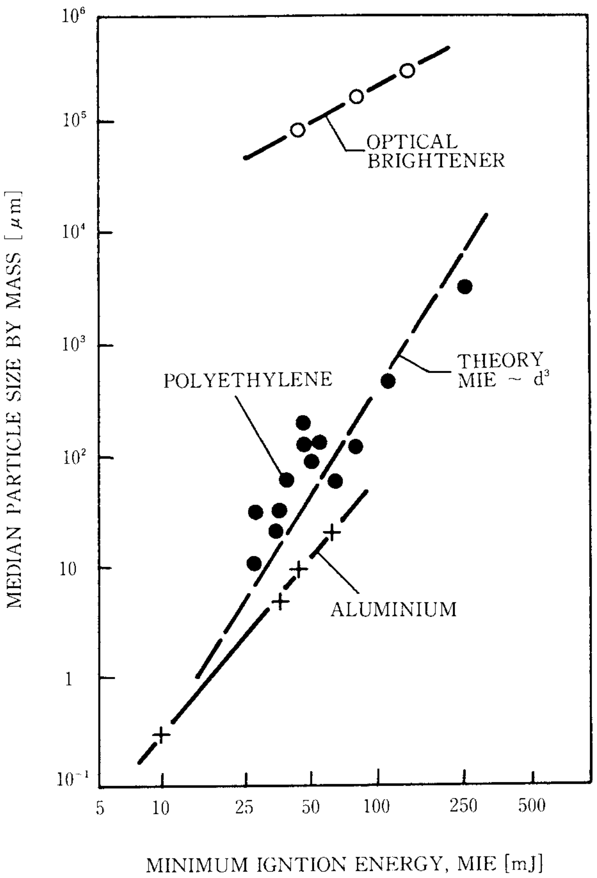

Fig. 4 Minimum electric spark ignition energy (MIE) of clouds in air of an optical brightener, polyethylene and aluminium, as functions of median particle size. (From Bartknecht [9]. Theoretical line for polyethylene from Kalkert and Schecker [10])

3. Degree of De-Agglomeration of Dust Particles

3.1 Nature of problem

The formation of explosible dust clouds from powder deposits implies that particles originally in contact within the powder deposit must be separated and suspended in the air. There are two points to consider. The first is the spectrum of forces originally acting on and between the particles in the deposit, resisting the separation of the particles. The second point is the energy required for the separation process under various practical conditions. Eckhoff [11] suggested that a global dispersibility parameter for a powder deposit may be defined by considering these two points. A given quantity of a given powder, at equilibrium with the ambient atmosphere, contains a finite number of inter-particle bonds, each of which requires a specific amount of work to be broken. The total minimum work W_{min} needed to break all these bonds in one unit mass of powder, could in principle be calculated by integrating the work required for breaking all the individual inter-particle bonds. The influence of gravity would depend on whether the particles would have to be raised into suspension or whether dispersion would be downwards. One could then define a theoretical upper limit value of the dispersibility for that specific powder deposit, in terms of mass of powder dispersed per unit of work performed:

$$D_{max} = \frac{1}{W_{min}} \quad (1)$$

However, no realistic dispersion process can be one-hundred per cent efficient. This could be accounted for by incorporating an efficiency factor, K:

$$D_{real} = \frac{K}{W_{min}},\ 0 < K < 1 \quad (2)$$

Inter-particle forces in powders include

- van der Waals' forces
- electrostatic forces (Coulomb-forces)
- forces due to liquids (liquid bridges, capillary underpressure)

In the dispersion of cohesive powders composed of very small particles (<5-10 μm), inter-particle forces play a major role, and inter-particle bonds cannot be broken unless the particle agglomerates are exposed to very large shear forces. This means that complete dispersion into primary particles is only possible in high-velocity flow fields, or if the particles are exposed to high-velocity impacts.

3.2 Influence of dust moisture on dust dispersibility

In his report on the dust explosion in Turin in 1785, Morozzo[1] wrote:

"The warehouse, at the time of the accident, contained about three hundred sacks of flour. Suspecting that this flour might have been laid up in the warehouse in a damp state, I thought it right to enquire into that circumstance. I found, upon examination, that it was perfectly dry; there was no appearance of fermentation in it, nor was there any sensible heat. The baker told me that he had never had flour so dry as in that year (1785), during which the weather had been remarkably dry, there having been no rain in Piedmont for the space of five or six months: indeed, he attributed the accident which had happened in his warehouse to the extraordinary dryness of the corn."

Professor Weber [12], one of the pioneers of dust explosion research in the 19th century, emphasized that the cohesion of wheat flour, caused by inter-particle adhesion, plays an important role with respect to the ability of the flour to disperse into explosible dust clouds. He suggested that two large dust explosion disasters, one in Szczecin (Stettin) and one in München, were mainly due to the high dispersibility of the flours. He also demonstrated, using simple but convincing laboratory experiments, that the dispersibility, or dustability, of a given flour increased systematically with decreasing moisture content in the flour.

The specific mechanisms by which moisture reduces both ignition sensitivity and explosion violence of clouds of organic dusts are complex, as illustrated by **Figure 5**. For some reason, the minimum ignition energy of the tapioca dust responded much more strongly to changes in dust moisture content than the other two dusts. In the dry state the tapioca gave the lowest minimum ignition energy of the three, which could indicate that this dust was the finest one.

3.3 Influence of intensity of dust dispersion process on degree of de-agglomeration of dust particles in industrial dust clouds

As already pointed out, the extent to which a certain powder or dust will appear in agglomerated form when dispersed in a cloud very much depends on the intensity of the dispersion process. The work by Yamamoto and Suganuma [14] constitutes an excellent experimental confirmation of this. Their findings are of significance both with respect to the real nature of the industrial dust explosion hazard, and to the design of experimental methods for its assessment. **Figure 6** shows the equipment used in the investigation by Yamamoto and Suganuma. The dust was first dispersed gently in the upstream air flow by feeding it into the supply pipe from a vibration feeder. For cohesive powders, this gave comparatively poor dispersion and large effective

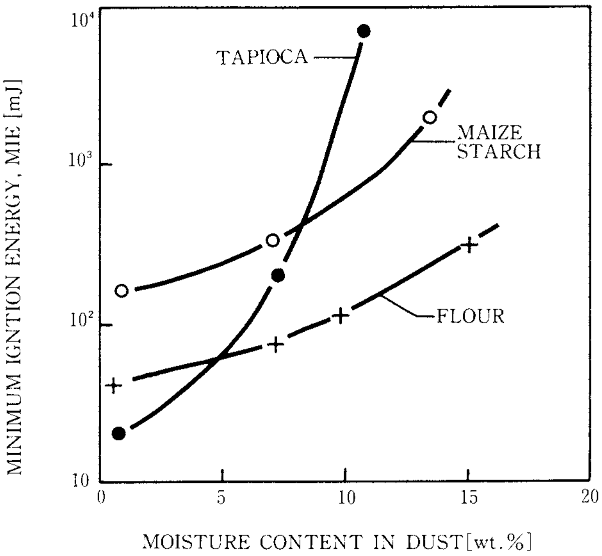

Fig. 5 Influence of dust moisture content on minimum electric spark ignition energy (MIE) for three dusts. (From van Laar and Zeeuwen [13])

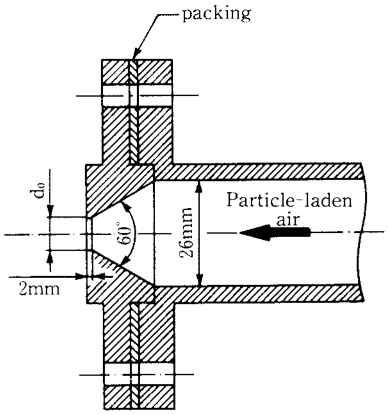

Fig. 6 Schematic view of nozzle for dispersing agglomerates of cohesive dust particles. (From Yamamoto and Suganuma [14])

particle size. The primary dust cloud was then forced through the narrow nozzle in which the agglomerates were dispersed to varying extent depending on the flow conditions in the nozzle. A sample of the secondary, dispersed dust cloud was sucked through a cascade impactor, from which the effective, aerodynamic in-situ size distribution in the secondary dust cloud was obtained.

As **Figure 7** shows, the distribution of effective particle sizes is shifted systematically towards smaller particles as the dispersion process becomes more intense, i.e. as the air velocity through the nozzle increases. At the highest air velocities in the nozzle, 168 m/s, the distribution of the sizes of 'effective' particles in the secondary dust cloud approached the size distribution determined by a sedimentation balance, with the primary particles effectively dispersed in a liquid.

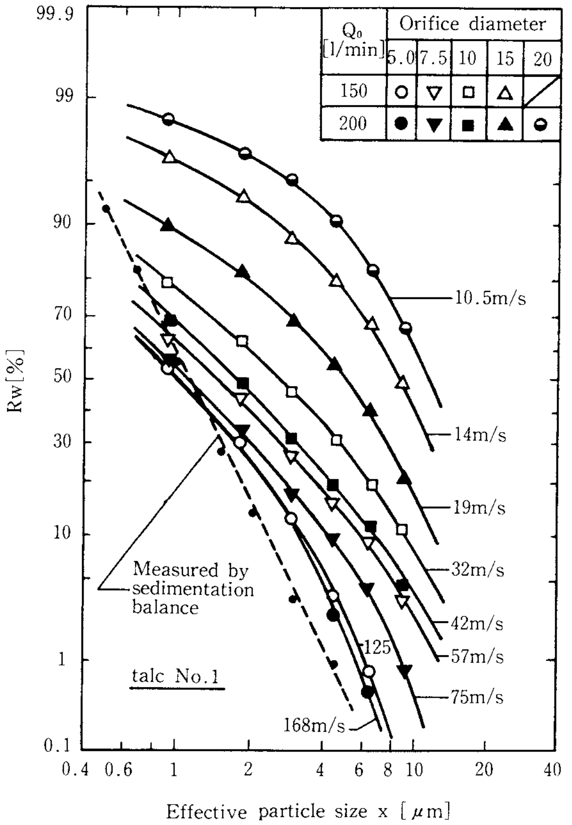

Fig. 7 Effective particle size distribution of an airborne talc dust after dispersal through different orifices. R_W is the percentage by weight of the effective 'particles' that are larger than the size x. (From Yamamoto and Suganuma [14])

3.4 Effect of degree of de-agglomeration on dust cloud burning rates

In his experimental studies of burning times of pulverized fuels, Bryant [15] found that persistent agglomeration, as illustrated in **Figure** 8, was the reason for comparatively long burning times for apparently small particles. Under such circumstances, a stable agglomerate behaves as a large single particle of the size of the agglomerate.

Eckhoff and Mathisen [16] investigated the influence of the degree of dispersion of maize starch grains of typical diameters 10-15 μm on the rate of pressure rise during explosions in a small 1.2-litre explosion bomb. **Figure 9** shows that $(dP/dt)_{max}$ increased systematically as the effective particle size decreased.

4. Dust Concentration

As also pointed out by Wolanski [4], explosive combustion of dust clouds cannot take place unless the dust concentration, i.e. the mass of dust per unit volume of dust clouds, is within certain limits. This is analogous with combustion of homogeneous mixtures of gaseous fuels and air, for which upper and lower flammability limits are well established. **Figure 10** indicates the explosible range typical of natural organic materials.

Explosible dust clouds have high optical densities,

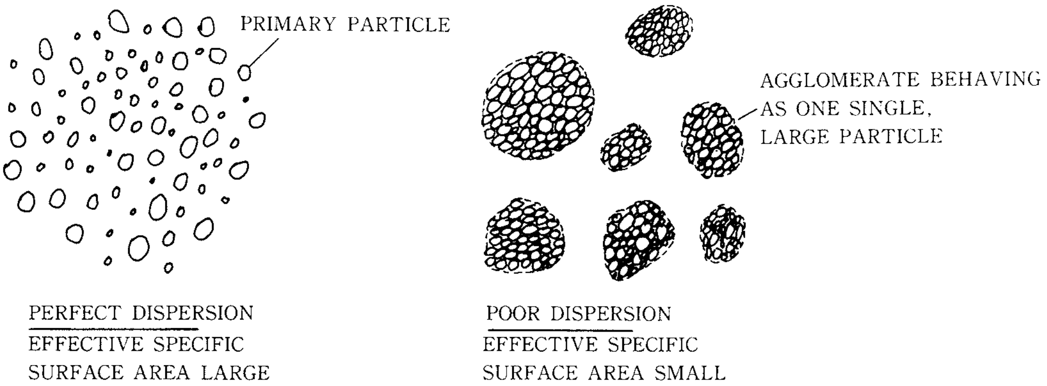

Fig. 8 Illustration of a perfectly dispersed dust cloud and a cloud consisting of agglomerates. (Eckhoff [2])

even at the lower explosible limit, and the unpleasant dust concentration levels in the general working atmosphere of a factory, which may draw the attention of industrial hygiene authorities, are far below the concentration levels that can propagate dust flames. For metals, the explosible ranges and the bulk densities are higher than for organic materials, because of the higher specific gravities of the metals.

Within the explosible range of dust concentrations, both the ignition sensitivity and the explosion pressure/rate of rise of explosion pressure vary with the dust concentration. **Figure 11** shows some results from large-scale experiments with maize starch in a 22-m-high experimental silo of volume 236 m^3, vented at the top. The results indicate a peak in the maximum vented explosion pressure at about 500 g/m^3, i.e. about twice the idealized stoichiometric concentration 235 g/m^3.

Figure 12 illustrates the influence of dust concentration on the electric spark ignition sensitivity.

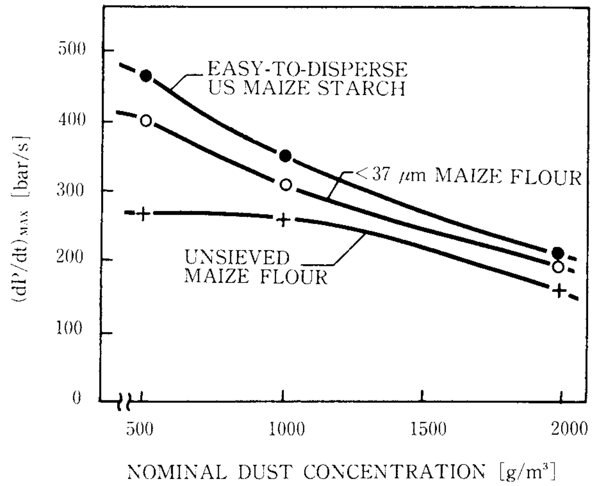

Fig. 9 Maximum rate of pressure rise in the 1.2-litre explosion bomb of maize starches containing different fractions of agglomerates. (From Eckhoff and Mathisen [16])

5. Dust Cloud Turbulence

5.1 General outline

The influence of the turbulence of the dust cloud is a very important aspect of dust explosions, which was sometimes overlooked in the past. In practical terms, turbulence is a process of rapid internal, more or less random movement of elements of the dust cloud relative to each other in three dimensions. If the cloud is burning, turbulence will give rise to a kind of three-dimensional alternating 'laminate' of burnt/burning/unburnt zones ('flamelets'). Therefore, a turbulent cloud will generally burn much faster than when a single laminar flame sheet propagates through a quiescent cloud.

In the case of ignition of the dust cloud, whether by an electric spark or a hot surface, the turbulence will disturb the heat transfer by removing heat from the ignition zone by rapid convection. Therefore, ignition of a turbulent dust cloud generally requires higher energies/temperatures than ignition of a quiescent cloud of the same dust.

5.2 Initial turbulence

In the context of dust explosion propagation, two kinds of turbulence, differing by their origin, have to be considered. The first is turbulence generated by the industrial process itself within the various process units in which dust clouds are formed, be they air jet mills, mixers, cyclones, bag filters, pneumatic transport pipes, or bucket elevators. This kind of turbulence is often called *initial turbulence*. The second kind, explosion-induced turbulence, is discussed in 5.3 below.

Figure 13 shows the strong influence of initial turbulence on the minimum electric spark ignition energies of dust clouds. The dust clouds were generated in a closed vessel by dispersing a given mass of

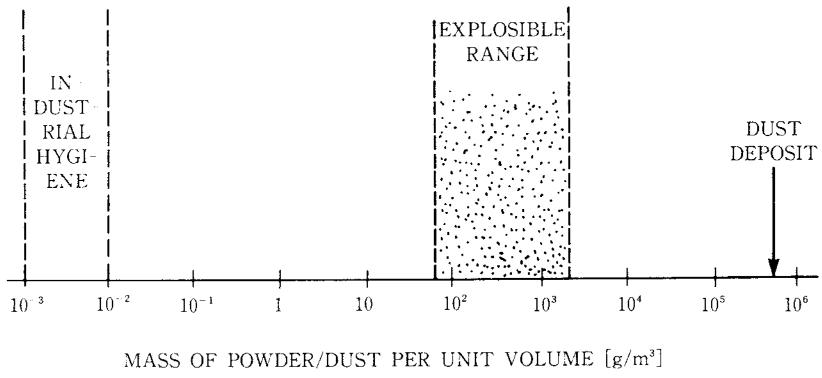

Fig. 10 Range of explosible dust concentrations in air at normal temperature and atmospheric pressure for a natural organic dust, e.g. maize starch, compared with typical range of maximum permissible dust concentrations in the context of industrial hygiene, and a typical density of deposits of natural organic dusts. (Eckhoff [2])

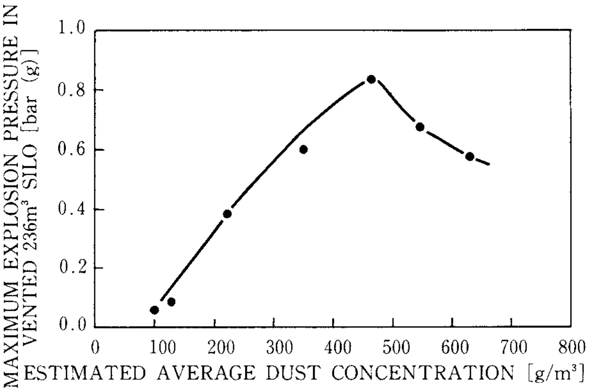

Fig. 11 Influence of estimated average dust concentration in exploding maize starch cloud in 236-m^3 silo of $L/D=6$, on maximum explosion pressure in vented silo. Vent area at top of silo 5.7 m^2. Ignition close to bottom of silo. (From Eckhoff et al. [17])

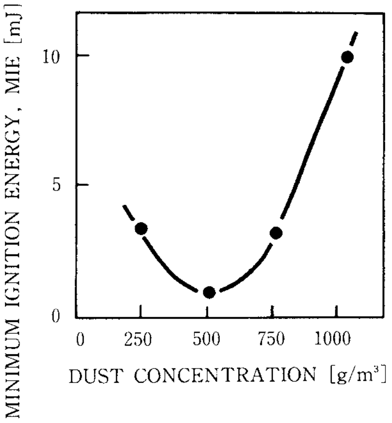

Fig. 12 Influence of average dust concentration in 1 m^3 ISO standard closed vessel on the minimum electric spark ignition energy of clouds of an antioxidant in air. (From Bartknecht [18])

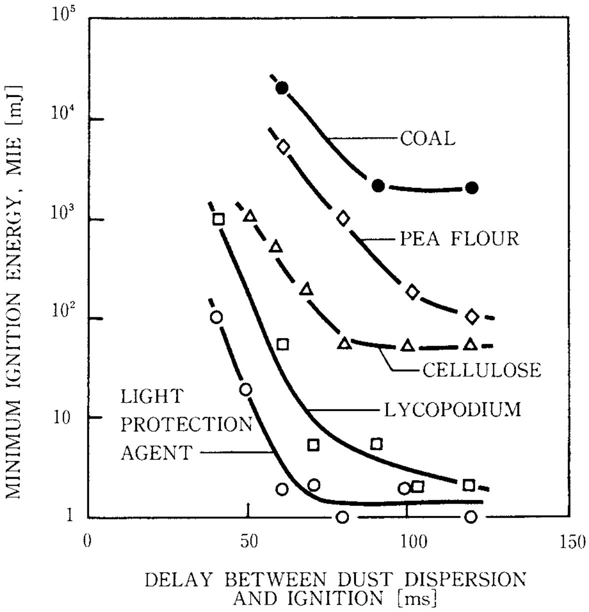

Fig. 13 Influence of initial turbulence on the minimum electric spark ignition energy of dust clouds. Experiments with various dusts in a 20-litre spherical explosion bomb. (From Glarner [19])

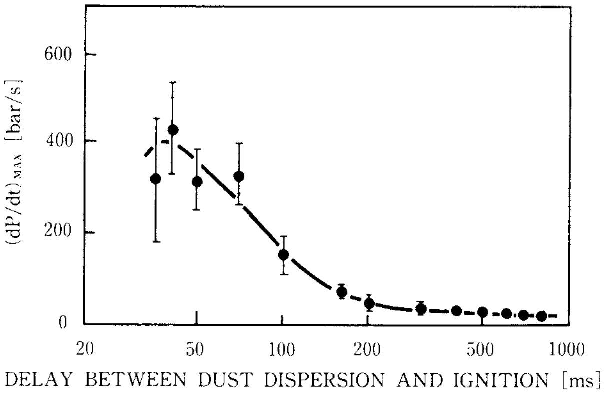

Fig. 14 Influence of initial turbulence on explosion rate of a dust cloud. Experiments with 420 g/m^3 of lycopodium in air in a 1.2-litre closed explosion bomb. Bars indicate ±1 standard deviation. (From Eckhoff [20])

dust by a short blast of air. In the early stages of dust dispersion, the dust cloud was quite turbulent, whereas the turbulence faded away with time after the dispersion air had ceased to flow. The effect exposed in Figure 13 is quite dramatic. High initial turbulence can give MIE values that are several orders of magnitude higher than for quiescent clouds. In the context of possible ignition by electrostatic discharges, this is fortunate, because triboelectric charging to high voltages normally requires dust clouds of high velocities and turbulence.

When it comes to the violence of the explosion, however, the effect of initial turbulence is to increase the hazard. **Figure 14** shows that the maximum gradient of the pressure rise versus time decreased markedly, by about an order of magnitude, with increasing ignition delay (decreasing initial turbulence) up to about 200 ms. Over this range of delays the maximum explosion pressure remained fairly constant, which indicates that the reduction in explosion rate was not due to the settling-out of the dust.

Comparatively little quantitative knowledge exists about the various processes by which dust clouds are generated in industrial plant, and the resulting levels of initial turbulence. As discussed by Eckhoff², some work has been done on the entrainment of dust particles by turbulent gas flows passing over dust layers and ridges in wind tunnels. However, quantitative relations between essential parameters of the dust cloud generation processes and the states of the resulting dust clouds are scarce, and more work, directed towards conditions of pratical dust cloud generation in industry, is needed.

An excellent example of this kind of work was performed by Hauert et al. [21]). They measured

RMS (root mean square) turbulent velocities, global velocities and dust concentrations in experimental dust clouds in a 12-m^3 silo where the dust was either blown in via a pneumatic transport pipe, or dropped from a screw conveyor at the silo top. This kind of work is essential, for example, for testing numerical codes for simulating dust cloud formation in real industrial situations. Such codes will in turn constitute an essential element in future comprehensive codes for simulating dust explosion propagation in industrial environments.

A challenging basic question needs to be considered: *What is the 'turbulence' of a dust cloud in the context of initiation and propagation of dust explosions ?* Could it be that the most important 'turbulence' mechanism is, in some cases, *the movement of burning particles in relation to unburnt ones, rather than the movement of the gas phase ?* Could it be, therefore, that the movement of the particles is, in fact, in some cases a more appropriate measure of 'turbulence' than the movement of the gas phase? The answer probably depends on the nature of the particles. Very rapid devolatilization with the combustion occurring mainly in the bulk of the gas phase is an extreme case where the gas movement is indeed important. If, on the other hand, the combustion mainly occurs close to the particle surface, the particle movement is the primary concern.

5.3 Explosion-induced turbulence

The second kind of turbulence in the context of dust explosions is the turbulence generated by the explosion itself by the expansion-induced flow of unburnt dust cloud ahead of the propagating flame. The levels of turbulence generated 'in situ' in this way depend on the speed of the flow and the geometry of the system. Obstacles such as the buckets in a bucket elevator leg enhance turbulence generation under such conditions. In long ducts or galleries, a positive feed-back loop can be established by which the flame can accelerate to very high speeds and even transit into a detonation. (Eckhoff [2])

Predicting this kind of positive feed-back process in real dust explosions in industrial plant is a major challenge. CMR in Bergen, Norway, has produced a comprehensive numerical model, FLACS, which is capable of predicting the development of turbulent gas explosions in complex geometries. This constitutes an excellent basis for developing a similar model for dust explosions in real, complex process plant. CMR has recently (1996/97) launched a major international co-operative effort in dust explosion research, DESPRO, aimed at accomplishing this demanding task.

6. Application to Practice

6.1 Dust explosion venting

The maximum explosion pressure in a vented dust explosion, P_{red}, is a result of two competing processes:

- Burning of the dust cloud inside the enclosure, which develops heat and increases the pressure.
- Flow of unburnt, burning and burnt dust cloud through the vent, which relieves the pressure.

The two processes are often coupled via turbulence induced by the flow out of the vent, which can increase the burning rate.

It is now generally accepted that the required minimum area of the vent opening depends on:

- Enclosure volume
- Enclosure strength
- Internal pressure for opening of vent cover
- Mass of vent cover
- Burning rate of dust cloud

The most complex problem by far is to make an adequate assessment of the dust cloud burning rate. In the past, it was sometimes believed that this was a constant property of a given dust, which could be determined once and for all in a standard closed vessel test (K_{St}-value). However, it is now generally accepted that in industrial reality, clouds of a given dust can have widely differing combustion rates depending on the dust concentration, the degree of de-agglomeration, and the turbulence in the actual process situation.

The influence of the initial turbulence intensity of the dust cloud on the maximum pressure in vented explosions was studied specifically by Tamanini [22] and Tamanini and Chaffee [23]. The turbulence intensity in the dust cloud at the moment of ignition was measured in terms of the RMS (root-mean-square) of the instantaneous velocity. **Figure 15** gives a set of data confirming a strong increase of the maximum pressure in the vented explosion with increasing initial turbulence of the cloud.

A series of experiments in a 500-m^3 silo of $L/D = 4$ was reported by Eckhoff and Fuhre [24]. Pneumatic upwards injection of dust through a 200-mm-ϕ pipeline was used for generating explosible dust clouds in the silo. The ignition point was close to the silo bottom. The experimental results are shown in **Figure 16** together with predictions based on a range of proposed vent sizing methods. The excep-

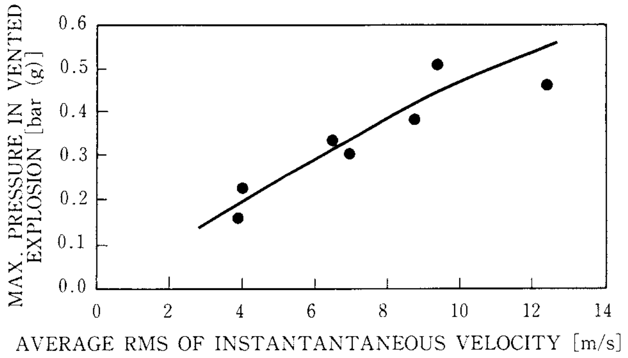

Fig. 15 Influence of turbulence intensity of burning dust cloud on maximum pressure in vented maize starch explosion in 64-m^3 rectangular chamber. Starch concentration 250 g/m^3. Vent size 5.6 m^2. Ignition source 5 J chemical igniter at the chamber centre. (From Tamanini [22])

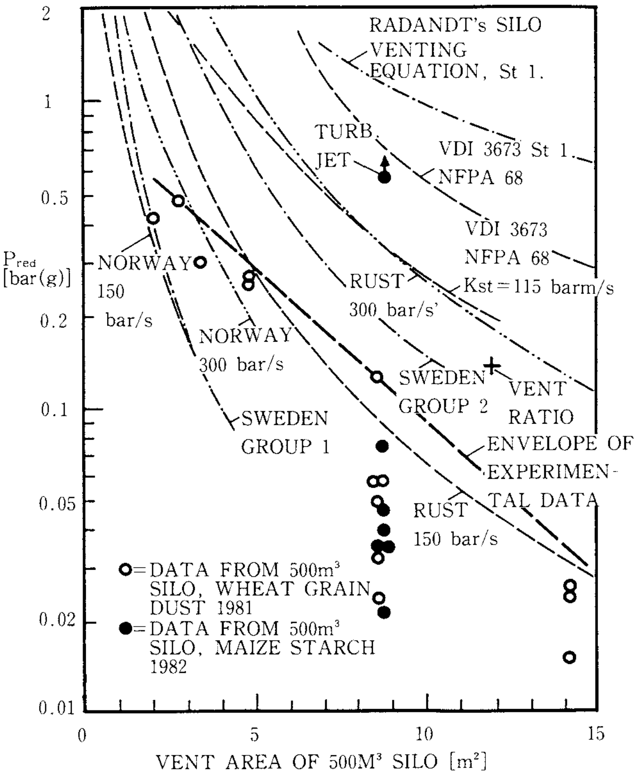

Fig. 16 Results from vented maize starch and wheat grain dust explosions in a 500-m^3 silo cell in Norway. Comparison with predicted P_{red}/vent area correlations by various vent sizing methods in current use. P_{red} means the maximum pressure in the vented enclosure during the explosion. (From Eckhoff and Fuhre [24] with adjustments by Eckhoff [25])

tion was the experiment marked 'Turb. Jet', in which the ignition source was activated while dust was still being blown into the silo, and the cloud was therefore still highly turbulent. In all the other experiments, dust injection was terminated a few seconds before ignition, allowing the dust cloud to become practically quiescent.

Figure 16 reflects the current situation: the wide range of vent area sizing codes in use differ in their vent area predictions by factors of up to 3-5 and even more. Large-scale experiments have confirmed the very strong influence of the state of the dust cloud at the moment of ignition on the dust cloud combustion rate in the vented enclosure. An excellent demonstration is provided by **Figure 17**.

The dust cloud in the silo was generated in three different ways, giving substantially different dust concentration distributions, degrees of dust de-agglomeration, and turbulence. The first was the traditional VDI-method for dust-cloud generation, giving very violent explosions, and the second was direct pneumatic pipeline injection of the dust. The third way was dust injection via a cyclone at the silo top, i.e. the dust cloud in the silo was generated by the gentle discharge of dust from the cyclone bottom via a rotary lock. With a vent area of 1.2 m^2, the latter method gave a maximum explosion pressure of only 0.2 bar(g), whereas direct pneumatic injection gave about 0.5 bar(g), and the traditional VDI-method (discharge of dust from pressurized bottles) about 0.75 bar(g). Consequently, for a given P_{red}, the required vent area varied substantially in the three cases.

Figure 18 gives some results from maize starch explosion experiments in a much larger silo, of volume 236 m^3, but with the same height-to-diameter ratio $L/D \approx 6$. In these experiments, the parameter of main concern was the location of the ignition point along the vertical axis of the silo. The dust cloud was essentially quiescent at the moment of ignition.

The hatched envelope of all experimental data shows a dramatic decrease of the maximum explo-

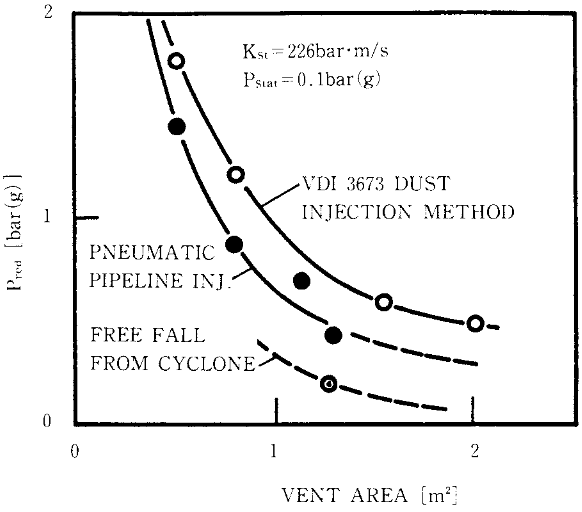

Fig. 17 Results from vented maize starch explosions in a 20-m^3 silo, demonstrating the marked influence of the mode of dust cloud generation on the maximum pressure P_{red} in the silo during the vented explosion. (From Bartknecht [9, 26])

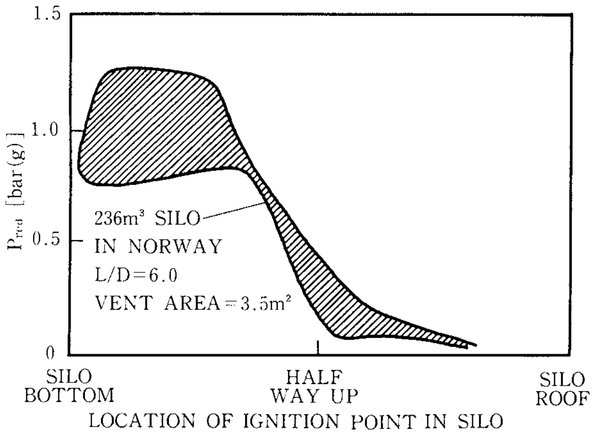

Fig. 18 Influence of location of the ignition point in a 236-m³ experimental silo in Norway on maximum vented explosion pressure. (From Eckhoff [25])

sion pressure when the ignition point was moved upwards along the silo axis. There is little doubt, therefore, that the marked increase of the maximum explosion pressure as the ignition point was shifted downwads in the silo was caused by flame acceleration due to explosion-induced turbulence. The basic mechanism is the following: as the still unburnt cloud is pushed towards the vent opening by the expanding combustion products, it becomes turbulent, and its combustion rate increases, causing the pressure inside the silo to raise. This is in complete accordance with what has been found in the past in numerous dust and gas explosion experiments in one-end-open tubes, ducts and galleries, e. g. in experimental coal mines.

6.2 Preventing explosion transfer between process units via pipes and ducts: Explosion isolation

There are three main reasons for preventing a dust explosion in one process unit from spreading to others via pipes and ducts. Firstly, there is always a desire to limit the extent of the explosion as far as possible. Secondly, a dust flame propagating in a duct between two process units tends to accelerate due to explosion-induced turbulence in the dust cloud ahead of the flame. For a sufficiently long duct, this may result in a vigorous flame jet entering the process unit at the downstream end of the duct. The resulting extreme combustion rates can generate very high explosion pressures even if the downstream process unit is generously vented. This effect was demonstrated in a dramatic way for flame-jet-initiated explosions of propane/air in a generously vented 50 m³ vessel, by Eckhoff et al. [27,28]. Wingerden et al. [29] reported very similar effects for dust explosions.

The third reason for employing explosion isolation is pressure piling. This implies that the pressure in the unburnt dust cloud in downstream process unit(s) increases above atmospheric pressure due to the compression caused by the expansion of the hot combustion gases in the unit where the explosion starts. Therefore, in a coupled system, because the maximum explosion pressure (abs) is proportional to the initial pressure (abs), higher transient explosion pressures can occur in secondary process units than would be expected at atmospheric initial pressure.

Devices for explosion isolation are most often located in ducts and pipes connecting various process equipment. As described by Eckhoff[2], there are two main categories of such devices, viz. passive and active. Passive devices are operated by the explosion itself, whereas the active types require extra explosion detection and activation equipment.

The boundaries for the applicability of the various types of passive devices have not been fully explored. The development of the burning rate in the entire system, with non-steady explosion-induced turbulence as a key parameter, is of prime importance.

As regards active explosion interrupters, the required closing times for fast-acting valves depend on the distance between the remote pressure or flame sensor and the valve, and indeed on the burning rate development in the dust cloud. Often closing times as short as 50 ms, or even less, are required. Explosion interruption by fast automatic injection of extinguishing chemicals ahead of the flame is another active method. This is a special application of the automatic explosion-suppression technique, which will be described in Section 6.3.

For the present, the design of explosion isolation systems for industrial process plant has to be based on full-scale experiments. In the longer term, however, codes for CFD 2-phase simulation of the entire coupled reactive flow during dust explosions in complex coupled process systems will most probably become available. (See 5.3.)

6.3 Automatic dust explosion suppression

The first patent for a fast fire-suppression system was allotted to a German company as early as 1912. The Second World War accelerated the development. As a result, new, fast-acting fire extinguishers were developed based on three main principles:

- Extinguishing agent permanently pressurized
- Large-diameter discharge orifice

- Very fast opening of valve for immediate release of extinguishing agent by means of an explosive charge

These principles, combined with a fast-response flame or pressure-rise detection system, form the basis of today's automatic explosion-suppression systems.

Moore [30] discussed the results of his own comprehensive experimental and theoretical research, which resulted in a logical basis for systematic design of industrial suppression systems. He introduced the concept of a critical mass M_t of suppressant that is just sufficient for suppressing the flame when evenly distributed throughout the flame volume. He assumed the existence of a critical minimum mass concentration of any given suppressant for suppressing a flame of a given dust, and that a suppressant cloud of this concentration or higher must occupy at least the flame volume for successful suppression. It then follows that the critical mass M_t increases with time because the flame volume increases with time.

A similar line of thought was applied to the mass of suppressant actually delivered at any time after onset of flame development. Successful suppression would result if $M_{t,delivered} > M_{t,required}$. This is illustrated in **Figures 19** and **20**.

As in the case of explosion venting, the performance of explosion-suppression systems, i.e. the reduction of the explosion pressure that is actually achieved, is a result of two competing processes, viz.:

- The rate of explosion pressure build-up due to the combustion process in the enclosure
- The quenching of the combustion process by the injected suppressant

In order for the suppressant, which is itself often a powder, to be able to penetrate sufficiently far into the burning dust cloud in a sufficiently short time, the suppressant ejection process is bound to be quite violent and generate considerable turbulence. This can in fact temporarily increase the rate of combustion of the dust cloud in initially comparatively quiescent clouds.

As reviewed by Eckhoff [2], much valuable empirical information has been acquired about the performance and feasibility of systems for automatic suppression of dust explosions. However, in the longer term, a more basic design approach, based on CFD 2-phase simulation of the entire explosion/suppression process, will probably become available. (See 5.3.)

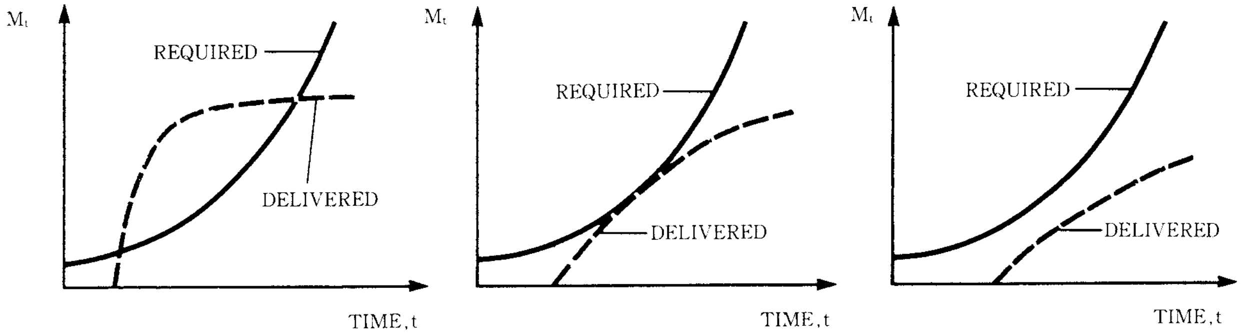

RELIABLE SUPPRESSION CRITICAL SUPPRESSION FAILED SUPPRESSION

Fig. 19 Illustration of mass of suppressant required and delivered as functions of time for reliable suppression, critical suppression and failed suppression. (From Moore [30])

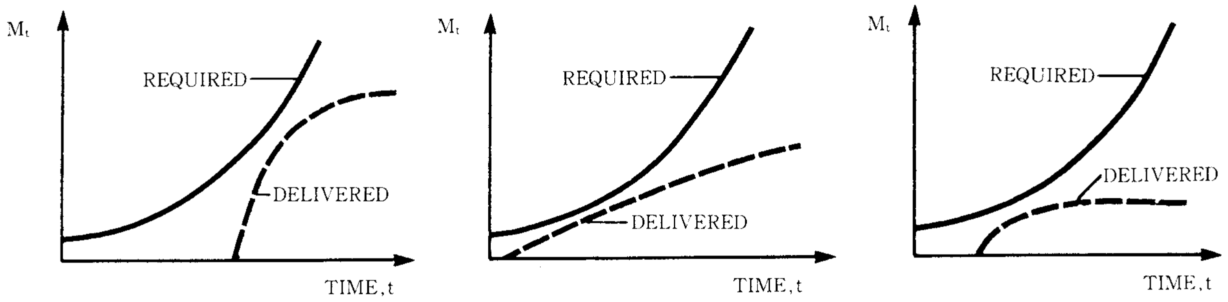

TOO LATE START TOO LOW RATE TOO SMALL QUANTITY

Fig. 20 Illustration of how failed suppression can result from too late start of suppressant injection, too low injection rate, and too small quantity of suppressant injected. (From Moore [30])

6.4 Secondary dust explosions

One important objective of dust explosion control is to avoid *secondary explosions* due to entrainment of dust layers by blast waves from primary explosions. **Figure 10** shows that there is a gap of at least two orders of magnitude between the maximum explosible dust concentration and the bulk density of dust layers and heaps.

The simple relationship between the bulk density of the dust layer ρ_{bulk}, the layer thickness, h, the height, H, of the dust cloud produced from the layer, and the resulting dust concentration, c, is:

$$c = \rho_{\text{bulk}} \frac{\mathrm{h}}{\mathrm{H}} \tag{3}$$

The consequence of this is illustrated in **Figure 21**.

As Figure 21 shows, a 1-mm layer of a dust of bulk density 500 kg/m^3 will generate a cloud of average concentration 100 g/m^3 if dispersed all over in a room of 5 m in height. Partial dispersion up to 1 m gives 500 g/m^3, i.e. in the middle of the most explosible range. This means that even apparently harmless dust layers can contain enough dust to become highly hazardous dust clouds.

If a dust layer of thickness h on the internal wall of a cylindrical duct of diameter D is dispersed homogeneously over the whole tube cross-section, one has

$$c = \rho_{\text{bulk}} \frac{4\mathrm{h}}{\mathrm{D}} \tag{4}$$

In the case of a tube diameter of 0.2 m, typical of many dust extraction ducts in industry, a layer thickness of only 0.1 mm of a dust of bulk density 500 kg/m^3 is sufficient for generating a dust concentration of 1000 g/m^3.

Tamanini [31] investigated the propagation of secondary maize starch dust explosions in a large-scale experimental gallery. A central objective was to determine the minimum quantity of dust, spread as a layer on the gallery floor, per unit gallery length, that was able to propagate a dust explosion sweeping along the gallery. The experiments showed that a dust flame propagated down the gallery even if the mass of the dust layer, per unit length of gallery, was considerably smaller than that corresponding to the minimum explosible concentration if dispersed uniformly over the whole gallery cross-section. This is because the dust was dispersed only in the lower part of the gallery volume and therefore gave higher, and explosible, dust concentrations there, in accordance with Figure 21c. It was observed that the height of the secondary dust flame, sweeping along the floor of the gallery, was considerably smaller than the total height of the gallery.

The course of an experiment of the type conducted by Tamanini [31] depends on a number of parameters, including the nature of the primary explosion. Therefore, few generally valid quantitative conclusions can be drawn from such experiments until the various processes have been theoretically coupled and comprehensive mathematical simulation models developed.

7. Concluding Remarks

Increased emphasis should be put on investigating the complex relationships between dust cloud generation processes in industrial plant and the structures of the resulting dust clouds. Such structures must be defined in terms of the spatial and temporal distributions of dust concentration, quality of dust dispersion (de-agglomeration), turbulence parameters and global velocities. At the same time, further work must be performed to clarify the complex relationships between the dust cloud structure and dust cloud combustion rate. Embarking on development of comprehensive 2-phase-reactive-flow CFD codes for simulating dust explosion propagation in real industrial geometries is timely. Finally, it should be emphasized that the systematic implemen-

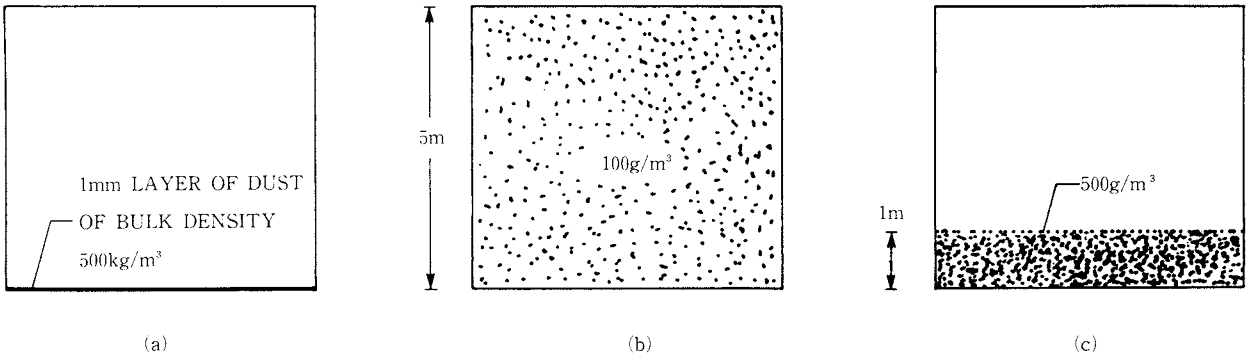

Fig. 21 Illustration of the potential hazard of even thin dust layers.

tation of powder science and technology in the optimization of process design may contribute significantly to increasing the level of inherent safety of process plant with regard to the dust explosion hazard. One classical example is the replacement of funnel flow by mass flow in silos and hoppers, which can produce a dramatic reduction of dust cloud formation during discharge operations.

8. References

1) Morozzo, Count : *Account of a violent explosion which happened in a flour-warehouse, at Turin, December the 14th, 1785, to which are added some observations on spontaneous inflammations*. The Repertory of Arts and Manufacturers 2 (1795) pp.416-432.

2) Eckhoff, R.K. : *Dust explosions in the process industries*, extended, updated 2nd edition, Butterworth-Heinemann, Oxford, UK (1997), 643 p., ISBN 0-7506-3270-4.

3) Faraday, M. ; Lyell, C. : *Report on the explosion at the Haswell Collieries, and on the means of preventing similar accidents*. Philosophical Magazine 26 (1845), pp. 16-35.

4) Wolanski, P. : *Dust explosions*. KONA No. 14 (1996), pp. 144-152.

5) Bartknecht, W. : Explosionen-Ablauf und Schutzmassnahmen. Springer Verlag. (1978)

6) Eckhoff, R.K. : *Dust explosion hazards in the ferro-alloys industry*. Proc. 52nd Electric Furnace Conference, Nov. 13-16, 1994, Nashv., TN, USA, pp.283-302. The Iron and Steel Society Inc., Warrendale, PA 15086, USA (1995). ISBN 0-932897-97-5, pp.283-302.

7) Eckhoff, R.K., Parker, S.J., Gruvin, B., et al. : *Ignitability and Explosibility of Silicon Dust Clouds*, J. Eletrochem. Soc. 133 (1986) pp.2631-2637.

8) Hertzberg, M., and Cashdollar, K.L. *Introduction to Dust Explosions. Industrial Dust Explosions*, ASTM Special Techn. Publ. 958 (eds K.L. Cashdollar and M. Herztberg) (1987) pp.5-32, ASTM, Philadephia, USA.

9) Bartknecht, W. : *Staubexplosionen-Ablauf und Schutzmassnahmen*. Springer Verlag. (1987)

10) Kalkert, N., and Schecker H.-G. : *Theoretische Überlegungen zum Einfluss der Teilchengröse auf de Mindestzündenergie von Stäuben*. Chem.-Ing. Techn. 51 (1979) pp.1248-1249.

11) Eckhoff, R.K.: *Factors affecting the dispersibility of powders*. Beretninger XXXIX, 3. Chr. Michelsen Institute, Bergen, Norway (1976), 20 p.

12) Weber, R. : *Preisgekrönte Abhandlung über die Ursachen von Explosionen und Bränden in Mühlen, sowie über die Sicherheitsmassregeln zur Verhütung derselben*, Verh. Ver. Gew. Fliess. (1878)

13) Laar, G.F.M. van, and Zeeuwen, J.P. : *On the Minimum Ignition Energy of Dust-Air Mixtures*. Archivum Combustionis 5 (1985) pp.145-159.

14) Yamamoto, H., and Suganuma, A. : *Dispersion of Airborne Aggregated Dust by an Orifice*. International Chemical Engineering, 24 (1984) pp.338-345.

15) Bryant, J.T. : *Powdered Fuel Combustion : Mechanism of Particle Size*. Combustion and Flame 20 (1973) pp. 138-139.

16) Eckhoff, R.K. : and Mathisen, K.P. : *Critical Examination of the Effect of Dust Moisture on the Rate of Pressure Rise in Hartmann Bomb Tests*. Fire Research 1 (1977/1978) pp.273-280.

17) Eckhoff, R.K., Fuhre, K., and Pedersen, G.H. : *Vented Maize Starch Explosions in a 236 m^3 Experimental Silo. Report* No. 843307-2, December (1985) Chr. Michelsen Institute, Bergen, Norway.

18) Bartknecht, W. : *Forschung in der Sicherheitstechnik*, Chemie-Technik 8 (1979) pp.493-503.

19) Glarner, Th. : *Mindestzündenergie-Einfluss der Tempertur*. VDI-Berichte 494 pp.109-118, VDI-Verlag GmbH, Düsseldorf. (1984)

20) Eckhoff, R.K. : *The Use of the Hartmann Bomb for Determining K_{St} Values of Explosible Dust Clouds*. Staub-Reinhaltung-Luft 37 (1977) pp.110-112.

21) Hauert, F., Vogl, A., and Radandt, S. : *Measurement of Turbulence and Dust Concentration in Silos and Vessels. proc. 6th Internat*. Coll. Dust Explosions, (Ed. by Deng Xufan and Piotr Wolanski), (Aug. 29-Sept. 2), Shenyang, P.R. of China, (1994) pp.71-80.

22) Tamanini, F. : *Turbulence Effects on Dust Explosions Venting*. AIChE Loss Prevention Symposium, Paper 12 a Session 8, April (1989) Houston, USA.

23) Tamanini, F., and Chaffee, J.L. : *Large-Scale Vented Dust Explosions-Effect of Turbulence on Explosion Severity*. Technical Report FMRC J.I. OQ2E2.RK, April (1989) Factory Mutual Research.

24) Eckhoff, R.K., and Fuhre, K. : *Dust Explosion Experiments in a Vented 500 m^3 Silo Cell*. J. Occ. Acc. 6 (1984) pp.229-240.

25) Eckhoff, R.K. : *Sizing of Dust Explosion Vents in the Process Industries. Advances Made During the 1980s*. J. Loss. Prev. Process Ind. 3 (1990) pp.268-279.

26) Bartknecht, W. : *Massnahmen gegen gefährliche Auswirkungen von Staubexplosionen in Silos und Behälter : Explosionsdruckentlastung beim Befüllen durch Flugförderung*,, Abschlußbericht Project No. 01 HK 664 AO, (1988) Bundesministerium für Forschung und Technologie.

27) Eckhoff, R.K. et al. : *Some recent large-scale gas explosion experiments in Norway*. CMI-report No. 790750-1, Jan. (1980), Chr. Michelsen Research AS, Bergen, Norway. 125 p.

28) Eckhoff, R.K. et al. : *Venting of turbulent gas explosions in a 50-m^3 chamber*. Fire Safety Journal 7 (1984), pp. 191-197.

29) Wingerden, K. van ; Pedersen, G.H. ; Eckhoff, R.K. : *Violence of dust explosion in integrated systems*. Process Safety Progress 14 (1995), pp.131-138.

30) Moore, P.E. : *Suppression of Maize Dust Explosions*. Industrial Dust Explosions, ASTM Special Techn. Publ. 958 (eds K.L. Cashdollar and dM. Hertzberg), (1987) pp.

281-293, ASTM Philadephia, USA.

31) Tamanini, F.: *Dust Explosion Propagation in simulated grain conveyor galleries*, Technical Report FMRC J.I. OFIR2. RK, July (1983) Prepared for National Grain and Feed Association, (NGFA) Washington D.C.

Author's short biography

Rolf K. Eckhoff

Rolf K. Eckhoff was born in Stavanger, Norway, in 1937. He was appointed at Chr. Michelsen Institute CMI), Bergen, Norway, in 1962, where he first established powder technology as a new research area. From 1970 he established dust explosions as another new field of research, and in 1976 he started the research into accidental gas explosions. From 1973 to 1988 Eckhoff was CMI's chief scientist in powder technology, and dust and gas explosions. From 1988 he was (CMI's from 1992 CMR) senior scientific adviser in Process Safety Technology (explosion research). In 1991 Eckhoff initiated a co-operative with the University of Bergen (UiB) to establish education and research in process safety technology at the University. He was appointed part time professor in 1992, and in 1996 he moved to a full time professorship in process safety technology at UiB, while maintaining a part time position as a scientific adviser at CMR.

Eckhoff is the author/co-author of more than 70 technical/scientific publications and more than 100 research reports on various aspects of powder technology, and dust, mist and gas explosions. He has advised industry on powder technology and explosion protection on numerous occasions, and lectured on courses, conferences and seminars in many countries in Europe, and in China, Australia and USA: He is also member of the editorial boards of several technical journals.

Honours: Permanently invited guest, WPMPS, Europ. Feder. Chemical Engineering, 1985. Concurrent professor of North Eastern University, Shenyang, P.R. of China, 1990. Member of the Committee of Honour of EuropEx, Belgium, 1991. Recipient of the W. Cybulski medal (Polish Academy of Science), 1992.

Review

Generating Aerosols[†]

by **Brian H. Kaye**
*Professor of Physics, Laurentian University**

Abstract

The generation of aerosols has always been an important concern in studies of the hazards of inhaled materials. In recent years the need to generate aerosols for test purposes has spread into many areas of technological endeavour. Literature dealing with the problems associated with the various techniques of aerosol generation has spread into a diversity of technical areas and the relevant literature is not always easy to retrieve, especially since the term "Aerosol Generation" rarely appears in the title of an article. For example, a study of the use of a diffractometer based method of measuring a size distribution would not state that efficient generation of aerosols is a major concern in the accuracy of the data.

In this review article, the diverse literature is focused to facilitate the retrieval of appropriate information for scientists who must generate aerosols as part of a larger investigation.

Section 1 Generating Sprays by Jet Break Up

One of the major ways of creating a spray is to direct with air a jet of liquid against a baffle. There are literally hundreds of systems available commercially to generate sprays for industry. See for example, the catalogues of a spray systems companies. In some systems, breakup of the jets is assisted by the use of ultrasonic vibrations [1-5].

In this review the focus will be on aerosol generation for laboratory tests. One of the major problems, from a scientific point of view, is that the breakup of an air driven jet results in a very wide size range of droplets [6-10]. If the droplets are of a volatile substance, there is a very rapid interchange of vapour between the droplets; if the droplets are of a non-volatile nature, a large size range of droplets persists. The actual range of droplets present in the spray jet depends upon the properties of the fluid, the configuration of the nozzle and the operating conditions. One area where there is very active research is in attempting to obtain greater fuel efficiency in systems such as diesel engines using heavy fuel oil. In **Figure 1**, size distributions for three different sprays generated under various conditions, noted on the diagram, are shown [11].

It should be noted that the ordinate of the graph of **Figure 1** is a special scale known as the Rosin Rammler distribution. This function is given by the relationship

$$\log\left(\log\left(\frac{100}{R}\right)\right)=k+n\log(d)$$

where d is the size of the particle and R is the weight percent larger than or equal to d.

This type of distribution function has been widely used to describe the distribution of drops in a spray system. It is known as a Rosin-Rammler distribution function after the original German scientists who described the function in 1932. (For an accessible discussion of this distribution function, see Reference 12.) The Rosin-Rammler distribution

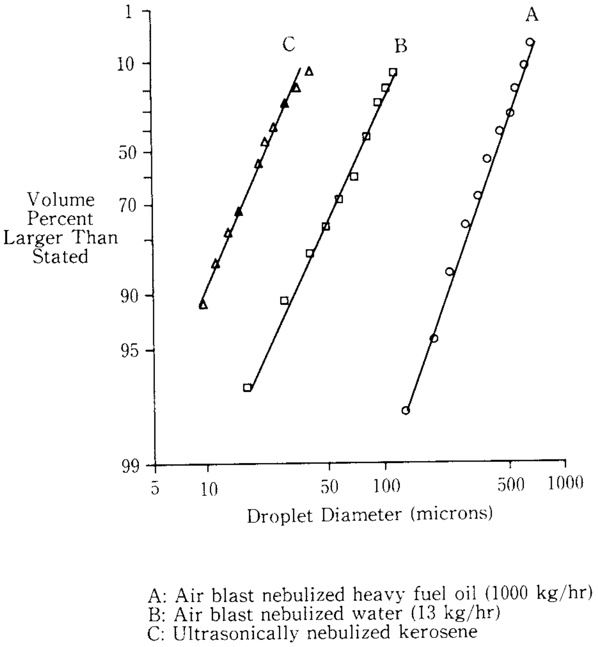

Fig. 1 A wide range of droplet sizes can be created by the break-up of a jet of fluid [11].

---

*Sudbury, Ontario Canada P3E 2C6

[†] Received may 1997.

involves taking the "logarithms of logarithms". In the words of Allen,

> "this relationship should be used with caution, since the device of taking logs always reduces the scatter (of data), hence taking logs twice is not to be recommended."

In the early days of the use of diffraction to study spray systems, the Rosin-Rammler distribution was assumed to be the appropriate descriptive function and was incorporated into the interpretive logic of some of these machines. The scale is so insensitive to fluctuations, that it has been shown that if one were to treat the sequence of numbers in a random number table as sieve residues obtained when studying crushed powders, nine out of ten random number tables would fit the Rosin-Rammler distribution! [12]

The simple type of spray bottles shown in **Figure 2** exploit Bernoulli's principle to aspirate water into a jet of air which was then driven against a baffle to generate an aerosol spray. This simple physical system was used in the 1935 design of what has become known as the Collison Nebulizer. This classic spray generator is still widely used in industry [13-16].

The basic system of the Collison Nebulizer is shown in **Figure 3**. Liquid to be nebulized is placed in the reservoir as shown in the diagram.

A feed tube draws liquid into the nebulizing head. It is drawn by the pressure drop in the head created by the dynamic pressure in the air forced down through the center tube. The spray emerges from a jet on the side of the nebulizing head as indicated in the figure, and impinges on a baffle, designed to remove the larger droplets from the spray which then fall back into the reservoir of fluid. The size of aerosol generated with this equipment varies according to the operating conditions. In the commercial version of the equipment, using an air pressure of 15-50 pounds per square inch at an airflow rate of 6-14 liters per minute, you can have a final droplet output of 3.5 milliliters per hour, with a mass median diameter of the order of 2 micrometres. The commercial equipment can have various jets on the nebulizing head according to the needs of the individual worker [13]. Historically, the Collison Nebulizer was devised to meet the needs of scientists studying inhalation therapy, but over the years, it has been used to generate various types of aerosols. W.H. Walton for example used it to nebulize a methylene blue solution for testing the penetration of respirator filters. Rapid evaporation of the water from the original droplets left an aerosol of very fine dye particles. This technique has been embodied into a British standard for testing filters [17].

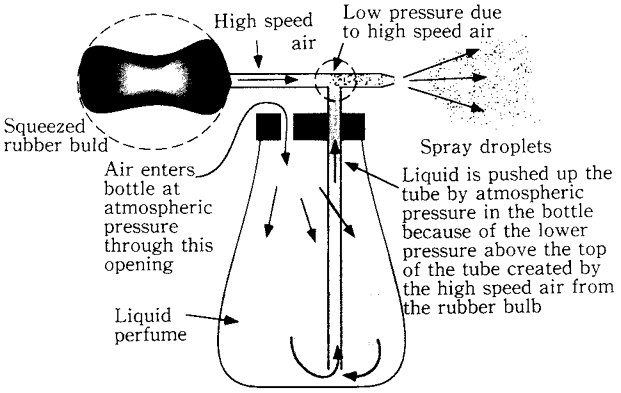

Fig. 2 Bernoulli's Principle is exploited to design aerosol generating equipment. Shown here is the operation of a simple scent spray bottle.

It can also be used to generate salt aerosols and aerosols of oily liquids by using a suitable solvent to create a solution which can be nebulized using the equipment. Another area where jet aerosol generators such as the Collison nebulizer are used is to provide aerosols of standard particles such as latex spheres for calibrating instruments such as the Climet and other optical stream counters. For this purpose, several companies provide suspensions of standard fineparticles in a liquid which is then used

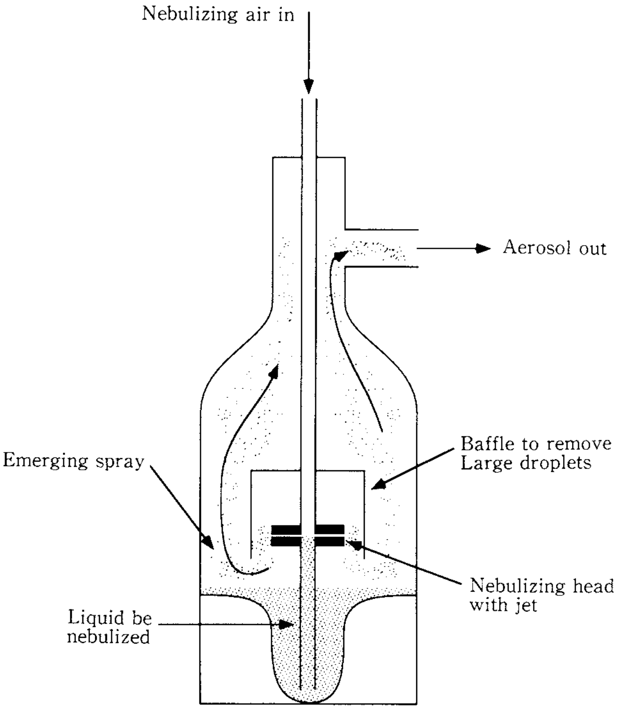

Fig. 3 Basic system of the Collison Nebulizer used to generate aerosols.

to generate a spray.

To generate aerosols of standard latex aerosols the solution is placed in a container and nebulized in a similar way to that in a simple spray generator, as shown in the diagram of **Figure 4** [18, 19, 20]. Again, the liquid stream is aspirated into the compressed air jet by Bernoulli's Principle. The emerging spray is directed to an impaction ball, which removes the larger aerosol particles from the airstream. Only droplets able to flow around the ball move towards the aerosol outlet. When one is generating a latex aerosol, one must pass the aerosol leaving the atomizer chamber through a column of dry air to evaporate the moisture from the drops carrying the latex spheres from the aerosol generation system.

One must be very careful to use only the cleanest water when diluting the suspension of latex particles, because small amounts of chemical in the water will show up as very tiny residual aerosols, as shown by the data reported by workers at the TSI company, shown in **Figure 4(b)**. [20]

It should be noticed that the various manufacturers of generators of aerosol systems use different vocabulary. For example, the term atomizer is used by the TSI company, I prefer to always use the term nebulizer since most certainly an atomizer does not reduce the system to its constituent atoms. Nebulizer, since it means to produce a cloud, is a technically more correct term. However, the term atomizer is so firmly entrenched in the literature, that one must learn to live with the various vocabulary used by different companies and workers.

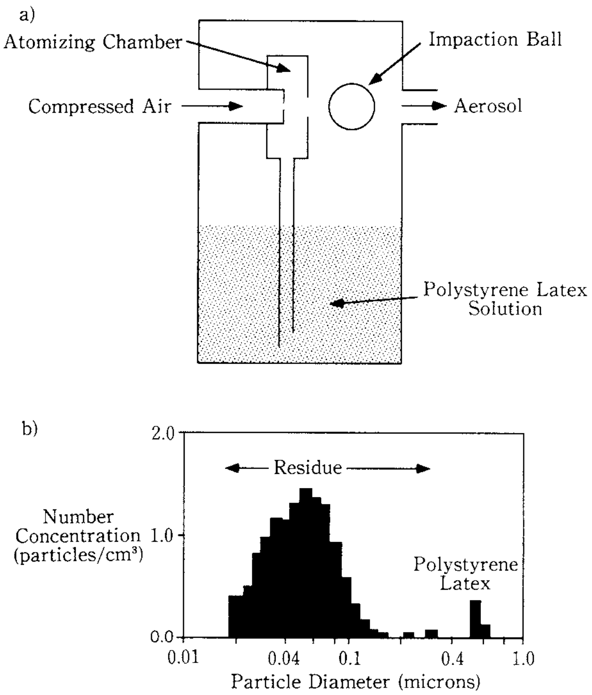

Fig. 4 Schematic diagram of the atomizer head in the TSI Model 3460 Tri-Jet aerosol generator and size distribution for a spray generated using a diluted suspension of polystyrene latex. Nominal size of the latex is 0.546 mm and the data is generated by a differential mobility analyzer.

If one uses the same basic system just discussed to generate aerosols of larger latex spheres, one must be sure to use a drying column pointing downwards, so that the larger aerosol particles are not removed from the airstream by gravity as one attempts to move them upwards in an airstream [21].

Chein and Lundgren have described a system for generating a monosized aerosol from a spray generator in which large particles are removed in an air column, and a cascade impactor with a virtual surface removes the fines [22].

The system described in **Figure 5** can be used to generate a steady stream of aerosols of fine silicon carbide which can be used to form smoke streams in a wind tunnel to make flow patterns visible [23].

It should be noted that most individual particles produced by nebulization and many other techniques have high electrostatic charges. Sometimes, if this is undesirable, one must provide a decharging element in the instrumentation. For example, some of the equipment manufactured by TSI Incorporated can be equipped with a Krypton 85 (Kr-85) radioactive source to neutralize the charges on the aerosols. In other equipment a sub-corona discharge is used to provide a flood of ions, which can neutralize the charge on the aerosol [18, 20].

A widely used instrument for generating monosized aerosols for test purposes was described in 1973 by Berlund and Liu [24]. The basic system used in their equipment, known as vibrating orifice aerosol generator is shown in **Figures 5(a)** and **(b)**. A jet of liquid is forced by a motor driven syringe to an orifice which is in close contact with a piezoelectric ceramic. As described by Keady and Nielson, the jet is naturally unstable, and when left alone, tends to break into non-uniform drops [20]. By applying a periodic vibratory disturbance to the jet, the breakup is controlled and generates more uniform droplets. One droplet is generated for each cycle of oscillation of the piezoelectric ceramic. Common solvents include water and isopropyl alcohol, which can be used to generate droplets of oils such as dioctylphthalate (DOP), olive oil, and oleic acid [25, 26]. Again, quoting Keady and Nielson,

> "once the droplets are generated, they must be dispersed and diluted to avoid coagulation. To

disperse the aerosol, a cover over the generating head forces air through a hole causing a turbulent air jet to surround and disperse the aerosol stream. Dilution air is added to the column to evaporate the volatile solvent from the droplets and carry the aerosol out of the column. An optional neutralizer can be used to reduce the number of electric charges the particles inherently acquire in the generation process. Neutralization reduces particle losses to the water tubes and chambers from electrical attraction." [20]

A system whereby the aerosol is dried and electrically discharged is shown in **Figure 5(b)**. Typical aerosols produced by the vibrating orifice aerosol generator are a methylene blue aerosol, already discussed, and a DOP aerosol. DOP, dioctylphthalate, has been widely used in filter test procedures. In recent years, however, there has been some suggestion that DOP is a potential carcinogenic substance and scientists have been developing alternative aerosols. The literature on aerosol generation and filter testing are full of references to DOP aerosols.

Modifications to the operational procedure of the vibrating orifice aerosol generator to generate large, solid, monodispersed calibration aerosols has been described by Vanderpool and Rubow [21].

Another type of generator for sprays is known as a spinning disc nebulizer. This basic system used in this device is shown in **Figure 6**. In **Figure 7**, some data for an aerosol system generated with a spinning disc nebulizer, reported by Dunn and Wallis are shown [27]. Items of interest in this graph are the fact that the droplet size distribution is relatively wide and that satellite droplets, are present in the data. If one wishes to use a spinning disc generator to generate relatively monosized distributions, the satellite particles must be removed. The other thing to notice from this data is that, even to generate a relatively coarse spray of 70 micrometre average size, the disc has to spin at 8000 R.P.M.. To produce small droplets of the order of 3 micrometres, it is obvious that the speed must be greatly increased and this becomes a challenging engineering problem. A spinning disc generator, also called a spinning top generator, which can be used to generate aerosols is marketed by Sierra Instruments [28]. The system available from Sierra instruments is shown in **Figure 8**. The spinning disc rotates at 60000 R.P.M. Liquid to be atomized drops onto the disc which rotates just above a baffle which has a air flow sufficient to suck satellite drops out of the main air stream. These satellite droplets are sent to a filter to remove them from the aerosol stream. The larger droplets are moved over the baffle plate

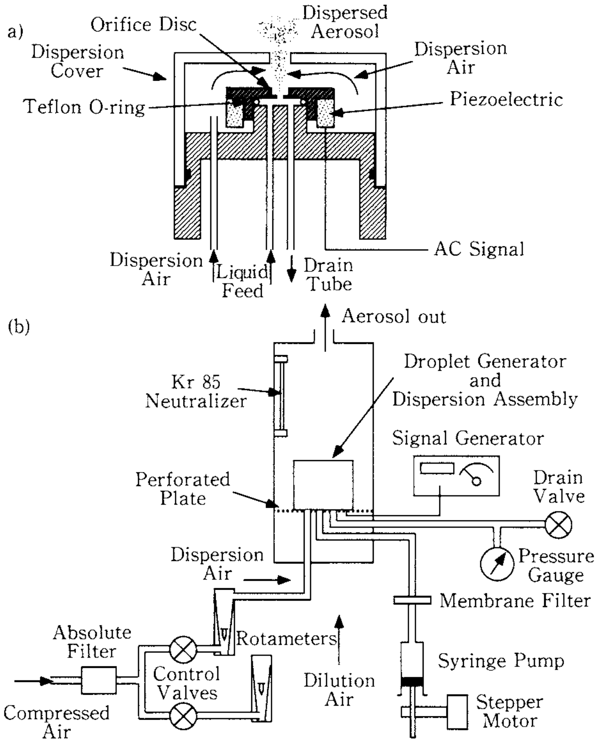

Fig. 5 The TSI model 3450 Vibrating Orifice Monodisperse aerosol generator, used to calibrate particle sizing equipment, and generate test aerosols for such tasks as filter testing. a) The aerosol generating head. b) Droplet drying and charge neutralizing equipment.

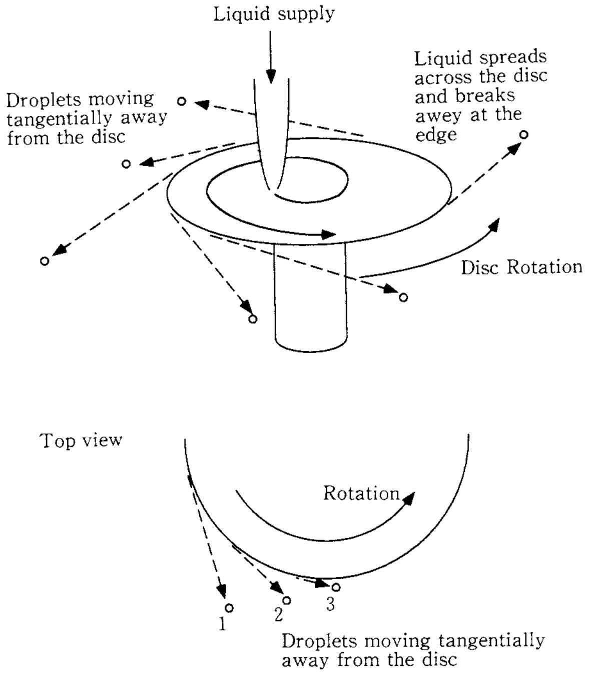

Fig. 6 The spinning disc nebulizer creates nearly monosized droplets by breaking the surface tension of the liquid at the edge of the rapidly rotating disc.

and sucked down by the main air flow. The aerosol stream passes through a charge neutralizer before being passed to the system where the test aerosol is to be used. In the trade literature published by Sierra it is stated that one can vary the particle size of the test aerosol over a range from one to five micrometres for solid particles placed in a liquid suspension and one to ten micrometres for liquid particles. Size is controlled by varying suspension or solution concentration. It is claimed that the geometric standard deviation for aerosols produced this way can be as low as 1.1 based on number size distributions [28, 29].

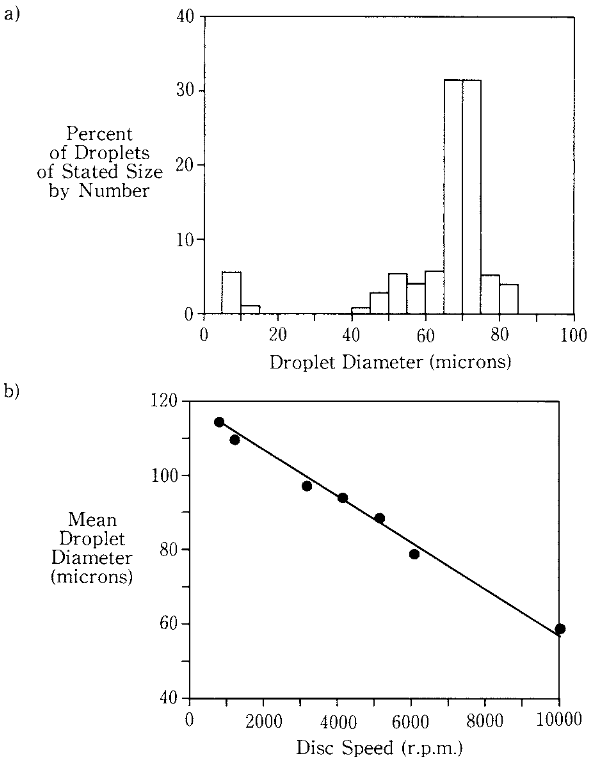

Fig. 7 The size distribution of droplets produced by a spinning disc nebulizer used for agricultural purposes have a narrow size range but contain a smaller population of satellite droplets. Data obtained by in-line holography. a) Typical droplet size distribution generated at a given disc speed. b) Variation in average droplet size at various disc speeds.

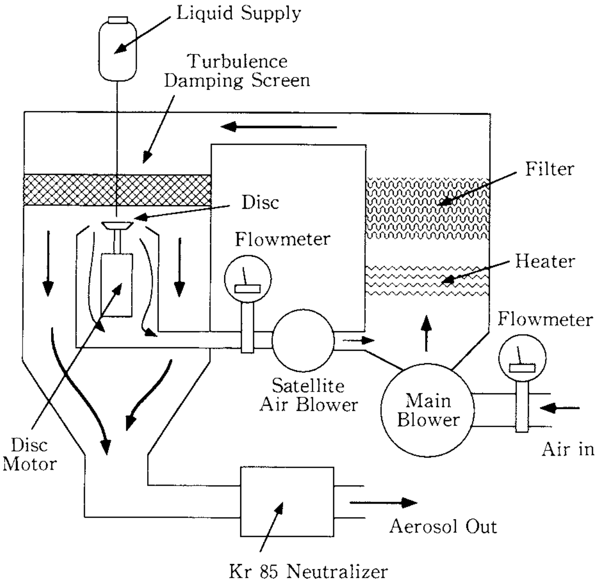

Fig. 8 In the Sierra Instruments spinning disc aerosol generator, the disc spins at 60000 r.p.m. Satellite drops are removed by an ancillary air stream.

Section 2 Generating Aerosols Directly from Powdered Material

The direct generation of aerosols from a powder is a difficult task. Pioneer work in this area was carried out by scientists investigating dust explosions and the problems of the use of aerosol systems in warfare [16]. The main problem which has to be faced when generating aerosols directly from a powder supply is the dispersion of aggregates and the maintenance of a steady stream of aerosol feed to the dispersing system. One of the devices which was developed at the National Bureau of Standards to study the health and explosion hazards of powdered coal in 1937 is known as the NBS dust generator. It is claimed that

> "this generator will redisperse virtually any dry dust which will flow through the hopper."

This statement illustrates the basic problem that one faces when one starts to look at the dispersion of cohesive powders which will not flow through the hopper. In the NBS dust generator, powder flows down into a gear situated under the spreader plate at the foot of the hopper. The quantity of dust trapped between teeth in the gear is carried around to a slit lying across three consecutive teeth. In the commercial literature describing the equipment it is stated that the speed of rotation may be infinitely varied from 0.25 to 10 R.P.M. The dust between the teeth is aspirated into the air stream. The air stream is fired through the vent and against an impaction disc to break up any aggregates.

For many years, a workhorse of the aerosol community used to generate aerosol clouds directly from powder was the Wright dust feed mechanism shown in **Figure 9**. In discussing the performance of the Wright dust feeder, Green and Lane make the following statements

> "Experiments have shown that any dust feed apparatus based on the manipulation of a dust or powder in the form of a loose aggregation is unsatisfactory. In most cases a much better con-

trol over the dust is obtained if it (the powder supply) is first converted to a solid cake by packing it tightly into a tube. The finely divided powders the particles, which are mostly less than ten micrometres, can be packed in this way quite uniformly provided that they are clean and dry and then they can be readily redispersed by scraping a very thin layer of the cake into an air stream". [16]

As can be seen from the **Figure 9**, in the Wright dust feeder the powder to be dispersed is packed into a column. A piston holds a scraper disc up against this packed powder bed. The column is rotated slowly by a set of gears. The disc which is rotated up against the powder has a spring on it's upper surface with a radial cut which is turned up to form the scraper. The remainder of the scraper disc is free so that it presses on the surface of the dust. The central hole allows the powder scraped off the powder bed to fall into the central air channel as shown. The driving air passes up the outside of the spindle which is hollow and is used to rotate the column. Air travels into the channel around the disc and passes, via the slot, and down the central tube. The dust tends to be scraped up as relatively large aggregates but as the airstream passes through the jet at the base of the equipment the aerosol stream impinges on an impact plate before leaving the apparatus. This strategy ensures that almost all the aggregates are completely dispersed in the aerosol stream. The system will not work if the dust has some oversize particles that can block the jet. It is claimed that this equipment can run for a period of half an hour with only plus or minus 20 percent variations in the flow. It is also stated that the equipment can generate many different dust levels and has been successfully used with coal dust, silica dust, aluminum powder and uranium dioxide [16]. Dusts which contain a great many coarse particles cannot be used in the Wright dust feeder satisfactorily. Such coarse dusts can however be relatively easily dispersed using the equipment such as the NBS dust generator.

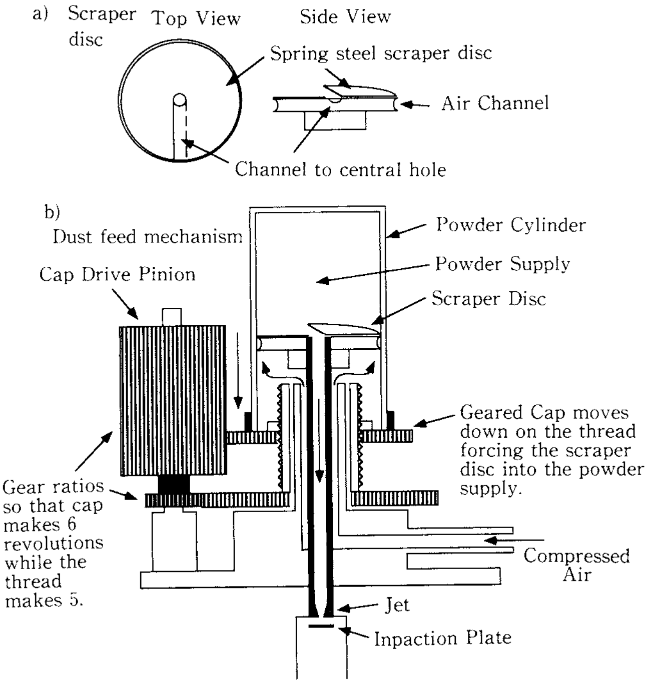

Fig. 9 In the Wright dust feeder, the powder to be dispersed is packed into a cylinder. A rotating disc scraper feeds the powder into a central tube and the emergent aerosol is driven against an impact disc to break-up agglomerates.

In recent years, equipment similar to the Wright dust feeder has been developed in which the scraper system is replaced by a wire brush. Thus in the **Figure 10**, the TSI model 3410 Dry Powder Disperser is shown [30]. In the operation manual of this dry dispersing system, it is stated that the equipment is based on research work carried out at the Institut für Mechanische Verfahrenstechnik und Umweltverfahrenstechnik, Technische Universität Clausthal, Germany. It is stated small particles have a natural tendency to cling together due to the considerable forces of adhesion that act between them. The smaller the particle, the more dominant

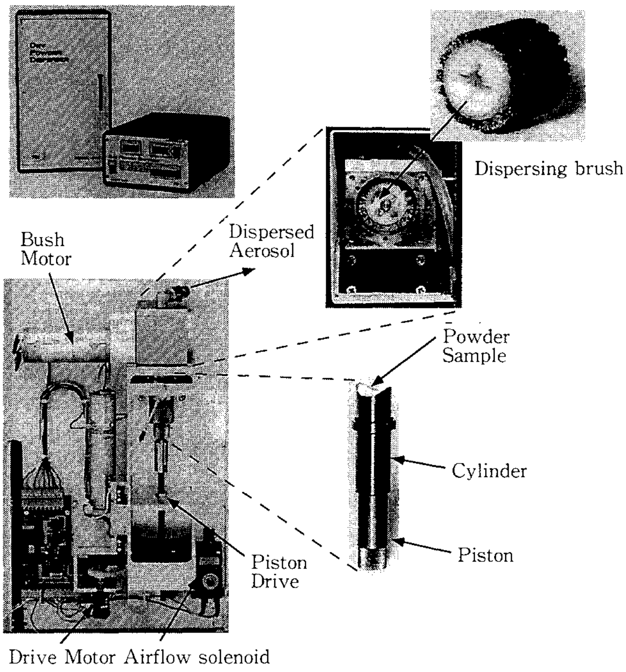

Fig. 10 In the TSI Model 3410 Dry Powder Disperser, a wire brush strips powder from the surface of a sample packed into a cylinder and driven upward by a piston. The powder is then suspended in an air stream.

are the adhesive forces and the more difficult the problem of dispersion.

The adhesive forces that act between particles include van der Waals forces, electrostatic, magnetic and forces due to liquid or solid bridges. Of these, van der Waals is by far the dominant one to overcome in dispersing dry powder. A discussion of what is meant by van der Waals force is beyond the scope of this review but the topic is covered in any standard first year chemistry text. In the operation of the equipment, the piston presses the powder cake against a stainless steel brush rotating at a constant rate of 3000 revolutions per minute. A jet of compressed gas blows across the top of the brush. It is claimed that together, the rotating brush and high speed gas jet, provides sufficient shear forces to overcome the van der Waals forces and deaggregate the powder [30].

In the last 20 years, several instruments have been developed for sizing fine particles in which the fine particles to be characterized are first dispersed as an aerosol. The aerosol particles are then studied in several ways. In some instruments, the aerosols are examined with a laser beam to generate a size information rich diffraction pattern. [31-36] Another technique is to study the dynamics of the particles as they are driven through an inspection zone. [18,37] Research carried out by various companies has resulted in the availability of several new dispersing techniques for generating aerosols from dry powder. It is useful to consider a particular instrument, known as the Amherst Process Instruments Inc. Aerosizer at this time, because it has been used to study the effect of different shear forces on the deaggregation of a powder to be turned into an aerosol [37].

For example, in the device known as Aerosizer, a stream of aerosol is sent down a central feed tube towards an interrogation zone, formed between two laser beams. The system is shown in **Figure 11**. Clean, sheath air is fed to the system so that the aerosol stream to be interrogated in the inspection zone is confined to a narrow stream. The particles scatter light from the laser beams as they pass through them, and the scattered light is picked up by photodetectors. Special electronic editors monitor the pulses generated in this way and, using the built in logic, one can actually measure up to 100,000 fineparticles a second. This machine can operate on aerosol particles from 0.1 to 700 micrometres. A comparable system is manufactured by TSI Instruments.

The confining of the stream of aerosol particles to be characterized by an auxiliary sheath of clean air is known as hydrodynamic focussing.

Of the various commercial systems for generating aerosols to study size characterization, the Aerosizer is the only one which currently provides for different dispersion severity when creating the aerosol to be characterized. The attachment available to study the effect of various dispersion forces with the Aerosizer is known as the Aerodisperser. The basic system of the Aerodisperser is shown in **Figure 12**. The powder to be dispersed is placed in the bottom of the sample cup. This sample cup has two streams of air. The first stream, labeled pulsed air stream in the figure, comes down the center of the equipment and impinges directly on the powder

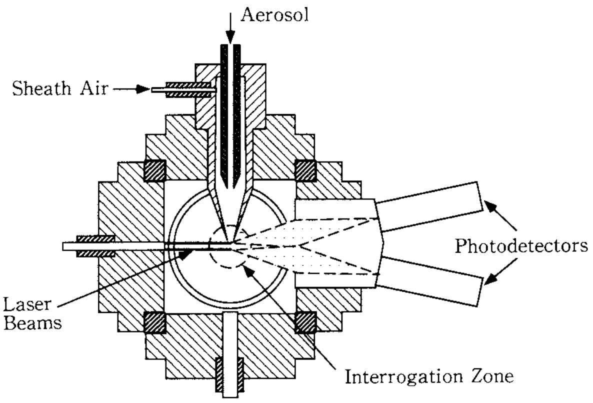

Fig. 11 Schematic diagram of the inspection zone of the Amherst Process Instruments Inc. Aerosizer® time-of-flight particle sizer.

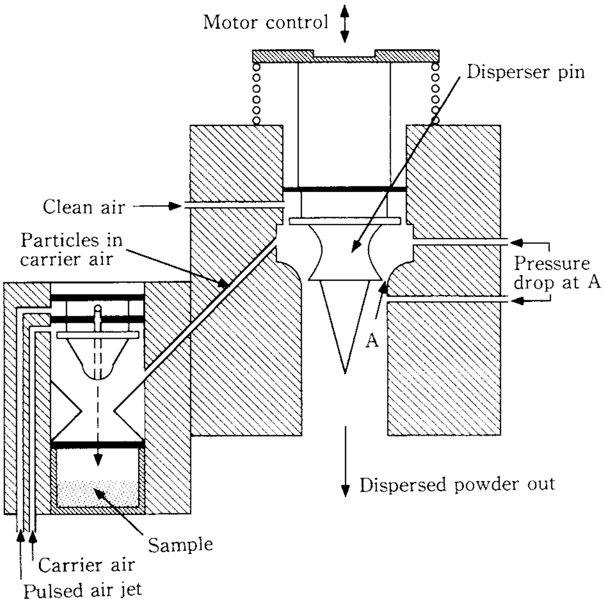

Fig. 12 The Aerodisperser attachment for the Aerosizer® of Figure 11, enables aerosol preparation using controlled shear rates to disperse the sample.

sample, stirring up the sample and aerosolizing it. The carrier air is a higher volume stream that carries the aerosol generated up the channel as shown. Clean air is introduced at the top of the dispersion unit. The disperser pin is made of stainless steel and vibrates to prevent powder buildup from the aerosol stream. The aerosol is carried past the disperser pin, which can be raised or lowered by the motor control. The pressure drop across the air gap A, can be measured using the channels shown in the figure. The diagram shown in **Figure 12** is not to scale, the larger gap A in this diagram is shown to give the location of the gap, but the gap, in reality, is much narrower. As the disperser pin is raised, the shear rate in the annular gap A drops. In the first model of this equipment a shear force at the gap A is recorded in terms of the pressure drop across the gap. This is not a fundamental variable, and the manufacturers have indicated that future models will express the shear rate in terms of the forces experienced by the aerosol in the shear gap. The effect of the shear rate on the dispersion of the aerosol is shown by some typical data, summarized in **Figure 13**. The powder studied to generate this data was intended for use in a therapeutic aerosol delivery system. In these devices, the shear rate of the powder at the point of dispersal is critical. When an aerosol was generated using 7 kPa of pressure across the annular gap, the generated aerosol contained many undispersed aggregates. Dispersal at 21 kPa improved the situation, but not until a dispersion force of 35 kPa was reached were the aggregates fully dispersed. If therapy was attempted with an aerosol generated at 7 kPa, most of the powder would have been ineffective, since it needs to be below 3 micrometres to be effective in reaching the appropriate areas of the lung. It can be anticipated that development of the various machines sold to size powders via aerosolization studies will, in the future, be fitted with equipment indicating the shear rate actually being experienced by the powder in the dispersion zone used by the equipment.

Another powder dispersion equipment used as a preliminary stage in diffractometer studies of the size of powders which have been aerosolized is available from the Horiba Company [32]. The basic system used in the Horiba equipment is shown in **Figure 14**.

In the Horiba powder feed system, the powder falls from a sample funnel into an airstream where it encounters a second airstream traveling at sonic

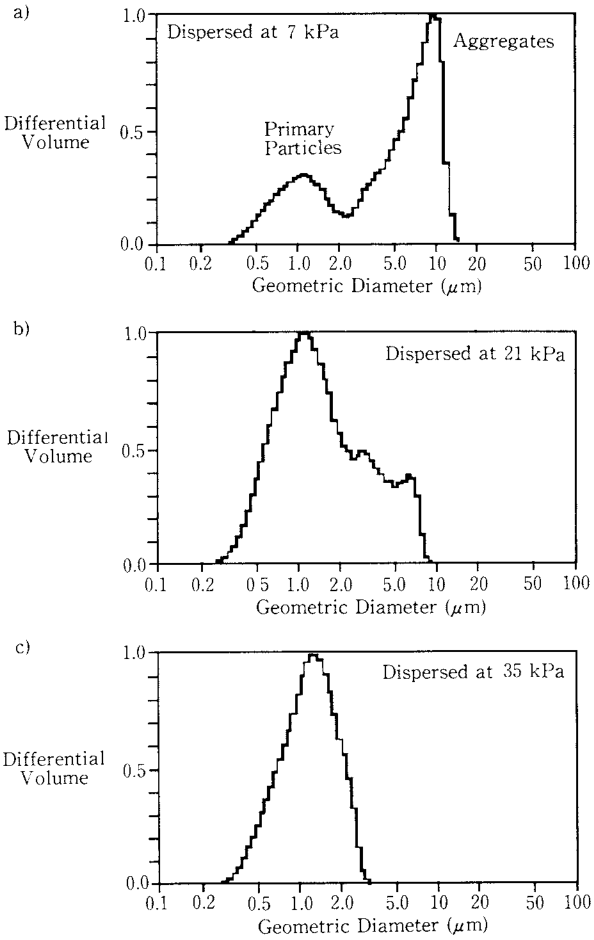

Fig. 13 The effect of various shear rates in the Aerodisperser of Figure 12 can be seen from these size distributions generated for a pharmaceutical powder intended for use as a therapeutic aerosol.

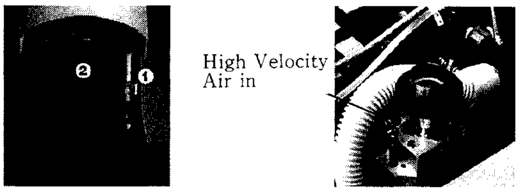

1. Dispenser
2. Vacuum control

Sample Cell in place

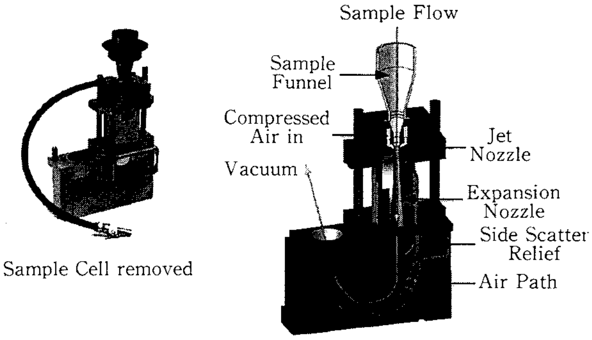

Internal operation of Sample Cell

Fig. 14 In the Horiba aerosolization equipment for dispersing dry powders, a sonic velocity jet mingles with the primary powder-air stream to create a high shear zone.

velocities. In the literature of the Horiba company, it is stated that :

> "the difficult dispersion of cohesive fine powders is automatically accomplished by feeding the sample through the variable pressure high velocity jet nozzle. Dispersion and deagglomeration are achieved by two processes. First, a high shear rate is created where high and low velocity air meet at the nozzle's exit. This imparts both tumbling and (shear) friction forces. Next, as agglomerated particles pass from the high to the low pressure region, the air in the agglomerate interstices expands, separating individual primary particles. The flow rate and pressure of the jet stream can be varied so that the proper amount of energy is applied to disperse but not fracture the particles. In powder jets, the sample is fed directly downwards from the dispenser, moving just a few inches in free fall to the nozzle. This approach prevents powder buildup clogging and the inconsistent rate of feed normally experienced in systems that use tubing to transport powder horizontally and upward to the sensing zone." [32]

In the above quotes, we have used the words used in the Horiba literature, but in fact, the term they should have used is aggregate. In powder technology, the word agglomerate means a system which stays together during the handling of the system because the word means "formed into a ball". Aggregate denotes a loser conglomeration of material, much like a flock of sheep, (the term aggregate, in Latin, means to bring together like a loosely assembled flock of sheep). An aggregate will break up during the handling of the conglomeration in the same way that a flock of sheep will disperse when the dog goes away. Unfortunately both terms are used interchangeably by different authors.

It should be noticed that the Globe Technology Corporation sells equipment to generate an aerosol of fluorescent powders of known particle size to use when testing filters. The idea is that particles caught in holes in the filter are easy to detect with ultraviolet light [38].

Leschonski and co-workers have been active not only in developing techniques for generating aerosols but also in the feeding of aerosols in equipment used to prepare fractions of powder of known size range known as classifiers. The commercially available instrument based on the work carried out by Leschonski and co-workers is known by the acronym RODOS [39, 40]. The RODOS disperser uses a wire brush to scrape powder from a powder supply into a high velocity air stream, but instead of using a power driven piston to deliver the powder material to the wire brush, a flexible hopper is used as shown in **Figure 15**. Thus in describing the system, Leschonski et. al. state

> "cohesive powders do not glide on inclined surfaces ; they form stable arches over openings of almost any kind and size. Therefore, a feeder with flexible hopper was designed, built and tested. The hopper walls consist of a flexible cylindrical rubber or plastic hose attached at its upper end to a circular ring which can be closed with a removable lid. At it's lower end, it is attached to a rectangular frame, the cross section of which slightly larger than the cross section of the flexible hose. Downward movement of the powder is achieved by gravity and arching is prevented by periodic deformation of the walls. This motion results from two rings around the hopper which are agitated with a speed adjustable motor. The lower end of the hopper is attached to the top of the brush feeder casing, the tips of the bristles of the brush when rotating scrape off particles from the powder into the airstream." [40]

Data published by Leschonski show that the RODOS system is very efficient at dispersing powders, Leschonski et. al. also suggest that aerosols can be created from powder stream using a pin mill [39, 40]. They built and tested a specially designed

a) Overview

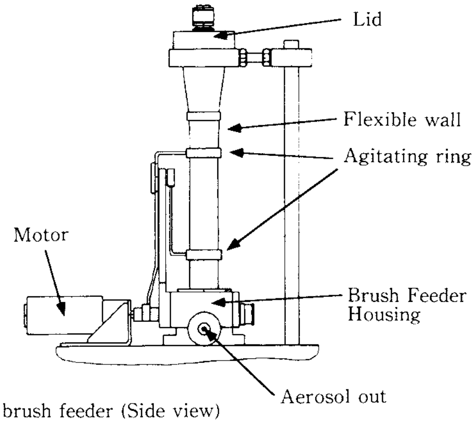

b) Detail of brush feeder (Side view)

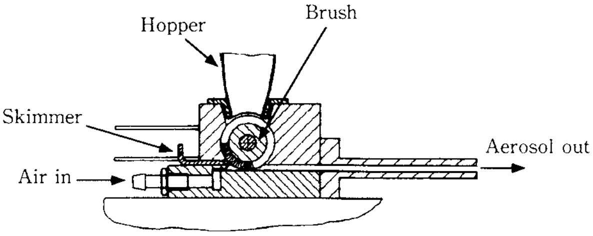

Fig. 15 In the RODOS system, developed by Leschonski and co-workers, flexiwalled hopper and wire brush system deliver powder into a high-velocity air stream [40].

pin mill in which the two counter rotating walls at the outer periphery were only 0.22 millimeters apart subjecting the dispersed powder leaving the mill to a very high shear rate. The system used in the pin mill disperser are shown in **Figure 16**.

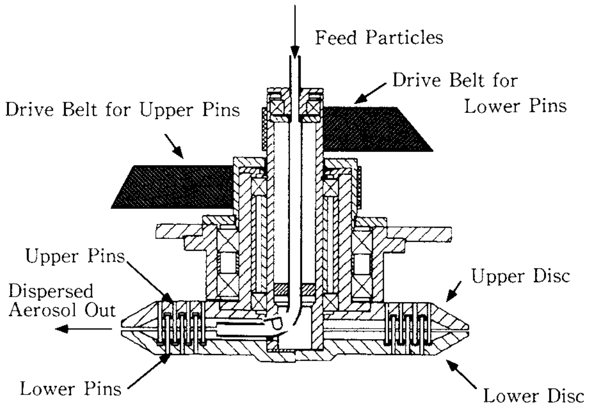

Fig. 16 Leschonski and co-workers have built a special pin mill to deaggregate and feed powder through a high shear zone to create an aerosol [40].

A more conventional design of a pin mill is shown in **Figure 17** [41]. Commenting on the performance of the two systems that he and his co-workers have designed, Leschonski states that the pin mill introduces the same amount of stress to the aggregates as the RODOS injector, but its air consumption and its energy consumption are much smaller.

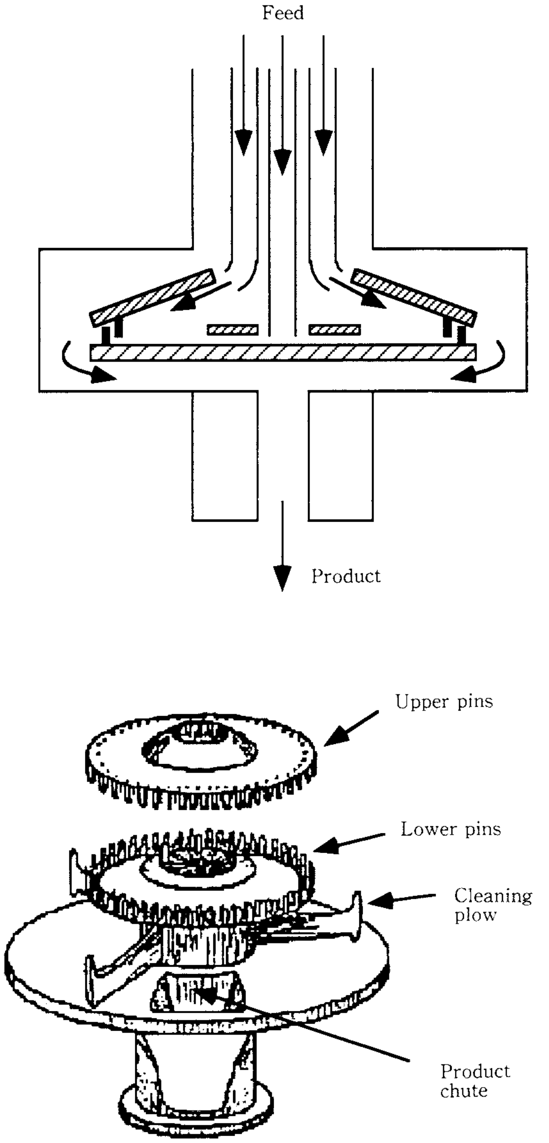

Fig. 17 Passing a powder through a pin mill can be a useful device for creating an aerosol system.

Another mill system devised for pulverizing a powder which could also be used to create a steady aerosol stream into a piece of equipment is the Trost jet mill shown in **Figure 18** [42]. In this system the feed to the mill is a hopper at the bottom of which is an air jet creating entrainment of powder from the hopper into the airstream by the Venturi effect (Bernoulli principle). At the start of the operation of the system, the air circulates around the classification chamber with the flow of the feed jet and the opposing jet shown in the diagram. After a short time, powder falling back into the opposing jet meets the incoming powder on the left hand side of the equipment. This could either reduce the size of the powder to create a fine aerosol, or simply deaggregate a powder system to be transformed into an aerosol system. As the air leaves the equipment from the centre of the classification chamber, only small aerosol fineparticles of a given size are allowed to exit with the airstream because the centrifugal force of the spiraling air, sends the larger particles back to the walls of the classification chamber and down into the impact

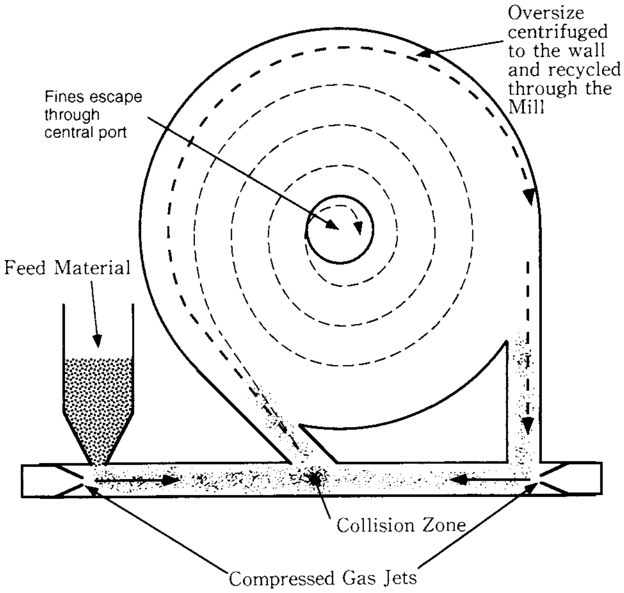

Fig. 18 The Trost mill could be used to create aerosols with a fixed upper size limit.

deaggregation chamber. By altering the velocity of the exiting airstream, one could alter the top size of the particle leaving the system.

Another technique which is being used to deaggregate a powder and entrain it into an air stream to create an aerosol is to feed the powder to be aerosolized into a fluidized bed as shown by the system shown in **Figure 19**. A typical system is available from TSI systems, a fluidized bed is created out of one hundred micrometre brass beads [18]. A steady stream of powder to be aerosolized is pulled by a chain of beads into the fluidized bed. The turbulent agitation of the brass beads deaggregates the incoming powder, the grains of which are then entrained in the upward moving air. At the top of the fluidized bed is a cyclone to remove any larger fineparticles that inadvertently leave the system, they fall back from the cyclone into the powder stream. The fluidized bed itself can be conical so that as the air stream moves upwards, the air velocity drops and the brass beads cannot move above a certain level at a given level of fluidization air supply.

A similar equipment to that of **Figure 19** has been used to generate relatively large amounts of dust for inhalation studies and other aerosol studies by Strek et. al. [43]. The equipment is shown in **Figure 20(a)**. In their apparatus, the screw feed takes powder from a hopper into a stream of fluidizing air. The fluidized bed itself contained sea sand with a particle diameter ranging from 0.12 to 0.20 mm. although for some experiments a larger size was used. The dust to be aerosolized, is fed into the fluidized bed and the ratio of dust to bed particles was varied from 1 to 10 to 1 to 3. Using this equipment, dispersions of asbestos and talc dust could be generated. Typical data obtained by Strek et al are shown in **Figure 20(b)**.

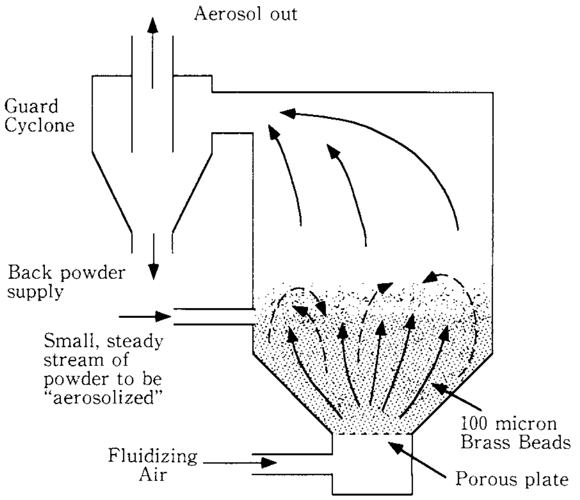

Fig. 19 Fluidized beds can be used to generate dry powder aerosols.

From the forgoing discussions, it can be seen that many different systems can be used to generate aerosols. Continuing research in this area can be anticipated to generate dry powder aerosols that are more monosized.

Conclusion

As pointed out in the text of this article, a major area of research required in the field of aerosol generation is the development of controlled shear rate dispersal of solid materials. Development in this area can be anticipated in the near future and hopefully this review has helped the technical community to exploit the existing literature, and indicated areas where more information is required.

References

1) News Article, "Safer aerosols using natural rubber", Rubber Developments, Vol. 41, No. 2, 1988, pp.37-40.
2) A.H. Lefebvre, "Atomization and Sprays", Hemisphere

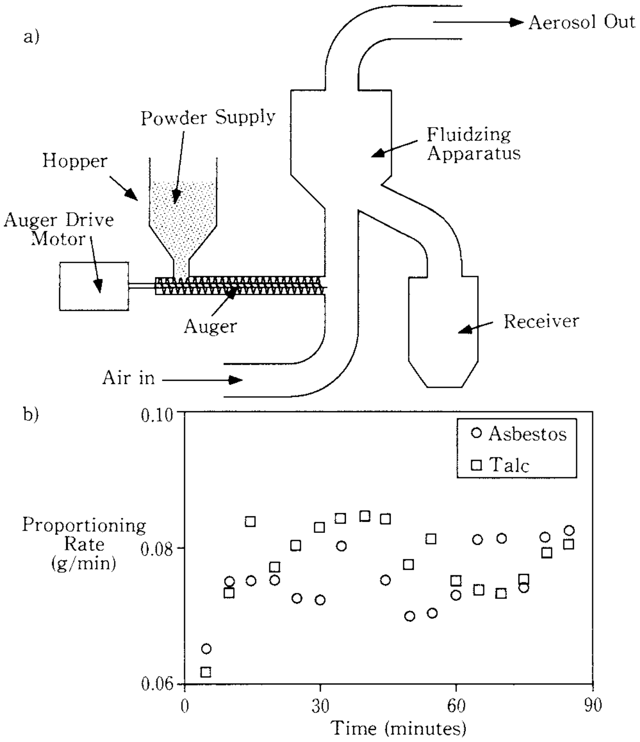

Fig. 20 Fluidized bed system used by Strek et al to generate aerosols.The sand in the bed was 0.12 to 0.20 mm in size, the air velocity was 6.2 cm/s and the ratio of dust to sand was 1:10. a) Schematic of the fluidized bed equipment. b) Typical performance data for the system of (a)

Publishing Corporation, New York, 1989.

3) Drain Systems Co., North Avenue at Schmale Rd, Wheaton, Illinois, 60187.

4) Flosonic Division, Fluid Kinetics Inc., 4859 Factory Drive, Fairfield, Ohio, 45014.

5) Heat Systems-Ultrasonics Inc., 38 East Mall, Plainville, New York, 11803.

6) "Fineparticles : Aerosol generation, Measurement, Sampling, and Analysis", Edited by Benjamin Yh Liu, Academic Press, 1976.

7) T.T. Mercer, "Aerosol Technology and Hazard Evaluation", Academic Press, 1973.

8) K. Freelander, "Smoke, dust and Haze", John Wiley, 1977.

9) "Fundamentals of Aerosols", Edited by D.T. Shaw, John Wiley & Sons Inc., 1978.

10) T. Allen, "Particle Size Measurement", Chapman and Hall, 2nd Edition, London, England, 1974.

11) Yule, A.J., Chigier, N.A., Cox, N.W., "Measurement of Particle Sizes in Sprays by the Automated Analysis of Spark Photographs". Proceeding of a conference at the University of Salford, England, 12-15 Sept. 1977, M.J. Groves (ed). Proceeding published by Heyden and Son, London, p.61-73.

12) B.H. Kaye, "The Use of Special Rosin Rammler Paper as an aid for Sieve Analysis of Powders" (in German), Staub Vol. 2d, March 1964.

13) W.E. Collison, "Inhalation Therapy Technique", Heinemann, London, 1935.

14) See commercial literature on the Collison Nebulizer and other aerosol generators sold by BGI Incorporated, 58 Guinan St, Waltham, Massachusetts, 02154.

15) The history of the Collison Nebulizer has been reviewed by K.R. May in "The Collison Nebulizer : Description, Performance and Application", Journal of Aerosol Science, Vol. 4, pp.235-243.

16) H.L. Green, W.R. Lane, "Particulate clouds, dusts, smokes and mists", E. VanNostrand & Co., Princeton, New York, 1957.

17) British Standard 2577, 1955, "Classification for Methylene Blue particulate test for respirator canisters", British Standards Institute, London, England.

18) See the trade literature of TSI Incorporated, 500 Cardigan Rd., P.O. Box 64394, St. Paul, Minnesota, 55164.

19) See Dow Diagnostics, P.O. Box 68511, Indianapolis, In, 46268.

20) P.R. Keady, and P.A. Nielson, "Monodispersed particle generators for calibrating aerosol instrumentation", Proceedings of the Institute of Environmental Science, pp.94-100, reprints available from TSI.

21) R.V. Vanderpool and K.L. Rubow, "Generation of large, solid, monodispersed calibration aerosols", Aerosol Science and Technology, Vol. 9, 1988, pp.65-69.

22) H.M. Chein, B.A. Lundgen, "High Output Size Selective Aerosol Generator", Aerosol Science and Technology, volume 23, pp.1510-1520, 1995.

23) For an introductory discussion of the use of visible smoke streams in wind tunnels, see B.H. Kaye, "Golf Balls, Boomerangs and Asteroids", VCH Publishers, Weinheim, 1996.

24) Berlund R.N. and Liu B.Y.H., "Generation of monodispersed aerosol standards", Environmental Science and Technology, Vol. 7, 1973, p.147. See also trade literature of the TSI Corporation and reference 17.

25) K.T. Whitby, D.A. Lundgren, and C.M. Peterson, "Homogeneous aerosol generators", International Journal of Air and Water Pollution, Vol. 9, 1965, pp.263-277.

26) B.P. Keady, F.R. Quant and G.J. Sems, "Differential mobility particle sizer : A new instrument for high resolution aerosol distribution measurements below 1 micron.", TSI Quarterly Nine, No. 2, 1983. Obtainable from TSI Industries, address given in reference 15.

27) P. Dunn, J.M. Wallis, "Droplet Size Distribution from an Agricultural Spray Using In-Line Holography". In the proceedings of a conference at the University of Saltford, September 12-16 1977. Proceeding edited by M.J. Groves, Published by Hayden and Son Limited, London, 1977.

28) Sierra instruments inc. 3756 north Dunlap street, St. Paul, Minnesota, 55112.

29) B.G. Simpkins, "Aerosols Produced by Spinning Disks : a Reappraisal", Aerosol Science and Technology, pp.2651-2654, 1997.

30) An aerosol disperser which uses a rotating wire brush plus airstream similar to that of the TSI system is available from the German company, Palais Gmbh Partikel and Lasermesstechnik, D7500 Karlsruhe 1, Hiad und Neu Strasse, 7-907. This company also makes other types of aerosol dispensers similar to the ones discussed earlier in this section.

31) Sympatec, Inc., Systems for Particle Technology Division., 3490 U.S., Route 1, Princeton, N.J., U.S.A., 08540.

32) Horiba Instruments Incorporated, Irvine Facility, 1761 Armstrong Ave., Irvine, California, 92714, USA.

33) CILAS U.S.A., agents Denver Autometrics Inc., 6235 Lookout Road, Bolder, Colorado, U.S.A., 80301 Company headquarters in France Osi 47, Rue de Javel, 75015 Paris, France.

34) Leeds & Northrup, A Division of MicroTrac, 351 Sumneytown Pike, North Wales, PA., U.S.A., 19454.

35) Shimadzu Scientific Instruments., Inc., 7102 Riverwood Drive, Columbia, MD., U.S.A., 21046.

36) See trade literature of Coulter Counter Electronics, 5990 West, 20th St. Hialeah, Florida, U.S.A., 33010.

37) See the commercial literature of Amherst Process Instrument Inc., The Pomeroy Building 7 Pomeroy Lane Amherst MA 01002-2941

38) Globe Technology Corporation, 938 Northeastern avenue, Los Angeles, California, 90063.

39) K. Leschonski, S. Roth, L.. Menzel, "A Special Feeder for Diffraction Pattern Analysis of Dry Powders", Particle Characterization, Volume 1, 1984, pp.161-166.

40) K. Leschonski, B. Benker, U. Bauer, "Dry Mechanical Dispersion of Sub-Micron Particles", Part. Part. Syst. Charact., 12, 1995, pp.295-298.

41) B.H. Kaye, "Powder Mixing", Chapman and Hall, Lon-

don, England, 1997.
42) The Trost mill is manufactured and sold by Garlock Inc., Plastomer Products, 23 Friends Lane, Newtown, PA., U.S.A., 18940-9990.
43) Strek, A. Haba, A. Rochowiecki, "Application of a Fluidizing Apparatus for Dispersing Small Amounts of Dust to a Gas Stream", Powder Technology, 34, 1983, pp. 107-108.

Author's short biography

Dr. Kaye

Dr. Kaye was educated at the university of London England, where he obtained his BSc., MSc., and Ph.D. For several years he worked on the design of atomic weapons, and in particular, studied the problems of aerosol fallout from detonated atomic bombs, he also studied the problems of fabrication of such substances as fuel rods for nuclear reactors and components of the atomic bomb. In 1960, he moved to Nottingham where, as a lecturer in the physics department, he conducted research into problems of occupational hygiene in the coal industry, and powder problems in the pharmaceutical industry. In 1963, he moved to Chicago to become a senior physicist on the materials group of the Illinois Institute of Technology Research Institute where he worked on many problems associated with powders such as the design of high reflectance coatings for spacecraft and new routes to ceramic raw materials. Since 1968, he has been professor of physics at Laurentian University at Sudbury, Ontario. He has published over 150 papers on powder science and technology and serves on the editorial board of Powder and Bulk Solids, and is North American editor of Particle and Particle Systems Characterization.

Review

Force Transmission in Granular Media[†]

C. Thornton
School of Engineering, Aston University, U.K.

Abstract

Powders and other granular media are composed of discrete particles and force transmission through a system of particles can only occur via the interparticle contacts. The distribution of contact orientations affects the magnitude of the contact forces which are not uniformly distributed. Since the contact stiffness and contact area are functions of the contact force, the manner in which the contact forces are distributed determines the shear strength, compressibility and conductivity characteristics of granular media. The paper reviews the current understanding of force transmission in granular media as gleaned from both physical experiments and numerical simulations and discusses the mechanical implications.

1. Introduction

Powders, and other granular media composed of discrete particles, exhibit very complex non-linear, hysteretic, stress-strain behaviour which is both stress level and stress path dependent. The complexity arises from the fact that the ensemble macroscopic response is a function of the spatial, size and shape distributions of the constituent particles and the distributions of other internal variables associated with the interactions between contiguous particles. The macroscopic state of stress is a function of the distribution of contact forces, Thornton and Barnes [1], and the ensemble moduli are related to the distribution of contact stiffnesses, Thornton [2]. The distribution of contact forces is also relevant to the fracture and crushing of constituent particles. The contact stiffnesses are functions of the contact areas and the distribution of contact areas controls the conductivity of granular media. Since the contact areas and contact stiffnesses are themselves functions of the contact forces, it is of scientific and industrial interest to understand how the intrinsic properties of the constituent particles affects the force transmission in granular media.

For any assemblage of discrete particles subjected to external loading, the transmission of force from one boundary to another can only occur via the interparticle contacts. Intuitively, therefore, we expect that the distribution of contacts will determine the distribution of forces within the system of particles and that the forces will not necessarily be distributed uniformly. Direct observations of stress distribution in photoelastic studies of two-dimensional arrays of discs have been reported by a number of researchers [3-7]. Konishi et al [8] used the same photoelastic technique to examine arrays of oval shaped particles. Photoelastic investigations of dynamic stress wave propagation in disc assemblies have been reported by Rossmanith and Shukla [9], Shukla [10] and dynamic photoelastic studies of regular arrays of elliptical discs have been performed by Zhu et al [11].

In all static photoelastic studies of disc assemblies it has been observed that the load is largely transmitted by relatively rigid, heavily stressed chains of particles forming a relatively sparse network of larger than average contact forces. Groups of particles separating the strong force chains are only lightly loaded. The implication is that, in a random system of particles, the applied load will search for the shortest and most direct transmission path, and the less ziz-zag the chosen pathway the higher the proportion of load that will be transmitted. The existence of strong force chains in three-dimensional packings of spheres has recently been demonstrated by Liu et al [12].

A more efficient alternative to photoelastic studies of force propagation in granular media is to perform numerical simulations of particle systems subjected to external loading regimes. A well established computational technique, which we have used at Aston since 1980, was developed by Cundall and Strack [13] and is commonly known as the Distinct (or Discrete) Element Method. In their paper, Cundall and Strack [13] simulated a simple shear test reported by Oda and Konishi [7] and demonstrated

---

*Aston Triangle, Birmingham B4 7ET, UK
[†] Received 19 June, 1997

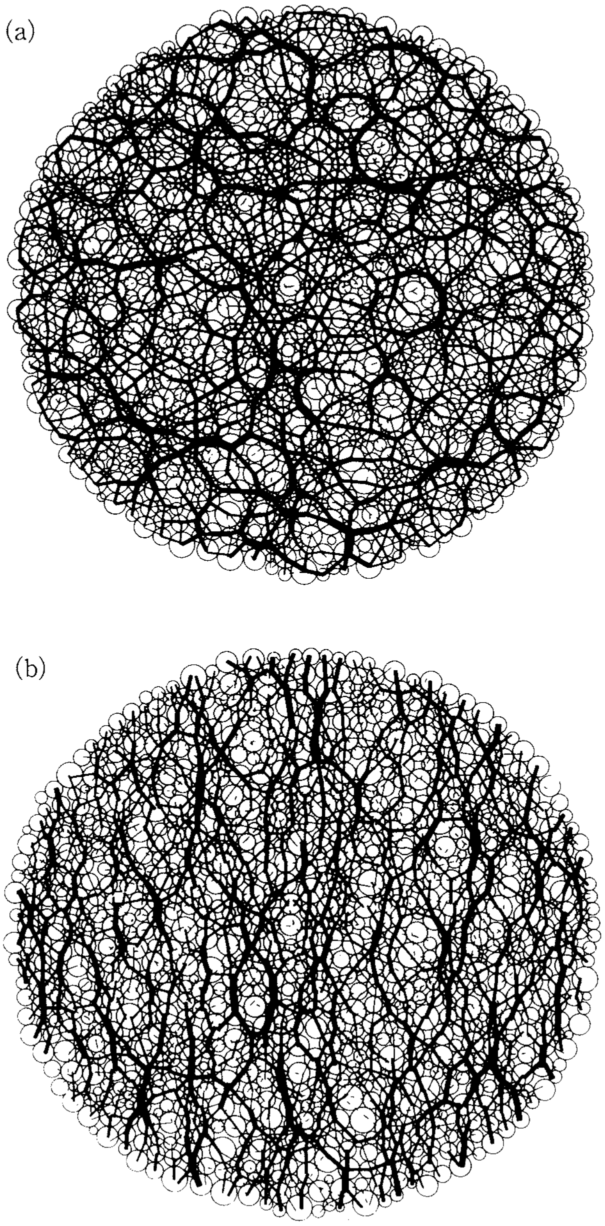

Fig. 1 Contact force transmision in a 2D array of polydisperse discs (a) isotropic stress state (b) deviatoric stress state.

good qualitative agreement obtained between the numerically simulated force transmission patterns with those obtained in the photoelastic experiment [7]. Sadd et al [14] have examined wave propagation in granular media using both photoelastic experiments and distinct element simulations. They demonstrated that, by using non-linear hysteretic normal and tangential interaction laws (similar to those used in the Aston version of the TRUBAL code), the relative errors between the experimental and simulated data were less than 15%.

2. Granular Dynamics

The computational technique may also be described as Granular Dynamics since the interactions between discrete particles are modelled as a dynamic process and the evolution of the system is advanced using an explicit finite difference scheme. The method is similar to Molecular Dynamics but with the difference that particles only interact when in contact and the contact interaction rules are more complex.

Application of the program involves cyclic calculations. At any time t, interparticle force increments are calculated at all contacts from the relative velocities of the contacting particles using incremental force-displacement rules. The interparticle forces are updated and, from the new out-of-balance force and moment of each particle, new particle accelerations (both linear and rotational) are obtained using Newton's second law. Numerical integration of the accelerations, using a small timestep Δt, provides new velocities which are then numerically integrated to give displacement increments from which the new particle positions are obtained. Having obtained new positions and velocities for all the particles, the program repeats the cycle of updating contact forces and particle locations. Checks are incorporated to identify new contacts and contacts that no longer exist.

In the original 2D simulation code BALL, linear springs and dashpots were used to model the interactions between contiguous particles [1, 13] and, in order to simulate quasi-static deformation, it was necessary to incorporate mass proportional damping terms into the equations of motion in order to dissipate sufficient energy. In the Aston version of the 3D simulation code TRUBAL, the interactions between contiguous particles are modelled by algorithms based on theoretical contact mechanics. Details of the contact mechanics theories used are provided by Thornton and Yin [15], Thornton [16]. Simulations of quasi-static deformation are performed using a representative volume element, with periodic boundaries, subjected to uniform strain fields and the bulk mechanical properties are calculated directly using statistical mechanics formulations [1, 2]. Mass proportional damping is no longer used in the TRUBAL code. Instead, the particle density is scaled up by a factor of 10^{12} in order to provide sufficient inertial damping to permit quasi-static simulations to be performed within a reasonable timescale.

3. Visualisation of force transmission pathways

Thornton and Barnes [1] reported two-dimensional simulations of quasi-static shear deformation of a compact polydisperse system of 1000 discs using the BALL code. The particles were initially randomly generated within a prescribed circular area such that there were no interparticle contacts. The boundary of the assembly was located by linking the centres of the peripheral particles to provide a convex boundary which enclosed all the disc centres. Deformation of the system was achieved by applying strain or stress control to the boundary particles, the effects of which then propagated through the system as the system evolved with time. In this way the system was subjected to isotropic compression followed by shear deformation during which the mean stress $(\sigma_1+\sigma_2)/2$ was maintained constant.

Figure 1a shows the force transmission pattern at the start of the shear stage when both the structure and the applied stress field are isotropic. The orientation of the contact forces is shown by the straight lines and the magnitude of each force is indicated by the thickness of the line, scaled to the current maximum force. It is clear from the figure that the force distribution is random. Macroscopically the orientation and distribution of the contact forces are both homogeneous and isotropic (i.e. there appears to be no regional preference regarding concentrations and no preferred contact force orientation). Microscopically, however, the distribution is inhomogeneous. Even when the stress state is isotropic, some contacts transmit forces several times those of others. Large forces tend to be transmitted along chains of particles which form the boundaries of enclosed, approximately circular, regions inside which there are relatively unloaded particles.

When a principal stress difference $(\sigma_1-\sigma_2)$ is applied to shear the system of particles, there is a rapid change in the force distribution as shown in **Figure 1b**. Macroscopically the distribution of forces becomes more and more anisotropic. The circular patterns initially formed by the large force chains rapidly adjust to form the boundaries of enclosed regions which are elongated in the direction of the compressive principal strain. The obliquity of contact forces along high force chains is low whereas the ratio of tangential to normal contact force is much higher in the unloaded regions. This indicates that, as confirmed from examining the simulation data, sliding is more likely to occur at contacts that carry small forces. Further discussion of the simulations in terms of the deformation mechanisms associated with the force transmission patterns shown in **Figure 1** are provided in [1].

Using the 3D simulation code TRUBAL, quasi-static deformation tests have been simulated in a periodic cell on polydisperse systems of 8000 elastic spheres. **Figure 2** illustrates the contact force transmission through such a system when subjected to an axisymmetric stress state $(\sigma_1>\sigma_2=\sigma_3)$. For clarity, sections through the mid-third of the periodic cell are shown. **Figure 2a** shows a view in the direction of σ_1. Although large forces are evident there appears to be no directional bias. This is due to the fact that both the structure and the state of stress are isotropic in the plane orthogonal to the viewing direction. However, when the force transmission is viewed in the direction of σ_3, as shown in **Figure 2b**, it is clear that strong force chains exist which tend to align themselves in the σ_1 direction.

4. Distribution of contact forces in terms of magnitude

It is necessary to characterise in a quantitative manner the force transmission behaviour described above. In this section, we consider the variation in magnitude only and leave any considerations of orientation until the next section.

Liu et al [12] used a layer of carbon paper on the inside surface of a cylindrical container to examine the distribution of forces on the base when the container was filled with beads. Their results indicated that the number of contacts carrying a given force decreased exponentially as the magnitude of the force increased. Similar exponential distributions of the contact force magnitude have been obtained in 3D simulations of isotropic compression of small assemblies of binary mixtures of 432 elastic spheres [17, 18].

A simple theoretical model was proposed [12] for the probability distribution of the magnitude of the normal contact forces. The model assumes that the inhomogeneity of the particle arrangement causes an unequal distribution of force transmission between contiguous particles which leads to chains of particles transmitting larger than average forces, as observed in photoelastic disc assemblies. Adopting a stochastic analysis, a mean field solution for the probability distribution P was obtained which may be written in the form

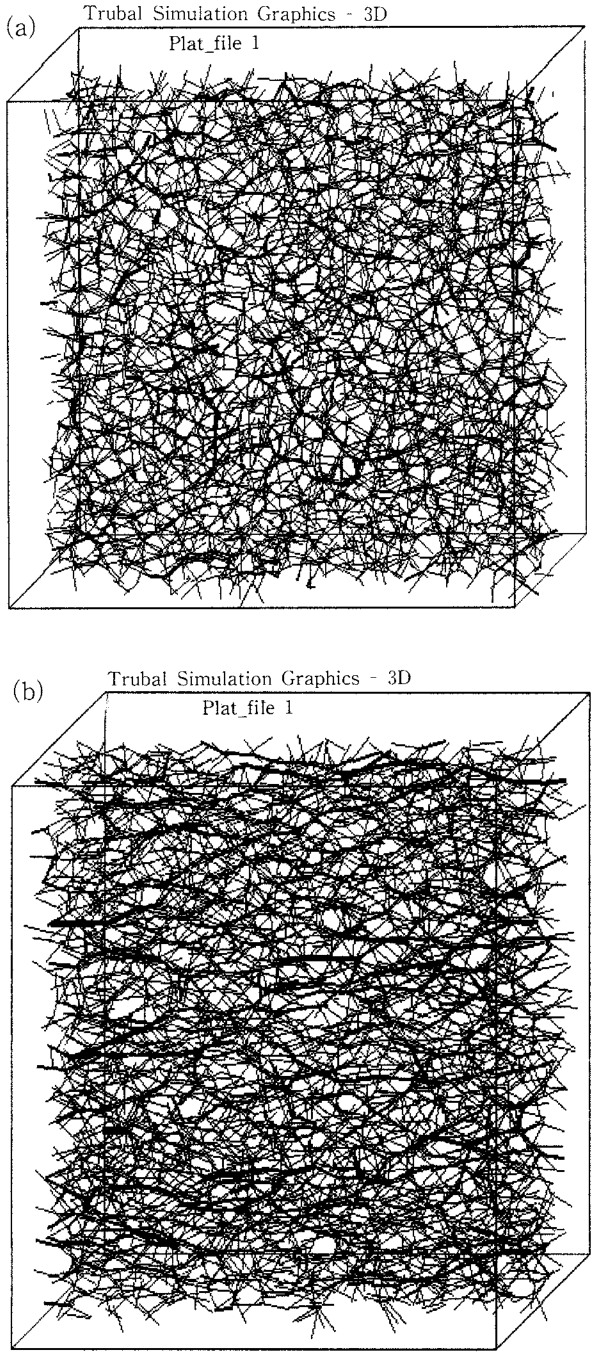

Fig. 2 Contact force transmission in a 3D array of polydisperse spheres (spheres not shown) during axisymmetric compression (a) view in direction of σ_1 (b) view in direction of σ_3.

$$P=\frac{k^k}{(k-1)!}\left(\frac{N}{\langle N\rangle}\right)^{k-1} exp\left[-k\left(\frac{N}{\langle N\rangle}\right)\right] \qquad (1)$$

where $\langle N\rangle$ is the average normal contact force. **Figure 3** illustrates how the distribution changes from an exponential distribution to an almost Gaussian distribution as the parameter k is varied from 1 to 12.

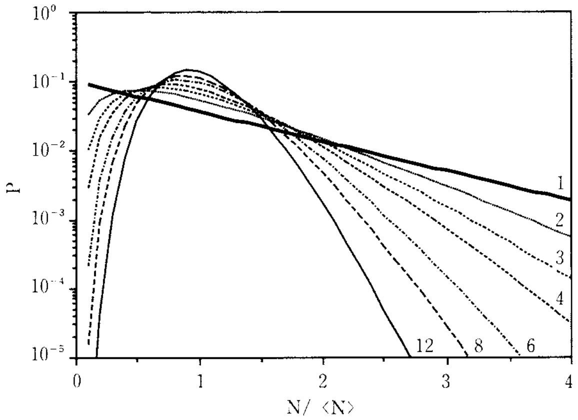

Fig. 3 Theoretical model for the probability distribution P of the normalised contact normal force magnitudes (N/⟨N⟩) given by equation (1) for values of k = 1 to k = 12.

Using a different simulation technique from that described in the previous section, Radjai et al [19] have examined force networks in two-dimensional systems of rigid spheres. In a rigid sphere array the contact force is not a function of the relative displacement of the two spheres forming the contact but is the result of the geometrical configuration of the whole system and the boundary conditions. The simulation technique has been termed the Contact Dynamics Method and is described by Radjai and Roux [20]. From the probability distributions obtained, Radjai et al [19] found that although the larger than average normal contact forces exhibited an exponential decay, the smaller than average normal contact forces had a power law distribution. They suggested that the probability P_N of the normal forces N takes the form

$$P_N \propto (N/\langle N\rangle)^{\alpha} \quad N<\langle N\rangle \qquad (2)$$

$$P_N \propto exp[\beta(1-N/\langle N\rangle)] \qquad (3)$$

Similar expressions were obtained for the probability P_T of the tangential forces T.

We have performed three dimensional simulations of two polydisperse systems of 8000 elastic spheres subjected to isotropic compression in a periodic cell. The only difference in the particle specifications was that one system was composed of "hard" spheres and the other of "soft" spheres. The particles in the hard sphere system were attributed with a Young's Modulus, E = 70 GPa; a Young's Modulus, E = 70 MPa was specified for the particles in the soft sphere system. Both systems were isotropically compressed to stress levels of 50 kPa, 100 kPa, 200 kPa and 400 kPa.

Figure 4 shows that the contact force distributions obtained for the hard sphere system are insensitive to stress level. Superimposed on the figure is the theoretical model given by (1) with k = 3. It can be seen that this simple one parameter model well describes the distribution of the larger than average

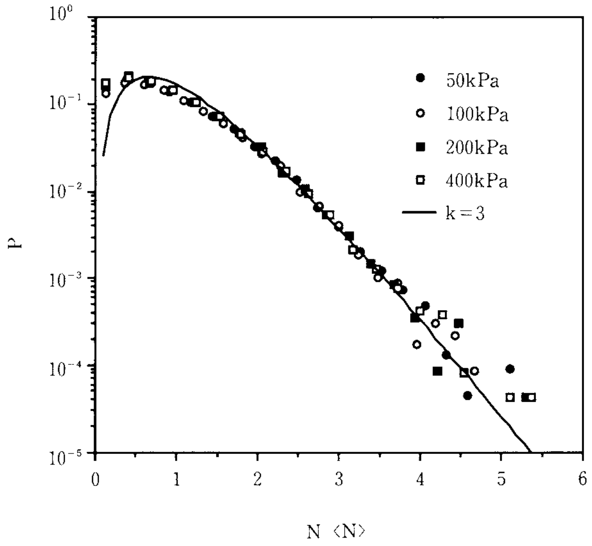

Fig. 4 Contact force distributions obtained at different stress levels for a polydisperse system of hard sheres compared with equation (1) using k=3.

contact forces. In **Figure 5** the data is replotted to compare with the alternative correlations given by (2) and (3). The fit to the data shown in **Figure 5a** was obtained with $\beta=2.15$ compared to a value of $\beta=1.4$ obtained in the 2D simulations of rigid discs reported in [19]. However, it can be seen that the exponential distribution is only reasonable for contact forces which are more than twice the magnitude of the average contact force. **Figure 5b** shows that the smaller than average forces tend to follow a power law distribution as suggested by (2) with $\alpha=-0.16$. Exactly the same exponent was obtained for the soft particle system and the value can be compared with the value of $\alpha=-0.3$ reported in [19].

The contact force distributions obtained for the soft particle system, **Figure 6**, clearly show that the distribution of the larger than average forces depends on the stress level and cannot be represented by the simple exponential relationship provided by (3). In **Figure 7**, a comparison of the results of the simulations with the predictions given by (1) for k=3 and k=4 suggests that, for soft particle systems, k increases with stress level. Although a fit to the larger than average forces in any one data set may be obtained by adjusting k, the distribution of the smaller than average forces tend to obey a power law which is independent of the elastic modulus of the particles and the stress level. Consequently, from the results of our own simulations, we conclude that there is no simple universal rule to completely characterise the contact force networks in granular media.

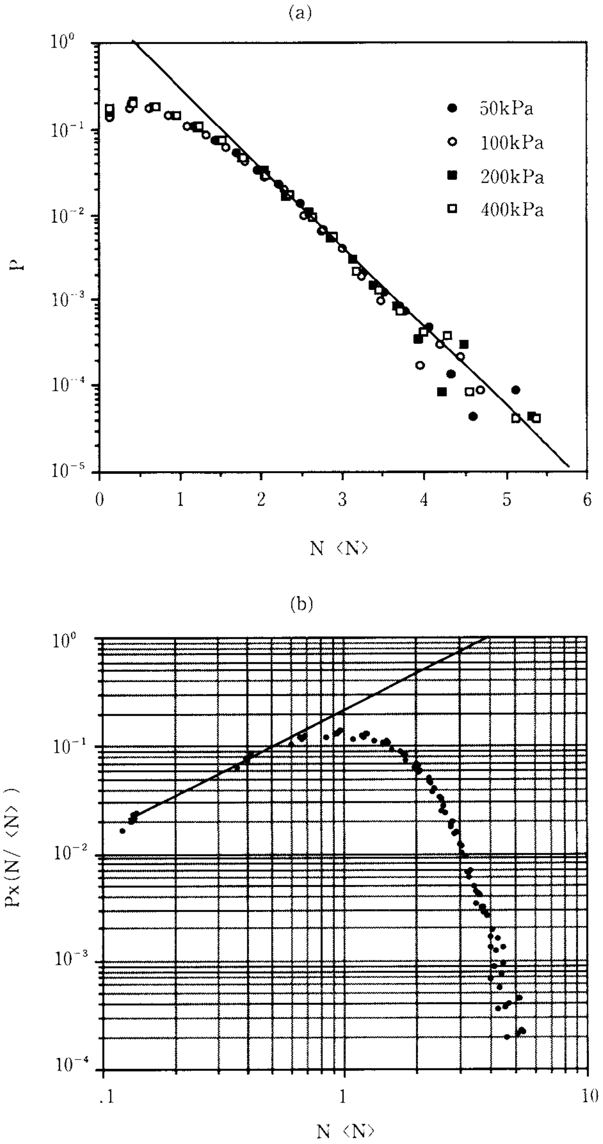

Fig. 5 Contact force distributions obtained at different stress levels for a polydisperse system of hard spheres (a) comparison with equation (3), $\beta=2.15$ (b) comparison with equation (2), $\alpha=-0.16$.

5. Distribution of contact forces in terms of magnitude and orientation

Granular media exhibit anisotropic characteristics. Consequently, it is necessary to take into account the contact orientations in order to provide descriptions of the macroscopic stress, modulus and conductive properties. Here we consider only the stress state.

For a large system of particles occupying a volume V the ensemble average stress tensor can be defined in terms of the interparticle contact forces P [1] by the equation

$$\sigma_{ij}=\frac{1}{V}\sum_{1}^{2M}x_iP_j=\frac{2M}{V}\langle x_iP_j\rangle \qquad (4)$$

where ⟨.⟩ denotes statistical average, $i=1, 3$; $j=1$,

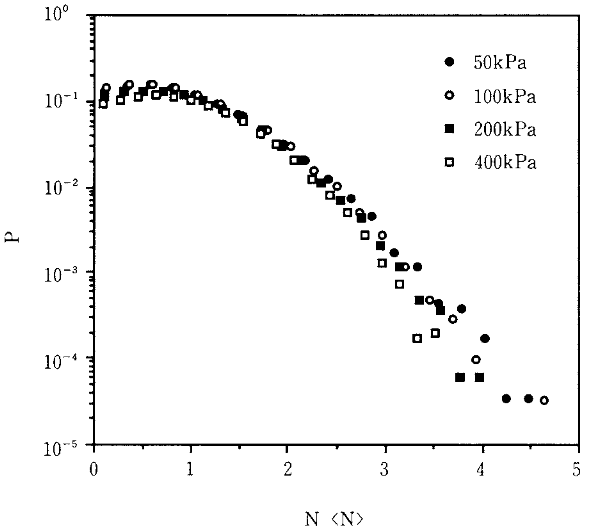

Fig. 6 Contact force distributions obtained at different stress levels for a polydisperse system of soft spheres.

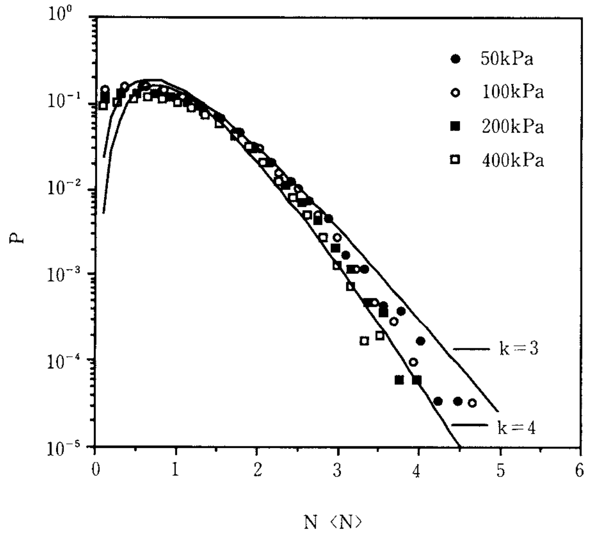

Fig. 7 Comparison of simulation data for the soft sphere system shown in figure 6 with equation (1) for k=3 and k=4.

3 and x_i defines the coordinates of the contact referenced to the particle centroid. The summation is performed over the M contacts in the system, each contact being counted twice.

For discs or spheres, the contact forces may be partitioned into their normal and tangential components (N,T) so that $P_i=Nn_i+Tt_i$ where n_i are the direction cosines of the unit contact normal vector and the vector t_i defines the direction of the relative tangential velocity at the contact. Also, the coordinates may be expressed in terms of the particle radius $x_i=Rn_i$ and (4) may be rewritten in terms of the normal and tangential force contributions to the stress tensor

$$\sigma_{ij}=\sigma_{ij}^N+\sigma_{ij}^T \qquad (5)$$

where

$$\sigma_{ij}^N=\frac{2M}{V}\langle RNn_in_j\rangle \text{ and } \sigma_{ij}^T=\frac{2M}{V}\langle RTn_it_j\rangle \qquad (6)$$

Since $n_in_i=1$ and $n_it_i=0$, (6) may also be written as

$$\sigma_{ij}=\sigma_{kk}\left[\left\langle\frac{RNn_in_j}{RN}\right\rangle+\left\langle\frac{RTn_it_j}{RN}\right\rangle\right]=\sigma_{kk}(N_{ij}+T_{ij}) \qquad (7)$$

where

$$\sigma_{kk}=\frac{2M}{V}\langle RN\rangle \qquad (8)$$

It follows from (7) that the anisotropy of the normal force contribution σ_{ij}^N is defined by the tensor N_{ij} which characterises the orientational distribution of contact normal forces. We may approximate the actual distribution with a continuous distribution by introducing a probability density function $P(\vec{n})$

$$N_{ij}=\left\langle\frac{RNn_in_j}{RN}\right\rangle\Rightarrow\frac{1}{4\pi}\int_\Omega P(\vec{n})\,n_in_jd\Omega \qquad (9)$$

which satisfies the conditions

$$\int_\Omega P(\vec{n})\,d\Omega=1 \text{ and } P(\vec{n})=P(-\vec{n}) \qquad (10)$$

The probability density function may be represented by a Fourier series expansion expressed in terms of even rank tensors [21]

$$P(\vec{n})=P_0+P_{ij}f_{ij}+\cdots\cdots \text{ where } f_{ij}=n_in_j-\delta_{ij}/3 \qquad (11)$$

and

$$P_0=\frac{1}{4\pi}\int_\Omega P(\vec{n})\,d\Omega=\frac{1}{4\pi} \qquad (12)$$

$$P_{ij}=\frac{15}{8\pi}\int_\Omega P(\vec{n})\,f_{ij}d\Omega=\frac{15}{8\pi}(N_{ij}-\delta_{ij}/3) \qquad (13)$$

Hence, we see that the orientational distribution of the normal contact forces may be represented by a tensorial Fourier series whose coefficients are functions of the deviatoric components of the normal force contribution to the stress tensor. The Fourier approximations to the normal contact force distribution may be further illustrated by polar diagrams, as shown in **Figure** 8.

Figure 8a shows the Fourier approximation to the normal contact force distribution during axisymmetric compression ($\sigma_1>\sigma_2=\sigma_3$). The distribution is clearly anisotropic and reflects the fact that the large contact forces tend to align in the σ_1 direction, as seen in **Figure 2**, and that contact separation tends to occur in directions orthogonal to the direction of σ_1. The 3D shape may be described as a peanut. For the case of axisymmetric extension ($\sigma_1=\sigma_2>\sigma_3$), the corresponding shape resembles a doughnut, as illustrated in **Figure 8b**. For general stress states ($\sigma_1>\sigma_2>\sigma_3$), there is a smooth continuous change in the shape of the normal contact force distribution, between the two extreme cases shown in **Figure** 8, as the intermedi-

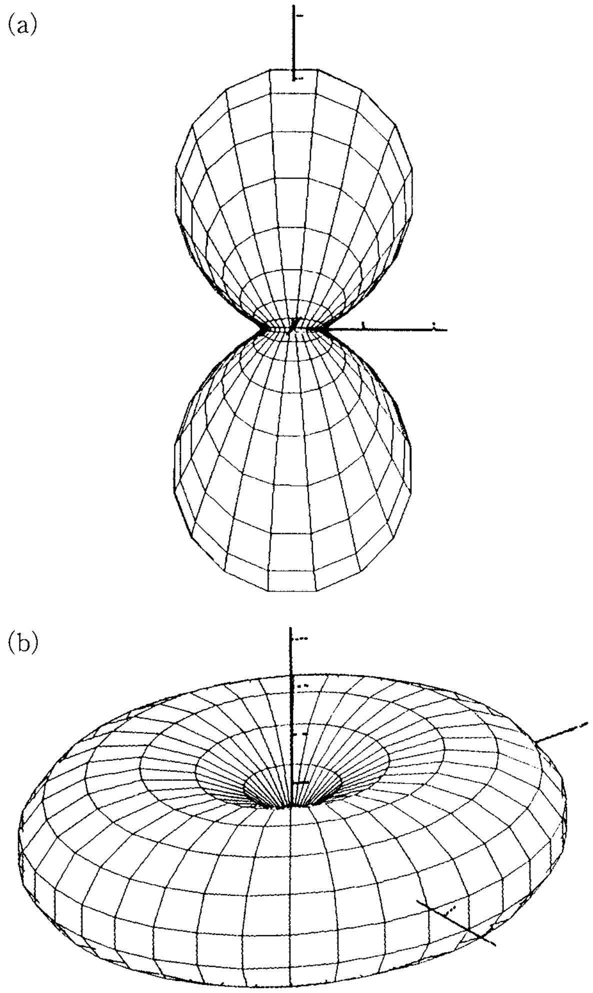

Fig. 8 Probability density distributions of contact normal forces represented by equation (11) for (a) axisymmetric compression and (b) axisymmetric extension.

ate principal stress σ_2 varies.

6. Force transmission during shear deformation

When subjected to an isotropic state of stress the tangential contact force contribution to the stress tensor is zero. Although tangential contact forces exist, the distribution of positive and negative shear directions is self-cancelling in the statistical averaging. During shear, the tangential contact forces contribute only to the deviatoric part of the stress tensor ; the normal contact forces contribute to both the isotropic and deviatoric parts.

Thornton and Sun [22, 23] reported numerical simulations of two polydisperse systems of 3620 elastic spheres, one dense the other loose, in which the mean stress, $(\sigma_1+\sigma_2+\sigma_3)/3=100$ kPa, was maintained constant during shear. **Figure 9** shows the evolution of the deviator stress $(\sigma_1-\sigma_3)$, the normal contact force contribution to the deviator stress $(\sigma_1-\sigma_3)^N$, and the tangential contact force contribution to the deviator stress $(\sigma_1-\sigma_3)^T$ during axisymmetric compression $(\sigma_2=\sigma_3)$ of the dense system. It is clear from the figure that the mobilised deviator stress is primarily a function of the normal force contribution and that the tangential force contribution is small. The results shown are for a coefficient of interparticle friction $\mu=0.3$. Increasing the interparticle friction increases the tangential force contribution but also increases the normal force contribution which remains the major contribution to the stress tensor. Similar trends were observed for the loose system. Results of recent, unpublished, numerical simulations indicate that this is also true for systems of non-spherical particles.

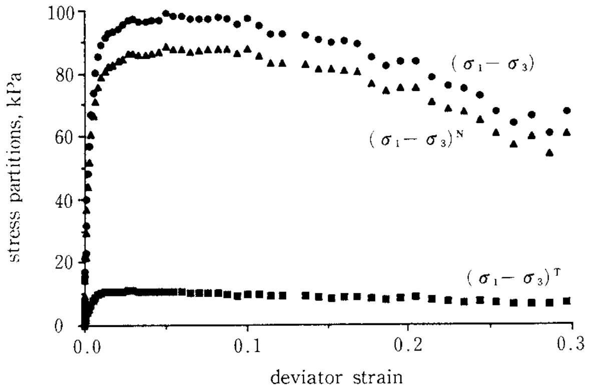

Fig. 9 Evolution of the deviator stress $(\sigma_1-\sigma_3)$, the normal contact force contribution to the deviator stress $(\sigma_1-\sigma_3)^N$ and the tangential contact force contribution to the deviator stress $(\sigma_1-\sigma_3)^T$ during axisymmetric compression of a dense polydisperse system of elastic spheres.

During shear, the distribution of contact orientations becomes anisotropic primarily due to contact separation in directions approximately orthogonal to the direction of the major principal stress and consequently, in dense systems, the total number of contacts decreases. The average number of contacts per particle, the coordination number, is normally defined by Z=2M/V. However, in all simulations it is found that there are always a number of particles which have only one or no contacts and, hence, such particles do not contribute to the force transmission through the system. Consequently, we define a mechanical coordination number

$$Z_m=\frac{2M-N_1}{N-N_0-N_1} \tag{14}$$

where N_1 and N_0 are the number of particles with only one or no contacts respectively. **Figure 10** shows the evolution of the mechanical coordination number during axisymmetric compression for both dense and loose systems. It can be seen that after a

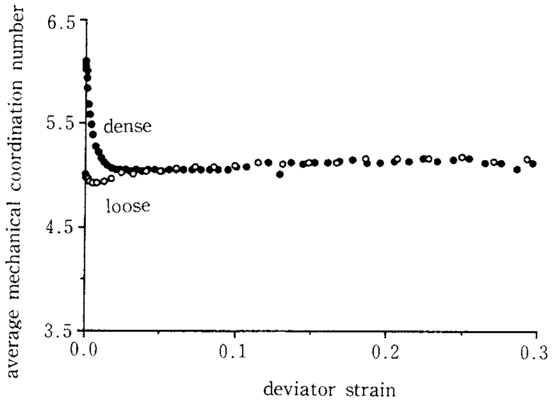

Fig. 10 Evolution of the mechanical coordination number, defined by equation (14), during axisymmetric compression of dense (●) and loose (o) polydisperse systems of elastic spheres.

small amount of straining the mechanical coordination number becomes essentially constant and independent of the initial packing density, irrespective of whether the system is expanding or contracting. This reflects an underlying stability requirement and corresponds, in statistical physics terminology, to a percolation threshold. If the coefficent of interparticle friction is increased, the critical mechanical coordination number decreases.

In other simulations which we have carried out we have found that the critical mechanical coordination number can momentarily drop below the critical value [24]. Since we impose a uniform strain field in periodic cell simulations, the critical coordination number is regained but fluctuations continue to occur. These fluctuations are coincident with fluctuations in the stress-strain curve and with transient jumps in the fluctuating kinetic energy density (granular temperature) which may be of one or two orders of magnitude. This phenomena indicates local transient instabilities in the columns of particles transmitting the larger than average contact forces. In the presence of real boundaries, we anticipate that strain localisation may occur when the mechanical coordination number falls below the critical value.

7. Concluding remarks

It has been demonstrated that, in granular media, load is transmitted primarily along relatively rigid, heavily stressed chains of particles forming a relatively sparse network of larger than average contact forces. Drawing an analogy with percolation theory, the heavily stressed chains of particles form the backbone to the percolating cluster. The distribution of the magnitude of the larger than average contact forces is exponential but for general states of stress it is necessary to account for the orientations of the contact forces by adopting a tensor representation of the force network. Nevertheless, it is the rapid development of strong force chains aligned in the direction of the major axis of compression that results in the deviator stress being primarily related to the normal contact force contribution to the stress tensor.

From our numerical simulations we observe that the system of particles acts in a way similar to that of a highly redundant space structure. There is a multiplicity of pathways along which force transmission may be achieved in order to establish a stable stress state. In order to achieve a stable state of stress it is not necessary that all the possible pathways are used. Hence, the system does not use all the potential pathways but naturally optimises the selection to match the loading direction. If the loading direction is suddenly changed then there is a rapid reselection of a more appropriate and efficient set of pathways. In terms of statistical physics, this is a percolation problem and the system can be considered to be self-organising. This self-organised optimisation of the force transmission is reflected in a critical value of the mechanical coordination number which corresponds to a percolation threshold. If the mechanical coordination number falls below the critical value then instabilities occur.

Numerical simulations have shown that increasing the interparticle friction does not produce a sigificant increase in the amount of energy dissipated but decreases the percentage of sliding contacts and reduces the value of the critical mechanical coordination number. This demonstrates that friction is, primarily, a kinematic constraint which permits reorientation of force transmission paths without undue particle rearrangement. Enhanced friction at the contacts increases the stability of the system and reduces the number of contacts required to achieve a stable configuration. When sliding does occur it tends to be at the relatively unloaded contacts in the regions between the chains of particles carrying the larger than average contact forces. Consequently the tangential contact force contribution to the stress tensor is small and the shear strength mobilised is primarily due to the development of the strong force network rather than due to work done in sliding particles over each other as implied in traditional soil mechanics.

Finally, it should be said that the above is true for “hard” particle systems but “soft” particle systems, and mixtures of hard and soft particles, may behave differently. Consider an equivalent space lattice which is composed of "branches" joining the centres of contacting spheres. Even when each branch has the same stiffness the effective stiffness depends on the direction of the applied loading. If we consider a hard sphere system, the space lattice consists, in effect, of a random array of stiff springs. Under load, branches which are favourably orientated will pick up the load with very little reduction in the branch length. Consequently, the load is not shared with other less favourably oriented branches. This leads to the type of force transmission networks described in Section 3. In contrast, the space lattice representing the soft particle system consists of a random array of highly compressible springs. Even though it will be the most favourably orientated branches which will initially pick up the load, the reduction in branch length as the applied loading is increased will permit load transfer to other less favourably orientated branches. Hence, in soft sphere systems, the force transmission is more uniformly distributed. However, we have observed that at very low stress levels the force transmission through soft particle systems is exponential, indicating that the force transmission also depends on stress level. At sufficiently high stress levels it is anticipated that hard particles will deform plastically and the force distribution will become more uniform.

References

1) Thornton C and Barnes D J : Computer simulated deformation of compact granular assemblies. Acta Mechanica 64 (1986) 45-61.
2) Thornton C : On the relationship between the modulus of particulate media and the surface energy of the constituent particles. J. Phys.D : Appl. Phys. 26 (1993) 1587-1591.
3) Wakabayshi T : Photoelastic method for determination of stress in powdered mass. In Proc. 7th Japan Nat. Cong. Appl. Mech. (1957) 153-158.
4) Dantu P : A contribution to the mechanical and geometrical study of non-cohesive masses. In Proc. 4th Int. Conf. on Soil Mechanics & Foundation Engineering (1957) 144-148.
5) de Josselin de Jong G and Verruijt A : Étude photoélastique d'un empilement de disques. Cahiers du Groupe Francais de Rheologie 2 (1969) 73-86.
6) Drescher A and de Josselin de Jong G: Photoelastic verification of a mechanical model for the flow of a granular material. J. Mech. Phys. Solids 20 (1972) 337-351.
7) Oda M and Konishi J : Microscopic deformation mechanism of granular material in simple shear. Soils and Foundations 14 (1974) 25-38.
8) Konishi J, Oda M and Nemat-Nasser S : Inherent anisotropy and shear strength of assembly of oval cross-sectional rods. In Deformation and Failure of Granular Materials (P A Vermeer and H J Luger, Eds.) Balkema (1982) 403-412.
9) Rossmanith H P and Shukla A : Photoelastic investigation of dynamic load transfer in granular media. Acta Mechanica 42 (1982) 211-225.
10) Shukla A : Dynamic photoelastic studies of wave propagation in granular media. Optics and Lasers in Engineering 14 (1991) 165-184.
11) Zhu Y, Shukla A and Sadd M H : The effect of microstructural fabric on dynamic load transfer in two dimensional assemblies of elliptical particles. J. Mech. Phys. Solids 44 (1996) 1283-1303.
12) Liu C-h, Nagel S R, Schecter D A, Coppersmith S N, Majumdar S, Narayan O and Witten T A : Force fluctuations in bead packs. Science 269 (1995) 513-515.
13) Cundall P A and Strack O D L : A discrete numerical model for granular assemblies. Gẽotechnique 29 (1979) 47-65.
14) Sadd M H, Tai Q M and Shukla A : Contact law effects on wave propagation in particulate material using distinct element modeling. Int. J. Non-Linear Mechanics 28 (1993) 251-265.
15) Thornton C and Yin KK : Impact of elastic spheres with and without adhesion. Powder Technology 65 (1991) 153-166.
16) Thornton C : Coefficient of restitution for collinear collisions of elastic-perfectly plastic spheres. J. Appl. Mech. 64 (1997) 383-386.
17) Cundall P A, Jenkins J T and Ishibashi I : Evolution of elastic moduli in a deforming granular material. In Powders & Grains (J Biarez and R Gourvès, eds.) Balkema (1989) 319-322.
18) Bagi K : On the definition of stress and strain in granular assemblies through the relation between micro- and macro-level characteristics. In Powders & Grains 93 (C Thornton, Ed.) Balkema (1993) 117-121.
19) Radjai F, Jean M, Moreau J-J and Roux S : Force distributions in dense two-dimensional granular systems. Phys. Rev. Lett. 77 (1996) 274-277.
20) Radjai F and Roux S : Friction-induced self-organization of an array of particles. Phys. Rev. E 51 (1995) 6177.
21) Onat E T and Leckie F A : Representation of mechanical behavior in the presence of changing internal structure. J. Appl. Mech. 110 (1988) 1-10.
22) Thornton C and Sun G : Axisymmetric compression of 3D polydisperse systems of spheres. In Powders & Grains 93 (C Thornton, Ed.) Balkema (1993) 129-134.
23) Thornton C and Sun G : Numerical simulation of general 3D quasi-static shear deformation of granular media. In Numerical Methods in Geotechnical Engineering (I M Smith, Ed.) Balkema (1994) 143-148.
24) Thornton C : Micromechanics of elastic sphere assemblies during 3D shear. In Proc. Workshop on Mechanics

and Statistical Physics of Particulate Materials, Institute for Mechanics and Materials Report No. 94-9, University of California San Diego, 64-67.

Author's short biography

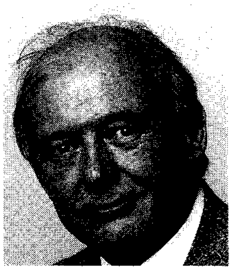

Colin Thornton

Colin Thornton graduated in Civil Engineering from Aston University where he also obtained his Ph.D and, since 1971, has lectured on soil mechanics and geotechnical engineering. He is a member of the International Society for Soil Mechanics and Foundation Engineering's Technical Committee on the Mechanics of Granular Materials, the Engineering and Physical Sciences Research Council's Process Engineering College and the IChemE Particle Technology Subject Group Commitee. In 1993, he organised the 2nd International Conference on the Micromechanics of Granular Media and edited the conference proceeding, Powders & Grains 93 (Balkema, Rotterdam). Since 1980 his reseach has focussed on the micromechanics of granular media and computer simulations of particle systems which have been applied to quasi-static shear deformation, hopper flow, particle/wall collisions and the coalescence, attrition and fracture of agglomerates.

Review

Wet Comminution in Stirred Media Mills[†]

Arno Kwade and Jörg Schwedes
*Kwade+Schwedes Zerkleinerungstechnik**
Institute of Mechanical Process Engineering
*Technical University of Braunschweig, Germany***

Abstract

The importance of stirred media mills in various industries as well as in research is steadily increasing because the quality requirements of comminution products, e.g. the product fineness, rise continuously. This paper gives a survey of different mill designs and of the influence of various operating parameters on the specific energy consumption. The specific energy necessary for a certain product fineness depends above all on the stress intensity, which is among other things a function of the grinding media size and the circumferential stirrer speed. At similar stress intensities, the influence of the stirrer and grinding chamber geometry is small and scale-up using the specific energy is usually possible. Moreover residence time behaviour, wear of grinding media and autogenous comminution are discussed.

1. Introduction

Stirred media mills are increasingly used for the fine and ultrafine grinding of minerals, ceramic materials, paint pigments, chemical products, microorganisms and other materials. In these mills which are mainly operated wet, the product particles are reduced in size between loose grinding media usually made of glass, steel or ceramic materials. Due to a very high number of stress events per unit time and unit volume and due to an appropriate stress intensity in the production of very fine particles, the specific energy consumption of stirred media mills is less than that of tumbling ball mills. The importance of stirred media mills increases steadily because of an increasing demand for fine and very fine particles and because of the advantages of stirred media mills compared with other mills. Therefore, many developments regarding minimization of specific energy, separation of very small grinding media, production of narrow particle size distributions and wear protection have been made in the last few years. Besides this, stirred media mills are increasingly the subject of scientific study, so that recently many new results have been published. Above all this paper covers experimental results, whereas simulation results using the population balance model or other models are not discussed.

2. History of development and different mill designs

Originally, tumbling ball mills were often used for wet fine and ultrafine grinding. But since the power consumption of tumbling ball mills is limited by the number of revolutions at which the grinding media are centrifugated at the chamber wall, the power density is relatively small. Thus, for the production of fine and ultrafine powders, very long comminution times are necessary. To improve the efficiency in fine grinding, in 1928 Szegvari (in [1]) proposed a mill with a vertical stationary grinding chamber in which spherical grinding media are moved by a slowly rotating agitator. An advanced design of this mill built in 1950 is shown in **Figure 1**. Such low-speed stirred media mills, also called "Attritors", with circumferential speeds up to approximately 6 m/s are still built and used, mainly for the fine grinding of minerals and ceramic materials. Parallel to the further development of this mill (e.g. increase in length/diameter ratio of the vertical chamber), high-speed stirred media mills were developed, which were operated with circumferential speeds of 8 to 20 m/s and with smaller grinding media. The industrial breakthrough of high-speed stirred media mills occurred in 1948 with the introduction of DuPont's "sand mill", which has been primarily applied as a pigment grinder in the paint industry. The product suspension is pumped through the vertical grinding chamber of the "sand mill" from the bottom to the open top, where the grinding

---

* Consultants, Rebenring 33, 38106 Braunschweig, Germany
**Volkmaroder Str. 4/5, 38104 Braunschweig, Germany
[†] Received August 1, 1997

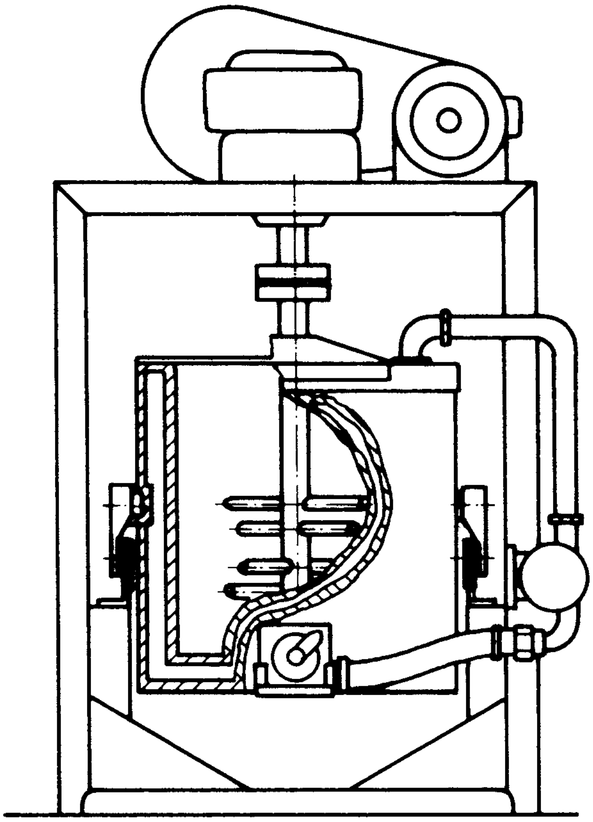

Fig. 1 Low-speed stirred media mill (Attritor) [1]

media are held back by a fixed sieve cage.

Since the power input and/or the volumetric power density of these open top mills are limited by the formation of spouts and other reasons (e.g. emission of solvents, inclusion of air, problems in processing highly viscous suspensions), these open top mills were largely replaced by closed-type mills. The grinding chamber of these closed stirred media mills can be arranged horizontally or vertically and is usually equipped with a water-jacket for cooling purposes. Usually 70 to 85% of the free grinding chamber volume is filled with a bulk of grinding media. Depending on the feed size and the feed material, different grinding media sizes (usually between 200 μm and 4000 μm) and different grinding media materials (e.g. glass, steel and ceramic materials) are employed. The grinding media are moved by a stirrer with circumferential speeds of up to 20 m/s, so that centrifugal acceleration rates of more than fifty times the acceleration due to gravity can be achieved. As a typical example of a closed-type stirred media mill the design principle of a mill with a disc stirrer is shown in **Figure 2**. The mill is equipped with a rotating gap for the separation of the grinding media. Today, closed-type stirred media mills are built with grinding chamber volumes of less than 1 litre (laboratory scale) up to more than 1 m^3 and with drive powers of more than 1 MW [2].

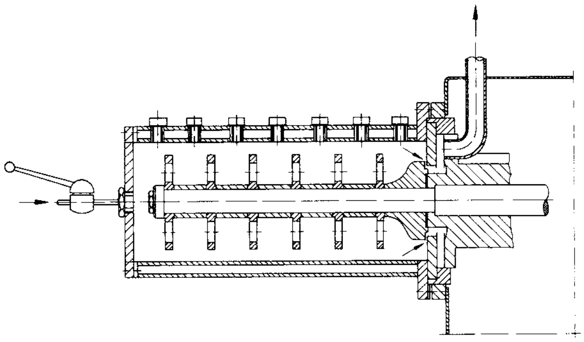

Fig. 2 Design principle of a closed-type stirred media mill with disc stirrer

A large number of different types of closed stirred media mills were developed by industry, especially in the last 10 years. The various mill designs differ above all in their chamber and stirrer geometry as well as in the separation device, which allows free discharge of the product but prevents the grinding media leaving the mill. Usually, the grinding media are held back in the grinding chamber by a screen (e.g. flat screens, screen cartridges [3], rotating or stationary cylindrical screens) or by a rotating gap (see **Figure 2**). In principle, the width of the rotating gap or the mesh width of the screen should be at least half the size of the grinding media. Usually, a rotating gap featuring self-cleaning properties is used for the processing of highly viscous suspensions. But rotating gaps are limited by the tolerance in the gap width and the relatively high pressure drop due to a very narrow gap width. Because grinding media with sizes of a few hundred microns are increasingly used, screens are being increasingly used instead of rotating gaps. They are usually designed and fixed such that they cause no dead zones in the grinding chamber, are exchangeable without having to empty the grinding chamber (screen cartridges), and/or that contact of the grinding media with the screen can be largely avoided by utilising the centrifugal force inside the mill or even by using a special kind of rejector-wheel classifier [2]. Due to specially designed grinding chamber geometries, the danger of accumulation and blocking of grinding media in front of the separation device can be significantly reduced.

Concerning the chamber and stirrer geometry, a distinction between three types of stirred media mills can be made:

- Stirred media mill with disc stirrer
- Stirred media mill with pin-counter-pin stirrer
- Annular gap geometry

Figure 3 shows schematically the three different geometries. The simplest stirrer geometry is the disc stirrer. Here, the energy is transferred from the stirrer to the grinding media/product mixture mainly by adhesion. The discs can be provided with holes, slots, slits, etc. and/or are fixed eccentrically, so that as a result of displacement forces, additional energy can be transferred from the stirrer to the grinding media/product mixture. The pin-counter-pin stirrer moves the grinding media/product mixture mainly by means of displacement forces. Especially if counter-pins (rotor/stator-system) are used, the power density is larger than that of a disc stirrer at an identical circumferential speed. The highest power density can be obtained in a grinding chamber of an annular gap mill. The width of the annular gap is usually small, i.e. approximately 5 to 20 times the grinding media diameter. Often, these mills consist of a smooth rotor and a smooth chamber wall, so that energy is transferred only by adhesion forces. In this case, the power density is very uniform and the residence time distribution is narrower than that of disc or pin-counter-pin stirrers. Some annular gap mills are also equipped with pins so that displacement forces act besides adhesion forces, permitting an even higher energy density to be obtained. Recently, annular gap mills have become very popular and most manufacturers of stirred media mills offer a specially designed annular gap mill. Annular gap mills are built with a single or double conical annular gap, with a single cylindrical or double cylindrical annular gap, or with a rotor shaped like a flat disc. Especially in some of the annular gap mills, the danger of accumulation and blocking of grinding media in front of the separation device is significantly reduced by means of an internal circulation of the grinding media.

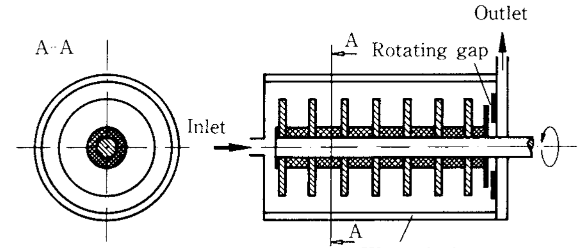

a) Disc stirrer

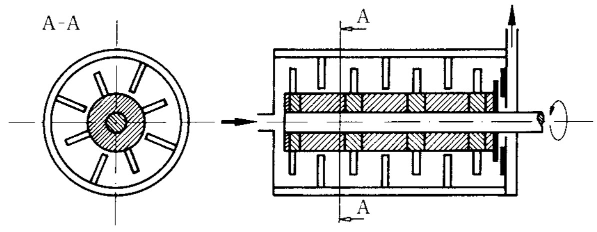

b) Pin-counter-pin stirrer

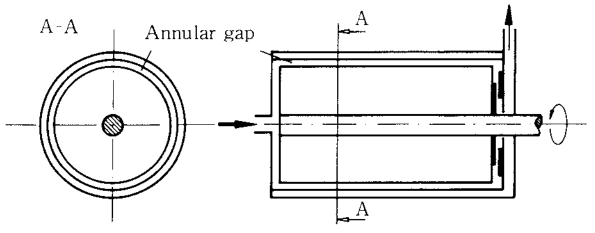

c) Annular gap mill

Fig. 3 Characteristic chamber and stirrer geometries

3. Motion of the grinding media

Bosse [4] was the first to investigate the motion of grinding media in a stirred media mill. Based on his work, further experimental and theoretical investigations were published [5-7]. Recently, numerical calculations concerning the flow field, the distribution of the specific energy and the motion of single grinding beads in a grinding chamber with disc stirrer have been carried out by Blecher, Kwade and Schwedes [8,9]. Although the calculations are based on the steady-state laminar stirring of a Newtonian fluid without grinding media, in principle the results correspond to the published experimental investigations.

A result of this study is given in **Figure 4**, in which a section of the grinding chamber, i.e. the upper part of a disc with the volumes shown next to the disc, is shown. On the left side of the disc, profiles of the tangential fluid velocity are depicted for a Reynolds number of 2000. On the right side, stationary trajectories of single beads in the radial-axial plane are presented. The profiles of the tangential fluid velocity, i.e. the velocity perpendicular to the plane of representation show that the tangential velocity is nearly constant except in the vicinity of the discs. Near the discs, high gradients of the tangential velocity and, therefore, zones of high power density exist in which the power density is higher than the mean power density. This zone is shown on the right side of the disc. Another zone of high power density is located at the grinding chamber wall. Although the volume of these zones is only about 10% of the net grinding chamber volume, at a Reynolds number of 2000, approximately 90% of the power is consumed in the zones of high power

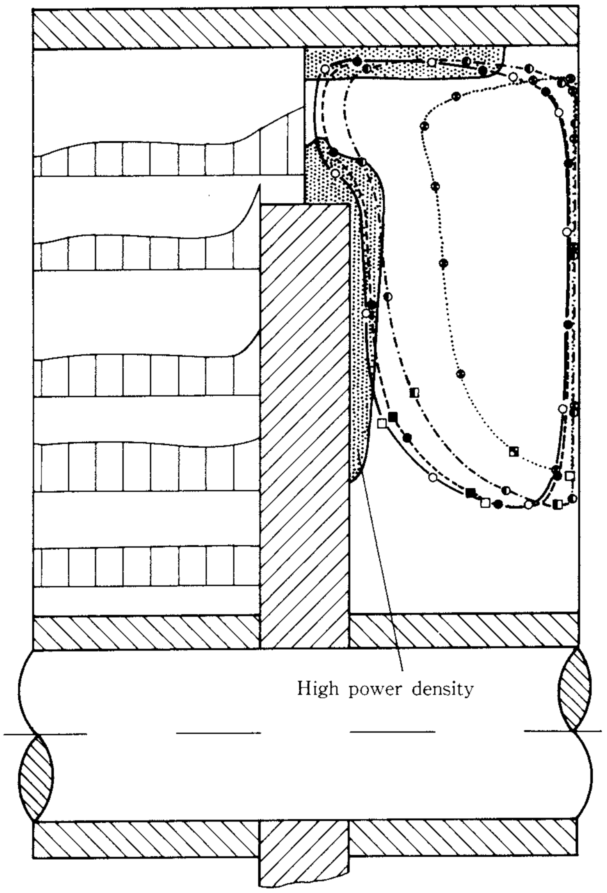

Fig. 4 Profiles of the tangential fluid velocity and stationary trajectories of single grinding beads in the axial-radial plane [8,9]

density.

Besides in tangential direction, the fluid and therefore the grinding beads also rotate in axial and radial direction. The beads move thereby through the zones of high energy density. In the zone around the stirrer discs, the grinding media are accelerated towards the grinding chamber wall. At the grinding chamber wall, the grinding media are turned round and move to the plane of symmetry between two discs. The grinding media move along the symmetry plane from the chamber wall back to the stirrer shaft because of the condition of continuity.

4. Effect of geometry and operating parameters on the comminution result

Several investigations concerning stirred media mills are occupied with the determination of the effect of various operating parameters on the relationship between product fineness and grinding time. But as the investigations show, the grinding time necessary for a certain product fineness cannot describe the influence of the several operating parameters on the comminution result. Therefore, this paper will focus on the relationship between the product fineness and the specific energy input (net energy input related to the product mass or net power input related to the product mass flow rate, respectively). The specific energy is well known to be an important influencing variable in most comminution processes. In the case of high-speed stirred media mills, Stehr, Weit and Schwedes [10-14] found on the basis of a large number of continuous grinding experiments with limestone as the grinding material that the specific energy input E_m is the main influencing variable on the comminution result for a wide parameter range. As it can be seen in **Figure 5**, in a first approximation, the specific energy describes the influence of mill size, circumferential speed of the stirrer, v_t, solids concentration of the suspension, c_V, density of the grinding media, ρ_{GM}, and throughput, $\dot{V}_{Susp}$, on the product fineness (integral mean size $\bar{x}_{1,3}$). Therefore, control of the specific energy input is often sufficient to guarantee a certain product quality in grinding plants [15].

Further investigations published more recently (Stehr [16], Mankosa et al. [17], Stadler et al. [18], Bunge [19,20], Thiel [21,22], Kwade et al. [23,24], Joost [25]), show that besides the specific energy input, the size of the grinding beads greatly affects the comminution result. For example, the influence of the media size on the relationship between the specific energy and the product fineness (median size x_{50}) is shown in **Figure 6** for batch comminution of limestone using glass beads. It can be seen that the specific energy consumption can be decreased considerably by adapting the grinding media size to suit the comminution problem. Using glass beads of a size larger than or equal to 838 μm, smaller beads yield a finer product at fixed specific energy inputs. For smaller glass beads (399 μm-661

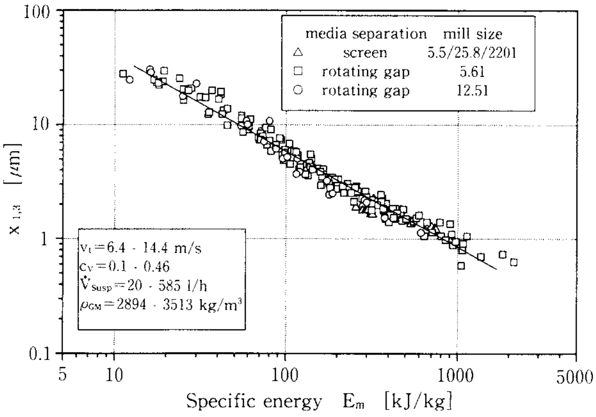

Fig. 5 Relationship between product fineness (integral mean size $x_{1,3}$) and specific energy for the comminution of limestone

μm), the position of the curve depends on the specific energy input: for low specific energies, larger glass beads yield a finer product, whereas for high specific energies, smaller glass beads are advantageous. For very small beads (97 μm and 219 μm), no progress in the product fineness can be found.

Moreover, Kwade et al. [23,24] and Reinsch et al. [26] show that as well as by the media size, the relationship between the product fineness and the specific energy is affected by the circumferential speed of the discs and the grinding media density. This influence is shown in **Figure 7**, in which the relationship between the median size obtained at a specific energy input of 1000 kJ/kg and the diameter of the grinding media is presented. The six curves plotted for different circumferential speeds of the discs and different densities of the grinding media have a characteristic shape. With increasing grinding media size, the median size of the product first declines down to a minimum. At this minimum, the corresponding grinding media size is most advantageous for a specific energy input of 1000 kJ/kg. For grinding media sizes larger than the optimum size, the median size of the product increases with increasing grinding media diameter and, moreover, with increasing circumferential velocity of the discs as well as with increasing media density.

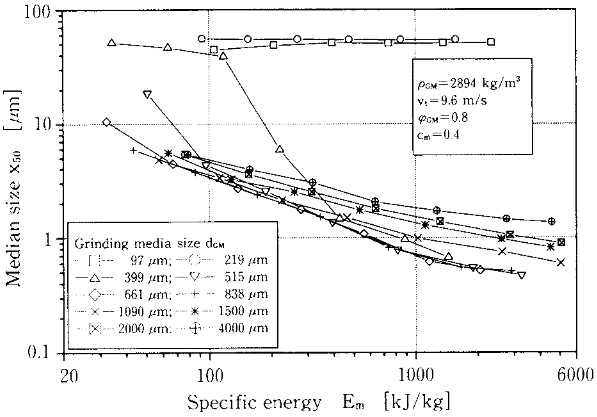

Fig. 6 Effect of grinding media size on the relationship between product fineness and specific energy

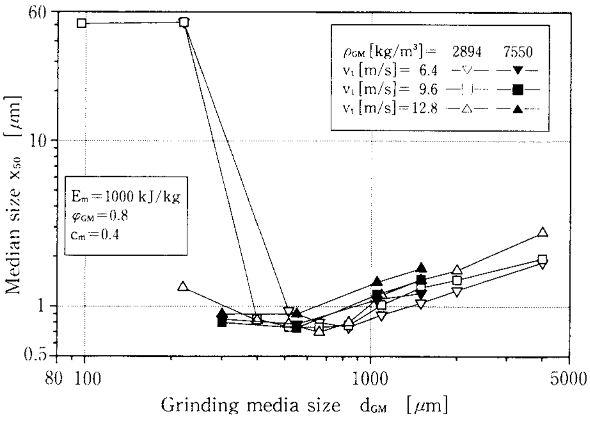

Fig. 7 Relationship between product fineness and media size for a constant specific energy input, but different circumferential speeds of the discs and different media densities

The following explanation can be given as a reason for the influence of the different operating parameters on the relationship between product fineness and specific energy [24]: The specific energy input can be considered as the product of the number of stress events and the specific energy consumed at a single stress event (i.e. the energy related to the product mass stressed between two grinding media). A measure for the number of stress events is the so-called stress number and a measure for the specific energy consumed at a single stress event is the stress intensity. The stress intensity in stirred media mills is determined above all by the kinetic energy of the grinding media. Therefore, the stress intensity is proportional to the mass of a grinding medium (bead) and to the square of the tangential velocity of the grinding media. Assuming that the tangential velocity of the grinding media is proportional to the circumferential speed of the discs, that the elasticity of the feed material is much less than that of the grinding media, and that only single particles are stressed intensively between the grinding media, the following expression can be taken as a measure of the stress intensity:

$$SI_{GM} = d_{GM}^3 \cdot \rho_{GM} \cdot v_t^2 \tag{1}$$

The parameter SI_{GM}, which is called stress intensity of the grinding media, is determined by the operating parameters (media size, d_{GM}, media density ρ_{GM}, and circumferential speed of the discs, v_t) and is constant during a comminution process. If the elasticity of the feed material is about the same or higher than that of the grinding media material (e.g. in grinding of ceramic materials), Young's modulus of the feed, Y_F, and Young's modulus of the grinding media material, Y_{GM}, have to be taken into account. The larger the Young's modulus of the feed material is compared to that of the media material, the larger is the deformation of the grinding media at each stress event and the less energy is transferred from the grinding media to the product particle. According to Becker and Schwedes [27], this influence can be described by the following definition of the stress intensity, which is a measure for the stress intensity acting on the feed or product particle:

$$SI_P = d^3_{GM} \cdot \rho_{GM} \cdot v_t^2 \cdot \left(1 + \frac{Y_F}{Y_{GM}}\right)^{-1} \tag{0}$$

The influence of the stress intensity on the relationship between the product fineness and the specific energy is shown in the following by means of the comminution of limestone, where the elasticity of the feed material is much less than that of the grinding media material. In **Figure** 8 the median sizes, which are already shown in **Figure 7**, are related to the stress intensity SI_{GM}. It can be seen that for a constant specific energy input, the stress intensity determines the product fineness. The specific energy and the stress intensity are the two main influencing variables for the comminution of limestone in stirred media mills.

Almost no comminution progress is obtained at small stress intensities because the stress intensities are too low for breaking the feed particles. Therefore, multiple stressing and more energy are required. With increasing stress intensity, the product fineness increases until a minimum is reached. At this fineness, the stress intensity has an optimum value. If the stress intensity is further increased while the specific energy input is held constant, the product fineness decreases because the number of stress events, and above all, the energy utilization (newly created surface related to the energy input) of each stress event decrease. Because of the decrease in energy utilization, the decrease in product fineness due to the decrease in stress number is higher than the increase in product fineness due to the increase in stress intensity. For example, the new surface achieved by stressing a particle volume only once with a certain stress intensity is smaller than the new surface created by stressing this particle volume twice with half stress intensity.

For different specific energy inputs, different relationships between the stress intensity SI_{GM} and the product fineness and thus different optimum values of the stress intensity exist. With increasing specific energy and therefore increasing product fineness, the optimum stress intensity decreases because with decreasing particle size, lower energies and lower forces of pressure are necessary to break a product particle. Therefore, the optimum and most advantageous stress intensity always depends on the demanded product fineness.

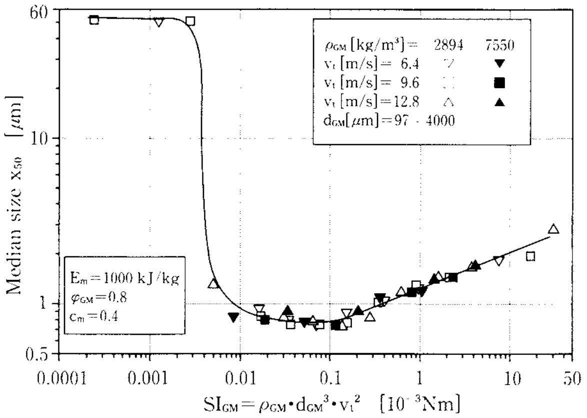

Fig. 8 Influence of stress intensity on median size for a specific energy input of 1000 kJ/kg

Besides the specific energy and the stress intensity, the filling ratio of the grinding media (bulk volume of the grinding media related to the grinding chamber volume) also affects the comminution result: Thiel [21], Joost [25] and Kwade [23] have shown that at a constant specific energy input and at a constant stress intensity of the grinding media, the product fineness increases with increasing filling ratio of the grinding media. Depending on other operating parameters and on the chamber geometry, the optimum filling ratio is in the range of 0.75 to 0.85. For filling ratios lower than the optimum value, Joost [25] and Kwade [23] found that the influence of the filling ratio on the comminution result can be described by the product of the specific energy and the filling ratio of the grinding media. This finding is shown in **Figure 9** for the comminution of limestone and can be explained as follows: In stirred media mills, the energy is transferred from the stirrer to the grinding media and the suspension. The larger the amount of grinding media inside the grinding chamber and therefore the larger the filling ratio is, the larger is the part of the energy which is transferred to the grinding media and not to the suspension. Thus, the product of the filling ratio of grinding media and the specific energy is a measure for that portion of the specific energy which can be used for comminution.

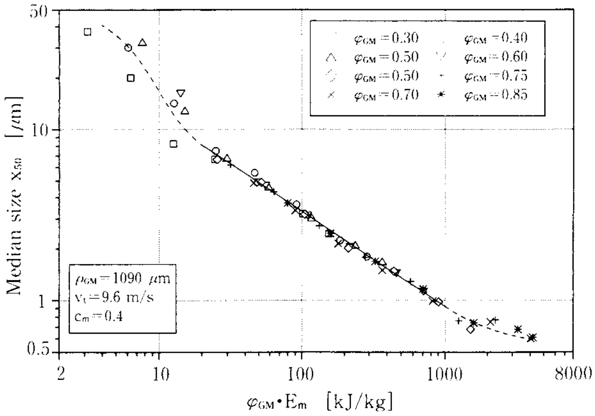

Fig. 9 Product fineness as a function of the product of the specific energy and the filling ratio of the grinding media

The solids concentration of the suspension is another operating parameter which can be described in a first approximation by the specific energy. But at low solids concentrations, more specific energy is required to achieve the same product fineness [23]. A possible reason for this behaviour is that at low solids concentrations, it is not at every grinding media contact that a product particle is stressed between the grinding media. Besides low solids concentrations, also high solids concentrations can make larger specific energy consumptions necessary for producing a certain product fineness because of disadvantageous suspension viscosities [21,25,28]. To overcome this problem, grinding aids or dispersants can be used to reduce the suspension viscosity. But as experiments of Wang et al. [28] show, dispersants have to be used carefully because too large an amount of dispersants can lead to higher specific energy consumptions.

Instead of with the specific energy, the product fineness can be correlated with the so-called stress number (sometimes also called stress frequency). The stress number is a measure for the number of stress events in a mill and can describe the influence of the grinding time as well as the influence of several operating parameters on the product fineness. Various authors [18-21,23,24] show that by choosing an appropriate relation for the stress number or stress frequency, the effect of several operating parameters on the comminution result can be described. For the comminution of limestone, Kwade and Schwedes [23,24] show that for a constant stress intensity, a certain relationship between the product fineness and the stress number exist. In contrast to these results, the effect of the stress intensity is different for the disintegration of microorganisms [19,20] and for the desagglomeration of pigments [18]. For the case that the stress intensity is higher than the stress intensity necessary for the disintegration of a microorganism or for the desagglomeration of an agglomerate, only one relationship between the disintegration rate or the product fineness and the stress number exist. The reason is that if a microorganism is disintegrated or an agglomerate is broken, a higher stress intensity has no additional advantage.

5. Effect of mill size and mill design on the comminution result

Weit and Schwedes [12,13] and recently Karbstein et al. [29] as well as Kwade [24] investigated the effect of the mill size on the specific energy necessary to obtain a certain product fineness. Weit used seven stirred media mills with disc stirrer and net volumina between 5.5 and 200 litres. Besides the mill size, he varied the circumferential speed of the discs, v_t, the volume flow rate, $\dot{V}_{Susp}$, and the solids concentration by volume, c_V. The comminution results shown in **Figure 5** prove that the specific energy required for a certain product fineness is more or less independent of the mill size. The results published by Karbstein et al. confirm the results of Weit for grinding chamber net volumes down to approximately 1 l. But the comminution experiments of Karbstein et al. and Kwade also show that by using grinding chambers with net volumes less than 1 l, the specific energy necessary for a certain product fineness increases. Among other things, the increase of the specific energy requirement using very small grinding chamber volumes can be attributed to a change in the stress intensity: At an unchanged circumferential stirrer speed, the centrifugal acceleration and thus the stress intensity of the grinding media increase with decreasing mill size. Therefore, as long as the stress intensity remains in the range of the optimum stress intensity, although the mill size has changed (see **Figure** 8), the effect of the mill size on the specific energy consumption is small. But if the stress intensity is much larger than the optimum stress intensity (for example, because of a relatively large grinding media size), the specific energy necessary for a certain product fineness increases with decreasing mill size.

Since the specific energy consumption is independent of the mill size for a wide range of mill sizes, the specific energy required for a certain product fineness can be determined by means of comminution experiments in a small mill. This specific energy has to be supplied to the large mill by choosing an appropriate flow rate and an appropriate circumferential stirrer speed. The required circumferential stirrer speed can be determined by using the power characteristic diagram, which is well known in stirring processes and where the Newton number is plotted versus the Reynolds number [11-13].

Joost and Schwedes [25,30], Reinsch et al. [26] and Karbstein et al. [29,31] investigated whether chamber and stirrer geometry influence the relationship between the product fineness and the specific energy. Joost and Karbstein et al. used three different geometries according to the three different types shown in **Figure 3**, whereas Reinsch et al. investigated a mill with a disc stirrer and different types of annular gap mills. All investigations show that at a certain specific energy input and at a comparable stress intensity, similar median sizes of the product are obtained with the different mill designs. Differences were found in the widths of the particle size distributions. For example, **Figure 10** shows particle size distributions obtained at four specific energy inputs using three different mill designs [25,30]. The particle size distributions prove that the narrowest particle size distribution can be achieved using the annular gap geometry because of a narrow residence time distribution and because of a relatively uniform power density or stress intensity, respectively. The widest particle size distributions were found for the pin-counter-pin stirrer because of intense radial mixing and axial remixing. The products achieved with the disc stirrer have particle size distributions which range between the others.

6. Transport behaviour and residence time distribution

As mentioned before, the width of the particle size distribution depends on the residence time distribution of the mill and thus on the axial flow through the grinding chamber. For the description of the axial transport of the product particles through the grinding chamber, two models can be used: Axial dispersion model [11,24,32,33] and cell model with backmixing [24,33,34]. The axial dispersion model bases on the notion that a mixing motion superposes the convective axial transport over the entire length of the grinding chamber. On the other hand, in the cell model with backmixing, the grinding chamber is divided into several cells. In the case of a grinding chamber with a disc stirrer, the number of cells corresponds to the number of discs and the cells are bounded by the symmetry planes between two discs. The product suspension flows through all cells from the inlet to the outlet. Besides that, a so-called backmixing flow rate connects two adjacent cells in both directions because of the backmixing behaviour.

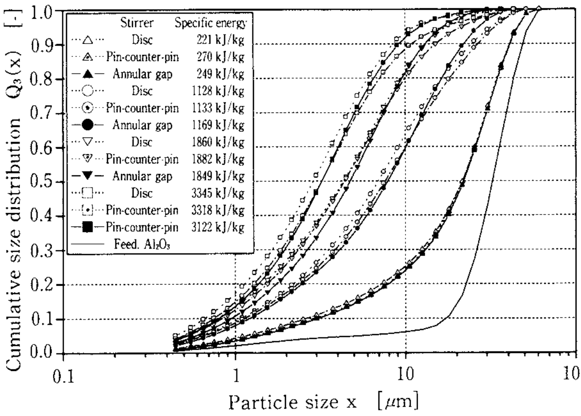

Fig. 10 Comparison of grinding results at the same specific energy input; three different grinding chamber geometries [25,30]

Up to now, the applicability of the two different transport models has only been proven for a mill with disc stirrer: Heitzmann [33], Berthiaux et al. [34] and Kwade [24] have shown that the residence time behaviour of a mill with disc stirrer can be described better by the cell model with backmixing than with the axial dispersion model. This is shown in **Figure 11**, in which a residence time distribution measured by Kwade is compared to the distributions calculated with the two models.

The residence time behaviour of the mill determines the residence time distribution of the product particles if the product flows only once through the grinding chamber. But often more than one pass is necessary to obtain the required product fineness. This can be done by using a cascade of mills or by pendulum operation. Besides the multi-pass mode, the circuit mode is very common, especially for the grinding of pigments where small batches are usual. Here, the suspension is pumped from a storage tank through the mill and then returned to the same tank [18,31]. Therefore, the residence time distribution in the grinding chamber is superposed by that in the storage tank and consequently the overall residence time distribution becomes wider. Especially at small comminution times, the circuit mode can lead to relatively wide particle size distributions with a tail of coarse particles. In contrast, the narrowest residence time distribution can be achieved by operat-

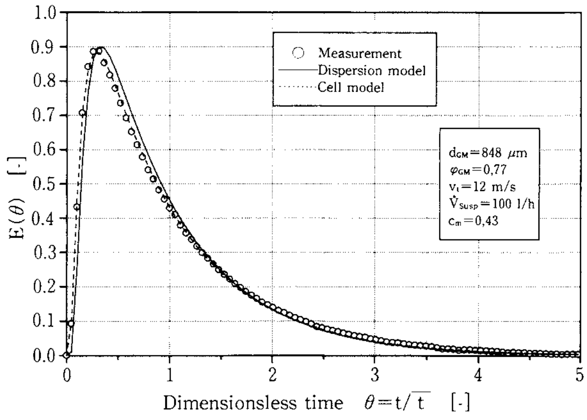

Fig. 11 Comparision of measured and calculated residence time distributions in a mill with disc stirrer

ing the stirred media mills in multi-pass mode: The more passes are carried out, the smaller the width of the particle size distribution. But because of high investment costs and a high expenditure for control technology, the multi-pass mode is not very common.

7. Wear of grinding media

The wear of grinding media was investigated extensively by Joost, Becker and Schwedes [25,27, 30], who made comminution tests with white fused alumina and other materials using varius grinding media materials. The wear of the grinding media was described by the ratio of the mass loss of the grinding media during the comminution process to the mass of the grinding media at the start of the comminution process, $\Delta m_{GM}/m_{GM}$. **Figure 12** shows that the influence of the following operating parameters on the wear of the grinding media can be described by the total energy input related to grinding chamber net volume, $E_{V,GC}$: circumferential stirrer speed, v_t, mass flow rate, $\dot{m}_{susp}$, and solids concentration by mass, c_m, of the product suspension, filling ratio, ϕ_{GM}, and size, d_{GM}, of the grinding media as well as grinding chamber geometry. Independent of the chosen operating parameters and independent of the grinding chamber geometry, a certain total energy input related to the grinding chamber net volume leads to the same media wear or to the same relative mass consumption of grinding media. Moreover, the media wear is affected by the properties of the media material and of the feed material, above all by the hardness of the two materials: The media wear decreases if harder grinding media or/and a softer feed material are employed.

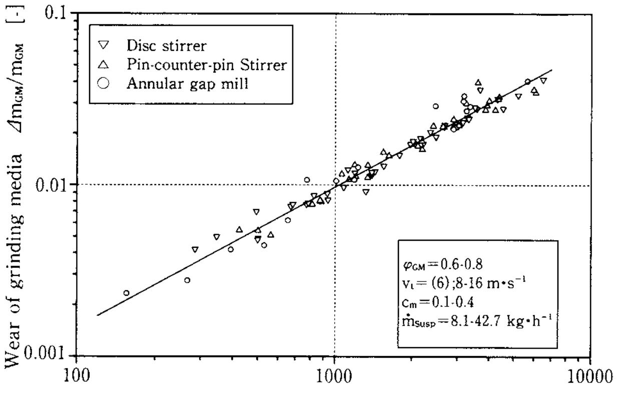

Fig. 12 Effect of different operating parameters on the media wear (comminution of white fused alumina) [25,30]

8. Autogenous comminution

By means of autogenous comminution, a product contamination caused by the breakage and abrasion of grinding beads can be avoided and grinding media costs can be largely reduced. Autogenous comminution in stirred media mills was scientifically investigated by The and Schubert [35] (silicon carbide), Kanda et al. [36] (limestone) and Kwade and Schwedes [24,37,38] (limestone, white fused alumina). In **Figure 13**, the cumulative size distribution by mass, Q_3, is depicted for batch autogenous pebble comminution of limestone [24,37]. With the exception of the absence of fine feed (i.e. only coarse particles are in the mill), a fully autogenous comminution process is comparable.

Before starting the comminution process, the hold-up is composed of the grinding media (about 200 to 1600 μm) and the fine feed (about 20 to 100 μm). After starting the comminution process, the feed particles are quickly reduced in size by the grinding media and a fine product with particle sizes smaller than 10 μm results. Besides the feed particles, small grinding media which are stressed between large grinding media as well as grinding media with internal cracks are reduced in size by complete fracture. Moreover, chipping fracture (removal of asperities from irregular particles) occurs. After a few minutes, almost no particles can be found in the particle size range between the fine product and the grinding media or the pebbles, respectively, because pebbles are reduced in size mainly by the abrasion of micro grains and because small pebbles are broken by large pebbles before they become smaller than 100 μm. This particle size range without particles is very important for the separation of product and grinding media. Since the smallest size of the grinding media is larger than

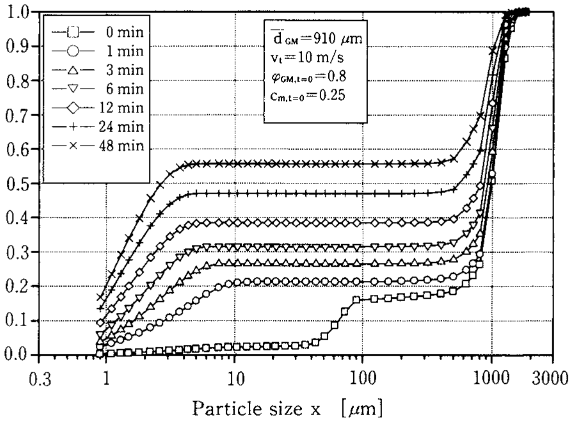

Fig. 13 Cumulative size distribution of the hold-up for batch autogenous pebble comminution of limestone

100 μm and the product is finer than 10 μm, a product finer than 10 μm can be achieved by sieving at a particle size of about 100 μm. Thus, a separation at a particle size of 10 μm is not necessary to obtain a product finer than 10 μm. A comparison with the comminution of limestone using glass beads showed that the specific energy consumption of an autogenous comminution process is comparable to that using glass beads. Enderle et al. [2] give an example of an industrial use of autogenous comminution in stirred media mills. They report on the autogenous regrinding of zinc/lead ores in stirred media mills with disc stirrer and a grinding chamber volume of about 3000 litres and a drive with a power of 1.1 MW.

9. Outlook

The importance of stirred media mills for the production of very fine particles is likely to increase further in the next years. Because of rising product qualities, further developments of stirred media mills regarding the use of very fine grinding media, the production of narrow product particle size distributions and wear are expected. The research work should focus above all on the operation of stirred media mills, e.g. on the blocking of the grinding media, on the use of grinding aids and on the scale-up. Moreover, progress in the simulation of the comminution process should be made in a manner such that a prediction of the comminution result (product fineness, specific energy consumption) is possible for a wide range of operating parameters.

References

1) John, W.: Von der Trommelmühle zur Ringkammermühle, Farbe und Lack, 79 (1973) 6, 537-542
2) Enderle, U., Woodall, P., Duffy, M. and Johnson, N.W.: Stirred Mill Technology for Regrinding McArthur River and Mount Isa Zinc/Lead Ores, XX International Mineral Processing Congress, 21.-26. 9. 1997, Aachen, Germany
3) Stehr, N.: Recent Developments in Stirred Ball Milling, International Journal of Mineral Processing, 22 (1988), 431-444
4) Bosse, D.G.: Development and Use of the Sand Grinder, Official Digest, (1958) 3, 251-276
5) Engels, K.: Die Dispergierverfahren in der Lack- und Farbenindustrie unter besonderer Berücksichtigung der schnellaufenden Rührwerksmühlen, Farbe und Lack, 71 (1965) 5, 375-385
6) Hashi, Y., Senna, M.: Motion of Grinding Media in Axial Direction and its Effect on Comminution in an Agitation Bead Mill, KONA, 14 (1996) 176-181
7) Jenczewski, T.J.: The Grinding of Organic Dyestuffs, The Canadian Journal of Chemical Engineering, 50 (1972) 2, 59-65
8) Blecher, L., Kwade, A., Schwedes, J.: Motion and Stress Intensity of Grinding Beads in a Stirred Media Mill. Part 1: Energy density distribution and motion of single grinding beads, Powder Technology, 86 (1996), 59-68
9) Blecher, L.: Strömungsvorgänge in Rührwerkmühlen, Dissertation, TU Braunschweig, 1993
10) Stehr, N., Schwedes, J.: Technological Investigations on the Comminution at a Continuously Operated Ball Mill, Intern. Symp. on Recent Advances in Particulate Science and Technology, Madras, India, 1982, Part 1, Preprints, B103-B119
11) Stehr, N.: Zerkleinerung und Materialtransport in Rührwerkskugelmühlen, Dissertation, TU Braunschweig, 1982
12) Weit, H., Schwedes, J.: Scale-Up of Power Consumption in Agitated Ball Mills, Chem. Eng. Technol., 10 (1987) 6, 398-404
13) Weit, H.: Betriebsverhalten und Maßstabsvergrößerung von Rührwerkskugelmühlen, Dissertation, TU Braunschweig, 1987
14) Weit, H., Schwedes, J. and Stehr, N.: Comminution and Transport Behaviour of Agitated Ball Mills, 1. World Congress Particle Technology, Nürnberg, 1987, Part II, Preprints, 709-724
15) Stehr, N., Weyand, C.: Control System for Agitated Media Mills, 7. European Symposium Zerkleinern, Ljubljana, 1990, 681-695
16) Stehr, N.: Naßfeinstmahlung mit Rührwerksmühlen in der Keramik-Grundlagen und technische Ausführungen, Keramische Zeitschrift 42 (1990) 3, 162/167
17) Mankosa, M.J., Adel, G.T., Yoon, R.H.: Effect of Media Size in Stirred Ball Milling Grinding of Coal, Powder Technology 49 (1986), 75-82
18) Stadler, N., Polke, R., Schwedes, J., Vock, F.: Naßmahlung in Rührwerksmühlen, Chem.-Ing.-Tech. 62 (1990) 11, 907-915
19) Bunge, F.: Mechanischer Zellaufschluß in Rührwerkskugelmühlen, Dissertation, TU Braunschweig, 1992
20) Bunge, F., Schwedes, J.: Mechanical Disintegration of Micro-Organisms, 7. Europ. Symposium Comminution, Ljubljana, June 1990, 55-77
21) Thiel, J.P.: Energiebedarf und Durchsatzverhalten der Kohlenaßzerkleinerung in einer Rührwerkskugelmühle, Dissertation, TU Braunschweig, 1993
22) Thiel, J.P., Schwedes, J.: Comminution of Coal in an Agitated Ball Mill, Ljubljana, June 1990, 667-680
23) Kwade, A., Blecher, L., Schwedes, J.: Motion and Stress Intensity of Grinding Beads in a Stirred Media Mill. Part 2: Stress Intensity and its Effect on Comminution, Powder Technology, 86 (1996), 69-76
24) Kwade, A.: Autogenzerkleinerung von Kalkstein in Rührwerkmühlen, Dissertation, TU Braunschweig, 1996

and Verlag Shaker, Aachen, 1997

25) Joost, B.: Zerkleinerung von Schmelzkorund und Mahlkörperverschleiß in Rührwerkskugelmühlen, Dissertation, TU Braunschweig, 1995

26) Reinsch, E., Bernhardt, C., Husemann, K.: Energy Consumption for Wet Grinding in Stirred Mills, Aufbereitungstechnik, 38 (1997) 3, 152-160

27) Becker, M., Schwedes, J.: Comminution of Ceramics in Stirred Media Mills and Wear of Grinding Beads, in Schwedes, J.: Feinste Feste Partikeln-Erzeugen, Klassieren, Abscheiden und Messen, Verlag Shaker, Aachen, 1997

28) Wang, Y., Forssberg, E.: Dispersants in Stirred Ball Mill Grinding, KONA 13 (1995), 67-77

29) Karbstein, H., Müller, F., Polke, R.: Scale-up for Grinding in Stirred Ball Mills, Aufbereitungstechnik, 37 (1996) 10, 469-479

30) Joost, B., Schwedes, J.: Comminution of White Fused Alumina and Wear of Grinding Beads in Stirred Media Mills, Ceramic Forum International, 73 (1996) 6 and 73 (1996) 7/8

31) Karbstein, H., Müller, F., Polke, R.: Producing Suspensions with Steep Particle Size Distributions in Fines Ranges, Aufbereitungstechnik, 36 (1996) 10, 464-473

32) Stehr, N.: Residence Time Distributions in a Stirred Media Mill and their Effect on Comminution, Chem. Eng. Process., 18 (1984), 73-83

33) Heitzmann, D.: Characterisation des Operations de Dispersion-Broyage, Dissertation, INPL Nancy, 1992

34) Berthiaux, H., Heitzmann, D., Dodds, J.A.: Validation of a model of a stirred bead mill by comparing results obtained in batch and continuous mode grinding, 8. European Symposium on Comminution, Stockholm, 17.-19. 5. 1994, Preprints, Part II, 723-733

35) The, L.X., Schubert, H.: Autogene Mahlung von SiC in Rührwerksmühlen ohne und mit Mahlhilfsmitteln, Aufbereitungs-Technik 33 (1992) 10, 541-550 and 33 (1992) 12, 661-664

36) Kanda, Y., Hasegawa, M., Hayashi, Y., Sano, S., Ishikawa, T., Nagaoka, H.: Production of Submicron Particles by Autogenous Grinding with a Stirred Mill, XVIII International Mineral Processing Congress, Sydney, 23.-28. 5. 1993, 245-249

37) Kwade, A., Schwedes, J.: Autogenous Comminution in Stirred Media Mills, 5th World Congress of Chemical Engineering, San Diego, 14.-18. 7. 1996, Preprints, 214-219

38) Joost, B., Kwade, A.: Feinstzerkleinerung in Rührwerkmühlen, in Reh, H.: Das Jahrbuch der Keramik, Bauverlag, Walluf, 1995, 23-38

Author's short biography

Dr.-Ing. Jörg Schwedes

Born 1938 in Berlin
Study of mechanical and chemical engineering at the Technical Unviersities of Karlsruhe and Munich. Dipl.-Ing. 1964 at Karlsruhe. Dr.-Ing. 1971 at Karlsruhe (Prof. Rumpf) with a thesis on the shear properties of slightly compressed cohesive granular materials.
1971-1976 with Bayer AG at Leverkusen as head of a research group working in the field of mechanical process engineering.
since 1976 Professor and Director of the Instiute of Mechanical Process Engineering, Technical University of Braunschweig.
main research activities:

- mechanics of bulk solids (measurement of flow properties, silo design, development and application of constitutive laws for bulk solids, instationary flow of gases in bulk solids, flow promoting devices, handing of contaminated soils)
- comminution (wet grinding in agitated ball mills, vibratory milling, grinding of micro-organisms, particle classification in the μm-range)

about 130 publications
1982-1984: Vicepresident of the Technical University of Braunschweig
1989-1991: Dean of the Faculty of Mechnical Engineering
since 1991: consultancy with Dr. Schulze on bulk solids technology

Dr.-Ing. Arno Kwade

Born 07. 01. 1965 in Nordhorn, Germany
1986-1992: Study of Mechanical Engineering with consolidation in process and chemical engineering at the Technical University of Braunschweig, Germany, and the University of Waterloo, Canada (1989-1990)
1992-1996: Research assistant at the Institute of Mechanical Process Engineering of the Technical University of Braunschweig, Germany
1996: Dr.-Ing with a thesis on autogenous comminution of limestone in stirred media mills
1996: Foundation of the consultant and engineering company Kwade+Schwedes Zerkleinerungstechnik, Braunschweig, Germany
research activities: fine grinding, especially comminution in stirred media mills, and bulk solids handing

Research

A New Constitutive Model for Alumina Powder Compaction[†]

O. Cazacu, J. Jin and N.D. Cristescu
Department of Aerospace Engineering,
Mechanics & Engineering Science
*University of Florida**

Abstract

Based on a systematic experimental investigation of the mechanical properties of alumina powder ***a new general 3-D constitutive model*** *for compaction of powders has been developed. A significant feature of the model is that it describes the time effects on compaction. These effects have been revealed by creep and relaxation phenomena and by the influence of the strain rate. Although the theory is applicable to general 3-D conditions all the parameters involved in the model can be derived from the results of a few number of conventional triaxial drained compression tests. The procedure to identify the model parameters from data is general. Unlike the models available in the literature, the model developed in the present paper accounts for both compressibility and dilatant behavior of powders. Thus it provides a realistic description and a better understanding of the mechanisms of powder pressing. The theory is able to model important aspects of powder behavior with a degree of accuracy which appears to make it useful in FEM analyses of stress and density distribution in a pressed compact.*

1. Introduction

Almost every industry handles powders/bulk solids, either as raw materials, intermediates in the production process, or as final products. Examples include: chemicals and chemical processing, foods, detergents, ceramics, minerals, pharmaceuticals, etc. However, the understanding of powder behavior, despite its economic importance, is yet limited compared to other classes of materials or disperse systems. Particularly, the mechanical behavior of cohesive bulk solids under external loads can be critical to the final performance and quality of the product. To mould an advanced ceramic shape, for example, the principal method is still pressing. High production rates and close tolerances can be achieved with dry pressing. However, important problems such as cracking and pore-formation, non-uniform density have yet to be overcome. Furthermore, flaws may not be visible by routine inspection and thus, the defects are carried out through sintering to the final product. Also the density variation in the green compact causes distortion or cracking during fire. In order to reduce density variation in the compact, moulding is restricted to simple geometrical shapes of relatively small sizes.

Modelling of the mechanics of compaction has thus developed through the necessity of controlling densification kinetics and shape change in order to optimize the design start up and processing of powders. A promising approach for practical applications appears to be to treat the powder as a homogeneous continuum. During the past decades considerable efforts have been undertaken to describe the behavior of granular materials within the framework of classical plasticity theory. Two main methods have been followed in order to formulate constitutive models. The first one, that can be referred to as the empirical procedure, is based on the best fitting of the data obtained from a series of tests by means of simple functions (polynomial, exponential, etc.). The characteristics of these functions are chosen just to meet the shape of the experimentally obtained pressure versus density diagrams. A list of the most used empirical laws can be found in the review paper by Shinohara [14]. The empirical laws lead to accurate results when applied to situations having boundary conditions, and loading paths similar to those used in the tests from which the laws have been formulated. However, the use of these laws for different conditions would in general lead to erroneous results.

---

*Gainesville, Fl. 32611-6250, USA

[†] Received April, 1996

A second procedure consists of developing a constitutive model, represented by a set of stress-strain (time) relationships having a sound mechanical basis. Afterwards, the values of the material parameters are calibrated from data. An adequate constitutive model generally lead to results reasonably close to those experimentally observed, even when applied to situations different from those considered for the determination of its parameters.

During the past decades considerable efforts have been undertaken to adapt existing models for granular materials (mainly soils) to powder-like materials. Generally, the theory used for establishing the yield locus is the Mohr-Coulomb theory:

$$\tau_f = C + \sigma_n \tan\Phi \tag{1}$$

where τ_f is the magnitude of the shear stress on the failure plane, σ_n is the normal stress on that plane (compression stresses are assumed to be positive), C is the cohesion, and Φ is the angle of internal friction. The cohesion and the slope of the yield locus ($\tan\Phi$) as well as the wall friction are measured using the Jenike cell. The Jenike Cell is still the most widely used flow-properties measuring device in industry and the yield locus [Eq. (1)] is generally considered for bin design.

The use of the Mohr-Coulomb criterion [Eq. (1)] is based on the assumption that the material is perfectly plastic, i.e., the yield locus is fixed in the stress space. Thus the yield locus coincides with the failure surface (Kamath *et al.* [9]). However, the experimental evidence suggests that for powders a clear distinction exists between the stress conditions at which the irreversible behavior initiates and those corresponding to failure. Recently, critical-state models have been applied to describe the yielding of dry cohesive powders (see Tripodi *et al.* [15], Puri *et al.* [11]). These models developed by the Cambridge group (see Roscoe *et al.* [12], Burland and Roscoe [1], Schofield and Wroth [13]) have been originally tailored to describe the behavior of clays and sands in triaxial compression and extension. These models are based on the observation of steady-state flow and the concept of critical state line. The critical-state concept states that if a sample of material undergoes an increasing deviatoric strain, it tends towards an ultimate condition defined by a zero volume change and a constant ratio of the deviatoric stress q over mean stress p

$$d\varepsilon_q \geq 0,\ d\varepsilon_v = 0,\ q = Np,\ \frac{v}{v_o} = \Gamma - \lambda \ln\left[\frac{p}{p_a}\right] \tag{2}$$

N, Γ and λ are material constants which do not depend on the initial volume v_o, v is the current volume of the sample and p_a is a reference pressure; p and q denote the stress invariants, ε_v and ε_e the strain invariants (see Nomenclature):

$$p = \frac{1}{3} tr\sigma,\ q = \left[\frac{3}{2} tr\sigma'^2\right]^{\frac{1}{2}},$$
$$\varepsilon_v = tr\varepsilon,\ \varepsilon_q = \left[\frac{2}{3} \varepsilon' : \varepsilon'\right]^{\frac{1}{2}} \tag{3}$$

The state of the material is therefore defined by the set (p, q, v). This concept seemed to be verified at least qualitatively in clays.

However, experimental data on powders reported by various authors [8, 14] suggest that there exists, for each confining pressure, a stress value for which the slope of the octahedric shear stress versus volumetric strain curve changes sign, i.e., above which the volume expands. Thus, the behavior of powders is not described correctly for undrained conditions by the critical state class of models. It appears then necessary to develop a constitutive model of enough generality to properly account for the complex volumetric behavior of powders.

All the models discussed so far neglect the time effect on compaction. However, it is well known that time has an important influence on the mechanical behavior of powders. This effect is revealed by creep and relaxation phenomena, and by the influence of rate of strain. Several points arise: (I) What is the importance of the viscous part of the behavior in comparison with the elasto-plastic behavior, which is generally the only one considered? (ii) How does one measure this effect without performing very long experiments which are inevitably expensive?

In the present paper an attempt is made to address these topics. First, we present the experimental results concerning the influence of time on compaction of alumina powder. Then, based on the data, we formulate a 3-D elastic/viscoplastic model which describes the behavior of the material under general loading conditions. Finally, data from conventional triaxial compression tests are used to demonstrate the capability of the model to reproduce the commonly observed features of powder's response.

2. Experimental studies

The bulk properties of alumina powder were investigated by means of hydrostatic and triaxial compression tests on cylindrical specimens 7 cm in diameter and 15 cm in length. To assure a similar specimen for each test and in order to minimize the variability in axial deformation and specimen volumetric change the two-layers filling method has been followed. This method consists of filling half of the triaxial mould with material, compressing it with uniform tamping and repeating this operation until the mould is completely filled. Thus for all tests the initial bulk density varied from 1.42 g/cm^3 to 1.427 g/cm^3. The arithmetic mean particle size varied from 40 μm to 200 μm. The specimen was saturated with water so that before testing the water content was 50% per volume.

2.1 Hydrostatic tests.

Figure 1 shows the results of a hydrostatic test with 4 unloading-reloading cycles. Here, and throughout this paper, compressive stresses and strains are assumed to be positive. ε_v denotes the volumetric strain, while σ is the mean stress which coincides with the applied hydrostatic pressure. Before passing from loading to unloading the pressure was held constant for a short period of time (10 minutes). A volume decrease by creep had been observed. After the material had reached a quasi-stable state (nearly zero decrease of volumetric strain) the unloading was performed. It is worthwhile to point out that in this way the viscous effects have been separated from unloading and therefore the obtained unloading curve is elastic. From its slope one can evaluate accurately the bulk modulus K. **Figure 1** shows that bulk modulus increases as pressure is increased. This nonlinear behavior can be attributed to the presence of pores.

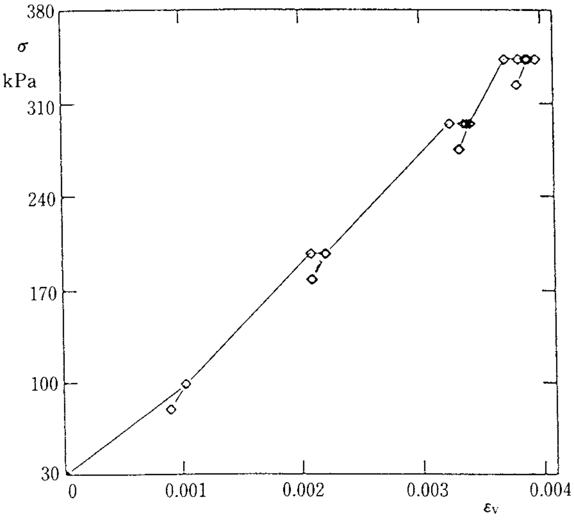

Fig. 1 Volumetric creep and compressibility of alumina powder. Partial unloadings are used to determine the bulk modulus.

Since the pores close as pressure is raised, at sufficiently high pressure, when most of the pores are closed, one can expect that further increase in pressure does not cause additional change in slope. An exponential type of law of the form

$$K(\sigma)=K^{\infty}-p_a a \exp\left[-b\frac{\sigma}{p_a}\right] \qquad (4)$$

seems to fit well the data. In Eq (4) K^{∞} is the constant value towards which the bulk modulus tends for high pressures ;p_a is a reference pressure expressed in the same units as K^{∞} and the mean stress σ ; a and b are dimensionless parameters. For alumina the numerical values of these parameters are : $a=10^7$, $b=-1.219\times10^{-4}$, $K^{\infty}=1\times10^7$kPa, $p_a=$ 1 kPa.

The test shows that alumina powder exhibits time-dependent properties (see **Figure 1**). The question which arises is whether the dominant properties of alumina are visco-elastic or viscoplastic. In other words, are the time-dependent properties influenced by the loading history ? In order to answer to this question, three additional hydrostatic tests with step-wise increase of pressure have been performed (**Figure 2**). The results obtained are revealing. For a stress path consisting of successive stress increments of equal magnitude, the smaller those increments are the larger the deformation is. It is clear that only an elastic/viscoplastic model can describe correctly the material behavior.

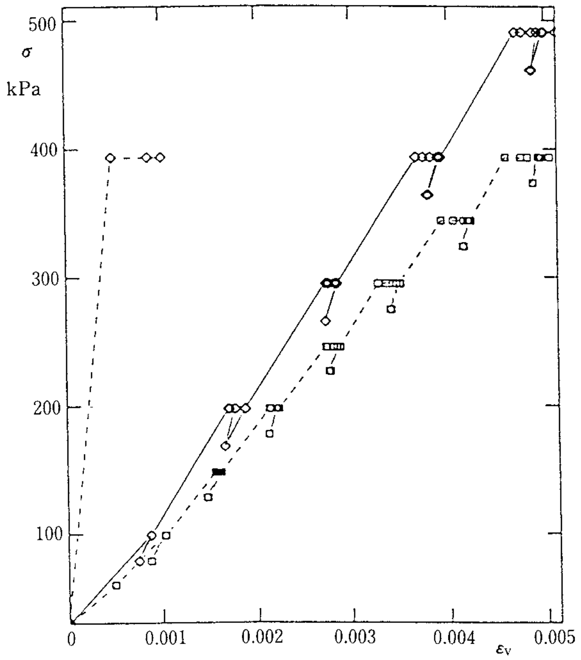

Fig. 2 Influence of the loading history on the hydrostatic response.

2.2 Drained triaxial compression tests

The realization of drained triaxial compression tests is presently well mastered in the laboratory. The cylindrical specimen was contained in a latex membrane to isolate it from direct contact with the surrounding water with which the testing cell is filled. The sample sat in the cell between a rigid base and a rigid top cap which is loaded by means of a ram passing out of the cell. The tests were run at a constant displacement rate of 0.1 mm/min. The rigid base is porous so that the pore fluid can drain from the sample. The quantities measured during any test were : the pressure in the cell fluid, the cell pressure σ_3 (which provides an all-around pressure on the lateral surface of the sample), the axial force applied to the loading ram, the change in length of the sample and the change in the volume of the sample. First the hydrostatic pressure was raised to a predetermined level, and afterwards σ_3 was kept constant while the axial stress σ_1 was further increased. Drained compression tests were carried out for 6 different pressures in the range 98-490 kPa. Three experiments were done for each confining pressure. From these experiments one can determine the elastic properties and draw conclusions about the deformation mechanism and the failure strength of the material.

The practical measurement of the Young modulus is not as easy as it seems because the test results can be strongly influenced by the rheological behavior of the material. This problem can be overcome by performing fast experiments where viscous effects have no chance to interfere. Since dynamic tests are difficult to perform, in most cases the elastic properties are measured from experiments with unloading-reloading cycles. However, during unloading-reloading cycles significant hysteresis loops are usually observed. A rather good estimation of the real value of E can be obtained from the slope of the middle part of the unloading curve which is generally nearly linear. The determination of the E modulus from such tests yields much smaller values than in dynamic tests. Nevertheless, these reduced values are often used in model computations and in practical applications and thus misleading results may be obtained.

An experimental procedure which allows the experimentator to determine more accurately the elastic properties by static methods has been proposed by one of the authors (see [4]). Thus, before passing from loading to unloading one has to keep the deformation constant for a certain time interval in order to permit the material to reach by relaxation a quasi-stable state. In this way the hysteresis loop can be practically eliminated. **Figure 3** shows the axial and radial strains as functions of the octahedral shear stress τ :

$$\tau=\frac{\sqrt{2}}{3}(\sigma_1-\sigma_3) \tag{5}$$

obtained in such test ($\sigma_3=392$ kPa). Note that the stress-strain curves are strongly non-linear. Five unloading-reloading cycles were performed. Before passing to unloading, the axial deformation was kept constant and the time dependent evolution of the axial stress σ_1 was measured. A significant stress relaxation was recorded within minutes. At each stress level about half of the stress reduction shown in **Figure 3** is due to relaxation. From the unloading slopes we were able to evaluate the Young modulus E. A dependence of this modulus on the mean stress is observed. To account for this variation we propose the following expression

$$E(\sigma):=E^{\infty}-p_a\beta\exp(-d\sigma) \tag{6}$$

where E^{∞} is a constant limiting value that E approaches as pressure increases while β, and d are dimensionless constants. For alumina $E^{\infty}=7\times10^5$ kPa, $\beta=6.95\times10^5$ and $d=0.002$. **Figure 3** also shows the developing of irreversible deformation and the steadily increasing elastic limit for alumina. Note also that first the volume decreases as τ increases. Thus, additional compaction is obtained in the deviatoric part of the test. However, as the applied load is further increased, the volume starts to expand (dilatancy). This phenomenon was observed for all the tests on alumina. A comparison of all volumetric profiles is shown in **Figure 4**. For each confining pressure, the intersection of the $\tau-\varepsilon_v$

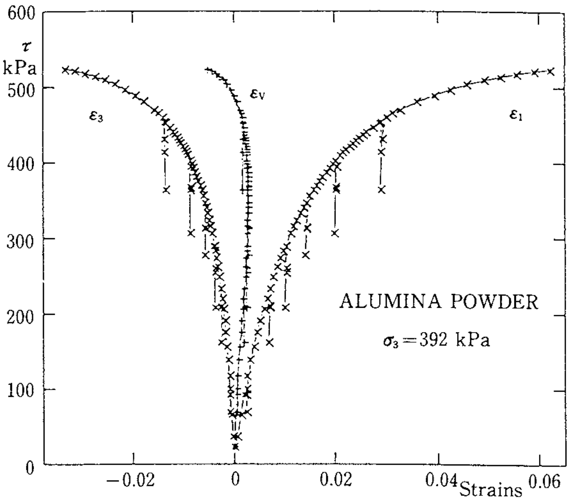

Fig. 3 Stress-strain curves for alumina in deviatoric tests. The stress decreases are due to relaxation and unloading.

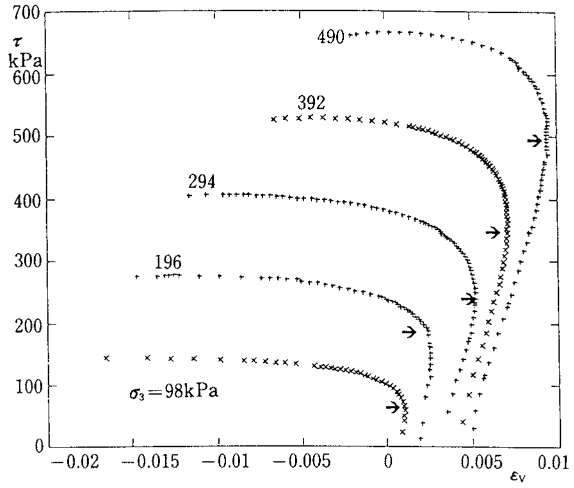

Fig. 4 Influence of confining pressure on the volumetric behavior. Arrows show the passage from compressibility to dilatancy.

curve with the horizontal axis represents the volumetric strain reached at the end of the hydrostatic part of the test. It is clearly seen that the stress value for which the slope of the $\tau-\varepsilon_v$ curve changes sign depends on the confining pressure. These critical points can be used to define in the $\sigma\tau$-plane the boundary between the compressible and dilatant domains (Cristescu [4,5]). For alumina this boundary can be expressed as $X(\sigma, \tau)=0$, where

$$X(\sigma, \tau)=0.555\sigma-\tau \tag{7}$$

Stress-states for which $X>0$ will produce compressibility, while stress-states for which $X<0$ produce dilatancy. Eq. (7) approximates this boundary for the range of pressures considered in our tests. For higher pressures this boundary may be nonlinear. The exact determination of the compressibility/dilatancy boundary is of great importance for industrial applications. For a given confining pressure, it provides the exact amount of axial stress to be applied in order to get maximal compaction.

2.3 Relaxation and rate-effect experiments

For each confining pressure relaxation tests have also been performed. The results obtained in such a test are shown in **Figure 5**. After a preloading up to $\tau=187.6$ kPa, the relative movement of the endfaces of the specimens is suddenly stopped ($\dot{\varepsilon}_1=0$). Then, the variation of the axial stress under constant deformation and constant lateral pressure is recorded. The axial stress decreases quite fast. After 15 minutes the relaxation practically ceases. The stress reduction is about 18% of the stress before relaxation. Afterwards loading is further performed. This cycle (loading-relaxation-reloading) is repeated eight times.

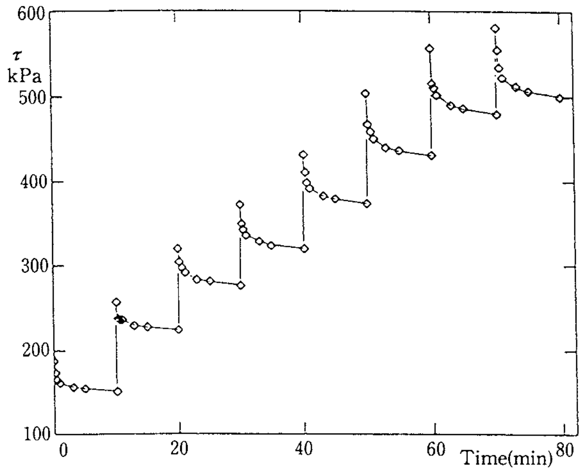

Fig. 5 Stress relaxation in triaxial tests under constant axial strain.

The fast relaxation observed for alumina is of great significance for industrial problems since it may influence both the compressibility and dilatancy characteristics of the powder. When pressing a powder in a die, for instance, one has to consider that the stresses may relax thus producing a change in the density distribution in the compact.

An experimental study of the influence of the strain rate on the mechanical properties of alumina has also been done. **Figure 6** shows the stress-strain curves obtained for two different axial strain rates (of $3.3\times10^{-4}s^{-1}$ and, $1.1\times10^{-5}s^{-1}$). Though the two strain rates are not significantly different, the influence of the strain rate on the mechanical response of the alumina powder is obvious. The $\tau-\varepsilon_1$ and $\tau-\varepsilon_2$ curves for the higher rate are above the ones obtained for the slower rate. Also, the curves $\tau-\varepsilon_v$

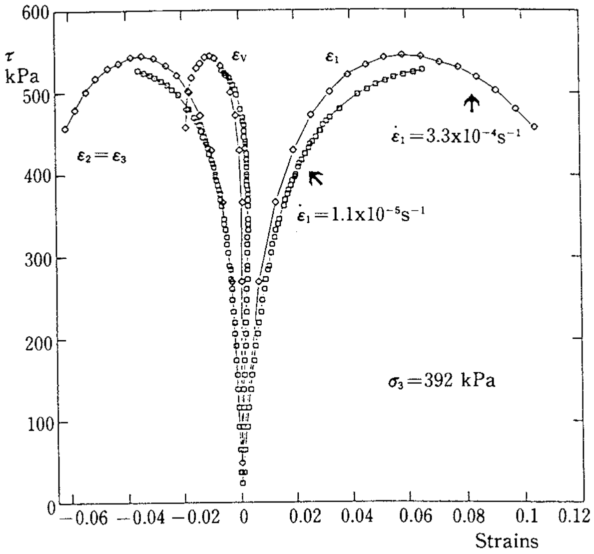

Fig. 6 Influence of the strain rate on the mechanical response of alumina in triaxial compression tests.

show that slower rates produce more compressibility and more dilatancy. This aspect is characteristic for powders and may also be important for industrial applications.

From the experimental results presented, we can conclude that the material exhibits irreversible time-dependent properties. Thus, in modelling the material behavior an elastic/ viscoplastic approach is adopted. The elastic/viscoplastic constitutive equation which will be presented in the next section, is applicable to general 3-D stress conditions and can describe the loading-history effects. The parameters involved can be obtained easily from the results of a series of conventional drained triaxial compression tests. Compared to other available theories, this model has an improved capability to describe several major aspects of the mechanical behavior of powders including the shear-dilatancy effects, stress-path effects, time-dependent effects.

3. Development of elastic/viscoplastic model for alumina powder

The development of the elastic/viscoplastic constitutive equation, applicable to powders under general 3-D stress conditions is based on the concepts of the viscoplasticity theory. In order to formulate an elastic/viscoplastic model three basic ingredients are required:

1) Yield function;
2) Flow rule;
3) Hardening rule.

The yield surface does not constitute a limit on possible stress states. The viscous effects are related to the stress exceeding the current yield limit. The distance between this stress-state and the current yield surface is called overstress. The concept of overstress is due to Ludwik [10].

The flow rule relates the viscoplastic strain rates to the stresses. The current yield surface is not fixed but its position depends on the amount of hardening experienced by the material. Also, a short-term failure surface defining the boundary of the constitutive domain, is to be defined.

In the model the irreversible stress work per unit of volume W is used as hardening parameter:

$$W(T)=\int_0^T \boldsymbol{\sigma}(t):\dot{\boldsymbol{\varepsilon}}^I(t)\,dt \qquad (8)$$

where $\dot{\boldsymbol{\varepsilon}}^I$ represents the irreversible strain rate and $\boldsymbol{\sigma}$ the stress tensor. W captures yielding in terms of shear strains as well as volumetric strains. It can be decomposed in two terms:

$$W(T)=\int_0^T \sigma(t)\,\dot{\varepsilon}_v{}^I(t)\,dt+\int_0^T \boldsymbol{\sigma}'(t):\dot{\boldsymbol{\varepsilon}}'^I(t)\,dt \qquad (9)$$

In Eq. (9) "prime" means deviator and the ":" denotes the tensorial product. The second right-hand side term is always positive and represents the energy related to the change in shape. The first right-hand side term is the energy related to volume change. It increases in the compressibility domain and decreases in the dilatancy one. Thus the irreversible volumetric work can be thought as a damage indicator.

The general form of the elastic/viscoplastic constitutive equation proposed is

$$\dot{\boldsymbol{\varepsilon}}=\frac{\dot{\boldsymbol{\sigma}}}{2G}+\left[\frac{1}{3K}-\frac{1}{2G}\right]\dot{\sigma}\mathbf{1}+k\left\langle 1-\frac{W(t)}{H(\sigma)}\right\rangle \boldsymbol{N}(\boldsymbol{\sigma}) \qquad (10)$$

(see Cristescu [4, 5, 6] and Cazacu [2]). In Equation (10) $\dot{\boldsymbol{\varepsilon}}$ is the rate of total strain, G and K are elastic moduli, k is a viscosity parameter while the symbol $< >$, known as Macaulay bracket, is used to denote the positive part of a function (i.e. $<A>=(1/2)(A+|A|)$). $H(\boldsymbol{\sigma})$ is the yield function, whereas $\boldsymbol{N}(\boldsymbol{\sigma})$ is a tensor valuated function which defines the orientation of the viscoplastic strain rates.

Let us observe that in contrast to the classical viscoplasticity models no assumption concerning the existence of a viscoplastic potential is done.

There are two main topics to be addressed: the determination of the yield function $H(\boldsymbol{\sigma})$ and that of the viscoplastic strain rate orientation tensor $N(\boldsymbol{\sigma})$.

3.1 Determination of the yield function $H(\boldsymbol{\sigma})$

As the material is isotropic the yield function $H(\boldsymbol{\sigma})$ depends on stress invariants only. For sake of simplicity, we assume that $H(\boldsymbol{\sigma})$ depends on the mean stress

$$\sigma=\frac{1}{3}(tr\boldsymbol{\sigma}) \qquad (11)$$

and on the octahedral shear stress τ, only

$$\tau=\sqrt{\frac{1}{3}\boldsymbol{\sigma}':\boldsymbol{\sigma}'} \qquad (12)$$

The yield function $H(\boldsymbol{\sigma})$ can be determined from data obtained in drained triaxial compression tests. Since in such tests, the first stage is hydrostatic and the second one is deviatoric, we assume that $H(\boldsymbol{\sigma})$ is the sum of two terms:

$$H(\boldsymbol{\sigma})=H_h(\sigma)+H_d(\sigma,\ \tau) \qquad (13)$$

such that $H_d(\sigma,0)\equiv 0$. Thus, for hydrostatic conditions the yield function reduces to H_h.

The procedure to determine H_h is the following: first compute the irreversible stress work in a hydrostatic creep test (as the one described in the section §2.1). Since the stresses are equal in all directions the irreversible stress work reduces to:

$$W(T)=\int_0^T \sigma(t)\,\dot{\varepsilon}_v^I(t)\,dt \tag{14}$$

where $\dot{\varepsilon}_v^I$ is the irreversible volumetric rate of deformation, and σ — the mean stress — is equal to the applied pressure. Next, plot the obtained values of $W(T)$ at creep-stabilization as a function of σ.

The irreversible stress work increases monotonically as the pressure increases. A second order polynomial matches well the data for alumina. Thus:

$$H_h(\sigma)=a_h\left(\frac{\sigma}{p_a}\right)^2+b_h\left(\frac{\sigma}{p_a}\right) \tag{15}$$

where $a_h=5.833\times10^{-6}$ and $b_h=1\times10^{-6}$.

Further, $H_d(\sigma,\ \tau)$ can be determined from the deviatoric part of the compression tests. The irreversible stress work is computed using the formula

$$W_d(T)=\int_{T_H}^{T}\left(\frac{3}{\sqrt{2}}\tau\right)\dot{\varepsilon}_1^I(t)\,dt+\int_{T_H}^{T}\sigma_3\dot{\varepsilon}_v^I dt \tag{16}$$

where T_H represents the beginning of the deviatoric part of the test, $\dot{\varepsilon}_1^I$ the axial irreversible rate of deformation.

Figure 7 shows the data for irreversible stress work obtained from 3 triaxial compression tests on alumina with confining pressures of 294, 392 and 490 kPa, respectively. A possible function which approximates accurately the irreversible work contours is

$$H_d(\sigma,\ \tau)=A\left(\frac{\tau}{p_a}\right)^9+B\left(\frac{\tau}{p_a}\right)^2 \tag{17}$$

It was found that A depends on the confining pressure and can be expressed as:

$$A(\sigma_3)=a_1\left(\frac{\sigma_3}{p_a}+a_2\right)^{-m} \tag{18}$$

where $a_1=0.27$, $a_2=37$ and $m=8.5$. B can be considered to be constant, i.e., $B=4.6\times10^{-5}$. Since $\sigma_3=\sigma-\tau/\sqrt{2}$ it follows that the expression of the yield function in terms of invariants is:

$$H(\sigma,\ \tau)=a_h\left(\frac{\sigma}{p_a}\right)^2+b_h\frac{\sigma}{p_a}$$
$$+a_1\left(\frac{\sigma-\frac{\tau}{\sqrt{2}}}{p_a}+a_2\right)^{-m}\left(\frac{\tau}{p_a}\right)^9+B\left(\frac{\tau}{p_a}\right)^2 \tag{19}$$

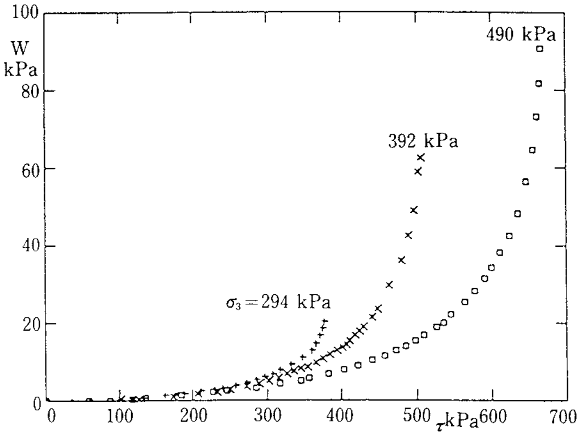

Fig. 7 Variation of the irreversible stress work as a function of τ for different confining pressures.

Figure 8 shows in a $\tau\sigma$-plane the shape of several surfaces $H=$constant. The short-term failure surface is represented as full line while the compressibility/dilatancy boundary as dotted line. The line $\partial H/\partial\sigma=0$ is shown as dotted line. In an associated model this last line would coincide with the compressibility/dilatancy boundary. For a saturated powder the domain between the compressibility/dilatancy boundary and the $\partial H/\partial\sigma=0$ line is a domain of possible loose of stability (Cristescu [3]). The domain between the compressibility/dilatancy boundary and the short-term failure surface is a dilatancy domain. All stress-states under the compressibility/dilatancy boundary produce compaction. The model reproduces accurately the shear-dilatancy effect. From this figure one can conclude that shear (i.e., τ) superposed on a hydrostatic pressure (i.e., σ) produces additional compaction. In fact for each value of σ the maximal compaction is obtained for the corresponding value of τ located on the compressibility/dilatancy boundary.

3.2 Determination of the viscoplastic strain rate orientation tensor $N(\sigma)$

In order to describe the orientation of the irreversible strain increments one has to determine

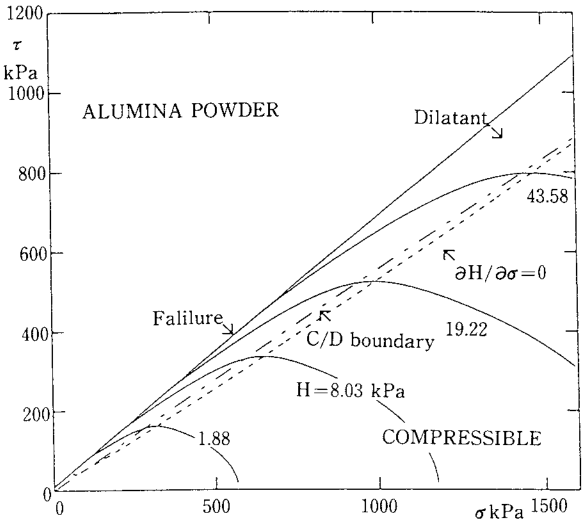

Fig. 8 Shape of several yield surfaces $H=$constant (solid lines), compressibility/dilatancy boundary (dash-dot line), stability boundary surface $\partial H/\partial\sigma=0$ (dotted line), and short-term failure surface (solid line).

the tensorial function $\boldsymbol{N}(\boldsymbol{\sigma})$. As the material is isotropic $\boldsymbol{N}$ must satisfy the invariance requirement

$$\boldsymbol{N}(Q\boldsymbol{\sigma}Q^T)=Q\boldsymbol{N}(\boldsymbol{\sigma})Q^T \tag{20}$$

for any orthogonal transformation Q. From classical theorems of representation of isotropic tensor functions follows that $\boldsymbol{N}$ can be represented as

$$\boldsymbol{N}(\boldsymbol{\sigma})=N_1\boldsymbol{I}+N_2\sigma+N_3\sigma^2 \tag{21}$$

where N_i are scalar valued functions of the stress invariants. In order to reduce the complexity of the problem we assume that $N_3\equiv 0$ and also we disregard the influence of the third stress invariant. Thus, we consider that $\boldsymbol{N}(\boldsymbol{\sigma})$ is of the form

$$\boldsymbol{N}(\boldsymbol{\sigma})=N_1\boldsymbol{I}+N_2\frac{\boldsymbol{\sigma}'}{\tau} \tag{21$'$}$$

where $\boldsymbol{\sigma}'$ is the stress deviator and $N_i=N_i(\sigma,\ \tau)$. Since

$$\dot{\varepsilon}^I=k\left\langle 1-\frac{W}{H(\boldsymbol{\sigma})}\right\rangle\left(N_1\boldsymbol{I}+N_2\frac{\sigma'}{\tau}\right) \tag{22}$$

it follows that

$$\dot{\varepsilon}_v{}^I=3k\left\langle 1-\frac{W}{H(\boldsymbol{\sigma})}\right\rangle N_1 \tag{23}$$

Afterwards, using Eq. (23), from the data obtained during the hydrostatic part of the test we determine $kN_1|_{\tau=0}$. We use the notation $kN_1|_{\tau=0}=\varphi(\sigma)$. A second order polynomial in σ seems to fit well the data. Thus

$$kN_1|_{\tau=0}=a_k\left(\frac{\sigma}{p_a}\right)^2+b_k\frac{\sigma}{p_a} \tag{24}$$

where $a_k=-8\times 10^{-11}$ and $b_k=1.641\times 10^{-6}$. Next, we must determine $N_1(\sigma,\ \tau)$ for $\tau\neq 0$. From Eq. (23) follows that this function must be positive in the compressibility domain and negative in the dilatancy one.

The simplest possible function satisfying these properties is

$$kN_1=\varphi(\sigma)+\frac{\tau}{p_a}sgnX(\sigma,\ \tau)\,\Psi(\sigma,\ \tau) \tag{25}$$

where $X(\sigma,\ \tau)$ is defined by Eq. (7). In Eq. (25) all the functions, except $\Psi(\sigma,\ \tau)$, have been already determined. By making use of Eq. (23), from Eq. (25) results

$$\Psi(\sigma,\ \tau)=\frac{\dfrac{\dot{\varepsilon}_v{}^I}{3\left\langle 1-\dfrac{W}{H(\sigma)}\right\rangle}-\varphi(\sigma)}{\dfrac{\tau}{p_a}sgnX(\sigma,\ \tau)}$$

where

$$sgnX(\sigma,\ \tau)=\begin{cases}1 & for\ X(\sigma,\ \tau)\geq 0\\ -1 & otherwise\end{cases} \tag{26}$$

Therefore, from data obtained in the deviatoric part of the triaxial compression tests and Eq. (25) one can determine $\Psi(\sigma,\ \tau)$ For alumina a possible expression of $\Psi(\sigma,\ \tau)$ can be

$$\Psi(\sigma,\ \tau)=z_c\left[\frac{\tau}{p_a}-y_a\left(\frac{\sigma-\frac{\tau}{\sqrt{2}}}{p_a}\right)-y_c\right]^5 \cdot\exp\left(z_b\frac{\sigma-\frac{\tau}{\sqrt{2}}}{p_a}\right) \tag{27}$$

where $y_a=0.842$, $y_c=-56.06, z_b=-0.01$ and $z_c=1.127\times 10^{-15}$.

From the flow rule Eq. (22) follows that

$$\begin{aligned}\dot{\varepsilon}_1{}^I&=k\left\langle 1-\frac{W}{H(\sigma)}\right\rangle\left(N_1(\sigma,\ \tau)+\frac{N_2(\sigma,\ \tau)}{\tau}\sigma_1'\right)\\ \dot{\varepsilon}_3{}^I&=k\left\langle 1-\frac{W}{H(\sigma)}\right\rangle\left(N_1(\sigma,\ \tau)+\frac{N_2(\sigma,\ \tau)}{\tau}\sigma_3'\right)\end{aligned} \tag{28}$$

By subtracting Eq. $(28)_2$ from Eq. $(28)_1$ we obtain

$$kN_2(\sigma,\ \tau)=\frac{3}{\sqrt{2}}\frac{\dot{\varepsilon}_1{}^I-\dot{\varepsilon}_3{}^I}{\left\langle 1-\dfrac{W}{H(\sigma)}\right\rangle} \tag{29}$$

From the deviatoric part of the same triaxial tests performed at $\sigma_3=294$, 392 and 490 kPa, in conjunction with Eq. (29) we found that kN_2 can be approximated by

$$kN_2=m_1\left(\frac{\tau}{p_a}\right)^{14}\exp\left[m_2\left(\frac{\sigma-\frac{\tau}{\sqrt{2}}}{p_a}\right)\right]+n_1\left(\frac{\tau}{p_a}\right)^2\exp\left[n_2\left(\frac{\sigma-\frac{\tau}{\sqrt{2}}}{p_a}\right)\right]+r \tag{30}$$

where $m_1=2.38\times 10^{-33}$, $m_2=-0.038$, $n_1=4\times 10^{-7}$, $n_2=-0.005$ and $r=8\times 10^{-4}$.

4. Comparison with the experimental results

The accuracy of the elastic/viscoplastic model described previously was evaluated by comparing predicted and measured strains in drained compression tests at different confining pressures.

Figure 9 shows a comparison between model prediction and experimental results for $\sigma_3=294$ kPa. Let us note that this test has not been used for the identification of the constitutive parameters. The axial and radial strains are predicted fairly accurately, both in magnitude and variation. The calcu-

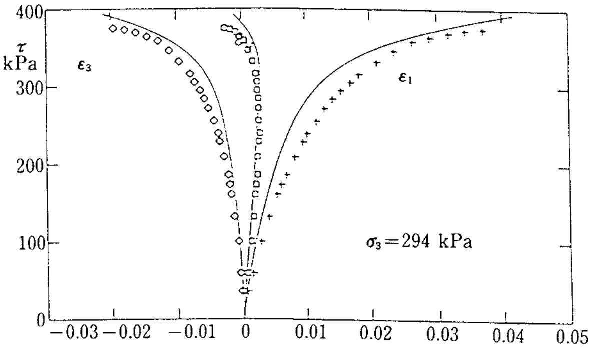

Fig. 9 Stress-strain curves for alumina in a triaxial test at $\sigma_3=294$ kPa confining pressure.

lated volume changes are slightly more compressive than those observed. However, it may be seen that the theory predicts correctly the variation of the volumetric strains throughout the test.

5. Conclusions and final remarks

The model presented was developed in the framework of non-associated viscoplasticity theory in order to simulate the nonlinear, stress-dependent and time-dependent behavior of powders. The form of the yield criterion used in the theory was chosen as simple as possible in order to arrive at an uncomplicated stress-strain relationship.

A significant feature of the proposed model is that it reproduces both the compressive and dilatant behavior of powders. No assumptions have been made concerning the existence of a viscoplastic potential. The sensitivity with which the flow rule reflects the actual powder behavior is best assessed by comparing measured and calculated volumetric compressibility and dilatancy. The good agreement between observed and predicted rates of compressibility and of dilatation indicates the accuracy of the flow rule employed. That is shown in **Figure 9**.

Unloading and reloading is modeled in the theory as being elastic, the magnitude of both E and K depending on the mean stress only. Although the theory developed is applicable to general 3-D stress conditions, all the parameters involved can be derived entirely from the results of 4 conventional triaxial drained compression tests.

The theory has been shown to be able to model several important properties of powders with a degree of accuracy which appears to make it useful in finite element analyses of stresses and density distribution in a pressed compact. The application of the model to the analysis of compaction by creep for a cylindrical part can be found in [7].

Acknowledgments

The authors would like to acknowledge the financial support of the Engineering Research Center (ERC) for Particle Science and Technology at the University of Florida, the National Science Foundation (NSF) grant # EEC-94-02989, and the Industrial Partners of the ERC.

Nomenclature

C	: Cohesion	[Pa]
E	: Young's Modulus	[kPa]
E^{∞}	: limit value of E	[kPa]
G	: shear modulus	[kPa]
$H(\sigma)$	: yield function	[kPa]
K	: bulk modulus	[kPa]
K^{∞}	: limit value of K	[kPa]
$N(\sigma)$	: viscoplastic strain rate orientation	[-]
p, σ	: mean stress	[kPa]
p_a	: reference pressure	[1kPa]
q	: equivalent stress	[kPa]
v	: current volume	[m^3]
v_0	: initial volume	[m^3]
$W(t)$	: irreversible stress work per unit volume	[Pa]
$X(\sigma,\tau)$	: compressibility/dilatancy boundary function	[Pa]
ε'	: strain deviator tensor	[-]
ε_q	: equivalent strain	[-]
ε_v	: volumetric strain	[-]
σ'	: stress deviator tensor	[Pa]
σ_n	: normal stress on the failure plane	[Pa]
σ_1	: axial stress	[Pa]
σ_3	: confining pressure	[Pa]
τ	: octahedral shear stress	[Pa]
τ_f	: shear stress on the failure plane	[Pa]
Φ	: angle of internal friction	[-]

References

1) Burland, I.B., Schofield A.N. and C.P. Wroth: On the generalized stress-strain behavior of wet clay. In: Heyman, J. and Leckie, F.A. (Eds). Engineering Plasticity. (1968) Cambridge University Press, Cambridge, U.K.

2) Cazacu, O.: Elastic/viscoplastic Constitutive Equation for Anisotropic Rocks: Ph.D. Dissertation, University of Lille 1, (1995) (in French).

3) Cristescu, N.D.: Int. J. Plasticity, 7. 41 (1991).

4) Cristescu, N.D.: "Rock Rheology." Kluwer Academic Publ., Dordrecht (1989).

5) Cristescu, N.D.: Viscoplasticity of Geomaterials. In: "Visco-plastic Behaviour of Geo-materials", N.D. Cristescu and G. Gioda. eds, Springer Verlag, Wien-New York, (1994) pp. 103-207.

6) Cristescu, N.D.: Int. J. Plasticity, 10. 103 (1994).

7) Cristescu, N.D. and Cazacu, O.: "Time effects on uniaxial compaction of powders", Proc. VIth Intern. Symp.on Plasticity and Its Current Applications, NEAT PRESS, FULTON, MARYLAND, (1997) pp. 303-304.

8) Hehenberger, M., Samuelson, S., Alm, O., Nilsson, L. and T. Olofsson: Experimental and theoretical studies of powder compaction. In: IUTAM Conference on Deformation of Granular Materials. (1982), pp. 381-390.

9) Kamath, S., Puri, V.M. and H.B. Manbeck: Powder Technology, 81. 293 (1994).

10) Ludwik, P.: "Elemente der technologischen Mechanik." Springer Verlag, Berlin (1909).
11) Puri, V.M., Tripodi, M.A., Manbeck, H.B. and G.L. Messing. KONA, Powder and Particle. 13. 135 (1995).
12) Roscoe, K.H., Schofield, A.N. and C.P. Wroth: Geotechnique, 9. (1968).
13) Schofield, A.N. and C.P. Wroth: "Critical State Soil Mechanics." McGraw Hill, London (1968).
14) Shinohara, K.: "Rheological properties of particulate solids." In: "Handbook of Powder Science and Technology" (Eds. M.E. Fayed, and L. Otten.) Van Nostrand Reinhold Comp., New York (1984). pp. 129-169.
15) Tripodi, M.A., Puri, V.M., Manbeck, H.B. and G.L. Messing. Powder Technol. 80. 35. (1994).

Author's short biography

Oana Cazacu

Oana Cazacu received her Msc degree in Mechanics from the University of Bucharest, Romania in 1990, and her Ph.D. in Civil Engineering from University of Lille I, France in 1995. Her current research activities focus on modelling the rheological behavior of powders and concentrated suspensions. She is a member of the Dispersion, Agglomeration and Consolidation thrust group at the Engineering Research Center for Particle Science and Technology at the University of Florida.

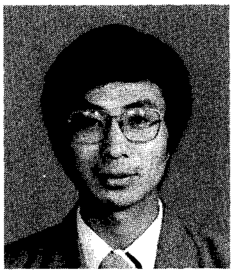

Jishan Jin

Jishan Jin received his B.S. degree in Mechanics from Zhejiang University, China in 1982, his M.S. degree from Peking University in 1987, and his Ph.D. from University of Florida in 1996. His reserch activities include experimental testing and numerical modelling of particulate materials.

Professor Nicolae D. Cristescu

Dr. Cristescu is a Graduate Research Professor in the Department of Aerospace Engineering, Mechanics & Engineering Science at the University of Florida and member of two Engineering Research Center's thrust groups: Dispersion, Agglomeration and Consolidation, and Transport and Handling. He received his undergraduate training as well as his doctoral degree from University of Bucharest, Romania. From 1951 to 1992 he held a succession of academic positions at the University of Bucharest (full professor since 1966, department chairman (1982-1990)). From 1990 to 1992 he served as President of the University of Bucharest. In 1992 he joined the University of Florida. His research interests include dynamic plasticity, theory of metal working, mechanics of composites, viscoplasticity of geomaterials, powder mechanics. He is the author and co-author of more than 150 papers, 16 books and textbooks. His books "Dynamic Plasticity", "Viscoplasticity" (with I. Suliciu), and "Rock Rheology" have been adopted worldwide. He also serves as Senior Editor of the International Journal of Plasticity, and in the Editorial Boards of International Journal of Mechanical Science, Mechanics Research Communications, and Mechanics of Cohesive-Frictional Materials. Most recently, he was the recipient of ASME 1995 Nadai award. He is a Fellow of Romanian Academy of Sciences.

Research

A Preliminary Model for Mechanofusion Powder Processing†

J. Chen, H. Herman
Dept. of Materials Science and Engineering
*State University of New York**
C. C. Huang
Hosokawa Micron Powder Systems
*Summit***

Abstract

Mechanofusion (MF) is a unique high energy powder processing technique, in which powder characteristics can be significantly modified. The effects of MF on powdered materials depend on MF operating conditions and the starting powders. This paper proposes a preliminary MF modeling concept to develop quantitative relationships among MF variables and their effects. In the modeling, an inner piece "action zone" is defined. It is believed that most MF effects are generated when the particles pass through the action zone. From the model, the pressure imposed on the powders by MF can be described via the geometry of the device, operation speed and material properties. In addition, some basic particle kinematics variables can be estimated. The results derived from the modeling are compared to reported experimental results.

1. Introduction

Mechanofusion (MF) is an advanced technology for processing powdered materials, allowing raw materials to be mechanically intermingled with sufficient energy to create a powder with new characteristics. Mechanofusion is similar to mechanical alloying, in that both utilize mechanical forces to process powdered materials. A fundamental difference is that the MF process in essence does not need ball medium, while which is an indispensable working component for mechanical alloying. However, when the medium is added, MF may be considered as a modification of mechanical alloying. In MF processing, the powders are intensively mixed and subjected to compression, attrition, frictional shearing and rolling. Therefore, mechanical-thermal energies are generated, resulting in a variety of distinct effects on powdered materials.

Many phenomenological observations of MF effects on powders have been published (1-16). However, the theoretical modeling of MF has lagged behind the experimental studies, although some schematic models for the MF effects on powders have been reported (4, 5, 11, 16). This paper attempts to establish a basic model so that the mechanism of MF can be better understood. In the following model, mathematical relationships among the device design, the operational variables and the MF effects will be proposed. The equations derived from the model will then be applied to explain some experimental results.

Most of the modeling here is a first attempt in MF research. The attempts are both simple and fundamental. More detailed investigations of the modeling will be necessary in the future.

2. Description of the Model

The modeling of particle movement is gradually developed from pure hypothetical conditions to more realistic operating situations, based on principles of mechanics, fluid mechanics and thermodynamics, as well as the geometry of the machine design. Then, a few mechanical variables are correlated, and their values are estimated. The results obtained here will provide a basis for further development.

2.1 Particles Motion without the Inner Piece

As described in Reference (5), during operation the chamber that contains the powder is spinning, while the inner piece is stationary. The powder therefore is squeezed through the gap between the

---

* Stony Brook, NY 11794-2275, USA
**NJ 07901, USA
† Received July, 1996

inner piece and the chamber wall. However, understanding the particle motion in a chamber without the inner piece can be considered as a starting point. As a first step, we assume that, if the inner piece is not installed or when the particles are moving in the outside region of the inner piece "action zone", which will be defined later, the powder rotates together with the chamber at the same angular speed. Therefore, at a given chamber rotation speed, the particles are moving in a circle with constant speed, i.e., uniform circular motion. It will be convenient to deal with such motion in cylindrical coordinates (r, θ, z). Provided that the powder movement is independent of the z direction, the particle motion can be essentially described by two dimensional polar coordinates. Under the above assumptions, when the chamber rotates at an angular speed ω, a particle at a distance r from the axis through the origin O has a linear speed

$$v = \omega r \tag{1}$$

and a radial acceleration

$$a_r = \frac{v^2}{r} = \omega^2 r \tag{2}$$

By choosing the rotational chamber as a reference frame, a particle at a distance r from the axis is subjected to a centrifugal force

$$f_c = m\omega^2 r \tag{3}$$

where m is the mass of the particle.

If the powder in the chamber is also considered as a fluid, the state of the powder can be derived. Take a small volume element within the powder at a distance r from the axis with a thickness dr and an area A, as indicated in **Fig. 1**. The mass of this element is ρ Adr, where ρ is the powder density, the powder considered as a continuum. The radial forces exerted on the element are the centrifugal force $\rho A\omega^2 r dr$, and those resulting from the pressures exerted on the element by the surrounding powder, PA and (P+dp)A.

Hence, for radial equilibrium

$$PA + \rho A\omega^2 r dr = (P + dp)A$$

rearrangement and integration of the equation gives

$$\int_{P_c}^{P} dp = \omega^2 \rho \int_0^r r dr$$

or

$$P = P_c + \frac{1}{2}\omega^2 \rho r^2 \tag{4}$$

where P_c is the pressure at $r=0$.

Therefore, the pressure imposed on the powder is proportional to the square of angular speed of the chamber.

Also, from fundamental physics and **Fig. 2**, we can have the slope of the powder surface, $tg\theta$, at a distance r,

$$tg\theta = \frac{\omega^2}{r} \tag{5}$$

and the shape of the powder surface,

$$Z = \frac{\omega^2}{2g} r^2 \tag{6}$$

i.e., the surface of the powder is a paraboloid of revolution.

The equations derived above are for some basic conditions of the powder in a chamber without the inner piece or in the outside region of the inner piece "action zone" during rotation. They can be applied to understanding some experimental phenomena, which will be presented later.

2.2 Inner Piece Action Zone

Now take into account the effects of the inner

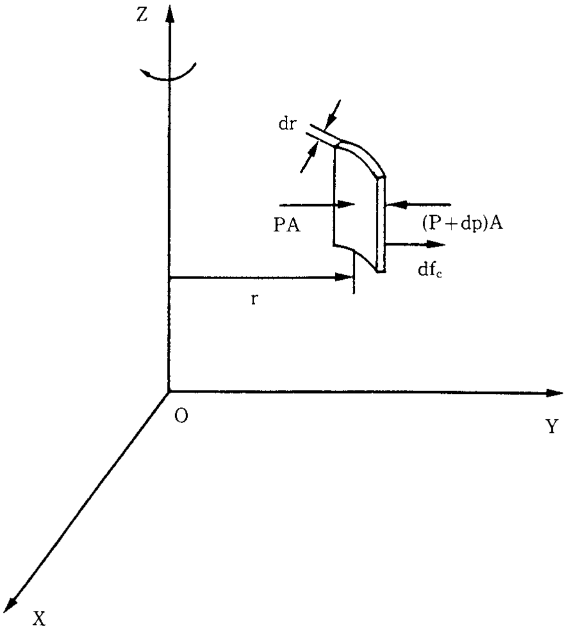

Fig. 1 Small volume element within the powder.

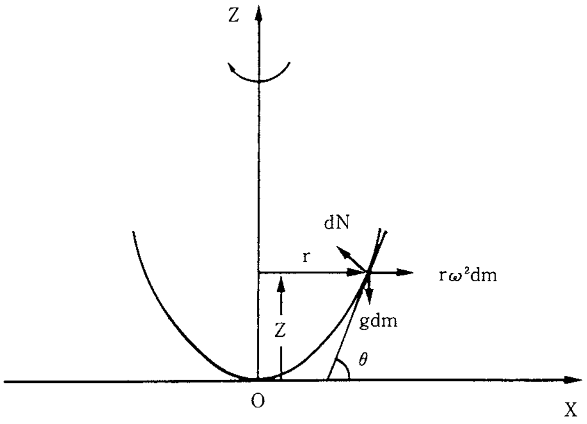

Fig. 2 Surface of the powder fluid within the chamber is a paraboloid of revolution during MF

piece on the powder. The inner piece action zone mentioned above is defined as the first half region between the inner piece and the chamber wall, whose cross-section is marked by ABCD* in **Fig. 3**, as we look downward on it from above, along the z-axis. It is believed that most MF effects are generated while the particles pass through this region.

For the powder within the inner piece action zone, ABCD, three major interactions may occur: inner piece-particles, particles-particles, particles-chamber wall. Here, only the small volume of the powders, the area labeled by AA′B′B in **Fig. 3**, is selected for analysis, and the particles contained inside the small volume are treated as an assembly. The system interactions with the inner piece and the chamber wall will be investigated. The relationships among the particles within the assembly are more complex and need to be further examined.

When the assembly enters the action zone, those particles immediately touching the inner piece or the powder within the small volume as a whole are subjected to the inner piece tangential force f_t. The average tangential force is related to the velocity of the particles by

$$f_t=\frac{\Delta M\upsilon}{t}+f_{tw} \tag{7}$$

where M is the mass of the assembly, υ represents the particles velocity, t is the time required for the particles to pass through the zone (or move from line AB to CD in **Fig. 3**), $\Delta M\upsilon$ is the change momentum of the particles during the time t and f_{tw} is the tangential force of the chamber wall acting on the particles.

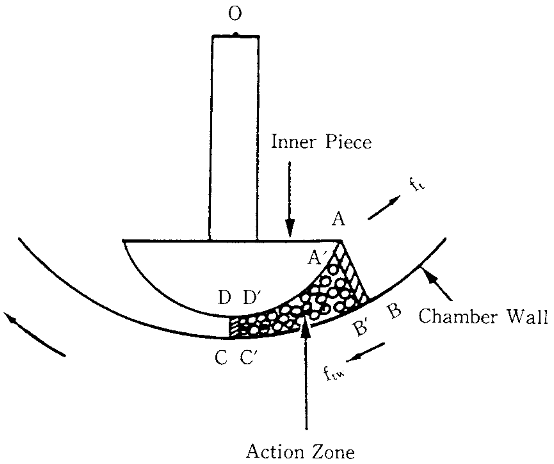

Fig. 3 The inner piece action zone ABCD.

If the powder is assumed to be a compressible fluid, and the particles are considered to have the same angular speed during their motion through the action zone (i.e., all powder in AA′B′B will move to CC′D′D after time t), we can introduce a compression ratio R, which is defined as:

$$R=\frac{V_{AA'B'B}}{V_{CC'D'D}} \tag{8}$$

or

$$R=\frac{AB}{CD}=\frac{AB}{D_g} \tag{8$'$}$$

where $V_{AA'B'B}$ is the volume of the powder in AA′B′B, and $V_{CC'D'D}$ is the volume of the same powder in CC′D′D. R is then determined by the geometry of the inner piece and the gap distance D_g, which is adjustable.

The Above hypotheses may apply only to some powders under certain conditions. In reality, the particles in AA′B′B may not move into CC′D′D concurrently. For a given powder, the higher chamber rotation speed, the actual compression ratio will be closer to that expressed in Eq. (8)′, since the powder with the higher speed has more momentum to push through the gap.

The volume change of the powder during moving through the action zone is due to a pressure imposed on the system. From thermodynamics, the relationship between the pressure (thus, forces) and the volume can be established through the compressibility of a system, which is defined as

$$\beta=-\frac{1}{V}\left(\frac{\partial V}{\partial P}\right)_T \tag{9}$$

β is the compressibility factor, or the fractional decrease in the volume of the system for unit increase of pressure acting on the system at constant temperature. The β depends on the material. V is the volume of the system, and P is the applied pressure. The negative sign is used in order to make β a positive number.

Thus, for an isothermal process (the temperature effect can be ignored here),

$$dP=-\frac{1}{\beta}\left(\frac{dV}{V}\right) \tag{10}$$

and integrating Eq. (10) with assuming that β is constant** gives

$$P=P_0+\frac{1}{\beta}\ln\frac{V_0}{V} \tag{11}$$

or

$$P=P_0+\frac{1}{\beta}\ln\frac{AB}{D_g}=P_0+\frac{1}{\beta}\ln R \tag{12}$$

Where P_0 is the initial pressure, and V_0 is the initial volume.

---

*We assume that the particle movement is independent of z direction, so in the following paragraphs the three dimensional issues are described in the terms of two dimensions.

**Note: β for the assembly may vary during the system passing through the action zone.

Equation (12) indicates that pressure (compression or forces) acting on particles increases with reducing gap distance, D_g, or with increasing compression ratio, R.

The pressure can be converted to radial force, f_r, and for particles sliding over the inner piece, f_r is connected to tangential force, f_t, by

$$f_t = \mu f_r \tag{13}$$

where μ is the friction coefficient.

The tangential forces are linked to shear and attrition. These forces are most responsible for grinding and friction. Also, a pair of tangential forces, such as f_t and f_{tw}, can exert a torque on the particles. It is this torque that causes the rolling of the particles and provides the fundamental mechanism for particle shape spheroidization. The radial forces are more related to compression and yield deformation and fragmentation or coalescence of the materials.

2.3 Particle Kinematics in the Inner Piece Action Zone.

A primary analysis of the kinematics of particles will offer valuable information about particle motion during MF. The maximum relative velocity ν_{max} of a particle with respect to the inner piece (i.e., slide velocity or impact velocity) can be calculated from the particle linear speed in Eq. (1), i.e.,

$$\nu_{max} = \omega Rs \tag{14}$$

where ω is the particle angular speed, and Rs is the radius of the chamber wall. For a rotation speed ω of 2500 rpm or 262 rad/s and the MF unit used in this research with radius Rs of 0.075 m, the maximum relative velocity ν_{max} can be as high as 20 m/s.

From Eq. (14), the minimum time required for a particle to travel through the action zone (i.e., the duration of each pass) can be estimated by the following formula,

$$t_{min} = \frac{BC}{\nu_{max}} \tag{15}$$

For a $\nu_{max} \approx 20$ m/s and BC ≈ 0.025 m, the t_{min} is about 1.25×10^{-3}s.

At the other extreme, if we hypothesize that a particle only rolls through the inner piece action zone without sliding, then the maximum turns of rolling, Π_{max}, for the particle during passing through the action zone, are approximated by

$$\Pi_{max} = \frac{AD}{\pi d} \tag{16}$$

where AD is the length of the arc in **Fig. 3**, and d is the particle diameter.

For a particle size of 30 micrometers or 3×10^{-5}m and an arc AD of 0.025 m, theoretically the particle has to make over 260 turns to pass through the action zone. However, a more realistic condition of particle movement in the action zone should be a combination of rolling as well as sliding with respect to one-another.

We can now apply the above results to explain the phenomena observed in the experiments.

3. The Model and Reported Data

The relationships of rotation speed-loading-force were reported by Yokoyama et al. (2) using a chamber diameter of 35 centimeters to process talc powder with an average size of 44 micrometers. Their results are presented graphically in **Figs. 4**, **5** and **6**. Here, efforts are made to interpret these figures based on the fundamental model proposed above.

3.1 Relationship of Loading and Force at a Given Speed

In **Fig. 4**, when a small charge is processed at a given low speed, the tangential force F_t exerted on the inner piece is small. As the load increases, the F_t increases accordingly. This can be explained roughly as follows. When the chamber rotates, there is a centrifugal force imposed on the powder, Eq. (3), in addition to gravity and forces among the particles. As a result, the surface of the powder within the chamber will appear as a parabolic shape, as indicated by Eq. (6), i.e., the powdered material rises near the chamber wall and descends as it approaches the center. At a given speed, the shape of the surface is fixed. For a small quantity of

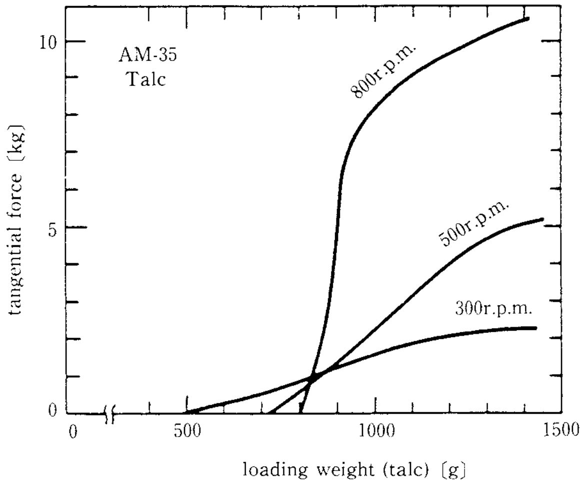

Fig. 4 Variation of the tangential force acting on the inner piece tip with loading weight and rotation speed (2).

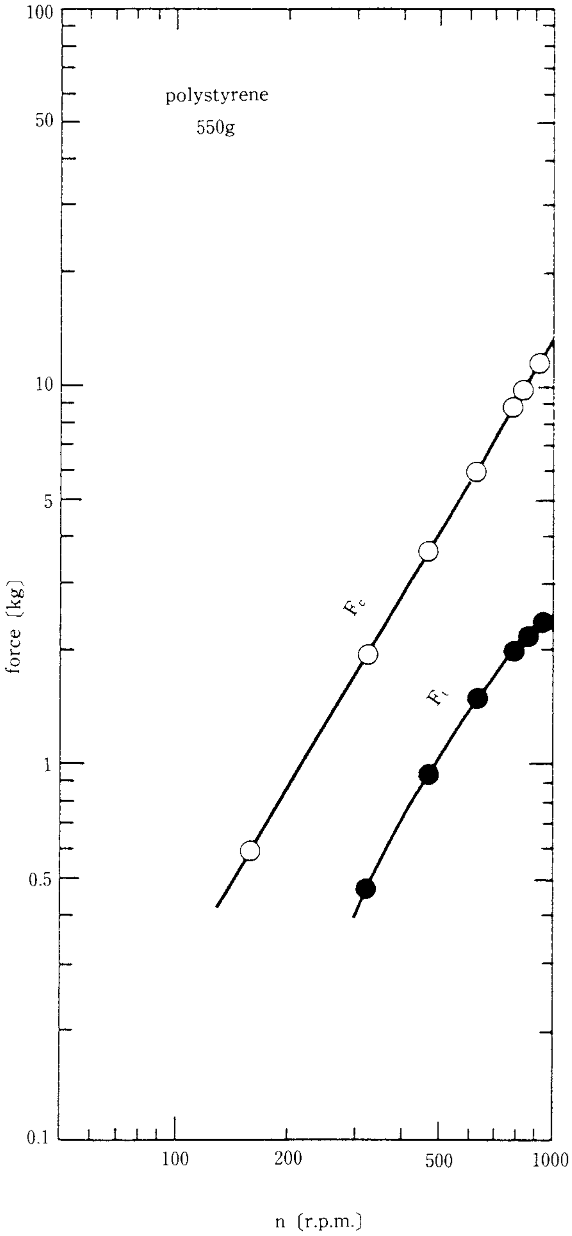

Fig. 5 Variation of the tangential force acting on the inner piece tip with rotation speed and materials (2).

powder, the inner piece is subjected to only minor action from the particles. Adding the charge increases the entire surface level, as shown in **Fig. 7**, and more particles will interact with the inner piece, yielding a larger F_t. Therefore, the curves shift upward with increasing loading at a given speed. This is more obviously shown in the first part of each curve or at lower charges in **Fig. 4**.

3.2 Relationship of Loading and Force at Varying Speeds

In **Fig. 4**, the starting point of each curve is observed to depend on the rotation speed. This may be due to the following. When the chamber rotation speed is increased, the shape of the powder surface within the chamber will change correspondingly. According to Eq. (5)

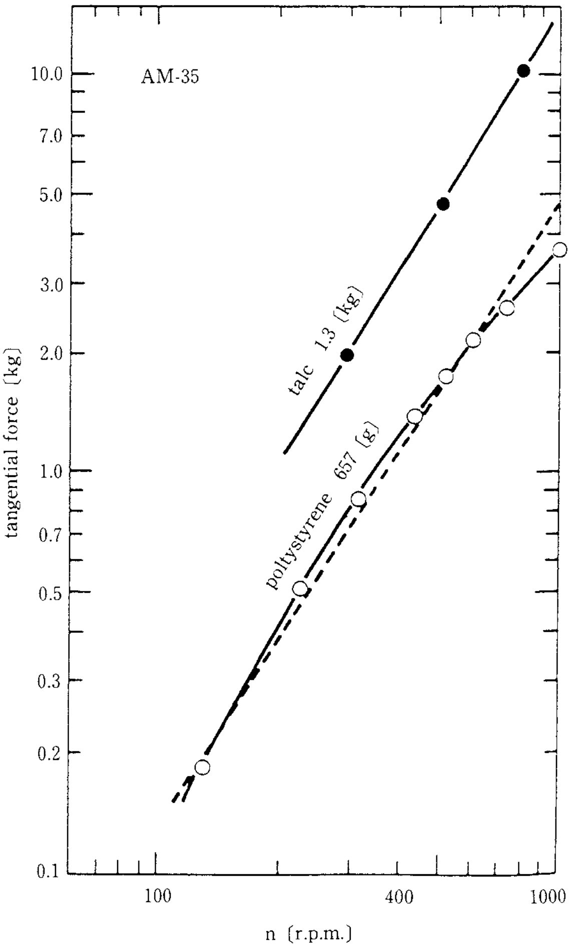

Fig. 6 Variation of the radial and tangential forces acting on the inner piece tip with rotation speed (2).

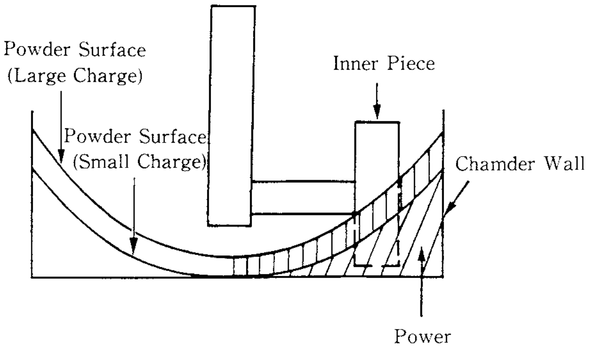

Fig. 7 Shape of powder surface within the chamber is fixed at a given rotation speed. Adding the charge increases the entire surface level.

$$\mathrm{tg}\theta=\frac{\omega^2}{g}r \qquad (5)$$

the slope or tgθ for a point on the surface at a distance r from the axis increases with angular speed, ω. For a limited quantity of charge, the powder will be pushed up and outward to the chamber wall, as shown in **Fig.** 8, so that its surface can satisfy the Eq. (5) condition.

Furthermore, from Eq. (4)

$$P = P_c + \frac{1}{2}\omega^2 \rho r^2 \qquad (4)$$

the pressure exerted on the particles also increases, resulting in a higher density of the powder. This means that for a given charge, the higher the rotation speed, the smaller the volume. Those two factors decrease the interaction area between the powder and the inner piece, especially for the relatively small amount of charge, since the inner piece is located at some distance away from the chamber wall, as illustrated schematically in **Fig.** 8. Consequently, the higher the rotation speed, the smaller is F_t. The F_t may even be reduced to zero. Thus, the starting point of the curves is shifted with the rotation speeds. The following paragraphs will further clarify this issue.

A phenomenon similar to pinning in ball milling will take place under the following two conditions. If the chamber rotation speed exceeds a critical value, which will be discussed in the next paragraph, the centrifugal force can "pin" the particles against the chamber wall, and if the volume of the charge V is also smaller than a critical volume V_c, the powder will form as a thin layer on the surface of the chamber wall with a thickness less than the D_g. This layer can pass through the gap without interaction with the inner piece. The critical volume V_c is given below,

$$V_c = 2\pi h R s D_g \qquad (17)$$

where Rs is the radius of the chamber wall, h is the height of the chamber, D_g is the gap distance.

A particle will be pinned if its weight

$$W = mg \qquad (18)$$

is balanced by vertical frictional force f_v. Using Eq. (3) gives

$$f_v = \gamma f_r = \gamma m \omega^2 R s \qquad (19)$$

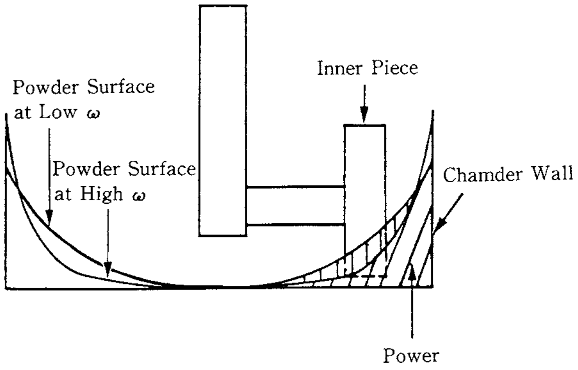

Fig. 8 Shape of the powder surface within the chamber varies with rotation speeds.

where m is the mass of the particle, g is the acceleration due to the gravity, γ is the coefficient of static friction, ω is the angular speed, can be expressed as $2\pi n$.

The rearrangement of Eq. (19) gives

$$n_c = \frac{1}{2\pi}\sqrt{\frac{g}{\gamma R s}} \qquad (20)$$

This value n_c is the critical speed in revolutions per second for pinning particles. The critical volume determined in Eq. (17) can also be considered as the minimum volume of powder required for the MF process, which is about 60 cm^3 for the unit used in this research.

Thus, when processing at 800 rpm, there is no force exerted on the inner piece until 800 g of talc is loaded, **Fig. 4**. Once the charge exceeds the critical volume expressed in Eq. (17), the powder has to "squeeze" through the gap, so the F_t increases steeply, approaching saturation.

3.3 Relationship of the Radical Force F_c and the Rotation Speed

Yokoyama et al (2) also reported that the radial force F_c acting on the inner piece varies with the rotation speed, **Fig. 5**. F_c displays a linear increase with the rotation speeds, n, in a log-log plot. This indicates that the relationship between F_c and n can be expressed approximately by

$$F_c = \lambda n^q \qquad (21)$$

where λ and q are experimental constants.

From the model of particle motion proposed in this study, when the powder first enters the action zone, or AA′B′B in **Fig. 3**, the initial pressure P_0 is given by Eq. (4), and is rewritten as,

$$P_0 = P_c + \frac{1}{2}(2\pi n)^2 \rho r^2 \qquad (22)$$

Hence, the pressure exerted on the inner piece in Eq. (11) becomes

$$P = P_0 + \frac{1}{\beta}\ln\frac{V_0}{V} = P_c + \frac{1}{2}(2\pi n)^2 \rho r^2 + \frac{1}{\beta}\ln\frac{V_0}{V} \qquad (23)$$

Equation (23) implies that the radical force Fc is a function of n^2. This result basically agrees with the linear relationship between the force and the rotation speed in the log-log plot shown in **Fig. 5**, i.e., the derived expression Eq. (23) is consistent with the empirical formula Eq. (21).

3.4 Relationship of Force and Material

It is no surprise that Ft also varies with the processed materials, such as polystyrene and talc investigated by Yokoyama et al. (2) and presented in **Fig. 6**. Because the compressibility factor β in

Eq. (23) depends on the material and powder characteristics, a soft material such as the polystyrene polymer will be expected to have a large β value, i. e., easier to be compressed as compared to talc. Therefore, as can be found in Eq. (23) and **Fig. 6**, force created in MF processing of the talc will be larger than that in MF processing of the polystyrene.

4. Conclusion

In this paper, through introducing a inner piece action zone, a primary MF model is established. Based on the model, the derived equations indicate that the pressure (force) acting on particles is proportional to the square of angular speed of the chamber, and increases with decrease in gap distance. These results are consistent with the reported data. The model also predicts that the forces imposed on powders vary with the processed materials, as has been observed by other researchers. Some basic particle mechanical variables can also be estimated from the model. For a rotation speed of 2500 rpm and the small MF unit (AM-15F) used in this research, which has a radius of 0.075 m, the maximum particle velocity can be as high as 20 m/s. Correspondingly, the time required for a particle to pass through the action zone is about 1.25×10^{-3}s. For a particle size of 30 micrometers, the particle may need to make over 260 turns to roll through the action zone. The minimum volume of powder required for processing is about 60 cm^3.

5. References

1) Yokoyama T., Urayama K., and Yokoyama T., KONA No. 1, 53-63 (1983).
2) Yokoyama T., Urayama K., Naito M., Kato M. and Yokoyama T., KONA No. 5, 59-68 (1987).
3) Yokoyama T., Urayama K., Kato M., Herman H. and Chen Z., Proc. of Second World Congress Particle Tech., Kyoto, Japan, 591-598 Sept. (1990).
4) Herman H., Chen Z.J., Huang C.C. and Cohen R., J. of Thermal Spray Technology, Vol. 1, No. 2, 129-135 (1992).
5) Chen Z.J., Herman H., Tiwari R., Huang C.C. and Cohen R., Proc. Inter. Therm. Spraying Conf., Orlando, edited by Berndt C.C., ASM International, Metals Park, OH, 355-361 (1992).
6) Chen Z.J., Herman H., Huang C.C. and Cohen R., "High-Temperature Ordered Intermetallic Alloys V", Materials Research Society Sym. Proc., Vol. 288, edited by Baker I., Darolia R., Whittenberger J.D. and Yoo M.H., Material Research Society, Pittsburgh, PA, 835-840 (1993).
7) Chen J et al., J. of Powder Metall., vol. 29, No. 4, 316 (1993).
8) Chen Z.J., Ph. D. Dissertation, State University of New York at Stony Brook, NY, U.S.A. (1995).
9) Bernard D., Usmani S., Chen Z.J, C.C. Berndt, H. Herman, Yokota O., Grimaud A and Fauchais P., "Thermal Spray Industrial Applications", edited by Berndt C.C. and Sampath S., ASM International, Metals Park, OH, 171-178 (1994).
10) Brogan J.A., Gross K.A., Chen Z., Berndt C.C and Herman H., "Thermal Spray Industrial Applications", edited by Berndt C.C. and Sampath S., ASM International, Metals Park, OH, 159-164 (1994).
11) Alonso M., Satoh M. and Miyanami K., Powder Technology, 59, 45-52 (1989)
12) Alonso M., Satoh M. and Miyanami K., KONA, No. 7, 97-105 (1989).
13) Davich K., Powder and Bulk Engineering, 50-54, Feb. (1990).
14) Ito H., Umakoshi M., Nakamura R., Urayama K. and Kato M., Proc. of 4th National Thermal Spray Conference, Pittsburgh, PA, edited by Bernecki T.F., ASM International, Materials Park, Ohio, 405-410 (1992).
15) Naito M. and Yoshikawa M., KONA No. 7, 129-132 (1989).
16) Tanno K., KONA, No. 8, 74-82 (1990).

Author's short biography

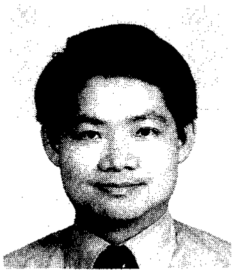

C.C. Huang

Dr. C.C. Huang is Director, Research and Development for Hosokawa Micron Powder Systems in Summit, New Jarsey. He holds an M.S. degree in Engineering from Illinois Institute of Technology and a Ph.D. degree in Chemical Engineering from West Virginia University. He has many years' experience in industrial R&D and academia in the field of powder technology and science, specializing in powder processing, powder characterization, powder granulation and fluidization. He has published numerous articles and is an active member in a number of science and engineering societies.

John Z. Chen

John Z. Chen, formerly a research assistant, Department of Materials Science & Engineering, State University of New York at Stony Brook, is a senior process engineer at Chromalloy New York, Orangeburg, New York.

Herbert Herman

Prof. Herman received his Ph.D. degree in 1961 from Northwestern University, following which he was a Fulbright Scholar at the University of Paris. From 1962 to 1963 he was a Research Associate at Argonne National Laboratory. He was on the Faculty of the University of Pennsylvania until joining the State University of New York at Stony Brook in 1968. He has been very active in the field of surface engineering, working with a wide range of industrial and govement orgnizations, with a special emphasis on thermal sprayed protective coatings. He played a key role in forming the Thermal Spray Division of ASM International, becoming the Division's founding Chairman in 1986. Sice 1983 Herman has been Editor-in-Chief of the international jeurnal, *Materials Science & Engineering*. Herman has over 200 scientific and engineering publications and nine patents. Herman is a Fellow of ASM International and the American Ceramic Society and was elected to the International Academy of Cemamics in 1992.

Research

Dry Coating Method Using Magnetically Assisted Impaction In a Randomly Turbulent Fluidized Bed†

Rajiv K. Singh, A. Ata, and J. Fitz-Gerald
and Ya.I. Rabinovich
Department of Materials Science and Engineering
*University of Florida**
W. Hendrickson
*Aveka Inc***

Abstract

Surface modified particulates have many potential industrial applications ranging from new technologies such as rechargeable batteries, flat-panel displays, etc. to a wide range of unit operation processes such as dispersion, transport and handling, and separation of particulate systems. Due to environmental constraints, there has been a strong interest in the development of dry methods (chemical and/or water free) for particulate coatings. In this paper, we report the feasibility of novel dry method based on a magnetically-assisted impaction coating (MAIC) process for synthesis of composite particulates. In the MAIC process, magnetic particles are accelerated in the chamber using an alternating electromagnetic field. The magnetic particles in turn collide with the core and with submicron sized fine particles (secondary particles) to form composite particles. The adhesion of the secondary particles on the core particles was found to be dependent on several factors including particle size, particle hardness, etc. and a number of processing parameters. Experiments were conducted on a wide variety of particles systems such TiO_2/PMMA, Alumina/PMMA, Ag/PMMA, TiO_2/Al_2O_3, etc to understand the effect of these parameters. PMMA were preferred to use as a core (primary) particle because of its smooth surface which minimizes surface roughness effects. The composite particles were characterized using standard materials techniques such as scanning electron microscopy, energy dispersive X-ray microanalysis, etc. The results show that MAIC process significantly improved the surface coverage compared to the coverage obtained from standard blending methods. High frequency ultra-sonication of composite particles was also conducted so that weakly adherent particles could be removed from the surface. The efficiency of the coating process was found to be decreased with increasing secondary particle size. High surface coverage was achieved for composite particle with soft cores (e.g PMMA). To understand the effect of particle hardness on the adhesion process, atomic force microscopy (AFM) studies were conducted as a function of the particle hardness. Based on experimental observations, a model for the particle coating process has been developed.

1. Introduction

The synthesis of engineered particulates i.e. particulates with tailored properties, have become increasingly important for a variety of industrial and technological applications (1-2). Methodologies are being developed to synthesize particulates with desired properties such as specific size, size distribution, and shape, etc. One important class of engineered particulates are composite particles in which the surface properties of the particle can be tailored for various applications. **Fig. 1** is a schematic diagram of the two types of engineered particulates with controlled surface architecture. The secondary particle adheres to the surface of the core particle, thereby modifying its surface properties. Various inter-particle forces such as Van der Waals, electrostatic, capillary forces, etc, are important in controlling the adhesion of the secondary particle to the core particle. Two different types of surface architecture are depicted in this diagram. In the first case, the secondary particles

---

* Gainesville, FL 32611, USA
**2045 Wooddale Drive, Woodbury, MN 55125
† Received October, 1996

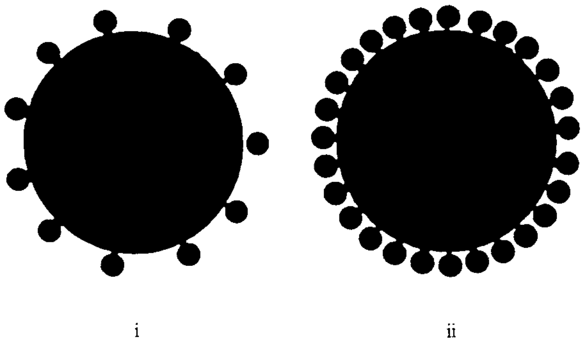

Fig. 1 Schematic diagram of (i) discrete and (ii) continuous engineered particulates with controlled surface architecture

form a continuous coating on the surface, while in the second case, a discrete discontinuous coating is formed. The size of the secondary particle can vary from ~1 nm to > 1 μm, while the size of the core particle can range from less than 1 μm to greater than 200 μm. Both discrete and continuous coatings may be important, depending on the nature of the application.

This class of engineered particulate has wide-ranging applications extending from synthesis of ceramic tungsten carbide/cobalt cutting tools, metal hydride based rechargeable batteries, to phosphors for flat panel display materials. In each of these application, it is desirable to obtain a surface property which is different from the bulk particle. To achieve this, particulate surfaces have to be designed so that the surface properties (e.g conductivity, sinterability, corrosion characteristics, flow behavior, etc.) are different from the bulk material. For example, the surface of phosphor powders should be conducting so that the charge introduced by cathodoluminescence can be dissipated, while in WC/Co cutting tools, the surface has to modified so that high-density sintering of the ceramic can be achieved at relatively lower processing temperatures. Also, the surfaces can be designed to have novel properties such as selective adsorption, high catalytic activity, etc.. Thus, the synthesis of specifically engineered particulates is expected to play an important role in the next generation particulate technologies. It should also be noted that by controlling the surface architecture of the coating, segregation effects can be also minimized. A uniformly coated composite particle represents a structured mixture of two systems (3-5).

Synthesis of engineered particulates of controlled architecture can be accomplished by both wet and dry processes. Typically in wet processes, the core particles are dispersed in an aqueous/non-aqueous solution, before the coating with the secondary particle takes place. The secondary particles can exist as second suspended phase before the mixing process, or can be in-situ precipitated on to the core particles. Wet techniques are characterized by the use of chemicals/water for the process. These techniques rely on the use of electrostatic, Van der Waals and steric forces for adherence of the secondary particle on the core particle.

Recently, there has been a concerted effort to develop coating processes which do not require the use of chemicals, or aqueous/non aqueous solvents. The development of new and existing "dry processes" for particulate coatings has become crucial for the development of next generation particulate coating technologies. Typically dry methods to synthesize composite particles use some type of grinding system. Almost every fine grinding machine appears to possess the ability to make various kinds of composite particles, aside from its primary function. To make the composite particles, the secondary particle is initially covered over the surface of the core particle, and then mechanical compressive and shear stresses are applied to enhance the adhesion process. There are a number of reports which claim the production of composite particles in a variety of combinations including plastics, metals, ceramics (2-7). One important development in this area has been the use of the *Mechano-fusion* system developed by Hosokawa Inc. Senna et. al. have analyzed in detail the use of this system to synthesize composite particulates and analyze the ratio of the tangential stresses to the normal stresses for optimum conditions in the machine (1-2).

In this paper, we show the feasibility of a new method to form engineered particulates with controlled surface architecture. This method is based on the use of a magnetic field to accelerate magnetic particles which further collide with the core and the secondary particles. The magnetically assisted impaction coating (MAIC) process results in efficient mixing and mechanical deformation, thereby leading to the formation of adherent coatings. Particulate coatings consisting of different core (PMMA, alumina) and secondary particles (titania, alumina, silver, cobalt oxide, etc.) were used for the experiments. The MAIC coating method was compared with other standard blending techniques. Studies were conducted to understand the effect of the processing parameters such as particle size, and hardness on the surface coverage

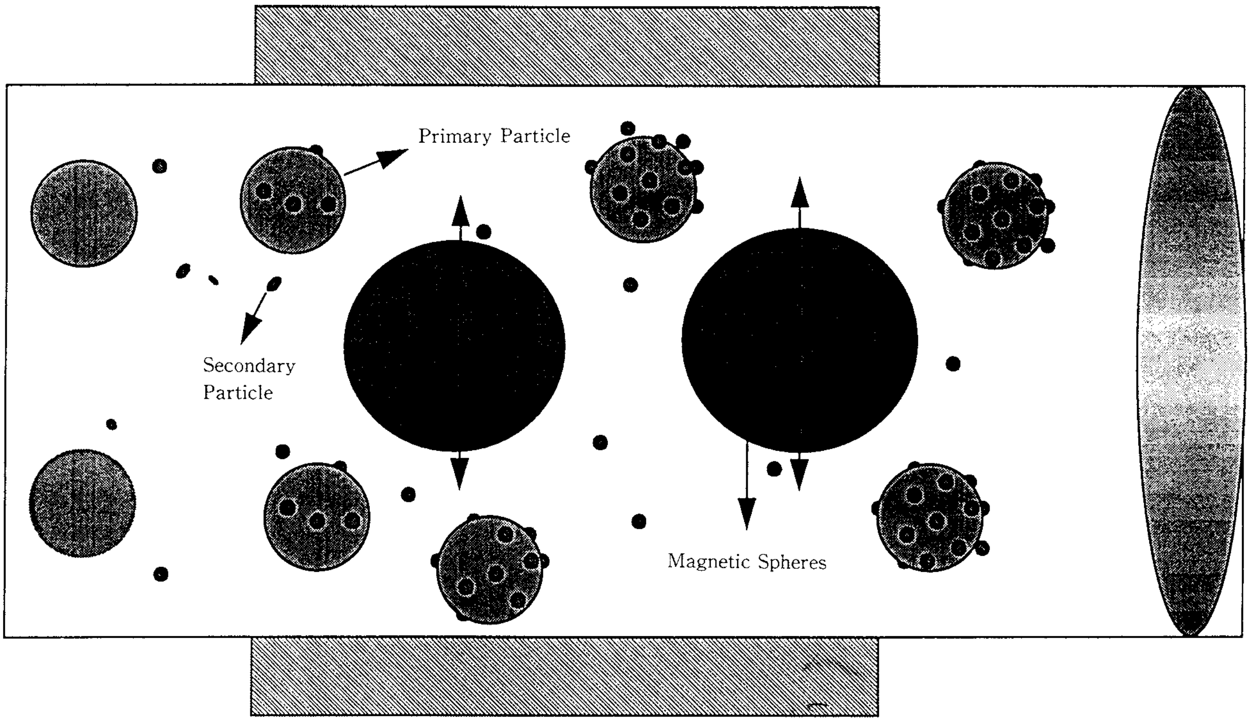

Fig. 2 Schematic diagram of the magnetically assisted impaction coating (MAIC) system

and degree of adhesion of the coating.

In order to understand the nature of adhesion in the composite particles, AFM studies were also conducted. Based on the experimental observations, the mechanisms for coating formation have been proposed.

2. Experimental

A schematic diagram of the magnetically assisted coating process (MAIC) is shown in **Fig. 2**. Briefly, this system consists of a long hollow cylindrical tube enclosed with a series of electromagnets. The flux inside the tube consists of the relatively large magnetic particles (size 200 μm-1000 μm), core (size 1 μm-200 μm) and secondary particles (5 nm-1 μm). **Figure 3** shows the magnetization as a function of the applied magnetic field (B-H hysteresis loop) obtained from a SQUID magnetometer. An alternating current (with varying frequency and amplitude) is applied to the electromagnets, thereby creating a weak (~100 Gauss) magnetic field. The alternating magnetic field, produces by the time varying field which accelerates the magnetic particles within the system. The magnetic particles are characterized by a high coercivity (approx 4000 Gauss) so that they do not reverse their polarity in a weak electromagnetic field. Therefore, the magnetic particles can be accelerated in the chamber. The magnetic particles in-turn collide with the core and secondary particles resulting in the formation of a psuedo-fluidized bed. As the magnetic response of each type of particle is different, the particle collide in a random manner. It is envisaged that these collisions lead to formation of a particulate coating.

After the formation of the coating, the magnetic particles are separated from the composite particles by standard magnetic separation methods. The adherence of the coating depends on a number of process parameters such as, electromagnetic field strength, frequency of the applied magnetic field, process time, particle loading and concentration etc. Materials parameters such as the hardness and

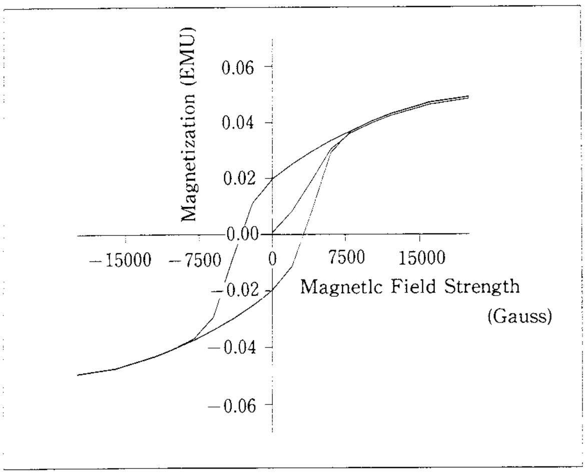

Fig. 3 Magnetization versus applied magnetic field for Iron Oxide used in the MAIC system

yield strength of the core and secondary particles, surface roughness and particle size also play a critical role in controlling the adhesion of the coating. In addition these parameters also control the surface architecture of the coating (distribution of particulates, particle density on the surface, etc.)

The composite engineered particulates were characterized for their surface architecture and composition, uniformity and texture by standard materials characterization techniques. Secondary electron microscopy (SEM) studies on these particles were conducted to determine the surface morphology of the coatings, while energy dispersive X-ray analysis (EDX) and wavelength dispersive X-ray analysis (WDX) were conducted to determine the surface composition and surface architecture of the films. It was observed that after the coating process, some of the particles appeared to be weakly adhering to the surface of the core particle. In some experiments, the composite particulates were treated to standard ultrasonic treatment (20 Khz, 1 minute) conditions, so that loosely attached/weakly adhered particles could be removed from the surface. The effect of deformation on adhesion characteristics was determined at the particulate level using atomic force microscopy (AFM) techniques and correlated with the particle ensemble behavior.

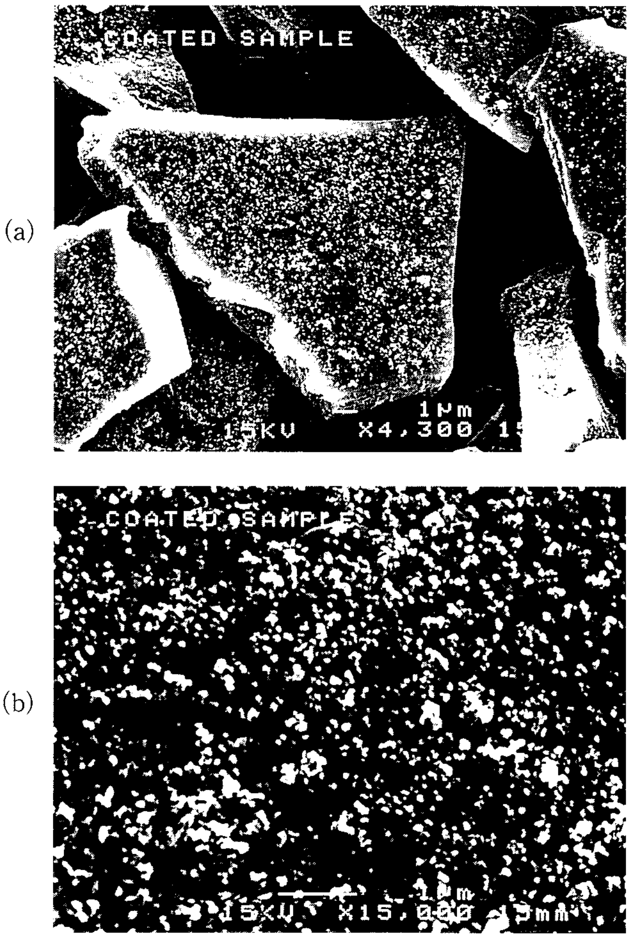

Fig. 4 SEM micrographs at (a) low and (b) high magnification of fumed silica particles coated on silicon carbide particles by the MAIC process

3. Results

Comparison of Other Coating Techniques

To determine the efficacy of the MAIC process, experiments were conducted and compared with standard blending techniques. These experiments were conducted with both soft-hard and hard-hard combination of secondary and core particles. **Fig. 4(a)** and **Fig. 4(b)** show the surface morphology at two different magnifications of fumed SiO_2 coatings on silicon carbide core particles synthesized by the MAIC process. Both these particles are relatively hard (Vickers hardness exceeding 1000 Kg/mm^2), thus significant plastic deformation is not expected to occur. The percentage of the weight ratio of fumed silica (average particle size $\sim$0.1 μm) was approximately 1%. No ultrasonic treatment or other cleaning operations were conducted on these samples. The SEM micrographs show that the coating is distributed uniformly on the surface without formation of large agglomerates. From image analysis, the surface coverage of the fumed silica was determined to be approximately 30%. **Fig. 5(a)** and **5(b)** show the surface morphology of ball-mill blended 1% silica particles on silicon carbide core particles at two different magnifications. The micrographs show that the surface coverage of fumed silica particles on the silicon carbide surface was less than the MAIC treated samples by a factor of three, even though the same weight ratio of the materials was used. Thus, these results shows that the MAIC process is a highly efficient process in the formation of coatings. It should be noted that the adherence strength for either of the coatings could not be determined because no ultrasonication studies were carried out on these samples.

Similar results were obtained for soft-hard combination composite particulate combinations. **Figure 6(a)** and **Figure 6(b)** show the surface of a PMMA particles (200 μm) coated with alumina with using (i) the MAIC process and (ii) standard blending. In these experiments the size of the secondary particles was approximately 0.2 μm. The weight ratio of the secondary to primary particles was adjusted so that under ideal conditions an 100% surface coverage could be achieved. The figure shows that the

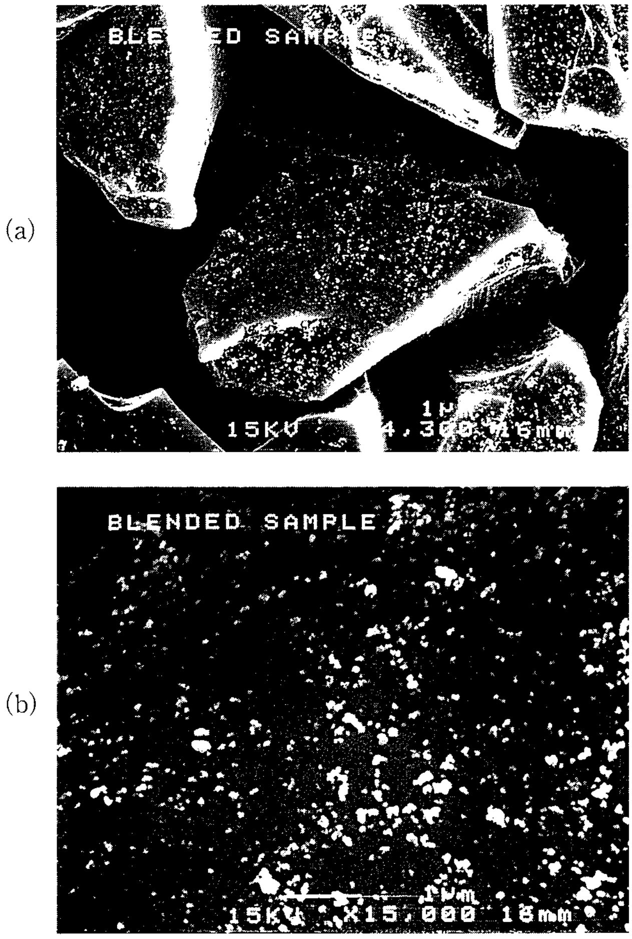

Fig. 5 SEM micrographs at (a) low and (b) high magnification of fumed silica particles coated on silicon carbide particles by blending method

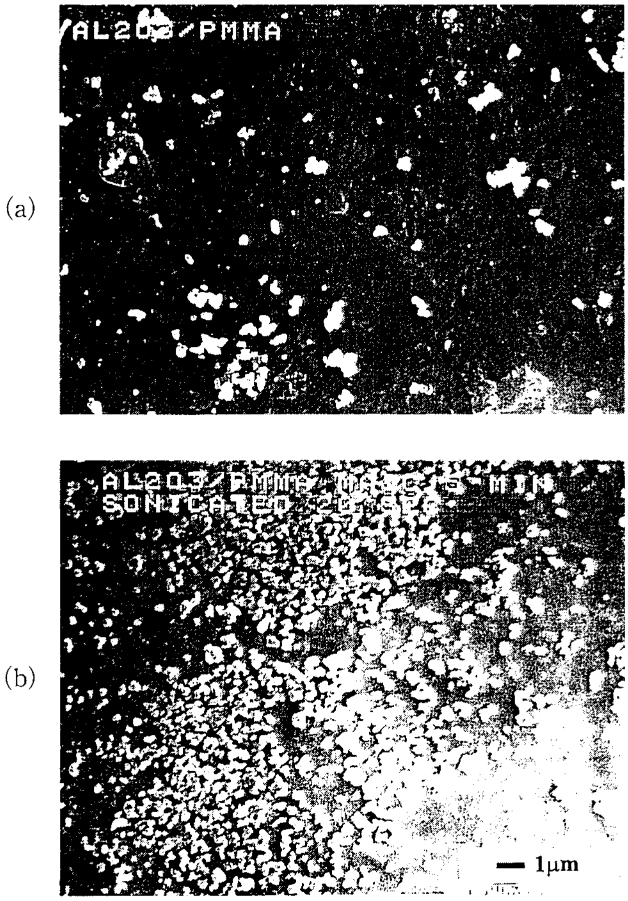

Fig. 6 Surface morphology of 0.4 μm alumina particles coated on PMMA particles obtained from (a) MAIC system and (b) standard blending techniques

surface coverage of the coating made by the MAIC process was more than an order of magnitude higher than the surface coverage observed from the blending method. The surface coverage values after ultrasonic treatment for both blended and MAIC treated samples is listed in **Table 1**. The ultrasonic treatment was conducted so that the loosely held particles from the surface can be removed. No appreciable detachment of the secondary particles was observed after ultrasonication for MAIC treated samples. However significant detachment of the particles was observed for composite particles prepared by standard blending methods.

Effect of Particle Size and Hardness

The size of the secondary particles was found to be an important factor controlling the degree of surface coverage and the efficiency of the coating process. Alumina secondary particles with size varying from 0.05 μm to 1 μm and primary PMMA particles (size ~200 μm) were used in these experiments. The weight ratio of the secondary to primary particles was adjusted so that under ideal conditions an 100% surface coverage could be achieved. **Figure 7** shows the surface coverage of

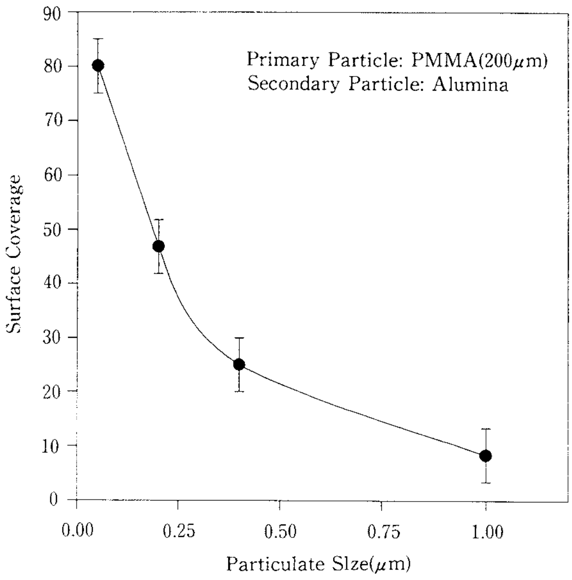

Fig. 7 Surface coverage of alumina particles on PMMA core particles as a function of particle size obtained from the MAIC method

the alumina particles as a function of secondary particle size for Al_2O_3/PMMA composite system. The surface coverage values were obtained from detailed image analysis of the SEM micrographs. No ultrasonic treatment or other cleaning techniques were applied on the particles. However it should be noted from **Table 1**, that the surface coverage of MAIC synthesized composite alumina/PMMA particles do not decrease significantly upon ultrasonic treatment. The graph shows that the surface coverage is very high (>80%) when the secondary particle size is less than 50 nm, and drops to nearly 10% when the secondary particle size is increased to 1 μm. The maximum slope of the graph which corresponds to highest decrease in the coating coverage occurs when the secondary particle size varies from 0.1-0.3 μm size range.

Table 1 Surface Coverage of the alumina particles on PMMA substrates before and after ultrasonication obtained from standard blending and MAIC techniques

Synthesis Method	Secondary Particle Size (μm)	Surface Coverage (%) (As synthesized)	Surface Coverage (%) (After Ultrasonication)
MAIC	0.2	45±4	40±4
MAIC	1	10±2	6±2
Blending	0.2	18±3	2±0.3
Blending	1	8±2	0.6±0.1

The mechanical properties of the secondary and core particles play an important role in the adhesion of the coatings. Materials with lower hardness can deform upon impact, thus creating a larger impact area, and reduced roughness of the contacting surfaces. These effects lead to increased Van der Waals attraction forces. In addition, the secondary and core particles can approach closer to each other, thereby enhancing physical adhesion and increasing the possibility of chemical interactions between the two particles. Thus, it is expected that the adhesion strength of the secondary particle with the core particles will improve if at-least one of the particles possesses a low hardness.

Fig. 8(a) and **Fig. 8(b)** show respectively the surface morphology of alumina/TiO_2 particles before and after the ultrasonication process. In this experiment, the ratio of the secondary to primary particles was adjusted so that under ideal conditions, 100% surface coverage is obtained. The size of the primary and secondary particles were 10 μm and 0.4 μm, respectively. Also, as both particles are relatively hard, little plastic deformation effects are expected in this coating process. The figure shows that the synthesized titania coatings completely coat the primary particle. However after ultrasonication, a much lower surface coverage is observed. These results can be contrasted to the result obtained from soft-hard (alumina/PMMA) composite particles shown in **Fig. 7**, and **Table 1**. PMMA is relatively a softer material compared to alumina, thus deformation takes place on impact. In contrast, both titania and alumina are relatively hard materials and do not plastically deform under MAIC treatment conditions.

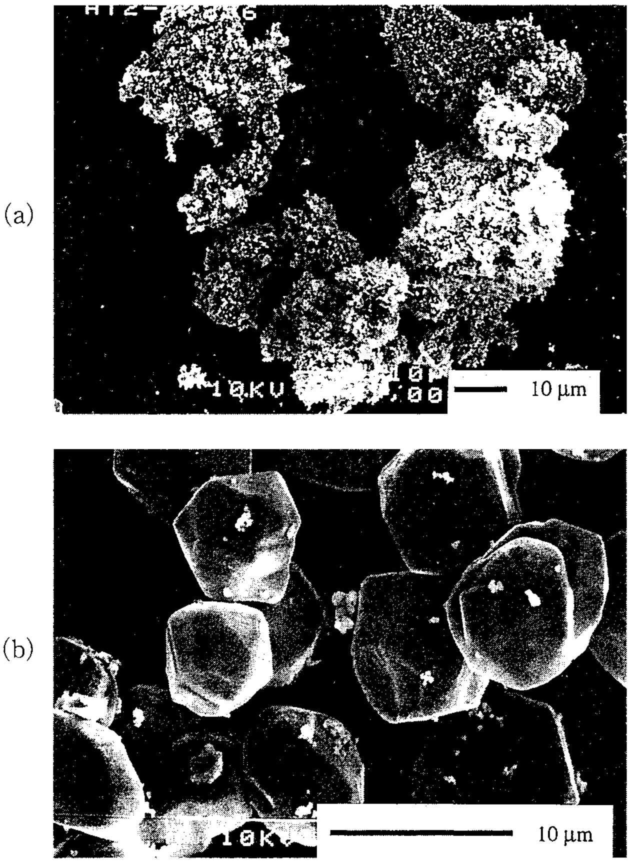

Fig. 8 Surface coverage of titania particles on alumina core particles after (a) MAIC synthesis and (b) MAIC synthesis followed by ultrasonication

It should be noted that besides particle hardness, other factors area also crucial in controlling the surface architecture and the adhesion of coatings (8-9). For example, the surface roughness, and the chemical affinity of secondary and core particle surfaces is expected to play a critical role in the adhesion and surface coverage of the coatings. The effect of other system and particle variables on the surface coverage and the adhesion of the coatings will be discussed in detail in a future publication.

4. Discussion

The above results shows that the intrinsic particle parameters such as hardness and particle size play a critical role in controlling the strength of adhesion and the surface coverage of the secondary particle coating. In this section, we outline the mechanisms which affect the formation of coating in the MAIC process. The primary forces which act to bring particles to the surface and hold it together are the Van-der Waals, electrostatic and the capillary forces (in presence of moisture) (9). As we are dealing with particle impact in the MAIC process, the present analysis will be limited to effect of particle impact in the Van der Waals attraction between the particles.

It is well known that non-polar and polar Van der Waals forces can be significantly increased if the cross-section area of contact between the particles can be increased. During particle impact, the deformation of the particle surface is expected to play a significant role in the adhesion process. The particles during impact may deform either by elastic or plastic deformation, however elastic deformation do not significantly increase the adhesion due to the stored energy effects (10). The amount of plastic deformation depends on the hardness of the secondary and the primary particle. As the secondary particle is much smaller than the core particle, the particle geometry can be approximated as a spherical particle attaching on a flat surface. The Van-der Waals adhesion force between the spherical particle and the flat surface is given by

$$F_{VdW} = \frac{AD}{12z^2} \qquad (1)$$

where z is the separation distance (approximated to be 4 Å) between the surfaces, D is the particle diameter, A is the Hamaker's constant. In the above equation, the Van-der Waals forces have been assumed to come from ideal point contact with no deformation of the secondary or the core particle. As indicated earlier, depending on the intrinsic properties of the particles (primary and secondary), significant deformation of the particle can occur both as a result of the intrinsic adhesion forces as well as the externally applied impact forces. The additional Van der Waals force due to deformation is a function of the increased contact area caused by the deformation and is given by

$$F_{VdW(def)} = \frac{A\rho^2}{6z^3} \qquad (2)$$

where 'ρ' corresponds to the radius of the contacting surface. The deformation of the particle surface can either be elastic or plastic in nature, however based on energy considerations, elastic deformations do not give rise to significant increase in the adhesion strength. The ratio of $F_{VdW(def)}$ and F_{VdW} represents and the adhesion force enhancement factor due to plastic deformation. The adhesion force enhancement factor is given by

$$\frac{F_{VdW(def)}}{F_{VdW}} = \frac{2\rho^2}{Dz} \qquad (3)$$

Figure 9 plots the adhesion force enhancement factor versus secondary particle diameter for two assumed deformation conditions (1% and 10% deformation). The percentage deformation is defined as the ratio of the plastic deformed radius to the particle radius expressed in a percentage value. This figure shows that there is a significant increase in the Van der Waals force due to plastic deformation. The adhesion force enhancement factor is higher for greater degree of deformation, and increases further when the diameter of the secondary particle is increased. This figure shows that impaction can lead to significant increase (factor of 10 to 100) increase in the Van-der Waals forces, which in turn can significantly increase the surface coverage and adhesion of the secondary particles. It should be noted the the amount of the deformation during the coating process will depend on the nature of impaction (particle velocity, size, angle) and the intrinsic properties of the particles (hardness, elastic properties, etc.) (10-12).

Several researchers have proposed models to calculate the contact radius between a particle and the substrate (13-16). A majority of the work has been concentrated on determination of the elastic contact radius. Derjaguin, Muller and Toporov

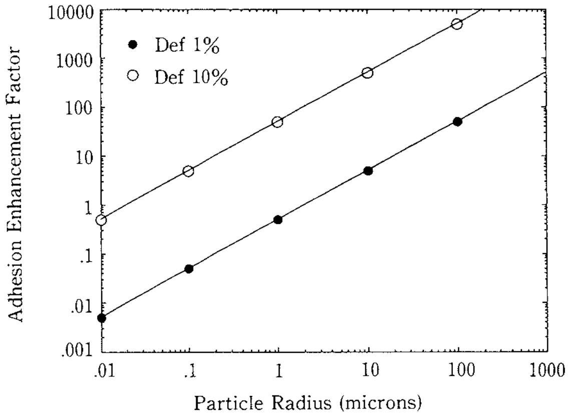

Fig. 9 The adhesion enhancement factor due to plastic particle deformation versus size of the secondary particle. In this graph only the Van der Waals forces has been shown.

(hereafter referred as the DMT model) proposed a model to calculate the contact radius by taking into account the tensile elastic interactions (14-15). Assuming that the shape of the contact region would be Hertzian, the DMT model predicts that half the interactions occurs outside the contact zone. This is in contrast to the Johnson, Kendall Roberts (JKR) model which assumes that all the interactions occur within the radius of contact (13). Further work in this area showed that both the models had a certain region of validity (16). However as mentioned earlier, the increase is contact radius with elastic deformation does not lead to an significant increase in the Van der Waals forces because of the "elastic rebound" effects.

Maguis and Pollock generalized the JKR model to include plastic deformation (17). They found out that in the case of plastic deformations, the contact radius "ρ" is related to the particle radius R and an externally applied load P by

$$p+2\pi W_a R=\pi\rho^2 H \tag{4}$$

where W_a is the thermodynamic work of adhesion, and the hardness "H" is related to the yield strength of the material Y by

$$H=3Y \tag{5}$$

Equation 4 suggests that if the impact forces are much larger than the intrinsic adhesion forces, the radius of the deformed area will be directly proportional to the applied load and inversely proportional to the hardness of the contacting surfaces. Thus based on equation (4) and (5), we can conclude that the hardness of the particle, and the impact load will play a significant role in the adhesion process.

To understand the effect of the particle impact on the adhesion forces we conducted AFM indentation studies on various two substrates (PMMA and sapphire). PMMA is relatively a soft material (Vickers hardness ~20 Kg/mm^2), while sapphire corresponds to a hard surface (Vickers Hardness ~2100 Kg/mm^2). These studies were conducted by loading the substrate surface with silicon nitride AFM tips under different loading conditions to simulate the experimental system. **Figure 10** shows the adhesion force on the AFM tip as a function of loading for two sapphire and PMMA substrates. This AFM experimental geometry simulates hard-hard and hard-soft particle impaction in the MAIC system. These experiments were conducted in dry air conditions so that the capillary effects could be eliminated. The figure show that for PMMA substrates, the adhesion force increases linearly as the loading force is increased. The linear increase in the Van der Waals forces is agreement with equations (2) and (4). In contrast, the adhesion forces on the sapphire substrates is independent of the loading force. This is attributed to the large hardness values of the substrate which does not result in plastic deformation.

The decrease in the surface coverage with increasing particle size for MAIC coated composite particle can be attributed to two effects (i) surface roughness of core and secondary particles and (ii) impaction effects. It is well known that the surface roughness plays a critical role in adhesion of materials (18). The van der Waals forces are significantly reduced due to asperities on the surface. Even though, theoretically the predicted Van der Waals forces for small particles (<10 μm) are much greater than the gravitational forces, in reality the gravitational forces become higher because of the reduced Van der Waals attraction due to surface roughness.

Figure 11 shows the effect of surface roughness on the Van der Waals attraction as a function of diameter of the secondary particle. This plots are based on the Van der Waals attraction between two spheres of different size assuming smooth surface contact and rough surface contact (19). The rough surface can be simulated by attaching a hemispherical particle to a flat surface. The figure shows that when the size of the secondary particle is relatively large (>1 μm), the Van der Waals forces for rough contacts are reduced by several orders of magnitude

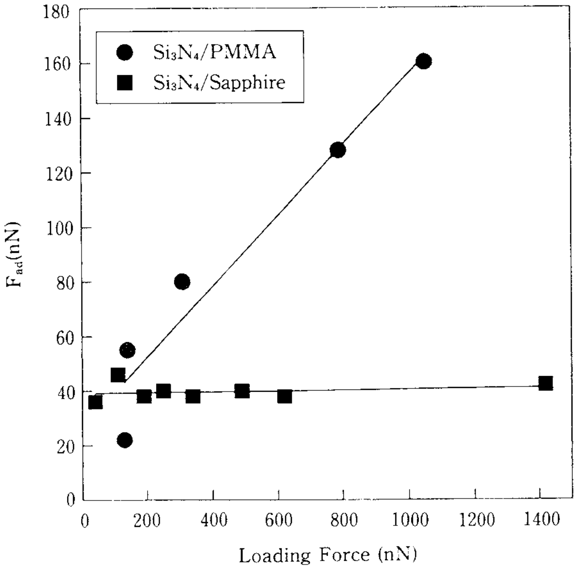

Fig. 10 The adhesion force between the AFM tip and PMMA and sapphire substrates as a function of loading. The loading leads to plastic deformation of the PMMA substrate while no plastic deformation in sapphire occurs.

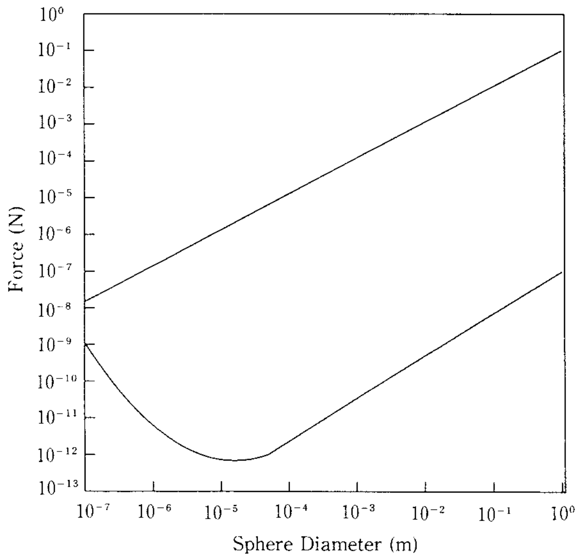

Fig. 11 Van der Waals forces between two spherical particles under (i) smooth contact and (ii) rough contact conditions

than expected from a smooth contact. However as the size of the secondary particle decreases, the Van der Waals for rough surfaces starts to increase. This increase is because the size of the asperity becomes comparable to the size of the secondary particle. As the size of the secondary particle is further decreased, the Van der Waals forces due to rough contact approaches the values expected from a smooth surface contact. Thus for small diameter secondary particles, Van der Waals forces becomes significantly larger. Similar effect of particle size has been obtained by the MAIC process (for example Alumina particles on PMMA). Significant secondary particle surface coverage has been obtained when the size of the secondary particle is small (~50 nm). With increase in particle size the surface coverage decreases rather significantly. It should also be noted that the deformation of the surface during impaction is also expected to play a role in modification of the surface roughness of the primary and secondary particles.

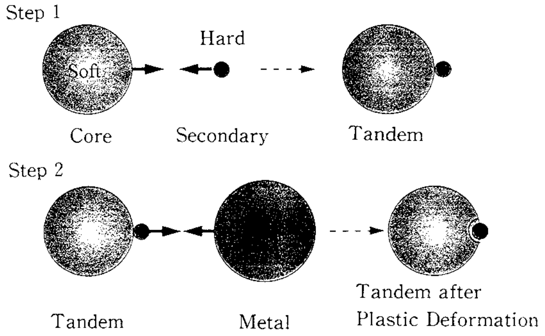

Fig. 12 Schematic diagram to deformation mechanisms which results in improved adhesion of the hard-soft coatings synthesized by the MAIC process

The impaction stresses are also affected with the size of the secondary particle. The coating process takes place via direct collisions of various species (secondary particles, core particles and the magnetic particles). The process is envisaged to occur in two steps. This is shown schematically in **Fig. 12**. In this figure we have assumed a soft core particle and a hard secondary particle. The first step involves random collisions the secondary particles with primary particles resulting in weak attachment. In the second step, collisions with large magnetic particles results in deformation of the primary particle, thereby enhancing attractive forces. For a fixed external impact load, the surface stresses increase with decreasing secondary particle size. Thus, the smaller secondary particles will cause larger deformation to occur, which result in increased Van der Waals attraction.

5. Conclusions

A novel dry method for particulate coatings has been developed. This method is based on the use of a magnetically assisted impaction process to induce uniform mixing, deformation and improve adhesion strength of the coating. The MAIC process for coating particles was found to be much more efficient than standard ball-mill blending techniques. Results show that the coating characteristics (surface coverage, adhesion strength) is strongly affected by the materials parameters such as particle hardness and size. Based on the experimental observation models to explain the nature of the coatings process in the MAIC system has been developed.

6. Acknowledgements

Part of this research is sponsored by the National Science Foundation funded Engineering Research Center on Particle Science and Technology via grant # EEC 94-0929. The authors would like to thank Brij Moudgil and Dinesh Shah for thought provoking discussions, and David Wright for helping to set-up the experiments.

References

1) K. Mizota, S. Fujiwara, and M. Senna, *"Microstructure and Adhesion Mechanism of Mechanically Prepared Composite Particles"* Materials Science and Engr. B 10,

139 (1991)

2) T. Yokoyama, K. Urayama, M. Naito, *"The Angmill Mechanofusion System and its Applications"* Kona, 5 59 (1987)

3) M. Satoh et. al., Proc 2nd World Congress on Particle Technology, 591 (1990)

4) M. Alonso, M. Satoh, K. Miyanami, *"Mechanism of Combined Mechanofusion Processing of Powders"* Powder. Tech. 59, 45 (1989)

5) M. Alonso, M. Satoh, K. Miyanami, *"Powder Coating in a Rotary Mixer with rocking Motion"* Powder Tech. 56, 135 (1988)

6) R.K. Singh *"Dry Coating Method for surface modification of Particulates"* Proceedings of the 10th International Conference on Surface Modification Technologies (in press)

7) R.K. Singh et. al., Appl. Phys. Lett, submitted for publication

8) D.S. Rimai, L.P. Demejo and R.C. Bowen, *"Mechanics of Particle Adhesion"* J. Adh. Sci & Tech. 8, 1333 (1994)

9) R.A. Bowling ": Particles on Surfaces 1 : Detection Adhesion and Removal" K.L. Mittal (eds.) Plenum Press NY (1989) pg. 129

10) J. Reed, "Particles on Surfaces 2 : Detection Adhesion and Removal" Edited by K. Mittal, Plenum Press pg .1, (1989)

11) S. Wall, W. John and S.L. Goren, "Particles on Surfaces 2 : Detection Adhesion and Removal", Edited by K. Mittal, Plenum Press pg .19, (1989)

12) K. Kendall and J.C. Padget, *"Latex Coalescence"* Intl .J. Adhesion Adhesives, 2, 149 (1982)

13) K.L. Johnson, K. Kendall and A.D. Roberts, *"Surface energy and Contact of elastic solids"* Proc. R. Soc. London Ser. A 324, 301 (1971)

14) B.V. Derjaguin, V.M. Muller and Y.P Toporov, *"Effect of Contact Deformations on the Adhesion of Particles"* J. Colloid and Interface Science 53, 314 (1975)

15) B.V. Derjaguin, V.M. Muller and Y.P Toporov, *"On the Role of Molecular Forces in Contact Deformations"* J. Colloid and Interface Science 67, 378 (1978)

16) D. Tabor, *"Surface forces and surface Interactions"* J. Colloid and Interface Science 58, 2 (1978)

17) D. Maugis and H.M. Pollock, *"Surface Forces, Deformation and Adherence at Metal Microcontacts"* Acta Metall, 32, 1323 (1984)

18) K. Kendall, Science, *"Adhesion : Molecules and Mechanics"* Vol 263, pg 1720 (1994)

19) H. Rumpf and H. Schubert, in "Ceramic Processing Before Firing", pg 357 edited by G.Y. Onoda and Larry L. Hench, J. Wuley and Sons, 1978

Author's short biography

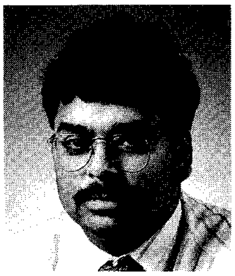

Rajiv. k. Sinsh

Dr. Rajiv Singh is currently a professor in the Materials Science & Engineering Department at the University of Florida. He has published over 200 papers in the area of innovative synthesis and processing of materials, thin film coatings, surface modification and photon solid interaction based processing of materials. Prof. Singh received his Ph. D degree from North Carolina State University in 1989. He is the reception of several awards involving NSF Young Investigation (NY1) award and TMS Hardy Gold Medal for outstanding contributions in materials science and engineering.

Ali Ata

Ali Ata graduated in Metallurgical Engineering from Middle East Technical University of Ankara Turkey and obtained his Masters degree in Materials Science from Technical University of Istanbul in 1993. He has done two years of research at the University of California, San-Diego and subsequently started his PhD program in Materials Engineering at the University of Florida. He is currently in the program studying Engineering Particulate Systems, adhesion phenomena in particulate system.

James Fitz-Gerald

James Fitz-Gerald is a graduate student in Materials Engineering at the University of Florida. He obtained his B.S degree in Mechanical Engineering from University of Massachuset, Lowell. His current research is on the development of thin coatings on particulate materials.

Ya. I. Rabinovich

Dr. Yakov Rabinovich is a scientist in Engineering Research Center at the University of Florida. His major research interest is surface forces between particles in gas and liquid media including adhesion of micro-particles.

W. Hendrickson

Dr. Hendrickson is the president of Aveka Inc. at Minnesota. He got his Ph.D in Chemical Engineering from the University of Florida and worked in 3M company. He is working on particulate processing including dry coating of particulate materials.

Research

A Contact Model for the Effect of Particle Coating on Improving the Flowability of Cohesive Powders[†]

Renwei Mei, Hong Shang
*Department of Aerospace Engineering, Mechanics & Engineering Science**
James F. Klausner, and Elizabeth Kallman
*Department of Mechanical Engineering, University of Florida**

Abstract

Coating or blending of fine particles on the surface of primary powder particles is often applied to improve and control the flow behavior of the powder. The effect of coating primary powder particles with fine particles on the cohesion force between primary powder particles is quantitatively examined. The JKR theory is extended to include the effect of particle coating on the force-displacement relationship due to surface energy and elastic deformation. It is shown that the cohesion force between two primary particles in the presence of a fine coating particle is directly proportional to the size ratio of the coating particle to the host powder particle and results in a drastic reduction in the cohesion force. Through discrete element simulation of powder flow, which uses the force-displacement relationship based on the extended JKR theory, the improved flowability is demonstrated. Competing effects of the coating and shear induced migration on the macroscopic behavior of the powder flow are discussed. The effect of coating on improving the flowability is also experimentally demonstrated by comparing the measured angles of repose at a static condition and the flow rates of the gravity driven flow through a funnel for powders with and without particle coating.

1. Introduction

Fine powders, 30 μm or less, are of significant industrial importance. Unfortunately, these materials are the most difficult to process and handle of all powders. Fine powders are characterized by cohesive behavior. Inter-particle surface forces, such as Van der Waals force, capillary force, electrostatic force and the like, are relatively strong. They play an important role in particle agglomeration which results in poor flow behavior. Many efforts have been made to improve the flowability using techniques such as aeration, vibration, and coating or blending with nanometer size particles [1, 2, 3, 4, 5] ; and there is an increasing use of the coating of fine particles (or flow conditioners) on the primary (or host) powder particles to improve the flowability of the otherwise cohesive powders. Experimental investigations on the effects of particle coating have been reported [6, 7]. By measuring the rheological parameters of bulk powder structure, represented by tensile strengths and plastic deformation coefficients of bulk powders, Kono et al. [7, 8] studied the working mechanism of flow conditioners (anti-caking agents, glidants or lubricants) under small deformation. Hollenbach et al. [9] demonstrated that the bulk properties of treated powder as a solid are strongly influenced by interactions between the host powder and the conditioner particles. However, a basic understanding of the underlying improved flowability mechanism on the microscopic level is lacking [5]. Quantitative modeling of powder flows in the presence of coating particles is scarce.

It has long been recognized that the attractive force between adjacent particles is responsible for the cohesive behavior. A better understanding of the flow of the cohesive powders would most likely come with a better understanding of the inter-particle forces. Visser [5] pointed out that the dominant interactive force between fine particles is the Van der Waals force of attraction. Other attractive forces, such as capillary and electrostatic forces, may also operate; but in general, they are smaller than the omnipresent Van der Waals force.

---

*Gainesville, FL 32611, USA

[†] Received November, 1996

For most of dry processes, the capillary force is negligible. The electrostatic force may be controlled by humidity.

In quantitatively discussing the effect of particle coating on reducing cohesion between the host particles, the Van der Waals force is difficult to use directly since it is singular upon the contact of two surfaces. Specifying an initial separation distance may be appropriate in some cases but the result will be very sensitive to the initial separation distance (*c.f.* Visser [5]). It is also difficult to implement in the simulation, modeling, or any quantitative estimation of powder flow behavior. From the view point of modeling cohesive powders, the following issues must be addressed:

i. How do coating particles change the microscopic behavior of the powder?
ii. How does the size of the coating particles affect cohesion and the flowability of the powder?
iii. How does the coating of fine particles affect the rheological behavior of the powder flow when the powder is in motion?

In this paper, the effects of fine particle coating on the surface of host powder particles is quantitatively examined. The first two issues will be addressed by extending the JKR theory [10] for the force-displacement relationship between two primary host particles in the presence of a coating particle and accounting for both the elastic deformation and the attractive Van der Waals force. Surface energy is used to represent the effect of Van der Waals force in order to model the force-displacement relationship at contact. Except for cases involving high pressure, high density compaction or high velocity impact, the deformation on the surface of the powder upon contact may be considered to be within the elastic range. The extended JKR theory shows that the cohesion force between two primary powder particles in the presence of a fine coating particle is directly proportional to the size ratio of the coating particle to the host powder particle resulting in a drastic reduction in the cohesion force. The third issue raised above is more involved. It is addressed by presenting the results obtained from a discrete element simulation of powder flows between a moving and stationary plate to illustrate the effect of coating on the velocity and concentration profiles. The model and simulation results indicate that the exact number of coating particles has only minor effect on the flowability once the cohesion force is reduced by one or more coating particles. For coated particles, the angle of repose is noticeably smaller than that for uncoated ones. For a gravity driven powder flow through a funnel, the treated powder flows easily while blockage occurs frequently with the untreated powders. Test results also show the angle of repose and flow rate are not sensitive to the exact number of coating particles on the host particle surface resulting from two different coating methods.

2. Reduction of the cohesion force and stiffness in the force-displacement relationship via particle coating

Consider the deformation of two primary powder particles of size R_1 and R_2 under a load P as shown in **Fig. 1**. In the absence of a fine particle, the JKR theory [10] gives

$$P=\frac{4E^*a^3}{3R^*}-2\sqrt{2\pi\Gamma E^*a^3}, \tag{1}$$

$$\alpha=a^2/R^*-\sqrt{2\pi\Gamma a/E^*}, \tag{2}$$

where

$$\frac{1}{R^*}=\frac{1}{R_1}+\frac{1}{R_2}, \tag{3}$$

$$\frac{1}{E^*}=\frac{1-\nu_1^2}{E_1}+\frac{1-\nu_2^2}{E_2}. \tag{4}$$

In the above, α and Γ are the relative displacement and the energy of cohesion of both surfaces, a is the radius of the contact area, E and ν are Young's modulus and Poisson ratio of the materials. For identical spheres, $R^*=R_1/2$. In (1) & (2), the respective first terms on the right hand side (RHS) result from the elastic deformation while the respective second terms result from the surface force. Due to the attractive surface force, the maximum tensile force $(-P_c)$ which is required to separate the particles at contact is given by

$$-P_c=\frac{3}{2}\pi\Gamma R^*. \tag{5}$$

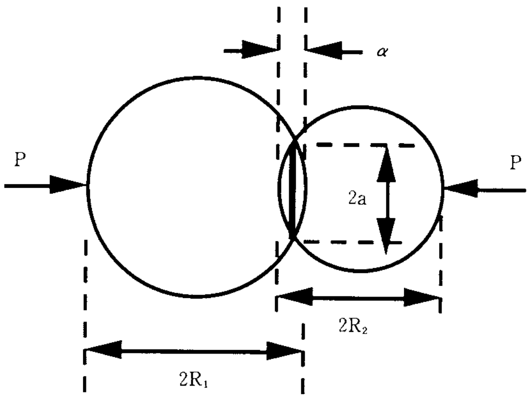

Fig. 1 Deformation of two primary particles under a load P.

At the point of separation, the displacement is given by

$$\alpha_s = -\frac{3}{4}(\pi^2 \Gamma^2 R^* / E^{*2})^{1/3}. \tag{6}$$

The maximum separation force $-P_c$ can also be interpreted as the adhesion force between two primary powder particles. If the effect of the surface energy is small, the second terms on the RHS of eqns. (1-2) may be neglected, and the force-displacement relationship for Hertzian contact results,

$$P = \frac{4}{3} E^* R^{*1/2} \alpha^{3/2} \qquad \text{for } \Gamma = 0. \tag{7}$$

For a fine particle of radius $R_2 = R_f \ll R_1$ in contact with the primary powder particles, R^* is approximately equal to R_f, as easily seen from (3).

Effect of one coating particle in the contact area

Consideration is now given to the load-displacement relationship between two identical spheres in the presence of a very fine coating sphere of radius $R_f \ll R_1$ as shown in **Fig. 2**. Assuming that the load is small so that the Hertzian contact theory can be applied locally at each contact, the force-displacement relationship at each contact is given by (1). In general, the material of the coating particle is different from that of the powder so that each material possesses different surface energy. The effective surface energy at the contact of dissimilar materials is given by

$$\Delta\gamma = \gamma_1 + \gamma_2 - \gamma_{12}. \tag{8}$$

where γ_1 and γ_2 are the intrinsic surface energies of solids 1 and 2 and γ_{12} is the energy of the interface in contact. For same materials, $\gamma_{12} = 0$ so that $\Delta\gamma = 2\gamma = \Gamma$ and is sometimes referred to as the cohesional energy. Since there are two contacts on the coating particle, the total displacement due to the relative motion of the host particles

$$-\alpha = \sqrt{(x_1 - x_2)^2 + (y_1 - y_2)^2 + (z_1 - z_2)^2} - 2R_1 - 2R_f \tag{9}$$

contributes only half to the surface deformation at contact, where (x_i, y_i, z_i) are the coordinates at the center of the ith host particle. Hence,

$$\frac{1}{2}\alpha \sim \frac{a^2}{R_f} - \sqrt{2\pi\Delta\gamma a / E_f^*}. \tag{10}$$

The load-contact area relationship at the contact is given by

$$P \sim \frac{4E_f^* a^3}{3R_f} - 2\sqrt{2\pi\Delta\gamma E_f^* a^3}. \tag{11}$$

In the above,

$$E_f^{*-1} = \frac{1-\nu_1^2}{E_1} + \frac{1-\nu_f^2}{E_f} \tag{12}$$

is the inverse of the effective Young's modulus of the primary particles in the presence of fine coating particles. The cohesion force, which must be overcome in order to separate these two primary particles, in the presence of a fine coating particle, is thus

$$-P_{cf} \sim \frac{3}{2}\pi\Delta\gamma R_f. \tag{13}$$

At the point of separation, the displacement is

$$\alpha_{sf} \sim -\frac{3}{2}\left[\frac{\pi^2(\Delta\gamma)^2 R_f}{E_f^{*2}}\right]^{1/3}. \tag{14}$$

Comparing (13) with (5), it is easily concluded that for a comparable surface energy, $\Delta\gamma/\Gamma = O(1)$, the cohesion force in the presence of a fine coating particle is much smaller than that for the untreated powders,

$$\frac{-P_{cf}}{-P_c} = \frac{2R_f}{R_1}\frac{\Delta\gamma}{\Gamma} \ll 1 \qquad \text{for } \frac{R_f}{R_1} \ll 1. \tag{15}$$

For a typical case of $R_f \sim 100$ nm and $R_1 \sim 5$ μm, it gives $2R_f/R_1 \sim 0.04$ which implies an order of magnitude drop in the cohesion force. Due to the drastic reduction in the cohesion force, $-P_{cf} \ll -P_c$, it is much less likely for the powders to adhere upon collision during flow.

The reduction in P_c also implies that the repulsive force due to elastic deformation now dominates over the surface force because of a much smaller value of R_f in (11). Neglecting the effect of $\Delta\gamma$ in (11), a leading order approximation for the force-displacement relationship is obtained

$$P \sim \frac{4E_f^* a^3}{3R_f} = \frac{4E_f^*}{3R_f}\left(\frac{\alpha R_f}{2}\right)^{3/2} = 2^{-3/2}\frac{4}{3}E_f^* R_f^{1/2}\alpha^{3/2} \tag{16}$$

which is valid except in a very small neighborhood near $\alpha = 0$. Near $\alpha = 0$, the absolute error in the P-α relationship given by (16) is still small due to a much reduced cohesion force $-P_{cf}$. It is interesting to note that while the cohesion force is reduced by a factor of $R_1/2R_f$, the stiffness is only reduced by a factor of $2(R_1/R_f)^{1/2}$ by comparing (7) with (16). In essence, the force-displacement relationship for the primary powder particles in the presence of coating

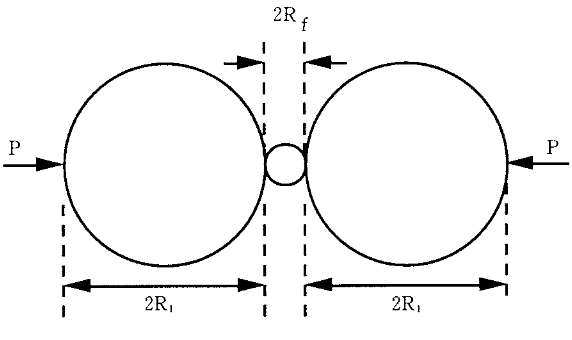

Fig. 2 A coating particle between two primary powder particles

particle behaves like that of cohesionless granular particles with a reduced stiffness (associated with the elastic deformation) for a given relative particle displacement α.

The importance of eqn. (15) is that it quantitatively relates the reduction in the cohesion force between two primary powder particles to the size ratio of the coating particle to the host powder particle. This quantitative relationship is not possible if the attractive surface force is described using the Van der Waals force expression due to the singular nature of the force at contact. The asymptotic relationship given by (16) clearly shows how the size of the coating particle, R_f, quantitatively changes the microscopic response of the powder particles to variations in the relative displacement.

Effect of multiple coating particles in the contact area

In reality, there may be more than one coating particle in the vicinity of the contact point between two host particles as shown in **Fig. 3**. Thus it is necessary to consider the effect of neighboring coating particles on the P-α relationship. Assuming that all coating particles adhere to host particles, it can be estimated that the average number of coating particles on the surface of each host powder particles is

$$n = x\frac{\rho_1}{\rho_f}\left(\frac{R_1}{R_f}\right)^3 \tag{17}$$

where x is the mass fraction of the coating particles, and ρ denotes density. Since the surface area of a spherical powder particle available for coating particle is $4\pi R_1^2$, the number of coating particles per unit surface area is $n/4\pi R_1^2$. It is easily seen that the average center-to-center distance, L, among the coating particles on each powder particle surface is

$$L = (4\pi R_1^2/n)^{1/2}. \tag{18}$$

However, in the contact region the other host powder particle also has, on average, an equal number of coating particles on its surface. Effectively, the area concentration of the coating particle at contact is double the amount given by (17) so that

$$\frac{L}{R_f} = \left[\frac{2\pi}{x}\frac{\rho_f}{\rho_1}\frac{R_f}{R_1}\right]^{1/2}. \tag{19}$$

For a typical case with $x=0.01$, $\rho_1 \sim \rho_f$, $R_1=5$ μm, and $R_f=0.1$ μm, the above gives $L/R_f \sim 3.5$.

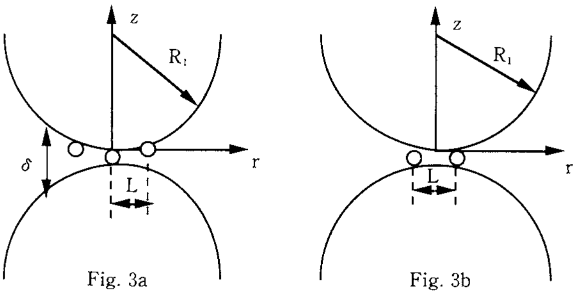

Fig. 3a

Fig. 3b

Fig. 3 Schematic of multiple coating particles near the contact point $(r, z)=0$ between two primary particle of radius R_1.

For a coating particle centered at $(r, z)=0$ as shown in **Fig. 3a**, the surface-to-surface distance between the host particles at r before the deformation is

$$\delta(r) \sim 2R_f + r^2/R_1 \qquad \text{for} \quad r \ll R_1. \tag{20}$$

At $r \sim L$, eqns. (19)~(20) give

$$\frac{\delta(L)-2R_f}{R_f} \sim \frac{2\pi}{x}\frac{\rho_f}{\rho_1}\left(\frac{R_f}{R_1}\right)^2. \tag{21}$$

For the typical case under consideration ($x=0.01$, $R_f/R_1=0.02$), one obtains $(\delta-2R_f)/R_f \sim 0.25$. This implies that the central coating particle in **Fig. 3a** would have deformed significantly before the neighboring coating particles can even contact with the other primary particle. Thus it is unlikely that the neighboring coating particles have an effect on the P-α relationship between two primary particles in this configuration.

However, for the configuration shown in **Fig. 3b**, it is possible to have 3 or even more coating particles undergoing simultaneous deformation between two host powder particles. As a first approximation, it is assumed that the mutual interaction caused by the neighboring coating particles on the global deformation of host particles be neglected so that each contact can be treated independently. Since the coating particles are close to $(r, z)=0$, the deformation may be treated as if each coating particle is at $(r, z)=0$. Thus the linear superposition gives the following approximate P-α relationship,

$$P \sim m\left(\frac{4E^*a^3}{3R_f} - 2\sqrt{2\pi\Delta\gamma E^* a^3}\right) \tag{22}$$

$$\alpha/2 \sim a^2/R_f - \sqrt{2\pi\Delta\gamma a/E^*} \tag{23}$$

where m is the number of fine particles in contact. Due to multiple contacts, the cohesion force $(-P_{cfm})$ is now given by

$$-P_{cfm} = m\frac{3}{2}\pi\Delta\gamma R_f. \tag{24}$$

Since the configuration in **Fig. 3b** is more stable than that in **Fig. 3a** in a nearly static condition and it takes three points to support a surface, it is conceivable that m may take a value of 3 when the particle collision velocity is low and the coating is dilute. At a high particle collision velocity, the particle collision time is shorter so that it is conceivable that the deformation may center only on one coating particle. Although the value of m is not known in general and a probabilistic approach for choosing m may be better to describe the effects of multiple coating particles, it is noted that a reduction in the cohesion force by a factor of $R_1/2mR_f$ is still quite significant even for $m=3$.

Fig. 4 shows the dimensionless force-displacement curve between two primary powder particles for three cases: i) no coating particle; ii) one coating particle ($m=1$); and iii) three coating particles ($m=3$). The scales $-P_c$ and $|\alpha_s|$ are given by (5-6). The size ratio is $R_f/R_1=0.02$ and $\Delta\gamma=\Gamma$. It is seen that the tensile portion of the P-α curve is drastically reduced in the presence of coating for both $m=1$ and 3. The slope of the curve, which is a measure of the stiffness, is also reduced for $m=1$ and 3. It is important to recognize that once the cohesion force becomes insignificant the powder behaves essentially as cohesionless granular particles, and the macroscopic behavior of the granular flow is in general insensitive to the exact stiffness. Thus, there should be only small differences in using either $m=1$, 2 or 3 in the discrete element simulation which allows the effect of fine particle coating on powder flow to be studied. As long as m is not very large the dynamic behavior of the powder flow should not be very sensitive to the exact concentration of coating particles. This hypothesis will be explored next.

3. Discrete element simulation for powders in a Couette flow

The numerical method used in this work is described in detail in Walton & Braun [10] and Walton [11]. The motions of a large number of individual particles between a plate moving with a constant velocity V and a stationary plate of height H are tracked (**Fig. 5**). A square array of hemispheres are placed on both plates to simulate the roughness of the wall or the effect of a moving layer of the same powder. The interactions among powder particles and between the particles with the wall are described by the above extended JKR model for the force-displacement relationship. Periodic boundary conditions are imposed on the mean flow (x) direction and the spanwise (z) direction. After the steady state is reached, the time-area averaged velocity and concentration profiles between the plates are analyzed. To illustrate the effects of coating on the macroscopic behavior of the powder, two average volume concentrations (ϕ_0) of the powders are considered. They are $\phi_0=0.42$ and 0.53. The rest of the parameters are kept the same and are given as follows. The velocity of the moving plate is $V=3.0$ m/s. $\Gamma=0.2$ N/m is used for untreated powder and $\Delta\gamma=0.2$ N/m is used for the treated powder. The radii of particles are $R_1=10$ μm and $R_f=0.1$ μm with $E_1=6\times10^{10}$ N/m^2, $\nu_1=0.25$, $\rho_1=2.6\times10^3$ kg/m^3, $E_f=6\times10^{10}$ N/m^2, and $\nu_f=0.25$. The friction coefficient (which is used in determining the maximum tangential contact force) is 0.4. A large value of H ($=60R_1$) is chosen so that the actual location of the stationary plate has little effect on the velocity profile of untreated powder. $L=W=18R_1$ are used.

Fig. 6a compares the mean velocity profiles, $u=V_x/V$, of the powder for treated ($m=1$ & 3) and untreated powders at a mean particle concentration $\phi_0=0.53$. The y-coordinate is normalized by H as $\eta=y/H$. Only a thin layer of the untreated powder

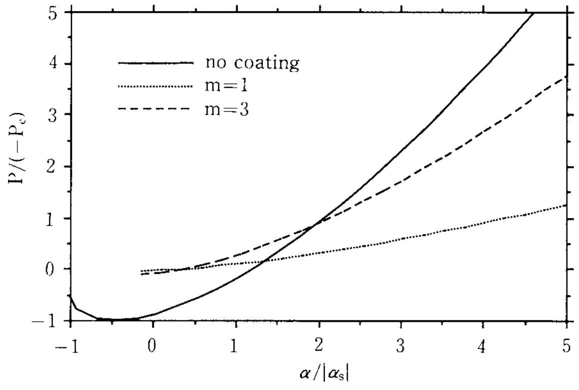

Fig. 4 Force-displacement relationship for primary particles with no coating, with one and three coating particles ($R_f/R_1=0.02$).

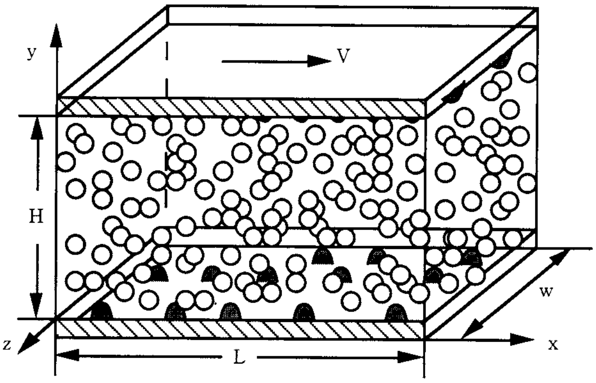

Fig. 5 Schematic of Couette flow simulation for cohesive powder.

moves under the shearing of the moving plate. The rest of the untreated powder remains nearly stationary, like a solid due to strong cohesion. For the treated powders ($m=1$ & 3), the particles in the middle region move as a plug with relative ease. The difference in the velocity profiles between $m=1$ and $m=3$ for the treated powders does exist ; but the difference is much smaller than between $m=3$ and the untreated powder. **Fig. 6b** compares the concentration profiles $\phi(y/H)$ for the treated and untreated powders under the same conditions. The treated powders ($m=1$ & 3) have more uniform distributions than the untreated powder. The particle concentration ϕ is around 0.56 in the lower shear region and is around 0.5 near $\eta \sim 1$. For the untreated powder, the particle concentration in the region $0.7 < \eta < 1$ where $\frac{\partial u}{\partial \eta}$ is finite is noticeably lower than that in the low shear region where $\phi \sim 0.58$ for $0.0 < \eta < 0.7$. Apparently, particles migrate from regions of high shear to regions of low shear. In the high shear region, the random fluctuating velocity component (or the kinetic energy) of the particle is also large and particles have larger mean free path than in the lower shear region. Since a larger mean free path implies a lower concentration, the lower shear region always has higher concentration than the high shear region if sufficiently long time is given to allow particles to adjust. However, this shear induced migration of particles is not so effective at $\phi_0=0.53$ for the treated particles as seen from **Fig. 6b**. Thus, coating at this high concentration range seems to reduce the extent of shear induced migration. Only small differences in the velocity and concentration of the treated powders between $m=1$ and $m=3$ are observed. This is consistent with the observation that the macroscopic behavior is insensitive to the actual number of coating particles.

Figs. 7a-b compares the mean velocity and concentration profiles of the powder for treated ($m=1$

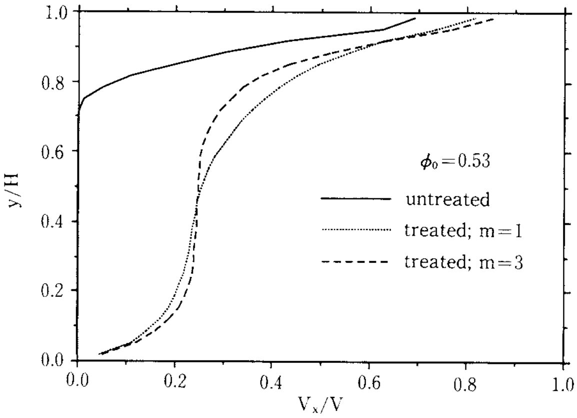

Fig. 6a Velocity profiles of treated ($m=1$ & 3) and untreated powders at average particle concentration $\phi_0=0.53$.

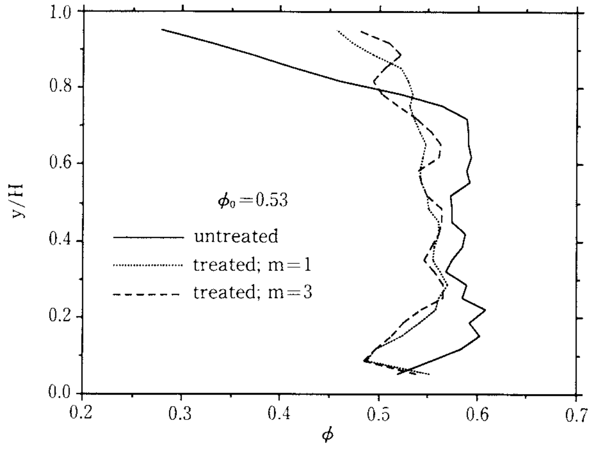

Fig. 6b Concentration profiles of treated ($m=1$ & 3) and untreated powders at average particle concentration $\phi_0=0.53$.

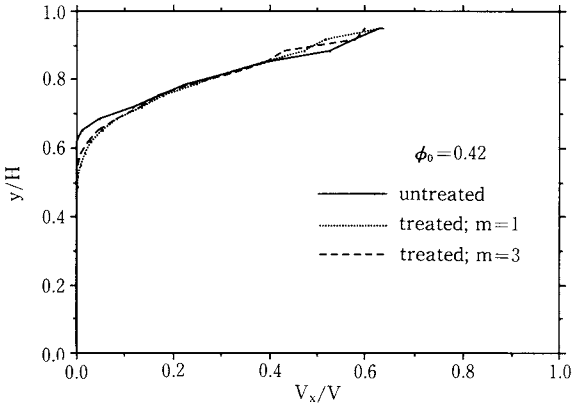

Fig. 7a Velocity profiles of treated ($m=1$ & 3) and untreated powders at average particle concentration $\phi_0=0.42$.

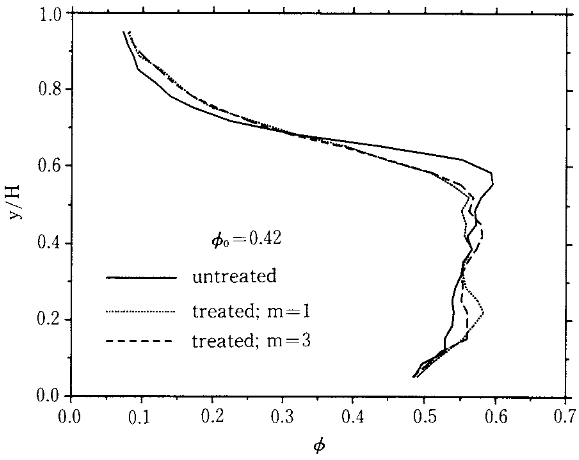

Fig. 7b Concentration profiles of treated ($m=1$ & 3) and untreated powders at average particle concentration $\phi_0=0.42$.

& 3) and untreated powders at a lower average particle concentration ($\phi_0=0.42$). While there is indeed very little difference in the velocity and concentration profiles for the treated powders between $m=1$ and $m=3$, the difference between untreated powder and the treated powder ($m=3$) is small as well, in contrast to the case with $\phi_0=0.53$. Apparently, the coating has little effect on the steady state average particle velocity and concentration profiles. This result appears surprising since $\phi_0=0.42$ cannot be considered as a truly low concentration case. It is interesting to note, however, that the concentration profiles for all three cases are highly non-uniform. The shear induced migration causes the powder to move to the low shear region ($0<\eta<0.5$). In the low shear region, the particle concentration is around 0.56 which is close to that of the treated powder in the case of $\phi_0=0.53$. Comparing **Fig. 6b** with **Fig. 7b**, it is seen that for $\phi_0=0.42$, the shearing at $\eta=1$ drives powder to the region of the lower shear and packs the powder to a concentration of around $\phi\sim0.56$. The rest of the powder is then distributed continuously in the high shear region. Using a linear variation to roughly approximate the concentration ϕ at $0.5<\eta<1$, the average concentration in the flow field is $\phi_0\sim0.56\times0.5+\frac{1}{2}(0.56+0)\times0.5=0.42$. Thus, for $\phi_0=0.42$, the dominant factor in determining the macroscopic behavior of the powder is the shear induced migration, whether the powder is coated or not. After a significant portion of the powder migrates to the lower shear region, the local concentration in the high shear region is much lower than the mean concentration and collisions occur less frequently so that the effect of fine particle coating is not as significant. Yet, small differences in the particle concentration profiles between $m=3$ and the untreated powder can be noticed for $0.5<\eta<1$.

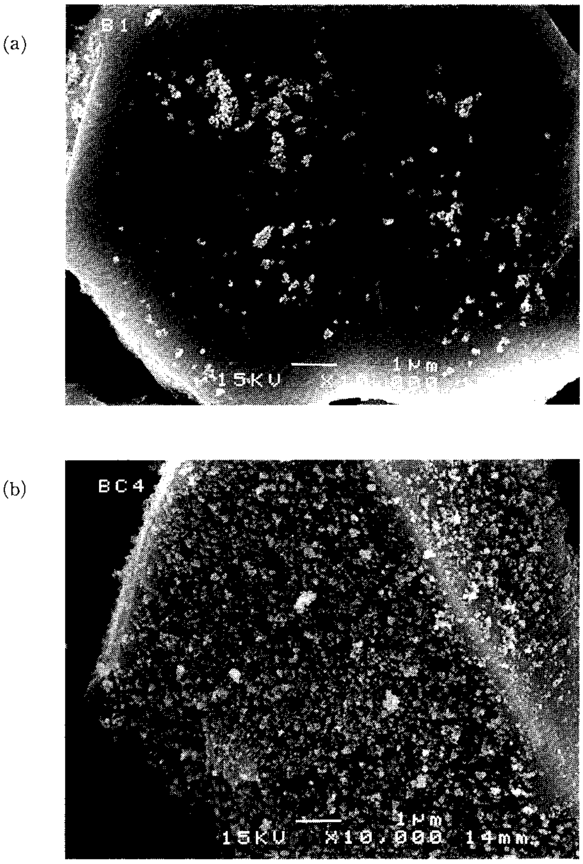

Fig. 8 Typical Scanning Electronic Microscope photographs of a) blended and b) coated powders. The untreated powder has almost smooth surface under the magnification of 10^5.

4. Experimental quantification of the effects of particle coating on powders

While the analysis on the force-displacement relationship provides insight into the mechanism of flowability improvement and the discrete element simulation demonstrates qualitatively how particle coating modifies the macroscopic velocity profile of the powder, the results are nevertheless limited to spherical particles. In reality, powder particles may be non-spherical and may have straight edges and flatter surfaces. The potential contact area can be larger than that of spherical particles. This implies a further increase in the cohesion force among untreated powder particles and a reduction in the flowability in comparison with spherical powder particles. To assess the effect of particle coating on the flowability of real powders, the static angle of repose and the gravity driven flow rate of powder through a funnel are measured for: i) silicon carbide powder coated with fine silica particles using a magnetic driven impact impingement process; ii) silicon carbide powder simply blended with fine silica particles; and iii) untreated silicon carbide powder. The untreated powder has a mean diameter of 10 μm and the coating particle has a mean diameter of 100 nm. **Fig.** 8 shows the surface morphologies of these two treated powders, obtained from Scanning Electronic Microscope photographs. It is noted that simple blending results in significantly less fine particles on the surface of the powder.

To measure the angle of repose, a pile of powder is prepared, illuminated with a light source, and projected on a screen. The image of the pile is recorded on a film negative from which the angle of repose is measured. The average value is obtained from 4 samples for each case. Table 1 compares the measured angle of repose for three cases. The angles of repose of the two treated powders are clearly lower than that of the untreated powder. Since the host powders are the same in these three cases, the reduction in the angle of repose is the direct consequence of the reduced cohesion force due to the presence of fine coating particles.

Table 1 also compares the mean and standard deviation of the flow rate (gram/sec) through a funnel obtained over 100 measurements for each case. The funnel is fabricated from Plexiglas. The cone angle is 10° and the vertical section has a length of 60 mm and discharge diameter of 5 mm. For the untreated powder, the flow is frequently blocked and the measurement is not meaningful. The treated powder flows easily. There is little difference in the measured flow rate for powders treated with blending and with coating. Although there are many more fine particles on the surface of host particles generated by the coating process than by simply blending (see **Fig.** 8), there is little difference in the angle of repose and flow rate with a nominal 1% mass fraction of the fine particles. This is consistent with the observation that the exact number of coating particles on the host particle surface has only minor effect on the flowability once the cohesion force is reduced by one or more coating particles.

Table. 1 Comparisons of angle of repose and flow rate through a funnel for untreated and treated powders

		untreated	blended	coated
Angle of repose		47.5°	36.5°	39.5°
Flow rate	mean(g/s)	(no flow)	21.3	23.3
	standard dev.(g/s)		4.2	5.3

5. Summary

The extended JKR model for the force-displacement relationship shows that the reduction in the cohesion force between two primary particles is proportional to the size ratio of the coating particle to the host powder particle. The drastic reduction in the cohesion force results in an improved flowability. For Couette flow at high average concentration, when the shear induced migration is not dominant, the treated powder exhibits a fluid-like behavior while the untreated powder shows a solid-like behavior under otherwise identical shearing conditions. When the shear induced migration dominates the mean flow behavior of the powder, the effect of coating is not obvious. The macroscopic behavior of the powder flow is not sensitive to the exact number of coating particles on the surface of host particles. Measurements of angle of repose and flow rate in a funnel support the results from the analysis and simulation.

The authors acknowledge the financial support of the Engineering Research Center (ERC) for Particle Science & Technology at the University of Florida, the National Science Foundation (EEC-9402989), and industrial partners of the ERC. Dr. O. R. Walton provided the Shear3D Code which serves as the basis for the present simulation of cohesive powder flow. The support and encouragement of Dr. W. Hendrickson at Aveka, Inc. are greatly appreciated.

Nomenclature

a : particle contact radius [m]
E : Young's modulus [N/m^2]
H : height of the Couette flow cell in simulation [m]
L : average distance between coating particles [m]
m : number of coating particles at contact [−]
P : loading on particle [N]
R : particle radius [m]
V : velocity of powder [m/s]
x : mass fraction of coating particles [−]

Greek Symbols:
α : displacement [m]
ϕ : volume concentration of solids [−]
$\Gamma, \Delta\gamma$: surface energy [N/m]
γ : intrinsic surface energy [N/m]
ν : Poisson ratio [−]
ρ : material density [kg/m^3]

Subscript:
c : cohesive force
f : in the presence of fine particles
m : multiple coating particles at a contact
s : separation
x : flow direction
1,2 : material 1 and 2

1. References

1) Wes, G. W. J., S. Stemerding and D. J. van Zuilichem : Control of Flow of Cohesive Powders by Means of Simultaneous Aeration and Vibration, *Powder Tech.* 61, 39-4 (1990)
2) Dutta, A. and L. Dullea : Effect of External Vibration and the Addition of Fibers on the Fluidization of a Fine Powder, *AIChE Symp. Ser.* No. 281 Vol. 87, 38-46 (1991).
3) Jaraiz, E., S. Kimura, and O. Levenspiel : Vibrating Beds of Fine Particles : Estimation of Interparticle Forces from Expansion and Pressure Drop Experiment, *Powder Tech.* 72, 22-30 (1992).
4) Liu, Y.-D. and S. Kimura : Fluidization and Entrainment of Difficult-to-Fluidize Fine Powder Mixed with Easy-to-Fluidize Large Particles, *Powder Tech.* 75, 189-196 (1993).
5) Visser, J. : An Invited Review : Van der Waals and Other Forces Affecting Powder Fluidization, *Powder Tech.* 58 , 1-10 (1989).
6) Molerus, O. : Effect of Interparticle Cohesive Forces on the Flow Behavior of Powders, *Powder Tech.* 20, 161-175 (1978).
7) Kono, H. O., C. C. Huang and M. Xi : Function and mechanism of flow conditioners under various loading pressure conditions in bulk powders, *Powder Tech.* 63, 81-86 (1990).
8) Kono, H. O., C. C. Huang and M. Xi : The effect of flow conditioners on the tensile strength of cohesive powder structures, *AIChE Symp. Ser.*, No. 270, Vol. 85, 44-48 (1989).
9) Hollenbach, A. M., M. Peleg & R. Rufner : Interparticle Surface Affinity and the bulk properties of conditioned powders, *Powder Tech.* 35, 51-62 (1983).
10) Johnson, K. L., K. Kendall and A. D. Roberts : Surface Energy and the Contact of Elastic Solids, *Proc. R. Soc. Lond.* A. 324, 301-313 (1971)
11) Walton, O. R. and R. L. Braun : Viscosity, Granular-Temperature, and Stress Calculations for Shearing Assemblies of Inelastic, Frictional Disks, *J. Rheology,* 30, 949-980 (1986).
12) Walton, O. R.: Numerical Simulation of Inclined Chute Flows of Monodisperse, Inelastic, Frictional Spheres, *Mechanics of Materials,* 16, 239-247 (1993).

Author's short biography

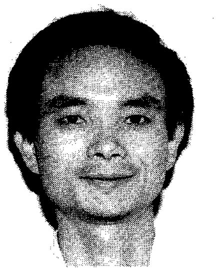

Renwei Mei

Dr. Renwei Mei is an Associate Professor in the Department of Aerospace Engineering, Mechanics & Engineering Science at the University of Florida. He received his B.S. in 1982 at Zhejiang Univeristy, China, and his Ph.D. in 1990 at University of Illinois at Urbana-Champaign. He joined the University of Florida as a faculty in 1990. His research interests include particulate multiphase flows and boiling heat transfer.

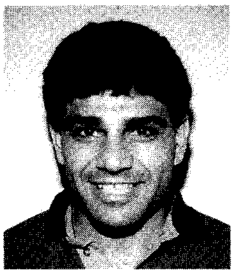

James F. Klausner

Dr. James Klausner is an Associate Professor in the Department of Mechanical Engineering at the University of Florida. In 1984 he received his B.S. degree in Marine Engineering from the United State Merchant Marine Academy and his M.S. and Ph.D. in Mechanical Engineering from the University of Illinois at Urbana-Champaign in 1986 and 1989, respectively. He joined the University of Florida in 1989 and has been engaged in research in multiphase flow and boiling heat transfer, photocatalytic oxidation, energy storage, and particulate mechanics.

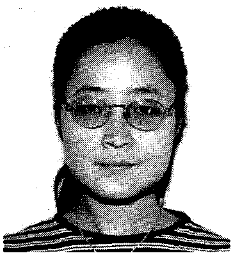

Hong Shang

Hong Shang received her B.S. and M.S. in Fluid Machinery Engineering in June 1988 and 1991, respectively, at Xi'an Jiaotong University, China. Currently she is working towards her Ph.D in powder flow mechanics at the Univeristy of Florida.

Elizabeth Kallman

Elizabeth Kallman received her B.S. in Mechanical Engineering in 1995 at the University of Florida. She is currently pursuing her Ph.D degree at UC Berkeley.

Research

A Laser-Optical-Sheet Based Technique for Monitoring Particle Charge Distributions[†]

Qin Tang, M.S. Klima and S. Chander
Mineral Processing Section
*The Pennsylvania State University**

Abstract

A system utilizing a coherent sheet of light obtained by a pulsed laser and appropriate optical components was developed to monitor a charged particle stream as it passes through an electric field. The deflection patterns of narrowly sized quartz particles (74×53 μm) were photographed and analyzed by a densitometer. The deflection and dispersion of a spot, representing a group of particles, can be used to determine the average charge and charge distribution in the particle stream. The results demonstrate the efficacy of this technique for determining the charge distribution of a particle stream. Such a device has the potential for monitoring particle charge in continuous airborne particulate streams.

1. Introduction

The prediction and control of electrostatic charge in a particle stream is important in various processes including electrophotography [1], electrostatic powder coating [2], electrostatic precipitators [3], electrostatic separation [4, 5,], powder handling [6], etc. Therefore, it is often desirable to measure the electric charge distribution of a particle stream rather than only the average charge-to-mass ratio. Such measurements are often required on a suite of particles rather than for individual particles. Further, a technique that can provide a rapid analysis, yet be simple in operation would be particularly useful for on-line monitoring.

The classical method uses a Faraday cup or "pail" coupled to a suitable monitoring circuit to measure the surface charge of an individual particle or the average charge for a group of particles [7, 8]. Based on the Faraday cup approach, the "blow-off" tribo method was developed [9] and improved [10] for measuring the average electric charge on a known amount of toner particles in electrophotography. Inculet [5] suggested using a Faraday cage-type instrument, called a "Separation Tower", to perform charge-to-mass ratio measurements. With this method, the average, net charge on some amount of particles is measured, but the magnitude and the sign of the charge on individual particles cannot be determined. Thus, this method is incapable of detecting a bipolar charging system, which is sometimes observed for powders.

Another approach for measuring the charge on the surface of a particle or droplet is based on Millikan's oil droplet experiment [11]. Several modified Millikan's apparatuses were used to measure the electric charge on a single particle [12-17]. The basic principle of Millikan's approach is rather simple. However, the charge measurements are tedious and time-consuming, because the particles must be measured, one at a time, to obtain a statistically meaningful distribution. Moreover, it becomes more difficult to trace each particle as the particle size decreases. As such, it is primarily used as a research tool and is not commercially available or suitable for industrial applications.

Charge spectrometers, commonly used in investigating the electrical behavior of commercial electrophotographic powders, have been used to measure the distribution of toner charge indirectly [18-21]. The spectrometer is particularly powerful because it can directly measure the amount of charge on toner particles. However, the concentration of toner particles must be kept low enough to minimize the number of touching particles but large enough to provide a statistically meaningful number of counts. Particle clusters or agglomerates would provide incorrect information about the particle size and electric charge. Another problem is that the collecting filter must be grounded to prevent the charge on the captured toner particles from distorting the trajectory of incoming particles. However, grounding the filter distorts the electric field at the

---

*University Park, PA 16802, USA

[†] Received February, 1997

bottom of the charge spectrometer. A modification of this technique was suggested by Takahashi et al. [22]. The problems associated with this modification are the long measurement time, complexity of operation, and poor separation of the toner particles from the carrier particles. Other charge characterization techniques used in electrophotography were reported by Kutsuwada et al. [23] and Mazumder et al. [24].

Several methods have been used for determining the charge distribution of an aerosol. Most of these methods are based on the measurement of the electrical mobility distribution of monodisperse or size-classified particles. Instruments used for measuring electrical mobility include the Millikan cell [25-28], parallel-plate electrical mobility spectrometer [29-33], and concentric electrical mobility analyzer (e.g., electric aerosol analyzer and differential-mobility analyzer) [34, 35]. A commercially available electrical aerosol analyzer and a differential mobility analyzer with a concentric configuration were developed mainly for particle-size measurement. However, if the particle size is determined by an independent method, such as an optical particle counter, these devices can also be used for the determination of the particle charges [34, 35].

An apparatus, utilizing a laser-based Phase Doppler Particle Analyzer (PDPA) for monitoring the particle component velocities, size, and number density, was developed to determine the charge on small particles [36]. This method provides high-speed data collection on a particle-to-particle basis. However, the major drawback of this approach is the high cost and complexity of the system.

A review of existing charge measurements shows that either the methods are only related to the average charge-to-mass ratio or the methods with charge distribution measurement have certain disadvantages, discussed above. In this paper, a new technique is developed, which allows the charge distribution of a particle mixture to be analyzed. For this study, the electrostatic charge on narrowly sized quartz particles was analyzed. This approach is presented and discussed, along with the results from the initial tests.

2. Experimental Approach

The basic principle of this new approach is based on the deflection of charged particles by an electric field. This approach is similar to the others in which particles are introduced into a laminar air flow stream across which an electric field is applied. The deflected distance of the particle is then a function of the charge on the particle. However, in the current approach, the trajectory of the entire particle stream in the electric field is recorded as it passes through a laser sheet, as opposed to tracing individual particles or collecting samples on the electrodes or in specially designed trays as in other techniques [5, 18-21]. This provides a means to estimate the electric charge distribution of a particle stream directly.

3. Test Set-Up

A Surelite I pulsed argon laser (Continuum) and necessary optical components including a mirror, prism, spherical lens, and cylindrical lens, were used to generate a laser sheet [37], shown in **Figure 1**. A schematic representation of the experimental set-up is given in **Figure 2a**. The test chamber (95×95×400 mm) was constructed out of 9 mm Plexiglas, with copper plates (75×75×150 mm) attached to two sides. The plates were connected to a DC power supply to vary the potential and polarity on the plates. The bottom of the separation chamber was open to the atmosphere. A slit was cut in the Plexiglas to allow the laser sheet to pass through the opening, eliminating the reflection in the chamber. The sheet was projected at 45° to the vertical plane. **Figure 2b** shows the change of spot shape in the laser sheet due to the electric force, which will be discussed later.

Crystalline quartz particles (U.S. Silica) were first wet screened at 25 μm (500 mesh), followed by dry screening. Narrow size fractions (74×53 μm) of the screened quartz were used for the charging experiments. The quartz sample was essentially pure SiO_2. The particles were tribocharged by contacting with a copper plate, attached to a vibrat-

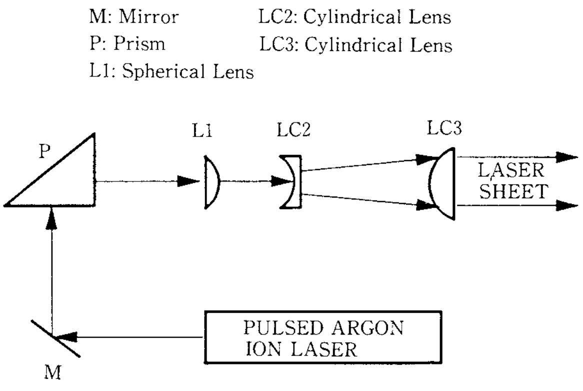

Fig. 1 Generation of laser sheet.

ing feeder, and fed into the top of the test chamber through a copper funnel. The particles fell freely through the chamber and were illuminated by the laser sheet. Photographs of the particle stream at different applied potentials were taken using a 35 mm still camera, which was placed perpendicular to the electric field.

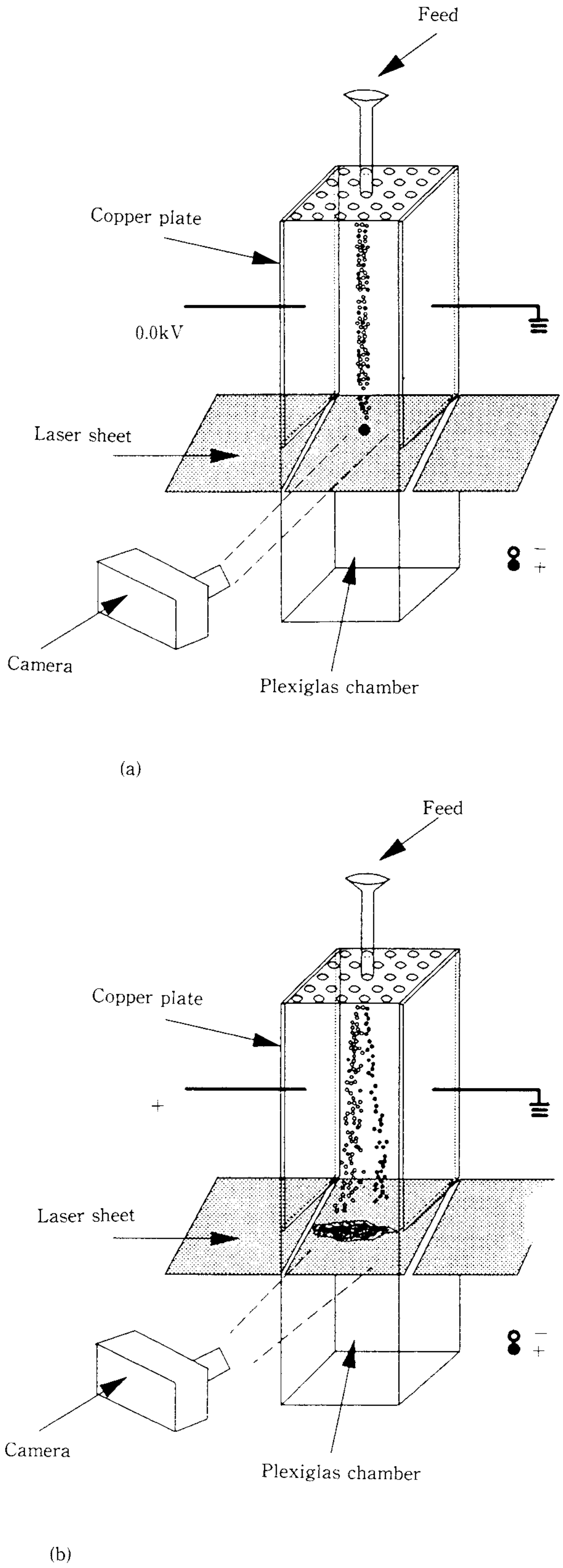

Fig. 2 Experimental set-up used for charge measurements: (a) without applied potential; (b) with applied potential.

Correct film exposure was determined by finding the proper combination of laser power, diaphragm opening (f-stop number), and exposure time (shutter speed). The Surelite I pulsed argon laser has a frequency of 20 Hz, which means a light pulse is generated every 0.05 seconds. Thus a long exposure time is required to eliminate the bias caused by the frequency of the pulsed laser. After the initial trials with different combinations of laser power, f-stop number, and exposure time, a laser power of 0.125 watts, f-stop number of 16, and exposure time of 0.5 seconds were selected. These settings provided the most consistent photographs of the particle stream. In all cases, 100 speed, black-and white Kodak film was used. Each negative frame was scanned with a Personnel Laser Densitometer to determine the optical density patterns on the frames resulting from the motion of particle in the electrical field. Image analysis was then performed on the scanned picture using the software package ImagequaNT (Molecular Dynamics, Inc.) from which the peak heights and peak positions were determined. This approach is commonly used in biotechnology research for displaying a scanned image and identifying cells based on the differences in optical density.

3. Results and Discussion

Figure 3 shows the change in the dispersion pattern with the applied potential for the quartz particles after contacting the copper plate. When no electric field was applied, the particles fell along the center line of separation chamber with almost no dispersion, as indicated by the spot in **Figure 3a**. When a positive voltage (i.e., 3.0 kV) was applied to the left electrode, the spot shifted slightly to the left side as shown in **Figure 3b**. This indicated that the particles carried more negative charges.

Davies [38] suggested that the sign of the charge that a particle or material will develop after contact is determined by the differential in work function between the particle and contact media. The work function, Ψ, is defined as the difference in potential between the Fermi level and a free electron state, where the Fermi level is the energy level at which 50% of the electron states are filled. When two materials with dissimilar work functions are contacted, the material with the higher work function gains electrons, producing a negative charge. The material with the lower work function loses electrons, producing a positive charge. This transfer occurs because the Fermi levels of materials in contact must equilibrate. Since the work function of quartz particles is higher ($\Psi=5.0$ eV) than that of copper ($\Psi=4.38$ eV), the quartz particles should charge negative, according to the solid state electron transfer theory.

As the applied potential was increased to 4.5 kV, the spot was more dispersed and moved more towards the left positive plate. No particles were found at the right side (**Figure 3c**). At higher applied potentials, the spot became narrower, and the particles were distributed between the copper plates (**Figures 3d-3f**). It can be seen that the

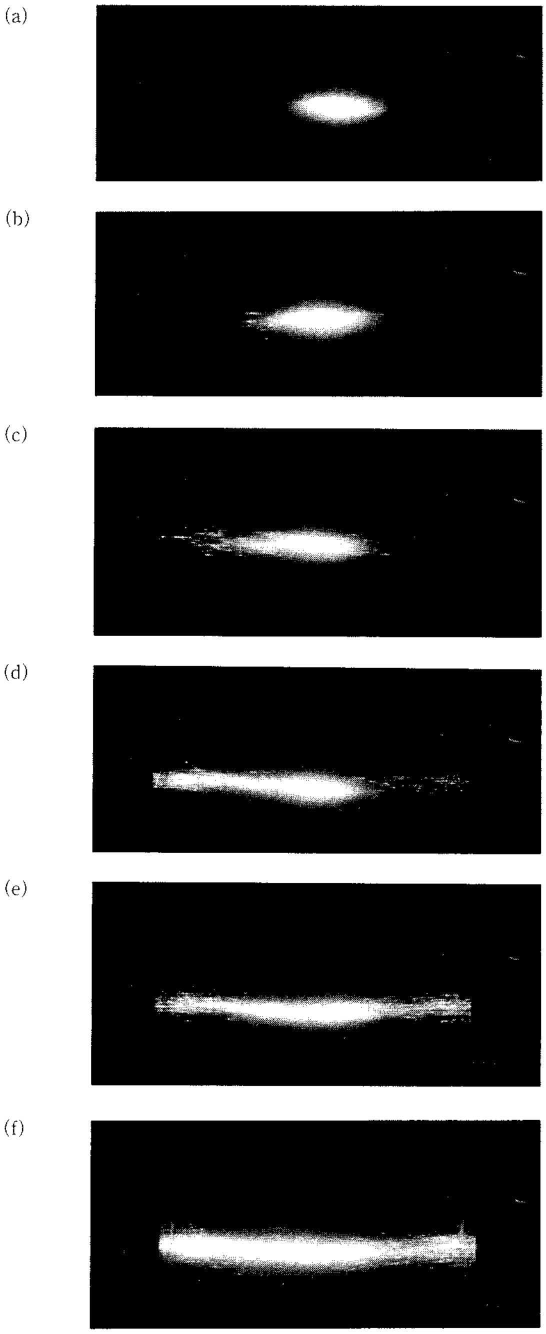

Fig. 3 Photographs of quartz particles (74×53 μm) on the laser sheet intersecting the chamber cross-section at an angle of about 45° at the bottom of the electric field after tribocharging by contact with a copper plate: (a) 0 kV; (b) 3.0 kV; (c) 4.5 kV; (d) 6.0 kV; (e) 7.5 kV; (f) 9.0 kV.

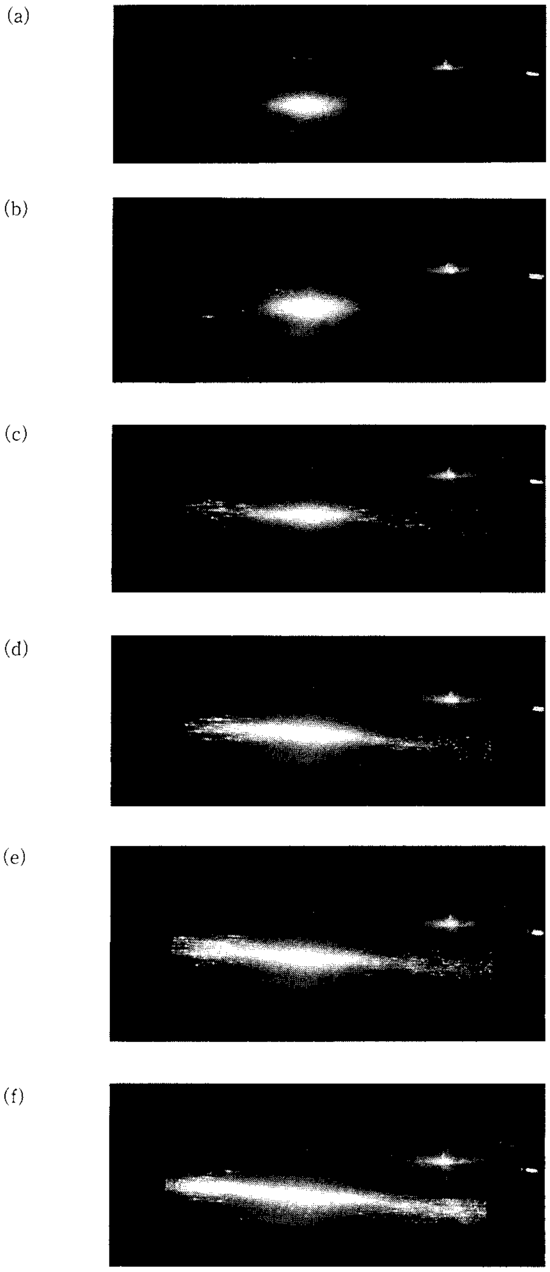

Fig. 4 Photographs of naturally charged quartz particles (74×53 μm) on the laser sheet intersecting the chamber cross-section at an angle of about 45° at the bottom of the electric field: (a) 0 kV; (b) 3.0 kV; (c) 4.5 kV; (d) 6.0 kV; (e) 7.5 kV; (f) 9.0 kV.

higher the applied potential, the greater the distribution of particles between the two plates. This occurs because the electric force is proportional to the applied potential for a given charged particle. It was found that some particles remained in the center of the chamber. One explanation for the lack of charging would be insufficient contact between the particles and copper plate while feeding. It was also observed that some particles actually deflected toward the right negative side, indicating a positive charge on the particles. This has also been found for silica particles tribocharged with copper [39]. Investigation of this phenomenon is continuing.

Figure 4 shows the change in the dispersion pattern with applied potentials for the quartz particles that were naturally charged. In this case, the particles were passed over a quartz spatula and through a glass funnel as opposed to contacting with copper. When no electric field was applied, the particles fell along the center line of separation chamber (**Figure 4a**), as in **Figure 3a**. When 3 kV was applied to the left electrode, no significant shift of the spot was observed, only some dispersion of the spot along the center separator line. As the applied potential was increased to 4.5 kV, the spot was more dispersed towards both ends (**Figure 4c**). At higher applied potentials, the spot became narrow, and the particles were evenly distributed between the separator plates (**Figures 4d-4f**). This indicates that the naturally charged particles carry about same amount of positive and negative charges.

As noted in the previous section, each negative frame was scanned with a densitometer and then subjected to image analysis. Optical density curves as a function of horizontal position in the chamber were obtained. A typical dispersion pattern as a function of the applied potential for the quartz particles is plotted in **Figure 5**. The x-axis in the figure is the actual distance along the separator chamber in the horizontal direction. The origin is defined as the center of the chamber.

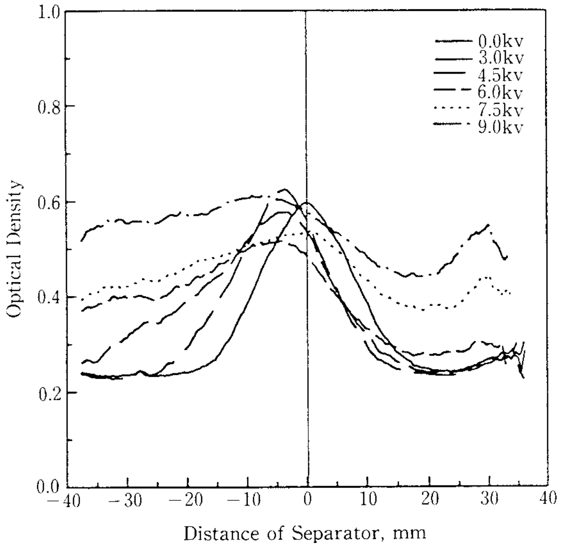

Fig. 5 Optical density curves as a function of applied potentials for quartz particles (74×53 μm) after tribocharging by contacting with a copper plate.

With no applied voltage, the optical density versus distance curve was normally distributed about the center of the chamber. As the positive voltage was increased to 3 kV, the curve shifted to the anode (left side). This indicates that the spot, as shown in **Figure 3b**, represented a group of particles having approximately same negative electric charge. The peak decreased and the curve broadened as the voltage was increased to 4.5 kV and 6.0 kV. Also, the optical density at the left end increased, whereas the optical density at the right end remained unchanged. This demonstrates that the majority of the silica particles acquired a negative charge. This is in agreement with that expected based on the material work functions and was also recently reported by Ban et al. [40]. They found that silica particles obtained under a gas flow after contacting with a copper loop showed negative charges on the majority of the silica particles. In their work, the electric charge was measured by PDPA.

Several replicate tests were made to determine the reproducibility of the results. **Figures 6a** and **6b** give several optical density versus distance curves at a given voltage. As can be seen, the curves were reproducible.

The naturally charged quartz particles (**Figure 4**) were also analyzed to determine the effectiveness of the charging apparatus. The optical density curves as a function of distance for various electric fields are shown in **Figure 7**. Comparing **Figures 5** and **7**, it can be seen that the response to the applied potential was different. The optical density versus distance curve are normally distributed at all voltages for the naturally charged particles. No peak shifts were observed, and the change at the each end was minimal. Broadening of curves was also found, but each curve was symmetric about the center of the separation chamber. As expected, particles charged by contacting with copper are more sensitive to the potential than particles naturally charged. The different behavior can be explained with the difference in the charging system.

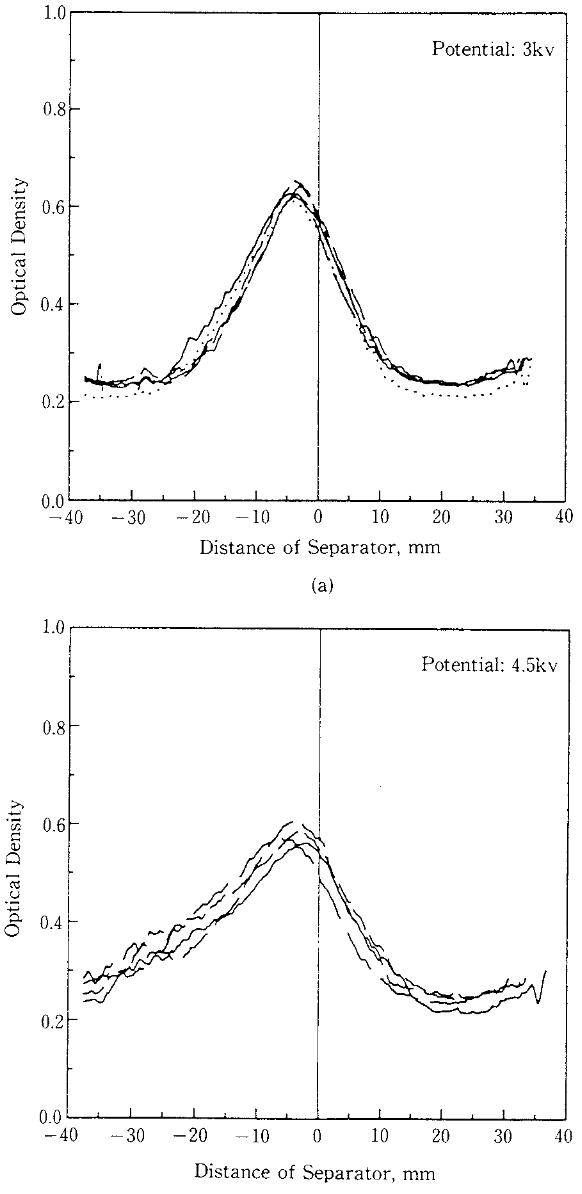

(a)

(b)

Fig. 6 Optical density curves of quartz particles charged by contacting with copper at a given applied potential: (a) 3.0 kV; (b) 4.5 kV.

5. Conclusions

A system using a coherent sheet of light, which was obtained by a pulsed laser and appropriate optical components, was designed to visualize particles and monitor the charge distribution of the particles after passing through an electric field. The particles passing through the laser sheet create a spot, which represents a distribution of particles. The average charge of the particles can be estimated by the deflection of the spot toward one of the electrodes. The dispersion shape of the spot provides information about the electric charge distribution in the particle stream, e.g., a wide spot indicates a broad charge distribution in the particle stream. An asymmetrical shape of the spot indicates that the particles are preferentially charged. It was shown that after contacting with a copper plate, a majority of sieved quartz particles (74×53 μm) were found to be negatively charged. On the other hand, the charge distribution of naturally charged particles was normally distributed under all voltages, indicating that the particles carried equal positive and negative charges. This technique was also shown to be very reproducible. Compared to other charge or charge distribution measurement techniques, this technique is relatively simple and fast, and is also suitable for on-line charge monitoring.

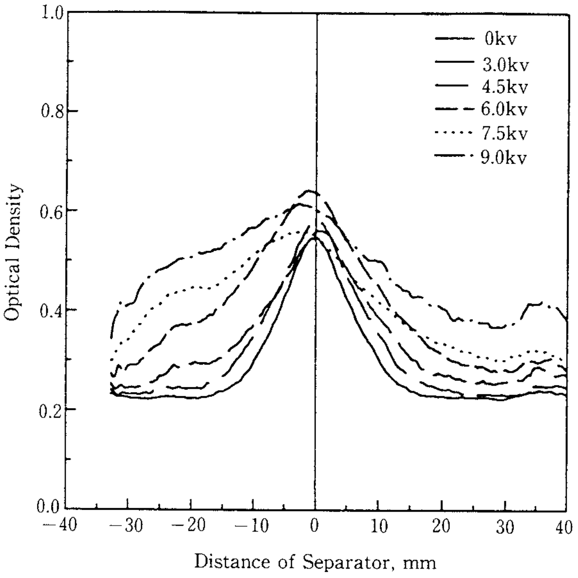

Fig. 7 Optical density curves as a function of applied potentials for naturally charged quartz particles (74×53 μm).

6. Acknowledgments

The authors acknowledge the support from the U. S. Department of Defense and from the Mineral Institutes Program under Grant No. 1145242 from the Bureau of Mines, U.S. Department of the Interior, as part of the Generic Minerals Technology Center for Respirable Dust, The Pennsylvania State University.

References

1) Schein, L.B.: Electrophotography and Development Physics, 2nd edition, Springer-Verlag, Berlin, (1992).
2) Hughes, J.F.: Electrostatic Powder Coating, Research

Studies Press LTD., Letchworth, (1985).

3) Taylor, D.M. and Secker, P.E.: Industrial Electrostatics, Research Studies Press LTD, Letchworth, (1994).

4) Lawver, J.E. and Dyrenforth, W.P.: "Electrostatic Separation", Electrostatic and Its Applications, Moore, A.D., ed., John Wiley & Sons, New York, Chapter 10, (1973).

5) Inculet, I.I.: Electrostatic Mineral Separation, Research Studies Press LTD., Letchworth, 16-22, (1984).

6) Glor, M.: Electrostatic Hazards in Powder Handling, Research Studies Press LTD, Letchworth, (1988).

7) Lawver, J.E. and Wright, J.L.: "The Design and Calibration of a Faraday Pail for Measuring Charge Density of Mineral Grains", Trans. AIME/SME, 241, 445-449, (1968).

8) Gupta, R.: "Dry Electrostatic Beneficiation of Illinois Coal and Eastern Oil Shales", Ph.D Dissertation, Illinois Institute of Technology, Chicago, (1990).

9) Donald, D.K. and Watson, P.K.: "The Influence of Electric Fields on Particle Adhesion in Xerographic Developer Mixtures", Photogr. Sci. Eng., 14, 36-41, (1970).

10) Schein, L.B. and Cranch, J.: "The Static Electrification of Mixtures of Insulating Powders", J. Appl. Phys., 46, 5140-5149, (1975).

11) Millikan, R.A.: "Isolation of an Ion, Measurement of Its Charge, and Correction to Stoke's Law", Physical Reviews, 32, 349-497, (1911).

12) Kutsuwada, N. and Nakamura, Y.: "A Measurement of Electrophotographic Toner Charge", The Journal of Imaging Technology, 15 (1), 1-6, (1989).

13) Kunkel, W.B. and Hansen, J.W.: "A Dust Electricity Analyzer", The Review of Scientific Instruments, 21 (4), 308-314, (1950).

14) Polat, M.: "Characterization of Freshly Generated Airborne Dust," M.S. Thesis, The Pennsylvania State University, (1990).

15) Masuda, S., Fujibayashi, K., Ishida, K. and Ogawa, T.: "Electrodynamical Behavior of a Charged Dust Particle Within AC Quadrennial Electric Fields-Experimental Study", Trans. Inst. Elect. Eng. Jap., 92b, 1, (1987).

16) Folan, L.M., Arnold, S., O'Keeffe, T.R. and Spoch, D.E.: "Electrometer for Repeated Charge Exchange Measurements Between a Microparticle and a Surface; Effect of Water Adsorption", Journal of Electrostatics, 25, 155-163, (1990).

17) Kutsuwada, N., Shohdohji, T., Okada, N., Izawa, H., Sugai, T., and Nakamura, Y.: "Measurement of Electric Charge of Electrophotographic Toner", The Journal of Imaging Technology, 37 (5), 480-484, (1993).

18) Lewis, R.B., Connors, E.W., and Koehler, R.F.: "A Charge Spectrophotograph for Xerographic Toner", Electrophotography, 22, 85, (1983).

19) Williams, E.M.: "The Physics and Technology of Xerographic Processes", Wiley, New York, 134, (1984).

20) Epping, R.H.: "Lifetime Simulation and Charge Related Parameters of Two Component Developers", Proceedings of the 4th International Congress on Advances in Non-Impact Printing, Springfield, VA, 102-112, (1988).

21) Terris. B.D. and Fowler, K.J.: "Charge Spectrometer for Mono- and Dual- Component Toner", The Journal of Imaging Technology, 17 (5), 215-222, (1991).

22) Takahashi, Y., Horiguchi, H., and Sakata, T.: "New Toner-Charge Measuring Method-Charge Measurement of a Toner Particle", The Journal of Imaging Technology, 15 (5), 235-238, (1989).

23) Kutsuwada, N. and Kashimada, H., Fukuda, M., Suzuhi, T. and Ohkawa, K.: "Electrostatic Properties of Electrophotographic Powder by Three-Dimensional Method", The Journal of Imaging Technology, 12 (4), 220-234, (1986).

24) Mazumder, M.K., Ware, R.E., Yokoyama, T., Rubin, B. and Kamp, D.: "Measurement of Particles Size and Electrostatic Charge Distributions on Toners Using E-Spart Analyzers", IEEE-IAS Ann. Meeting Conf. Record, 1606-1614, (1987).

25) Millikan, R.A.: "Electrons, Protons, Photons, Neutrons, and Cosmic Rays", The Exact Evaluation of e, The University of Chicago, Chicago, 90-124, (1935).

26) Sano, I., Fikitan, F., and Sakata, S.: "Colloid Chemistry of Tobacco Smokes, Distribution of Size and Charge of the Particles", J. of Chem. Soc. Japan; Pure Chem. Sec., 74, 664-668, (1953).

27) Ivanov, V.D., Kirichenko, V.N., Shan'gin, B.V., and Berezhnoi, V.M.: "Method and Apparatus for Investigation of the Electrical Charging of Beta-Active Hot Aerosol Particles", Colloid J. USSR, 36, 427-430, (1974).

28) Arnold, S.: "Determination of Particle Mass and Charge by One Electron Differentials", J. Aerosol Sci., 10, 49-53, (1979).

29) Megaw, W.J. and Wells, A.C.: "A High Resolution Charge and Mobility Spectrometer for Radioactive Submicrometre Aerosols", J. Sci. Instrum. Series 2, 2, 1013-1016, (1969).

30) Maltoni, G.G., Melandri, C., Prodi, V., Tarroni, G., DeZaiacomo, A., Bompane, G.F. and Formignani, M.: "An Improved Parallel Plate Mobility Analyzer for Aerosol Particles", J. of Aerosol Sci., 4, 447-455, (1973).

31) Takahashi, Y. and Kudo, A.: "Electrical Charging of Aerosol Particles by Bipolar Ions in Flow Type Charging Vessels", J. Aerosol Sci., 4, 209-216, (1973).

32) Yeh, H.C., Newton, G.J., Raabe, O.G., and Boor, D.R.: "Self-Charging of 198Au-Labeled Monodisperse Gold Aerosols Studied with a Miniature Electrical Mobility Spectrometer", J. Aerosol Sci., 7, 245-253, (1976).

33) Porstendorfer, J., Hussin, A., Scheibel, H.G. and Becker, K.H.: "Bipolar Diffusion Charging of Aerosol Particles-II. Influence of the Concentration Ratio of Positive and Negative Ions on the Charge Distribution", J. Aerosol Sci., 15, 47-56, (1984).

34) Whitby, K.T. and Clark, W.E.: "Electric Aerosol Particle Counting and Size Distribution Measuring System for the 0.015 to 1 (m Size Range", Tellus, 18, 573-586, (1966).

35) Knutson, E.O. and Whitby, K.T.: "Accurate Measurement of Aerosol Electric Mobility Moments", J. Aerosol Sci., 6, 453-460, (1975).

36) Schaefer, J.L., Stencel, J.M., and Ban, H.: "Non-Intrusive Measurement of Particle Charge Relating to Electrostatic Dry Coal Cleaning," Proc. of Ninth Annual International Pittsburgh Coal Conference, Pittsburgh, 259-264, (1992).
37) Diemunsch, G. and Prenel, J.P.: "A Compact Light Sheet Generator for Flow Visualizations", Optics and Laser Technology, 19 (3), 141-144, (1987).
38) Davies, D. K.: "The Generation and Dissipation of Static Charge on Dielectrics in Vacuum", Proceeding of 2nd Conference on Static Electrification, Institute of Physics, Conference Series, No. 4, 29-36, (1967).
39) Ban, H., Schaefer, J.L., and Stencel, J.M.: "Particle Tribocharging Characteristics Relating to Electrostatic Dry Coal Cleaning", Fuel, 73 (7), 1111-1113, (1994).
40) Ban, H., Schaefer, J.L., and Stencel, J.M.: "Electrostatic Separation of Powdered Materials: Beneficiation of Coal and Fly Ash", Energeia, University of Kentucky, Center for Applied Energy Research, 6 (4), 1-3, (1995).

Author's short biography

Qin Tang

Qin Tang obtained a B.S. from the Shanghai University of Science and Technology, China, in 1987. After graduating, she worked at the Shanghai Institute of Metallurgy, Academia SINICA as an assistant engineer (1987-1990). She received her M.S. from the University of Kentucky in 1993 and her research was in the field of comminution. Currently, she is a Ph.D candidate on the Department of Mineral Engineering at the Pennsylvania State University. Her research project involves electrostatic separation of fine particles and dust control.

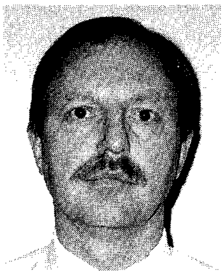

Mark S. Klima

Mark S. Klima received a B.S. degree in Mining Engineering and M.S. and Ph.D. degrees in Mineral Processing from the Pennsylvania State University. His research interests center on the evaluation and simulation of physical beneficiation processes, especially in the area of fine particle separations. He is a registered Professional Engineer in Pennsylvania and is currently Associate Professor of Mineral Processing at Penn State.

S. Chander

S. Chander received his B.S. from Indian Institute of Technology in Metallurgical Engineering and M.S. and Ph.D. from University of California, Berkeley, in Materials Science and Mineral Engineering. He is currently Professor of Mineral Processing at the Pennsylvania State University. His main research interests include surface and colloid science, particle technology and process engineering.

Research

Colloidal Zeolite-Preparation, Properties and Applications[†]

Brian J. Schoeman and Johan Sterte
*Lulea University of Technology, Sweden**

Abstract

A method for the preparation of stable colloidal suspensions containing discrete molecular sieve crystals is presented. The hydrothermal synthesis of the all-silica tetrapropylammonium silicalite-1 molecular sieve illustrates the preparation. The discrete colloidal crystals (< 150 nm) are aggregates of plate-like primary particles and they are stabilized in aqueous solution via steric forces that arise as a result of the strong adsorption of the tetrapropylammonium cation on the siliceous surface. The silicalite-1 surface charge is a function of pH as shown by electrophoretic measurements. These properties may be utilized for fabricating advanced materials. An example of the application of the colloidal materials is illustrated by the preparation of a thin silicalite-1 film on a non-charged gold substrate. Knowledge of the surface chemistry of the participating interfaces and the properties of the colloidal crystals allows for the preparation of microporous films with a thickness less than 300 nm.

1. Introduction

There are well over 150 known synthetic zeolites such as zeolite Na-Y, Na-A, ZSM-5 and zeolite Beta besides the approximately 34 naturally occurring counterparts, e.g. clinoptilolite, faujasite and mordenite. The synthesis procedures have been developed over the past 50 years, with much of the pioneering work performed by Barrer [1] and Milton [2,3]. The interest in these microporous aluminosilicates stems from their well-defined micropore channel geometries. The pore size range, approx. 3 to 8 Å, is similar to the sizes of numerous molecules of commercial interest. Hydrothermal treatment (normally ≥100°C) of hydrous alkaline amorphous aluminosilicate gels for extended periods of time (typically a few hours to several days) results in the crystallization of crystalline aluminosilicates or zeolites. The crystalline phase obtained is a function of the gel composition, the nature of the reagents, crystallization temperature and time [1]. Following completed crystallization, the precipitated solid phase is separated from the supernatant by conventional suction filtration and washed with water. Upon drying of the solid phase, a powder consisting of crystals with an average size >1 μm is obtained. The factors influencing crystal size are, among others, crystallization temperature, synthesis mixture composition and dilution and the source of the raw materials. While the majority of synthesis procedures describe the crystallization of zeolite from heterogeneous gels, there are (relatively few) reports dealing with the crystallization of zeolite from clear "homogeneous" solutions [4,5]. Irrespective, however, of whether the formation of zeolite takes place in the presence of a visible macroscopic solid phase or not, the final crystallization product is in most cases a material consisting of a large crystal size (termed conventional crystals) and with a broad crystal size distribution.

The conventional large-sized zeolite crystals have found applications in fields of commercial importance - notably as catalysts (cracking and reforming catalysts within the petrochemical industry) [6] and ion exchangers (zeolites A and P as a substituent for phosphates in laundry detergents) [7]. Several other promising application fields in which zeolites may be utilized are sensors, optical devices, supramolecular catalysis, photochemistry and electrochemistry.

It has been anticipated that certain applications require a zeolite with a smaller crystal size or a narrow crystal size distribution. An example is the molecular sieve TS-1 [8], a Ti-substituted silicalite-1, that has been shown to possess attractive properties as a mild oxidation catalyst in the presence of aqueous H_2O_2. The crystal size strongly influences the product distribution in reactions that are diffusion-limited - smaller crystallites resulting in

---

*Department of Chemical Technology, S-971 87 Lulea, Sweden

[†] Received : May 23, 1997

higher selectivities and activity [9]. A second example in which crystal size is anticipated as being of importance is within sensor technology. It is expected that in order to obtain shorter response times and higher selectivity and sensitivity in sensor composites, the active layer should be thin [10]. There is therefore a need to synthesize microporous materials with tailor-made properties. The property of interest in this respect is crystal size. Smaller crystals with a well-defined size and narrow size distribution are therefore interesting materials. In an effort to satisfy this demand, we have prepared several zeolite phases in the form of stable colloidal suspensions. These phases include silicalite-1, ZSM-5, N-Y, N-A, TS-1 and Beta [11-15]. In all cases, the average crystal sizes are less than 150 nm. Furthermore, the crystals exist as stable discrete entities in solution.

Our interest in this field of research is to utilize the colloidal properties of zeolites to prepare advanced materials, an example of which is the preparation of ultra-thin microporous films. In order to achieve this goal, however, it is necessary to understand the fundamental processes at work during the hydrothermal synthesis and the properties of the synthesized materials. The purpose of this report is to present the procedure used for the synthesis of discrete colloidal zeolite crystals, their properites and their application in thin-film fabrication. The all-silica tetrapropylammonium (TPA) silicalite-1 molecular sieve [11] has been chosen to illustrate the related nature of these three topics.

2. Experimental

Colloidal TPA-silicalite-1 synthesis

The silica source used in the syntheses of TPA-silicalite-1 was tetraethoxy silane, (TEOS, $>98\%$, <5 ppm Al, Aldrich-Chemie) and the tetrapropylammonium hydroxide source was a 1M TPAOH in water (TPAOH, Na<5 ppm, K<5 ppm, Sigma). In those cases where aluminium and sodium were required, the aluminium was derived from aluminium isopropylate (Sigma) and the NaOH was NaOH pellets (Riedel-de-Haen, p.a.). Double-distilled water was used in all experiments.

Colloidal suspensions of TPA-silicalite-1 were prepared by hydrothermal treatment of synthesis solutions with the molar compositions

$$9\mathrm{TPAOH}\ 25\mathrm{SiO_2}\ x\mathrm{H_2O}\ 100\mathrm{EtOH}$$
$$(\mathrm{EtOH}=\text{ethanol})\ ;\ x=480,\ 1500$$

in polyethylene flasks submerged in a preheated silicone oil bath at 100°C with reflux under static conditions. A typical synthesis was performed as follows: TEOS was transferred to a polyethylene flask and an aqueous TPAOH solution was added. The mixture was placed on a gyratory shaker for at least 12 h until a single homogeneous phase was obtained, thus marking the completion of the hydrolysis reaction. The resulting clear synthesis mixture (denoted the precursor solution) was heated in the polyethylene flask for a period of up to 7 days. The reflux columns were capped to prevent the loss of ethanol (formed by the hydrolysis reaction).

Thin-film preparation

Gold-plated silver substrates were used for growing thin TPA-silicalite-1 films. Prior to use, the surface was cleaned at room temperature for 15 min. with acetone (p.a.) in an ultrasonic bath, rinsed with water and thereafter, the plates were treated with a solution having the molar composition: $9\mathrm{H_2O_2} : 15\mathrm{NH_3} : 280\mathrm{H_2O}$ for 10 minutes. After this cleaning procedure, the plates were rinsed several times with distilled water. The gold surface was silanized by treating the substrate in a 10mM gamma-mercaptopropyltrimethoxysilane (MPT, OSi Specialties) solution in methanol. The silane was hydrolyzed in a 0.10M HCl solution for 15 h at room temperature.

Discrete negatively charged colloidal TPA-silicalite-1 crystals were synthesized according to the method presented above using a synthesis mixture molar composition

$$9\mathrm{TPAOH}\ 25\mathrm{SiO_2}\ 480\mathrm{H_2O}\ 100\mathrm{EtOH}$$
$$(\mathrm{EtOH}=\text{ethanol})$$

The product sol was purified with high-speed centrifugation as described below. The purified colloidal suspension contains discrete negatively charged TPA-silicalite-1 crystals (90 nm). A 4.2 wt% TPA-silicalite-1 suspension was deionized to pH 3.4 to yield a suspension of positively charged discrete crystals which were subsequently adsorbed onto the negatively charged siliceous interface by contacting the substrate with this suspension. Excess colloidal material was rinsed off with excess water whereafter the composite was calcined at 300°C in air for 1 h as above. The composite was contacted with a precursor solution with the molar composition

$$3\mathrm{TPAOH}\ 25\mathrm{SiO_2}\ 1500\mathrm{H_2O}\ 100\mathrm{EtOH}$$
$$(\mathrm{EtOH}=\text{ethanol})$$

and prepared as described above. The crystallization was performed at 100°C with reflux for varying periods of time in a preheated silicon oil bath.

3. Analysis

The as-synthesized aqueous TPA-silicalite-1 suspensions were purified by centrifugation in a Jouan High-Speed Centrifuge, model KR22i, with a relative centrifugal force of 50,000 g for 1 hour. The liquid phase was carefully decanted and the solid phase was redispersed in double-distilled water by ultrasonic treatment. This rinsing procedure was repeated 3-4 times. Purified and redispersed samples were freeze-dried and the organic template was removed by calcining samples at 550°C in air for approx. 3 hours.

Particle size analysis of dilute as-synthesized aqueous suspensions of silicalite-1 was performed using a Brookhaven Instruments ZetaPlus. The use of the light scattering technique for particle size analysis has been described in detail in a previous report [16]. The non-negative least squares (NNLS) data analysis method was used to determine the diffusion coefficients. Dust was removed from the precursor solution by filtration through a Gelman Sciences Supor Acrodisc membrane filter, 0.2 μm pore size, prior to the light scattering measurements.

SEM micrographs were taken with a Philips XL 30 scanning electron microscope (SEM). Dilute aqueous samples of purified suspensions were dried on a glass plate and thereafter coated with a thin carbon film. Crystal phases were identified by X-ray powder diffraction (XRD) with a Philips PW 1710 diffractometer using CuKα radiation. Powder samples for XRD analysis were prepared by freeze-drying purified sols followed by calcination of the powder at 550°C for three hours in air.

The DRIFT spectra of freeze-dried powder samples were obtained using the KBr wafer technique with a Perkin Elmer PE 2000 FT-IR spectrometer. Data were collected with 200 scans and a resolution of 4 cm^{-1} in the frequency range 370-1300 cm^{-1}.

Specific surface areas of freeze-dried powder samples were measured by N_2-adsorption according to the BET method with a Micromeritics ASAP 2010 Surface Area Analyzer. The samples were outgassed at 200°C for 5 hours in vacuum before measurement. The N_2 adsorption isotherms were recorded at 77K.

Electrophoretic mobility [17] measurements were performed using a Laser Zee Meter instrument (PENKEM Model 501). Purified sol samples were diluted with a KCl solution to 10 mM KCl. The suspension pH was adjusted by the addition of NaOH or HCl. The samples were equilibrated for 2 h at room temperature by stirring. Before measurement, each solution was subjected to ultrasonic treatment for a few minutes, whereafter the pH was measured and a part of the solution injected into the sample cell to measure the electrophoretic mobility. The zeta potential was calculated from the electrophoretic mobility data with Smoluchowski's equation [17].

4. Results and Discussion

Synthesis of colloidal silicalite-1

The addition of TPAOH to TEOS results in two immiscible phases and hence the mixture requires a period of agitation during which the hydrolysis of the silane may take place. The resulting precursor sols with the molar compositions

9TPAOH $25SiO_2$ xH_2O 100EtOH ; $x = 480, 1500$

following hydrolysis are water-clear suspensions with the apparent absence of particles. Dynamic light scattering (DLS) studies of the clear precursors show, however, that the greater part of the silica is in the form of polymeric species with an average diameter in the range 2.5-3.5 nm depending on the precursor composition [18]. It was observed that the average particle size increases with increasing dilution, from 2.6 nm in the concentrated precursor to 3.5 nm in the dilute precursor. Similar trends in the change in particle size of amorphous silica have been observed upon dilution with water [19]. Cryo-TEM analyses (not shown here [20,21]) confirm the DLS results. FT-IR, **Figure 1a**, and FT-Raman (not shown) data show the characteristic spectra of the MFI phase vide infra (MFI = structure code for the silicalite-1 and ZSM-5 phases) [22]. The results therefore indicate that the subcolloidal particles possess a structure similar to that of the MFI phase and hence they are believed to play an important role in the crystallization of silicalite-1. Although the exact role of these subcolloidal particles is not fully understood, certain subcolloidal particles are believed to serve as nuclei that, upon hydrothermal treatment, grow to larger crystal sizes.

Following hydrothermal treatment (approx. 30 h at 100°C), the precursor sol with the molar composition - 9TPAOH $25SiO_2$ $480H_2O$ 100EtOH yields a colloidally stable suspension containing discrete TPA-silicalite-1 crystals as shown in the SEM micrograph in **Figure 2**. The average size is 95 nm and the particle size distribution is narrow. The crystal size is confirmed by light scattering analyses (DLS) as shown in **Figure 3** where the DLS particle size distribution (PSD) was recorded at a scattering angle of 90°. The PSD is narrow and consists of a single particle population (i.e. no aggregates). Aggregation of the primary particles (95 nm) to larger entities would have been detected with ease using this technique since the scattering power of larger particles is considerably larger than that of smaller particles even if the former are present in small amounts. Despite the small size of the crystals, they are highly crystalline as shown by the XRD pattern in **Figure 4**. All peaks may be assigned as being due to silicalite-1. The IR data presented in **Figure 1b** show the characteristic bands of the MFI phase, approx. 550 cm^{-1} (due to the presence of double-rings of tetrahedra in the MFI framework) and 1220 cm^{-1} (due to external asymmetrical stretching). A weak band at approx. 970 cm^{-1} is also evident and is thought to be due to external (dissociated) silanol groups. Considering the colloidal nature of the crystals (implying a high external surface area), the number of such silanol groups is expected to be large and hence their presence is expected to be detected with this technique. The FT-IR spectra of a truly amorphous colloidal silica is included in **Figure 1** as a comparison. From this spectra it is evident that the non-crystalline silica does not exhibit the absorption bands at approx. 550 and 1220 cm^{-1}. Specific surface areas as calculated with the BET equation are typically in the range 450-550 m^2/g - common for this class of microporous materials. It may be noted that the internal pore volume is only available to the N_2 molecules once the structure-directing agent (TPAOH) is removed

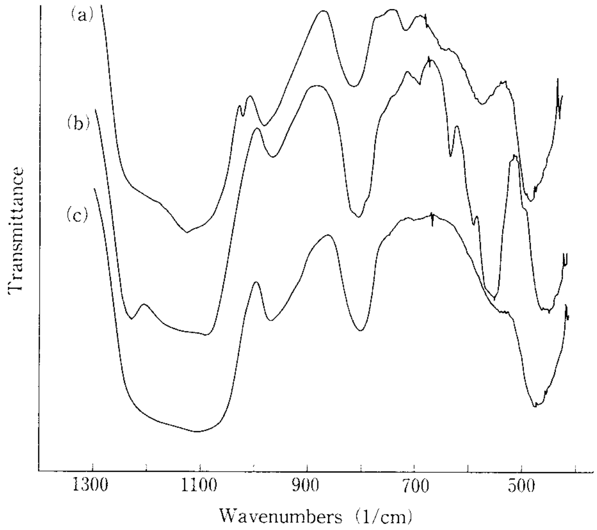

Fig. 1 The FT-IR spectra of (a) a freeze-dried precursor sol containing subcolloidal siliceous particles with an average size of 2.6 nm, (b) colloidal TPA-silicalite-1 (95 nm) -both spectra (a) and (b) show the characteristic absorption bands at approx. 550 and 1220 cm^{-1} due to the MFI phase, and (c) a freeze-dried sample of a commercial amorphous silica sol, Ludox SM (particle size approx. 7 nm), showing the absence of the absorption band at approx. 550 cm^{-1}.

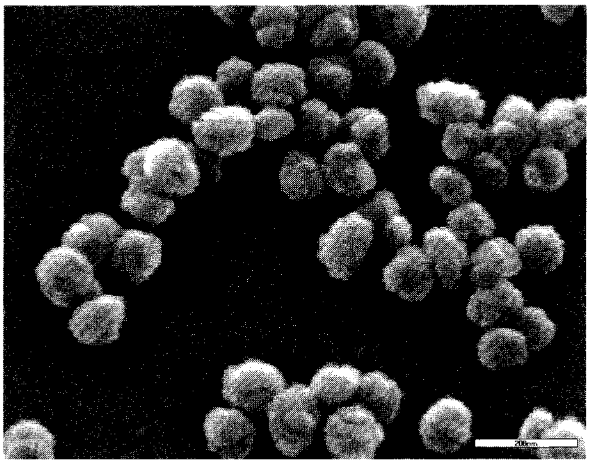

Fig. 2 SEM micrograph of colloidal TPA-silicalite-1 crystals following hydrothermal treatment of a precursor sol with the molar composition 9TPAOH $25SiO_2$ $480H_2O$ 100EtOH at 100°C for 24 h.

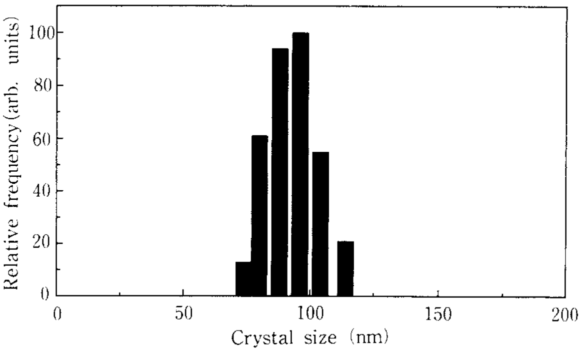

Fig. 3 The crystal size distribution of a colloidal dispersion of TPA-silicalite-1 measured using dynamic light scattering.

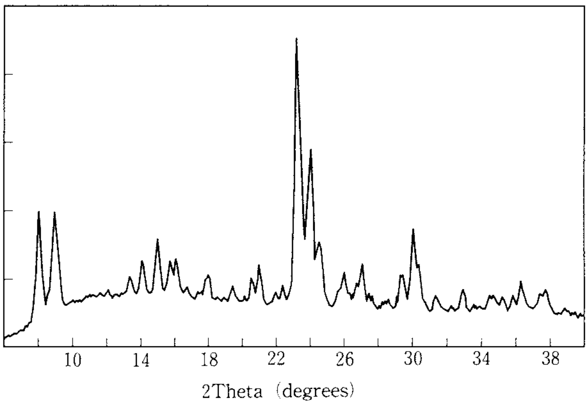

Fig. 4 The XRD pattern of colloidal TPA-silicalite-1 (95 nm) showing the characteristic peaks due to the MFI phase.

by calcination, a fact that is of significance when preparing thin microporous zeolite films vide infra. The characterization methods used, the results from which are given above, show that the colloidal crystals are discrete crystalline silicalite-1 particles with a size less than 100 nm.

The second precursor mixture composition ($9TPAOH\ 25SiO_2\ 1500H_2O\ 100EtOH$) represents a dilution of the first mixture. It was shown above that the size of the sub-colloidal particles in the dilute precursor was slightly larger than those in the concentrated mixture. Hydrothermal treatment of the dilute precursor yields silicalite-1 crystals with an average size of 180 nm. Furthermore, the crystal number concentration is less by a factor 14 and the kinetics of crystallization are faster by a factor 2.5 [11]. If one assumes from the hypothesis above that only certain sub-colloidal crystals grow to a larger size, the fraction of which is the same in each precursor, then it is reasonable that the size of the product crystals in the dilute system is larger since fewer crystals grow while consuming the same amount of nutrient material (silica conversions in the concentrated and dilute precursors are 64 and 68%, respectively).

Although there are several parameters influencing the size of the product crystals and the crystallization kinetics, the water content is a suitable parameter with which these properties may be manipulated.

Colloidal properties

Of interest is the stability of the colloidal crystals - a property that allows one to maintain the discrete nature of the particles. The high electrolyte content in the synthesis mixture would suggest that the crystals should aggregate to form larger secondary particles. Evidence, however, points to the fact that the growing crystals do not increase in size via the aggregation of similarly sized crystals but rather via a surface reaction controlled process [23]. The question is therefore, what imparts stability to these colloidal crystals? Besides the van-der-Waals attractive forces and the electrostatic repulsive forces (which are far weaker than the former due to the high electrolyte content), forces due to steric hindrance are known to stabilize colloidal material. The quarternary ammonium cations, e.g. TPA^+ as is the case in this work, are also known to stabilize colloidal amorphous silica particles and serve as dispersants [19]. The TPA cations are thought to be strongly adsorbed onto the external surface of the crystals thus preventing aggregation upon collisions during growth. Taking into account the fact that the crystals are centrifuged down to form a solid mass at high speeds, corresponding to relative centrifugal forces of typically 50,000 g-during the above-mentioned purification process and spontaneously redisperse upon standing, it would appear reasonable that the organic cations afford a barrier against aggregation. A purified suspension of silicalite-1 (i.e. free from excess TPAOH and unreacted silica) was characterized with respect to surface charge. The surface charge calculated from electrophoretic data and shown in **Figure 5** shows clearly that the zeta potential is a strong function of pH, as may be expected. An unexpected result, however, is that the point of zero charge (p.z.c.) is at a pH of approx. 6, whereas the p.z.c. for amorphous silica is at approx. 2 [19]. The reason for this behaviour is possibly due to the fact that the surface charge is a function of the TPA surface coverage. This topic deserves further investigation. It is, however, clear that the TPA is associated with the crystal surface, imparting colloidal stability within a wide pH range except for pH values in the vicinity of the p.z.c. The fact that the crystals are negatively and positively charged in distinct pH ranges allows one to electrostatically adsorb the particles onto positively and negatively charged surfaces, as will be discussed below.

The surface charge behaviour of aluminium-containing zeolite materials has been investigated. As one may expect, the crystalline aluminosilicates are negatively charged throughout the measurable pH range, i.e approx. 4.5-12. The crystal structure collapses in the pH interval below approx. 4.5 and hence the aluminosilicates do not exhibit a p.z.c., as seen in **Figure 5**.

A second aspect of interest is the morphology of

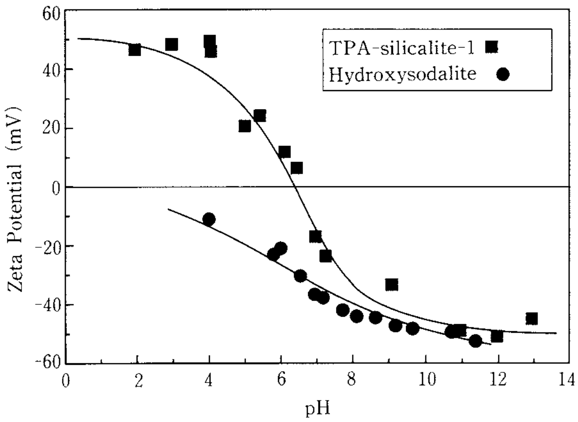

Fig. 5 The zeta potential of zeolite crystals in a 10-mM KCl solution as a function of pH at room temperature.

the colloidal crystals. Cryo-TEM micrographs (not shown here) clearly show that the colloidal particles are aggregates of plate-like primary particles. **Figure 6** shows the idealized morphology of the MFI phase. The colloidal crystals may be envisaged as being built up of several such ideal lathe-like crystallites with the (010) planes as the common interface. The morphology is of interest with regard to the preparation of thin microporous films, as will be discussed below. The plate-like morphology is believed to influence the orientation of the adsorbed crystallites and the orientation of the deposited crystalline material in the following hydrothermal treatment which leads to the formation of the thin film.

Thin-film preparation

A schematic illustration of the principle of the seed-film method is shown in **Figure 7**. The basic steps constituting this method are (i) substrate surface modification, steps A and B in **Figure 7**, (ii) electrostatic adsorption of charged colloidal zeolite seed crystals, step C, and (iii) hydrothermal treatment of the substrate/seed composite in a fresh precursor solution to close the void spaces and form a continuous zeolite film, step D. The seed-film method is, in principle, applicable to all solid surfaces once the surface chemistry of the interfaces (substrate and seed crystal) are taken into account.

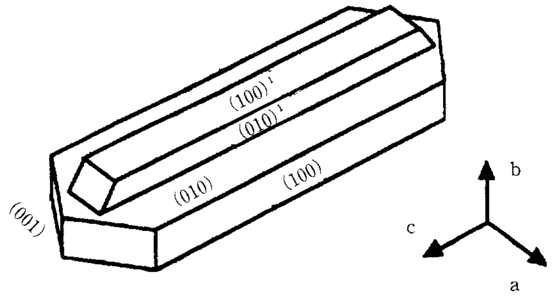

Fig. 6 A schematic representation of an idealized MFI crystal showing the lathe-like morphology.

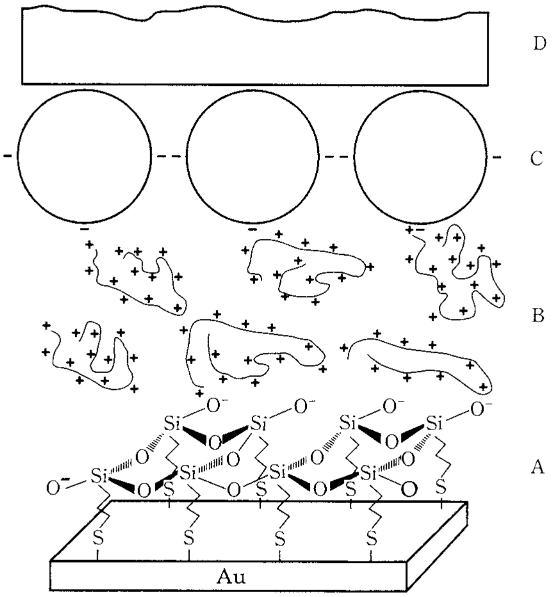

Fig. 7 A schematic representation of the various stages in the preparation method used to synthesize thin microporous films on gold substrates.

An area where thin microporous films may find an important application is that of electrochemistry (size and shape selective electrodes), wherein surface-modified gold electrode surfaces are encountered. The following example therefore illustrates the preparation of a thin silicalite-1 film on a modified gold surface. The surface of the noble metal substrate is modified by the adsorption and hydrolysis of a bi-functional silane to yield a negatively charged siliceous interface upon which charged colloidal crystals may be adsorbed. If the adsorption of the colloidal crystals is carried out in an acidic medium at a pH lower than the p.z.c. of the crystals (i.e. positively charged particles), adsorption occurs spontaneously and may therefore take place in a single step. If the adsorption is to take place at a pH higher than the p.z.c., the negatively charged interface must be charge-reversed by, for example, the adsorption of a cationic polymer to create a positively charged interface (see step B in **Figure 7**). It may be noted that no crystals are adsorbed onto the non-modified gold surface. In the following example, the gold surface was silanized in an acidic solution to yield a negatively charged interface. Silicalite-1 seed adsorption was achieved in an acidic solution in which the seed crystals are positively charged, approx. +55 mV. From **Figure 8a**, it is seen that the substrate is essentially fully covered by the adsorbed seed crystals. The composite (substrate and seed crystals) is then calcined at 250°C for 1h, whereafter it is exposed to a precursor solution at 100°C for varying periods of time. The precursor sol composition was chosen on the basis of previous results obtained from kinetic studies of the crystallization of TPA-silicalite-1 [11] and presented above, viz dilute solutions with relatively low TPA concentrations allow for rapid crystallization thus facilitating rapid closure of the voids between the adsorbed seed crystals. The adsorbed crystals serve as seeding agents in the crystallization process. The seed crystals are envisaged as growing in a lateral as well as a perpendicular direction. Growth in lateral direction ceases once

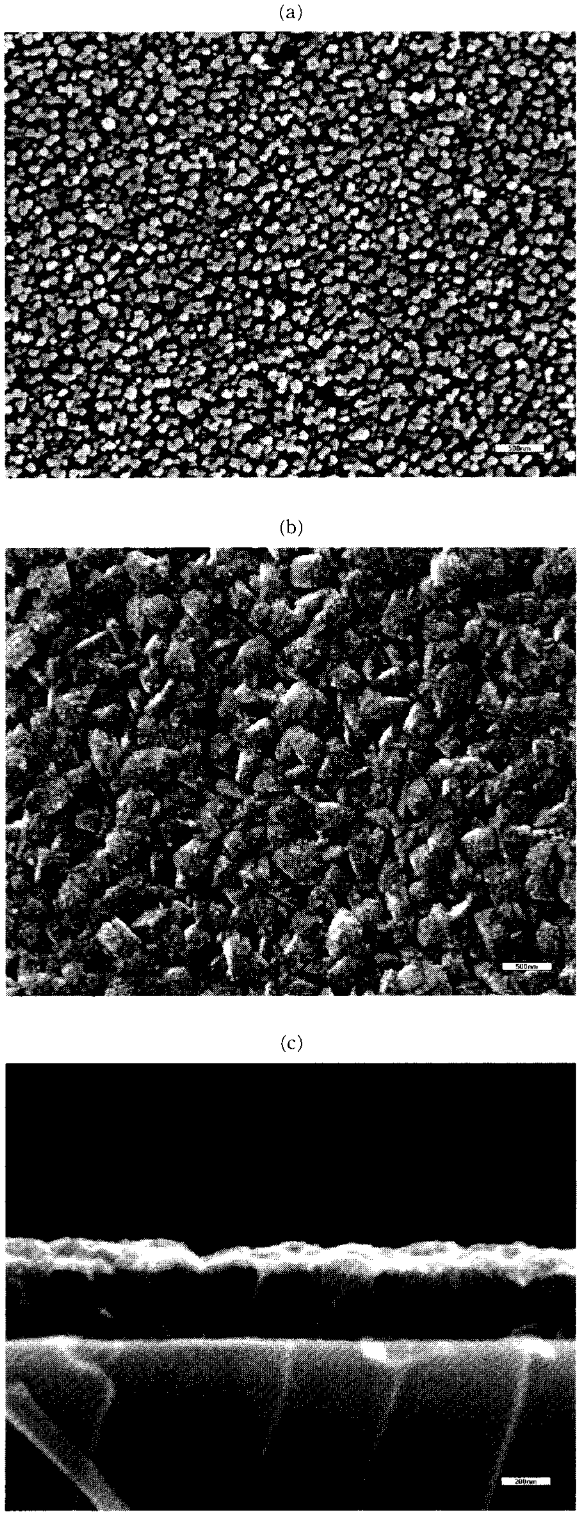

Fig. 8 SEM micrographs of (a) electrostatically adsorbed silicalite-1 seed crystals on a modified gold substrate (scale bar = 500 nm), (b) a top view of the closed silicalite-1 film (scale bar = 500 nm) and (c) a side-view of a silicalite-1 film after hydrothermal treatment of the composite shown in (a) (scale bar = 200 nm).

the crystal faces intergrow, whereafter growth is only in perpendicular direction. The uni-directional growth results in the orientation of the growing crystals - their orientation being determined by the orientation of the adsorbed seed crystals. The XRD pattern shown in **Figure 9** after a 20 h crystallization period shows that only certain peaks are present, thus indicating a degree of orientation. The top-view image of the film, **Figure 8b**, shows the individual, apparently oriented crystallites constituting the film. In addition, there is no halo in the XRD pattern, indicating the absence of amorphous material. The SEM micrograph shown in **Figure 8c** shows a side-view image of the cracked composite. It is evident that the film is of uniform thickness and, more importantly, that it is continuous with a thickness of approx. 250 nm. Permeation data show that the films are gas-tight prior to calcination [24]. It is anticipated that the film thickness may be controlled by the suitable choice of (i) seed size and (ii) precursor sol composition (e.g. water and TPAOH content).

The seed-film method has important advantages when compared with conventional film preparation methods : thin-film preparation is relatively insensitive to the chemical and physical nature of the substrate, flexibility in determining film thickness and the possibility of influencing crystal orientation. Furthermore, the seed-film method is applicable to other zeolite phases [15] once knowledge of the crystal surface charge as a function of pH is known.

5. Summary

Stable colloidal suspensions of molecular sieves may be prepared in the presence of structure-directing agents such as illustrated by the synthesis of silicalite-1 in the presence of TPAOH. The pre-

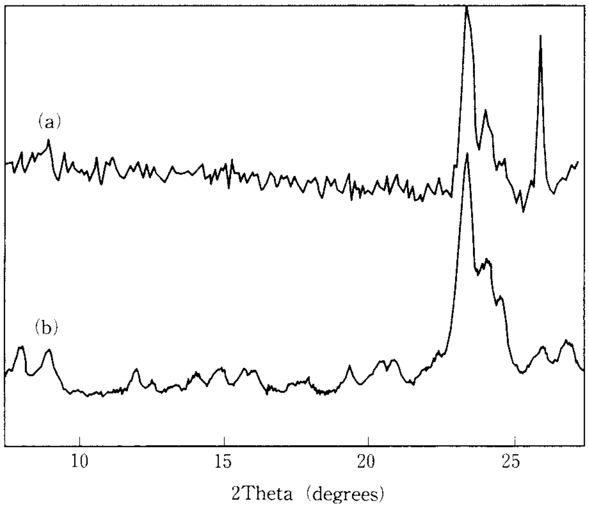

Fig. 9 The XRD pattern of (a) a silicalite-1 film on a gold substrate showing only certain MFI peaks and (b) a silicalite-1 sample taken from the bulk solution.

cursor solutions contain sub-colloidal (<4 nm) siliceous particles with a structure resembling the product crystals, and hence it is believed that certain sub-colloidal particles serve as growth centres. The crystals grow as discrete entities via a mechanism whereby monomeric or very small oligomeric species attach to the growing crystal surface. A mechanism in which growth takes place by the aggregation of either similar-sized or dissimilar-sized particles may be ruled out on the basis of the inherent stability of the crystals. The colloidal stability of the crystals has also been observed experimentally. The colloidal stability is derived from the surface-active structure-directing agent that imparts steric stability to the growing crystals.

The colloidal crystals serve as growth centres in the preparation of thin microporous materials. Knowledge of the surface chemistry of the participating interfaces is necessary in order to facilitate the adsorption of the charged crystals onto substrates of varying chemical nature. A high surface coverage of the substrate with adsorbed seeds allows for the rapid closure of the growing film to yield a continuous gas-tight film suitable for membrane and sensor applications, to name only a few.

6. Acknowledgements

The authors would like to thank the Swedish Council for Engineering Sciences (TFR), the Preem Environmental Foundation and the Carl Trygger Foundation for their financial support of this work.

7. References

1) Barrer, R.M.: "Hydrothermal Chemistry of Zeolites", Academic Press, London (1982).
2) Milton, R.M.: US Patent 2, 882, 243, (1959).
3) Milton, R.M.: US Patent 2, 882, 244, (1959).
4) Ueda, S. and M. Koizumi: Am. Miner., 64. 172 (1979).
5) Kasahara, S., K. Itabashi and K. Igawa: "New Developments in Zeolite Science and Technology", Kodansha/Elsevier, Tokyo (1986).
6) See, for example, Szostak, R.: "Molecular Sieves-Principles of Synthesis and Identification", Van Nostrand Reinhold, New York (1989).
7) See, for example, Breck, D.W.: "Zeolite Molecular Sieves", Wiley, New York (1974).
8) Taramasso, M., G. Perego and B. Notari: US Patent, 4, 410, 501 (1983).
9) van der Pol, A.J.H.P., A.J. Verduyn, J.H.C. van Hooff: Appl. Catalysis A, *92*. 113 (1992).
10) Mintova, S., B.J. Schoeman, V. Valtchev, J. Sterte, S. Mo and T. Bein: Adv. Materials *9*, 585 (1997)
11) Persson, A.E., B.J. Schoeman, J. Sterte and J.-E. Otterstedt: Zeolites, *14*. 557 (1994).
12) Persson, A.E., B.J. Schoeman, J. Sterte and J.-E. Otterstedt: Zeolites, *15*. 611 (1995).
13) Schoeman, B.J., J. Sterte and J.-E. Otterstedt: Zeolites, *14*. 110 (1994).
14) Zhang, G., J. Sterte and B.J. Schoeman: Chemistry of Materials, *9*. 210 (1997).
15) Schoeman, B.J., E. Babouchkina, V. Valtchev, S. Mintova and J. Sterte: Manuscript in preparation.
16) Schoeman, B.J., J. Sterte and J.-E. Otterstedt: J. of Porous Materials, *1*. 185 (1995).
17) Hunter, R.J.: "Foundations of Colloid Science", Vol. 1, Clarendon Press, Oxford, England, (1987).
18) Schoeman, B.J. and K. Higberg: Manuscript in preparation.
19) Iler, R.K.: "The Chemistry of Silica", Wiley, New York (1979).
20) Schoeman, B.J.: Zeolites, *18*. 97 (1997).
21) Schoeman, B.J.: Microporous Materials *9*, 267 (1997).
22) Coudurier, G., Naccache and Vedrine J.C.: J. Chem. Soc., Chem. Commun., 1413 (1982).
23) Schoeman, B.J., J. Sterte and J.-E. Otterstedt: Zeolites, *14*. 568 (1994).
24) Unpublished results.

Author's short biography

Brian Schoeman

Brian Schoeman was born in South Africa, December 1961 and received his MScEng (chem) in 1989 from Chalmers University of Technology, Göteborg, Sweden in 1994. This work entailed the development of synthesis procedures for the preparation of stable colloidal zeolite suspensions. Post-doctoral studies were carried out at the Luleå University of Technology, Sweden. During the period 1994-1997, emphasis has been placed on the synthesis of colloidal microporous materials, nucleation and growth mechanisms and the application of such materials.

Johan Sterte

Johan Sterte graduated in chemical engineering from Chalmers University of Technology, Göteborg, Sweden in 1982 and gained a PhD in Chemical Technology at the same university in 1987. In 1994 he was appointed to his current position of professor of Chemical Technology at Luleå University of Technology. His research interests are concerned with the preparation, modification, characterization and applications of small particle systems and porous materials.

Research

Spherical Crystallization : Modeling of the Emulsion Solvent Diffusion Technique[†]

F. Espitalier, B. Biscans and C. Laguerie
*University of Toulouse, France**
M. Deleuil
*Rhone-Poulenc, France***

Abstract

Kawashima developed the spherical crystallization technique to produce shaped and sized particles with improved properties. He presented two methods : Spherical Agglomeration (SA) and Emulsion Solvent Diffusion (ESD). It was established that ESD proceeds from a spontaneous emulsion of the drug solution into a non-solvent liquid, whereas the solvent and the non-solvent are miscible.

We investigated the general pharmaceutical case of a drug substance (DS) which is highly soluble in acetone (S), and moderately soluble in water (NS). The phase diagram DS/S/NS confirms that a concentrated DS/S solution poured into an NS will generate a biphasic liquid/liquid system (DS/S emulsion into NS), which then moves into a triphasic liquid/liquid/solid one (DS into DS/S emulsion into NS), by counter diffusion S ↔ NS.

Droplet size and mixing conditions are major determinants of where and at which speed solid growth will occur in the droplet. In large droplets, the solid growth takes place on the surface and extends in layers to the center. In small droplets, a homogeneous texture is obtained.

This article presents a complete kinetic model of these mechanisms, which show how a specific texture can be selected and the whole process controlled.

Two kinds of grains were produced and compared according to the micromeritic criteria required for direct tableting. The question of tablet cohesion is not critical with the drug we tested, and both grains are effective with regard to flowability whereas the powder produced from the standard crystallization technique is not suitable. With other drugs, a particular texture may be preferred, depending on cohesion and dissolution rate.

1. Introduction

Whether issuing from chemical or biological synthesis or extracted from natural substances, most pharmaceutical drug substances are isolated in solid form by crystallization. Generally speaking, crystallization produces fine particles (5 to 100 μm), which are in fact agglomerates of even finer crystals.

Depending on the process which the particles will undergo, particle sizes may be suitable or they may be too big or too small. If particles are too big, their surface can be reduced by crushing or by micronization. If they are too small, they can be adjusted using the particle size enlargement technique. This is particularly true for compression, when the drug substance content is high, and for microencapsulation, when the grain is coated by a protective film.

There are many different ways of obtaining grains ranging from 100 to 1500 μm. The method selected will depend on the ultimate manufacturing process retained, i.e. dry compaction, wet granulation, extrusion-spheronization, atomization, prilling, etc. In the 70s, Capes and Kawashima suggested performing particle size enlargement at the same time as crystallization (1-3), thus controlling crystal agglomeration in order to obtain large spherical grains. This was made possible by the two methods of spherical crystallization finally developed by Kawashima.

The first method is known as Spherical Agglomeration (SA) and consists of precipitating fine crys-

---

* Laboratoire de Génie Chimique UMR CNRS 5503, ENSIGC/INPT ; 18 Chemin de la Loge, 31078 Toulouse CEDEX 4, France.
** Rhône-Poulenc Rorer, Centre de Recherche de Vitry-Alfortville ; 13 quai Jules Guesde BP 14, 94403 Vitry-sur-Seine, France.
[†] Received June 23, 1997

tals of drug substance then aggregating them using a non-miscible liquid. The second method is referred to as Emulsion Solvent Diffusion (ESD), in which a quasi-emulsion is formed by droplets of solvent containing the drug in a medium in which the drug is non-miscible, with the solvent diffusing to the outside of the droplets and into this medium. The two methods, SA and ESD, are both Spherical Crystallization (SC) techniques.

Spherical agglomerated crystals are suitable for various uses (4, 5). Their specific properties are much documented (6-11), and it is known that these microspheres show specific properties with regard to flowability and compressibility (11), sustained release (6, 7, 10), etc. These fundamentals of the SC techniques can be applied to obtain products as diverse as microcapsules (5), microballoons (7), nanospheres (9), or directly compressible products (11), thus illustrating the advantages of particles generated by SC.

Kawashima has summarized the basics of the SA and ESD methods (12, 14). A recent article further details the mechanisms of the SA method (13). The rate constant and the effect of temperature were studied (14, 15). For the ESD method, however, thermodynamic and kinetic aspects have yet to be developed to make sure that crystallization is reproducible and feasible on an industrial scale.

This article contributes to modeling the ESD method. It describes the crystallization of an acetone-soluble pharmaceutical drug substance.

2. Materials and methods

2.1 Experimental design and standard operating procedure

Figure 1 shows the apparatus used to study the ESD crystallization process. It consists of a dissolution tank (I), a pressurized flow system (II), and a crystallizer (III). Temperature control is achieved by circulating water from thermostatically-controlled baths through a double-jacket system fitted round the various parts of the unit. The two tanks have removable baffles and marine impellers for stirring. The flow rate of the drug substance solution from the dissolution tank (I) to the crystallizer (III) is controlled.

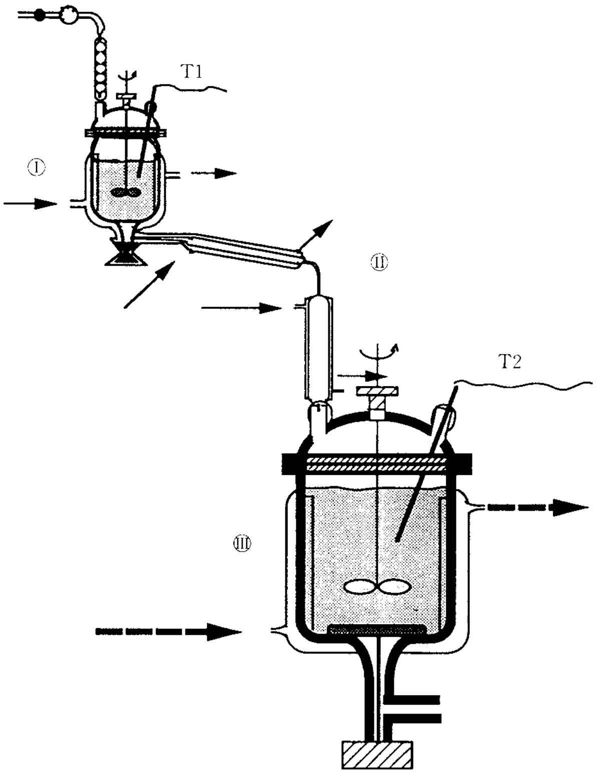

Fig. 1 ESD process. I-Dissolution tank ; II-Pressurized system ; solution runs down through a capillar orifice ; III-Batch crystallizer.

A drug substance solution is prepared in the dissolution tank (I) by dissolving a batch of the drug substance in acetone at temperature T_1. Double-distilled water is poured into the crystallizer (III) together with several hundred ppm of Mowiol® and maintained at temperature T_2. The solution is added when conditions in both tanks have stabilized.

An emulsion made up of acetone droplets saturated with the drug substance then forms in the crystallizer. These droplets quickly become spherical agglomerates consisting of a multitude of microcrystals of the drug substance. The suspension is then stirred for at least 20 minutes in the crystallizer. At the end of the procedure, the grains are removed from the bottom of the crystallizer. They are filtered using a Buchner funnel and washed with double-distilled water before drying in an oven at 50°C for 24 hours.

2.2 Products

The drug substance is a crystallized product with a purity of over 99.9%, density of $\rho_s = 1270 \pm 20$ kg/m^3 at 20°C, melting point at $T_m = 94.2 \pm 0.5$°C and melting enthalpy at $\Delta H_m = 28230 \pm 250$ J/mole. The water used is double-distilled and the purity of the acetone is over 99.7%. Mowiol® is a polyvinyl alcohol used as a dispersant and supplied by Hoechst.

2.3 Drug substance solubility in acetone, water and acetone/water mixtures

Figure 2 shows the apparatus used to determine the equilibrium of binary and ternary mixtures as a function of temperature. For the binary mixture (**Figure 2(a)**) the procedure is quite standard. Solutions containing an excess of solid are stirred under thermostatically controlled conditions. The saturated solutions in 25-ml flat-bottom flasks, fitted with condensers, are placed in a thermostatically controlled bath and stirred magnetically. Samples of supernatant are filtered and analyzed during the process.

With the test apparatus (**Figure 2(b)**), samples can be drawn from the two liquid phases of ternary mixtures without disturbing the equilibrium. It consists of a thermostatically controlled tank with six sampling points. Syringes fitted with needles are introduced into sampling points to remove samples of the liquid phases without disturbing the equilibrium.

2.4 Evaluation of physical characteristics

The conditions under which crystallization is carried out determine the texture of the grains ; it is this texture which then defines the functional properties of the powder bed. In order to control the reproducibility of this process, a certain number of physical properties were evaluated. Since the material and methods are standard, they are only presented in tabular form in **Table 1**.

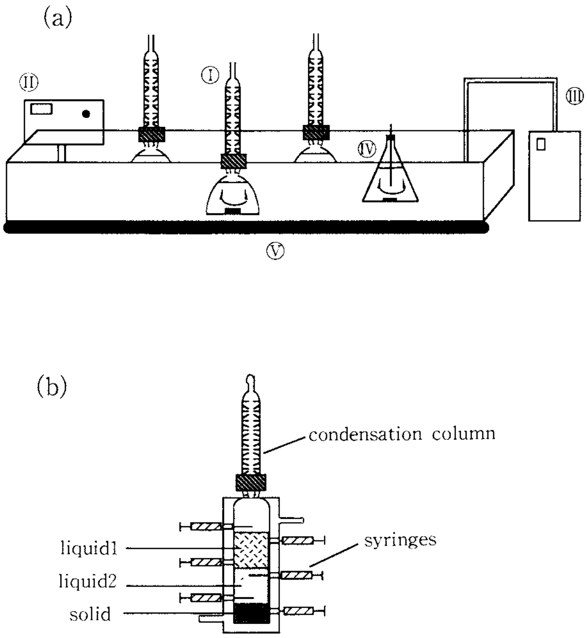

Fig. 2 Apparatus used for measuring liquid/liquid equilibrium (a) and liquid/liquid/solid (b) equilibrium.
(a) Ⅰ-Drug substance solution
Ⅱ-Temperature control
Ⅲ-Temperature-controlled stirring tank (±0.1°C)
Ⅳ-Control vessel for temperature measurements
Ⅴ-Magnetic stirring

Table 1 Measurement of spherical grain properties

Property measured	Methods
Crystal structure	X ray diffraction
Density	Pycnometry
Apparent density ρ_{app}	$\rho_{app}=m_p/V_0$ m_p : powder mass-V_0 : apparent volume
Tapped apparent density ρ'_{app}	$\rho'_{app}=3/2\ [(V_{500}/m_p)+(V_{100}/m_p)]$ V_{100} and V_{500} : apparent volumes after 100 and 500 taps
Carr index	$100\ (\rho'_{app}-\rho_{app})/\rho'_{app}$
Size distribution	Particle Size Analyzer Galai CIS1
Porosity	Micromeritics Autopore II 9215 apparatus
Shape	Scanning Electron Microscopy
Flowability	Flow rate of 100g of powder in a standard funnel
Compaction	With 0.5% of Mg stearate in a uniaxial Frogerais A0 press Matrix : 1cm^3, flat pattern of area : 11.28 cm^2

3. Results and discussion

3.1 Solubility profile

The drug substance/acetone/water ternary mixture yields a phase diagram with five regions. The Mowiol® does not penetrate the droplet under transformation so this ternary mixture is the one about to crystallize. **Figure 3** shows the appearance of this diagram at 20°C.

The monophasic DS/acetone/water liquid region depicted is in equilibrium with the different phases as a function of the mass ratio of acetone in the water/acetone mixture (Ra=acetone/(water+acetone)). In region A (Ra=1), DS is highly soluble in acetone (approximately 0.4 kg of DS/kg of solu-

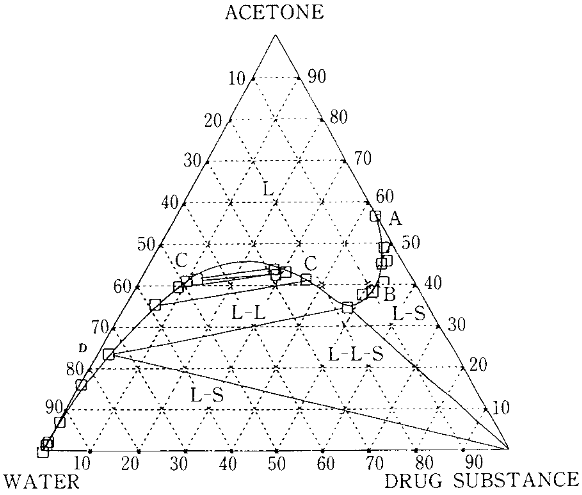

Fig. 3 Drug substance/acetone/water equilibrium at 20.2°C.

tion at 20°C). In region B (Ra=0.925), DS is even more soluble. Dissolvability of the molecule is enhanced by the increase in the number of hydrogen bonds resulting from the presence of a certain percentage of water. In region C (Ra=0.67), solubility decreases markedly. Whereas between regions A and C, the monophasic region was in equilibrium with the biphasic liquid/solid region (crystallization of DS), from regions C to D, the monophasic region is in equilibrium with the biphasic liquid/liquid region. A liquid with a high DS concentration which is non-miscible in a liquid with a low DS concentration appears and forms an emulsion. The liquid with a high DS concentration is itself in equilibrium with a triphasic region, made up of the two liquids and the crystallized DS. In region D (Ra=0.24), the aqueous medium limits solubility to 2‰ so the liquid/liquid region disappears, yielding an equilibrium L≪L/S, between regions D and E. When Ra tends toward 0, solubility decreases to 0.1‰ (crystallization of DS).

3.2 Grain texture

3.2.1 Grain shape, size and texture

Scanning electron microscope studies revealed that the shape and roughness of the grain surface depends mainly on the mass ratio (Ra) and on the difference in temperature $\Delta T = T_1 - T_2$ used. The grains produced were classified into five groups which are presented in **Figure 4**.

In regions I, II and IV of **Figure 4**, the grains are spherical whereas in regions III and V they are deformed, i.e. they appear slightly elongated. Sphericity decreases as the acetone: water ratio increases. Ratios exceeding 0.060 kg acetone: kg water systematically produced elongated grains. The difference in temperature may cause droplets to coalesce and grains to agglomerate in the crystallizer (region III).

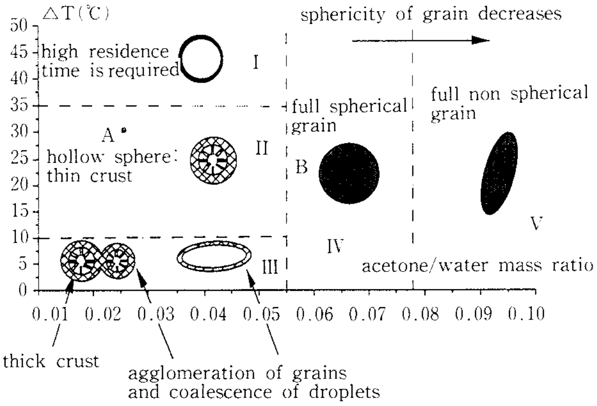

Fig. 4 Grain structure as a function of the operating conditions.
A and B: Operating procedure for producing grains used in tableting.

Acetone : water ratios of less than 5% (**Figure 4**) produce grains with an internal texture characterized by several layers. Acetone : water ratios of 6% or more produce grains with a homogeneous internal texture. If the difference between T_1 and T_2 is marked (>35°C), scanning electron microscope studies show small, spherical grains with a thick outer crust and no preferential orientation of crystals. The core is hollow (region I). These grains remain soft for a long time, indicating that a high residence time in the crystallizer is required before filtration. If there is an average difference between T_1 and T_2 (10 to 35°C), grains remain spherical, may have a hollow core, but are made up of two layers (region II). The outer crust is less dense and the surface is covered with crystals. The internal layer is very porous and the crystals are oriented towards the center. If the difference between T_1 and T_2 is less than 10°C, the outer crust is more porous and clusters of grains form (region III). **Figure 5** shows the photographs of solid and hollow grains. Grain size depends on stirring conditions, the flow system and the Mowiol® concentration.

3.2.2 Internal porosity of the grains

Products prepared under the conditions represented by points A and B shown in **Figure 4** were compared. A represents group II and B represents group IV. The intraparticulate volumes of A and B are equal (0.4 cm³/g), but are not distributed in the same way. Product A has pore diameters over 6 μm opening into the central cavity, whereas product B pores are of smaller diameter and are more often situated in the micropore region (**Table 2**).

Table 2 Intraparticle volume (cm³/g) as a function of diameter

Pore diameter (mm)	Product A	Product B
6 to 15 μm (macroporosity)	0.25	0.10
0.2 to 6 μm	0.10	0.15
0.06 to 0.2 μm (microporosity)	0.05	0.15

The volume of mercury retained between the particles corresponds to a density of 1.10 g/cm³, which is even lower than the density measured by pycnometry, but high microporosity indicates that there is a certain amount of closed porosity. After crushing, the volume of mercury indicates grains with a density of 1.22 g/cm³, which is close to the triclinical crystal habitus. The disparity between

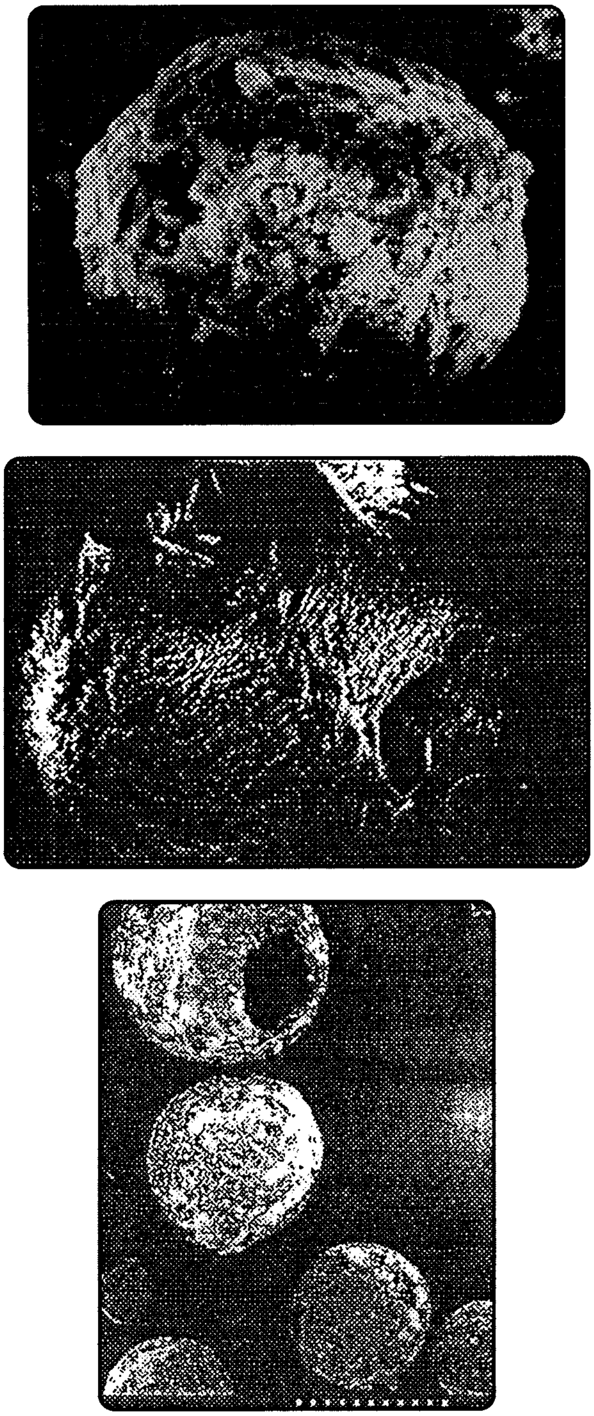

Fig. 5 Texture of spherical crystals: (a) type I; (b) type II; (c) hollow crystals.

the expected result (1.27 g/cm^3) and the pycnometric data (1.16 g/cm^3) is explained by the closed porosity.

Diagrams similar to that presented in **Figure 4** were prepared by Kawashima for many other substances and solvent/non-solvent combinations (19, 20). Similar results were found for all the other cases we tested. It seems possible, therefore, to make the following generalized statement: the ESD method yields three types of spherical grains (regions I, II and IV), which differ with regard to their internal structure and surface appearance. And second, two other types of grains can be obtained (regions III and V), but they are irregular and non-reproducible.

Two important questions then arise: Do these differently textured grains have different properties? And what are the kinetic aspects giving rise to these differences?

3.3 Functional properties of the grains

Once dried, all the spherical grains of the I, II, and IV groups flow freely. All Carr indices are less than 12, and all tapped apparent densities are greater than 0.50 g/cm^3. **Table 3** shows the results for products A and B.

Table 3 Products A and B-Mean size and properties

	Product A	Product B
Poured density (g/cm^3) (number of taps=0)	0.47	0.49
Tapped density (g/cm^3) (number of taps=500)	0.53	0.52
Carr index	11	5.8
Mean diameter (μm)	230	270
$\% < 100$ μm and $\% > 500$ μm	26 and 8	5 and 7

The size, shape, hardness and density of the spherical particles indicate good flowability. They can be coated easily because of their surface smoothness. Their size can be adapted for filling capsules or for mixing with direct tableting excipients (grain size 75-175 μm), by optimizing the stirring conditions. The flowability required for tableting is ensured. Types I, II and IV do not differ with regard to all these points. When coating, holes which are occasionally observed on the surface of the grain are to be avoided (**Figure 5**).

Extensometric criteria (**Table 4**) were used to compare agglomerates A (hollow spheres) and B (homogeneous spheres) with powder P made up of individual crystals (5-50 μm plate-like crystals) developed using standard crystallization procedures. The matrix of the tableting machine was filled manually, since P was unsuitable for automatic filling. It was, however, possible to fill automatically with products A and B.

Tensile strength (R_0) was adequate (aspirin $\doteqdot 1.0$ MPa and spray-dried lactose $\doteqdot 10$ MPa) and sensitivity to porosity low ($\gamma < 12$), producing a tablet ($R = 0.8$) with adequate porosity ($\varepsilon = 15\%$) under

Table 4 Extensometric results

Products	A	B	P
R_0 (MPa)	3.8	4.1	5.6
γ	10.8	10.5	11.5
P_y (MPa)	37	43	60
E (J/g)	25	21	53
P_1 (MPa)	150	200	80
$R = R_0 e^{-\gamma\varepsilon}$	R = tensile strength (Schleuniger) γ = sensitivity of R to ε ε = porosity after relaxation		
$n = n_0 e^{-P/P_y}$	n = porosity under stress (%) P_y = yield pressure (MPa)		
P_1 = minimum capping pressure (MPa)	E = specific compression energy (area of the curve P/movement)		

moderate pressure (70 MPa). In terms of this criterion, A and B are equivalent and similar to P, suggesting that it is the molecule itself which determines cohesion. The two spherical products are plastic ($P_y < 55$ MPa), whereas the crystallized P lies between plasticity and fragility. Specific compression energy (E) shows that P absorbs more energy than A and B. This energy, however, does not contribute to tablet cohesion so effectively since R_0 and γ are similar. The minimum capping pressure (P_1) at which tablets start capping confirms that P tablets are not as tough as A tablets, and A tablets are not as tough as B tablets.

Finally, the tableting profiles of A and B are quite similar. Under low pressure, the spherical grains fragment, redistribute and deform plastically. The tablet is obtained simply with no risk of capping. P crystals rearrange themselves less easily than the A and B fragments, and deform less under working pressure (70 MPa). Tablets obtained are acceptable, but tend to cap if high hardness values are required (R = 1.2 MPa).

The ESD method produced grains with many flaws (non-oriented crystals, microporosity, closed porosity). These flaws enable pressure to interact in a more isotropic and plastic fashion than it does with the powder obtained using the standard crystallization technique.

All the tablets of pure DS were unusable since the hydrophobic solid is practically insoluble and therefore does not dissolve well. Dissolution is the only problem related to formulation with spherical grains. There is a wide dissolution range and the problem can be solved by the addition of 5-10% of the excipients. With P, the formulation must be flowable, wettable and avoid capping. This requires a granulation procedure and the addition of 30-60% of the excipients.

4. Grain formation pattern by the ESD technique

Knowing the mechanism of grain formation should help in obtaining the chosen texture (**Figure 4**), in controlling surface appearance and checking for any cavities (**Figure 5**), and in obtaining the parameters required for optimization and scale-up of the process. Three steps are to be taken into account: droplet formation, supersaturation and crystallization of DS in droplets.

4.1 Droplet formation

Droplet size depends mainly on flow conditions, on stirring and on the surface tension between the droplet and the solution. Supposing that the droplets circulate in the continuous phase at the terminal settling velocity, it was calculated that 700-μm spheres circulate a hundred times quicker than 70-μm spheres (8.1×10^{-3} versus 8.81×10^{-5} ms^{-1}). Using the three-dimensionless numbers of Reynolds, Morton and Eotvos, Clift (21) determined which form a droplet takes at the terminal settling velocity. Under our test conditions as shown in **Figure 6**, droplets remained spherical. If surface tension is increased, droplets above 500 μm are subject to

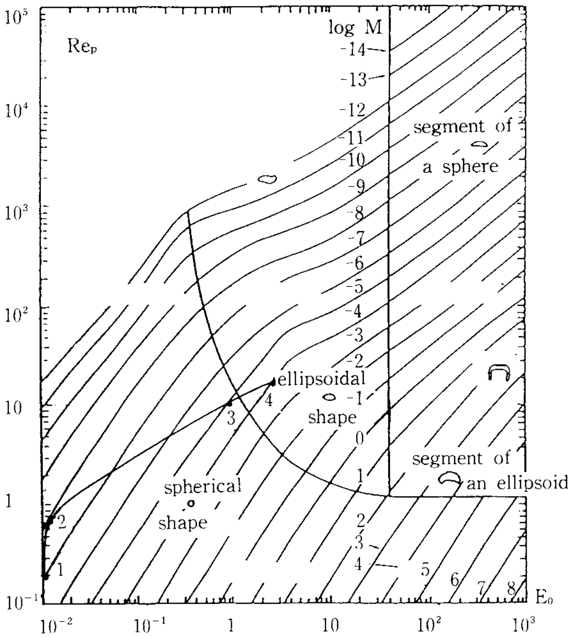

Fig. 6 Shape and size of a droplet free-falling in a liquid (from reference 21)
Re_p : Reynolds number ; E_0 : Eotvos number. Diameters of particles as a function of points on the scale : 1-70 μm ; 2-300 μm ; 3-750 μm (low surface tension) ; 4-500 μm (high surface tension)

deformation. Ellipsoidal or crescent shapes found in some cases by several researchers can be explained by high Reynolds and Eotvos numbers.

The movement of droplets within the medium induces circulation inside the droplets. The intensity of this internal circulation depends on the movement speed. Modeling showed that internal circulation is substantial in large droplets (450-1500 μm), less in medium-sized droplets (300-450 μm) and non-existent in small droplets (<300 μm).

4.2 Supersaturation

The drug substance is supersaturated from 20 to 25°C. Therefore cooling at $(T_1 - T_2) > 30°C$ does not have the same effect as cooling at $(T_1 - T_2) < 20°C$.

Since the droplets are spherical they can be represented as a pile of n concentric crowns in which supersaturation is S^j, where $j=1$ on the surface, and $j=n$ in the center. The acetone content increases with j (exit of acetone towards the exterior), and the water content decreases with j (penetration of water). The acetone: acetone+water mass ratio (Ra) increases markedly as a function of j.

When a hot droplet comes into contact with cold water, supersaturation occurs which is more marked on the surface than at the center. The solid therefore tends to appear on the surface of the droplet.

At constant temperature, DS is more soluble in acetone/water mixtures with a low water content. When water is added to the mixture (**Figure 3**), DS becomes less soluble. Supersaturation obtained by adding water is not possible at constant temperature for Ra between 0.7 and 1. But if the overall temperature of the droplet is decreased to temperature T, the critical Ra value is modified and it is a particular internal crown (S^i) which first reaches supersaturation. As a function of the size and the position of the droplet, i can include all values between 1 and n.

When internal circulation occurs in a droplet, it tends to homogenize concentration within the droplet. Supersaturation is then identical throughout and crystals will appear in a uniform fashion throughout the droplet.

4.3 Crystallization

All the possibilities are summarized in the three

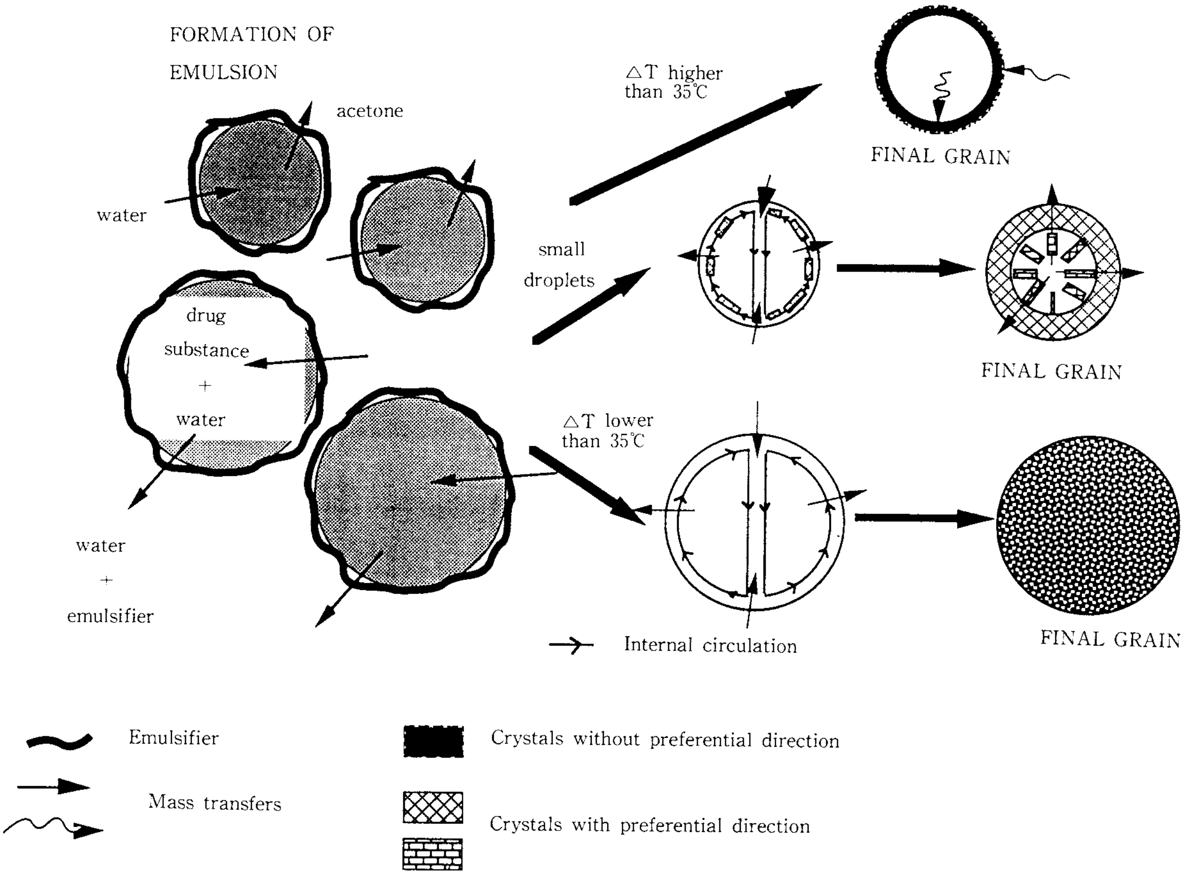

Fig. 7 Formation mechanism

cases shown in **Figure 7**.

4.3.1 Hollow grains with a single outside layer

Small-sized droplets (i.e. <300 μm) subjected to cooling at $(T_1-T_2)>35$°C very rapidly reach a state of supersaturation where the heat transfer takes place (S^1). A crust of nuclei is formed and increases by diffusion, rapidly filling any cavities. A single-layered grain with non-oriented crystals is thus formed (Type I).

4.3.2 Hollow grains with two outside layers

Larger-sized droplets (i.e. 450 μm) which undergo less rapid cooling ($T_1-T_2\cong 25$°C) also start nucleating where the heat transfer takes place (S^1). However, because circulation is quite marked, it inhibits radial diffusion and favors tangential movement, so the crystals grow at right angles to the radius until circulation is stopped (solidification) and diffusion slowed down (low porosity). Growth then changes both in direction and speed, and well-developed axial crystals form in the intermediate Si layers (Type II).

4.3.3 Homogenous grains

Large-sized droplets (>450 μm) originate from the competition between the internal circulation and acetone-water transfers. When the acetone : water ratio is high, the speeds generated by the mass transfer are higher than those generated by the internal circulation. As the mass transfer for the drug substance tested is very rapid, there is a time lag before nucleation during which internal circulation facilitates mixing within the droplet resulting in homogenization of the concentration. Under these conditions, when the nuclei appear they are well dispersed, very fine and cluster together forming a network of micropores.

4.3.4 Grain clusters and grains with cavities

Cooling at too low a temperature (difference $T_1-T_2<10$°C) produces grain clusters (pairs of coalescent droplets). Some grains have a large cavity (**Figure 5**) which can be explained by coalescence : the shocks received by the coalescent grains during stirring (against the tank wall and the impellers) cause them to separate into two parts : one grain retains a cap, the other a cavity. Surface tension also influences agglomeration and cavity formation.

Finally, cooling has an effect on the roughness of the grain surface. When the temperature is high (38°C) there are no crystalline facets on the surface. When it is lower, lines appear which represent the outward growth of crystalline facets and when the temperature is low, the grains are deformed, have cavities and agglomerate.

To summarize, for a specific physicochemical system and in given hydrodynamic conditions, there is a critical grain size. Below this critical size, grains are hollow, with one or two layers depending on the difference in temperature T_1-T_2 ; above this critical size ; they are homogeneous or have a slight hollow in the center depending on the solvent : non-solvent ratio.

5. Conclusion

The ESD spherical crystallization method developed by Kawashima is attractive because the crystallized grains produced are functional. As it is neither a purification phase nor a product-recovery phase, but a functionalization phase, it resembles granulation. However, the basic data and mechanisms involved are typically those of crystallization.

With such a polyphasic system, physicochemical complexity and related technological problems were to be feared. Amongst the solvent/non-solvent combinations suggested by Kawashima, those of acetone/water and ethanol/water are suitable for pharmaceutical purposes since they are authorized liquids and can be applied to a large number of products.

The research presented here concerns the acetone/water/DS combination and specifies the thermodynamic and kinetic bases of the technique used.

From the thermodynamic viewpoint, S (acetone) must be a very good solvent and NS (water) a non-solvent miscible in S in such a way that in the presence of the solute (DS), S emulsifies in NS. By controlling surface tension and stirring, the size of the emulsion droplets can be regulated. The use of a phase diagram S/NS/DS, at all working temperatures and with or without dispersant, is indispensable for this study.

From the kinetic viewpoint, the droplets quickly assume the bath temperature. The mass transfer is the following : diffusion of S in NS, diffusion of NS in S, circulation of S+DS inside the droplet and nucleation of DS. The principal parameters are droplet size, the initial concentration of S in NS, and the difference in temperature at the time S+DS are introduced into NS. The area of these three dimensions covers a region with spherical crystals and a region with deformed crystals. The spherical region subdivides into grains with hollow centers and homogeneous grains. Moreover, there are three types of solid texture around the central cavity. These various possibilities (**Figures 4** and **7**) are now modelized. The ESD method can be used to produce grains with a large variety of shapes, sizes (1 to 2000 μm) and internal textures.

Sizes of the order of 100 and 750 μm were tested by direct tableting. They are spherical and contain various types of grains which can be homogeneous or hollow. For DS, these grains are all of high quality and have similar profiles. It is possible, therefore, to create conditions to optimize production and reproducibility (**Figure 4**, Types II or IV).

The ESD method is similar in complexity to that of crystallization. There are no particular problems concerning solid/liquid separation or drying. The formulation and tableting process is consequently simplified.

Acknowledgments

The authors wish to acknowledge Rhône-Poulenc-Rorer and the French Ministry of Higher Education and Research (Ministère de l'Enseignement Supérieur et de la Recherche (MESR)) for their financial support to this project. They would also like to thank Professor Dominique CHULIA from the School of Pharmacy, University of Limoges (Faculté de Pharmacie), for her participation.

Nomenclature :

E : specific compression energy
Eo : Eotvos dimensionless number ($=g\Delta\rho d^2/\sigma$)
m_p : powder bed mass
P_y : yield pressure (MPa)
P_1 : minimum capping pressure (MPa)
R : tensile strength (MPa)
Ra : mass ratio of acetone in the water/acetone mixture (kg acetone per kg water/acetone mixture)
Re_p : Reynolds particle number ($=\rho\ d_g\ U^\infty/\mu$)
T : temperature (°C)
T_1 : initial temperature of the dispersed phase (°C)
T_2 : initial temperature of the continuous phase (°C)
U^∞ : terminal settling velocity in the continuous phase (ms^{-1})

Greek characters :

ε : porosity (%)
μ : viscosity (Pa.s)
ρ_{app} : apparent density of powder bed (kg/m^3)
ρ'_{app} : tapped apparent density of powder bed (kg/m^3)
σ : surface tension between the droplet and the continuous phase (Nm^{-1})

References

1) Kawashima Y. and C.E. Capes, Powder Technology, 10, (1974), 85.
2) Kawashima Y. and C.E. Capes, Powder Technology, 13, (1976), 279
3) Kawashima Y. and C.E. Capes, Ind. Eng. Chem. Fundam., 19, (1980), 312
4) Kawashima Y., SC : a new tool for micromeretic design of crystal and preparation of drug delivery systems, Int. Symp. on agglomeration, Nov. 15-17, Nagoya, Japan, 487-492.
5) Kawashima Y. and coll., Preparation of pharmaceutical agglomerated crystals for direct tabletting and microencapsulation, Int. Symp. on agglomeration, Nov. 15-17, Nagoya, Japan, 526-531.
6) Kawashima Y. and coll., Preparation of controlled release microspheres of Ibuprofen with acrylic polymers by a novel quasi emulsion solvent diffusion method, J. Pharm. Sci., 78, (1989), 68-72.
7) Kawashima Y. and coll., Preparation of controlled release microsponge and microballoon of Ibuprofen with acrylic polymers by SC technic, Chim. Pharm. J., 41, No. 3, (1989), 167-169.
8) Gordon M.S. and Z.T. Chowan, Naproxen particles via SC, Drug Dev. and Ind. Pharm., 16, No. 8, (1990), 1279-1290.
9) Kawashima and coll., Preparation of D/L lactide/glycolide copolymer nanospheres with a water-soluble or insoluble drug by a novel spontaneous emulsification solvent diffusion method, Proc. 6th Int. Conf. Pharm. Tech. Paris, vol. III, (1992), 32-40.
10) El-Helv A. and coll., Utilization of SC in the preparation of sustained release Furosemide tablets, STP Pharma Sci., 4, No.6 (1994), 409-413.
11) Kawashima Y. and coll., Improvements in flowability and compressibility for direct tabletting by ESD, Powder Technology, 78, (1994), 151-157.
12) Morishima K. and Y. Kawashima, Powder Technology, 76, (1993) 57-64.
13) Chow A.H.L. and M.W.M. Leung, A study of the mechanisms of wet SA of pharmaceutical powders, Drug Dev. and Ind. Pharm., 22, No. 4, (1996), 357-371.
14) Kawashima Y., Application of SC to particulate design of pharmaceuticals, in Powder Tech. and Pharm.Proc., Elsevier, Amsterdam, chap. 14, (1992), 493-512.
15) Kawashima Y. and coll., Powder Technology, 34, (1983),

255-260.
16) Kawashima Y. and coll., Powder Technology, 39, (1984), 41-47.
17) Svarovski L., Powder testing guide, Elsevier Applied Science Publisher, N.Y. (1987), 146p.
18) Celik M., Overview of compaction data analysis techniques, Drug Dev. and Ind. Pharm., 18, Nos. 6 and 7, (1992), 767-810.
19) Kawashima Y., Spherical Crystallization of pefloxacin mesylate, Conference to the Japanese Ass. of Particle Technology, 27-29 October 1988.
20) Kawashima Y. and coll., Preparation of spherically agglomerated crystals of an antibacterial drug for direct tabletting by a novel spherical crystallization technique, Int. Symp. Agglom. 5th, 3, 228-234 (1989), Inst. Chem. Eng. Rugby Publishers, UK.
21) Clift R. and coll., Bubbles, drops and particles, Academic Press ED., N.Y. (1978).

Authors' short biographies

Fabienne ESPITALIER

Dr Fabienne ESPITALIER was born in 1968. She graduated from the Ecole Nationale Supérieure de Génie Chimique of Toulouse in 1991. She prepared a PhD thesis on spherical crystallization by the quasi-emulsion technique in the Chemical Engineering Laboratory of Toulouse (UMR CNRS 5503) and obtained her doctor's degree in 1994. She is now assistant professor in the Ecole des Mines d'Albi Carmaux, in charge of crystallization research.

Béatrice BISCANS

Dr Béatrice BISCANS was born in 1958. She graduated from the Ecole Nationale Supérieure de Génie Chimique of Toulouse (ENSIGC) in 1982. She prepared a PhD thesis on the separation of proteins by ion exchange chromatography in the Chemical Engineering Laboratory of Toulouse (UMR CNRS 5503) and obtained her doctor's degree in 1985. She then undertook post-doctoral research on the electrophoretic separation technique.

Since 1987, she has developed and supervised several studies in the field of crystallization as a researcher of CNRS (French National Scientific Centre of Research), working in the Chemical Engineering Laboratory of Toulouse (UMR CNRS 5503). In particular, her work involves the development of research studies on spherical crystallization.

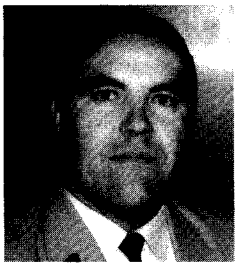

Michel DELEUIL

Dr Michel DELEUIL graduated from the Chemical High School of Lyon (ESCIL). In 1968, he joined Rhône-Poulenc Company, where his work focussed on powder processes (mixing, milling, handling, drying, particle size enlargement). He was instrumental in the development of new processes such as industrial chromatography, plaster dry compaction, prilling, and electrofiltration. Since 1989, he has been in charge of pharmaceutical formulations at Rhône-Poulenc Rorer. He is co-editor of a handbook (Powder Technology and Pharmaceutical Processes, Elsevier, 1994), and associate engineer of the Rhône-Poulenc Group. He considers Dr Kawashima's studies on spherical crystallization to be particularly relevant, and initiated the present study with Dr Kawashima in the role of consultant.

Claude LAGUERIE (1947-1995*)

Professor Claude LAGUERIE died* in July 1995. He was head of the Ecole Nationale Supérieure de Génie Chimique of Toulouse (ENSIGC). During his lifetime, he developed and supervised many studies in the fields of fluidization, chemical reactor engineering, crystallization, drying and solids processing. He published more than 100 papers in international journals and also gave expert advice on spherical crystallization processes, which was also the subject of one of his last research projects.

Research

Comparison Between Flow Velocity Profiles in Conical and Cylindrical Hydrocyclones

B. Chiné
*UCSC Catholic University, Faculty of Engineering**
G. Ferrara
*University of Trieste, Chemical, Environmental and Raw Materials Engineering Dpt.***

Abstract

Both conical and cylindrical cyclones are used in the size classification and density separation of particles. Conical hydrocyclones have a more general use and have been thoroughly studied concerning both flow velocity profiles and their classification performance. Cylindrical cyclones with peripheral underflow discharge have been used less and studied less, but there has recently been renewed interest. This concerns particularly density separation as well as size classification in two-stage cylinder-cyclone systems.

Tangential velocity profiles differ in conical and cylindrical cyclones. In conical cyclones, they approach the theoretical free vortex profile (with a forced vortex region confined near the axis); in cylindrical cyclones with peripheral underflow discharge they approach the forced vortex profile in a large part of the vessel. These results have been obtained by making Laser Doppler Velocimetry (LDV) measurements on 100-mm diameter cylindrical cyclones with peripheral and axial discharges under different flow conditions and with different ratios between overflow and underflow flow rates. It has been demonstrated that the occurrence of the one or the other vortex type does not depend on the vessel shape alone but on the inward radial flow patterns inside the vessel. This depends on how the fluid is fed and discharged as well as on the vessel shape.

Finally, the paper discusses the influence that the different tangential and axial velocity profiles in conical and cylindrical cyclones have on separation sharpness, in both size classification and density separation processes.

1. Introduction

The conical hydrocyclone was first patented in 1891 by Bretney but was not significantly applied until the 1940s, when it was used in mineral processing and coal preparation by the Dutch State Mines. Afterwards, the hydrocyclone became an important process unit in particle technology and was used in the chemical, textile and metalworking industries as well as many others.

Different cyclone shapes were proposed as described by Hoffmann (1953). However, it is only the conical and the cylindrical shapes which have been applied industrially. The conical cyclone is the most widespread dynamic classifier. The cylindrical vessel is used much less, and its more important applications are not in classification processes but in dense medium separation processes. As a dense medium separator, it was introduced in the USA by Rakowsky (1959), and is known as the Dynawhirlpool (DWP). The DWP was then modified to attain different separators such as the Tri-Flo developed in Italy and the Larcodems developed in the UK (**Fig. 1**). The conical cyclone is also the most widely used in dense medium separation at the present time. However, as a multi-stage separator (Ferrara, 1995), the Tri-Flo is attracting interest because it ensures high separation sharpness. The Larcodems has gained interest because it is large and can treat coals up to 100 mm top-size (Shah et al., 1986).

As a classifier, the cylindrical vessel has been used more frequently as the first stage of a two-stage arrangement where the second stage is a conical cyclone. In this application, the cylindrical vessel has a peripheral underflow discharge which

---

* Concepcion, Chile
**Trieste, Italy

† Received: 1 Sept., 1997

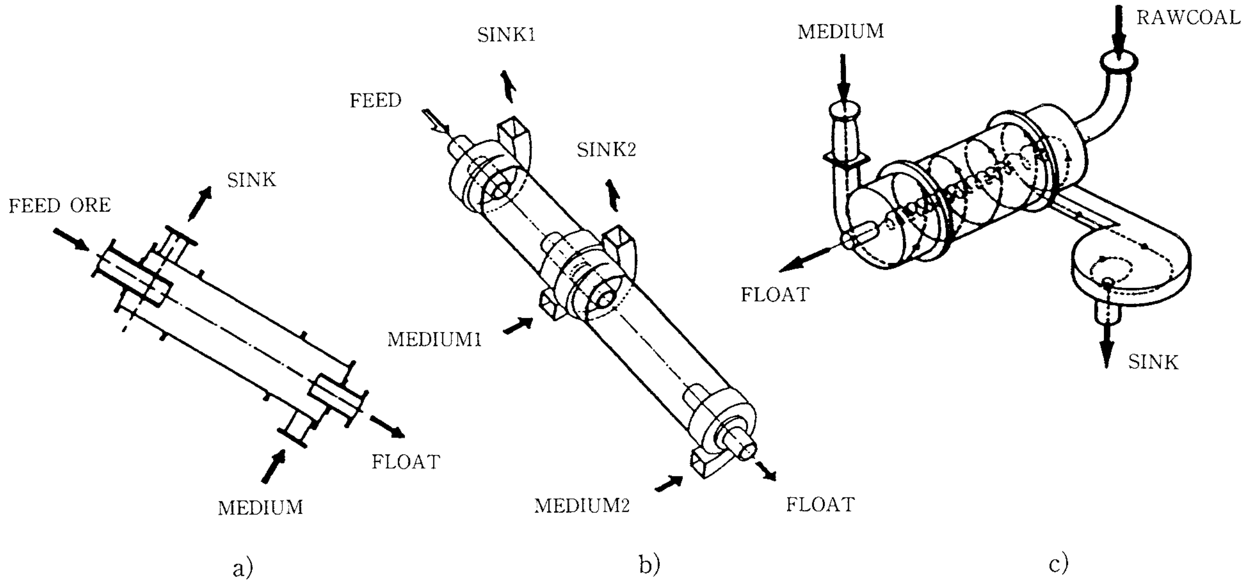

Fig. 1 Cylindrical dense medium separators: (a) Dynawhirlpool (DWP); (b) Tri-Flo; (c) Larcodems.

tangentially exits the bottom of the cylinder. The underflow also tangentially enters the conical cyclone (**Fig. 2**). A classifier of this type was described by Povarov (1961) and manufactured by Krebs (1965), who installed two-stage cyclones for both classification and upgrading values long ago. Multi-stage cylinder-cyclone systems have been used for different purposes, such as degritting mine water prior to pumping (Kelsall and Holmes, 1958), dissolving gypsum for agricultural purposes (Kelsall et al., 1960), and improving classification of ball mill discharge to reduce overgrinding (Kelsall et al., 1974).

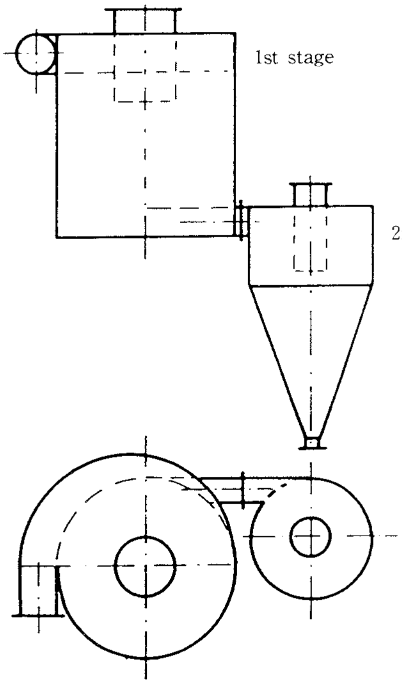

Fig. 2 Two-stage arrangement with a cylindrical and a conical cyclone.

More recently, the Twin Vortex cyclone (TC-cyclone) was developed in Finland (Heiskanen et al., 1987). The primary cylindrical section in this design has a central adjustable cone at the bottom; the underflow enters through the gap formed between the cone and the cylinder into an expanded cylindrical section (under the cone) with a peripheral discharge which feeds the second-stage conical cyclone. Wash water is injected into the expanded cylindrical section. The authors claim better efficiency (lower imperfection values) and a great reduction of the bypass flow of fines to underflow.

Another application of the two-stage arrangement was proposed by Restarick (1989 and 1991). In this design, a variable concentric aperture valve was interposed between the peripheral underflow discharge of the first-stage cylinder and the second-stage standard cyclone. Partial closure of this inter-stage valve decreases the flow rate and increases the pulp density of the cyclone feed, producing higher density cyclone overflow and coarser classification. The author claims a better separation sharpness, compared with single units, the possibility of shifting the cut-size by simply adjusting the inter-stage flow control valve, and flexibility in coping with variations of feed properties in closed grinding circuits.

Trawinski (1981 and 1984) proposed an application of the cylindrical vessel as a single classifier. In this design known as the CBC (circulating bed classifier) hydrocyclone, the underflow exits the center of the bottom of the cylinder (**Fig. 3**). Hence, there is no difference in discharges between Trawinski's vessel and conical hydrocyclones: in both, the discharges are located along the cyclone's axis, as opposed to the previous cylindrical vessels, and this greatly influences the flow velocity profiles as we will explain later. In the CBC-cyclone, strong convectional circulation has been observed near the bottom, due to the vortex being slowed down by wall friction. The circulating flow is downward in direction near the walls and upward in the center. At the bottom, the flow is inward and assists the discharge of the solid, thus making discharge possible without using a cone.

The solids concentrate in this circulating flow and form a circulating fluidized bed ; as the flow is upward in the center, it tends to relieve the underflow orifice. Consequently, the underflow discharge can be throttled much more than in the conventional cyclones without choking ; hence cut-sizes of up to 800 μm may be reached. Therefore, the cut-size can be easily controlled by throttling the underflow while the underflow concentration remains almost constant. Trawinski claims that the CBC-cyclone allows you to change the cut-size over a wide range (i.e. by a factor 6 instead of 2), the effect on the cut-size produced by variations in the feed size distribution and concentration is limited, and the values of the imperfection are lower than in conventional cyclones.

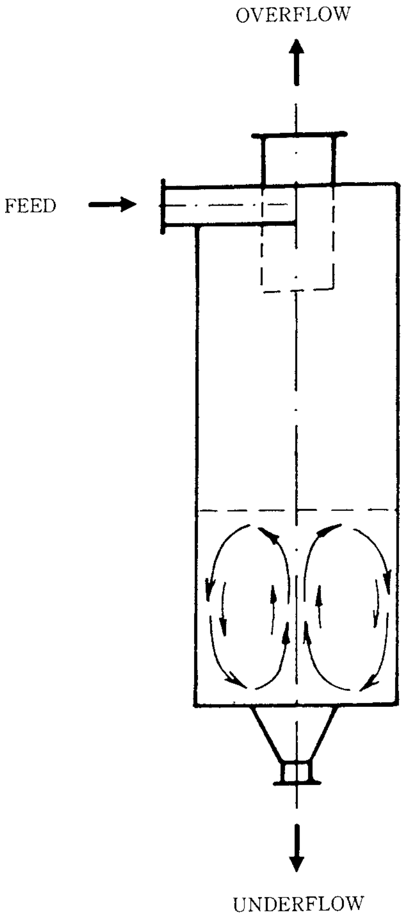

Fig. 3 Cylindrical cyclone with axial underflow discharge (CBC-cyclone) (Trawinski, 1981).

A great amount of operational data about performance, such as separation sharpness, partition curves, and predictive models, is available for the conical cyclone. In contrast, few data about particular operating conditions are available for cylindrical classifiers. This gap needs to be closed, also because recent investigations have revealed interesting properties of the cylindrical vessels.

2. Swirling flow in confined geometry

Swirling or vortex flow systems are frequently encountered in nature and technological applications. For example, large bodies of fluids form vortex systems in the atmosphere and the oceans, while swirling flows are applied in industry by using different cyclonic devices, to separate gases with different molecular weights, particles of different sizes and densities, or particles from gases or liquids.

A vortex may be of two types : (a) the forced vortex, where the tangential velocity is proportional to the radius ($w=k \cdot r$) and there is no shear rate between the concentric fluid layers (the fluid rotates as a rigid body) ; and (b) the free vortex, where the tangential velocity is inversely proportional to the radius ($w=k/r$) and there is a high shear rate between the concentric fluid layers.

The occurrence of one or the other vortex does not depend on the vessel shape alone but also on the radial flow patterns inside the vessel; this depends on how the fluid is fed and discharged as well as on the vessel shape. If the fluid enters the vessel tangentially at the external wall and exits at the axis, a free vortex occurs since-according to the law of conservation of angular momentum-the fluid elements increase their tangential velocity as the radius decreases ($w \cdot r=\text{constant}$). If the fluid enters the vessel at the external wall and exits at a peripheral discharge, no increase of the tangential velocity occurs with the radius and a forced vortex takes place.

In a conventional conical hydrocyclone, a combination of both vortex types occurs known as Rankine's vortex. It basically consists of two parts as shown in **Fig. 4** : a forced vortex-equivalent to a rotating rigid body (rotational flow)-between the

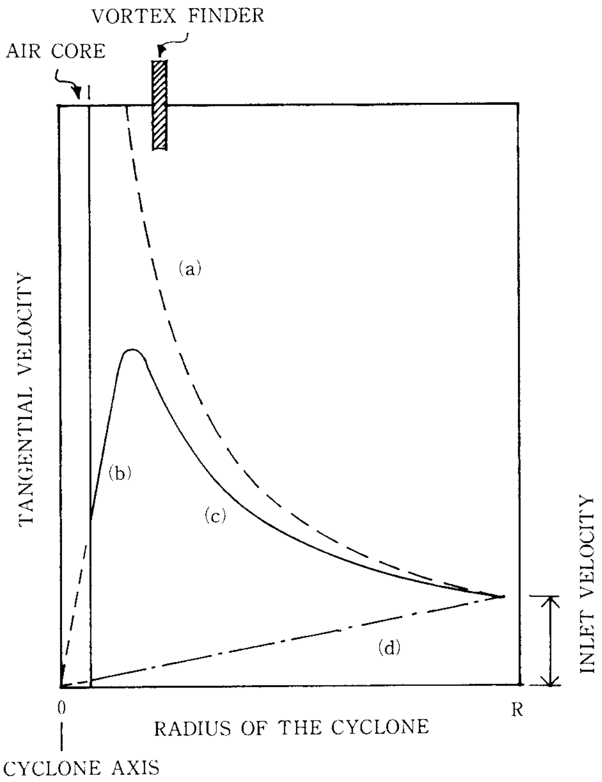

Fig. 4 Tangential velocity profiles for different vortex types: (a) theoretical free vortex ($w\cdot r=$ constant); (b) + (c) Rankine's vortex [where (b) forced vortex and (c) free vortex]; (d) theoretical forced vortex ($w/r=$ constant).

vertical axis of the vessel and a radius close to the radius of the vortex finder (a zone where the radial component of the velocity is virtually zero), and a free vortex or potential flow (irrotational flow) between the vortex finder and the wall (a zone with an inward radial component of the velocity). The region with the forced vortex is the central viscous or turbulent vortex region and is defined as a vortex core or viscous core.

In a cylindrical cyclone, different vortex types may take place: (a) if both overflow and underflow discharges are axial, as in Trawinski's CBC-cyclone (1981 and 1984), Rankine's vortex occurs as in a conical hydrocyclone; (b) if the overflow is axial and the underflow peripheral, the vortex type approaches a forced vortex when the underflow flow rate prevails (high value of the ratio: underflow flow rate/feed flow rate), it approaches Rankine's vortex if the overflow flow rate prevails. This behavior of cylindrical cyclones has been demonstrated in our experiments.

2.1 Theory

Working with cylindrical coordinates we consider Rankine's vortex in the plane (r,θ); this is a circular forced vortex flow with radius r_b and constant vorticity $\zeta=\nabla\times\mathbf{v}$ which is limited externally by an irrotational vortex. By excluding axial and azimuthal variations, we define the radii of two circular trajectories delimiting the forced vortex as $r_1<r_b$ and $r_2>r_b$, and w_1 and w_2 as the tangential velocity of the fluid for $r=r_1$ and $r=r_2$. By applying Stokes' theorem to the flux of ζ through two circular surfaces of radius r_1 and r_2, we obtain:

$$\iint_{S_1}(\nabla\times\mathbf{v})\cdot\mathbf{e}_z dS_1=\oint_{C_1}\mathbf{v}\cdot rd\theta\mathbf{e}_\theta \text{ for } r=r_1 \tag{1}$$

$$\iint_{S_2}(\nabla\times\mathbf{v})\cdot\mathbf{e}_z dS_2=\oint_{C_2}\mathbf{v}\cdot rd\theta\mathbf{e}_\theta \text{ for } r=r_2 \tag{2}$$

where e_θ and e_z are unit vectors. Then we obtain the two circulations Γ_1 and Γ_2:

$$\zeta\pi r_1^2=\Gamma_1=2\pi r_1 w_1 \tag{3}$$

$$\zeta\pi r_b^2=\Gamma_2=2\pi r_2 w_2 \tag{4}$$

which can be used to calculate the values of the tangential velocities of Rankine's vortex:

$$w_1=\frac{\Gamma_1}{2\pi r_1}=\frac{1}{2}\zeta r_1 \tag{5}$$

$$w_2=\frac{\Gamma_2}{2\pi r_2}=\frac{1}{2}\zeta\frac{r_b^2}{r_2} \tag{6}$$

If ω is the angular velocity of rotation of the rigid body, then:

$$2\omega=\zeta \tag{7}$$

and hence from Eqs. (5) and (6) one obtains:

$$w_1=\frac{\Gamma_1}{2\pi r_1}=\omega r_1 \tag{8}$$

$$w_2=\frac{\Gamma_2}{2\pi r_2}=\omega\frac{r_b^2}{r_2} \tag{9}$$

Eq. (8) demonstrates that a forced vortex corresponds to the rotation of a rigid body with an angular velocity ω, where $w(r)$ is a linear function of r, whereas for a free vortex $w(r)$ is a hyperbole (**Fig. 4**). If $k_1=\omega$ and $k_2=\omega r_b^2$ for a generic radius r we obtain:

$$w=\frac{\Gamma}{2\pi r}=k_1 r \text{ forced vortex} \tag{10}$$

Table 1 summarises the results obtained for the Rankine vortex flow.

Variables	Definition	Forced vortex	Free vortex
Tangential velocity	–	$w=k_1r$	$w=k_2/r$
Angular velocity	–	$\omega=w/r$	–
Vorticity	$\alpha=\nabla\times\mathbf{V}$	$\zeta=2\omega$	0
Circulation	$\Gamma=\iint_S(\zeta\cdot\mathbf{n})dS$	$\Gamma=2\pi\omega r^2$	$\Gamma=2\pi k_2$

$$w = \frac{\Gamma}{2\pi r} = \frac{k_2}{r} \text{ free vortex} \tag{11}$$

3. Flow velocity profiles of conical and cylindrical vessels

The flow velocity profiles of conical cyclones have been known for a long time (Kelsall, 1953), and more recently a number of authors reported their measurements made with Laser Doppler Velocimetry (Upadrashta et al., 1987 ; Fanglu et al., 1987 ; Monredon et al., 1992 ; Rajamani et al. 1994). All these authors found tangential flow velocity profiles that can be represented by Rankine's vortex.

Kirchberg and Schulze (1968) and Hacioglu and Turner (1985) made measurements for the cylindrical cyclone using intrusive methods such as the Pitot tube ; the flow velocity profiles have been determined by LDV measurements only recently (Chinê 1995 and 1997 a). The experimental test rig, details on the LDV equipment and on the test procedure are reported elsewhere (Chinê 1995 ; Chinê et al., 1997). The dimensions of the cyclones used in the experimental work are given in **Table 2** (Tri-Flo and cylindrical vessel) and **Table 3** (Trawinsky's CBC-cyclone).

3.1 Tangential velocity profiles

The experimental study has been conducted in different steps.

(1) *Tangential velocity profiles of a cylindrical vessel with peripheral underflow discharge (one stage of the Tri-Flo separator).*

The study was initially conducted in order to achieve a better knowledge of the Tri-Flo used as a dense medium separator, so appropriate operating conditions were selected to meet this purpose. Values of the underflow flow rate/feed flow rate ratio in the 50-80% range were therefore used. **Figure 5** shows the axial and tangential velocity profiles of the first stage of the Tri-Flo obtained in one of the tests. It can be observed that the tangential velocity profiles greatly differ from those known for the conical cyclones. As the radius decreases in conical vessels, the tangential velocity increases up to a maximum value corresponding to the vortex finder (**Fig. 4**). As the radius increases, for a large part of the cylindrical vessel on the medium inlet side, the tangential velocity increases up to a maximum value near the wall (**Fig. 5b**) ; the tangential velocity in the middle of the vessel is roughly constant, then its trend changes near the sink discharge as shown in the same figure.

Table 2 Dimensions of the Tri-Flo and the cylindrical vessel model are identical

Tri-Flo	Dimensions (mm)	Cylindrical vessel	Dimensions (mm)
Inner diameter	100	Inner diameter	100
Length of each cylindrical section	345	Length of the cylindrical section	345
Inlet section	20×20	Inlet section	20×20
Underflow discharge section	25×25	Peripherical discharge section	25×25
Overflow discharge section	30	Axial discharge diameter	30
Wall width	10	Wall width	10

Table 3 Dimensions of the Trawinsky's CBC-cyclone model

	Dimensions (mm)
Inner diameter	102
Length of the cylindrical section	301
Length of conical section	9,6
Included angle of the cone (flat bottom cyclone)	154°
Inlet section	43×16
Underflow discharge diameter	32
Overflow discharge diameter	19
Wall width	5,5

In other words, the fluid motion in a hydrocyclone is typically similar to that of a free-forced vortex, or more precisely, that of the so-called Rankine's vortex, a combination of the forced vortex close to the air core, and a free vortex affecting the largest part of the vessel (**Fig. 4**). The motion approaches that of a forced vortex, i.e. that of a centrifuge, for a large part of the vessel in a cylindrical vessel with peripheral underflow discharge.

(2) *Tangential velocity profiles of a cylindrical vessel where the discharge is entirely axial or peripheral.*

In order to find an explanation for the tangential velocity profiles of **Fig. 5b**, the following operating conditions for a cylindrical vessel have been explored :

(a) The entire feed flow rate entering the vessel exits an axial discharge. The tangential veloc-

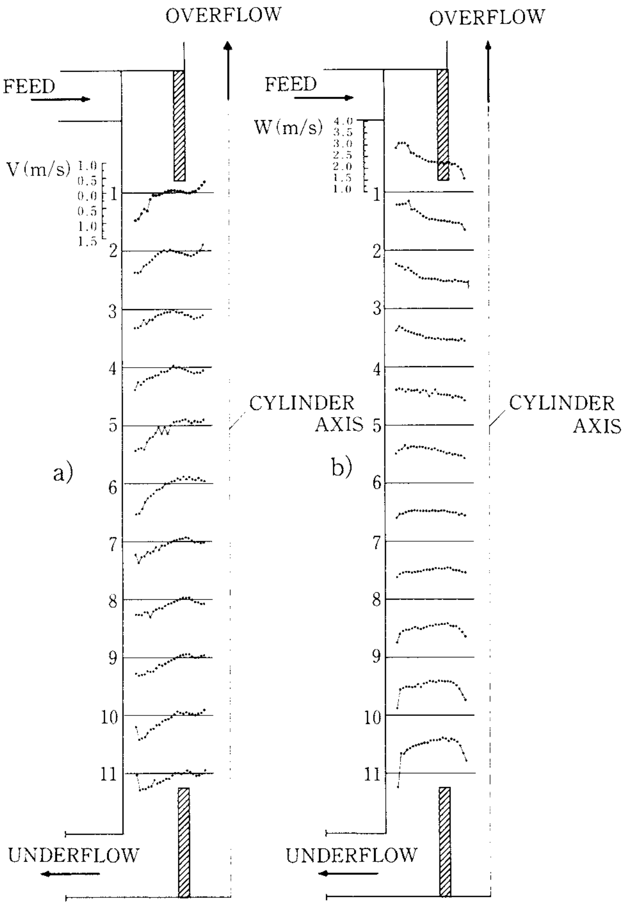

Fig. 5 LDV measurements of the axial (a) and tangential (b) velocity profiles in a cylindrical cyclone with peripheral underflow discharge. Underflow flow rate/feed flow rate ratio = 76.4%.

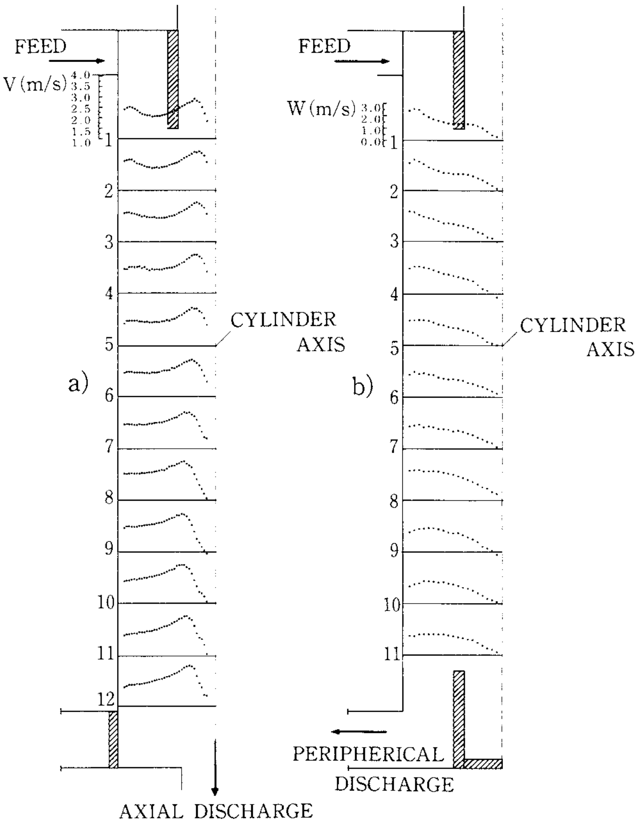

Fig. 6 Tangential velocity profiles in a cylindrical vessel under different discharge conditions:
(a) the entire feed flow rate entering the vessel exits an axial discharge;
(b) the entire feed flow rate entering the vessel exits a peripheral discharge.

ity profiles of **Fig. 6a** have been obtained under these conditions, and these show that Rankine's vortex occurs in the same way as in conical cyclones where free vortex conditions prevail in a large part of the vessel.

(b) The entire feed flow rate entering the vessel exits a peripheral discharge. The tangential velocity profiles (**Fig. 6b**) under these conditions show that forced vortex conditions occur.

Hence, it is experimentally verified that the occurrence of free or forced vortex conditions in cyclones depends on the radial flow patterns inside the vessel according to the law of conservation of angular momentum, as explained in Section 2. During normal operation of cylindrical vessels with peripheral underflow discharge, the tangential velocity profiles depend on the ratio underflow flow rate/feed flow rate: if this ratio is close to zero or to 1, free-forced vortex (Rankine's vortex) or forced vortex conditions, respectively, will prevail. For intermediate values of the ratio, intermediate conditions will occur.

(3) *Tangential velocity profiles of a cylindrical vessel with axial underflow discharge* (*Trawinski's CBC-cyclone*).

Another cylindrical vessel has been manufactured in Perspex based on Trawinki's design and LDV measurements have been carried out to determine the flow velocity profiles. The axial and tangential velocity profiles are reported in **Figs. 7a** and **b**. It can be observed that Rankine's vortex occurs; free vortex conditions prevail in a large part of the body and forced vortex conditions are restricted to very close to the axis (where measurements were difficult and only a few points have been determined). These results further prove the preceding statements.

3.2 Axial velocity profiles

The axial velocity profiles of conical and cylindrical cyclones also differ. There is an upward flow near the axis and a downward flow near the wall in both. However, the transition of the axial velocity profile between the upward and downward flow regions is sharp in conical cyclones (there is a

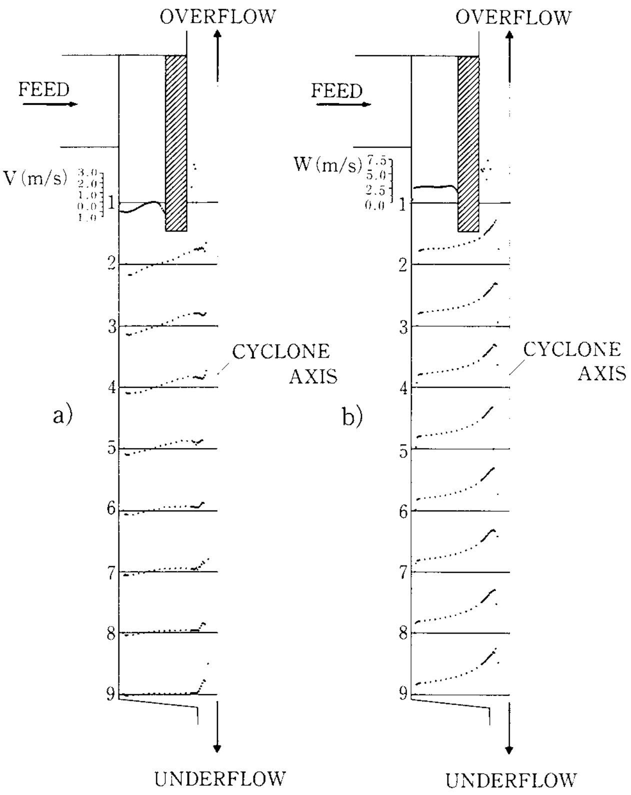

Fig. 7 Mean velocity profiles in a cylindrical flat-bottom cyclone: (a) axial component; (b) tangential component.

zero-velocity locus), while the transition is gradual in the cylindrical vessels with peripheral underflow discharge, with a wide zone where the axial velocity is zero or near zero (**Fig. 5a**).

The presence of a wide zero-velocity zone in the axial velocity profiles of the cylindrical cyclones may be interpreted as a favorable condition for high separation sharpness. In fact, some authors have studied a modification of the conical cyclone (using a thicker wall vortex finder) to obtain a wider zero-velocity zone (Fanglu et al., 1987; Luo Quian et al., 1989; Xu Ji Run et al., 1991). **Figure** 8 shows the axial velocity profiles determined by Luo Quian et al. (1989) for a standard conical cyclone and a cyclone with a thicker wall vortex finder. The above-mentioned authors claim that the presence of this zone, as opposed to the zero-velocity locus, reduces the probability of different size particles being misplaced, thus increasing separation sharpness. This statement was verified by Xu Ji Run et al. (1991) by producing the partition curves in some tests, but it requires further experimental proof in classification. On the other hand, it is proved in dense medium separation by the higher efficiency of the Tri-Flo cylindrical separator as opposed to the conical dense medium cyclone.

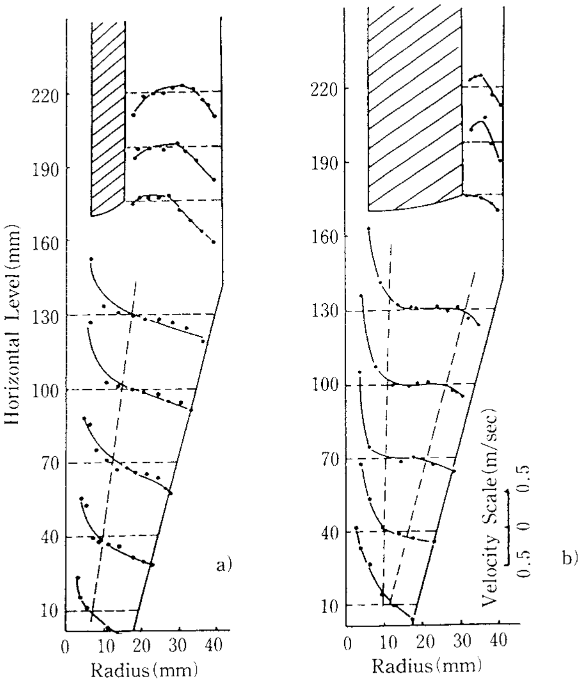

Fig. 8 Axial velocity profiles for a standard conical cyclone and a cyclone with a thicker wall vortex finder (Luo Quian et al., 1989).

As far as the cylindrical cyclone with central underflow discharge is concerned, LDV measurements have shown that not only the tangential but also the axial velocity profiles are similar to those found for the conical cyclones (sharp transition of the axial velocity profile between the upward and downward flow regions), excluding the region at the bottom where Trawinski observed a secondary vortex that he named "circulating fluidized bed". The measurements have shown that this secondary vortex exists and that it has a large core where the axial velocity is almost zero (Chiné 1997).

4. Discussion and conclusions

(a) The flow velocity profiles in cyclones are strongly influenced by vessel shape. However, as to tangential velocity profiles, this influence is basically due more to the position (axial or peripheral) of the discharges than to the vessel shape itself. In fact, Rankine's vortex takes place where free vortex conditions prevail in the separation zone in both conical vessels (standard hydrocyclone) and cylindrical vessels (CBC-cyclone)-having axial overflow and underflow discharges. Under these conditions, the tangential velocity is $w = k'/r^n$ where n may be in the 0.77-0.84 range for increasing under/over flow rate ratio (Kelsall, 1953). Therefore, the tangential velocity at a generic radius in the separation zone is much higher than its value at the inlet radius, as well as the centrifugal acceleration given by $a_c = k''/r^{(2n+1)}$.

By contrast, in cylindrical vessels with peripheral underflow discharge, the tangential velocity profiles depend on the ratio of underflow flow rate/feed flow rate. When this ratio is low, the tangential velocity profiles approach the free-forced vortex profile (Rankine's vortex); as this ratio increases, the tangential velocity profiles gradually change towards forced vortex conditions. When operating with an underflow flow rate/feed flow rate ratio in the 60-70% range, forced vortex conditions ($w = k''' \cdot r$) prevail in a large part of the vessel on the medium inlet side, while the tangential velocity may be assumed as being roughly constant ($w = k^{iv}$) in the remaining part of the vessel. Therefore, the tangential velocity at a generic radius in the separation zone is lower than its value at the inlet radius (or roughly equal). Consequently, centrifugal acceleration in cylindrical vessels may be much lower than in conical vessels.

(b) Although the cylindrical vessels with peripheral underflow discharge operate at lower centrifugal acceleration than in hydrocyclones, they can equally effect a fine separation. In fact, in cylindrical vessels the radial velocity (towards the axis)-which determines the drag force-is lower than in conical vessels. Therefore, a finer separation size (d_{50}) should be attained by using either a conical or a cylindrical vessel depending on the ratio between the centrifugal force and the drag force acting on a particle. As it is easier to adjust operating conditions in the cylindrical cyclone, it seems to have good potential as a classifier in both the fine and coarse size range.

Unfortunately, there are not enough data in the literature to give a comprehensive picture of the cylindrical vessel performance. Restarick (1989) reports the partition curves obtained in the Clayton and Mt. Isa plants with combined cylinder-cyclone classifiers, which show a fine cut-size for the cylinder with peripheral discharge (13 μm), while the combined cylinder-cyclone unit gives 47 μm cut-size. Trawinski (1994) reports that if the cylinder length in the CBC-cyclone is modified, the cut-size can be varied over a wide range (between 15 and 300 μm) without changing the solids content of the feed stream. The same author (1981) makes a comparison between the imperfection values obtained with a cylindrical 200-mm-CBC-cyclone and a standard conical cyclone under different operating conditions: the CBC-cyclone gives lower imperfection values, particularly in the fine cut-size range. In contrast, Restarick (1991) asserts that a properly operated conventional cyclone is slightly more efficient than a cylinder.

(c) As a consequence of the different tangential velocity profiles, the shear rate in the swirling flow in conical cyclones and cylindrical vessels with peripheral underflow discharge is different. It is very high in conical cyclones, where a free vortex occurs; it is very low or practically zero in cylindrical vessels, where a forced vortex occurs. Consequently, the conical cyclone cannot be used as a clarifier of flocculated suspensions because the high shear rate breaks the flocs; for this application cylindrical vessels work much better. In contrast, when de-sliming is the main function of the unit, the conical cyclone is more efficient.

(d) Particles of different shape behave differently in conical and cylindrical vessels as a consequence of the different shear rate. In conical cyclones, flat particles are oriented perpendicular to the radii: therefore, they are easily dragged to the cyclone axis and the overflow discharge. Particles of almost spherical shape rotate, thus producing a lifting effect (Magnus effect) towards the cyclone axis (Ferrara and Schena, 1987). In cylindrical vessels with peripheral underflow discharge, the influence of the particle shape on separation should be much lower. The behavior of differently shaped particles in cyclones of different shape deserves to be studied further.

(e) The cylindrical cyclones with peripheral underflow are suitable for connection in series, with the injection of fresh water at each stage, thus achieving a multiple classification of the overflow and reducing the cut size d_{50} or obtaining a better separation when used as a clarifier. This solution can even be implemented with only one pump for many stages; in contrast, in conical cyclones, a pump would be necessary for each stage. A similar solution has already been applied to perform multi-stage dense medium separation using the Tri-Flo separator (Ferrara et al., 1994).

(f) As far as dense medium separation is concerned, the results of the flow pattern in cylindrical separators with peripheral sink discharge (e.g., the Tri-Flo) explain the advantages of these separators over conventional conical cyclones:

reduced densifying effect of the medium and correspondingly lower values of the density differential, lower value of the "offset" (difference between cut-density and medium density), possibility of working at "zero offset" (a condition corresponding to sharper separation), and higher stability of the cut-density, etc. (Bozzato et al., 1997). These advantages have already been recognised by some authors and users (Kirchberg and Schulze, 1968 ; Burt et al., 1988 ; Machirori and Thomas, 1988).

In conclusion, the LDV measurement of the flow velocity profiles of cylindrical cyclones with peripheral underflow discharge and the comparison with the corresponding profiles of other cyclones (conical cyclones, cylindrical CBC-cyclone) show interesting properties for the cylindrical cyclones, not only for dense medium separation processes where their use is well established, but also for classification processes where their use is now very limited. These properties show that the cylindrical cyclones deserve greater attention as potential efficient classification tools or devices to solve particular problems such as fine classification, multi-stage classification, clarification, and separation according to particle shape.

List of symbols

C : circular trajectory in the plan (r,θ)
d_{50} : cut size diameter
$\mathbf{e}_r,\mathbf{e}_\theta,\mathbf{e}_z$: unit vectors in r, θ and z directions, respectively
k : constant in the forced/free vortex equations (Eqs. 10 and 11)
n : unit vector perpendicular to the S surface
n : exponent in the free vortex equation
r,θ,z : radial, azimuthal and axial coordinates (r is the radial distance from the axis of simmetry)
r_b : radius of the surface between the forced and the free vortex
R : radius of the cyclone
S : circular surface in the plan (r,θ)
u,w,v : velocity components in r, θ and z directions, respectively
v : velocity vector

Greek letters

Γ : circulation
ω : angular velocity
ζ : vorticity

Subscripts

1 : in the forced vortex region $(r<r_b)$
2 : in the free vortex region $(r>r_b)$

References

1) Bozzato, P., Bevilacqua, P. and Ferrara, G. : "Static and dynamic stability in dense medium separation processes," Engineering Foundation Conf., Rheology in the Mineral Industry, San Diego, California, 1977.
2) Bretney, E. : U.S. Patent No. 453,105 (1891).
3) Burt, R.O, Flemming, J., Simard, R. and Vanstone, P.J. : Industrial Minerals, January 1899, pp.53-59.
4) Chiné B. : "Studio idrodinamico del separatore centrifugo multistadio Tri-Flo," PhD Thesis, Dicamp-University of Trieste, 1995.
5) Chiné B. : "Estudio experimental del flujo con vortice en los hidrociclones," MSc Thesis, Departamento de Ingenieria Metalurgica, Universidad de Concepcion, Chile, 1997 a (in preparation).
6) Chiné B, Ferrara, G. and Concha, F : "Flow patterns in the Tri-Flo cylindrical dynamic separator," Proc. XX Int. Mineral Processing Congress, Aachen, Germany, 1997 b.
7) Ferrara, G. and Schena, G. : Proc. 3rd Int. Conf. on Hydrocyclones, Oxford, England, 1987, pp.101-107.
8) Ferrara, G., Machiavelli, G., Bevilacqua, P. and Meloy, T.P. : Minerals and Metall. Processing, 11, No. 2, May 1994, pp.63-73.
9) Ferrara, G. : Mineral Processing : Recent Advances and Future Trends, eds. S.P. Meh-rotra & R. Shekhar, Allied Publisher Ltd., New Dehli, 1995, pp.311-331
10) Fanglu, G. and Wenzhen, L. : Proc. 3rd Int. Conf. on Hydrocyclones, Oxford, England, 1987, pp.65-74.
11) Hacioglu, E. and Turner, J.F. : Proc., XV Int. Mineral Processing Congress, 1985, Cannes, France, pp.244-257.
12) Heiskanen, K., Vesanto, A. and Eronen, H. : ditto, pp. 263-268.
13) Hoffmann, E. : Glueckauf, Heft 5/6, 89. Jahrgang, 1953.
14) Kirchberg, H und Schulze, G. : Forschungsinstitut für Aufbereitung, Freiberg, Germany, 1968, Report N° 156.
15) Kelsall, D.F. : Recent Developments in Mineral Dressing, Inst. Min. & Met., London, 1953, pp.209-227
16) Kelsall, D.F. and Holmes, J.A. : Trans. Inst. Min. Metall., 68, 1958, pp.549-553.
17) Kelsall, D.F., Crockford, R.H. and Davey, E.T. : J. Agric. Eng. Res., 5, 1960, p.355.
18) Kelsall, D.F., Stewart, P.S.B. and Restarick, C.J. : Proc., First European Conf. on Mixing and Centrifugal Separation, Cambridge, 1974, pp.83-93.
19) Krebs Ltd. : The Model EE Krebs Cyclones, 1965.
20) Luo Quian, Deng Changlie, Xu Ji Run, Yu Lixin and Xiong Guangai : Int. J. Mineral Processing, 25, 1989, pp. 297-310.
21) Machirori, N.N. and Thomas, G.W.W. : "Heavy media

separation of Bikita pegmatites" 8th Industrial Minerals International Congress, Boston, 1988.
22) Monredon, T.C., Hsieh, K.T. and Rajamani, R.K.: Int. J. Mineral Processing, 35, 1992, pp.65-83.
23) Povarov, A.J.: Gidrociklony (in Russian), Gasgortechizdat, 1961, Moscow.
24) Rakowski, V.: U.S. Patent No. 2,917,173 (1959).
25) Rajamani, R.K. and Devulapalli, B.: Kona-Powder and Particle, 12, 1994, pp.95-104.
26) Restarick, C.J.: Int. J. Mineral Processing, 26, 1989, pp. 165-179.
27) Restarick, C.J.: Minerals Engineering, Vol. 4, No. 3/4, 1991, pp.279-288.
28) Upadrashta, K.R., Ketcham, V.J. and Miller, J.D.: Int. J. Mineral Processing, 1987, Vol. 20, pp.309-318.
29) Trawinski, H.F.: Erzmetall, 34, 1981, No. 6, pp.354-360.
30) Trawinski, H.F.: Proc. 2nd Int. Conf. on Hydrocyclones, Bath, England, 1984, pp.393-412.
31) Shah, C.L., Shaw, S.R., Strike, E. and Deeley, W.T.: 10th Int. Coal Prep. Congress, Edmonton, Canada, (1986), pp. 339-354.
32) Xu Ji Run, Luo Quian and Qiu Ji Cun: Int. J. Mineral Processing, 31, 1991, pp.1-10.

Author's short biography

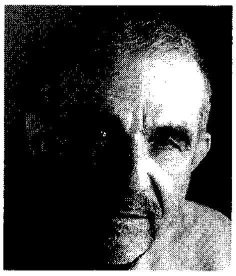

Gianfranco Ferrara

Gianfranco Ferrara obtained his degree in Mining Engineering in 1954 at the University of Cagliari (Italy). At the same University he was appointed Research Assistant in 1955 and Assistant Professor in 1960. In 1971 he was appointed to his present position of Professor of Mineral Processing at the University of Trieste, where from 1979 to 1992 has been Chairman of the Mineral Engineering, Division.

Consultant for the evaluation of the research activities financed by the Commission of the European Communities in the framework of the Primary Raw Materials and Recycling R&D programme from 1980 to 1989.

Member of the Steering Committee of the IMPC's, International Mineral Processing Congresses. Regional Editor for Europe of the journal Minerals Engineering. Member of the Editorial Board of the journals Coal Preparation and KONA-Powder and Particle.

For the research activity he has been appointed Adjunct Professor of the West Virginia University, USA.

To date he has produced more than hundred publications concerning mineral and coal processing research, characterisation of particulate solids, mineral liberation, comminution, mechanical, hydraulic and pneumatic classification of solids, dense medium separation processes in centrifugal field of ores and coals, rheology of dense suspensions, electrostatic separation, modelling and simulation of the separation processes of minerals, coals and particulate solids.

Author of a number of patents in the field of dynamic dense medium separation processes, which are applied in industrial plants operating in many countries of Europe, in Canada, South America, South Africa and China.

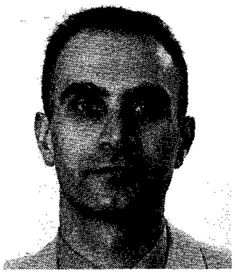

Bruno Chiné

Bruno Chiné is a Mineral Engineer from University of Trieste-Italy (1986) and Ph.D. in Mineral Engineering from the same University (1995). He worked as researcher in the Metallurgical Department of the University of Concepción (Chile) and actually his researches are in the field of experimental and computational fluid mechanics.

The Quantitative Measurement of Forces Acting on a Powder Bed During a Specific Mechanical Process for Preparation of Composite Particles[†]

Hiroyuki Yoshino, Yoshihiro Taya
and Hisashi Kaga
*Hokkaido Industrial Technology Center**
Ken-ichi Mukaida
*Muroran Inst. of Technol***

Abstract

Using the mechanical processing method called mechanofusion to prepare composite particles, the authors conducted a study on the preparation of metal-ceramic composite particles in a vacuum. The major principle in forming composite particles is the application of mechanical forces to a mixed powder in the apparatus used. The measurement of those forces, however, has seldom been attempted. Here we used strain gauges in an attempt to quantitatively measure the forces acting on a powder bed.

An experiment using glass beads as the raw material showed that (1) if the drum's rotational speed is high and the powder charge is large, great compressive and frictional forces are generated, and (2) compressive force is several times larger than frictional force. These forces were measured during the preparation of composite particles using $Cu\text{-}Al_2O_3$ *mixed powder under reduced pressures, and both forces appeared to be higher when atmospheric pressure was reduced.*

1. Introduction

There are now many attempts to create composite particles by affixing one kind of particle to the surface of a different kind, and these attempts often use devices derived from pulverizers and mixers. Methods using such mills to make composite particles are termed mechanical compositing processes. One of these methods, called mechanofusion, applies to powders such forces as compression, friction, shearing, and rotation between a rotating drum (mortar) and a fixed inner piece (pestle), and in this way composite particles are said to be formed [1,2]. Researchers are making the most of the simplicity, low contamination, and other advantages of this process to pursue research and development, and there are hopes for its industrialization[3].

The authors and others have demonstrated that, in the formation of composite particles by mechanical processing under a vacuum using $Cu\text{-}Al_2O_3$ mixed powder, the lower the residual pressure, the greater the extent to which compositing proceeds[4,5]. Analyses of particle surfaces revealed that the reduced pressure could alleviate the process of oxidation[6,7].

Even though forces acting on powders are a main factor in compositing, there is very little research on analyses of these forces in compositing processes[8], and even research reports on compositing that have appeared thus far include only a few that, in terms of test conditions in compositing, explicitly present the factors influencing these forces, instead writing only about the drum's rotational speed. From now on, however, it will be necessary to perform quantitative evaluations of these forces in order not only to scale up the devices used in the manufacturing process of composite particles by mechanical processing, but also to elucidate in detail the process by which compositing occurs.

This research involved developing a way to measure the frictional force and compressive force generated on the tip of the inner piece used in this mechanical process, and measuring the forces using

---

* 379 Kikyo-cho, Hakodate 041
**27-1 Mizumoto, Muroran 050
[†] This report was originally printed in J. Soc. Powder Technology, Japan. 32, 866 (1995) in Japanese, before being translated into English by KONA Editiorial Committee with the permission of the editiorial committee of the Soc. Powder Technology, Japan.

glass beads, as well as assessing the soundness of the measurement method with the coincidence of calculated and measured values for power consumption. The research also examines, in accordance with the results of force measurements, the effect of a vacuum on compositing using the Cu-Al_2O_3 mixed powder under a vacuum.

2. Experimental

2.1 Measurement Method Principle

The device used in the experiment was a model AM-15AF mechanofusion apparatus (made by Hosokawa Micron Corporation), to which we had added functions to perform composite processing under a high vacuum. **Fig. 1** shows detailed diagrams. The apparatus is designed to load 150 cc of powder and to directly exhaust the container interior during mechanical processing. It can maintain a high vacuum on the order of 10^{-2} Pa.

We measured the frictional force and compressive force generated on the part of the inner piece that makes contact with the powder while processing it, and determined the central point of contact with the powder on the inner piece head where these forces begin to arise (the mechanical action origin).

Figs. 2(a) and **(b)** schematically show strain gauge positions, while **Fig. 2(c)** schematically shows the relation among forces at point PL, the center of contact with the powder.

The equations below are used to calculate the forces generated where the inner piece and the powder make contact, with calculation based on the stress that is determined through strain measured by the strain gauges on the inner piece's arm.

$$F_c = f_c \cos\theta - f_f \sin\theta \tag{1}$$

$$F_f = f_f \cos\theta + f_c \sin\theta \tag{2}$$

Where :

f_c is compressive force acting on the area of contact,
f_f is frictional force acting on the area of contact,
F_c is the horizontal component of the inner piece's arm, and
F_f is the vertical component of the arm.

Stresses in these locations, i.e., σ_n, σ_n' (n=1, 2, 3), and σ_4, σ_4', are as follows.

$$\sigma_n = -\frac{F_c}{A} - \frac{F_c l}{Z} + \frac{F_f l_n}{Z} \tag{3}$$

$$\sigma_n' = -\frac{F_c}{A} + \frac{F_c l}{Z} - \frac{F_f l_n}{Z} \tag{4}$$

$$\sigma_4 = -\frac{F_c}{A} - \frac{F_c l'}{Z} \tag{5}$$

$$\sigma_4' = -\frac{F_c}{A} + \frac{F_c l'}{Z} \tag{6}$$

Solving Equations (3) through (6) for F_c and F_f yields :

$$F_c = -A\frac{\sigma_4 + \sigma_4'}{2} \tag{7}$$

$$F_f = \frac{Z}{(l_3 - l_1)} \frac{(\sigma_3 - \sigma_3') - (\sigma_1 - \sigma_1')}{4} \tag{8}$$

And because

$$\sin\theta = \frac{l}{R},\ \cos\theta = \frac{\sqrt{R^2 - l^2}}{R} \tag{9}$$

we obtain from Equations (1) through (9)

$$f_c = F_c\frac{\sqrt{R^2 - l^2}}{R} + F_f\frac{l}{R} \tag{10}$$

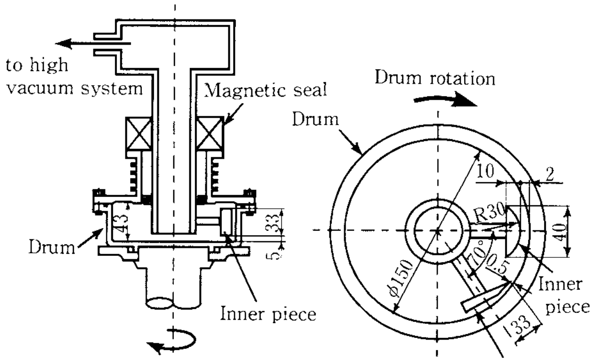

(a) (b)

Fig. 1 Schematic diagrams of vacuum mechanical preparation apparatus (a) and of the drum section (b). (mm)

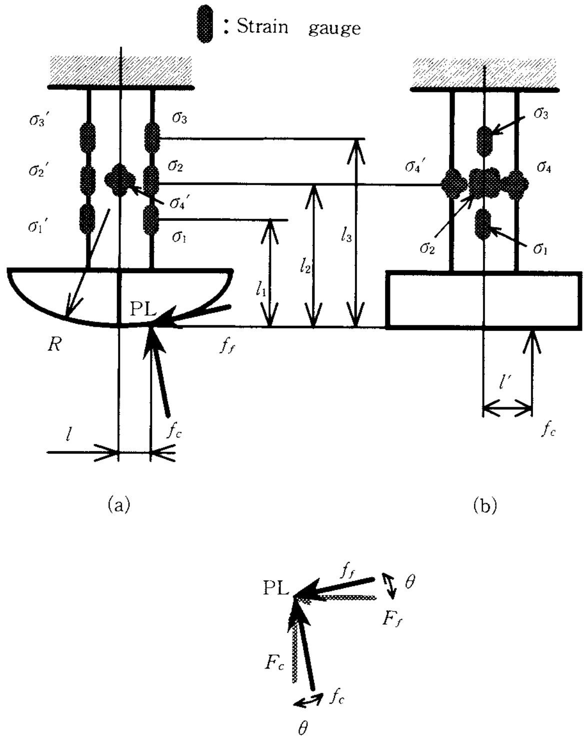

(a) (b)

(c)

Fig. 2 The position of the strain gauges in Fig. (a) and (b), and the relation of forces at the point PL in Fig. (c).

$$f_f = F_f \frac{\sqrt{R^2 - l^2}}{R} - F_c \frac{l}{R} \tag{11}$$

$$l = \frac{Z}{F_c}\left(\frac{F_f l_2}{Z} - \frac{\sigma_2 - \sigma_2'}{2}\right) \tag{12}$$

Thus, measuring σ_1 through σ_4 and σ_1' through σ_4' makes it possible to find compressive force F_c, frictional force F_f, and the distance from the inner piece center to the center of contact. This measurement method involves using the four active gauge method[9] with temperature-compensating circuits, forming three bridges, measuring $(\sigma_3 - \sigma_3') - (\sigma_1 - \sigma_1')$, $(\sigma_2 - \sigma_2')$, and $(\sigma_4 + \sigma_4')$, and using Equations (7) through (12) to determine the frictional force and compressive force arising at the area of contact between the inner piece and the powder, and the distance l to the mechanical action origin.

The strain gauges shown in **Fig. 2** also register apparent strain owing to structural effects, i.e., frictional heat from the tip of the inner piece and from drum atmosphere. Although all bridges have temperature-compensating circuits as mentioned above, the microdisplacement structure makes it difficult to completely cancel out the effects of temperature. For that reason we attached thermocouples near the strain gauges to measure gauge temperature and compensate for the apparent displacement due to temperature rise.

2.2 Basic Evaluation of Measurement Method

We mounted the inner piece shown in **Fig. 2** on a stationary bracket, imposed a load on the inner piece's tip, and measured the voltage output from each bridge at that time. **Figs. 3** and **4** show the basic characteristics of the imposed load and voltage output.

In **Fig. 3** we imposed a load on the inner piece head at a right angle (parallel to the arm) and measured the relationship of voltage output to the compressive load. As the compressive load increases, the voltage output of $(\sigma_4 + \sigma_4')$ increases linearly. By contrast, the voltage outputs of $(\sigma_3 - \sigma_3') - (\sigma_1 - \sigma_1')$ and $(\sigma_2 - \sigma_2')$ are 0 V, showing that the bending component has been canceled.

Fig. 4 shows the relationship of voltage output to bending load when a load is imposed on the inner piece head in a tangential direction (perpendicular to the inner piece arm). Voltage outputs of $(\sigma_3 - \sigma_3') - (\sigma_1 - \sigma_1')$ and $(\sigma_2 - \sigma_2')$ increase linearly as the bending load increases. On the other hand, we noted that the voltage output of $(\sigma_4 + \sigma_4')$ is 0 V, uninfluenced by the bending load, and that the compressive component is canceled. The results of **Figs. 3** and **4** confirmed that this measurement method is able to measure only the bending load and compressive load components.

As shown in **Fig. 5(a)**, in order to evaluate contact point l, we next applied a 98N point load to the inner piece surface, moved the load position in the X and Y directions, and investigated the relationship between the actual contact position L, and l as calculated using Equation (12). As **Fig. 5(b)** shows, even if the distance d along the Y direction shifts ± 5 mm from the inner piece center, it remains very close, within ±0.2 mm, to the value of l obtained according to the load position. This confirmed that the method is capable of accurately measuring the load's mechanical action origin.

2.3 Powder and Experimental Method

2.3.1 Experiment with Glass Beads

We installed the inner piece of **Fig. 2** in the mechanofusion apparatus shown in **Fig. 1** and

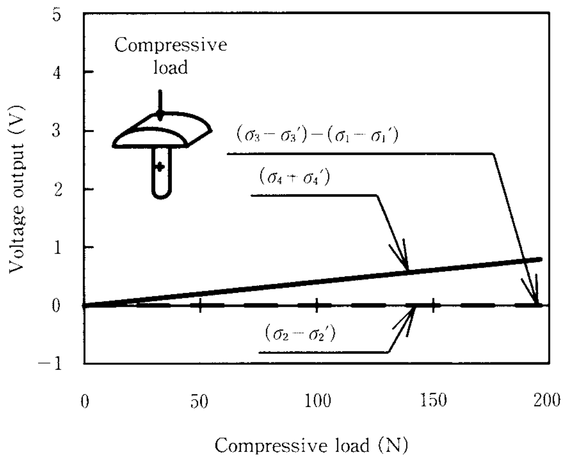

Fig. 3 Linear relationship between compressive load to the arm of inner piece and voltage output from strain gauges.

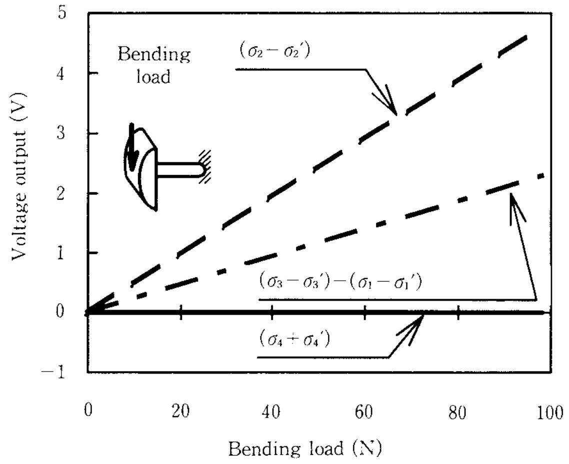

Fig. 4 Linear relationship between bending load to the arm of inner piece and voltage output from strain gauges.

mechanically processed glass beads whose average diameter was 100 μm. The processing atmosphere was air. We loaded the apparatus with 100～200 g (70～140 cc) of glass beads, and set the gap between the drum and inner piece at a constant 2 mm. Drum rotational speed was 10～23.3 s^{-1}, and was changed in stages of 3.3 s^{-1} between these two speeds. We had determined in a preliminary experiment that this rotational speed range was below the limit at which the glass beads would be pulverized.

Simultaneously measured items were compressive force, frictional force, contact position between glass beads and inner piece, temperature of strain gauges, drum rotational speed, and power consumption of the motor that rotates the drum. The values were obtained by averaging the values over periods of about 30 seconds after the drum stabilized at a new rotational speed. There were no major variations in measured values during these time periods.

2.3.2 Experimental Method Using Mixed Powder

We measured forces during mechanical composite processing in the same manner as in section 2.3.1. Powders used in the experiment were the same as in a previous report[5]: spherical Cu core particles with average diameters of 30 μm, and 0.5 μm α-Al_2O_3 adhering particles. We loaded the drum with 200～400 g (38～76 cc) of a mixed powder comprising 2 mass % Al_2O_3-98 mass % Cu (below, $2Al_2O_3$-98Cu), and subjected the mixture to composite processing at rotational speeds of 6.7～23.3 s^{-1} after evacuating the drum to prescribed pressures of 5.0×10^{-2} Pa (high vacuum), 5.0×10^{2} Pa (low vacuum), and 1.0×10^{5} Pa (atmospheric pressure). Items measured during processing and the method of measurements were the same as with glass beads in section 2.3.1.

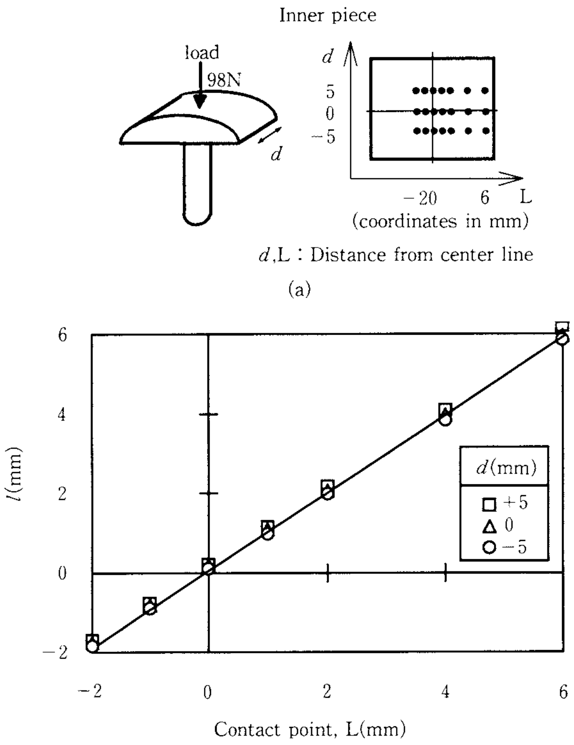

(a)

(b)

Fig. 5 The points as shown in the top view, loaded 98N on the inner piece head (a), and coincidence of the distances to the points under actual loads and calculated from strain.

3. Results and Discussion

3.1 Measurements with Glass Beads

3.1.1 Effects of Rotational Speed

Fig. 6 shows the changes in frictional force and compressive force corresponding to drum rotational speed and the amount of glass beads loaded. Frictional force and compressive force increase linearly as rotational speed increases. At the same rotational speed, the more glass beads loaded, the higher the frictional and compressive forces. However, frictional and compressive forces increase to about the same extent with rotational speed. We found that compressive force is about eight times greater than frictional force.

If one assumes friction between the inner piece

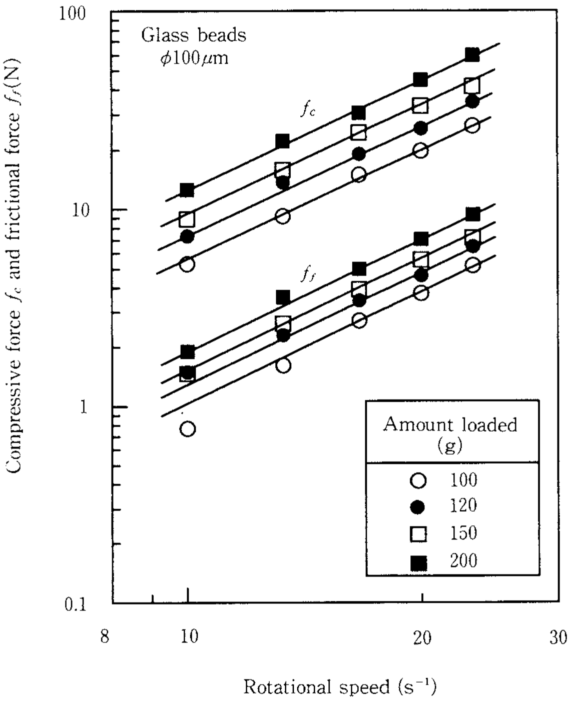

Fig. 6 Variation in frictional and compressive forces according to rotational speed of drum, as a parameter of the amount of glass beads loaded.

and glass beads in accordance with Coulomb's law[10], the relation between compressive force and frictional force is shown by the following equation.

$$f_f = \mu \cdot f_c \tag{13}$$

Here μ is the coefficient of friction, whose determination has nothing to do with rotational speed. We used Equation (13) to find μ, and plotted it against rotational speed. Results appear in **Fig. 7**, which shows that the coefficient of friction is nearly a constant value that is not dependent on rotational speed. These results support the soundness of our measured values for frictional force.

Fig. 8 shows the change in the mechanical action origin l, where the inner piece and the powder make contact, as a function of rotational speed. l falls as rotational speed increases, and becomes nearly constant beginning at a certain speed. The greater the amount of glass beads loaded, the bigger l becomes.

This shows that the higher the rotational speed, and the lower the amount of beads loaded, the more the contact location approaches the inner piece's center. One conceivable reason that this position approaches the center with a low bead load is a simple geometrical factor: because the amount of beads carried between the inner piece and drum is small, the thickness of beads pressed against the drum's interior wall is small. In terms of rotational speed effect, however, the reason is probably as follows. Because the centrifugal force acting on the beads is weak at low rotational speeds, they collect on the lower part of the drum wall. In effect this is conceivably the same situation as when the glass bead load is large, and a thick layer of beads is pressed against the drum wall, because of which the contact location moves away from the inner piece's center.

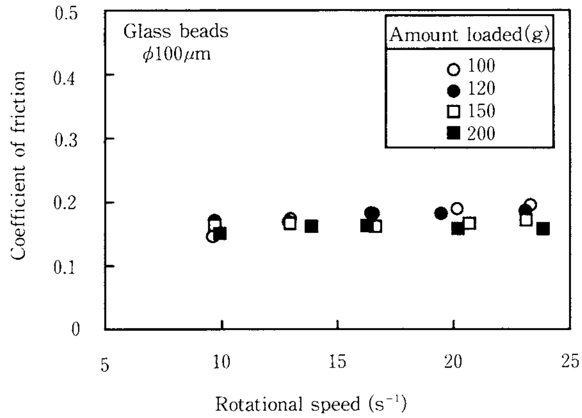

Fig. 7 Variation in the coefficient of friction acoording to rotational speed of drum, as a parameter of the amount of glass beads loaded.

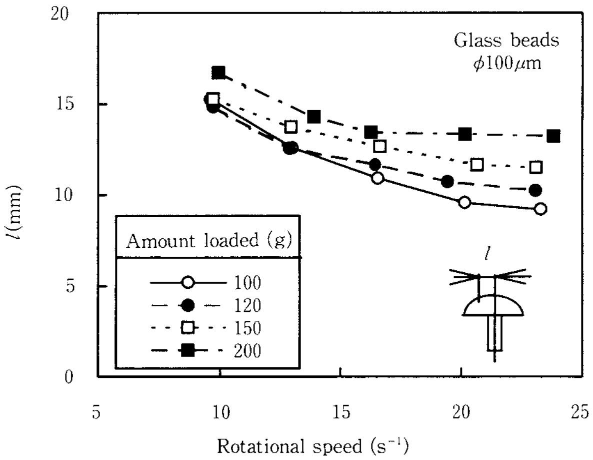

Fig. 8 Variation in the mechanical action origin according to rotational speed of drum, as a parameter of the amount of glass beads loaded.

On the other hand, at high rotational speeds a strong centrifugal force acts on the glass beads, producing a stronger force pressing the beads against the drum wall, and pushing them up even against the top portion of the wall, which forms the beads into a thin layer. We surmise that as a result, the contact location with the glass beads approached the inner piece's center.

3.1.2 Effects of Amount Loaded

Fig. 9 shows the change in compressive force as a function of the amount of glass beads loaded. There is a linear proportional relationship between the amount loaded and compressive force, in which compressive force increases with the amount loaded. The extent to which compressive force increases as the amount loaded increases will differ according to drum rotational speed: the higher the rotational speed, the larger will be its rate of

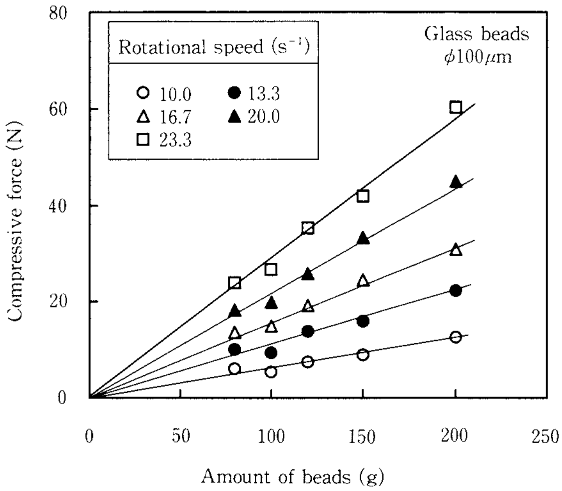

Fig. 9 Variation in the compressive force generated by the amount of glass beads, as a parameter of the rotational speed of the drum.

increase. This shows that compressive force per unit volume of powder for each rotational speed is constant. In other words, the total compressive force acting on the inner piece increases when the load of beads increases, but there is no change, per unit of powder loaded, in the mechanical energy needed for compositing.

However, this applies to the loaded amount of powder as a whole, because the energy expended on each individual particle differs according to factors such as surface area of contact and the movement of particles. Research results[11] show that in compositing experiments with Cu-Al_2O_3 mixed powder, composite particles assume different forms, even at the same rotational speed, depending on the amount of powder loaded, and that as the amount loaded increases, particles increasingly exhibit the kind of composite behavior observed at high rotational speeds. When in this way conceiving the mechanical energy expended on compositing in terms of total compressive force, there is a contradiction between this and actual compositing phenomena. If one is going to rigorously examine compositing behavior in relation to mechanical behavior, it will be necessary to elucidate the stress acting on a powder bed. Quantifying that stress will necessitate a detailed analysis in terms of the contact area size and stress distribution of the inner piece and powder bed, as well as the dynamic behavior of the powder itself.

3.1.3 Power Consumption

To examine the soundness of this mechanical measurement method, we compared the measured value for net electric power consumed during processing with the motive power calculated from the frictional force and bending stress acting on the inner piece (below called the calculated value of power consumed), which were determined in the previous sections.

Here net power consumed means the electric power value when rotating the mass of the glass beads (the value of power used only for rotation as measured when imposing the mass of the glass beads on the drum) subtracted from the electric power value when processing the glass beads. Usually, in order to check agreement with calculated values, it would also be necessary to subtract, from this net power consumption, the power required by the scraper to dislodge powder from the drum wall. In this case, however, we ignored this amount of power as very small because the spherical glass beads have low compaction and high fluidity.

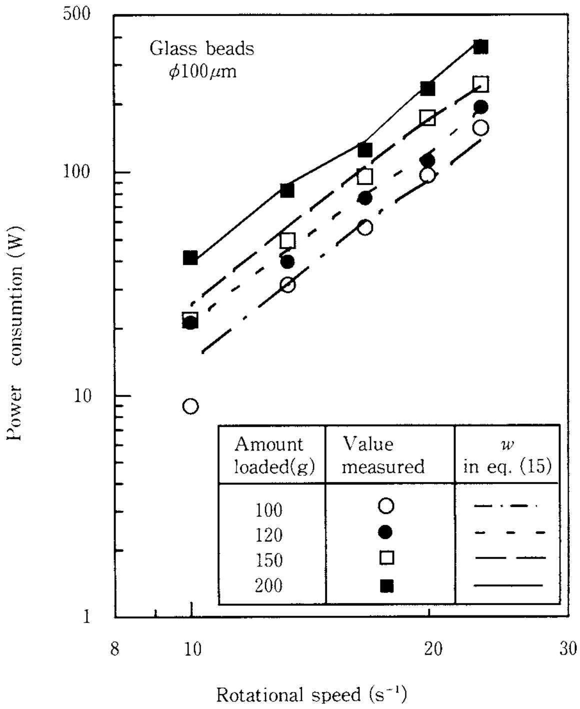

Fig. 10 Variation in power consumption with drum rotational speed as a parameter of amount of glass beads. The symbols and lines correspond to the measured values and the lines calculated by Eq. (15), respectively.

Equations (14) and (15) convert to motive power P (kg·m/s) and electric power w (W). Here T is the torque determined by the vertical component of force along the inner piece arm (F_f) that is imposed on the inner piece head and the drum radius, while n is drum rotational speed.

$$P = T \cdot 2\pi \cdot n \tag{14}$$

$$w = P \cdot 9.8 \tag{15}$$

Fig. 10 shows net electric power and motive power calculated with Equation (15), plotted as a function of rotational speed. Lines are calculated values, and points are measured net power used. Calculated and measured values are very close in all four bead loading amounts. This corroborates the fact that the method used through the previous section to measure forces can accurately detect the forces generated during processing, which suggests that we were right in assuming it is all right to ignore the power consumed by the scraper, as mentioned above.

3.2 Measurements with Al_2O_3-Cu Mixed Powder

3.2.1 Changes in Strength due to Residual Pressure

We loaded $2Al_2O_3$-98Cu mixed powder into the drum and exhausted it to the prescribed residual pressure, then performed composite processing at drum rotational speeds of 6.7 to 23.3 s^{-1}. **Fig. 11** shows the frictional force and compressive force measured while processing. Powder loaded was 400 g, and measurement results were taken over 300 seconds from the start of processing. Frictional force and compressive force increase as rotational speed increases. At the same rotational speed, frictional force and compressive force tended to increase as pressure fell, and the higher the rotational speed, the more marked the increase in frictional and compressive forces in relation to pressure.

Fig. 12 shows the changes in mechanical action origin l in conjunction with pressure. It contrasts the results obtained at 60 and 300 seconds after the start of compositing with loads of 200 and 400 g. Rotational speed was 11.7 s^{-1}. The value of mechanical action origin l becomes smaller as pressure drops. Also, the value of l was larger for the 400 g powder load than for 200 g. This value is smaller at 300 seconds after the start of processing than at 60 seconds, meaning that the contact location with the powder was approaching the inner piece center.

The reasons are as follows. When much powder is loaded, a large volume of powder is brought between the inner piece and the drum. Because a thick powder bed is formed by centrifugal force pressing powder against the drum wall, the value of mechanical action origin l becomes large, thus showing that the contact position moves away from the inner piece's center.

Next we shall examine the effects of residual pressure on l. The particles that scatter when dislodged from the drum wall by the scraper either directly reach the wall or reach the bottom of the drum by sedimentation or the like, and move to the drum wall by centrifugal force. Particles are subject to fluid resistance, a force acting opposite to their direction of movement. This fluid resistance is proportional to the product of projection area to the direction of particle movement, and kinetic energy $\rho \cdot v^2/2$.[12] Here v is particle and fluid relative speed, and ρ is fluid density. Because fluid density ρ is proportional to residual pressure, fluid resistance is higher at atmospheric pressure than under a high vacuum. This shows that the the lower the residual pressure, the faster particles move, and the less time it takes for them to reach the drum wall. Thus the amount of powder stuck to the drum wall per unit time becomes larger, but as the powder's force for climbing vertically through the drum is also large, in effect it is the same as if the powder bed on the interior wall were thin. This we can see as being equivalent to the phenomenon in **Fig. 11**, wherein frictional and compressive forces increase under low residual pressure. Conceivable causes for the decrease in l under low residual pressure include decreased volume of powder between the inner piece and the drum owing to increased tapping density caused by vacuum, and higher fluidity due to

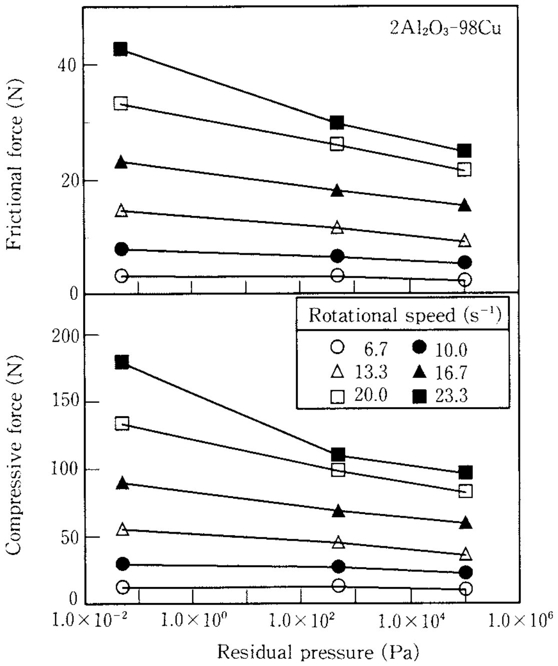

Fig. 11 Variation in the compressive and frictional forces for various residual pressures at the processing time of 300s, as a parameter of the rotational speed of drum, for $2Al_2O_3$-98Cu mixed powder.

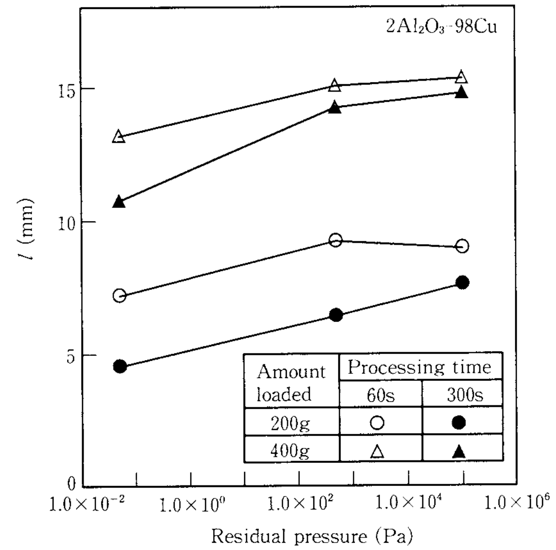

Fig. 12 Change in the mechanical action origin at various residual pressures, as a parameter of the amount of $2Al_2O_3$-98Cu mixed powder and the processing time.

vacuum drying, but this is still not clear. *l* is smaller at 300 seconds than at 60 seconds, the reason being perhaps that specific surface area decreases as compositing proceeds, which results in a decrease in the thickness of the mixed particle bed on the drum wall. The authors surmise that the change in *l* was large because compositing proceeds faster under a high vacuum than at atmospheric pressure.

Fig. 13 shows the power consumption 300 seconds after starting processing of 400 g $2Al_2O_3$-98Cu mixed powder in relation to residual pressure and drum rotational speed. Power consumption here is the value obtained by subtracting the consumption required to simply rotate mixed powder of 400 g mass. The higher rotational speed, the more power is consumed. Meanwhile, at the same rotational speed, power consumption rises as residual pressure declines, with the change in the rate of power consumption rise increasing as rotational speed increases.

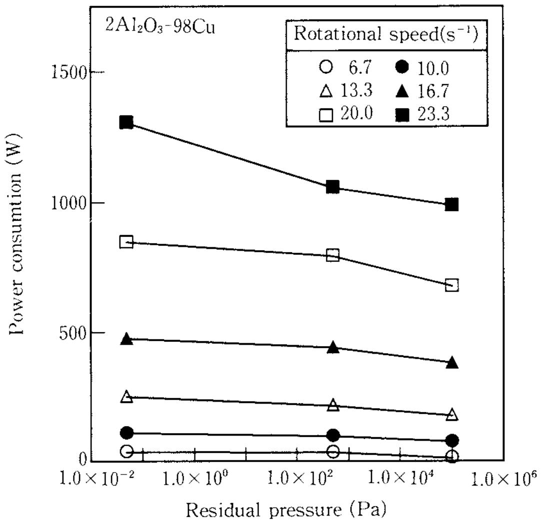

Fig. 13 Variation in power consumption at various residual pressures, as a parameter of the rotational speed of drum with constant amount (400g) of $2Al_2O_3$-98Cu mixed powder.

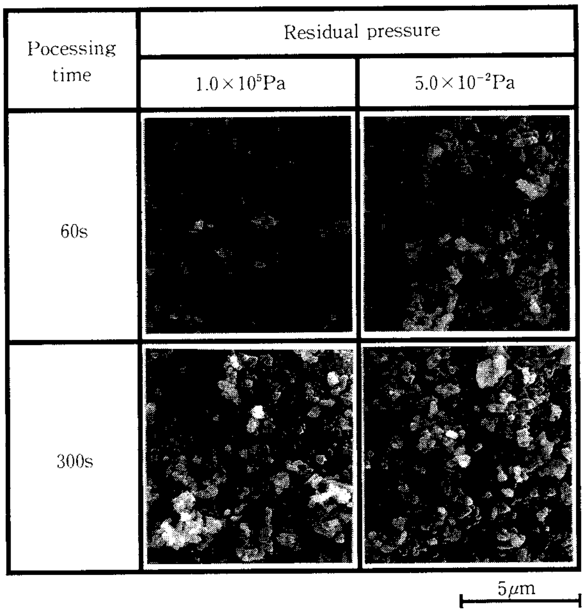

Fig. 14 Micrographs of the surface layers of the composite particles obtained from $2Al_2O_3$-98Cu mixed powder by changing the residual pressure and processing time.

After performing mechanical measurements on the $2Al_2O_3$-98Cu mixed powder, we made SEM observations of the composite particles' surfaces. These appear in **Fig. 14**. The minute surface particles are the Al_2O_3 adhering particles. Al_2O_3 dispersion and adherence have already begun 60 seconds after the start of processing, but 300 seconds after the start of processing the adherence of Al_2O_3 particles has advanced even more than after 60 seconds. Also, at the same processing time, Al_2O_3 adheres better and appears to composite faster under a high vacuum than at atmospheric pressure. As in **Fig. 11**, a high vacuum is more effective than atmospheric pressure in generating frictional force and compressive force during composite processing, and makes compositing proceed better. With the added effect by which Cu oxidation is suppressed as previously reported[7], compositing proceeds rapidly under a vacuum.

4. Conclusion

We developed a method of measuring the compressive force and frictional force generated on the inner piece during mechanical processing, and used this method to conduct basic mechanical measuring tests during processing with glass beads. We also conducted mechanical measurements on $2Al_2O_3$-98Cu mixed powder when processing under a vacuum, and studied how these forces are associated with how compositing proceeds. These tests revealed the following items.

(1) From the stress determined by the strain gauges on the inner piece's arm, it was possible to measure the compressive force and frictional force arising between the powder being mechanically processed and the inner piece, as well as the distance to the mechanical action origin at which those forces arose.

(2) The higher the drum's rotational speed, the greater the compressive force and frictional force generated on the inner piece. Increasing the amount of powder loaded especially increases

compressive force, but there is no change in compressive force per unit mass. As rotational speed increases, the mechanical action origin approaches the center of the inner piece.

(3) The electric power directly measured from the motor while processing powder closely matched the motive power value calculated from the mechanically measured value, which confirmed the soundness of these mechanical measurements.

(4) The compressive force and frictional force generated on the inner piece head differ according to residual pressure. As residual pressure drops, these forces become greater and the contact location between the inner piece head and the powder approaches the center of the inner piece head. The lower the residual pressure, the higher the power consumption during composite processing.

(5) After only 60 seconds from the beginning of composite processing the mixing/dispersion and compositing of adhering particles begins, and compositing proceeds faster under a vacuum than at atmospheric pressure.

Finally, we would like to express our appreciation to Chief Researcher Masaru Otani at the Hokkaido Industrial Research Institue for his cooperation in our experiments.

Nomenclature

f_f : frictional force (N)
f_c : compressive force (N)
F_f : vertical component of f_f and f_c (N)
F_c : horizontal component of f_f and f_c (N)
σ_n, $\sigma_n{}'$ $(n=1\sim4)$: stress (N/mm²)
A : cross-sectinal area of shaft (mm²)
Z : modulus of section (mm³)
R : radius of curvature of inner piece (mm)
μ : coefficient of friction (-)
P : motive power (kg·m/s)
n : rotational speed of drum (s^{-1})
T : torque (kg·m)
w : electric power (W)

References

1) Yokoyama, T., Urayama, K. and Naito, M.: *Funtai to Kogyo, Japan*, **19**, 47 (1987)
2) Tanno, K. and Yokoyama, T.: *J. Soc. Powder Technol., Japan*, **27**, 153 (1990)
3) Naito, M., Kondo, A. and Yokoyama, T.: *ISIJ Intenational*, **33**, 915 (1993)
4) Kaga, H., Shimono, I., Taya, Y., Takamura, T., Sugawara, T. and Katayama, H.: *J. Japan Soc. Powder and Powder Metallurgy, Japan*, **37**, 995 (1990)
5) Kaga, H., Tara, Y., Shimono, I. and Katayama, H.: *ibid.*, **39**, 546 (1992)
6) Kaga, H., Taya, Y., Katayama, H. and Hamaguchi, Y.: *ibid.*, **39**, 553 (1992)
7) Kaga, H., Taya, Y., Hamaguchi, Y., Katayama, H. and Mukaida, K.: *Kona*, **12**, 145 (1994)
8) Naito, M.: *Funtai to Kogyo, Japan*, **21**, 77 (1989)
9) Kanno, A.: "Ohryoku Hizumi Kaiseki", p.41, Asakura Syoten (1986)
10) Moriguchi, S.: "Shotou Rikigaku", p.171, Baifukan (1959)
11) Kaga, H., Taya, Y.: *Report of the Hokkaido Industrial Technology Center*, **2**, 27 (1992)
12) Takahashi, K.: "Kiso Aerosol Kougaku", p.10, Youkendo (1982)

Author's short biography

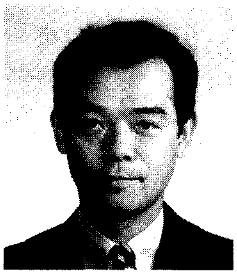

Hiroyuki Yoshino

Hiroyuki Yoshino studied mechanical engineering at the Akita University of Japan. He joined a motor company to design the motor car for 6 years.
Since 1987, he has been working at the Hokkaido Industrial Technology Center. He is a chief at the Department of Mechanical Engineering and has been mainly researching and developing new technologies of marine machinery. He has also been involved in the project of quantitative measurement of forces acting on a powder bed during a specific mechanical process since 1991.

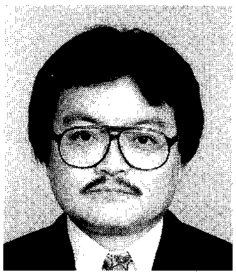

Yoshihiro Taya

Yoshihiro Taya graduated in the Department of Chemical Engineering from Doshisha University. He did research and development at the air conditioning machinery company for 4 years. He joined the Department of Research and Development at Hokkaido Industrial Technology Center from 1986, and has been studying on the vacuum machineries.

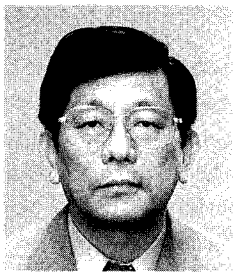

Dr. Hisashi Kaga

Hissashi Kaga graduated in Metallurgical Engineering from Muroran Institute of Technology, and subsequently obtained and MEn from Tohoku University. After 13 years in the research institute of the steel company, he joined the department of research and development at Hokkaido Industrial Technology Center since 1986. He obtained his doctorate (1993) concerning physical preparation of composite particles. His major research interests are the preparation of the composite particles by physical processing and the preparation of high performance materials from the composite particles.

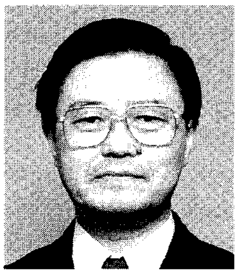

Prof. Dr. Ken-ichi Mukaida

Ken-ichi Mukaida graduated in Chemical Engineering from Muroran Institute of Technology (MIT) in 1961 and the graduate school of Engineering of Hokkaido University in 1963. He became an assistant professor of the Department of Chemical Engineering at MIT starting the research of the preparation, characterization, and modification of solid acid catalysts. He shifted to the department of Materials Science and Engineering in 1990, and thereafter he studies surface modification, metal-oxide composite physical-preparation and solid superacid catalysts.

Numerical Simulation of Three Dimensional Fluidized Bed Using Nozzles at Bottom and Experimental Verification†

Shinichi Yuu, Kenji Ikeda, Toshihiko Umekage and Kouki Nohara
Department of Mechanical Engineering,
*Kyushu Institute of Technology**

Abstract

For better understanding of gas and particle motion in a fluidized bed, we numerically solved the locally averaged three-dimensional Navier-Stokes equations and the Lagrangian equations for particle motion while taking into account the collisions between particles, and gas-particle mutual interaction. Finite difference methods were used. This simulation obtained locally averaged variables, such as gas velocities, by averaging point variables over the very small region of one computational cell. Small stress terms caused by fluctuations in locally averaged values were ignored at the present stage. In calculating collisions, particles were regarded as hard spheres with a collision time of zero, meaning that collisions occur between only two particles. Results show that the hard sphere collision model can be used to simulate flow fields in fluidized beds whose particle concentrations are relatively dilute.

Introduction

Fluidized beds are used in a wide variety of industrial fields, and even now their range of application continues to expand, so that there is a never-ending accumulation of design data for fluidized bed devices. However, air and particle motions in fluidized beds include three-dimensional unstable flows, making them extremely complex, and there are many important phenomena that are not yet understood theoretically (Muchi et al., 1983).

To begin with, there have been numerical simulations using a binary-fluid model to simulate air flows and particle motions in fluidized beds (Bouillard et al., 1989). The binary-fluid model involves calculations that see fluids and particles as discrete continuous fluids affecting each other, and it requires a variety of models and experimental constants in order to close the equation system. As a particle mass is regarded as a continuum from the very beginning, few analyses have succeeded in expressing characteristics that are based on the discrete nature of particles. In recent years researchers have started performing fluidized bed analyses with the discrete element method (DEM), which treats particles as soft spheres (Kawaguchi et al., 1993). Calculating particle fluid phenomena with DEM necessitates assumptions including physical characteristic values, and a limitation is that it can perform three-dimensional calculations for 10, 000 particles at most. Nevertheless, qualitatively DEM explains grain movement well, and in a sense one might say it also comes close quantitatively. But it is difficult for computers of present capacity and performance to carry out numerical simulations of fluidized beds of actually used size.

For these reasons our research involved numerical simulations of a three-dimensional fluidized bed using the hard sphere model, which can calculate more particles than DEM, specifically about 3.3×10^5. For the air flow field we simultaneously solved in an Eulerian manner the Navier-Stokes equations and continuous equations, and determined particle trajectories with Lagrangian motion equations, performing calculations while taking into account the interactions of both. To assess the soundness of the calculations, their results were compared with experimental results obtained under identical conditions. A Laser Doppler Velocimeter (LDA) was used to measure air velocity in a fluidized bed, and particle velocity was found by recording with a video camera.

---

*Sensuicho 1-1, Tobata, Kitakyushu 804, JAPAN
TEL/FAX:093-884-3174/093-871-8591
E-mail:yuu@mech.kyutech.ac.jp

†This report was originally printed in Kagaku Kougaku Ronbunshu, 22, 67(1996) in Japanese, before being translated into English by KONA Editiorial committee with the permission of the editiorial committee of the Soc. Chemical English, Japan.

The objective of this research was to show to what extent the hard sphere model can be used to simulate fluidized beds of near actual size; specifically, if it is possible to express with calculations the large-scale unstable flows in fluidized beds, and the extent to which it is possible to express things such as ordinary experimental results for average velocity distributions of air jets and particles. Also, at this stage these calculations lack a measure of exactness, one reason being that, when finding localized averages, they ignore stress caused by microvariation in air flows, but the main purpose was to establish a starting point for numerically simulating actual fluidized beds.

1. Calculation Method

Because particles exist throughout a large region, for basic air flow equations our calculations did not use the Navier-Stokes equations and continuous equations, which take only ordinary flows into account; in addition to these equations, we considered within a single calculation cell the ratio occupied by air flow, i.e., the void ratio, and used equations averaged locally within one calculation lattice. This approach is exactly the same as large eddy simulation.

The following equations find the spatial average value $\boldsymbol{v}$, which averages the spaces in which air flows and particles are found (Anderson and Jackson, 1967).

$$\boldsymbol{v}=\frac{1}{V_0}\int_{V_0} g\boldsymbol{v}dV=\varepsilon\boldsymbol{v} \tag{1}$$

$$\varepsilon=\frac{1}{V_0}\int_{V_0} g dV \tag{2}$$

Where:

$\boldsymbol{v}$ is the local spatial average determined by averaging only the space with air flow, ε is void ratio, and g is a function that is 0 in a space occupied by particles, and 1 in a space occupied by air flow.

The Navier-Stokes equations and continuous equations are locally averaged, i.e., the spaces where air and particles exist are averaged, Equations (1) and (2) are substituted, and made nondimensional by means of nozzle diameter, jet velocity at nozzle exit, atmospheric pressure, air density, and kinematic viscosity of air, which yields Equations (3) and (4). The τ in Equation (3) is the viscous stress tensor in a space with an air flow, and is found with Newton's law of viscosity.

$$\frac{\partial(\varepsilon\boldsymbol{v})}{\partial t}+(\nabla\cdot\varepsilon\boldsymbol{v}\boldsymbol{v})+(\nabla\cdot\varepsilon\boldsymbol{v}'\boldsymbol{v}')$$

$$=-\nabla\varepsilon P-\frac{1}{Re}\nabla\cdot\varepsilon\tau-Sp \tag{3}$$

$$\frac{\partial\varepsilon}{\partial t}+\nabla\cdot\varepsilon\boldsymbol{v}=0 \tag{4}$$

Substituting Equation (4) for Equation (3) yields Equation (5).

$$\varepsilon\frac{\partial\boldsymbol{v}}{\partial t}+(\varepsilon\boldsymbol{v}\cdot\nabla\boldsymbol{v})+(\nabla\cdot\varepsilon\boldsymbol{v}'\boldsymbol{v}')=$$

$$-\nabla\varepsilon P-\frac{1}{Re}\nabla\cdot\varepsilon\tau-Sp \tag{5}$$

Where:

$\boldsymbol{v}$, P, and τ are the nondimensional localized averages obtained by averaging only the space with air.

$\boldsymbol{v}'\boldsymbol{v}'$ in the third term on the left side of Equation (5) is the average of the product of localized variable values, and the stress term arising from variable values, but we ignored it at this stage because it is thought to be so small as to influence little the movement of the large particles with approximately 1.5 mm diameters used in this research.

When using Schiller and Naumann's experimental equation for the resistance coefficient, which is applicable when the particle criterion of Reynold's number, Rep, is below about 1000 (Schiller and Naumann, 1933), the term Sp in Equation (5) appears as in Equation (6) (Squires and Eaton, 1990).

$$Sp=\frac{3\pi\overline{D_p}}{Re\Delta x\Delta y\Delta z}(1+0.15Re_p{}^{0.687})\,n(\boldsymbol{v}-\boldsymbol{v}_p)\frac{1}{\phi(\varepsilon)} \tag{6}$$

Where:

$\overline{D_p}$ and n are nondimensional particle diameter and the number of particles in a lattice, and Re_p is the particle criterion Reynold's number, which is shown by this equation.

$$Re_p=\frac{\rho|\boldsymbol{v}-\boldsymbol{v}_p|U_0D_p}{\mu} \tag{7}$$

Because the velocity at the present time is unknown, the velocity used when calculating Re_p uses the value for one calculation time step previous as an approximated value because, as noted below, the calculation time step amplitude in these calculations is very small ($\Delta t=0.01$, 3.27×10^{-6}s actual time equivalent). $\phi(\varepsilon)$ is the correction function for determining the resistance undergone by one particle in a mass as experimentally determined by Steinour (Steinour, 1944), and it is found by Equation (8).

$$\phi(\varepsilon)=10^{-1.82(1-\varepsilon)} \tag{8}$$

Difference calculus is used to calculate the air flow field, with the basic equations being the Navier-Stokes Equation (5), and the continuous equation (4).

In actual numerical calculations we used the divergence in the Navier-Stokes Equation (5), and used the relaxation method to solve Poisson's equation (Equation (9)) on the pressure obtained (Harlow and Welch, 1963) (Yuu et al., 1992).

$$\nabla^2(\varepsilon P) = -\frac{\partial}{\partial t}(\nabla \cdot \varepsilon \boldsymbol{v}) - \nabla \cdot (\varepsilon \boldsymbol{v} \cdot \nabla \boldsymbol{v}) - \frac{1}{Re}\nabla^2 \cdot \varepsilon \tau - \nabla \cdot Sp \tag{9}$$

When calculating the inertia term with Equation (9) as it is, kinetic energy is conserved only to the value dependent on the size of the numerical error allowed by the continuous equation, and the error accumulates in the solution. The present calculations therefore use the method of Piacsek and Williams (Piacsek and Williams, 1970), which applies a tertiary upwind difference method after converting the inertia term to an energy conservation type (Equation (10)) (Yuu et al., 1992).

$$\varepsilon \boldsymbol{v} \cdot \nabla \boldsymbol{v} = \frac{1}{2}[(\varepsilon \boldsymbol{v} \cdot \nabla \boldsymbol{v}) + \nabla \cdot \varepsilon \boldsymbol{v}\boldsymbol{v})] \tag{10}$$

The other terms use a secondary central difference method.

Particle trajectories were calculated with an equation for particle Lagrangian motion, and a motion equation for particle rotation. The nondimensional equations of motion are as follows.

$$\frac{\Psi\phi(\varepsilon)}{1+0.15{Re_p}^{0.687}}\frac{d^2\boldsymbol{s}}{dt^2} + \frac{d\boldsymbol{s}}{dt} - \boldsymbol{v} + \frac{G\phi(\varepsilon)}{1+0.15{Re_p}^{0.687}} = 0 \tag{11}$$

$$\frac{C\phi(\varepsilon)}{32.1+6.45{Re_{p\omega}}^{0.5}}\frac{d\boldsymbol{\omega}}{dt} + \boldsymbol{\omega} + \frac{1}{2}\nabla \times \boldsymbol{v} = 0 \tag{12}$$

$$\boldsymbol{s} = (x_p, y_p, z_p),\ \boldsymbol{G} = (G,0,0),\ \boldsymbol{\omega} = (\omega_{xp}, \omega_{yp}, \omega_{zp}),$$

$$\Psi = \frac{1}{2}St = \frac{\rho_p {D_p}^2 U_0}{18\mu D},\ G = \frac{\rho_p {D_p}^2 g_c}{18\mu U_0},\ C = \frac{4\pi}{15}\frac{\rho_p {D_p}^2 U_0}{\rho D \nu},$$

$$Re_{p\omega} = \left|\boldsymbol{\omega} - \frac{1}{2}\nabla \times \boldsymbol{v}\right| {D_p}^2/4\nu$$

Where ϕ is the inertial parameter made nondimensional by the representative length of the stop distance when a particle is subject to Stokes resistance in an air flow, and G is nondimensional sedimentation velocity in which Stokes sedimentation velocity was made nondimensional by representative velocity. When air velocity is constant in meshes, Equations (11) and (12) can be solved analytically in each mesh, and particle velocity and location are determined; particle trajectories are found by combining these.

As an example, the following equations show particle velocity u_p in the x direction and particle angular velocity ω_{px} around the x axis in Equations (11) and (12), as solved by the following equations.

$$u_p|_{t=m\Delta t} = \frac{|u_p|_{t=m\Delta t} - u|_{t=m\Delta t} + G'|}{u_p|_{t=m\Delta t} - u|_{t=m\Delta t} + G'} \times |u_p|_{t=(m-1)\Delta t} - u|_{t=(m-1)\Delta t} + G'| \times e^{-\Delta t/\Psi'} + u|_{t=m\Delta t} - G' \tag{13}$$

Where $G' = \frac{G\phi(\varepsilon)}{1+0.15{Re_p}^{05687}}$, $\Psi' = \frac{\Psi\phi(\varepsilon)}{1+0.15{Re_p}^{0.687}}$

$$\omega_{px}|_{t=m\Delta t} = \frac{\left|\omega_{px}|_{t=m\Delta t} - \frac{1}{2}(\nabla \times v)_x|_{t=m\Delta t}\right|}{\omega_{px}|_{t=m\Delta t} - \frac{1}{2}(\nabla \times v)_x|_{t=m\Delta t}} \times \left|\omega_{px}|_{t=(m-1)\Delta t} - \frac{1}{2}(\nabla \times v)_x|_{t=(m-1)\Delta t}\right| \times e^{-\Delta t/C'} + \frac{1}{2}(\nabla \times \omega)_x|_{t=m\Delta t} \tag{14}$$

Where $C' = \frac{C\phi(\varepsilon)}{32.1+6.45{Re_{p\omega}}^{0.5}}$

In the above equations $u|_{t=m\Delta t}$, for instance, is velocity in the x direction of air flow at the m calculation time step, and is an unknown sought via the S_p term in the Navier-Stokes equations, so the present calculations use the already found $u|_{t=(m-1)\Delta t}$ in place of $u|_{t=m\Delta t}$, i.e., they substitute the pre-Δt value. And in Equation (13), for example, where $u_p|_{t=m\Delta t}$ appears on both the left and right sides, the solution is found by convergence using successive calculations. If the $u|_{t=m\Delta t}$ obtained is substituted for the Sp term and the Navier-Stokes equations solved, they yield the air flow velocity, which includes particle effects. But if at that time there are inter-particle collisions and particle-wall collisions, particle velocity will change instantaneously (time zero), yielding the value found by a particle collision equation, which is then substituted for the S_p term.

For particle collisions, particles are considered to be hard spheres. In accordance with particle location after Δt time, which is determined by the particle motion equation, we assumed that collisions occur only between two particles with the largest contact capacity, and that those collisions (which require no time because particles are hard spheres) change the particles' velocity and angular velocity, which are then sought. The computations involve transforming the XYZ coordinate system into a relative coordinate system (a spherical coordinate system with a certain particle at the origin), and solving for various values. The motion equations for particle collisions differ depending on whether the particle surface state is completely or incompletely rough. It is not known from the beginning if slippage will occur or not, so at first equations are solved assuming no slippage and shock strength is calculated. If $F \leqq \mu_p R$, that is the solution, and if $F > \mu_p$R, the problems should be re-solved using equations for slippage. The same procedure is used for particle-wall situations. The Appendix shows representative equations. The void ratio ε is found with the following equation using the volume of the calculation cell V_0 and the particle volume portion of that volume, which is V_p.

$$\varepsilon=(V_0-V_p)/V_0 \tag{15}$$

V_p should be calculated separately for situations in which particles are completely inside the lattice, and in which some particles are outside.

As shown in **Fig. 1**, we performed calculations for a situation in which an air flow was expelled at a nondimensional initial velocity of 1.0 (dimensional initial velocity $U_0=21.4$ m/s) from nozzles in 10 locations. The initial particle state comprised two particles in each direction in a computational cell, for a total of eight in a lattice, and an ordered arrangement with a total of $80\times64\times64=3.28\times10^5$ particles for the whole. But in actuality there are any number of conceivable initial particle arrangements, so there is concern that a flow field calculated assuming an ordered initial particle arrangement does not express an actual fluidized bed field that has a variety of different initial particle arrangements. For that reason, in order to investigate the effect of differing initial particle arrangements on a fluidized bed flow field, the authors carried out two experiments with widely differing initial particle arrangements, one that was sparse, and the other dense. Experimental conditions except for initial particle arrangement were all identical, and the procedure was to expel air jets from the nozzles into static flow fields, and to record by video and compare the variation per 1/60th s (0.01667 s) in the flow field from the moment the jet began. Results showed that when there is no particle size distribution as in this research, even when there are large differences in the initial particle arrangement the entire flow field becomes fluid, that the time needed until the influence of initial particle arrangement disappears from the entire flow field is considerably shorter than 1/30 s (0.03333 s) (about 0.03 s is thought to be quite sufficient), and that the flow field subsequently assumes nearly the same fluid state. Owing to these results, for these calculations we decided on the above-described ordered initial particle arrangement because it is the easiest, then used visualized results and flow characteristic values to compare experimental results with the calculated results obtained after elapse of the actual time equivalent of 0.03 s (100 nondimensional time units), which is the time needed for the difference owing to initial particle arrangement to more or less disappear from the entire flow field.

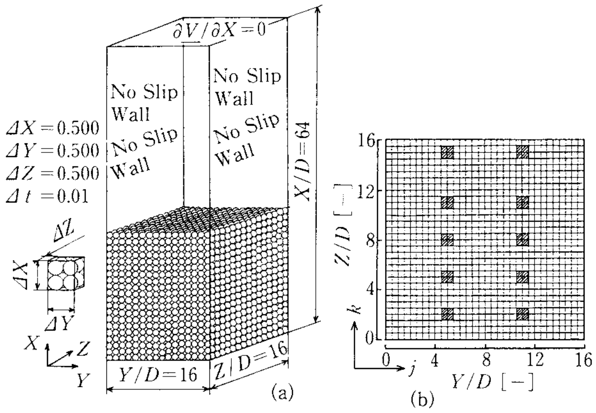

Fig. 1 (a)Computationsl domain, (b)layouts of nozzle exits (X/D=0).

This research calculated the fluidized bed's flow field from the moment the jet from the nozzle started until 320 nondimensional time units elapsed (equivalent to about 0.1 s actual time). Thus, when in these calculations we sought the average velocity distributions of air jets and particles, and turbulence intensity distribution, we computed them by averaging the instantaneous data for each $\varDelta t$ during $t=$ 100 to 320 (actual time equivalent, approx. 0.07 s) (however, for the three data items $X/D=12$, 16, and 20 in **Fig. 8**, which are regions far from nozzle exits, we averaged data over the interval of $t=160$ to 320 (actual time equivalent, approx. 0.05 s)). As this shows, the averaged time for flow characteristic values in our calculations is short, at about 0.07 s actual time equivalent, but the statistical error this causes is small, as explained below. The range $X/D\leqq4$, within which this research sought the air flow velocity distribution, has the fewest incidents of velocity variation. Thus the number of turbulent eddies n passing during the averaged time of $X/D=4$, about 0.07 s, which is thought to contain the largest error for averaged values, is $n=195$ to 896 when calculated using values measured by Gibson (Gibson, 1963) and Laurence (Laurence, 1956) on an integral scale in a nozzle jet (an integral scale in a jet does not change very much even in the presence of particles, and as shown in **Fig. 7** below, in a fluidized bed the axial velocity attenuation of a jet begins near the nozzle exit, and at $X/D=4$ it is thought to already have formed the same flow as the developed region in a free jet; here, therefore, we performed calculations by applying the results of Gibson (Gibson, 1963) and Laurance (Laurence, 1956) on developed regions in free jets). The estimated error when averaging those events with the median limit theorem is $896^{-1/2}$ to $195^{-1/2}=0.033$ to 0.072, which comes to 3.3% to 7.2%. Meanwhile, particles in flow fields are moving under the influence of air flows, so when there are many air flow velocity variation events during the approximately 0.07 s averaged time, it is possible that there are also many particle velocity variation events. With particles, however, unlike an air flow in which one can continuously measure all the velocity variation events passing through a measuring point, one can measure only the discrete velocity of particles passing through the point, which means that even when there are many air flow velocity variation events during the averaged time of about 0.07 s, the number of particles passing through the measuring point will determine the statistical error in the computation results. In these calculations the number of particles for which we were able to average the velocity during the approximately 0.07 s equivalent actual time was at least 200 directly over the nozzle where particle velocity was fast, and at least 100 even in places near the wall where particle velocity was slow. Thus, the estimated error when averaging those events according to the median limit theorem is $200^{-1/2}$ to $100^{-1/2}=0.071$ to 0.10, or 7.1% to 10%. If a still longer time is taken for numerical calculations it is possible to further reduce statistical error, but even when the actual computation time is about 0.1 s as in our research, there is little statistical error in the time-averaged values for air and particle velocities.

Table 1 Conditions of calculation and experiment.

Nozzle diameter D	[mm]	7.0
Particle diameter D_p	[mm]	1.56
Nondimensional particle diameter $\overline{D}_p$	[−]	0.25
Particle−particle restitution coefficient e_p	[−]	0.90
Particle−wall restitution cooefficient e_W	[−]	0.95
Nondimensional settling velocity G	[−]	3.42
Reynolds number Re	[−]	9980
Nondimensional time step Δt	[−]	0.01
Air velocity at nozzle outlet U_0	[m/s]	21.4
Particle density ρ_p	[kg/m^3]	1.03×10^3
Particle−particle friction coefficient μ_p	[−]	0.25
Particle−wall friction coefficient μ_W	[−]	0.30
Inertia parameter Ψ	[−]	22836
Nondimensional cell size	[−]	0.5×0.5×0.5
Number of computational cells	[−]	128×32×32
Number of particles	[−]	80×64×64

Table 1 shows the calculation conditions. Computations were performed on a FACOM VP-2600.

2. Experimental Apparatus and Method

Fig. 2 shows the experimental apparatus. As its particles, this experiment used plastic spheres 1.56 mm in diameter. For their initial state, particles were filled to a height of 125 mm in a transparent acrylic container measuring 900 mm × 100 mm × 100 mm, and a net was placed in the container to keep the particles from falling. Air brought in from a centrifugal blower is taken into the container. To alleviate turbulence in the container a honeycomb 100 mm thick and with 9 mm cells was installed. This rectified air was streamed into the container through 10 square-shaped nozzles at 21.4 m/s, and the jet velocity could be adjusted with a control valve. A Laser Doppler Velocimeter (LDA) was used to measure air velocity in the fluidized bed. The seed particles used when measuring air flow velocity with the LDA were ammonium chloride fume (average diameter 0.8 μm) made by causing hydrochloric acid and aqueous ammonia to react in the gaseous phase by producing an air flow with a compressor. The LDA used a backscattering differential mode. A photomultiplier received the backscattered light when seed particles passed through the measured volume where two laser beams intersected. The Doppler signal produced by the backscattered light passed through a frequency shifter, and a frequency tracker converted this into an analog signal corresponding to seed particle speed. In regions where there were enough seed particles passing through the observed volume per unit time, average seed particle speed was measured by directly running an analog signal to the signal indicator, and performing measurements while checking wave form with an oscilloscope. Owing to LDA structure, however, measurements are impossible in the region

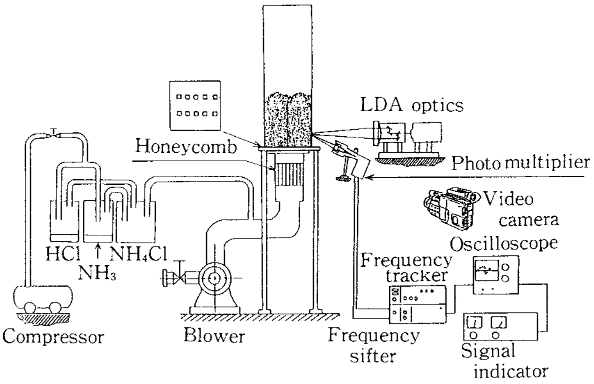

Fig. 2 Experimental apparatus.

where the laser beams' intersection is blocked by particles, and regions with an insufficiency of seed particles. Therefore the only data used were those obtained directly above nozzle openings.

Measurements of particle velocity and their turbulence intensity involved recording particle fluid motion with a video camera, and determining the values for particle locations from their amount of movement each 1/60th s (0.01667 s). Nevertheless, even then it was possible to measure only particle movement that was visible near walls. **Table 1** shows the experiment conditions. Conditions were the same as those for calculations.

3. Comparison of Calculation Results and Experimental Values

Figs. 3a, **4a**, and **5a** show the results of instantaneous particle location calculations, which cover the time frame of 0.047 s to 0.060 s actual time equivalent, beginning with the initial state. The particles shown by calculations are only the particles in the width of one calculation cell in the depth direction (*Z* direction). Because, $Z/D=16$ is the wall position, $Z/D=15$ to 15.5 is the particle location near the wall toward the inside to the distance of one calculation cell width from the wall. In **Fig. 3** ($t=144$, actual time equivalent 0.047 s) the air from the nozzle has already reached the top of the particle bed, and has formed bubble-like flows with low particle density in various places. In **Fig. 4** ($t=160$, actual time equivalent 0.052 s) one bubble-like flow has grown near the left wall, while in **Fig. 5** ($t=183$, actual time equivalent 0.060 s) particles are lifted by air from the upper surface. Thus calculated results have clearly shown a large-scale, unstable flow. We then performed the experiment mentioned in the previous section in which both the number of particles and the dimensionally converted conditions are identical, and verified this kind of large-scale, unstable flow. **Figs. 3b**, **4b**, and **5b** are video shots of the particles' instantaneous flow state. When making measurements all visible particles are included. Initial particle arrangement and the time elapsed after air begins streaming from the

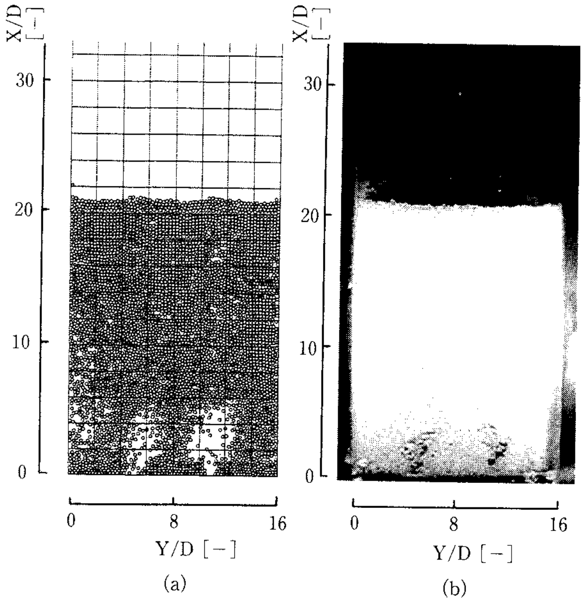

(a) (b)

Fig. 3 Instantaneous locations of particles, (a)Calculated result(X/D-Y/D plane, Z/D=15, t=144), (b)Experimental result.

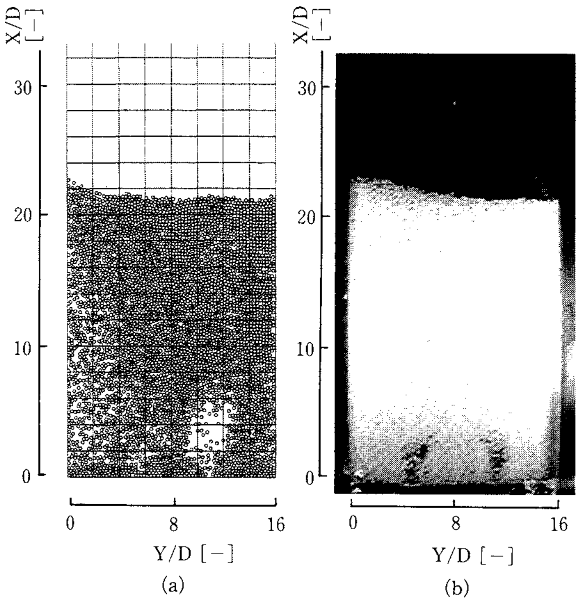

(a) (b)

Fig. 4 Instantaneous locations of particles, (a)Calculated result(X/D-Y/D plane, Z/D=15, t=160), (b)Experimental result.

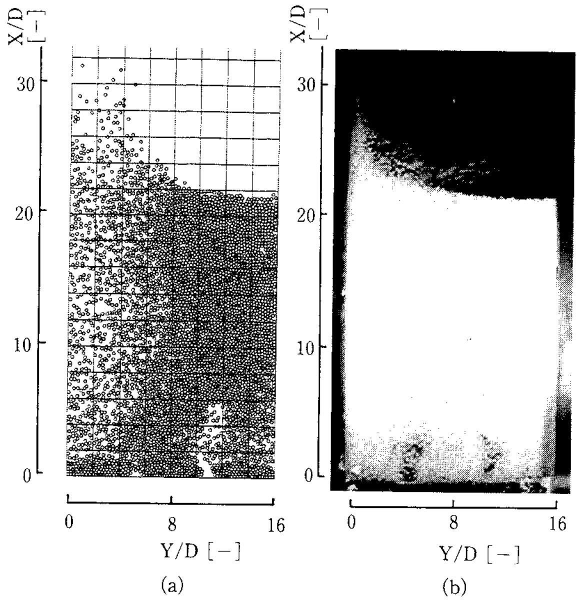

(a) (b)

Fig. 5 Instantaneous locations of particles, (a)Calculated result(X/D-Y/D plane, Z/D=15, t=183), (b)Experimental result.

nozzles are not the same in both the *a* (calculated) and *b* (experimental) parts of these three figures, but as noted previously, under the conditions used in this research, after the passage of about 100 nondimensional time units (actual time equivalent of approximately 0.03 s) since air begins issuing from the nozzles, the stationary particles have become fluid even in the regions farthest from the nozzle openings, which nearly eliminates any flow field differences owing to initial particle arrangement. Thus calculation results obtained after about 100 nondimensional time units (actual time equivalent of approximately 0.03 s) likely express the phenomena in actual fluidized beds operating continuously. Accordingly, if one excerpts phenomena similar to calculated results (in these calculations, phenomena occurring near the $Y/D=0$ wall in which large-scale particle lifts are caused by bubbles) from among the frequently occurring large-scale, unstable flows recorded by video, and compares and contrasts them with calculated results, it will be possible to compare both using information such as the rate at which bubbles rise, and the location and height of particle lifts. It is on this basis that **Figs. 3** through **5** compare the calculated results on instantaneous particle location over time after 144 nondimensional time units (actual time equivalent 0.042 s) with continuous photos of actual large-scale unstable flows (1/60th s (0.01667 s) intervals) very similar to calculated results. The figures show that the state of flows shown by calculation results—especially large-scale, unstable flows—assume about the same form as measured results, showing that they actually exist. Comparing these calculated and experimental results in detail reveals differences in the shape and other characteristics of bubbles appearing near nozzle exits, but these are due to the fact that there are no two flow fields with exactly the same flow pattern from one instant to the next, and the authors have confirmed from video shots that experimental results obtained at another instant reveal nozzle-exit bubbles that are nearly the same in form to calculated results. **Fig. 6** is two snapshots of calculated results showing lateral sections of a fluidized bed, in this case the $Y-Z$ surface, and their particle locations. As seen in **Fig. 1**, air jets are emitted from 10 nozzles on the bottom ($S/D=0$) of the fluidized bed, but at $X/D=8$ there is hardly any sign that an air jet is being emitted from each nozzle, and the situation is characterized by a large bubble-like flow, and by small bubble-like flows in various places. At $X/D=16$ the large bubble-like flow becomes even larger, which reduces the number of small bubble-like flows by a corresponding amount.

We next compared quantitative calculation and experimental results as detailed below. **Fig. 7** shows the mean time values of air velocities along the center line of a nozzle, i.e., along the center line of the jet issuing from a nozzle, near the fluidized bed wall ($Z/D=15$). As particles with diameters of 1.56 mm blocked the observation region, the LDA was only able to measure along the nozzle center line nearest the acrylic transparent wall. In this situation as well, velocity was determined by using a calculator to subtract the value for the time when a

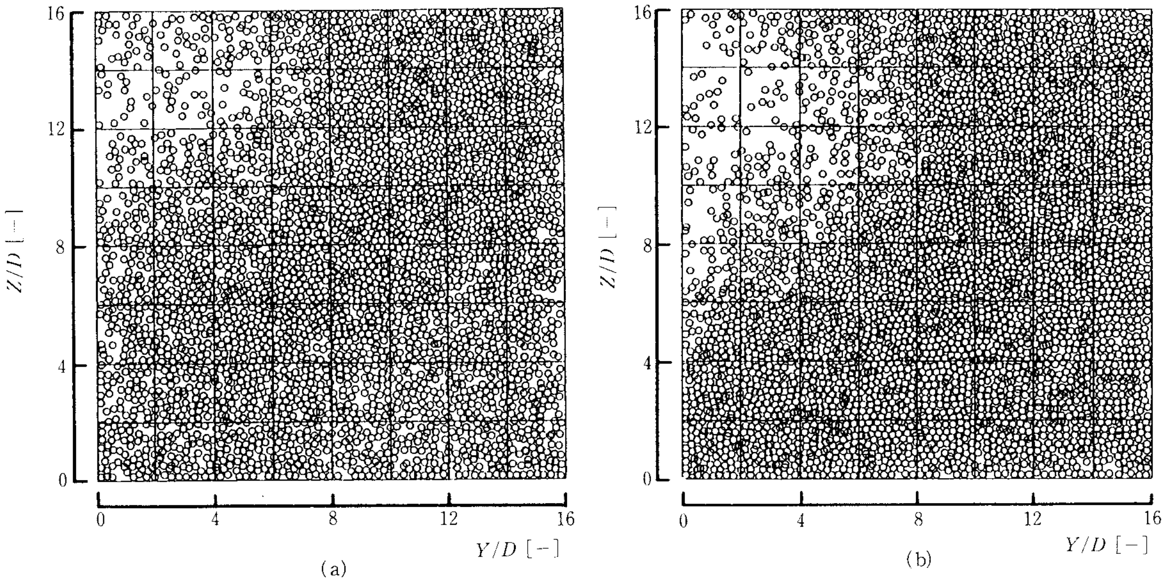

Fig. 6 Calculated instantaneous locations of particles(Y/D-Z/D plane, t=186). (a)X/D=8, (b)X/D=16.

1.56 mm particle passes through the measurement region from the value obtained by digitizing LDA output. Calculation results are average values for a time of about 0.07 s actual time equivalent. This is not long enough for averaged time, so averaged values include some error. Still, because X/D is up to 4 along the jet axis, and because the region is near the nozzle exit, the change in velocity is not great, and the error is probably not that large. As **Fig. 7** illustrates, the calculated results closely match the experimental results. At $X/D=4$ the calculated values are considerably lower than experimental values, but one cannot be sure of the reason with only these data.

Fig. 8 shows the average particle velocity distribution along the center line of a nozzle near the wall ($Z/D=15$). The calculated values are averages for the 100 to 200 particles passing through that point, while experimental values are averages for about 100 particles. Subsequent data are all for the wall vicinity, and the averaged number of particles is also the same. As particle inertia is great (inertia parameter for jet velocity standard at nozzle exit $\Psi=2.3\times10^4$), particle velocity is far slower than jet velocity near nozzle exits, but this difference diminishes as particles near the top. However, as we are dealing with a phenomenon that happens over the short time of 0.07 s, particles rise and then fall again, thus to a certain extent moving in a cycle, while the 0.07 s represents only the zone in which a large-scale, unstable current is rising, so values differ from those that would express movement over a sufficiently long time. Experimental values likewise are average values for phenomena occurring over a short time (about 0.07 s), which corresponds roughly to calculated values. Although calculated values roughly express experimental values, overall the calculated values are higher. This is perhaps because of slight divergence between the calculated and experimental values for the aforementioned short-time phenomenon. **Fig. 9** shows horizontal distributions of mean particle velocities in the axial (vertical) direction. Nozzle locations are $Y/D=4.5$ to 5.5 and $Y/D=10.5$ to 11.5 at $X/D=0$ (i.e., the fluidized bed's bottom). Near jet stream centers in the vicinity of the bottom the calculated values are very near experimental values, but as distance from them lengthens, calculated values become higher than experimental values. Especially near the wall, the particles are stationary in the experiment, while calculations show them to be moving with considerable velocity. As we are dealing with phenomena occurring over the short time of about 0.07 s, it would seem the results are affected by the disparity between calculations and experimental phenomena, but because there are large discrepancies between the two at whatever section, we think this reflects a shortcoming of the hard sphere model, which considers only two-particle collisions. Even when particle density is high and each particle has contact with many others, the hard sphere model calculates only two-point contact, which results in a high particle speed assessment in regions with high particle density.

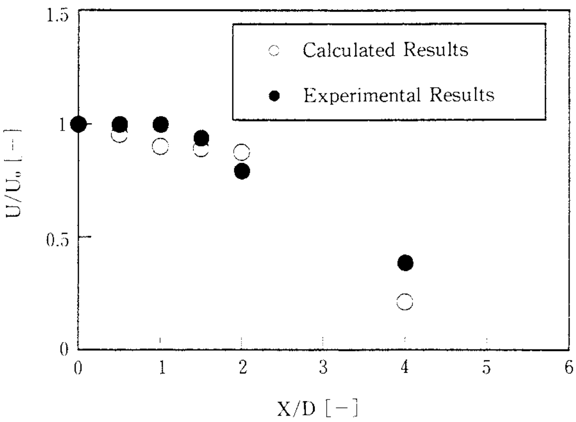

Fig. 7 Axial air mean velocities on jet center-line(Z/D=15).

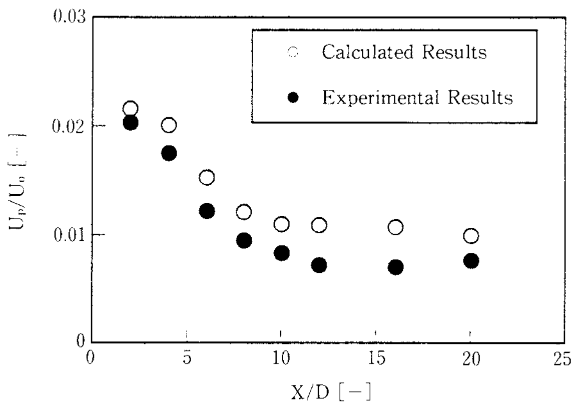

Fig. 8 Axial particle mean velocities on jet center-line(Z/D=15).

Fig. 10 shows horizontal distributions of the intensities of variation in particle velocity in the axial (vertical) direction. As these are averages for the short time of at most 0.07 s, both calculated and experimental values serve as little more than reference data, but as calculated values are higher at almost all sections, results are perhaps affected by the aforementioned hard sphere model shortcomings, and by ignoring the stress term generated by micro-variations. It will be necessary to investigate in more detail these variation intensities and other variation characteristics.

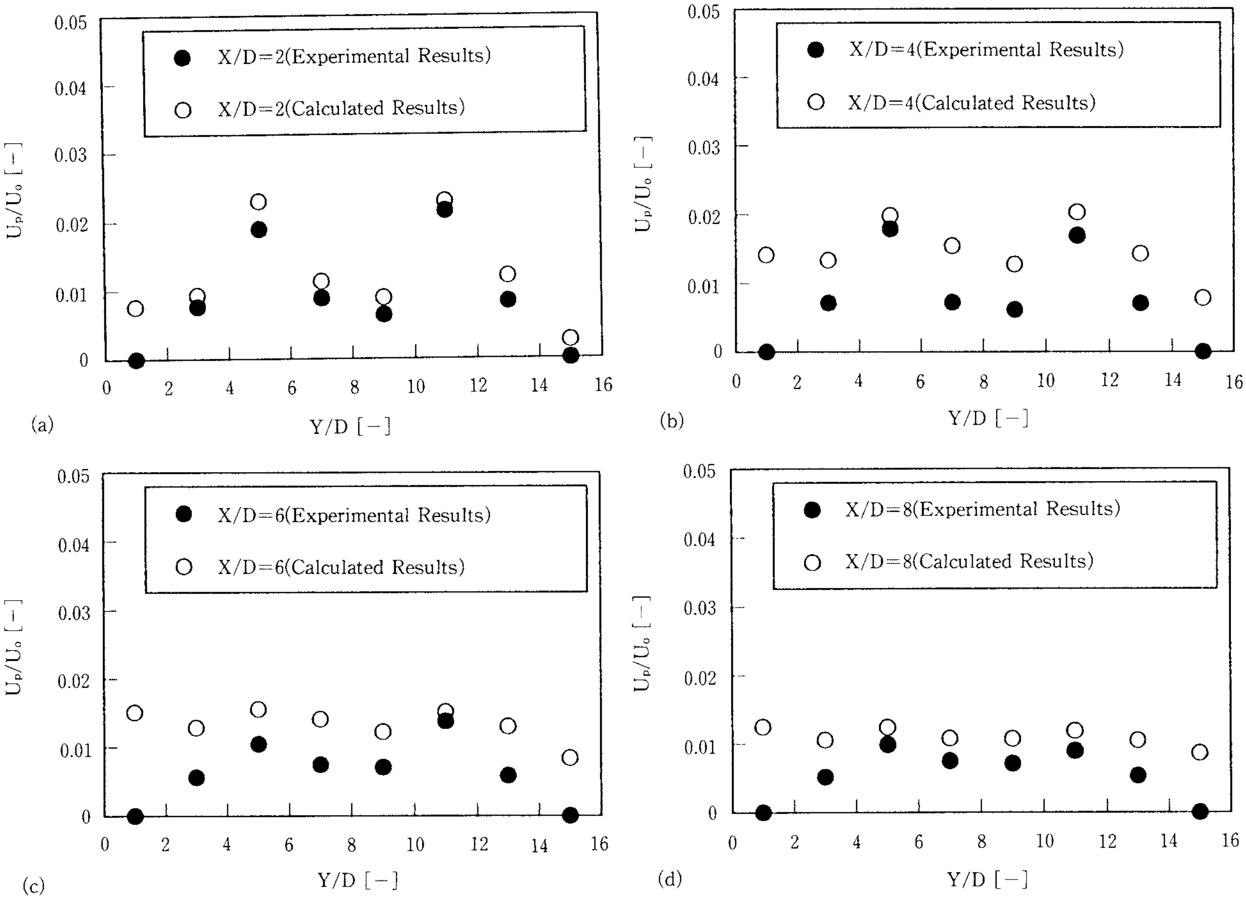

Fig. 9 Axial particle mean velocity distributions(Z/D=15), (a)X/D=2, (b)X/D=4, (c)X/D=6, (d)X/D=8.

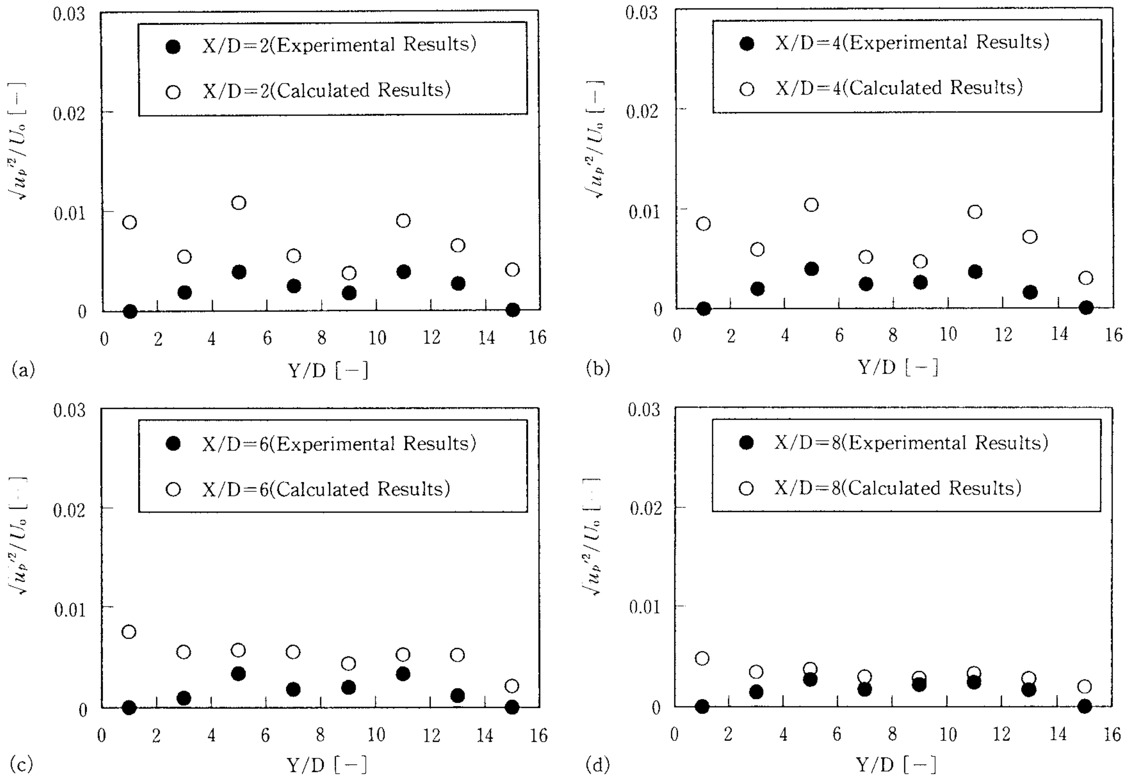

Fig. 10 Axial particle turbulent intensity distributions (Z/D=15), (a)X/D=2, (b)X/D=4, (c)X/D=6, (d)X/D=8.

Conclusion

We used the hard sphere model for particle collisions, and simultaneously solved the Navier-Stokes equations for locally averaged air flow in a single calculation cell (in this case, however, we ignored the stress term generated by micro-variation in a single calculation cell) and Lagrangian particle movement equations. By this means we sought the motions of air streams and particles in a three-dimensional fluidized bed with 10 nozzles installed on the bottom and expelling air jets. We then conducted experiments under conditions identical to those of the calculations to test the soundness of calculation results. Experiments showed that the calculations expressed well the large-scale, unstable flows that actually appear, and that this method can more or less predict them. We also found that calculation results can express average particle velocity distributions and other ordinary experimental results, except for places where particle density is so great as to make multi-particle contacts predominant. At this stage calculations lack a certain degree of precision for reasons that include the ignoring of micro-variations in a single calculation cell, but we believe that this research has succeeded in establishing a starting point for numerical simulations of actual fluidized beds. Most in need of improvement is perhaps this method's calculation of phenomena lasting only about 0.1 s, which must be lengthened to several seconds. It is also necessary to increase somewhat the number of particles by improving the algorithm, and to make it possible to directly apply the Monte Carlo method (DSMC method). This would probably make it possible to numerically analyze fluidized beds of fine particles.

Appendix

To solve for collisions, convert an XYZ absolute coordinate system into a spherical coordinate system whose origin is the center of a certain spherical particle, then ultimately restore this to an XYZ absolute coordinate system and perform calculations. The collision equations for colliding particles i and j are as follows.

$$\begin{aligned}
&m_p(v'_{ni}-v_{ni})=R,\\
&m_p(v'_{ti}-v_{ti})=F_t,\\
&m_p(v'_{bi}-v_{bi})=F_b,\\
&I_p(\omega'_{ni}-\omega_{ni})=0,\\
&I_p(\omega'_{bi}-\omega_{bi})=\frac{D_{pi}}{2}F_t,\\
&I_p(\omega'_{ti}-\omega_{ti})=\frac{D_{pi}}{2}F_b,\\
&m_p(v'_{nj}-v_{nj})=-R, \qquad \text{(A-1)}\\
&m_p(v'_{tj}-v_{tj})=-F_t,\\
&m_p(v'_{bj}-v_{bj})=-F_b,\\
&I_p(\omega'_{nj}-\omega_{nj})=0,\\
&I_p(\omega'_{bj}-\omega_{bj})=\frac{D_{pj}}{2}F_t,\\
&I_p(\omega'_{tj}-\omega_{tj})=\frac{D_{pj}}{2}F_b,\\
&v'_{ni}-v'_{nj}=e_p(v_{nj}-v_{ni})
\end{aligned}$$

Conditional equations for totally rough, non-slipping particles are as follows.

$$v'_{ti}+\omega'_{bi}\frac{D_{pi}}{2}=v'_{tj}+\omega'_{bj}\frac{D_{pj}}{2} \qquad \text{(A-2)}$$

$$v'_{bi}+\omega'_{ti}\frac{D_{pi}}{2}=v'_{bj}+\omega'_{tj}\frac{D_{pj}}{2} \qquad \text{(A-3)}$$

For partly rough, slipping particles, $F=\sqrt{F_t^2+F_b^2}\geqq\mu_pR$, the equations are as follows.

$$F_t=\mu_pR\frac{F_t}{F} \qquad \text{(A-4)}$$

$$F_b=\mu_pR\frac{F_b}{F} \qquad \text{(A-5)}$$

If Equation (A-1) is solved using Equations (A-2) and (A-3), or using Equations (A-4) and (A-5), impact strength and post-impact velocity are found. Variables with prime symbols denote post-impact velocity.

Nomenclature

D	: nozzle diameter	[m]
D_p	: particle diameter	[m]
$\overline{D_p}$	: nondimensional particle diameter ($=D_p/\Delta x$)	[-]
e_p	: particle-particle restitution coefficient	[-]
e_w	: particle-wall restitution coefficient	[-]
F	: shear force	[N]
g	: weighting function used in defining local average	[-]
g_c	: gravitational acceleration	[m/s^2]
I_p	: moment of inertia ($=(1/10)m_pD_p^2$)	[kgm^2]
m_p	: particle mass	[kg]
n	: particle number in a computational cell	[l/m^3]
P	: static pressure	[Pa]
R	: normal force	[N]
Re	: Reynolds number ($=DU_0\rho/\mu$)	[-]
Sp	: interaction term between air and particles	[N/m^3]
$\bar{t}$	: time	[s]

t : nondimensional time $(=\bar{t}\,U_0/D)$ [-]

Δt : nondimensional computational time step [-]

U_0 : air velocity at nozzle outlet [m/s]

V_0 : computational cell volume [m^3]

v : nondimensional locally averaged air velocity vector $(=(u,\ v,\ w))$ [-]

V_p : particle volume [m^3]

v_p : nondimensional particle velocity vector $(=(u_p,\ v_p,\ w_p))$ [-]

$X,\ Y,\ Z$: rectangular coordinates [m]

$\Delta x,\ \Delta y,\ \Delta z$: cell sizes [m]

ε : void ratio [-]

μ : air viscosity [kg/ms]

μ_p : friction coefficient of particles [-]

μ_w : particle-wall friction coefficient [-]

ν : μ/ρ [m^2/s]

ρ : air density [$\mathrm{kg/m}^3$]

ρ_p : particle density [$\mathrm{kg/m}^3$]

τ : nondimensional viscous stress [-]

ω : nondimensional particle angular velocity vector $(=(\omega_{xp},\ \omega_{yp},\ \omega_{zp}))$ [-]

Literature cited

1) Anderson, T.B. and R. Jackson : "A Fluid Mechanical Description of Fluidized Bed", *I. E. C. Fundamentals*, **6**, 527 ~539 (1967)

2) Bouillard, J.X., Lyczkowski, R.W. and D. Gidaspow : "Porosity Distributions in a Fluidized Bed with an Immersed Obstacle", *AIChE J.*, **35**, 908~922 (1989)

3) Gibson, M.M. : "Spectra of turbulence in a round jet", *J. Fluid Mech.*, **15**, 161~181 (1963)

4) Harlow, F.H. and J.E. Welch : "Numerical Calculation of Time Dependent Viscous Incompressible Flow of Fluid with Free Surface", *Phys. Fluids*, **8**, 2182~2189 (1965)

5) Kawaguchi, T., Nishi, S., Tanaka, T. and Y. Tsuji : "Numerical Simulation of Fluidized Bed using Discrete Element Method (Effect of the Depth)", *Proceedings of Konsoryu Symposium* '93, 5~8 (1993)

6) Laurence, J.C. : "Intensity, Scale, and Spectra of Turbulence in Mixing Region of Free Subsonic Jet", *NACA Report 1292* (1956)

7) Muchi, I., Mori, S. and M. Horio : "Ryudoso no Hannokogaku", Baifu Kan (1983)

8) Piacsek, S.A. and G.P. Williams : "Conservation Properties of Convection Difference Scheme", *J. Comp. Phys.*, **6**, 392~405 (1970)

9) Schiller, V.L. and A. Naumann : "ber die Grundlegenden Berechnungen bei der Schwerkraftaufbereitung", *Z. Vereines Deutscher Inge.*, **77**, 318~321 (1933)

10) Squires, K.D. and J.K. Eaton : "Particle response and turbulence modification in isotropic turbulence", *Phys. of Fluids A*, **2**, 1191~1203 (1990)

11) Steinour, H.H. : "Rate of Sedimentation, Nonflocculated Suspensions of Uniform Spheres", *I. E. C.*, **36**, 618~624 (1944)

12) Yuu, S., Kawaseki, Y. and T. Nagasue : "Direct Numerical Simulation of Three-Dimensional Navier-Stokes Equations for Free Jet and Experimental Verification", *Kagaku Kogaku Ronbunshu*, **18**, 101~107 (1992)

Author's short biography

Shinichi Yuu

He graduated from the graduate school of Kyoto University in 1970 and obtained the Doctor degree of Engineering. He was appointed Associate Professor of Kyushu Institute of Technology in 1973, and Professor in 1979. He was Visiting Scholar in University of California, Berkeley from 1980 to 1981. He has been Dean of Faculty of Engineering, Kyushu Institute of Technology since 1996. His major research interests are numerical simulations for gas-solid two-phase turbulent flows (gas-solid two-phase jets, fluidized beds and graunlar flows), and statistics and dynamics of granular materials by using numerical approaches.

Kenji Ikeda

He graduated from the graduate school of Kyushu Institute of Technology with M. Emg. in 1994. He has worked in Asahi Chemical Industry, Co., Ltd. since 1994.

Toshihiko Umekage

He graduated from the graduate school of Kyushu Institute of Technology with M. Emg. in 1987. He had worked in Kobe Steel, Ltd. from 1987 to 1990. He was Research Assistant of Kyushu Institute of Technology in 1990, and Lecturer in 1994. He obtained the Doctor degree of Engineering from Kyushu Institute of Technology in 1994. His research interests are almost same as those of Professor S. Yuu.

Kouki Nohara

He graduated from the graduate school of Kyushu Institute of Technoloogy with M. Emg. in 1996. He has worked in Nippon Light Metals, Co., Ltd. since 1996.

Dynamic Shape Factors of Regular Shaped Agglomerates and Estimation Based on Agglomerate Symmetry[†]

—For Rectangular Parallelepiped, V- and W-shaped, Hexagonal and H-shaped Agglomerates—

Tohru Niida, Shinichi Ohtsuka
Dept. of Chem. Eng.,
*Osaka Prefecture University**

Abstract

Dynamic shape factors for regular-shaped agglomerates, such as rectangular parallelepipeds, V- and W-shapes, and others, have been calculated from their measured terminal settling velocities in the Stokes regime. Experimental results have been analyzed by using a new correlation based on two-sphere hydrodynamic resistance as presented in a previous work. Estimated and experimental dynamic shape factors are in good agreement, with deviation smaller than 5%. The correlation can estimate the dynamic shape factor of a double-sized symmetrical agglomerate from its components, and also in a direction with an unstable settling orientation.

1. Introduction

Studies on the dynamic shape factors of agglomerates have mainly been empirical to date. Previous researchers performed theoretical analyses for a few classes of agglomerates, showing that very short chains consist of a few spheres of equal size. Happel and Brenner[4] obtained the analytical solutions in a series by using the method of reflection for two spheres in contact and separated from one another in the horizontal and vertical directions. Numerical solutions of the dynamic shape factors of chain-like agglomerates consisting of 30 or less primary spheres were performed by Geller et al[2]., who formulated results in a form similar to those for the case of long prolates.

Experimental determinations of dynamic shape factors have been reported for chain-like agglomerates[1,7-9,12], and for some regular and arbitrarily shaped cluster-like agglomerates[7,9,10-12]. The dependency of the dynamic shape factor of agglomerates on their shapes and on the number of primary spheres in them is not explicitly correlated either by observation or by theory, except in the work of Niida and Ohtsuka[10,11].

In the present research we determined the dynamic shape factors of agglomerates whose shapes include those that are rectangular parallelepiped, V-shaped, W-shaped, and hexagonal. They have regular forms that are somewhat complex from the viewpoints of analytical calculation and numerical method. The experimental results are correlated by using parameters which characterize the motion of model agglomerates.

To account for the experimental results, we first applied the results of Happel and Brenner to the motion of a pair of spheres in a viscous fluid in a creeping flow regime to evaluate the dynamic shape factors of nonspherical and symmetrical particles. An expression developed according to an analogy was tested using the experimental results. This procedure can be applied to an agglomerate if it has some symmetrical planes dividing it into at least two parts that are mirror images of each other in directions that are parallel and perpendicular to the axis of settling motion. Each mirror image in a symmetrical agglomerate may be a primary particle or an agglomerate itself. But we excluded planes of symmetry dividing a primary particle into two incomplete parts. In general, the plane of symmetry inclines in an arbitrary direction. The dynamic shape factor in the direction of three principal axes indicates those in any direction of motion by means of an analytical expression[3] shown below. Here we assume for the restricted motion of an object that the direction of gravity along which the agglomerate settles is on the plane of symmetry of a model

---

*1-1 Gakuen-cho, Sakai, Osaka, Japan 599-8531

[†] This report was originally printed in Kagaku Kougaku Ronbunshu, 22, 98 (1996) in Japanese, before being translated into English by KONA Editiorial Committee with the permission of the editiorial committee of the Soc. chemical Engineers, Japan.

particle. When the plane of symmetry is perpendicular to the line of gravitational direction, the expression for falling motion[3,4] with the particle shape parameters must be different from that given above.

2. Theory

2.1 The interaction between a pair of spheres of equal size, and the dynamic shape factor

When two spheres of equal size settle side by side and the line of their centers is perpendicular to the line of gravitation, the fluid force acting on a sphere is given by the following equation[4].

$$F = 6\pi\mu a_1 u\lambda \tag{1}$$

$$\lambda = 1-(3/4)x+(9/16)x^2-(59/64)x^3+(465/256)x^4 - (15813/7168)x^5+2x^6/(1+x) \tag{2}$$

where $x = a_1/L$, L is the distance between the centroid of spheres. When they are in contact x is 1/2.

2.2 Estimation of dynamic shape factor when an agglomerate moves in the plane of symmetry

Eqs. (1) and (2) were derived from the basic equation of spheres in the creeping flow regime. In general they must not be applied to nonspherical or irregular particles including agglomerates. We assume here the dynamic shape factor for agglomerates with a form similar to that described above, which is a particle consisting of a symmetrical particle as a component; the volume equivalent radius and the dynamic shape factor when the particle moves with the same orientation are a_v and x_1, respectively (**Fig. 1**). The hydrodynamic resistance acting on a particle is,

$$F = 6\pi\mu a_v u\lambda x_1 \tag{3}$$

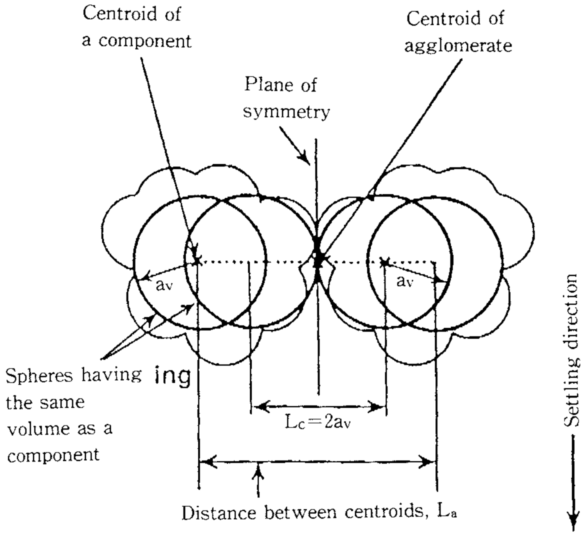

$$x \equiv a_v/L = (a_v/2L_c)^{1/2}$$

Fig. 1 Illustration of a symmetrical agglomerate to calculate dynamic shape factor using Eg.(5)

The net hydrodynamic resistance acting on a symmetrical agglomerate must be doubled by taking into account the effect of contact as follows:

$$F_2 = 2F = 6\pi\mu(2a_v)u\lambda x_1 = 6\pi\mu a_{v2} u x_2 \tag{4}$$

where x, instead of in Eq. (2), is $x = a_v/L$ by replacing a with a_v. In Eq. (4), the volume equivalent radius of an agglomerate consists of two particles of equal size in which a_{v2} is replaced with $2^{1/3}a_v$. Then:

$$x_2 = 2^{2/3}\lambda x_1 \tag{5}$$

The next assumption is that L in Eq. (5) is calculated as a function of two different distances, one (L_a) is that between the centroids as they locate, the other (L_c) is that occurring when two spheres with equal radiuses and equal volume equivalents ($L_c = 2a_v$) come into contact. We tried to determine the function with an expression as simple as possible assuming the arithmetic mean, the geometric mean, and so on, under empirical correlations by testing the experimental data on the dynamic shape factors obtained from the gravitational settling velocities of a number of shapes. We found an expression, which may be applied to the shapes of agglomerates used in the present work, whose geometrical means of L_a and L_c enable us to characterize the distance between components in an agglomerate when it settles along the axis in the plane of symmetry. Thus:

$$L = (L_c L_a)^{1/2}, \text{ or } x = (a_v/2L_a)^{1/2}$$

2.3 Dynamic shape factor in an arbitrary orientation

For a chain-like agglomerate, the dynamic shape factor in an arbitrary orientation where the angle $\theta/2$ is between the moving axis and the principal axis along a chain is[8]:

$$1/x_\theta = 1/x_\perp + (1/x_{/\!/} - 1/x_\perp)\cos^2(\theta/2) \tag{6}$$

3. Experimental

The dynamic shape factor of a model agglomerate is determined from the terminal settling velocity in a cylindrical container filled with silicone oil whose kinematic viscosity is about 10^{-2} m²/s, and by using the linear correction for the effect of the container wall[5,10].

The model agglomerates used here had the three shape categories as shown in **Fig. 2 (a)-(c)**, including 37 different shapes and two or three different

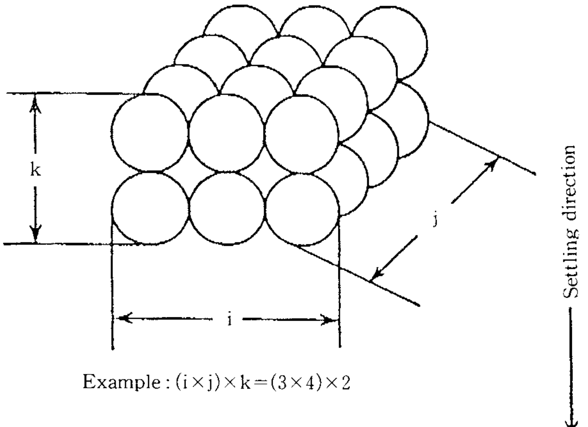

(a) Rectangular parallelepiped agglomerate (RPAs)

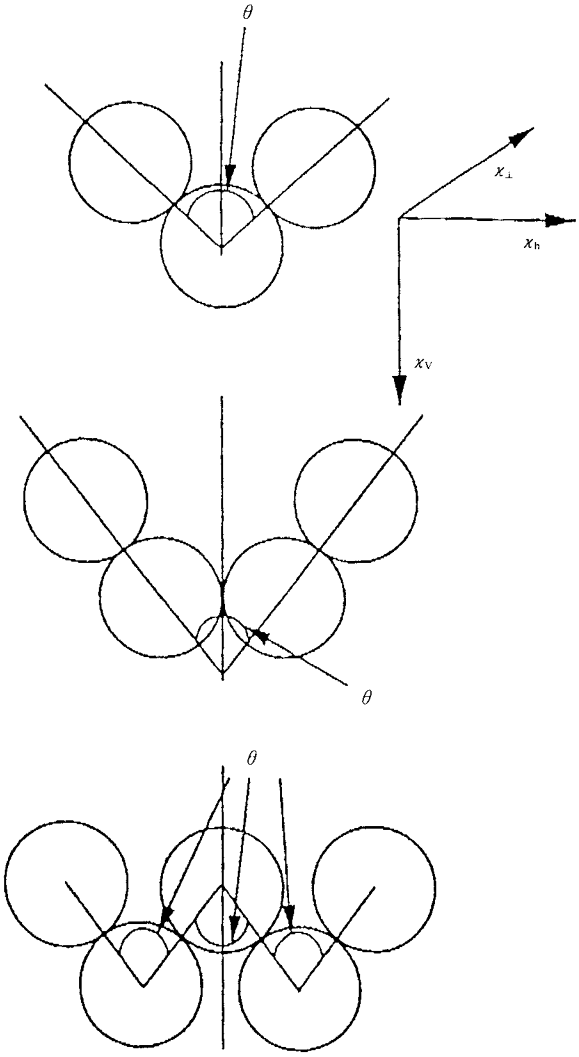

(b) V-and W-shaped agglomerates

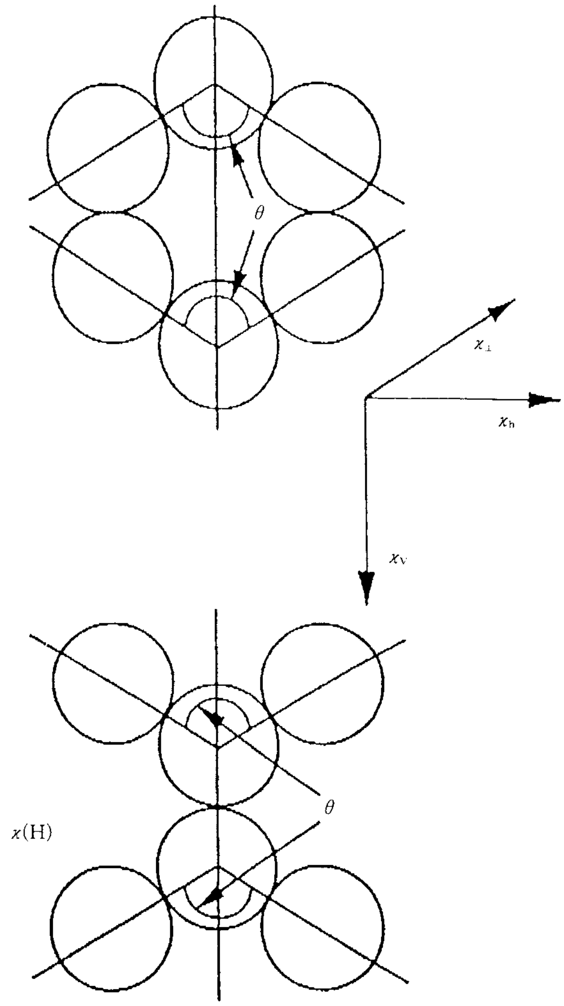

(c) Hexagonal ring and H-shaped agglomerates

Fig. 2 Illustration of the shapes of Agglomerates used in experiments

sizes, but similar to each other for each shape. All of these agglomerates consist of spherical primary particles of equal size in each model.

The first model agglomerate category has the rectangle parallelepiped shape shown as $(i \times j) \times k$, where i and j are the number of primary particles on the side of the rectangular surface perpendicular to the settling axis, and k is the number of spheres in the direction parallel to settling motion. Here i and j are mutually exchangeable. The top and middle in **Fig. 2(b)** shows V-shaped agglomerates consist of odd and even numbers of primary spheres, respectively. The corner angle between branches is 60° to 180° for the odd number, and 0° to 180° for the even. In W-shaped agglomerates, shown in **Fig. 2(b)** bottom, the angles of corners are the same (error ; ±1° or less) and between 60°-180°. The last category includes two types, but both consist of a pair of V-shaped components, one hexagonal, and the other the modified H-shape as shown in **Fig. 2 (c)**. The dynamic shape factor is measured in all of the different orientations corresponding to the principal axis when the projection and settling directions differ from each other.

Throughout the experiments, the particle density of chrome steel is 7.79×10^3 kg/m^3, and the diameters of primary spheres are 2.00-4.00 mm. Each shape has one or two model particles of different sizes, and the volume equivalent diameter of all model particles is 9.5 mm or less. The inside diameters of the cylindrical oil tank are 66.4 mm (effective settling depth, 202 mm), 50.0 mm (190 mm), 38.0 mm (150 mm), and 27.9 mm (100 mm). Thus, the resulting values of the particles' Reynolds number, which is based on the volume equivalent diameter of the agglomerate, are less than 1.67×10^{-2}, and the ratio of the volume equivalent diameter of the agglomerate and the cylinder diameter is less than 0.2. The experimental procedure, not described here, and the method for manufacturing agglomerates are as described in a previous paper[10].

4. Results and discussion

4.1 Properties of silicone oil and measurement accuracy

The viscosity and density of silicone oil, and the density, size, mass, and shape of primary and model agglomerates are measured prior to experiments [10,11]. Agglomerates consisting of 20 or more primary spheres are subject to inaccuracy, although not serious, so model agglomerates having better configurations were chosen and used in the experiments.

The accuracy of terminal settling velocity measurements was estimated at about 0.2% based on errors in time measurement (between 11 s and 36 s, ±0.1%) between graduations (±0.3 mm, with the thickness), repeated five times for each agglomerate. Other accuracies are: viscosity (±1%), particle density (±0.1%), shape error (distortion), and the error during graphic extrapolation. From the error sources considered here, we estimated roughly that the final net error is a few percentage points in dynamic shape factor values.

4.2 Rectangular parallelepiped agglomerates

The dynamic shape factors of the rectangular parallelepiped agglomerates in the present research and those in the literature[9] are plotted in **Fig. 3** and listed in **Table 1**. **Fig. 3** shows the change in dynamic shape factors with agglomerate size (i, j, and k). Here the observed dynamic shape factor values are shown below each shape. The direction of arrows in the horizontal, diagonal, and vertical directions show the increase in the numbers of primary particles in i, j and k, respectively, in the same order. The solid (or dotted) arrows show that the dynamic shape factor increases (or decreases) from the left (beginning) to the right (end). The dynamic shape factor ratios in this research and by Lee et al., χ (exp.)/χ (Lee), are close to unity as 1.01±0.04.

Table 1 Dynamic shape factors of rectangular parallelepiped agglomerates (RPAs)

n	(i×j)×k*	χ exp.**	χ Lee et al.[9]	n	(i×j)×k	χ exp.	χ Lee et al.[9]
2	(1×1)×2	1.03	1.02	9	(1×3)×3	1.24	–
	(1×2)×1	1.16	1.15		(3×3)×1	1.54	–
3	(1×1)×3	1.07	1.07	12	(1×3)×4	1.27	–
	(1×3)×1	1.26	1.28		(1×4)×3	1.39	–
4	(1×1)×4	1.10	1.11		(3×4)×1	1.61	–
	(1×4)×1	1.37	1.38	12	(2×2)×3	1.20	–
4	(1×2)×2	1.10	1.09		(2×3)×2	1.28	–
	(2×2)×1	1.24	1.38	16	(2×2)×4	1.21	1.11
6	(1×2)×3	1.15	–		(2×4)×2	1.33	1.25
	(1×3)×2	1.24	–	18	(2×3)×3	1.22	–
	(2×3)×1	1.37	–		(3×3)×2	1.33	–
8	(1×2)×4	1.19	1.14	24	(2×3)×4	1.19	–
	(1×4)×2	1.31	1.27		(2×4)×3	1.29	–
	(2×4)×1	1.48	1.41		(3×4)×2	1.36	–
8	(2×2)×2	1.16	1.12	27	(3×3)×3	1.24	–

* i and j are interchangeable.

** Experimental results in this research.

Fig. 3 shows that the rate of increase in the

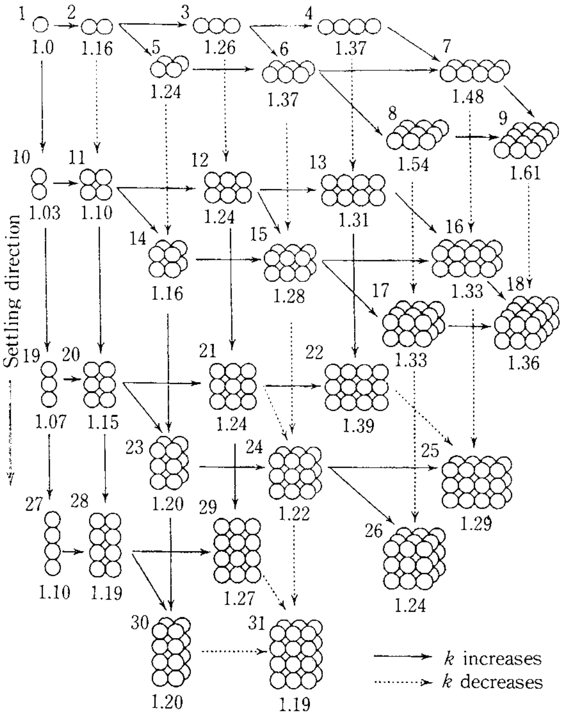

Fig. 3 Dynamic shape factors and shapes of parallelepiped agglomerates

dynamic shape factor from small agglomerates to large in the horizontal direction, which corresponds to the increase in the cross section perpendicular to the direction of fall, such as 11→12, 14→15, etc., is faster than that for the change of *k* in the vertical direction. This tendency of the change in dynamic shape factor corresponds exactly to that of prolate spheroids in the parallel orientation to the axis of revolution. When dynamic shape factor decreases or when *i*, *j* or *k* increases, the parallelepiped agglomerate changes its shape much like cube as seen in **Fig. 2**, that is 5→14, 3→12, 15→24, while the ratios *i*/*j*, *i*/*k*, and *j*/*k* approach unity. The dynamic shape factor increases whenever *k* increases from unity to 2 ($n>2$) and also when n is large the dynamic shape factor increases along the horizontal directions (*i* and *j*), that is, 29→31, 22→25, etc., as before. Other cases like 24→31 and 30→31 have decreasing dynamic shape factors for no clear reason, perhaps because of minor measurement error.

For special cases, the agglomerates whose cross sections are square in horizontal, where *i* and *k* are equal to 2 for different *j* values (11→14→15→16), show almost the same dynamic shape factor values, within experimental error, as the solid parallelepiped with a square cross section, or the square cylinder[6], as compared in **Table 2**.

Table 2 Comparison between dynamic shape factors of RPA* (2×j)×2 and square prisms

j	1	2	3	4
RPA	1.10	1.16	1.28	1.33
square prism**	1.08	1.16	1.24	1.34

* Rectangular parallelepiped agglomerates

**Derived from Fig. 5-11. 3 in Happel and Brenner 1965b.

4.3 V-shaped and W-shaped agglomerates

The dynamic shape factor χ_v of the V-shaped and W-shaped agglomerates consisted of from three to five primary particles of equal size, with some different branching angles that are listed in **Table 3**. The dynamic shape factors shown in **Table 3** correspond to the direction parallel to the symmetrical axis of the agglomerate, and particle motion orientation coincides with the most stable of those among multiple directions in motion.

Table 3 Dynamic shape factors of V-shaped and W-shaped agglomerates comprising 3,4, and 5 spheres of equal size

V-shaped								
	$n=3$							
θ[deg]	60	72	90	100	120	133	152	180
κ_v	1.09	1.12	1.16	1.19	1.22	1.24	1.26	1.26
	$n=4$							
θ[deg]	0	28	64	97	128	180		
κ_v	1.10	1.18	1.25	1.32	1.36	1.37		
	$n=5$							
θ[deg]	61	92	119	145	180			
κ_v	1.23	1.33	1.41	1.48	1.50			
W-shaped($n=5$)								
θ[deg]	62	91	122	153	180			
κ_v	1.21	1.35	1.45	1.50	1.50			

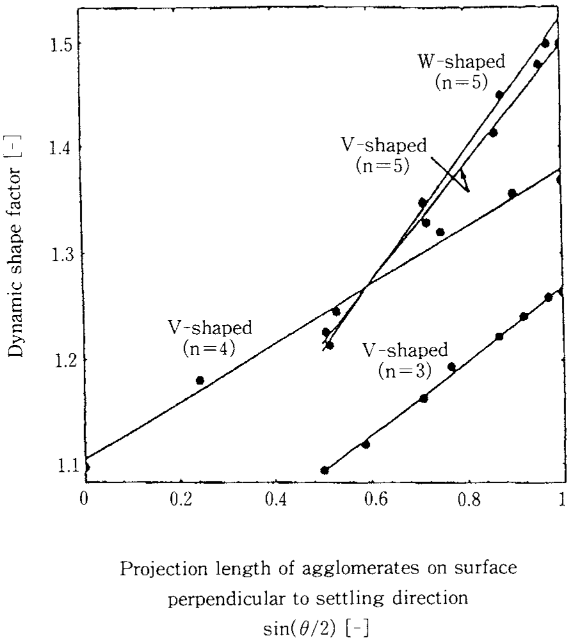

Fig. 4 Dynamic shape factors of V-and W-shaped agglomerates

The dynamic shape factors shown above correlate with the parameter sin ($\theta/2$), as shown in **Fig. 4**. The figure shows that the dynamic shape factor is a linear function of sin ($\theta/2$) or the particle length normal to the direction of motion. The correlation shows that the dimensionless parameter χ_p expressed by Eqs. (7) and (8) is introduced to find a function and is replotted in **Fig. 5** for the even and odd numbers of primary particles in an agglomerate.

$$\chi_\mathrm{p}=1+(n-1)\sin(\theta/2) \quad n=3 \text{ and } 5, \text{ odd} \tag{7}$$

$$\chi_\mathrm{p}=2+(n-2)\sin(\theta/2) \quad n=4, \text{ even} \tag{8}$$

Here, the dynamic shape factor χ_v is again correlated as a linear function of χ_p within a 4% error, as follows:

$$\chi_\mathrm{v}=0.847+0.131\chi_\mathrm{p} \tag{9}$$

The result clearly shows that the above correlation can be applied both to even and odd numbers of primary particles in an agglomerate, and also that W-shaped agglomerates have dynamic shape factors similar to those of V-shaped agglomerates

Table 4 Dynamic shape factors of hexagonal agglomerates

θ[deg]	60	91	120	140	180	120(H)*
Area**	6.38	7.09	7.31	7.21	6.55	
$\varkappa_v$	1.11	1.16	1.21	1.23	1.24	1.30
$\varkappa_h$	1.25	1.22	1.21	1.18	1.15	1.30
$\varkappa_\perp$	1.36	1.37	1.40	1.38	1.37	1.47

* H-shaped agglomerates(Fig. 2(c))

** Area $=4(1+(2/\pi)\sin(\theta/2)(1+\cos(\theta/2))$, is the ratio of total cross section of the agglomerate (including void space) to the primary particle cross section.

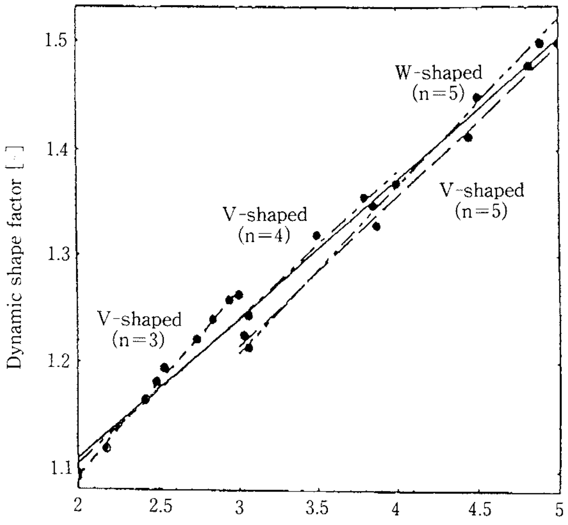

Fig. 5 Dynamic shape factors of V-and W-shaped agglomerates

consisting of the same number of primary spheres and having the same opening angle.

4.4 Hexagonal and H-shaped agglomerates

The dynamic shape factors of hexagonal rings as shown in **Fig. 2(c)** are listed in **Table 4** together with those of H-shaped agglomerates, and plotted in **Fig. 6** ($\varkappa_v$ and $\varkappa_h$) and **Fig. 7** ($\varkappa_\perp$). Both shapes consist of six primary particles. Here, $\varkappa_v$ is the dynamic shape factor along the symmetrical axis of the hexagonal shape, $\varkappa_h$ is in the direction along the open side of the symmetrical V-shape, and $\varkappa_\perp$ is in the direction normal to the plane where all primary spheres are located, as shown in **Fig. 2(c)**.

In **Fig. 6**, the linear correlation is found in dynamic shape factors with sin ($\theta/2$) and cos ($\theta/2$) for $\varkappa_v$ and $\varkappa_h$, respectively. The plot of dynamic shape factor $\varkappa_\perp$ to the whole cross section including the internal void space, again shows the linear relation between them, with the largest value at the regular hexagonal cross section, where the projection to the direction of motion is the largest. When the hexagonal and H-shaped agglomerates move in the direction normal to their planes, the dynamic shape factor $\varkappa_\perp$ of the hexagonal agglomerate is smaller than that of the H-shaped agglomerate. The difference between them must be interpreted because the distance between centroids of two components in hexagonal agglomerates is shorter than

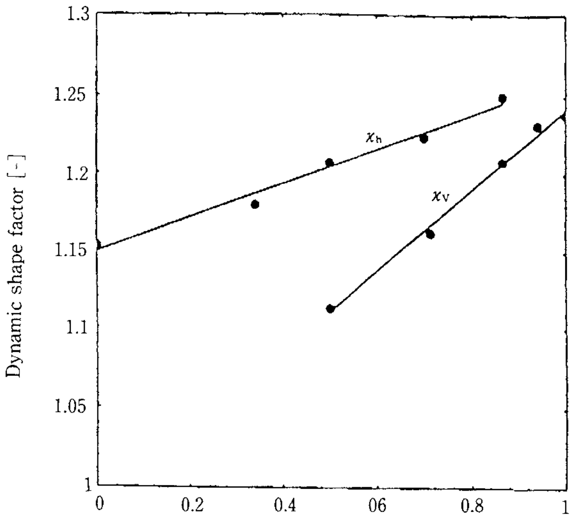

Fig. 6 Dynamic shape factors $\varkappa_v$ of hexagonal ring

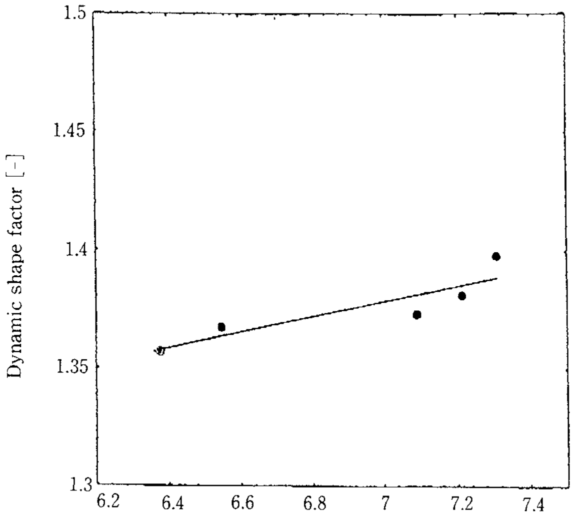

Fig. 7 Dynamic shape factors of $\varkappa_\perp$ of hexagonal ring
Area : See Table 4

that in H-shaped agglomerates.

4.5 Estimation of dynamic shape factors based on agglomerate symmetricity

Here we focus the discussion on the estimated results of dynamic shape factors for agglomerates consisting of a pair of symmetrical components by using the procedure described in section 2.2.

Rectangular Parallelepiped Agglomerates

In **Fig.** 8 the dynamic shape factor of parallelepiped agglomerates are shown with each shape. Here the dynamic shape factor is obtained by three procedures: The first is obtained experimentally and shown just below each shape; the second is the dynamic shape factor of the mother agglomerate (κ_2), estimated by combining the dynamic shape factor of two mirror image components (κ_1), and is shown over the right hand directional horizontal or diagonal arrows; the last is the result of an estimation (κ_1) for each component by decomposing a symmetrical mother agglomerate (κ_2) using Eq. (5), and is shown below the opposite-facing arrows. The ratio of values ($\kappa_{\text{estimated}}/\kappa_{\text{observed}}$) provides a mean value, 1.002, that is estimated from the dynamic shape factors of components, which yields 0.997 by using those from the mother agglomerates. The largest error in both estimation procedures is about 5% or less. It is suggested that the error in the empirical dynamic shape factor likely comes from errors in measurements, such as time measurement, settling distance, or the like, because these errors cancel each other.

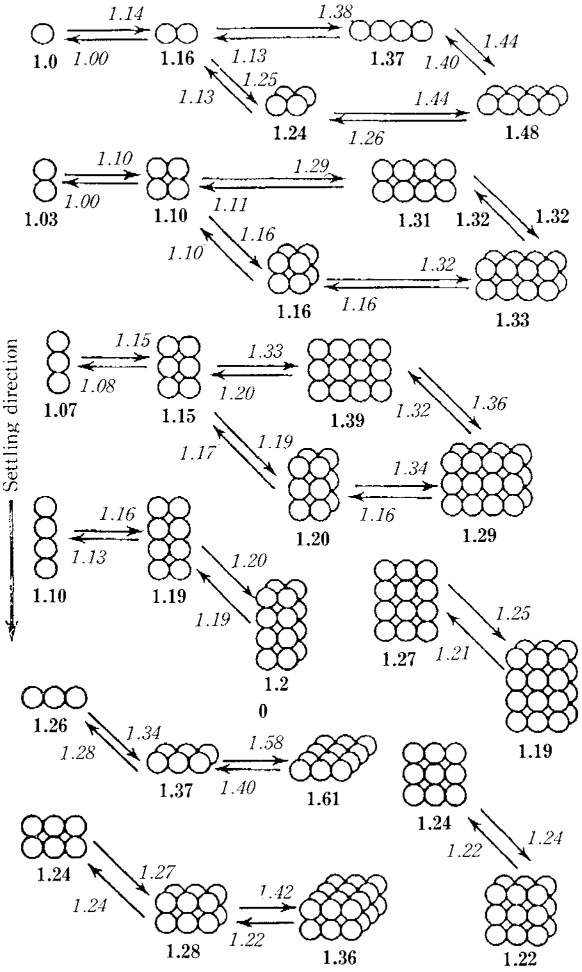

Fig. 8 Comparision among dynamic shape factors of parallelepiped agglomerates:
gothic: experimental result
italic: estimated by using Eq.(5)

Fig. 8 shows that, on the whole, differences between estimated and observed dynamic shape factors are closer when agglomerates consist of a lesser number of primary spheres, and that the dynamic shape factors estimated from the more cluster-like agglomerates have values closer to observed values than those from other routes from plate-like agglomerates when there are two different routes of estimation, for example (2,4,2) from (2,2,2) and from (1,4,2). But the differences seem at most not to exceed the overall errors that arise in experimental procedure, ca. 2% in dynamic shape factors. The present method described here now enables us to make estimates for the rectangular parallelepiped agglomerates having the side ratios of i/j and/or i/k between 1/4 and 4.

V-shaped Agglomerates (n=4)

The results are shown in **Table 5**, where κ_1 (ana.) is the analytical value for the inclined orientation with $\theta/2$ from Eq. (6) of two sphere agglomerate by using of $\kappa_{/\!/}=1.024$ and $\kappa_{\perp}=1.137^4$. Here κ_1 (est.) obtained from decomposing by using of Eq. (5) and κ_2 (exp.) the experimental results of V-shaped ($n=4$) in **Table 3**. κ_2 (est.) from κ_1 (ana.) and Eq. (5). It is found in **Table 5** that both κ_1 (ana.) and κ_1 (est.),

Table 5 Comparison between experimental dynamic shape factors and those predicted by eq.(5) for V-shaped agglomerates with n=4(κ_2) and tilted double spheres(κ_1)

θ[deg]	0	28	64	97	128	180
κ_1(ana.)$^{a)}$	1.02	1.03	1.05	1.08	1.11	1.14
κ_1(est.)$^{b)}$	1.00	1.04	1.07	1.11	1.13	1.13
κ_2(exp.)	1.10	1.18	1.25	1.32	1.36	1.37
κ_2(est.)$^{c)}$	1.10	1.17	1.23	1.29	1.34	1.38

a) Calculated from analytical values for double spheres with parallel and perpendicular orientation using Eq. (6) for each θ.

b) Estimated from κ_2(exp.) for V-shapes using Eq.(5).

c) Estimated from κ_1(ana.) using Eq.(5).

and $\varkappa_2$ (exp.) and $\varkappa_2$ (est.) coincide within the experimental error.

Hexagonal and H-shaped agglomerates

Table 6 Estimation of dynamic shape factors of V-shaped agglomerates($\varkappa_h$ and $\varkappa_\perp$) using $\varkappa_2$ for hexagonal agglomerates in Eq.(5)

θ[deg]	60	91	120	140	180	120(H)
$\varkappa_{h2}$	1.25	1.22	1.21	1.18	1.15	1.30
$\varkappa_{h1}$(est.)	1.09	1.07	1.08	1.06	1.08	1.12
$\varkappa_{h1}$(exp.)	1.09	–	–	–	1.07	–
$\varkappa_{\perp 2}$	1.36	1.37	1.40	1.38	1.37	1.47
$\varkappa_{\perp 1}$(est.)	1.18	1.21	1.24	1.25	1.28	1.26
$\varkappa_{\perp 1}$(exp.)	1.19	–	–	–	1.26	–
$\varkappa_{av}$*	1.12	1.15	1.18	1.18	1.19	–

* $\varkappa_{av}$ is calculated from $\varkappa_v$ for n=3 in Table 3 and the estimated $\varkappa_{h1}$ and $\varkappa_{\perp 1}$.

Table 6 lists the dynamic shape factor of V-shaped agglomerates by decomposing the $\varkappa_h$ and $\varkappa_\perp$ (see **Fig. 2(c)**) of hexagonal agglomerates. $\varkappa_h$ and $\varkappa_\perp$ for V-shaped agglomerates (see **Fig. 2(b)**) may not be determined experimentally, except for the opening angles of 60° and 180°. It must be emphasized that Eq. (5) enables us to estimate the dynamic shape factor in a certain direction where the dynamic shape factor cannot be determined experimentally because its motion is unstable during gravitational settling. It is natural that the estimated dynamic shape factors of V-shaped component agglomerates must coincide with each other when they are estimated from hexagonal shapes and from H shapes. Both results in **Table 6** are within the experimental error.

Table 6 show that $\varkappa_h$ is almost constant, 1.08±0.02, and $\varkappa_\perp$ increases about 8% from 1.18 at 60° to 1.28 at 180°. Spatial averaged dynamic shape factors $\varkappa_{av}$ are then calculated and shown in **Table 6**. $\varkappa_{av}$ slightly increases (ca. 5%) from 1.12 at 60° to 1.18 at 120°, but is almost constant between 120° and 180°.

The accuracy of symmetrical estimation

The values estimated by using Eq. (5) and the observed values of dynamic shape factors for symmetrical agglomerates are plotted in **Fig. 9**. Though the mean of the ratios of estimated dynamic shape factors and the observed value is 1.02±0.06, which is slightly larger than that of rectangular parallelepiped agglomerates, both seem to agree well within experimental error.

Even Eq. (1) can be applied in limited cases for the horizontal orientation of a two-sphere agglomerate. It is rigidly derived through a method of successive approximation based on the basic equations for the creeping motion of Newtonian fluid. On the other hand, Eqs. (3) and (4) are formulated on the basis of a certain analogy to Eq. (1), and then these equations are used here to estimate dynamic shape factor, which must be considered subject to errors arising from unknown factors. But these equations are still useful in estimating the dynamic shape factors of symmetrical agglomerates consisting of many primary particles because of the difficulty of evaluating complex-shaped agglomerates by analytical or numerical methods. We should suggest once again the applicability of Eqs. (3) and (4) because many classes of agglomerate shapes, such as the rectangular parallelepiped, V shapes, W shapes, and hexagonal and other shapes, can be evaluated by their dynamic shape factors as shown in the above description.

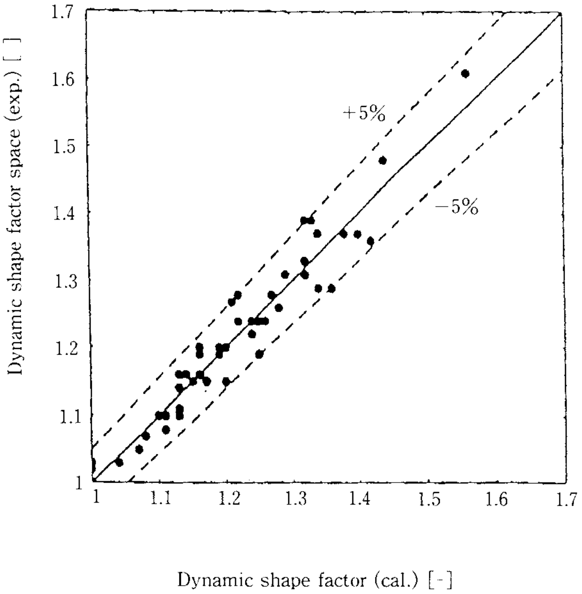

Fig. 9 Comparision between experimental and calculate (Eq.(5)) dynamic shape factors

5. Conclusion

The dynamic shape factors of regular-shaped agglomerates consist of up to 27 primary spheres, and their rectangular parallelepiped, V, W, hexagonal, and H shapes have been experimentally determined and correlated with semi-empirical equations to make estimations based on agglomerate symmetricity. The dynamic shape factors of observed and estimated values agree well within a difference about 5% when the latter are estimated using Eqs. (3) and (4) regarding the composing and decomposing of agglomerates.

Another correlation for V-, W-, hexagonal, and H-shaped agglomerates is carried out based on the projection length or projection area of an agglomerate in the direction of settling motion, and presented by linear functions.

According to Eqs. (3) and (4), the dynamic shape factor of one mirror-image element in a symmetrical agglomerate or a double-sized agglomerate consists of a pair of mirror-image elements, and can be evaluated from that of the whole agglomerate or from an element of the agglomerate. Moreover, it enables us to calculate the dynamic shape factor of an agglomerate's orientation when it cannot be determined by experimental measurement.

List of symbols :

a	: particle radius	[m]
a_v	: volume equivalent radius	[m]
D	: inner diameter of cylindrical container	[m]
d_{pv}	: volume equivalent diameter	[m]
F	: drag force	[N]
L	: distance between centroids	[m]
n	: number of primary particles in an agglomerate	[-]
x	: =a/L	[-]
x_p	: projection length	[-]
u	: terminal settling velocity	[m/s]
θ	: angle	[rad]
κ	: dynamic shape factor	[-]
λ	: coefficient of resistance	[-]
μ	: viscosity of fluid	[Pa s]

Subscripts

1 : agglomerate component
2 : combined agglomerate
av : average orientation
v : vertical orientation
h : horizontal orientation
θ : for angle θ
// : parallel orientation
$\perp$: perpendicular orientation

Literature cited

1) Durlofsky, L., J.F. Brady and G. Bossis: "Dynamic Simulation of Hydrodynamically Interacting Particles", *J. Fluid Mech.*, **180**, 21-49 (1987).

2) Geller, A.S., L.A. Monday, D.J. Rader and M.S. Lunber: "Boundary Element Method Calculations of the Mobility of Nonspherical Particles-1. Linear Chains", *J. Aerosol Sci.*, **24**, 597-609 (1993).

3) Happel, J. and H. Brenner: *Low Reynolds Number Hydrodynamics*, pp.183-207, Prentice-Hall, Inc., Englewood Cliffs, N.J. (1965a).

4) Happel, J. and H. Brenner: ibid., pp.249-270 (1965b).

5) Happel, J. and H. Brenner: ibid., p.318 (1965c).

6) Happel. J. and H. Brenner: ibid., p.231 (1965d).

7) Horvath, H.: "The Sedimentation Behavior of Nonspherical Particles," *Staub*, **34**, 197-202 (1974).

8) Kasper, G., T. Niida and M. Yang: "Measurements of Viscous Drag on Cylinders and Chains of Spheres with Aspect Ratios Between 2 and 50," *J. Aerosol Sci.*, **16**, 535-556 (1985).

9) Lee, C.T. and D. Leith: "Drag Force on Agglomerated Spheres in Creeping Flow," *J. Aerosol Sci.*, **5**, 503-513 (1989).

10) Niida, T. and S. Ohtsuka: "Dynamic Shape Factors of Regular Shaped Agglomerates," *Kagaku Kogaku Ronbunshu*, **21**, 173-180 (1995a).

11) Niida, T. and S. Ohtsuka: "The Dynamic Shape Factors of Close Packed Agglomerates and Hollow Agglomerates," *Kagaku Kogaku Ronbunshu*, **21**, 821-823 (1995b).

12) Stöber, W., H. Flachsbart and D. Hochrainer: "Der aerodynamische Durchmesser von Latexaggregaten und Asbestfasern," *Staub*, **30**, 277-285 (1970).

Author's short biography

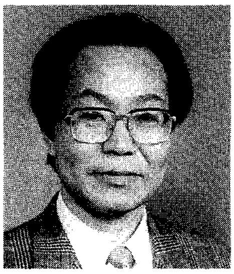

Tohru Niida

Tohru Niida graduated from Osaka Prefecture University (1964) and received his D. Eng. Degree (1978). He majored in Chemical Engineering. Since graduation he engaged in research on fluid dynamics and heat transfer and since 1980 on the fine particle characterization and behavior in gase and liquid phases.

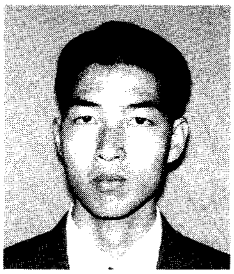

Shinichi Ohtsuka

Shinichi Ohtsuka graduated in Chemical Engineering from Osaka Prefecture University (1993) and obtained M.S. (1995). He studied the heterogeneous agglomeration and motion of nonspherical particles. Since graduation he has been working at Hitachizosen Co. Ltd. in the field of the purification of exhaust gas from the incinerator.

A Consideration of Constitutive Relationship between Flowing Particles†

Junya Kano
*Institute for Advanced Materials Processing, Tohoku University**
Atsuko Shimosaka and Jusuke Hidaka
*Department of Chemical Engineering and Materials Science, Faculty of Engineering, Doshisha University***

Abstract

In order to analyze the flow behavior of particles by the application of continuum mechanics, a new constitutive equation is derived from considerations of energy dissipation during the flow of the particles. This dissipation mechanism was investigated by computer simulation of the flow behavior of particles on an inclined trough. The energy of flowing particles is dissipated by friction and collision with neighboring particles. The constitutive equation was derived by considering both dissipation mechanisms of energy. The velocity distribution of flowing particles on the inclined trough was estimated by the application of a constitutive equation. The estimated velocity distribution agrees well with the measured one.

1. Introduction

Computer simulations now provide very useful information on powder systems, and they have become a highly important tool in the study of powder phenomena. In particular the particle element method[1] provides very detailed spatial and temporal information on the flow behavior of particles, and it has demonstrated its great usefulness in the essential understanding and mechanical analysis of powder behavior[2]. However, as this method entails tracking the movements of individual particles in Lagrangian method, there is a severe limitation on the number of particles in the system being studied, which means it is impossible to simulate particle behavior inside an apparatus working with a very large number of particles. This is a serious problem for the particle element method, which has accomplished much.

Further advances in particle simulations will therefore necessitate the devising of a new simulation method that is unrestricted by the number of particles. One requirement for this new simulation method is quite clear : It should basically be grounded in continuum mechanics, and have a high degree of freedom in element movement in terms of expressing the discrete character of powder behavior. Achieving this kind of simulation method requires, more than anything else, the ability to suitably express powder flows with continuum mechanics.

In this connection, people have for many years assiduously pursued research using polar fluid theory grounded in Cosserat's continuum theory[3]. Kanatani[4] in particular developed a theory of powder flow on the basis of polar fluid theory. In his work he derived a constitutive relationship for powder flows from macroscopic considerations that assume a particle bed is a continuum, and from microscopic considerations on the state of movement of constitutive particles. The constitutive equations derived are highly useful because they take into consideration the rotation of constitutive particles, which is a characteristic of particle flows, and because there are few parameters that must be obtained experimentally.

But as there was no means of obtaining detailed information on the flow state of a particle bed, there was no consideration of the energy dissipation occurring in conjunction with particle collisions, which have a large effect on particle flow.

As detailed in this report, we used the results[5] from a particle element method simulation of a flow in an inclined trough, which is a comparatively simple particle bed flow, to perform a detailed examination of energy dissipation in a flowing

---

* 2-1-1, Katahira, Aoba-ku, Sendai 980-77, Japan
**1-3, Tataramiyakodani, kyotanabe, kyoto 610-03, Japan

† This report was originally printed in J. Soc. Powder Technology, Japan. 33, 95(1996) in Japanese, before being translated into English by KONA Editiorial Committee with the permission of the editiorial committee of the Soc. Powder Technology, Japan.

particle bed, and derive a constitutive relationship that takes into consideration energy dissipation caused not only by inter-particle friction, but also by particle collisions. We then applied this constitutive relationship to analyze the flow state of a particle bed in an inclined trough and verified its soundness.

2. Controlling Equations of a Flowing Particle Bed

2.1 Fundamental Equations

Let us assume that a particle bed with a particle size distribution flows in a comparatively dense state, and that inertial force controls its flow. Further, we'll assume that the particles in a flowing bed are always rotating independently instead of submitting to the flow. This being so, the equation of continuity, equation of motion, and equation of angular momentum are as follows.

$$\frac{\mathrm{d}\rho}{\mathrm{d}t}+\rho\partial_k v_k=0 \tag{1}$$

$$\rho\frac{\mathrm{d}v^i}{\mathrm{d}t}=f_i+\partial_j\sigma^{ji} \tag{2}$$

$$\rho\frac{\mathrm{d}\omega_{ji}}{\mathrm{d}t}=\frac{10}{{D_s}^2}\{2\sigma^{[ji]}+\partial_k\mu^{kji}\} \tag{3}$$

Where :

v is particle velocity,

ρ is bulk density,

σ is stress,

f is external force,

ω is rotational velocity,

μ is couple stress, and

D_s is particle diameter of mean surface.

2.2 Energy Dissipation in a Flowing Particle Bed

Generally constitutive equations are determined by two controlling functions : free energy and a dissipation function. We'll assume that in the flow of a particle bed the collective has no internal energy, all internal force being dissipation energy. On the basis of this assumption, Kanatani focussed on the energy dissipation of particle mass, and derived a constitutive equation by determining the equivalent stress which causes that dissipative work.

This method requires detailed information on energy dissipation. The authors previously used the particle element method, which provides detailed information on the behavior of flowing particle beds, to simulate a particle bed flowing in an inclined trough^5. **Figs. 1** and **2** show the initial particle fill in a trough, and the particle velocity distribution at the side of the inclined trough, respectively. **Table 1** shows the calculation conditions and physical constants used in the simulation. **Figs. 3(a)** and **(b)** show the dissipated energy by friction Φ_f and dissipated energy by collision Φ_c obtained from simulation results. **Table 2** shows the ratio R of energy dissipated by collisions to total dissipated energy. As the trough's angle of inclination becomes greater, the dissipated energy caused by both fric-

Table 1 Physical constants used in simulation calculation

Young's modulus	4.9×10^9	[Pa]
(wall)	3.9×10^9	[Pa]
Poisson's ratio	0.23	[−]
(wall)	0.25	[−]
Number of particles	3752	[−]
Particle diameter	20	[mm]
Time step	1.0×10^{-5}	[s]
Coefficient of repulsion	0.8	[−]
Coeffisient of friction	0.466	[−]
(particle-wall)	0.268	[−]
Particle dnsity	2.65×10^3	[kg/m^3]

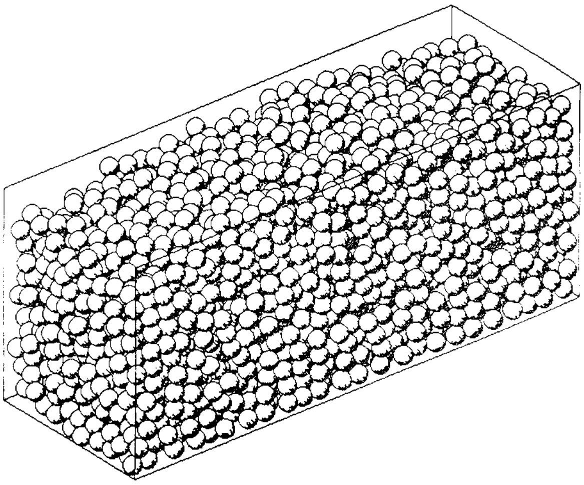

Fig. 1 Initial fill of particles in trough

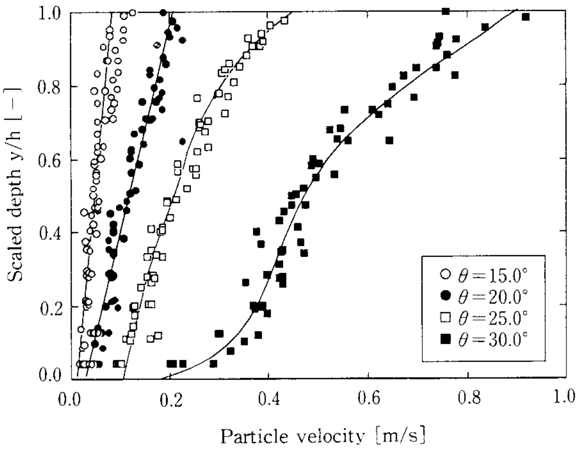

Fig. 2 Velocity profiles obtained in 3D simulation calculation of chute flow

Table 2 Mean dissipation energy of flowing particles and ratio of energy dissipated by collisions to total dissipation energy

θ[°]	E_f[J]	E_c[J]	R[−]
10.0	0.134	2.00×10^{-2}	0.129
15.0	0.252	3.90×10^{-2}	0.134
20.0	0.482	9.36×10^{-2}	0.163
25.0	0.983	0.257	0.207
30.0	1.663	0.921	0.356

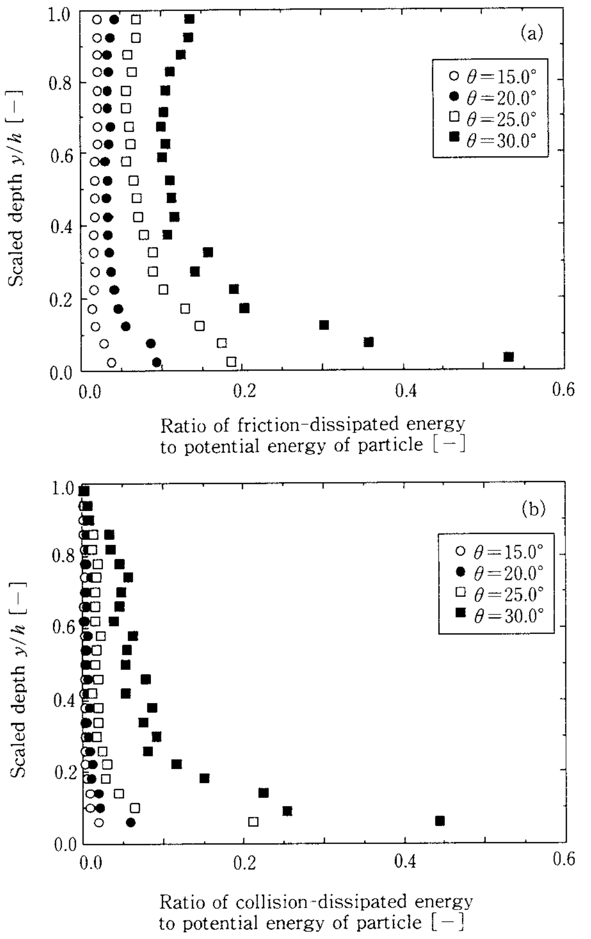

Fig. 3 Dissipation energy of flowing particles on chute

tion and particle collisions becomes greater, and the ratio of collision-caused dissipated energy to total dissipated energy grows. Especially when chute flow becomes large, the ratio of collision-caused dissipated energy to total dissipated energy attains 30 or 40%, a value that cannot be ignored. Thus, in the derivation of a constitutive equation applied to particle bed flows, one must take into consideration collision-caused dissipated energy in addition to friction-caused dissipated energy.

2.3 Constitutive Equation for a Flowing Particle Bed

The total dissipated energy Φ_m of a flowing particle bed is the sum of dissipated energy by friction Φ_f and dissipated energy by collision Φ_c, as shown in this equation.

$$\Phi_m = \Phi_f + \Phi_c \tag{4}$$

Next these values for dissipated energy are determined by using a model of the flowing particle bed. In particle flows with comparatively little mutual inter-particle action and high fluidity, individual particles flow while continuously colliding with nearby particles. This flowing particle movement can be demonstrated using the cell model[4] in **Fig. 4**. It shows that a certain particle with microscopic velocity v' moves randomly in a spherical space with diameter D_r, and that it flows while continuously colliding with the cell wall (i.e., nearby particles in the first stratum). We have already examined in detail the applicability of the cell model to particle bed flows using the results of a particle element method simulation of a particle bed flowing in an inclined trough[5]. On the basis of this cell model it is possible to determine the flowing particle bed's friction- and collision-caused dissipated energy.

a) Energy Dissipated by Friction

When a certain particle collides with its cell wall, the compressive force acting on the wall is $\pi D_r^2 P$ when average pressure is P, and frictional force is $\mu_i \pi D_r^2 P$ when μ_i is the frictional coefficient. If the tangential component of collision velocity at the point of collision is ξ_i, the energy dissipated by friction that is caused by the collision is expressed as $\mu_i \pi D_r^2 P \xi_i$. Thus the energy dissipated by friction

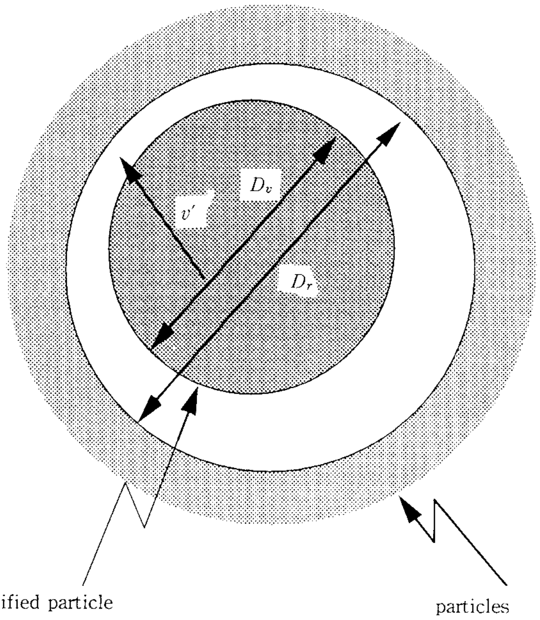

Fig. 4 Cell model of flowing particles

per unit volume and unit time of the flowing particles is determined by the following equation.

$$\Phi_f = \frac{\pi}{2m}\mu_i D_r^2 \rho P \xi_i \tag{5}$$

Because the particle continuously collides with its spherical cell wall, the mean pressure P in Equation (5) can be found in the same way as in the kinetic theory of gases. In other words, the distance that the particle can move without colliding with the wall of its spherical cell, whose diameter is D_r, is $(D_r - D_v)\sin\zeta$ when the collision angle is ζ. Thus, the number of collisions n per unit time is $2v'e/(1+e) \times (D_r - D_v)\sin\zeta$, using v' for particle microscopic velocity and e for the coefficient of repulsion. Each collision transmits a momentum of $mv'(1+e)\sin\zeta$ to the cell wall, meaning that a force of $nmv'(1+e)\sin\zeta$ acts on the wall per unit time. As cell surface area is πD_r^2, mean pressure P is found by the following equation.

$$P = \frac{2mv'^2 e}{\pi D_r^2 (D_r - D_v)},\ m = \frac{\pi}{6} D_v^3 \rho_p,\ D_r = D_v \sqrt[3]{\frac{\rho_0}{\rho}} \tag{6}$$

Where:

ρ_0 is the bulk density of the initial particle fill.

Thus, if Equation (6) is substituted with Equation (5), energy dissipated by friction is found by this equation.

$$\Phi_f = \frac{\mu_i e v'^2 \rho \xi_i}{D_r - D_v} \tag{7}$$

b) Energy Dissipated by Collisions

Because the energy dissipated by one collision is $(1/2)\,mv'^2 \times (1-e)^2$, the energy per unit time is $(1/2)\,nmv'^2 \times (1-e)^2$. Thus the dissipated energy according to collisions per unit volume is determined by this equation.

$$\Phi_c = \frac{1}{2}\frac{\rho v'^3}{D_r - D_v}\frac{e(1-e)^2}{(1+e)\sin\zeta} \tag{8}$$

If Equation (4) is substituted for Equations (7) and (8), total dissipated energy of a flowing particle bed is determined in the following manner.

$$\Phi_m = \frac{\mu_i e v'^2 \rho \xi_i}{D_r - D_v} + \frac{1}{2}\frac{v'^3 \rho}{D_r - D_v}\frac{e(1-e)^2}{(1+e)\sin\zeta} \tag{9}$$

The following equations determine the tangential component ζ_i of the relative velocity in collisions between the particle and its cell wall[4].

$$\xi_i = \frac{\sqrt{6}}{3} D_s \hat{\omega},\ \hat{\omega} = \sqrt{\frac{3}{10}E_{ji}E_{ji} + \frac{1}{2}R_{ji}R_{ji} + \frac{D_s^2}{40}(\Omega_{kkj}\Omega_{llj} + \Omega_{kji}\Omega_{kji} + \Omega_{kji}\Omega_{kij})} \tag{10}$$

$$E_{ji} = D_{(ji)} - \frac{1}{3}\delta_{ji}D_{kk},\ D_{ji} = \partial_j v_i,$$

$$R_{ji} = \omega_{ji} - D_{[ji]},\ \Omega_{kji} = \partial_k \omega_{ji} \tag{11}$$

Substituting Equation (9) for Equation (10), total dissipated energy is determined by the following equation.

$$\Phi_m = C(\rho)\,\hat{\omega}^3$$

$$C(\rho) = \frac{\sqrt{6}}{30} \cdot \frac{\mu_i e T D_s^3 \rho}{D_r - D_v} + \frac{\sqrt{10}}{200}\frac{T\sqrt{T}D_s^3\rho}{D_r - D_v}\frac{e(1-e)^2}{(1+e)\sin\zeta} \tag{12}$$

Where:

T is the ratio of the particle's translational kinetic energy $(1/2mv'^2)$ to rotational kinetic energy.

Macroscopic dissipated energy Φ_s, however, can be obtained from the law of energy conservation. Assuming that power by external force is equal to the increase in kinetic energy and the dissipated energy per unit time, the following equation determines macroscopic dissipated energy[4].

$$\Phi_s = \tilde{\sigma}^{ji}E_{ji} - \sigma^{[ji]}\omega_{ji} + \frac{1}{2}\mu^{kji}\Omega_{kji}$$

$$\tilde{\sigma}^{ji} = \sigma^{ji} - \frac{1}{3}\delta_{ij}\sigma^{kk} \tag{13}$$

Combining the microscopic dissipated energy found by the cell model (Equation (9)) with the macroscopic energy determined by the law of energy conservation yields the following constitutive equations[4].

$$\sigma^{ji} = C(\rho)\,\hat{\omega}\left(\frac{2}{5}\frac{\partial v_j}{\partial x_i} - \frac{1}{10}\frac{\partial v_i}{\partial x_j} + \frac{1}{2}\omega_{ji}\right) \tag{14}$$

$$\sigma^{ii} = \frac{1}{5}C(\rho)\,\hat{\omega}\frac{\partial v_i}{\partial x_i} - P \tag{15}$$

$$\sigma^{[ji]} = \frac{1}{2}C(\rho)\,\hat{\omega}\left(\frac{1}{2}\frac{\partial v_j}{\partial x_i} - \frac{1}{2}\frac{\partial v_i}{\partial x_j} + \omega_{ji}\right) \tag{16}$$

$$\mu^{kji} = \frac{D_s^2}{40}C(\rho)\,\hat{\omega}\frac{\partial \omega_{ji}}{\partial x_k} \tag{17}$$

Now we shall use the fundamental equations in section 2.1 and the constitutive equations obtained here to attempt an analysis of a typical particle flow state.

2.4 Numerical Analysis of Particles Flowing Through an Inclined Trough

We conceived a flow such as that in **Fig. 5** in order to compare the constitutive equations proposed here with the analysis results given by Kanatani's equations, which do not take into consideration the energy dissipation caused by collision. Following are the equations of motion for this particle flow.

$$\rho\frac{\mathrm{d}u}{\mathrm{d}t} = C(\rho)\frac{\partial}{\partial y}\left\{\hat{\omega}\left(\frac{2}{5}\frac{\partial u}{\partial y} + \frac{1}{2}\omega\right)\right\} + \rho g \sin\theta \tag{18}$$

$$\rho\frac{\mathrm{d}\omega}{\mathrm{d}t} = \frac{10C(\rho)}{D_s^2}\left\{\hat{\omega}\left(\frac{1}{2}\frac{\partial u}{\partial y} + \omega\right) + \frac{D_s^2}{40}\frac{\partial}{\partial y}\left(\hat{\omega}\frac{\omega}{\partial y}\right)\right\} \tag{19}$$

$$\hat{\omega} = \sqrt{\frac{1}{2}\left(\frac{1}{2}\frac{\partial u}{\partial y} + \omega\right)^2 + \frac{3}{40}\left(\frac{\partial u}{\partial y}\right)^2 + \frac{D_s^2}{10}\left(\frac{\partial \omega}{\partial y}\right)^2} \tag{20}$$

By contrast, Kanatani's equations for the same

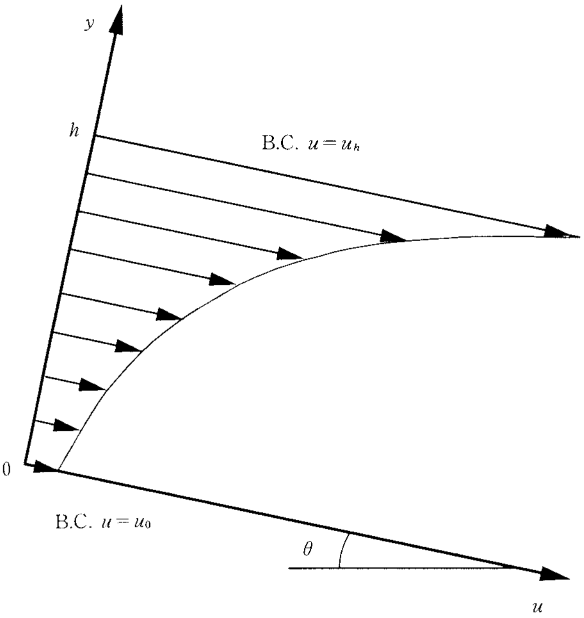

Fig. 5 Boundary condition for calculation of velocity distribution of flowing particles on chute

flow are as follows.

$$\rho\frac{\mathrm{d}u}{\mathrm{d}t}=B(\rho)\frac{\partial}{\partial y}\left\{\bar{\omega}\left(\frac{2}{5}\frac{\partial u}{\partial y}+\frac{1}{2}\omega\right)\right\}+\rho g\sin\theta \tag{21}$$

$$\rho\frac{\mathrm{d}\omega}{\mathrm{d}t}=\frac{10B(\rho)}{D_s^2}\left\{\bar{\omega}\left(\frac{1}{2}\frac{\partial u}{\partial y}+\omega\right)+\frac{D_s^2}{40}\frac{\partial}{\partial y}\left(\bar{\omega}\frac{\partial\omega}{\partial y}\right)\right\} \tag{22}$$

$$B(\rho)=\frac{\sqrt{6}\pi}{60}\frac{T\mu_iD_r^2D_p^3}{m}\frac{\rho_0\rho^2}{\rho_0-\rho} \tag{23}$$

Where :

D_p is particle size.

For each equation of motion, one approximates by forward difference for time and central difference for space, and obtains numerical solutions using the finite difference method. By way of boundary conditions, for particle velocities u_0 and u_h at the lowest and highest lattice points we assigned the particle velocity values observed for the bottom and top of the particle bed in a flow experiment with the inclined trough (**Fig. 6**)^5. For initial conditions we used the particle velocities yielded by the following equation.

$$u=(u_h-u_0)y/h+u_0 \tag{24}$$

In **Table 3** are the calculation conditions and physical constants used in these calculations. We assumed a constant bulk density for the state of particle flow, and made the ratio T of the particle's translational energy to rotational energy match the observed values for particles flowing through the trough.

Table 3 Physical constants used in FDM analysis

Δt	1.0×10^{-5}	[s]
Δy	5.0×10^{-4}	[m]
e	0.78	[−]
μ_i	0.380	[−]
D_s	2.0	[mm]
D_v	2.0	[mm]
D_p	2.0	[mm]
ρ_0	1.563×10^3	[kg/m^3]
ρ	1.548×10^3	[kg/m^3]
h	4.0×10^{-2}	[m]

3. Results and Discussion

Figs. 7(a) and **(b)** show the particle velocity distributions obtained by numerical calculations using the same conditions as in the flow experiment that yielded the particle flow distribution in **Fig. 6**. **Fig. 7(a)** shows the results of Equations (21) and (22) proposed by Kanatani, while **Fig. 7(b)** presents the results of Equations (18) and (19), which are proposed in this report. Estimated velocities according to the constitutive equations proposed here are in all cases smaller than those based on Kanatani's constitutive relationship; even in a low particle velocity region when the trough's incline is low, there is a slight difference in the velocity distributions. When the angle of incline θ is 15.5° and 16.9°, i.e., inclinations at which particle velocity increases, the difference between the distributions grows. Furthermore, overall the particle velocity distributions estimated using the constitutive equations proposed here more closely match measured values than Kanatani's results.

Figs. 8(a), **(b)**, and **(c)** illustrate the effects of the coefficient of friction μ_i on particle velocity distribution. A decrease in the frictional coefficient makes for an increase in the difference between the particle velocity obtained under Kanatani's theory and that obtained under the theory proposed here,

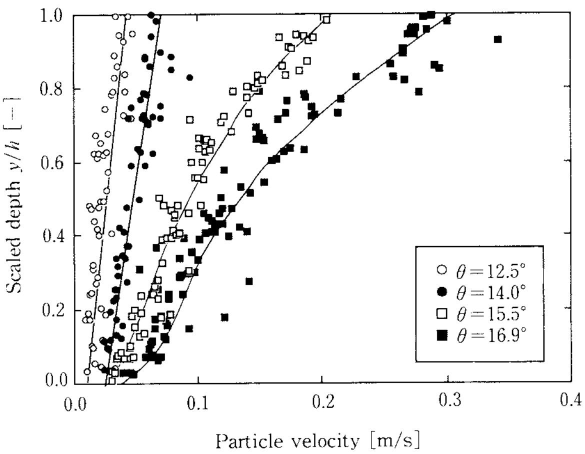

Fig. 6 Velocity profiles obtained in chute flow test

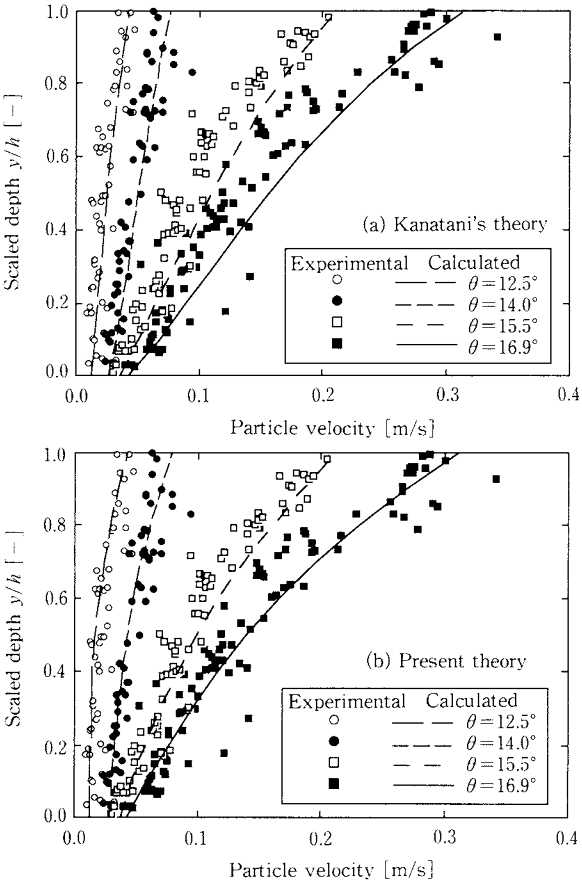

Fig. 7 Velocity profiles estimated by numerical analysis using proposed constitutive equation

signifying an increase in the effect of energy dissipation by collisions.

Fig. 9 shows the ratio of collision-caused dissipated energy to the total dissipated energy derived from numerical calculation results. As the inter-particle frictional coefficient and the inter-particle coefficient of repulsion become smaller, it becomes impossible to ignore energy dissipated by collisions.

The foregoing results show that when an ordinary powder (frictional angle of 20° to 30°) flows at a comparatively high velocity, the energy dissipated by collisions has a large effect on powder flow ; and that the constitutive equations proposed here are useful over a broad range, from slow to fast flows.

4. Conclusion

The authors performed research on constitutive relationships in flowing powder beds so that it would be possible to examine particle flow behavior in terms of continuum mechanics. Using simulations according to the particle element method to carefully observe flow behavior in a powder bed, we found that it is necessary for the flow model and constitutive equations derived by Kanatani to take collision-caused energy dissipation into account. For this purpose we derived constitutive equations that incorporate the coefficient of repulsion, and used them to obtain velocity distributions for a flowing particle bed in an inclined trough by means of the finite difference method. Calculated velocity distributions closely matched the plots of measured distributions, demonstrating the soundness of incorporating the coefficient of repulsion and modeling it. As the powder flow velocity in powder devices is

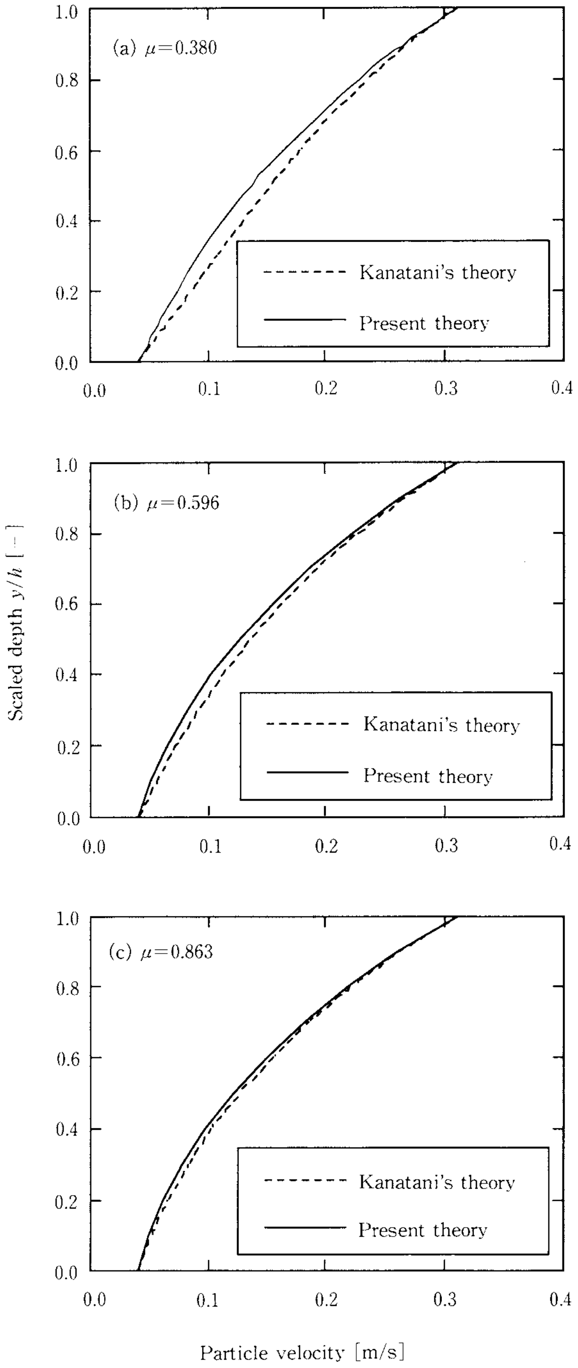

Fig. 8 Effect of coefficient of friction between particles on particle velocity distribution

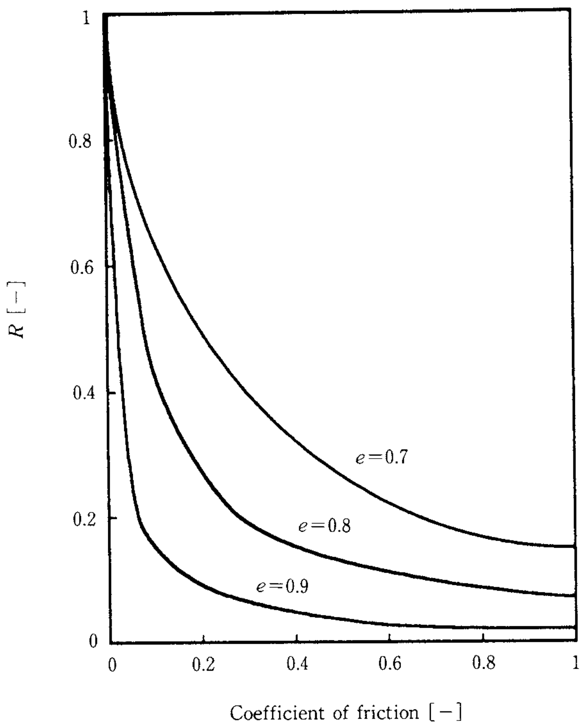

Fig. 9 Effect of coefficient of friction on the ratio of dissipation energy with collision to total dissipation energy

quite fast, we believe that in performing analyses of actual powder behavior it will prove useful to employ the proposed constitutive relationship, which takes collision-caused energy dissipation into account.

Nomenclature

B : function of ρ defined by Eq.(23) (kg/m)
C : coefficient in Eq.(12) (kg/m)
D_{ji} : tensor of velocty gradient defined by Eq.(11) (1/s)
$D_{(ji)}$: $\frac{1}{2}(\partial_j v^i + \partial_i v^j)$ (1/s)
$D_{[ji]}$: $\frac{1}{2}(\partial_j v^i - \partial_i v^j)$ (1/s)
D_p : particle diameter (m)
D_r : diameter of cell (m)
D_s : particle diameter of mean surface (m)
D_v : particle diameter of mean volume (m)
E_{ji} : tensor of velocity gradient deviator defined by Eq.(11) (1/s)
e : coefficient of repulsion between particles (-)
f : external force (N)
g : gravitational acceleration (m/s^2)
h : depth of powder bed (m)
m : mass of particle (kg)
P : pressure (Pa)
R_{ji} : relative rotational velocity of particle defined by Eq.(11) (1/s)
T : ratio of kinetic energy of specified particle to rotational kinetic energy (-)
t : time (s)
u : x-component of particle velocity (m/s)
u_0 : x-component velocity of particle at the bottom of powder bed (m/s)
u_h : x-component velocity of particle at the top of powder bed (m/s)
v : particle velocity (m/s)
v' : speed of specified particle (m/s)
y : height of particle in powder bed (m)
δ_{ij} : Kronecker's delta (-)
θ : inclinational angle of chute (deg)
μ : couple stress (Pa/m)
μ_i : coefficient of friction (-)
ζ : angle of collision (deg)
ξ_i : tangential component of relative velocity (m/s)
ρ : bulk density of flowing particles (kg/m^3)
ρ_0 : bulk density at initial packing of particles (kg/m^3)
ρ_p : density of particle (kg/m^3)
σ : stress (Pa)
$\sigma^{(ji)}$: $\frac{1}{2}(\sigma_{ji} + \sigma_{ij})$ (Pa)
$\sigma^{[ji]}$: $\frac{1}{2}(\sigma_{ji} - \sigma_{ij})$ (Pa)
Φ_c : dissipation energy by collision (J/s)
Φ_f : dissipation energy by friction (J/s)
Φ_m : microscopic dissipation energy (J/s)
Φ_s : macroscopic dissipation energy (J/s)

References

1) Hidaka J.: *J. Soc. Powder Technol., Japan*, **29**, 465 (1992)
2) Hidaka J., J. Kano and A. Shimosaka: *Kagaku Kogaku Ronbunshu*, **20**, 397 (1994)
3) Oshima N.: *Zairyo Kagaku*, **5**, 294 (1972)
4) Kanatani K.: *Nihon kikai Gakkai Ronbunshu*, **45-392**, 507 (1979)
5) Kano J., A. Shimosaka and J. Hidaka: *J. Soc. Powder Technol., Japan*, **30**, 183 (1993)

Author's short biography

Junya Kano

Junya Kano is a research associate at the Institute for Advanced Materials Processing (IAMP), Tohoku University. He graduated in the postgraduate course of department of chemical engineering, Doshisha University in 1995 and took a doctorate in engineering from Doshisha University in 1997. His main fields of research are in the computer simulations of powder flow and balls' behavior in mills and material science of ceramic powder.

Atsuko Shimosaka

Atsuko Shimosaka is a lecturer of Chemical Engineering and Material Science Department of Doshisha University since 1993. Her main fields of research are in the mechanical analysis of granular behavior using computer simulations. Currently, she is an editor of Journal of The Society of Powder Technology, Japan.

Jusuke Hidaka

Prof. Jusuke Hidaka has been at Doshisha University since 1976. His major research interests lie in mechanical analysis of powder flow using computer simulation, classification and instrumentation of powder industrial processes using acoustic emission. He is the secretary of the Society of Powder Technology, Japan.

Effect of Packing Conditions of a Fine Powder on Powder Pressure in a Bin[†]

Hisato Eitoku, Mitsuaki Hirota,
Michitaka Suzuki and Toshio Oshima
*Dept, of Chem, Eng., Faculty of Eng., Himeji Inst. Technol**

Abstract

We examined the effect of packing conditions on the pressure of a fine powder in a bin. Results of experiments on filling fine powders through sieves of different mesh sizes confirmed that the powder pressure and the charge of a fine powder in a bin are influenced by packing conditions. This is because the mechanical properties of a fine powder change considerably in accordance with packing conditions, i.e., normal stress acting on the bed, state of agglomeration, packing structure, filling rate, and the like. The pressure and charge of a fine powder in a bin can be estimated by Janssen's equation using mechanical properties that depend on packing conditions.

1. Introduction

The mechanical properties of powders are basic to predicting powder behavior in actual operations, and a great deal of research has been performed on ways to measure and assess them. Nevertheless, the mechanical properties of fine powders are determined not only by the particles' own physical characteristics, but also depend greatly on packing fraction, and it is known that they are also affected by usage conditions in actual operations, such as the particles' agglomeration conditions and packing structure. Yet, there is little research that takes these effects into account while considering the relationship between fine powders' operational characteristics and powder mechanical properties.

The authors focussed on the storage of powders, which is one operation involving the handling of fine powders, and, by using as a function of packing fraction the mechanical property values obtained from compression and shear tests on fine powders, studied a method of calculating powder pressure and the powder charge in a fine powder bed on the basis of Janssen's equation[1]. In order to further investigate the effects of usage conditions on actual operations, we varied the mesh of sieves through which powders were fed to a container, thereby changing items such as the filling rate and powder agglomerating conditions. By this means we studied the effects of packing conditions on powder pressure and powder charge. We also determined the mechanical properties of a bed packed under more or less the same conditions as these various packing conditions, and these properties were used in estimating powder pressure and powder charge.

2. Sample Powders and Mechanical Property Tests

2.1 Sample Powders

Our three sample types were fly ash, silica powder, and precipitated calcium carbonate. **Table 1** shows these sample powders' 50% particle diameters (measured by laser diffraction particle size analysis microtrack FRA) and particle density. The 50% particle diameter given here is the primary particle diameter measured when samples were dispersed in liquid, while it is thought that within a bin the silica powder and precipitated calcium carbonate form agglomerates that are much larger

Table 1 50% Particle diameter and particle density of sample powders

Sample powder	50% Particle diameter $D_{50}[\mu m]$	Particle density $\rho_P[kg/m^3]$
fly ash	13.2	2320
Silica	3.2	2650
$CaCO_3$	3.6	2550

---

*2167 Shosha, Himeji-shi, 671-22, Japan

[†] This report was originally printed in J. Soc. Powder Technology, Japan. 33, 102(1996) in Japanese, before being translated into English by KONA Editiorial Committee with the permission of the editiorial committee of the Soc. Powder Technology, Japan.

than primary particles.

2.2 Mechanical Property Tests

We used varying sieve mesh sizes to loose-pack the samples, then performed compression and shear tests on powder beds whose packing states are expected to differ, and investigated how sample powder properties are affected by differences in mesh sizes when packing a bin. In our experiments sieves of three different mesh sizes for each sample were used. Sizes for silica powder and $CaCO_3$ were 500, 2000, and 3360 μm, while those for fly ash were 1190, 2000, and 3360 μm because it contains a very small proportion of primary particles larger than 500 μm.

2.2.1 Shear Testing

Fig. 1 shows the powder yield loci (PYLs) for all samples at pre-consolidation stresses σ_1 of 0.6, 1.2, and 1.8 kPa. The PYL of sample fly ash at a 1190 μm mesh was slightly lower than those at 2000 and 3360 μm, and as the graphs show, the sieve mesh has little effect. But when using large meshes (2000 and 3360 μm) for silica powder and calcium carbonate, the PYLs were quite low in comparison with the small mesh (500 μm), so the effect of mesh size is evident. This tendency becomes increasingly evident as pre-consolidation stress σ_1 and normal stress σ become smaller. It is known that in fine powders with strong adhesion, PYLs change according to the particle agglomeration state even when using the same sample[2]. The main reason is conceivably that the agglomeration state changes when changing sieve mesh*. Generally it is believed that fine powders form agglomerated particles that are much larger than their primary particles[3]. Because more large agglomerated particles are found in powder beds when using a large-mesh sieve than a small one, they will exhibit shearing properties similar to those of samples with large primary particle diameters, which lowers PYL. But as σ_1 and σ increase, large agglomerated particles are broken down during powder bed pre-consolidation or the shearing process, which lessens differences in agglomerated particle size due to the sieve mesh. This makes it harder for PYL to be affected by mesh size. We then focussed on large meshes (2000 and 3360 μm) and noted almost no PYL differences even in fine powders. Powder beds loose-packed through a 3360 μm mesh sieve likely have more agglomerated particles than when using a 2000 μm mesh, but the strength of agglomerated particles (tertiary agglomerated particles) becomes smaller as the diameter of their constituent agglomerated particles (secondary agglomerated particles) becomes larger. Thus, it would seem that when the mesh enlarges to a certain point, large agglomerated particles will be broken down during pre-consolidation even when using a sieve with a different mesh size; change in particle agglomeration state is no longer much observed, and effect on PYL is manifested only with difficulty.

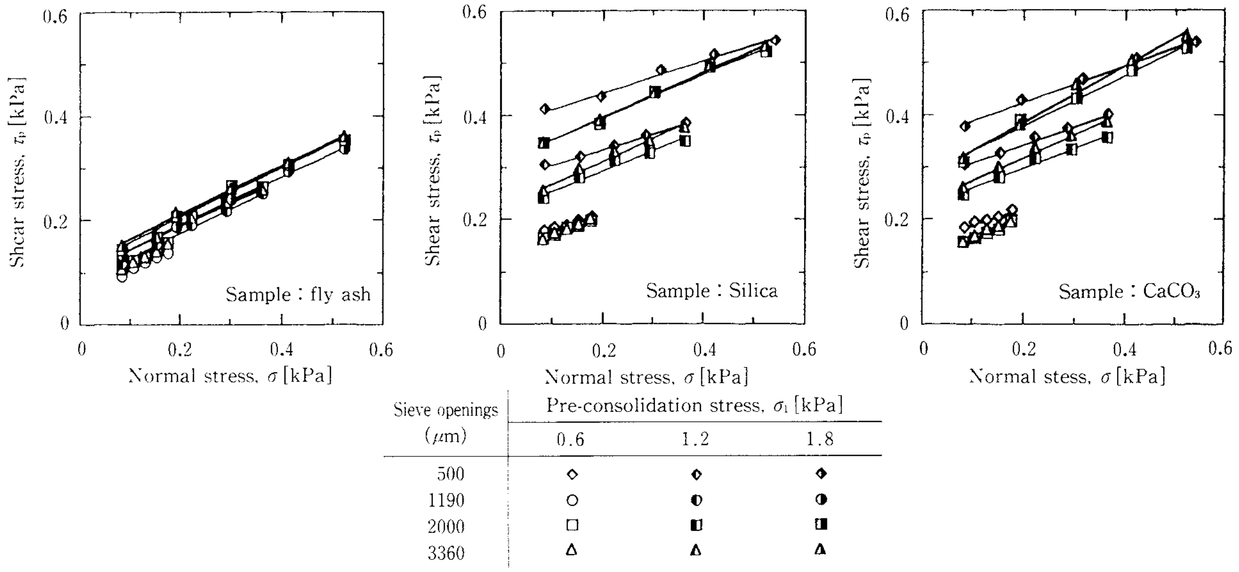

Fig. 1 PYLs of sample powders

[footnote]

* Because particle agglomeration state, packing structure, filling rate, and other items change

according to packing conditions, PYL and other mechanical properties also possibly change. As this experiment did not quantitatively assess these factors, no definite conclusions can be drawn, but research reports and empirical findings submitted thus far on adhesive fine powders suggest that changes in particle agglomeration states due to packing conditions have the greatest effect on changes in mechanical properties.

Fig. 2 shows the particle-wall yield loci (WYLs) of silica powder and precipitated calcium carbonate when sieve mesh is small and its effects were strongly manifested in PYLs. Just as with PYLs, WYLs have smaller values when mesh is larger than when it is small.

Fig. 3 shows the inter-particle critical state lines (CSLs) for all samples. As the graphs show, even if pre-consolidation stress σ_1 and sieve mesh are changed, CSL is always a straight line passing through the origin, and the inter-particle kinetic friction coefficient is not dependent on particle packing conditions. Similarly, the particle-wall kinetic friction coefficient is not dependent on sample packing conditions if the sample and wall material are the same.

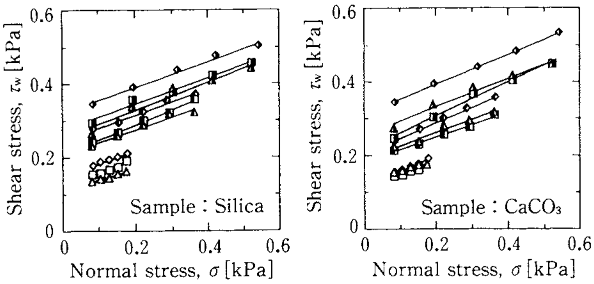

Sieve openings (μm)	Pre-consolidation stress, σ_1 [kPa]		
	0.6	1.2	1.8
500	◇	◈	⬖
2000	□	◧	◨
3360	△	◭	◮

Fig. 2 WYLs of sample powder

2.2.2 Compression Testing

Fig. 4 shows the results of compression tests on all samples. Fly ash shows less influence of sieve mesh size than the other fine powders, so the curves for all compression tests nearly coincide. This is probably because fly ash is low-adhesion and forms almost no agglomerations. On the other hand, silica powder and precipitated calcium carbonate are high-adhesion fine powders, so that when mesh size is large (2000 and 3360 μm) bulk density is considerably larger than when mesh is small (500 μm), and the initial packing fraction in particular is about 20% different (when normal stress σ is zero). When adhesive fine powders are used, differences in compression properties are especially large in powder states near loose packing; bulk density increases because large agglomerated particles are formed, and compression properties change in conjunction with that. But just as in shearing test results, the effects of mesh size nearly disappear as normal stress increases.

The foregoing demonstrates that the mechanical property values of high-adhesion fine powders change greatly in accordance with the sample packing conditions in a bin.

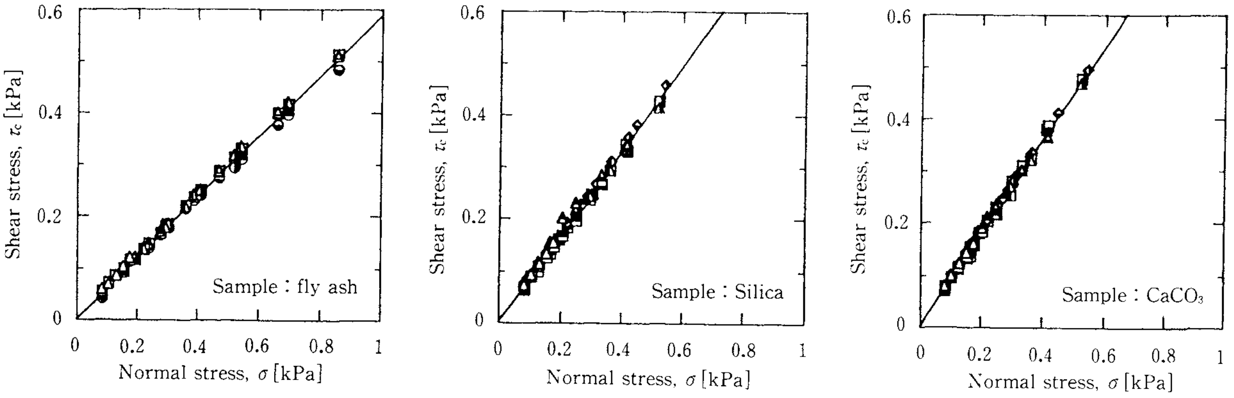

Seve openings (μm)	Pre-consolidation stress, σ_1 [kPa]						
	0.6	0.9	1.2	1.5	18	2.4	3.0
500	◇	⬘	⬖	⬙	⬗		
1190	○		◐		◑	◓	◓
2000	□	⬒	◧	⬓	◨	◫	⊟
3360	△	△	◭	△	◮	△	△

Fig. 3 CSLs of sample powders

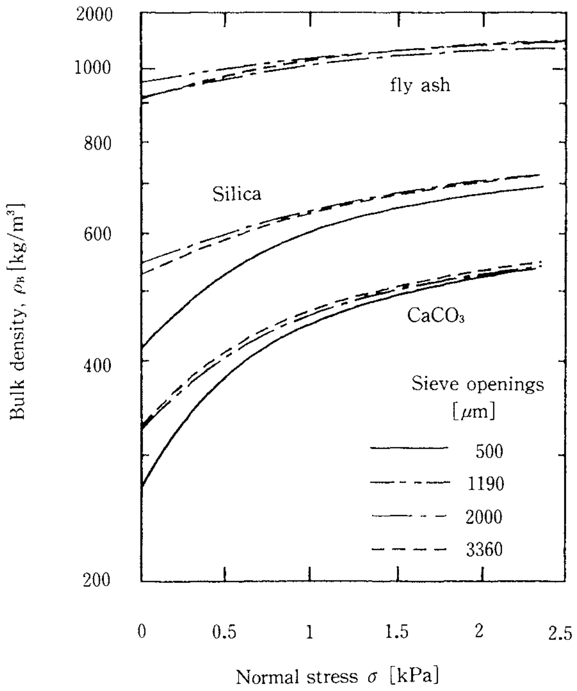

Fig. 4 Relation between bulk density and normal stress

3. Experimental Apparatus and Method

The experimental apparatus was the same as that in **Fig. 5** of our previous report[1]. A powder sample is passed through a sieve into a cylindrical container (inside diameter 0.14 m) in such a way that the powder bed surface is as level as possible. The powder bed height is changed from 0.05 m to 0.6 m in 0.05 m increments. At each of these powder bed heights we measured bottom pressure and determined the powder bed's pressure change in the vertical direction. At the same time we measured powder input mass. At this time we passed samples through different mesh sizes to vary their agglomeration states, filling rates, and other items, and investigated what effects these differences would have on powder pressure and powder charge. **Table 2** shows sample filling rates (charge per unit time) for different mesh sizes. As the table indicates, with fly ash there is an approximate 30-fold difference in the filling rate of sample into the container between the small 1190 μm mesh size and the large 3360 μm size, so it was possible to greatly vary the filling rate just by changing the mesh size of the sieve used when putting a sample into the container. However, it is likely that with fly ash there is hardly any change in the particle agglomeration state by merely changing mesh size. With silica powder and precipitated calcium carbonate, on the other hand, when using the small 500 μm mesh and the large 2000 and 3360 μm meshes, the differences in agglomeration states and other properties of the filled particles revealed differences in their respective mechanical property values as well. Additionally, between the 500 and 2000 μm meshes there was an approximate 10-fold filling rate difference, while between 500 and 3360 μm there was an approximate 40-fold difference. As mechanical property test results also show, when the 2000 and 3360 μm sieve mesh sizes are used, little difference is discerned in the mechanical property values of these adhesive fine powders when filling, but there is a large four- or five-fold differ-

Table 2 Filling rates of sample powders

Sample powder	Sieve Openings [μm]	Filling rate [kg/s]
fly ash	1190	1.3×10^{-3}
	2000	1.7×10^{-2}
	3360	3.7×10^{-2}
Silica	500	5.3×10^{-4}
	2000	5.4×10^{-3}
	3360	2.0×10^{-2}
$CaCO_3$	500	3.9×10^{-4}
	2000	3.8×10^{-3}
	3360	1.8×10^{-2}

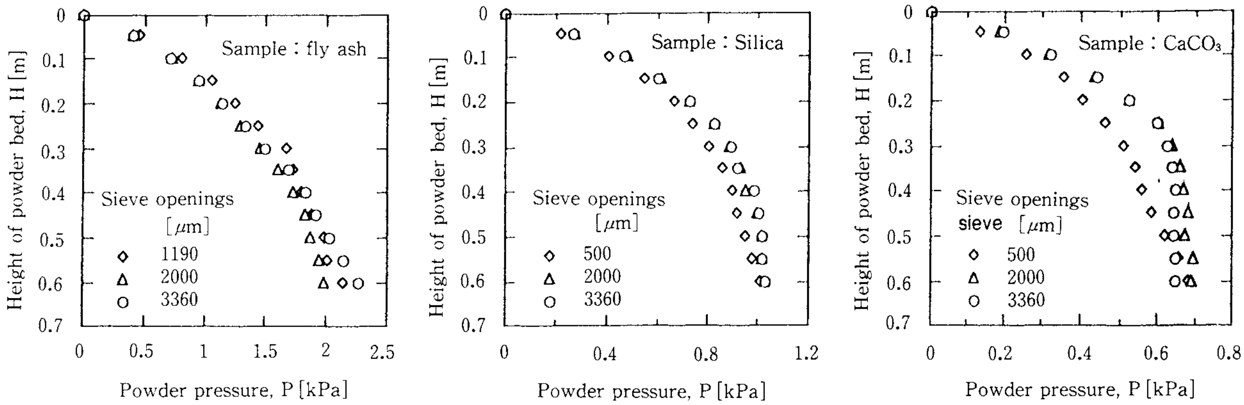

Fig. 5 Relation between height of powder bed and powder pressure

ence in the filling rate.

4. Experiment Results and Discussion

Fig. 5 shows the effect of sieve mesh size on vertical pressure change in a powder bed. When mesh size for fly ash is 1190 μm and powder bed height is low, powder pressure is slightly larger than when mesh size is 2000 and 3360 μm, but packing conditions do not have a clear effect on pressure change. With silica powder and precipitated calcium carbonate, on the other hand, powder pressure tended to become higher at the large mesh sizes (2000 and 3360 μm). As the results of mechanical property tests show, when adhesive fine powders are filled through large-mesh sieves, apparent fluidity is greater than with small mesh sizes. Thus powder bed bulk density is greater, and powder pressure is higher. And when mesh size is 2000 and 3360 μm, there is an approximate four- to five-fold difference in the rate at which the sample is put into the container, but powder pressure change is almost equal no matter which sieve is used. This suggests that changes in powder mechanical properties occurring because of changes in things such as the particle agglomeration state have a greater effect on powder pressure than the filling rate.

With all samples we noted a tendency in which, as bed height rises, bottom pressure gradually approaches a certain value instead of being dependent on packing conditions.

Let us now consider the calculation of powder pressure and powder charge using Janssen's equation. As explained in our previous report[1], because the mechanical property values of fine powders are largely dependent on pressure, they cannot be treated as unchanging in a bin. In our calculations, therefore, we used as a function of pressure the mechanical property values obtained only from fine powder compression and shear tests. And because powder in the bin bottom is compacted by that at the top, there are likely two regions in the bin : one of static balance, and one of dynamic balance. So when postulating not only the plastic equilibrium state, but also the steady state, we calculated powder pressure and powder charge while taking into account changes in mechanical property value due to each state in the bin's vertical direction.

Table 3 compares measured and calculated values for bin bottom pressure and powder charge with a powder bed height of 0.6 m. As seen in **Fig. 5** as well, powder pressure in all samples when bed height is 0.6 m tends to be affected little by packing conditions. On the other hand, the charges of fine powders of silica and precipitated calcium carbonate increase considerably with large mesh sizes (2000 and 3360 μm), suggesting the strong influence of changes in powder mechanical properties caused by mesh size difference. Comparing these measured values with those calculated shows that, even if sample packing conditions change, the powder pressures of fine powders of silica and precipitated calcium carbonate can be estimated within their calculated ranges when the plastic equilibrium state and the steady state have been postulated. Meanwhile, the calculated values for fly ash powder pressure were slightly larger than those measured. The reason is not clear, but it is perhaps because fly ash is more fluid and has higher flashing than the other samples, which influence the results. In all samples, measured values for powder charge could be estimated within the calculated range without

Table 3 Powder pressure and charge of sample powders

Sample	Sieve openings [μm]	Powder pressure [kPa]			Charge [kg]		
		Experimental data	Theoretical value		Experimental data	Theoretical value	
			Plastic equlibrium static	Steady state		Plastic equlibrium static	Steady state
fly ash	1190	2.13	2.48	2.61	9.60	9.69	9.73
	2000	1.99	2.34	2.66	9.98	9.60	9.64
	3360	2.25	2.43	2.63	9.96	9.75	9.80
Silica	500	1.00	0.59	1.32	4.80	4.74	5.26
	2000	1.03	0.82	1.43	5.65	5.64	5.88
	3360	1.03	0.92	1.41	5.64	5.57	5.81
$CaCO_3$	500	0.68	0.52	0.98	3.34	3.27	3.61
	2000	0.70	0.54	1.20	3.92	3.58	3.93
	3360	0.65	0.57	1.11	3.90	3.67	3.96

depending on packing conditions.

5. Conclusion

We investigated the effects on the powder pressure and powder charge of a fine powder bed in a bin brought about by changes in particle packing conditions (filling rate, powder agglomeration state, etc.). Differences in powder pressure caused by packing conditions were noted when the bed height is low, but when bed height rises to a certain extent it becomes hard to discern differences in powder pressure due to packing conditions. On the other hand, we confirmed that the powder charge varies substantially depending on packing conditions. However, we found that for all samples it is possible to estimate powder pressure and charge if one uses powder mechanical properties that have been measured while taking into account the packing conditions when a sample was put into the container.

Acknowledgment

We would like to thank Mr. Shinsuke Yamada and Mr. Yoshikazu Iwata for their cooperation in performing this experiment.

Nomenclature

D_{50} : 50% particle diameter (μm)
H : height of powder bed (m)
P : powder pressure (kPa)
ρ_P : particle density (kg/m^3)
ρ_B : bulk density (kg/m^3)
σ : normal stmess (kPa)
σ_1 : pre-consolidation stmess (kPa)
τ_C : particle-particle shear stress at steady state (kPa)
τ_P : particle-particle shear stress at plastic equilibrium state (kPa)
τ_W : particle-wall shear stress at plastic equilibrium state (kPa)

References

1) Eitoku, H., M. Hirota, M. Suzuki, T. Oshima : *J. Soc. Powder Technol., Japan*, 31, 652 (1994)
2) Hirota, M., Y. Iwamoto, T. Kobayashi, T. Oshima : *J. Soc. Powder Technol., Japan*, 21, 69 (1984)
3) Tsubaki, J., K. Kato, J. Jimbo : *J. Soc. Powder Technol., Japan*, 18, 873 (1981)

Author's short biography

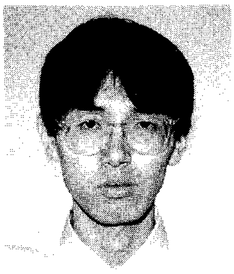

Hisato Eitoku

Hisato Eitoku received his BE (1991) and MS degree (1993) from Chemical Engineering Department of Himeji Institute of Technology. He received his Doctor's degree in 1996 from the same University for the work on the mechanical properties of powder and its applications for powder technology. After graduating, he works for Hosokawa Micron Corp., Japan as aresearch staff. The main subject of his recent research is the powder composite processing with Mechanofusion system.

Toshio Oshima

Toshio Oshima is Emeritus Professor of Himeji Institute of Technology.His major research interests are mechanical properties of powder and its application for powder technology. He retired in 1996 from Professor of Himeji Institute of Technology.

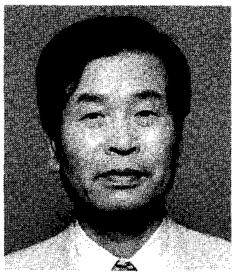

Mitsuaki Hirota

Mitsuaki Hirota is Professor of Chemical Engineering Department of Himeji Institute of Technology since 1996. His major research interests are mechanical properties of powders, pneumatic transport of powders, and pressure distribution of powders in bins.

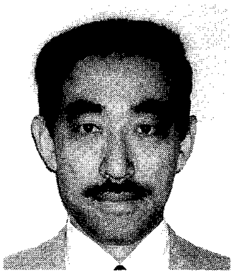

Michitaka Suzuki

Dr. Michitaka Suzuki is Associate Professor of Chemical Engineering Department of Himeji Institute of Technology since 1996. His major research interests are particle packing structure, utilization of Fractal dimension on powder technology, and the effect of particle surface condition on powder mechanical properties.

The Formation of Ultrafine Particles of Metal Sulfide by the Electrostatic Spray Pyrolysis Method[†]

Kikuo Okuyama, I. Wuled Lenggoro
and Norikazu Tagami
Department of Chemical Engineering,
*Hiroshima University**
Shinkichi Tamaki
Department of Industrial Engineering,
*Kinki University***
Noboru Tohge
Department of Metallurgical Engineering,
*Kinki University***

Abstract

In the preparation of fine particles of metal sulfide such as zinc sulfide and cadmium sulfide using the spray pyrolysis method, the electrostatic spray method was applied to atomize the starting solutions. The optimum operation conditions where the droplets could be generated from a Taylor cone were examined experimentally. It was shown that the use of the electrostatic spray pyrolysis method is available for preparing the several dozens nanometer-sized fine particles, in comparison with a typical ultrasonic spray pyrolysis method that produced the several hundreds nanometer size.

1. Introduction

Functional fine particles were used as raw materials of ceramics, pigment, electronics, magnetic, fluorescence materials. It is important to control their size, distributions, composition/chemistry, and morphology of the prepared fine particles. Among the production methods of particles, spray pyrolysis has been widely used to prepare continuously spherical, high purity, chemistry-controlled products at relatively high production rate. Using this method, the authors have recently prepared several metal oxide and composites particles[1-5].

Generally, in spray pyrolysis technique, aqueous solutions of metal salts were used as starting solutions to be sprayed to droplets by mechanical atomizations. The droplets thus generated would be introduced to heated furnace and then pyrolyzed to product the solid particles as the final products. Usually, some typical atomizers such as the ultrasonic or the twin-fluid flow nozzles used in spray pyrolysis method can generate droplets with 4-5 μm in average, as the lower limits. As the results, the prepared particles have their average sizes in submicron order, 0.1 to 1.0 μm, and it is difficult to prepare the ultrafine particles below 0.1 μm. By keeping the composition and the spherical shape of the prepared particles, there are two ways to reduce the particle sizes. First, by decreasing the concentration of the starting solutions and another way is by using an atomizer method that can generate finer droplets down to submicron order. The electrostatic sprays have been reported as the method that can generate finer droplets. By controlling the properties of the liquids, the droplet diameter could be attained down to 1 micron or submicron. The applications of electrospray method as an atomizer in spray pyrolysis process to produce some functional particles such as SnO_2 or Y_2O_3 have been reported[6,7].

In this study, the availability of the electrospray pyrolysis, on the preparation of fine particles of zinc sulfide, ZnS and cadmium sulfide, CdS are firstly presented. First, the relation of the experimental parameters and the optimum production rate, i.e., the number concentration of generated droplets of the device is investigated. The composition, size,

---

* 1-4-1, Kagamiyama, Higashi-Hiroshima 739 Japan.

**3-4-1 Kowakae, Higashi-Osaka 577 Japan.

[†] This report was originally printed in J. Soc. Powder Technology, Japan. 33, 192 (1996) in Japanese, before being translated into English with the permission of the editiorial committee of the Soc. Powder Technology, Japan.

and morphology of prepared metal sulfide particles are compared to those prepared by an ultrasonic spray pyrolysis, previously[9,10]. Both CdS and ZnS, the materials prepared in this study are mainly used as fluorescence materials, which are able to emit the fluorescence by the excitements of some sources such as electrons or X-rays. For example, by doping ZnS fine particle with Ag, the blue color emitting can be generated and the image display in Braun tube is one of its application. In fact, in the practical use of that fluorescence materials, several microns or somewhat larger particles were used, so it is interested in preparing finer metal sulfide particles.

2. The principle of electrospray

Electrospray phenomenon has been described in the beginning of this century, and there were considerable studies and reports on it, including their various applications such as spraying methods for liquid painting, ink-jet printer, and mostly in mass spectrometry areas. The principle of the droplet formation using the electrospray technique is shown in **Figure 1**. **Figure 1(a)** shows a metal nozzle serving both as a liquid supplier and an electrode where D.C. high voltage was applied, and a metal plate used as a grounded electrode. At the nozzle tip, a liquid meniscus was charged by electrostatic forces, and with a balance of surface tension or gravity, the meniscus is formed to a liquid cone. The expression "Taylor cone" is often used for the cone, since Taylor[11] has reported for the first time an analytical study on the formation of liquid cone. When the electrostatic force exceeds the liquid surface tension, the cone apex will be exerted to a liquid jet, and due to its instability, the droplets are generated by the breakup of the jet.

In this study, at first the experimental conditions such as applied voltages, liquid flow rates and solution concentrations where the stable Taylor cones can form, are investigated. Then the preparation of fine metal sulfide particles by using the device, is presented.

3. Experimental system and procedure

As starting solutions, ethanol was chosen as a solvent to dissolve the solutes containing the low cost cadmium nitrate $Cd(NO_3)_2$, or zinc nitrate $Zn(NO_3)_2$, with thiourea $(NH_2)_2SC$, as the sources of Cd, Zn and S, respectively in room temperature. In the solutions, thiourea complexes are formed, and the droplets containing these complexes can be thermally decomposed to form CdS or ZnS particles.

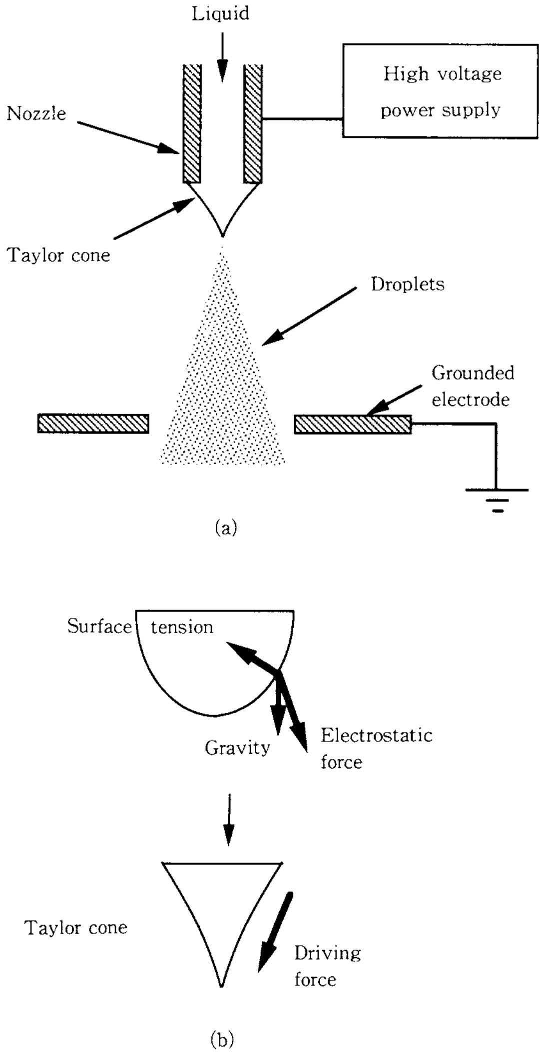

Fig. 1 Schematic of the droplet formation by electrospray atomization

$$Cd(NO_3)_2+(NH_2)_2SC \rightarrow Cd[SC(NH_2)_2]_2(NO_3)_2 \rightarrow CdS \quad (1)$$

$$Zn(NO_3)_2+(NH_2)_2SC \rightarrow Zn[SC(NH_2)_2]_2(NO_3)_2 \rightarrow ZnS \quad (2)$$

The use of solutions containing thiourea complexes also have been already reported to prepare metal sulfide films by the dip-coating and other processes [12-15]. In this study, the molar ratio of cadmium nitrate or zinc nitrate to thiourea was kept at 1:2, respectively[16].

The electrospray pyrolysis system used for the preparation of ZnS and CdS fine particles is schematically shown in **Figure 2**. The system is consisted of i) an atomizer, which generates the droplets from the solutions, ii) a reaction furnace, where the solution droplets decompose to form fine particles, and iii) a diffusion charging-type electrostatic

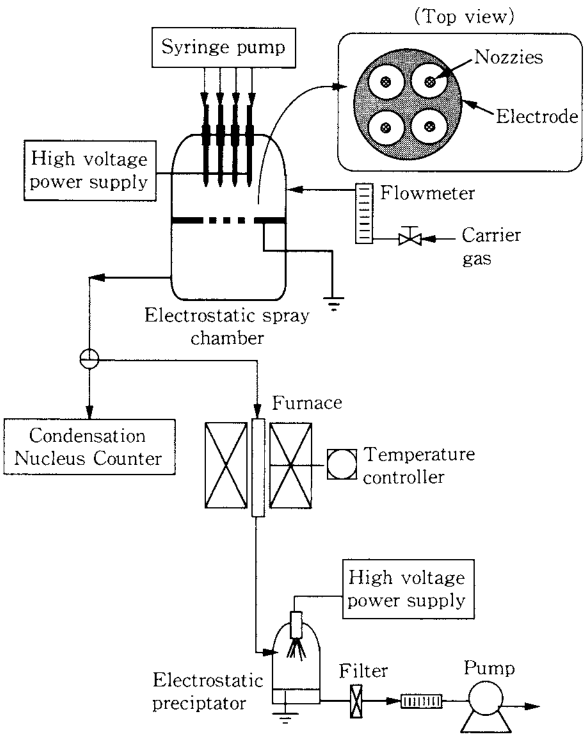

Fig. 2 The experimental system of the electrostatic spray pyrolysis, with details of the 4 nozzles position

precipitator.

The electrospray system was consisted of brass nozzles which have outer and inner diameter of 10 and 1 mm and a porous disk type brass plate used as a grounded electrode. Their distance was kept constant at 15 mm. In a complete set, four nozzles were set to configure a square with each side length is 45 mm. The tubular furnace used in the present study was a quartz glass tube of 15 mm-inner diameter and about 100 mm-length. The starting solution was supplied, by syringe pump (Harvard Apparatus, Model 55) that allows a constant liquid flow rate, to metal nozzles where the potential difference is applied between that and the metal plate. The generated droplets were carried to the reaction furnace by an inactive N_2 gas, at the flow rate of 2. 0 l/min. After passing some phenomena occurred inside the droplet, such as the evaporation of ethanol and thermal decomposition, the solid metal sulfide particles are formed. The particles generated from the furnace outlet are collected using an electrostatic precipitator. The composition, size and morphology of particles are examined by X-ray diffraction, transmission and scanning electron microscopy (TEM and SEM), respectively. A Condensation Nucleus Counter, CNC (TSI, model 3020) was also placed at the furnace outlet to count the number concentration of generated droplets or particles in aerosol state.

4. Result and discussion

4.1 Effects of operating conditions on droplet generation

First, the influences of the experimental parameters on the number concentration of generated droplets or particles were investigated, mainly by spraying ZnS-preparation solution (zinc nitrate, thiourea and ethanol) by using one to four nozzles. **Figure 3** shows that the particle number concentrations increase with increasing applied voltages at one and four nozzles. The liquid flow rate supplied to each nozzle was 10 ml/h and the solution concentration was fixed to be 0.05mol/l. The experimental values were averaged since there were some fluctuations in the counting of the CNC. Especially in the range between 6 and 7 kV, the particle number concentrations increase drastically because the liquid meniscus began to form a Taylor cone at near 7 kV. The Taylor cone cannot be formed in the voltage less than 6 kV. The number concentration increases gradually at the applied voltage greater than 7 kV. At the voltage greater than 9 kV, some spark discharges are frequently observed and the particle number concentration increases to the value out of the measurable range of the CNC ($>10^7$ particles/cm^3).

Figure 4 shows the changes in particle number concentrations when the supplied solution flow rate was varied at a constant applied voltage (8 kV) and at single or four nozzles cases. Both cases show a slight increase in particle number concentration as flow rate was increased. In single nozzle case, when

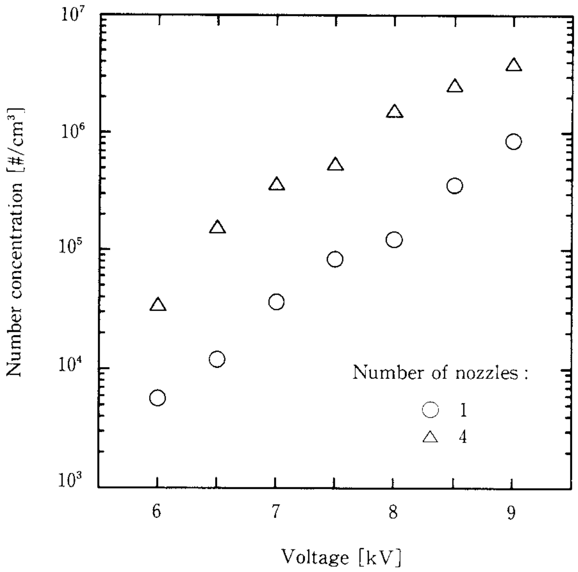

Fig. 3 Influence of voltage on droplet number concentration. (Solution concentration is 0.05 mol/l, flow rate is 10 ml/h)

flow rate was changed from 5 to 10 ml/h, the number concentration increases about two times, but not as the change from 10 to 20 ml/h where the number concentration is only increased slightly. This is due to the requirement of the liquid at the amount of flow rate to form a stable Taylor cone at an arbitrary applied voltage. In the experimental conditions of **Figure 4**, the stable Taylor cones were formed at flow rate less than 10 ml/hr, and at higher value, of 20 ml/h, the unstable cones were formed and that cone apex or the jet was skewed towards impermanent directions. This behavior enhanced the deposition of the droplets onto the chamber walls, and as a result it made a slight increase in particle number concentrations and decreased the throughput efficiency of the spray chamber. In the other words, it is necessary to use the other electrode configurations to form a stable Taylor cone at higher liquid flow rates.

The change of the particle number concentrations is shown in **Figure 5** when the solute concentrations of spray liquid were varied at four nozzles case. Generally, the particle number concentration increases with increasing solution concentrations, but it is almost constant above 0.01 mol/l. The droplet number concentrations of ethanol or 0.005 mol/l solution are two order smaller compared to the highest value. It was easier to form and control the stable liquid cones at lower solution concentration. At higher solution concentrations, the formation of unstable liquid cones were frequently observed. A further investigation is necessary, since the concentration changes of the solutions also will change the liquid physical properties, such as electrical conductivity, permitivity, viscosity and surface tension, which have been considered as the main parameters in the electrosprays[17].

Table 1 shows the influence of the number of nozzles on particle number concentrations, at applied voltage of 8 kV and liquids flow rate of 10 ml/h were supplied to each nozzle. Changes of 1 to 2 or 2 to 4 nozzles increased the number concentrations about twice, but there are only a slight increase from 2 to 3 nozzles, not a linear relation. The asymmetrical configuration of 3 nozzles makes a different electrical field than the others, and this may be influence the stability of the Taylor cones.

Table 1 Influence of the number of nozzles on droplet number concentration. (Solution flow rate is 10 ml/h, solution concentration is 0.05 mol/l, voltage is 8 kV)

Number of nozzles	Droplet number concentrations [#/cm³]
1	6.20×10^5
2	1.20×10^6
3	2.25×10^6
4	2.50×10^6

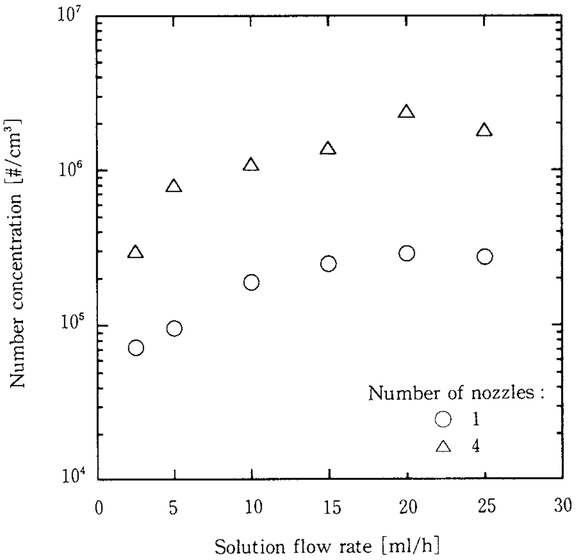

Fig. 4 Influence of solution flow rate on droplet number concentration. (Voltage is 8 kV, solution concentration is 0.05 mol/l)

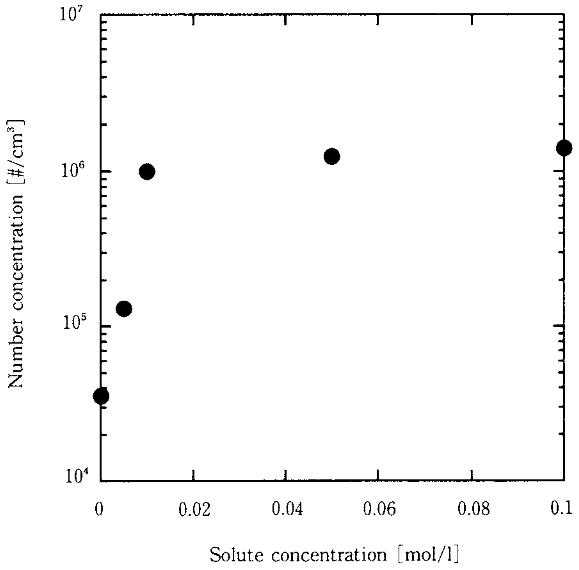

Fig. 5 Influence of solution concentration on droplet number concentration. (Flow rate is 10 ml/h,voltage is 8 kV, 4 nozzles)

It should be noted that in this study the droplets size was not measured directly, but only the changes of the droplet number concentrations are investigated. The droplet sizes are predicted from the SEM or TEM photographs of prepared particles and by using the calculation described later.

After considering some experimental conditions, the fine particles of CdS and ZnS were prepared and sampled. The experimental condition which could generate the highest droplet number concentration, i.e., the highest production rate, was used as a basis condition and it was four nozzles, 8 kV applied voltage, 10 ml/h liquid flow rate per nozzle.

4.2 Experimental results

The concentrations of CdS-preparation solutions were changed 3 runs ; 0.001, 0.005, 0.01mol/l, and those of ZnS were 6 runs ; 0.005, 0.01, 0.03, 0.05, 0.07, 0.1mol/l, respectively. Their characteristics were investigated with the furnace temperatures at 500°C and N_2 carrier gas of 2.0 l/min.

Figure 6 shows X-ray diffraction patterns of CdS particles. This result verifies the availability of the electrospray pyrolysis as a method to prepare the fine metal sulfide particles. Comparing to the particles prepared by an ultrasonic spray pyrolysis, electrospray pyrolysed particles have broader diffraction peaks. One reason might be that the decreasing crystalline size of those ultrafine particles, as mentioned later, makes the diffraction waves interference weaken, not due to the poor crystallization during the process.

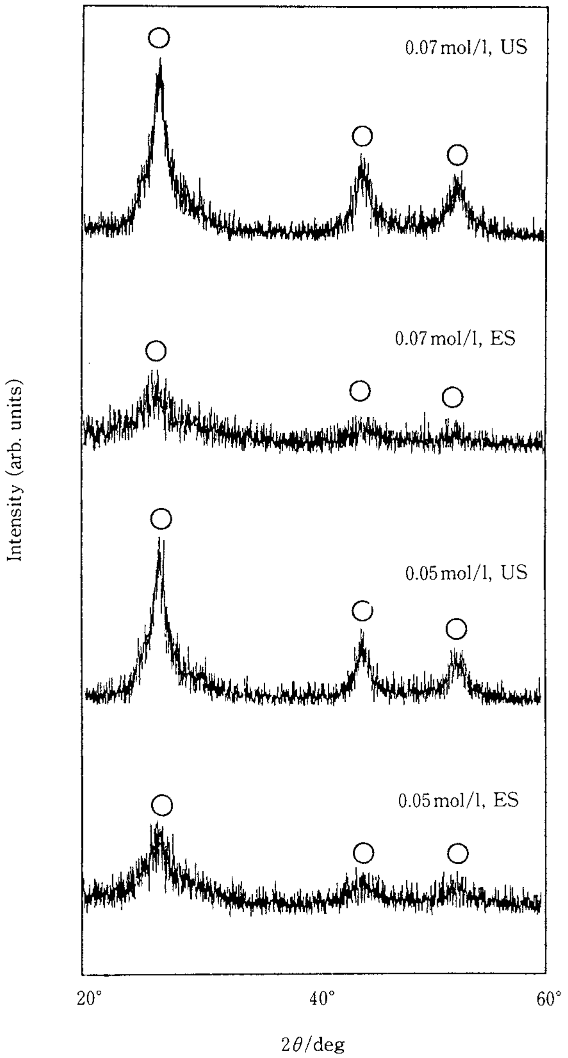

Fig. 6 X-ray diffraction patterns of CdS particles prepared at different solution concentrations, using ultrasonic (US) and electrostatic (ES) spray pyrolysis, respectively. (Symbol O represents the hexagonal CdS phase)

SEM photographs of CdS are shown in **Figure 7**. CdS is aggregate particles having rough surface, which were constructed from nanometer sized primary particles. The aggregate particles prepared by electrospray pyrolysis are finer than those by ultrasonic spray pyrolysis. It is interesting to study further on the size of their primary particles, since the size of electrospray pyrolysed primary particles seems to be larger than those of ultrasonic spray pyrolysis.

Figure 8 shows TEM photographs of CdS, which also verify the previous results. About 200 particles were picked up randomly from **Figure** 8 to evaluate the mean volume diameter of the particles. The results are shown in **Table 2**. As also mentioned in

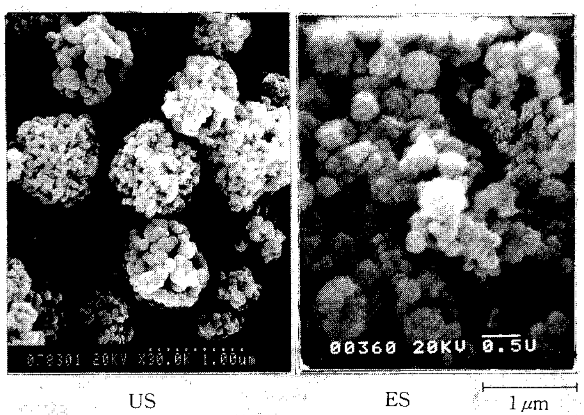

Fig. 7 SEM micrograph of CdS particles prepared by ultrasonic (US) and electrostatic (ES) spray pyrolysis, respectively. (Solution concentration is 0.05 mol/l)

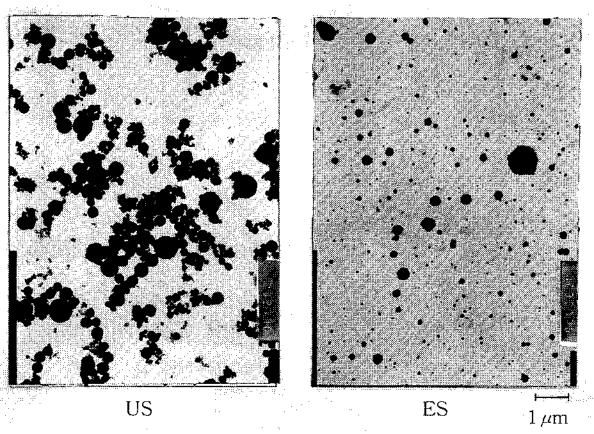

Fig. 8 TEM micrograph of CdS particles prepared by ultrasonic (US) and electrostatic (ES) spray pyrolysis, respectively. (Solution concentration is 0.01 mol/l)

the previous results, electrospray pyrolysis prepares finer particles than ultrasonic spray pyrolysis method. From these results, the availability of this method to generate the ultrafine particles below 0.1 μm could be confirmed.

Table 2 Relation between the solution concentrations and the mean volume diameter of CdS particles prepared by ultrasonic (US) and electrostatic (ES) spray pyrolysis, respectively.

Solution concentration [mol/l]	Mean volume diameter [μm]	
	Ultrasonic	Electrostatic
0.001	–	0.056
0.005	0.309	0.058
0.010	0.352	0.090

X-ray diffraction patterns of ZnS particles are shown in **Figure 9** with peaks of the cubic ZnS phase. Comparing with particles prepared by ultrasonic spray pyrolysis, electrostatic spray pyrolysed particles show broader diffraction peaks. These are similar to CdS case and due to the same reason as its case.

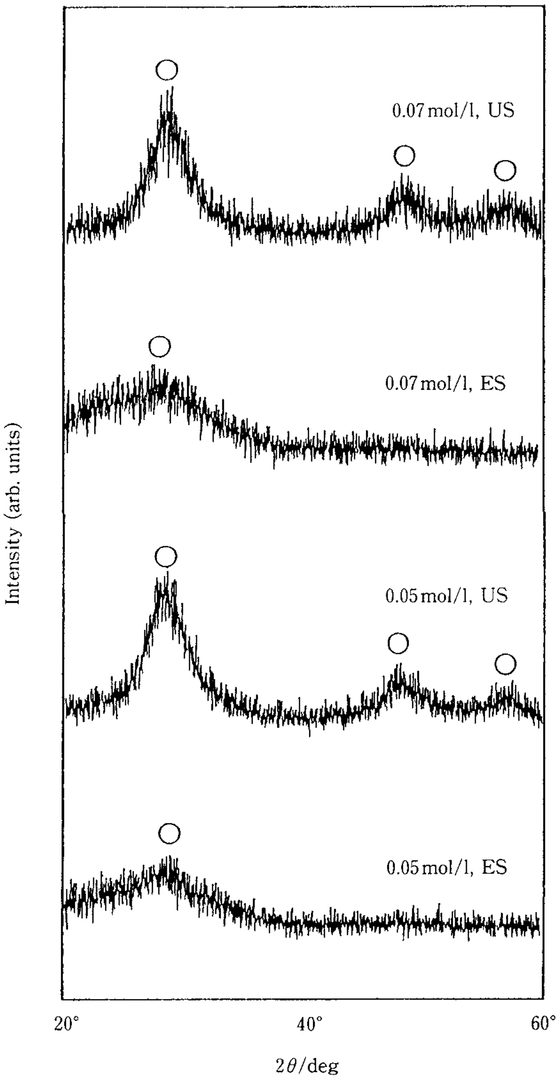

Fig. 9 X-ray diffraction patterns of ZnS particles prepared at different solution concentrations, using ultrasonic (US) and electrostatic (ES) spray pyrolysis, respectively. (Symbol O represents the cubic ZnS phase)

Figure 10 shows TEM photographs of ZnS particles prepared by those two methods. Although there is a broad size distribution, these pictures also verify that electrospray pyrolysis method generates finer ZnS particles than ultrasonic spray pyrolysis. **Figure 11** shows the relation between the solution concentrations and the mean volume diameter of ZnS particles, and also supports the previous tendencies.

It is necessary to predict the droplet diameter generated during the process. In spray pyrolysis,

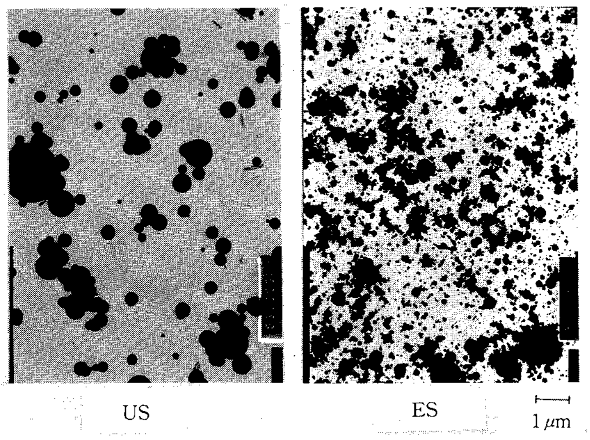

Fig. 10 TEM micrograph of ZnS particles prepared by ultrasonic (US) and electrostatic (ES) spray pyrolysis, respectively. (Solution concentration is 0.05 mol/l)

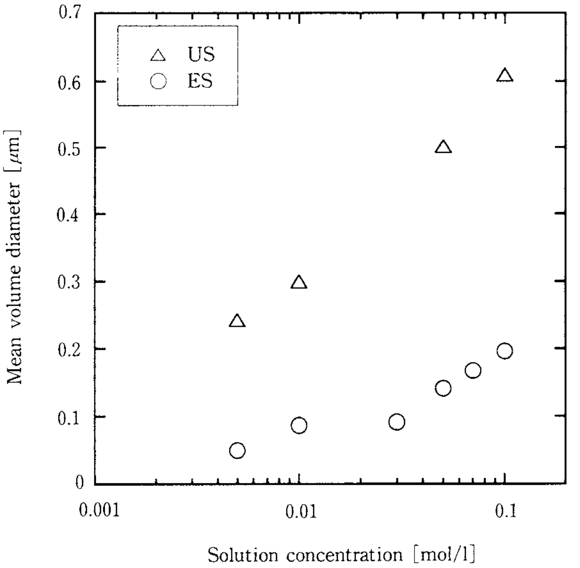

Fig. 11 Relation between the solution concentrations and the mean volume diameter of ZnS particles prepared by ultrasonic (US) and electrostatic (ES) spray pyrolysis, respectively.

one sprayed droplet is assumed to change into one dense spherical particle inside the reaction furnace. The following equation can be derived from the relation between one droplet (concentration of the solution, C_s ; volume mean diameter, D_d ; molecular weight, M) and one dense particle (final volume mean diameter, D_p ; theoretical density, ρ_p).

$$D_p = D_d (MC_s/\rho_p)^{1/3} \tag{3}$$

By using Eq. (3), the droplet diameters can be predicted from the generated particle diameters. The prediction results indicate that generation of the droplets with volume mean diameters of 0.8-0.95 μm range are possible.

This study also shows that electrospray pyrolysis can generate particles of about 10 nm. By further adjusting the experimental conditions, it is hoped that relatively large amount of ultrafine particle in this smaller class will be produced practically.

5. Conclusion

On the preparation of metal sulfide fine particles at the same solution concentration the electrospray pyrolysis technique could produce particles smaller by one order of magnitude as compared to ultrasonic spray pyrolysis. Without lowering the solution concentrations, the electrospray could exceed the lower limit of the generation of 0.1 μm fine particles on the spray pyrolysis process. While it was difficult to prepare the particles at that range by the typical (atomizer) spray pyrolysis methods, even the concentration of the starting solution was reduced. It is required further studies to facilitate the effective control of multiple parameters of the electrospray system including the liquid physical properties, as well as their relation to the generated particle sizes.

Acknowledgement

The support of the Ministry of Education, Culture and Science of Japan (Grant No. 08650893), the Hosokawa Powder Technology Foundation and the Electric Technology Research Foundation of Chugoku, is gratefully acknowledged.

Nomenclature

C_s : solute concentration in starting solution (mol/l)
D_d : droplet diameter (m)
D_p : particle diameter (m)
M : molecular weight of particle (-)
ρ_p : density of particle (kg/m^3)

References

1) Tohge, N., M. Tatsumisago, T. Minami, K. Okuyama, M. Adachi and K. Kousaka, Jpn. J. Appl. Phys., 27, L1086 (1988)
2) Tohge, N., M. Tatsumisago, T. Minami, K. Okuyama, K. Arai and K. Kousaka, Jpn. J. Appl. Phys., 28, L1175 (1989)
3) Ohshima, K., K. Tsuto, K. Okuyama and N. Tohge, Kagaku Kogaku Ronbunshu, 18, 288 (1992)
4) Ohshima, K., K. Tsuto, K. Okuyama and N. Tohge, Aerosol Sci. Technol., 19, 168 (1993)
5) Okuyama, K., T. Seto, M. Shimada and N. Tohge, J. Mater. Sci. Mater. Elec., 5, 210 (1994)
6) Rulison, A.J. and R.C. Flagan, J. Amer. Ceram. Soc., 77, 3244 (1994)
7) Vercoulen, P.H.W., D.M.A. Camelot, J.C.M. Marijnissen, S. Pratsinis and B. Scarlett, Proc. Int. Workshop on the Synthesis of Measurements of Ultrafine Particles (J.C. M. Marijnissen and S. Pratsinis Eds.), Delft, 71 (1992)
8) Tohge, N., S. Tamaki and K. Okuyama, Jpn. J. Appl. Phys., 35, L207 (1995)
9) Tamaki, S., N. Tohge and K. Okuyama, J. Mater. Sci. Lett., 14, 1388 (1995)
10) Meesters, G.M.H., P.H.W. Vercoulen, J.C.M.Marijnissen and B. Scarlett, J. Aerosol Sci., 23, 37 (1992)
11) Taylor, G.I., Proc. Roy. Soc. London, A280, 383 (1964)
12) Feigelson, R.S., A. N'Diaye, S.-Y. Yin and R.H. Bube, J. Appl. Phys., 48, 3162 (1977)
13) Rajaram, P., R. Thangaraj, A.K. Sharma, A. Raza and O. P. Agnihotri, Thin Solid Films, 100, 111 (1983)
14) Richards, D., A.M. El-Korashy, R.J. Stirn and P.C. Karulkar, J. Vac. Sci. Technol., A2, 332 (1984)
15) Krunks, M., E. Mellikov and E. Sork, Thin Solid Films, 145, 105 (1986)
16) Tohge, N. and T. Minami, SPIE Proc. Sol-Gel Optics II, 1758, 587 (1992)
17) Rosell-Llompart, J. and J. Fernandes de la Mora, J. Aerosol Sci., 25, 1093 (1994)

Author's short biography

Kikuo Okuyama

Professor Kikuo Okuyama graduated from Dept. of Chemical Engineering in 1971 and from Graduate School of Chemical Engineering in 1973, of Kanazawa University. He received the Doctor degree of Engineering in 1978 from University of Osaka Prefecture. He was appointed to Research Associate in 1973, Assistant Professor in 1984 and Associate Professor in 1986, of Dept. of Chemical Enginering, University of Osaka Prefecture. He has been Professor of Dept. of Chemical Engineering, Hiroshima University, since 1990.

His research interest covers preparation of new material particles and thin films by aerosol methods, analysis of aerosol reactor, development of aerosol size analysis technique, particle contamination control in semiconductor preparation process, gas-to-particle conversion process of polluted gas.

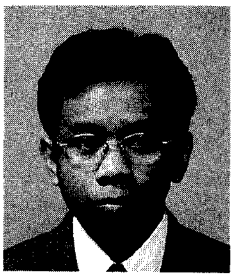

I. Wuled Lenggoro

Wuled Lenggoro studied Chemical Engineering at Hiroshima University and received master degree in 1995. Since then he is a doctorate student of Prof. Okuyama in Department of Chemical Engineering at Hiroshima University.

His current research are the preparation and characterization of fine particles in spray pyrolysis process.

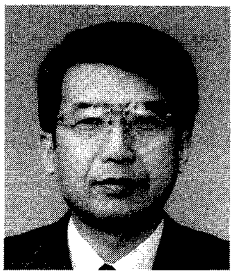

Noboru Tohge

Professor Noboru Tohge graduated from Dept. of Applied Chemistry in 1971 and from Graduate School of Electrical Engineering in 1974, of University of Osaka Prefecture. He received the Doctor degree of Engineering in 1980 from University of Osaka Prefecture. He was appointed to Research Associate in 1974, Assistant Professor in 1986 and Associate Professor in 1989, of Dept. of Applied Chemistry, University of Osaka Prefecture. He has been Professor of Dept. of Metallurgical Engineering , Kinki University, since 1993.

The main fields of his current research activity are the sol-gel processing of advanced thin films and the characterization of spray-pyrolyzed fine-particles.

Characteristic Shearing Curves of a Powder Bed Measured with a Rotary Intrusion Rheometer†

Munetake Satoh, Tomohiro Iwasaki and Kei Miyanami
*Dept. of Chem. Eng., Osaka Pref. Univ.**

Abstract

A rotary intrusion rheometer with a conical rotor was improved to detect the intruding stress as well as the shearing torque at a cell bottom. The characteristic curves of shearing torque versus a rotor's depth of intrusion in a powder bed, and normal stress versus depth of intrusion were measured simultaneously under various operating conditions. Two experimental coefficients C and m were introduced to characterize the relationship between the shearing torque and the depth of intrusion. The coefficient m indicates the compressibility tendency of the powder bed during rotor intrusion. The friction property of powders is discussed based on the coefficient C measured at m = 1 (without the compressive condition).

1. Introduction

To handle powder appropriately, it is very important to understand its dynamic physical characteristics, such as flow and shear. Various methods have been proposed and actually used to clarify these characteristics. Some evaluations involve measuring the angle of repose in a rotating cylindrical vessel, while others measure the velocity of powder outflow from an orifice. A number of new approaches to such analyses have been reported recently: e.g., evaluation of powder fluidity by measuring the transfer resistance of a metal sphere in a vibrating powder bed[1], evaluating change in particle surface physical properties by measuring the frequency transfer characteristic of a vibrating power bed[2], and evaluating physical properties by measuring a powder's specific frequency absorption characteristics using an acoustic tube, thereby obtaining guidance in sound-absorbing/vibration-proof material design[3].

Until now, powder flow characteristics have been evaluated on the basis of rotor frictional resistance or mechanical stirring of a powder bed. For certain kinds of powders, a liquid viscometer has been used to measure the relation between the friction coefficient and the shear rate. Powder dynamic physical properties have been evaluated on the basis of change in torque over time, as measured with a rotary shear tester using rotors of various shapes[4]. Further development of this method made it possible to use a rotary intrusion rheometer with a conical rotor to detect slight powder physical property changes achieved through wax-coating[5].

In the present study, we improved the above-mentioned rotary intrusion rheometer[5] to make possible the simultaneous measurement of changes in the shearing torque of a powder bed and in the normal load applied to the bed bottom by rotor intrusion. Variation curves of torque and intruding load were obtained using this improved rheometer. Using the shape-determining parameters of these mechanical characteristic curves, we then investigated the stress and friction status in a powder bed to evaluate equipment characteristics and powder dynamic physical properties.

2. Experimental Apparatus and Procedure

2.1 Experimental Apparatus

Figure 1 schematically shows the experimental apparatus used to simultaneously measure the shearing torque and intruding load on a powder bed. The main body design is based on the structure of a double-cylinder type rheometer ①. A circular cone with a 60° vertical angle and 44 V-shaped grooves on its circumference is used for the powder-shearing rotor ②. A test cell ③, which is a cylindrical vessel with a 58 mm inside diameter and 95 mm in height, is fixed on the linear head ⑧ (stroke: 50 mm) via

---

*1-1 Gakuen-cho, Sakai 599 Japan TEL. 0722-52-1161

†This report was originally printed in J. Soc. Powder Technology, Japan. 33, 510 (1996) in Japanese, before being translated into English by KONA editiorial committee with the permission of the editiorial committee of the Soc. Powder Technology, Japan.

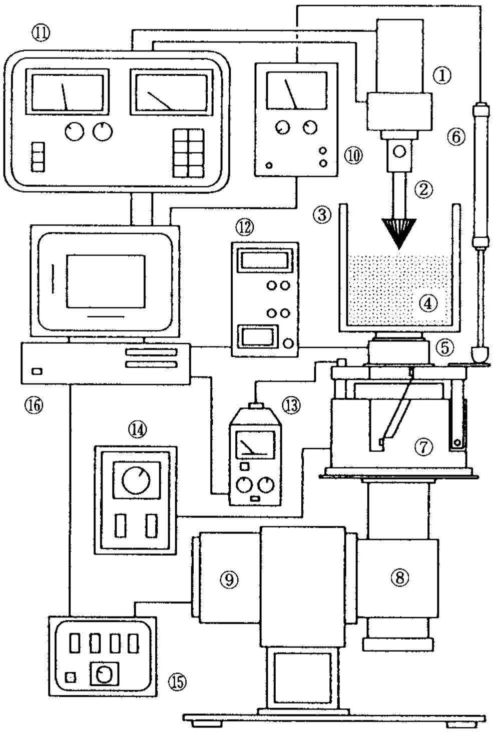

Fig. 1 Schematic diagram of the rotary intrusion rheometer for powder beds.
①Motor and torque meter, ②Conical rotor, ③Test cell, ④Powder sample, ⑤Load cell, ⑥Displacement sensor, ⑦Vibrator, ⑧Linear head, ⑨Motor, ⑩Amplifier, ⑪ Speed controller and amplifier, ⑫Amplifier, ⑬Accelerometer, ⑭Vibration controller, ⑮Speed controller, ⑯ Personal computer

a load cell ⑤ (capacity : 98 N). An electromagnetic vibrator ⑦ is provided between the load cell and the linear head to adjust the powder bed's initial packing condition by applying torsional vibration at 60 Hz in a direction 20° upward from the horizontal plane. Signal outputs of rotor rotational speed N_R, intrusion depth of rotor h, shearing torque T, and intruding load L_i are measured continuously using a personal computer ⑯ through an A/D converter.

2.2 Experiment Procedure

The test cell, filled with a specified amount of sample powder, was set on the load cell ⑤ mounted on the vibrator, which was then operated at constant acceleration (2G) for pre-packing. When powder bed height stabilized, the vibrator was stopped. As the conical rotor (30 mm in maximum diameter) was then rotated at a specified speed, the linear head was operated to raise the test cell so that the rotor intruded the powder bed. During this operation, the shearing torque, intruding load, and intrusion depth were measured simultaneously. When the intrusion depth exceeded the range within which the rotor could maintain stable rotation and torque becomes excessive, the linear head was stopped. The test cell was then immediately lowered to its original position with the rotor and vibrator still in operation. The vibrator was then stopped, and the test cell was raised again, enabling the rotor to intrude into and shear the powder bed. This series of operations was repeated until measurements for each powder sample stabilized. An average of at least five measurements was taken as shear characteristic data for each sample.

Table 1 gives the sample powders used in the experiment, and their physical property values. We used the apparatus shown in **Figure 2(a)**, Shinto Scientific Co., Ltd.'s Heidon Model 10 with modified sliding surface, to measure the sliding friction coefficient. Measurements were taken as follows: First, the sample powder was allowed to adhere to two-sided adhesion tape applied to one side of a plane weight (35×75 mm). The weight was placed gently, with the adhesion tape side down, on sample powder in a tray set on the flat board, which was then inclined gradually. This apparatus is designed so that the board automatically stops inclining at the moment the weight begins to slide. The normal stress imposed by the weight can be varied through a range from 0.76 to 1.23 kPa. At various normal stresses of the weight, sliding friction coefficient μ_s was calculated from the tangent of the maximum inclination angle $\theta_{s,max}$ of the flat board the moment it stopped inclining. The above operation was repeated 50 times, and the average of 50 measure-

Table 1 Physical properties of powders used in this work.

Powder material	Average diameter (μm)	Density (kg/m^3)			Compressibility (%)	Angle of repose* (deg)	Sliding friction coeff.** (-)
		True	Loose	Pack*			
Calcium carbonate	2.38	2600	532	805	33.9	54	0.832
Cornstarch	13.9	1475	467	757	38.3	52	0.717
PMMA MB-8	8.4	1190	500	617	19.0	55	0.619
Toyoura sand	200	2550	1590	1630	2.45	34	0.679
Zircon sand	130	4660	2700	3000	10.0	33	0.610

*Powder Tester (Hosokawa Micron Co., Ltd.) **Heidon (Shinto Scientific Co., Ltd.)

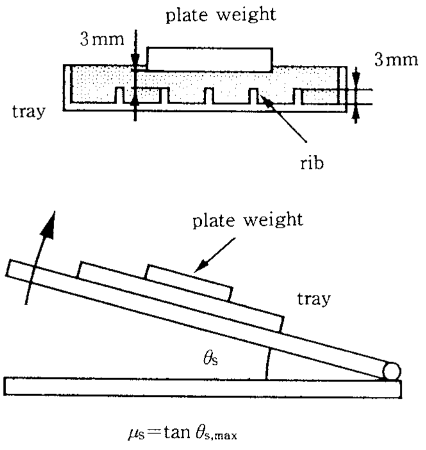

(a) Testing apparatus for sliding friction coefficient μ_s.

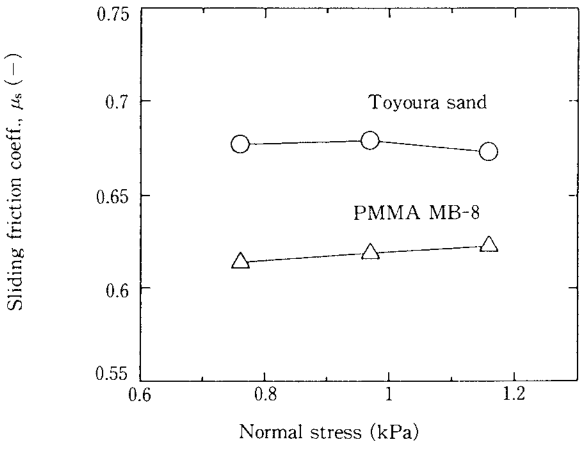

(b) Sliding friction coefficient μ_s vs. normal stress.

Fig. 2 Measurement of sliding friction coefficient μ_s.
(a) Testing apparatus for sliding friction coefficient μ_s.
(b) Sliding friction coefficient μ_s vs. normal stress.

ments was taken as the sliding friction coefficient. **Figure 2(b)** shows one of the measurement results. μ_s is virtually constant regardless of normal stress. Similar results were obtained for other samples, as shown in **Table 1**. This implies that μ_s represents one aspect of powder physical properties.

3. Results and Discussion

3.1 Torque and Intruding Load Characteristic Curves

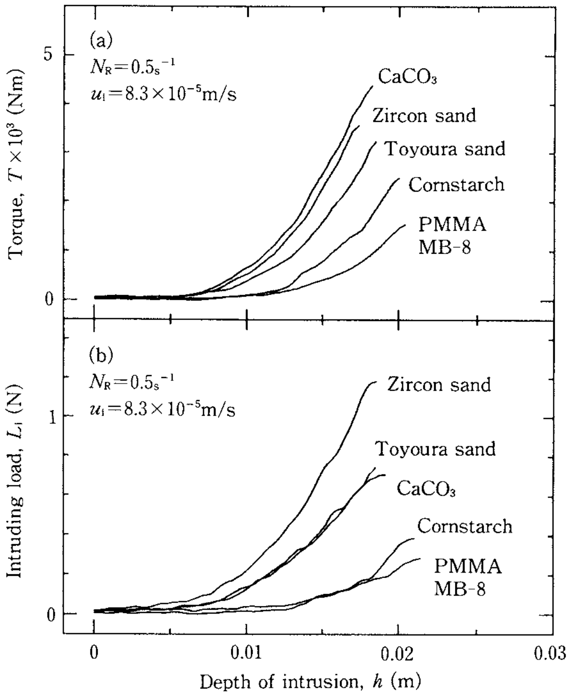

Fig. 3 Relation between torque T and intruding load L_i and depth of intrusion h for powder samples.

Torque T and intruding load L_i were measured at various rotational speeds N_R and intrusion rates u_i. **Figure 3** shows the torque and intruding load characteristic curves thus obtained. T and L_i increase with intrusion depth h, their increase rates differing according to the sample powder, owing to differences in the shear plane area increase among particles with rotor intrusion, as well as differences in the powder bed's rotor compression characteristics. In other words, differences in these characteristic curves are presumably attributable to differences in powder physical properties such as friction and packing characteristics. The following paragraphs discuss powder physical properties from this viewpoint.

3.2 Shear Characteristic

Infinitesimal area d_s on an inverted cone of vertical angle α, at arbitrary depth h in a powder bed can be expressed by the following equation:

$$ds = \frac{\tan(\alpha/2)}{\cos(\alpha/2)} h \, dh \, d\theta \qquad (1)$$

Therefore, if normal stress σ applied to a shear plane is of uniform distribution, shear torque T, required to rotate a conical rotor at an intrusion depth of h in powder bed, can be calculated by the following equation, which is obtained by integrating Equation (1) in the domains of $0 \leqq h \leqq h$ and $0 \leqq \theta \leqq 2\pi$5).

$$T = \frac{2\pi \tan^2(\alpha/2)}{3\cos(\alpha/2)} \sigma \mu h^3 \qquad (2)$$

where μ is the powder bed friction coefficient.

As indicated by Equation (2), T is proportional to the third power of h. Measured values for T and h, plotted on logarithmic graph paper, should therefore have a linear relation slope of 3. **Figure 4** shows an example of the relation between T and h, plotted on a log scale. The slope of the straight line is nearly 3, although it varies somewhat depending on measurement conditions. Normal stress σ and the friction coefficient μ can vary due to interaction among various factors, such as stress distribution changes caused by rotor intrusion, and adhesion resistance generated in the sheared powder bed. Coefficient C, containing σ and μ, was therefore introduced to define the following equation, on the assumption that T is proportional to the $3m$ power of h.

$$T = f(\alpha)\, C h^{3m} \tag{3}$$

where C is $(\mathrm{N \cdot m^{1-3m}})$, and

$$f(\alpha) = \frac{2\pi \tan^2(\alpha/2)}{3\cos(\alpha/2)} \tag{4}$$

Parameters C and m represent the degree of change in T with variation in h. If C and m are large values, T changes greatly. m indicates the degree of deviation from Equation (2). When $m=1$, Equation (3) coincides with Equation (2). C and m were obtained from the relation between T and h using the least squares method, and sample powders' dynamic characteristics were studied on the basis of the C and m values thus obtained, which change depending on measuring conditions.

Figure 5 shows changes in C and m for calcium carbonate at various rotational speeds N_R and constant intrusion rate u_l. Both C and m decrease, and m approaches unity, as N_R increases. This corresponds to the phenomenon in which, as N_R increases, powder bed friction changes from a static to a dynamic state, causing fluidization to progress, which results in lower shearing stress.

Figure 6 shows changes in C and m for calcium carbonate, at various intrusion rates u_l and constant rotational speed N_R. Both C and m increase with u_l, increasing sharply when u_l exceeds approximately 1×10^{-4} m/s. This is because at such a high u_l value, the powder bed compressive effect becomes apparent due to the imbalance between the powder scraping rate and the rotor scraped powder removal rate. By contrast, at u_l values below 1×10^{-4} m/s, i.e., in the region where rotor intrusion is semi-static, changes in C and m are relatively small, m being close to unity, due to the slight compressive effect of the powder bed.

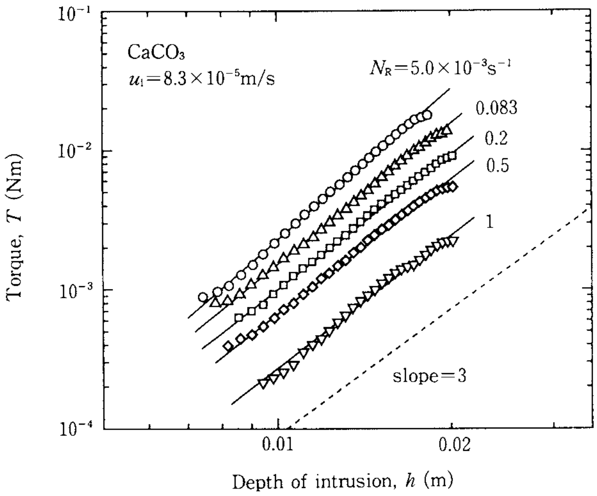

Fig. 4 Relation between torque T and depth of intrusion h for $CaCO_3$.

C and m therefore represent powder bed frictional status and degree of compression, m being the index.

3.3 Intrusion Characteristics

From Equation (1), infinitesimal force dF applied vertically to infinitesimal area d_s is given by:

$$dF = \frac{\tan(\alpha/2)}{\cos(\alpha/2)} \sigma h \, dh \, d\theta \tag{5}$$

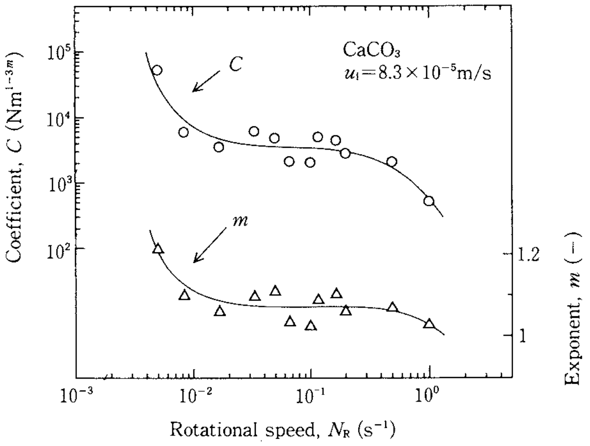

Fig. 5 Changes in C and m with the rotational speed N_R for $CaCO_3$.

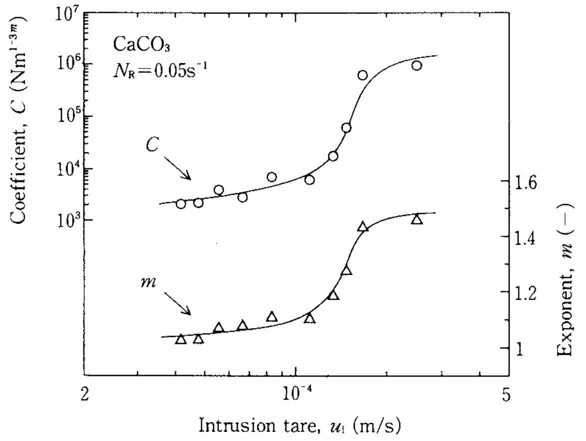

Fig. 6 Changes in C and m with the intrusion rate u_l for $CaCO_3$.

Assuming that σ is constant, vertical component F_V of the force the rotor receives from the powder bed at intrusion depth h is obtained by integrating Equation (5), as follows:

$$F_V = \pi \tan^2(\alpha/2)\,\sigma h^2 \qquad (6)$$

If F_V is equal to the intruding load of rotor L_I, the following equation holds:

$$L_I = F_V = g(\alpha)\,\sigma h^2 \qquad (7)$$

where

$$g(\alpha) = \pi \tan^2(\alpha/2) \qquad (8)$$

Therefore, σ can be obtained from the linear relation between L_I and $g(\alpha)\,h^2$. **Figure 7** shows an example of measured L_I values plotted against $g(\alpha)\,h^2$. L_I and $g(\alpha)\,h^2$ have a linear relation except when N_R is low, i.e., compressive effect is large. Slope σ of a straight line becomes lower as N_R increases, due to the change in frictional status, as mentioned previously. When N_R is low, the relation between L_I and $g(\alpha)\,h^2$ yields a descending convex curve, indicating that σ increases with h, reflecting the process in which the powder bed is compacted as the rotor intrudes. Therefore, since change in σ against h represents powder bed compressive status, σ is expressed by the following equation:

$$\sigma = kh^n \qquad (9)$$

where k and n are constants. In the following paragraphs, the relation between compression index m mentioned earlier, and n, which represents the degree of dependence of σ on h, is determined.

By substituting Equation (9) into Equation (7), the following equation is obtained:

$$L_I = kg(\alpha)\,h^{n+2} \qquad (10)$$

n is obtained by applying Equation (10) to the measured relation between L_I and h. Simultaneously, m is obtained from the measured relation between T and h. The calculated n and m data are then arranged to show the relation between them, as in **Figure** 8. n increases with m, confirming that m expresses definitely the powder bed's compressive status. n is close to 0 at $m=1$, which indicates that under the measuring conditions satisfying $m=1$, σ is constant; namely, $\sigma = k = \sigma_0$ (constant). In other words, normal stress is virtually constant on the shear plane, irrespective of rotor intrusion. This fact leads to the reasonable conclusion that, under the above-mentioned measuring conditions, the rotor can always form a new shear plane as it intrudes, without compressing the powder bed.

When rotor intrusion rate u_I is high, m takes a large value due to the large compressive effect. As rotational speed N_R is increased, however, the powder removal effect increases, making compression less likely to occur, which results in a tendency for m to decrease. Therefore, the compression or non-compression of a powder bed depends on the balance between u_I and N_R. There are several different measuring conditions, that is, several combinations of u_I and N_R, in which m equals unity. Even if the measuring conditions vary, the coefficient C obtained at $m=1$ is virtually constant for the same sample powder, although it differs for different sample powders. The following section discusses the relation between the physical properties of powder and C_0, which is the value of C obtained under the measuring conditions in which $m=1$.

3.4 Relation Between C_0 and Powder Physical Properties

As mentioned previously, C represents the frictional characteristic of powder. The relation

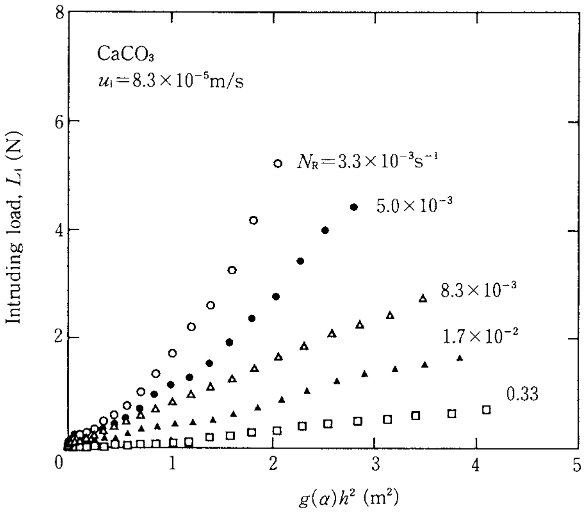

Fig. 7 Relation between L_I and $g(\alpha)\,h^2$ for $CaCO_3$.

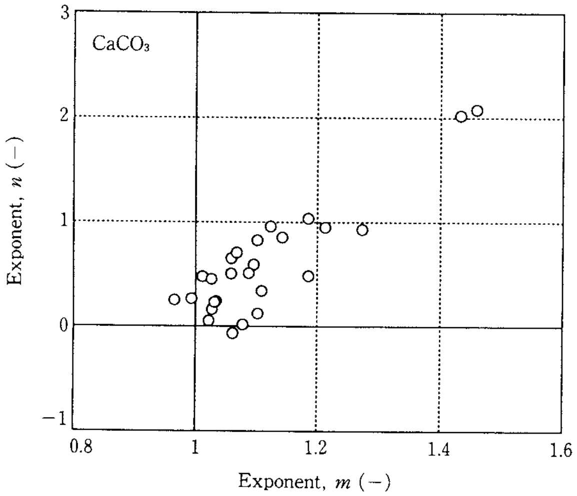

Fig. 8 Relation between n and m for $CaCO_3$.

between C_0 and the angle of repose, a typical index representing powder fluidity, was therefore determined. **Figure 9** shows this relation for various sample powders. C_0 differs greatly among calcium carbonate, corn starch, and PMMA (Polymethylmethacrylate) MB-8, although the angle of repose is almost the same, which indicates that C_0 represents subtle differences in the frictional characteristic and fluidity among different powders.

We therefore sought to calculate the internal friction coefficient from C_0. Essentially, C is expressed as the product of normal stress and the friction coefficient. Therefore, the following simplest form of the equation was used to calculate the internal friction coefficient μ_0.

$$C_0 = \mu_0 \sigma_0 \tag{11}$$

Normal stress σ_0 was obtained by plotting k of Equation (10) against m, and extrapolating to $m=1$, as shown in **Figure 10**. μ_0 was calculated using Equation (11), to identify the relation between μ_0 and sliding friction coefficient μ_s. **Figure 11** shows the result. There is a definite correlation between μ_0 and μ_s. In this correlation, μ_0 is always smaller than μ_s, because μ_s is obtained in the static state, whereas μ_0 is obtained in the dynamic state.

4. Conclusions

The rotary intrusion rheometer was improved to enable simultaneous measurement of shearing torque and intruding load. Experiments conducted with this improved rheometer yielded the following information:

(1) Introduction of the two parameters C and m to characterize the relation between measured shearing torque and intrusion depth made it possible to accurately describe the compressive effect and the change in frictional status under varying measuring conditions.

(2) Under the measuring conditions satisfying $m=1$, normal stress on the rotor remains constant regardless of rotor intrusion. Coefficient C obtained under such conditions represents such dynamic physical properties of a powder bed as stress and the friction coefficient.

(3) At present, the stress distribution in a powder bed is estimated from the intruding load detected at the sample cell bottom. Our future task is therefore to evaluate intruding load, taking powder bed load transfer characteristics into account. It is also necessary to conduct experiments using different powder bed initial void fractions, and evaluating the results.

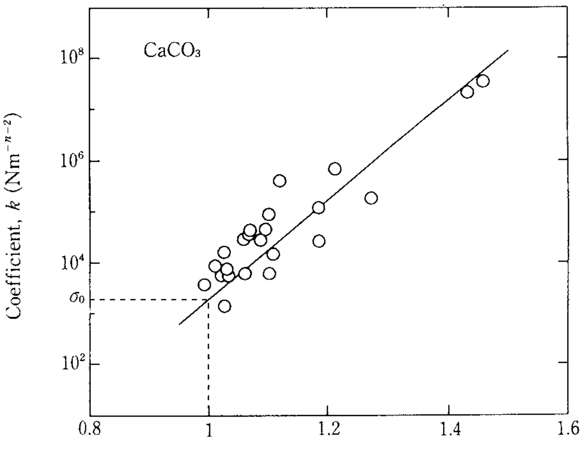

Fig. 10 Plots of k against m for $CaCO_3$.

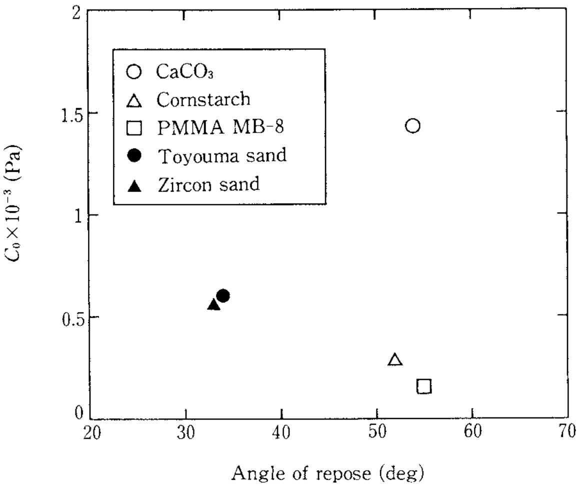

Fig. 9 Relation between C_0 and angle of repose for sample powders.

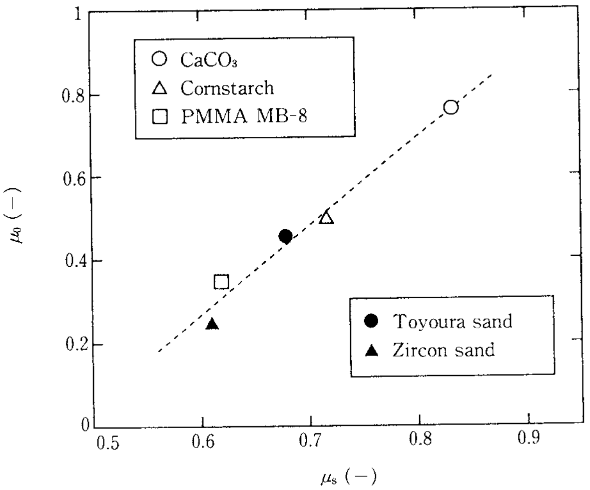

Fig. 11 Relation between μ_0 and μ_s (sliding friction coefficient).

Nomenclature

C : coefficient defined by Eq. (3) $(\mathrm{N \cdot m^{1-3m}})$
C_0 : coefficient at $m=1$ (Pa)
F : force acting vertically on the conical surface (N)
F_v : vertical component of force F (N)
$f(\alpha)$: function of α defined by Eq. (4) (-)
$g(\alpha)$: function of α defined by Eq. (8) (-)
h : depth of intrusion (m)
k : coefficient defined by Eq. (9) $(\mathrm{N \cdot m^{-n-2}})$
L_i : intruding load (N)
m : coefficient defined by Eq. (3) (-)
N_R : rotational speed of the rotor $(\mathrm{s^{-1}})$
n : coefficient defined by Eq. (9) (-)
s : area of the shearing zone $(\mathrm{m^2})$
T : torque $(\mathrm{N \cdot m})$
u_i : intrusion rate of the rotor $(\mathrm{m \cdot s^{-1}})$
α : vertical angle of the conical rotor (rad)
θ : central angle of the developed conical surface (rad)
θ_s : angle of inclination plate (rad)
$\theta_{s,max}$: maximum inclination angle (rad)
μ : friction coefficient (-)
μ_s : sliding friction coefficient (-)
μ_0 : friction coefficient defined by Eq. (11) (-)
σ : normal stress (Pa)
σ_0 : normal stress at $m=1$ (Pa)

References

1) Satoh M., S. Komura and K. Miyanami : *J. Soc. Powder Technol. Japan*, **22**, 530 (1985)
2) Satoh M., T. Fujimoto, T. Shigemura, F. Hamano and K. Miyanami : *J. Soc. Powder Technol. Japan*, **25**, 609 (1988)
3) Okudaira Y., Y. Kurihara, H. Ando, M. Satoh and K. Miyanami : *Powder Technol.*, **77**, 39 (1993)
4) Satoh M., T. Fujimoto and K. Miyanami : *J. Soc. Powder Technol. Japan*, **24**, 462 (1987)
5) Satoh M., N. Kondo, T. Iwasaki, K. Miyanami, Y. Okudaira and H. Ando : *J. Soc. Powder Technol. Japan*, **31**, 783 (1994)

Information Articles

The 31st Symposium on Powder Technology

The 31st Symposium on Powder Technology, sponsored by the Hosokawa Powder Technology Foundation, was held on August 28, 1997 at Senri Life Science Center in Osaka, and attended by some 150 people with a great success.

This year, emphasis was placed on the subject of environmental preservation technology, and a total of five general lectures were given under the theme "Environmental Preservation Technology and Powder Technology", followed by a special lecture, commemorating the grant of the KONA Award, by the awardee.

The 31st Symposium Powder Technology

Theme: Enviromental Preservation Technology and Powder Technology

Morning Session

Chairmanship: T. Oshima (Emeritus Prof. of Himeji Institute of Technology.)

● Waste management and Powder Technology	Kei Miyanami (Univ. of Osaka Prefecture)
● Rare Earth Extraction from Urban Resources Utilizing the Mechanochemical Approach	Fumio Saito (Tohoku University)

KONA Award Special Lecture

Chairmanship: Y. Kousaka (Univ. of Osaka Prefecture)

● Numerical Simulation of Gas-Solids Multiphase Flow and Powder & Granular Material Fluidization	KONA Awardee, Sin-ichi Yuu (Kyushu Institute of Technol.)

Afternoon Session

Chairmanship: Yoshitaka Kuwahara (National Industrial Research Institute of Nagoya)

● Separation and Segregation of Powder & Grannular Matesials – Application to Recycle System –	Masunori Sugimoto (Toyama Univ.)
● Examples of Wastes Treatment for Recovery	Hisashi Yamashita (Hosokawa Micron Corp.)
● Particle Separation mainly by High-Temperature Dust Collecting Technology	Chikao Kanaoka (Kanazawa Univ.)

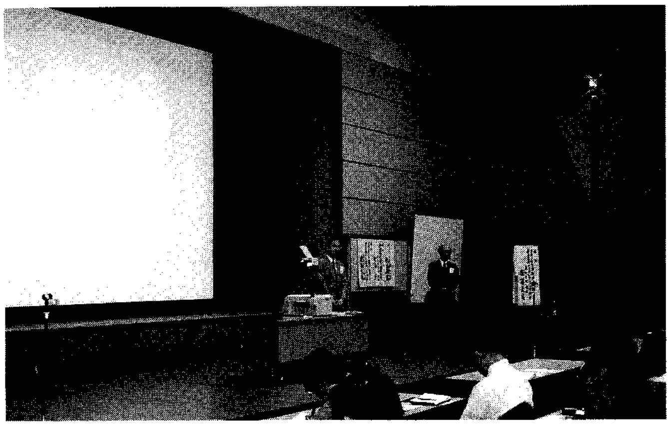

The 6th KONA Award

The 6th KONA Award sponsored by Hosokawa Powder Technology Foundation and given to the scientists or groups who have achieved excellence in the rerearches related to the basic powder technology, was presented to Professor Sin-ichi Yuu of Kyushu Institute of Technology by Masuo Hosokawa, President of the Foundation on January 22, 1997 at the R&D Center of Hosokawa Micron Corporation in Hirakata.

Professor Yuu is one of the pioneers in computer simulations of powder flow dynamics, and has over the past twenty years made many research achievements in that area. Among those achievements the research into the behavior of solid particles in gas-particle turbulent jet was particularly outstanding, in which Professor Yuu derived a stochastic model that takes into consideration the interaction between a vortex and particles, and provided an approach for predicting a particle motion that takes place in an actual turbulent flow such as a jet and a tubular flow. In addition, Professor Yuu derived a theoretical formula for diffusional transportation of particles by turbulent flow, which made it possible to determine a turbulent diffusion coefficient, average velocity distribution and concentration distribution of particles.

These basic researches provide the basis for making a simulation approach to various industrial problems related to a gas-particle turbulent jet, a phenomenon that is extremely complex.

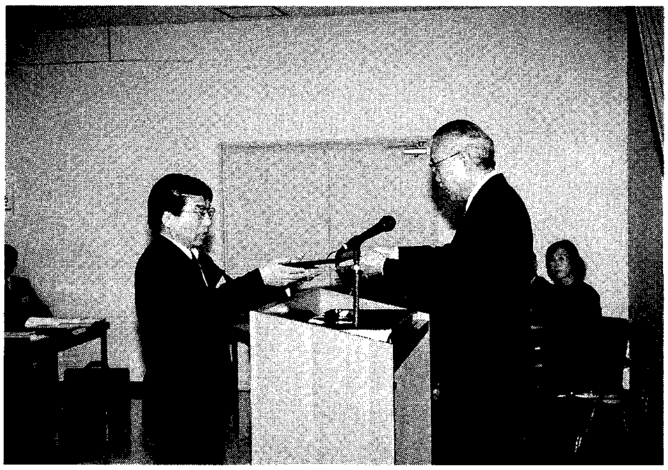

9TH EUROPEAN SYMPOSIUM ON COMMINUTION

8, 9 and 10 September 1998

Albi, (near Toulouse) France.

Further information from:
Professor J.A. Dodds
Ecole des Mines d'Albi
Campus Jarlard
81013 Albi Cedex
France
Tel: (33) 05 63 49 30 00
Fax: (33) 05 63 49 30 99
e-mail: dodds@enstimac.fr

Academic publication concerning powder technology in Japan (1996)

Journal of the Society of powder technology, Japan Vol.33 (1996)

Title	Author(s)	Page
〈Research Papers〉		
●Consolidation Analysis —Mechanical Characteristucs of a Particle Bed—	X. WU, A. Mukunoki and Y. Nagase	4—9
●Consolidation Analysis —An Approximate Theory of Consolidation—	X. WU, H. Itou, K. Ono and Y. Nagase	10—16
●The Preparation of Composite Fine Particles by the Addition of a Surfactant	K. Osaka, K. Kubota and A. Hamamoto	17—22
●The Direct Synthesis of Surface-modified Ultrafine Silica Particles	S. Shioji, K. Tokami, M. Kawaguchi and H. Yamamoto	23—30
●The Study of a Deposit Prevention System on a DryingChember Wall in Spray Drying Process —The Effect of Various Deposit Prevention Systems in Kampo Medicine Production—	M. Koyama, K. Masters, T. Kimura H. Kitazaki, M. Nagasawa and I. Endo	90—94
●AConsideration of the Constitutive Relation ship between Flowing Particles	J. Kano, A. Shimosaka and J. Hidaka	95—101
●Effect of Packing Cnditions of a Fine Powder on Powder Pressure in a Bin	H. Eitoku, M. Hirota, M. Suzuki and T. Oshima	102—107
●The Characteristics of Pressure Fluctuation Damping and the Error in the Flow Volume of the Gas Solid Suspension Flow System in the Pipe	T. Haraguchi	108—114
●The Dry Granuration of a Fine Powder Using a Spouted Bed	S. Hatano, R. Yamazaki and S. Mori	115—120
●Pressure Drop in Plug-phase Conveyance and the Scale-up of Conveyance Lines	M. Futamura	121—128
●The Accurate Air Classification of Fine Particles	Z. Tanaka and M. Uchiyama	248—252
Forms of the Rotor Blades System and Pressure Loss within a Cage-type Centrifugal Air Classifier	M. Ito, Y. Miyabe and F. Kawano	253—261
●The Separation of Binary Mixture of Particles and Pressure Distribution in a Fluidized Bed	Z. Tanaka and X. Song	262—265
●Estimation of Mixing Index Based on Contact Numbers by Coordination Nimber Sampling from a Multicomponent Mixture	K. Ura and H. Shindo	266—272
●The Preparation of Fine Porous Ammonium Perchlorate by the Spray-drying Method	M. Kohga and Y. Hagihara	273—278
●A Numerical Study on Convection of Particles in a Bin during Vertical Vibration	J. Yoshida	279—286
●The Dynamics of Aggregate in Planetary Mills	T. Morikawa	360—370
●The Correlation Between the Casting Behaviour and the Prticle Aggregated Structure of Fine Ceramics in a Concentrated Slurry	T. Kimura, S. Sakaguti and M. Nakamura	371—378
●Various Characteristic of Vinylon Fiber-reinforced Building Materials using Globular Cement	S. Taniguti, M. Nakamura and Y. Kohno	379—384
●Elimination of Ilon Guest Particles from a Comminuted Product	Z. Tanaka, S. Okada, Y. Kimura and R. Utsumi	385—388

Title	Author(s)	Page
●The Flocculation Behavior of Ceramic Powder Slurries with Cationic Polyelectrolyte −Relationship of Floc Size, Rheological Parameters and Surface Charge of Particles−	S. Murata, M. Nakamura and T. Kimura	389−395
●The Flocculation Behavior of Ceramic Powder Slurries with Cationic Polyelectrolyte −Discussion of Interaction among Flocs in Flocculated Slurries from a Rheological Viewpoint−	S. Murata, M. Nakamura and T. Kimura	395−403
●The Simultaneous Measurement of Crystal Sizes and Mass in a Fluidized Crystallizer	E. Obata, M. Maruyama, Y. Ohira M. Akiyoshi and K. Ando	456−461
●Functions of a Rotary Disk and Agitator in a Fluidized-bed Granulator	N. Takei, K. Nishiyama, K. Miyata and H. Saito	462−467
●On the Effect of Fluidized Bed Viscosity on Solid Circulating Rate Across a Tube Bank	K. Naruse, T. Oshita, M. Tsukada M. Horio, S. Shinozaki and T. Sugiyama	468−475
●Improvement of Surface Treatment and Blending of Milk Casein with Titanium Oxide	S. Taniguti, M. Nakamura, T. Konishi and T. Higuchi	487−499
●The Synthesis of Composite Particles made up of Titanium Nitride Nano Particles and Carbon Black	A. Towata, A. Tsuge and M. Sando	500−504
●The Necessary Powder and Pulverizing Rate in Planetary Mills	T. Moriwaki	505−509
●Characteristic Curves of Shearing for a Powder Bed Measured with a Rotary-intrusion-type Rheometer	M. Satoh, T. Iwasaki and K. Miyanami	510−515
●A Gradational Packing Using Fluidization for Functional Materials	Z. Tanaka, Y. Tuji and T. Takahasi	542−546
●Dust Properties and Char Recovery Cyclone as Factors in the Pressure Loss of Ceramic Candle Filters in Hot Coal Gas Filtration	S. Ito, T. Tanaka and S. Kawamura	547−532
●Quantitive Evaluation and Control of Delamination and Change in the Physico-chemical Properties of Talc by Wet Grinding	K. Hamada, S. Yamamoto and M. Senna	533−558
●Microstructure and Frost Durability of Vinylon Fibers-reinforced Building Materials using Globular Cement	S. Taniguti and M. Nakamura	624−631
●Preparation by Spray Drying of Microcapsules with a Core of a Water Soluble Substace and a Shell of Ethylcellulose	N. Yamada, H. Nakamura and E. Abe	632−637
●The Effectiveness of Inorganic Compounds on the Improvement of the Compressibility in the Crude Drug Tablets	M. Sofue and Y. Ueda	638−642
●The Characteristics of Fine Granules and Evaluation of their Dispensing Characteristics	M. Ohkuma, K. Ohtsuki, T. Ishikawa A. Ohishi, K. Kawano, S. Takamatsu K. Kawada and S. Nakajima	643−648
●AC Corona Charging Behaviors of Polymer Powder Layers of Various Particle Sizes	C. Yamaguchi, T. OU, F. Kaneko and M. Takeuchi	649−654
●The Discharge Characteristics of Fine Powders from a Screw Feeder with Deaeration	T. Ishikura and H. Nagashima	700−705

Title	Author(s)	Page
●Fluidization of Fine Particles in Spouted Bed with a Draft-tube	K. Ijiti, Y. Uemura, Y. Hatate and Y. Tanaka	706−710
●The Effects of Frequency and Amplitude on the Powder Coating of Fluidizing Particles in Vibro-fluidized Bed	H. Kage, M. Oba, H. Ishimatsu, H. Ogura and Y. Matsuno	711−716
●The Effect of Binder Adsorption on the Rheological Behavior of Silicon Nitride Suspensions	K. Shibata, H. Yanagisawa, T. Yamada and Y. Kohtoku	717−721
●The Characterization of Agglomerates from Pressure Swing Granulation with Surface Treatment	Y. Iwadate, H. Kamiya and M. Horio	722−727
●The Continuous Formation of Small Binary Composite Granules by a Single Rotating Conical Vessel with rinding Media	T. Kawakami, K. Yamamoto, M. Sugimoto and Y. Daidai	728−733
●The Development of Surface-treated Cements for Cement Powder Grouting	A. Nakamura, Y. Yamaguti, E. Onuma and Y. Sasaki	734−739
●The Change in Wettability and Structure of Silica Powder Surfaces Modified with Hexamethyldisilazane	M. Fuji, H. Iwata, T. Takei, T. Watanabe and M. Chikazawa	740−746
●Grinding Rate Improvement Using a Composite Grinding Ball Size for an Ultra-fine Grinding Mill	W.S. Choi	747−752
●Friction Characteristics of Graphite for Brake Friction, Materials	Y. Sugai, K. Iida, M. Arai and K. Seki	782−787
●The Packing Characteristics of Equal Spheres in Vertically Oscillating Cylinders	Y. Nakanishi, S. Hashimoto, H. Fujimoto and K. Gotoh	788−794
●Wet Classifier with Laminar Flow	M. Yamamoto, Y. Zhao, N. Nakamura and N. Watanabe	795−802
●Low Temperature Sintering of α-alumina with the Aid of Abrasive Powder in Wet Grinding	Y. Yoshizawa and F. Saito	842−847
●The Preparation and PTCR Properties of Semiconductive $BaTiO_3$-Indium Complex Particles by Forced Electrification Processing	T. Dan, M. Egashira, J. Kyono, H. Fudouzi and N. Shinya	848−854
●A Fundamental Study of Dry and Wet Grinding from the Viewpoint of the Creep Testing of Glass	Y. Kanda, Y. Abe, M. Okuyama and K. Kato	900−904
●The Power Requirement of an Agitating Impeller in Spherical Agglomeration in a Tank	H. Takase and K. Sanami	905−910
●The Shape Effect of Particles on Their Packing and Discharging Characteristics	M. Sugimoto, K. Yamamoto, T. Miyajima and T. Kawakami	911−918

Kagaku Kougaku Ronbunshu Vol.22 (1996)

Title	Author(s)	Page
●Numerical Simulation of Three Dimensional Fluidized Bed Using Nozzles at Bottom and Experimental Verification	S. Yuu, K. Ikeda, T. Umekage and K. Nohara	67−75
●Dynamic Shape Factors of Regular Shaped Agglomerates and Estimation Based on Agglomerate Symmetry −For Rectangular Parallel-piped, V-and W-Shaped,Hexagonal and H-Shaped Agglomerates−	T. Niida and S. Ohtsuki	98−105

Title	Author(s)	Page
● Evaluation of Fine Grindability of Ball, Vibration and Planetary Mills by Corresponding Work Index Rotating Cylindrical Membrane Filter	N. Kotake, Y. Watanabe, T. Ishizaki and Y. Kanda	106－112
● Mechanism of Formation of Particle Deposition Layers by an Aerosol Flow By Gas in a Packed Bed	I. Adhiwidjaja, S. Matsusaka and H. Masuda	127－133
● Particle Reentrainment under Reduced Pressure	S. Matsusaka, K. Fujita and H. Masuda	177－183
● A System to Trace Individual Solid Partieles in a Fluidized Bed	T. Kikkawa, M. Ishida and H. Hatano	277－286
● Fluidizing behaviour of Magnesia and Silica Ultra-Fine Powders at Elevated Temperature	K. Ushiki, T. Hibino, T. Sato and M. Mizuno	326－333
● On the Study of Measurement Apparatus for Particle Concentration and Estimation of Particle Size by Log-Normal Distribution in Gas-Solid Pipe Flow	H. Yoshida, S. Matsuura, K. Kanagawa, K. Nagahasi, T. Akahori and H. Makino	350－355
● Particle Coating Mechanism of Fine Particles by High-Speed Gas Impact : Wall Effects	K. Shinohara, K. Takayashiki, M. Otani and T. Uchiyama	356－364
● Effect of Milling Condition of a Tumbling Ball Mill on Comminution Kinetics Parameters and Production capacity of Closed-circuit grinding	M. Ito, K. Nagano and K. Hino	503－511
● Surface Roughness and Porosity for Thin Particle Layer	M. Sese, K. Hashimoto, H. Yoshida and S. Kawamura	575－581
● Effect of Rotation Method of Internal Blade and External Cylinder on Media Particles and Grinding Characteristics in Horizontal Type Sand Mill	H. Yoshida	597－602
● Experimental Investigation on Lifting Criteria of an Induction-Charged Spherical Particle in a Field with Horizontally Set Parallel Plate Electrodes	Y. Ohkubo, Y. Takahashi	603－609
● A Study on Size Segregation of Particles Using Distinct Element Analysis	J. Yoshida, K. Gotoh and H. Masuda	622－628
● Filtration Characteristics and Cake Properties in Microfiltration of Binary Mixtures of Fine Particles	E. Iritani, H. Nagaoka and T. Murase	648－654
● Mechanical Properties of Surface Composite Particles Coated with Finer Particles	T. Uchiyama, M. Otani, Y. Otomura and K. Shinohara	655－661
● Collection Efficiency of Granular Bed Filters with Reentrainment of Particle	K. Kiura and H. Takahashi	756－762
● Simple measurement of electric field intensity profiles and heating characteristic of a resin powder by microwave irradiation	H. Yoshida, Y. Itaya and M. Hasatani	808－814
● Effect of Blade Geometry on Motion of Media Particle and Grinding Characteristics in Horizontal Type Sand Mill and Development of a New Type of Blade	T. Teshida, M. Takao, S. Komori, Y. Murakami and H. Yoshida	830－836
● Separation Characteristics and Pressure Drop for Deep Bed Filtration of Heavy Oil/Water Emulsion by Flow through Granular Beds	H. Nakakura, M. Sambuichi and K. Osasa	854－860

Title	Author(s)	Page
● Measurement of Solid Fraction Distribution in a Three-Dimensional Jetting Fluidized Bed	H. Matsuo, C. Luo, S. Uemiya and T. Kojima	867－874
● Preparation of Micron-Size Monodisperse Silica Particles by Seed Growth Method	M. Kimata, M. Koizumi and M. Hasegawa	1366-1372
● Fine Particle Coating in a Circulating Fluidized Bed by Rapid Expansion of Supercritical Fluid Solutions	A. Tsutsumi, M. Nakata, T. Mineo and K. Yoshida	1379-1383
● Process Development of Effective Semi-Dry Flue Gas Desulfurization by Powder-Particle Spouted Bed	G. Qimin, I. Noriaki and K. Kato	1400-1407
● Evaluation of Friction Characteristics of Powder Bed by Intrusion Method using Conical Rotor	M. Satoh, T. Iwasaki and K. Miyanami	1435-1441

TECHNOLOGY AND EQUIPMENT FOR THE CONFECTIONERY INDUSTRIES

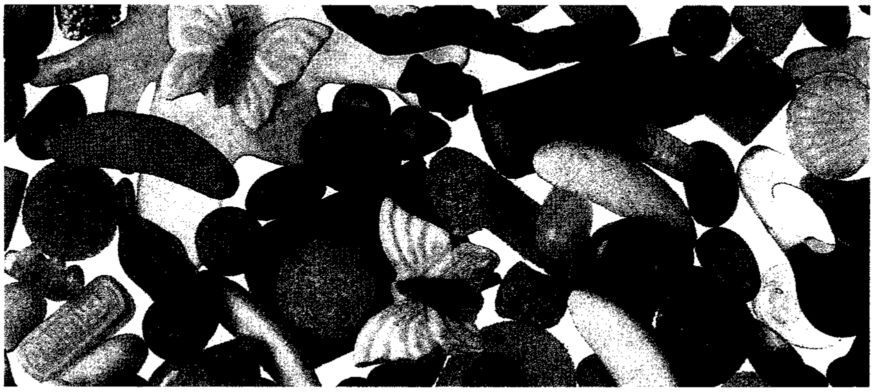

Ter Brack
is a leading supplier of process technology for batchwise and continuously operating dosing. dissolving, cooking, aerating and mixing installations for all kinds of aerated and non-aerated bars, as well as equipment for binders of any consistency for the production of cereal bars.

Bepex
supplies forming machines which practically operate completely pressureless for aerated or pressure-sensitive masses of any consistency.

Kreuter
supplies standard and distinctive special purpose enrobing technology, consisting of tempering and enrobing machines, cooling tunnels and auxiliaries.

HOSOKAWA BEPEX GmbH
P.O. Box 1152
D-74207 Leingarten / Germany
Tel.: +71 31 / 40 08 2
Fax: +71 31 / 40 36 07
Delivery address:
Daimlerstraße 8
D-74211 Leingarten / Germany

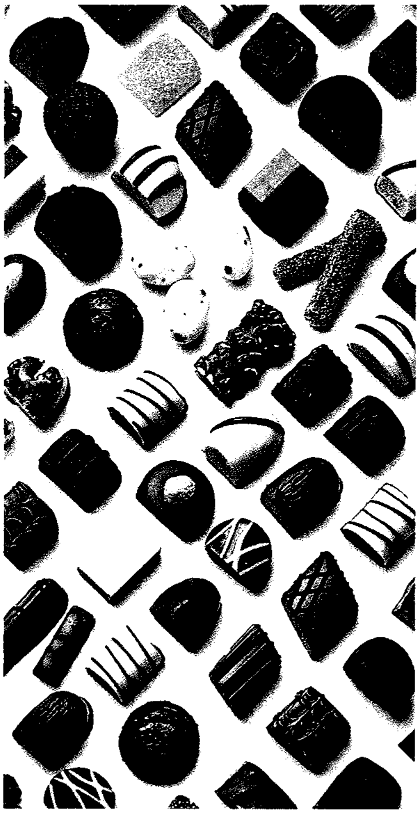

HOSOKAWA CONFECTIONERY & BAKERY GROUP

HOSOKAWA MICRON CORPORATION

HUTT • KREUTER • TER BRAAK • HUTT • KREUTER • TER BRAAK • HUTT • KREUTER • TER BRAAK

New product News

INTENSIFIER

Hosokawa Micron BV has developed the "Intensifier", which enhances the performance of the Vrieco-Nauta® Conical mixer.
The Intensifier is to provide the Vrieco-Nauta® mixer with the capability of high shear mixing and dispersing capabilities.
The Intensifier is a high speed mixing element, which is installed at the centre of the orbit arm and extends into the powder bed.
The Intensifier has it's own drive and is operated independently of the mixing screw and orbit arm.
The speed is variable. The Intensifier can be supplied with a multiple deflector for particle size reduction capabilities.

Special Feature

- fast and intensive mixing of powders
- easily installed on new or existing equipment
- compact energy efficient drive design
- optional capability for direct liquid injection
- optional capability for size reduction of powders
- low cost, high shear mixing requirements
- provides for dispersion, de-agglomeration and granuation options
- easy to inspect and clean

Applications

- intensive mixing of cohesive powders, pastes and slurries
- moistening of powder
- colouring
- flavouring

CYCLOMIX

A new type of mixer which has proven its excellence in the mixing of extremely cohesive materials. This mixer offers a high level of homogeneity in the end product, which is frequently demanded by various industries, such as food, chemical, plastic, toner, mineral, cosmetic and pharmaceutical. The working principle differs markedly from existing mixing techniques owing to the specific interaction between mixing element and vessel wall.

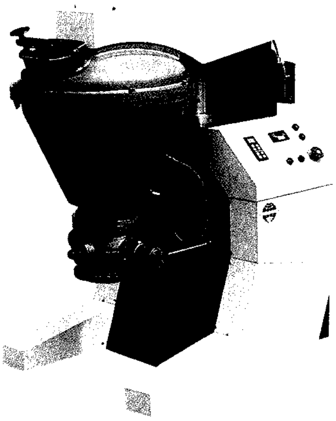

Features

- very fast, intensive mixing (mixing times from 30 seconds to 5 minutes)
- wide range of applications
- fully self-emptying vessel
- no bearings or seals in the product zone
- good control of product temperature

Applications

- intensive mixing of cohesive powders, pastes and slurries
- moistening of powder
- coating
- granulating
- flavouring
- colouring

For more information contact;
HOSOKAWA MICRON B.V.
P.O. Box 98, 7000 A.B Doetinchem Gildenstraat 26, 7005
BL Doetinchem / Holland
Tel. (0314) 373333 / Fax (0314) 373456, ING Bank 69.30.11.564
Website:http://www.hosokawamicron.com

New product News

Tubular Wet Electrostatic Precipitator-WEP-T

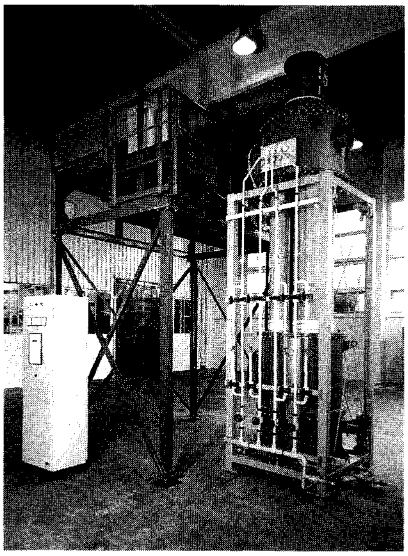

A new type of wet electrostatic precipitator has been developed for the efficient removal of finest particles (liquid or solid), especially from humid or corrosive gases. The collected particles are rinsed from the collection electrode continuously by a liquid film. This can be achieved either by an irrigating liquid or by condensation of vapour from the process gas. Typical applications are in the chip board and glass fiber industry, sulphuric acid or pigment production plants, incineration plants for hazardous or medical waste, soil regeneration, sinter, coating, hardening and galvanising plants as well as shredders, iron, steel and rolling mill plants.

Features:

- excellent collection efficiency, also in the particle size range below 1 μm (considerably better compared to alternative processes)
- low energy consumption and operating costs
- high throughput with compact design
- caking of sticky particles can reliably be avoided
- high flexibility in material selection

MikroCut Air Classifier-MC

The MikroCut is a new developed air classifier for in-and off-line operation. Due to its special design a high sharpness of classification, even in the range of 1 μm, can be achieved. The MikroCut is available in various sizes that are adapted to the throughput of the ACM-grinding systems of Hosokawa MikroPul. Typical applications are classification of powder coatings, pharmaceutical products, fillers, fine mineral materials etc.

Features:

- cut sizes from a few ten micron down to the submicron range
- high sharpness of classification
- no coarse particles in the fine
- high yield of product
- low energy consumption due to optimised rotor design
- easily cleanable

For more information contact; **HOSOKAWA MIKROPUL GmbH**
Welserstraße 9-11
D-51149 Köln, Germany
Tel.: +49-2203-308-0
Fax: +49-2203-308-293
E-mail: info@hmgmbh. hosokawa. com

HOSOKAWA ALPINE TSP TONER CLASSIFIER

The TSP is a totally new design for the special demands of the toner industry. It is designed for high efficiency fines removal with high coarse product yields from ground toner powder. In combination with the Hosokawa Alpine Fluidized Bed Jet Mill AFG, the TSP offers optimum perfomance for the steepest particle size distributions. The TSP can handle product at the rate from 60 to 360 kg/h.

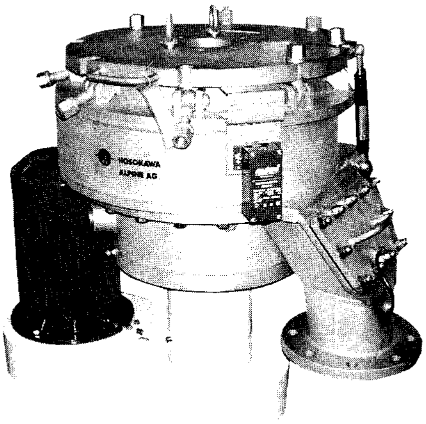

TSP Classifier Features and Benefits:

- Ultrafine classification in the range of 2-20 μm.
- High coarse product yields result in improved product quality and higher profits.
- All product contact parts are vertically removable for easy cleaning.
- Low energy on the particles reduces melting and particle degradation.
- Optimized velocities avoid build-up even with low melting point polymers.
- Moderate differential pressure reduces energy cost.
- Applicable for other materials where high product quality is required, such as thin film powder coatings.
- Gravity feed inlet and product discharge.

For more information contact; **HOSOKAWA ALPINE Aktiengesellschaft**
P.O. Box 98, 101109 D-86001 Augsburg, Germany
Tel: +821/5906-0 Fax: +821/57 35 58

Hosokawa Micron POWDER TESTER PT-R

The newly developed Powder Tester model PT-R has made a revolutionary epoch in the history of the development of Powder Tester. Its original was invented about 30 years ago for the characterization of various important mechanical properties of powders including the flowability and floodability after the Carr's proposal as well as the fundamental factors such as bulk densities and angle of repose, etc. The automatic measurements of angles with higher reliability have been realized using the laser technique. The integrated touch-panel computer and the software have made the measurements much easier and quicker.

Features

- Latest model of powerful touch-panel computer integrated
- GUI (Graphical User Interface) for easy and userfriendly operation
- New software for "Short-cut" operation and whole data transfer to PC in its spread sheet for further analysis and data logging
- Automatic measurement of angles of repose/spatula by laser sensor
- Easy and quick disassembling for cleaning and washing of stainless steel parts
- Corresponding to JIS/ISO standards

Applications

- Quality control of powder products
- Development of new powder materials
- Design of powder handling processes
- Validation for processing pharmaceutical powders

Hosokawa Micron BULK TAPNER

Bulk Tapner is a unit to reduce the volume of powder materials filled in various types of bags or containers such as container bags, fiber drums and plastic bags, giving the strong periodical shocks to the powders by tapping. Its high performance in reducing the powder volume leads to the drastic reduction of transportation costs and quick filling of bulky powder materials.

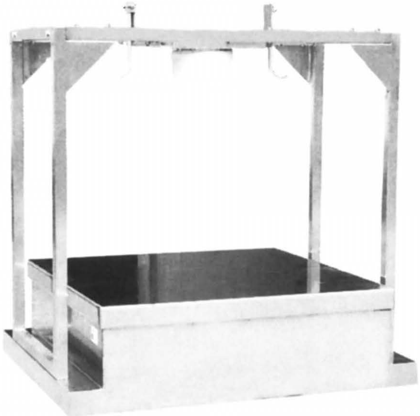

Features

- Save your transportation costs
- Realize steady and speedy filling of fine powders
- High performance but low running cost
- Weighing with tapping during filling

Applications

- Reducing volume of bulky powder materials of any kind filled in various type of plastic bags, drums or container bags.

For more information contact: **HOSOKAWA MICRON CORPORATION**
5-14, 2-chome, Kawaramachi, Chuo-ku,
Osaka 541, JAPAN
Telephone : 81-6-233-3968
Facsimile : 81-6-229-9267

HOSOKAWA MICRON

Hosokawa Micron is a member of the Hosokawa Micron Group, responding to global needs through an emphasis on materials science and engineering. The Group is an international provider of equipment and systems for powder and particle processing, thermal processing, product recovery, industrial filtration and plastics processing. The Group maintains facilities for research, engineering, manufacturing, and service in each of the world's major industrial markets.

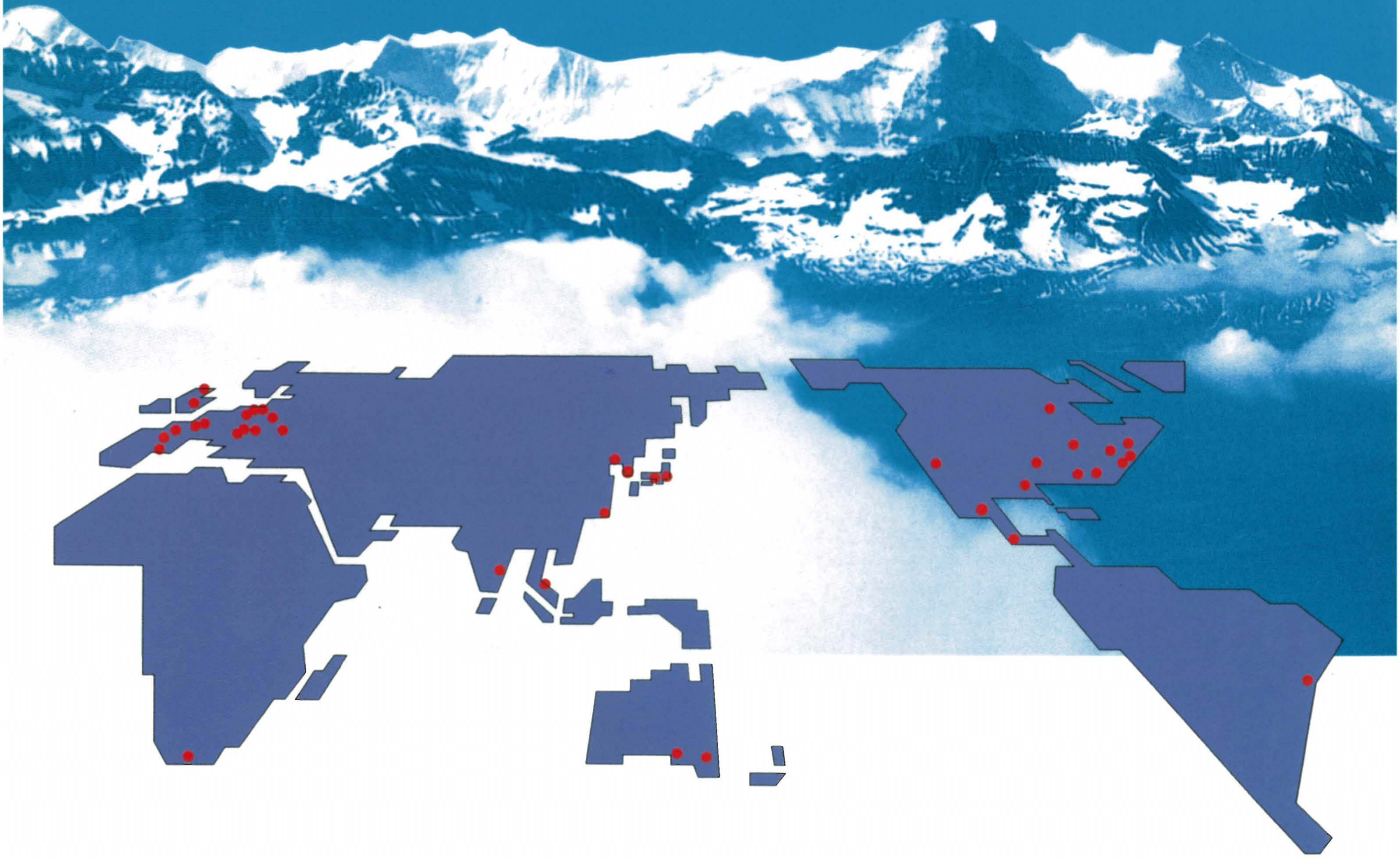

Process Technology for Tomorrow

HOSOKAWA MICRON

Headquarter Locations;

HOSOKAWA MICRON CORPORATION

5-14, 2-chome, Kawaramachi, Chuo-ku,
Osaka 541, Japan
Tel: 81-6-233-3968
Fax: 81-6-229-9267

HOSOKAWA MICRON INTERNATIONAL INC.

780 Third Avenue, New York,
NY 10017, U.S.A
Tel: 1-212-826-3830
Fax: 1-212-826-6612

HOSOKAWA MICRON INTERNATIONAL B.V.

World Trade Center, Strawinskylaan
249, 1077XX Amsterdam, Holland
Tel: 31-20-673-5571
Fax: 31-20-676-2061